

Microstructure and Microtribology of Polymer Surfaces

About the Cover

An elegant micro-flower of 8 μm across represents a fascinating example of directional distribution of friction forces at the microscale within a multidomain Langmuir film formed by chiral phospholipids. This image is cordially provided by researchers from the Swiss Federal Institute of Technology (for details, *see* Chapter 7 in this volume and the article in *Science* **1998**, 280, 273).

Microstructure and Microtribology of Polymer Surfaces

Vladimir V. Tsukruk, EDITOR
Iowa State University

Kathryn J. Wahl, EDITOR
Naval Research Laboratory



American Chemical Society, Washington, DC

**American Chemical Society
Library**

1155 16th St., N.W.

Washington, D.C. 20036

In Microstructure and Microtribology of Polymer Surfaces; Tsukruk, V., et al.; ACS Symposium Series; American Chemical Society: Washington, DC, 1999.



Microstructure and microtribology of polymer

Library of Congress

Microstructure and microtribology of polymer surfaces / Vladimir V. Tsukruk, editor, Kathryn J. Wahl, editor.

p. cm. — (ACS symposium series, ISSN 0097-6156 : 741)

Includes bibliographical references and indexes.

ISBN 0-8412-3682-8

1. Polymers—Surfaces Congresses. 2. Contact mechanics—Congresses. 3. Tribology Congresses.

I. Tsukruk, V. V. (Vladimir Vasil'evich) II. Wahl, Kathryn J., 1964— . III. Series.

QD381.9.S97M53 1999
547.7'0453—dc21

99-16494
CIP

The paper used in this publication meets the minimum requirements of American National Standard for Information Sciences—Permanence of Paper for Printer Library Materials, ANSI Z39.48-94 1984.

Copyright © 2000 American Chemical Society

Distributed by Oxford University Press

All Rights Reserved. Reprographic copying beyond that permitted by Sections 107 or 108 of the U.S. Copyright Act is allowed for internal use only, provided that a per-chapter fee of \$20.00 plus \$0.50 per page is paid to the Copyright Clearance Center, Inc., 222 Rosewood Drive, Danvers, MA 01923, USA. Reproduction or reproduction for sale of pages in this book is permitted only under license from ACS. Direct these and other permissions requests to ACS Copyright Office, Publications Division, 1155 16th Street, N.W., Washington, DC 20036.

The citation of trade names and/or names of manufacturers in this publication is not to be construed as an endorsement or as approval by ACS of the commercial products or services referenced herein; nor should the mere reference herein to any drawing, specification, chemical process, or other data be regarded as a license or as a conveyance of any right or permission to the holder, reader, or any other person or corporation, to manufacture, reproduce, use, or sell any patented invention or copyrighted work that may in any way be related thereto. Registered names, trademarks, etc., used in this publication, even without specific indication thereof, are not to be considered unprotected by law.

PRINTED IN THE UNITED STATES OF AMERICA

**American Chemical Society
Library**

1155 16th St., N.W.

Washington, D.C. 20036

In Microstructure and Microtribology of Polymer Surfaces; Tsukruk, V., et al.; ACS Symposium Series; American Chemical Society: Washington, DC, 1999.

Advisory Board

ACS Symposium Series

Mary E. Castellion
ChemEdit Company

Arthur B. Ellis
University of Wisconsin at Madison

Jeffrey S. Gaffney
Argonne National Laboratory

Gunda I. Georg
University of Kansas

Lawrence P. Klemann
Nabisco Foods Group

Richard N. Loeppky
University of Missouri

Cynthia A. Maryanoff
R. W. Johnson Pharmaceutical
Research Institute

Roger A. Minear
University of Illinois
at Urbana-Champaign

Omkaram Nalamasu
AT&T Bell Laboratories

Kinam Park
Purdue University

Katherine R. Porter
Duke University

Douglas A. Smith
The DAS Group, Inc.

Martin R. Tant
Eastman Chemical Co.

Michael D. Taylor
Parke-Davis Pharmaceutical
Research

Leroy B. Townsend
University of Michigan

William C. Walker
DuPont Company

Foreword

THE ACS SYMPOSIUM SERIES was first published in 1974 to provide a mechanism for publishing symposia quickly in book form. The purpose of the series is to publish timely, comprehensive books developed from ACS sponsored symposia based on current scientific research. Occasionally, books are developed from symposia sponsored by other organizations when the topic is of keen interest to the chemistry audience.

Before agreeing to publish a book, the proposed table of contents is reviewed for appropriate and comprehensive coverage and for interest to the audience. Some papers may be excluded in order to better focus the book; others may be added to provide comprehensiveness. When appropriate, overview or introductory chapters are added. Drafts of chapters are peer-reviewed prior to final acceptance or rejection, and manuscripts are prepared in camera-ready format.

As a rule, only original research papers and original review papers are included in the volumes. Verbatim reproductions of previously published papers are not accepted.

ACS BOOKS DEPARTMENT

Preface

This book is a first collection of chapters dealing with tribological studies of polymeric materials, both on a macroscopic scale and at the microscopic scale. Although friction and wear of polymers and polymer composites have been widely studied on a macroscopic scale for many decades, the complexities of these surfaces provide challenging problems for scientists to understand and for tribologists to overcome. The advent of new analytical techniques during the past two decades has allowed investigation of polymer tribology and materials properties on a microscopic scale. This has resulted in not only improvements in both spatial and depth resolution but also has contributed to new insights and observations of fundamental properties of polymer surfaces. However, the rapid development of experimental techniques to probe these surfaces is at times faster than the ability to adequately model and interpret the results. For example, we are still struggling with ways to distinguish between and to model different types of energy dissipation observed in the dynamic experiments for viscoelastic materials. Time- and temperature-dependent measurements of surface properties at the microscale are now possible, but the parameters required for measurements remain difficult to control. We believe that we are only beginning to learn about the properties of polymer surfaces at the microscale.

The contributions in this book were presented at an international symposium organized at the American Chemical Society National Meeting in Boston, Massachusetts, August 1998. A total of 62 presentations were delivered by participants from 15 countries. A majority of the oral presentations were invited lectures reviewing selected subjects and original contributions were presented at the poster session. The major focus of this symposium was on the relationship between microstructural, micromechanical, and tribological properties of polymeric materials, and on bridging the gap between microstructural and macroscopic surface properties. Symposium topics encompassed a variety of experimental and theoretical investigations of micromechanical and tribological properties of polymeric materials: polymers, composites, coatings, ultrathin films, and molecular layers. Industrial applications of polymeric materials were considered in a separate session as well.

Leading researchers, who presented papers at this symposium, were invited to contribute original articles and reviews to this volume. The 30 chapters collected here address a range of problems from treatment of contact mechanics for compliant, viscoelastic materials to relationships between polymer microstructure and surface properties. Although no single book can encompass all of the current research and scientific issues in this topic area, we hope that this book will provide an overview of the present state of knowledge of polymer surface tribology, microstructure, and mechanics. A general introductory chapter written by B. J. Briscoe from Imperial College gives a brief overview of the current status of the field of polymer tribology. The rest of the book is divided into four topic areas.

Contact Mechanics of Polymeric Materials

Tribological properties of polymers are strongly influenced by adhesion and elastic, and viscoelastic properties as well as by surface forces. K. L. Johnson reviews progress in

extending the JKR theory to viscoelastic spheres, enabling prediction of adhesion hysteresis and rate-dependent adhesion observed experimentally. J. C. Charmet et al. review how the mechanical behavior of contacting solids is influenced by both surface adhesion and bulk viscoelastic properties of rubberlike material. They explain spontaneous peeling, rolling contact, and Shallamach waves as well as the rebound behavior (or lack of!) for balls bounced against soft elastomers. Creep effects in viscoelastic polymers are discussed by W. N. Unertl, who concludes that creep effects may dominate over crack-tip effects for nanoscale contacts to low moduli materials. K. Vorvolakos and M. K. Chaudhury's studies (utilizing fluorescent particle velocimetry to observe slippage at surfaces) describe how release of adhesive contacts is governed by interfacial friction. M. O. Robbins and A. R. C. Baljon compare experiments and simulations of thin films undergoing oscillatory shear and discuss the effects of confinement on behavior including glass transitions, stick-slip phenomena, and memory effects in thin films.

Micromechanics and Microtribology

This section introduces a variety of proximal probe techniques to study response of polymer surfaces and thin films. A variety of techniques have been implemented (both dc and ac) to examine adhesion, friction, wear, and micromechanics of polymers; both time- and temperature-dependent effects are examined. F. Oulevey et al. describe changes in mechanical properties of polymer blends in response to temperature changes, as well as friction anisotropies and asymmetries in Langmuir-Blodgett films that they ascribe to molecular tilt. S. Kopp-Marsaudon et al. describe and compare the mechanical response of polymer films to different atomic force microscope (AFM) techniques employing both contact and intermittent contact operational modes. R. M. Overney et al. discuss friction effects, mechanical properties and dewetting of ultrathin, spin-cast polymer films, and relate these responses to flow, disentanglement, and surface strain. Z. Huang et al. describe experiments using cantilever beam-bending techniques with an AFM to compare surface micromechanical properties from a variety of compliant and glassy polymers. G. Meyers et al. use AFM and nanoindentation to study adhesion and mechanical properties of polymer surfaces. O. Marti and S. Hild used AFM techniques to investigate adhesion and stiffness of polystyrene films as a function of temperature and molecular weight. R. H. Schmidt et al. describe the flow response of polystyrene to raster scanning with an AFM tip at various temperatures and relate the patterns formed at different scanning rates and temperatures using the time-temperature superposition principle. C. Basire and C. Fretigny present work on sliding transitions and mechanical properties of viscoelastic contacts using AFM. G. S. Blackman et al. use a combination of AFM and a micro-scratch tester to study wear modes of polymer materials at both micro- and nanoscales.

Surface Microstructures of Various Polymers

This section contains chapters that deal with chemical and microstructural properties of polymer surfaces. K. Feldman et al. examine the influence of chemistry (e.g., pH, polarity, or termination) and mechanics on the behavior of nanoscale contacts for various polymers. Hammerschmidt et al. present work on temperature-dependent behavior of

nanoscale frictional contacts to polymers and attribute the responses to relaxation and viscoelastic losses. B. Nysten et al. describe AFM-based experiments investigating mechanics of copolymer surfaces. G. J. Vancso and H. Schönherr describe nanoscale friction anisotropies found on polymer single crystals and highly oriented polymer fibers. T. Fujii et al. examine surface morphology and frictional anisotropy of high-density polyethylene single crystals as a function of molecular weight. S. Sheiko et al. investigate morphology of monolayer films of polymer brushes and actual shape of isolated cylindrical macromolecules at surface. Ph. Leclere et al. examine transitions in surface morphology of triblock copolymers as a function of composition and molecular weight. A. Balazs et al. model polymer–clay interactions to predict conditions under which the polymer will exfoliate the layers within the clay particles.

Testing Polymer Applications

Polymers are widely used in applications throughout industry. This section presents a sampling of the various ways in which polymers are used in practical applications, and methods that researchers use to characterize performance of these materials. K. Budinski reviews the basic wear tests for plastics and the criteria for selecting an appropriate test methodology for various applications. C. M. Mate and J. Wu describe a new polymer lubricant layer to protect hard disk surfaces as well as discuss the use of contact angle measurements to evaluate lubricant behavior on surfaces. N. S. Eiss and E. Lee examine surface texture effects on plastics used in automobile interiors in an effort to reduce stick–slip occurrences (observed by vehicle occupants as noise). L. Lin et al. describe micro-scratch tests of automobile topcoats (protecting basecoat paint) to quantitatively characterize the scratch and mar behavior and to determine damage mechanisms. W. Shen and F. N. Jones also examine mar resistance, damage mechanisms, and healing behavior of coatings using AFM. M. T. Dugger et al. use AFM and specially fabricated microelectromechanical systems (MEMS) device to examine frictional behavior of nanoscale lubricated contacts. Finally, A. Liebmann-Vinson examines the tribological performance of syringes and methods used to control and measure frictional behavior of these biomedical devices.

Acknowledgments

We hope that readers of this volume will enjoy the images depicted on the cover. An elegant “micro-flower” of about 8 μm across represents a fascinating example of directional distribution of friction forces at the microscale within a multidomain Langmuir film formed by chiral phospholipids. This image is cordially provided by researchers from Swiss Federal Institute of Technology (for details, see the chapter in this volume and the article in *Science*, 1998, 280, 273). Complimentary cover image shows an AFM cantilever in a torsional deformational mode (a bit exaggerated though) used to collect friction force microscopic data frequently discussed in this volume and images similar to that presented on the cover. The finite element analysis model displayed here was built by J. Hazel, Western Michigan University (for details, see the article in *Thin Solid Films*, 1999, 339, 249).

We are grateful for all the hard and time-consuming work that the symposium lecturers and poster contributors devoted to this meeting. Also, we are especially appreciative of the efforts of the many authors who provided written chapters comprising this volume, and of the reviewers for their comments. The willing participation of researchers from a broad cross-section of science and engineering disciplines, especially those from the more “macroscopic” perspective, was essential to the success of such a meeting, and provided the necessary framework upon which discussions were built.

Finally, we acknowledge the sponsors who supported the symposium, which became a basis for this volume: the American Chemical Society Division of Polymer Chemistry, Inc., The Surface Engineering and Tribology Program of The National Science Foundation, the Air Force Office of Scientific Research, and The Petroleum Research Fund. We also are especially grateful to all the students who worked very hard to ensure the smooth running of the symposium: John Hazel, Kirsten Larson, Zheng Huang, and Melbs Lemieux.

VLADIMIR V. TSUKRUK
Department of Materials Science and Engineering
Iowa State University
Ames, IA 50011

KATHRYN J. WAHL
Tribology Section, Code 6176
Naval Research Laboratory
Washington, DC 20375-5342

Chapter 1

Tribology of Polymers: A Perspective

B. J. Briscoe

**Department of Chemical Engineering, Imperial College,
London SW7 2BY, United Kingdom**

The present review seeks to provide a broad and comprehensive personal reflection on the subject of the tribology of polymers and to offer an indication of the scale and very extensive spectrum of content within the subject. It introduces conventional tribology, such as bearings and slideways, but also covers those areas which are less well recorded. These include areas such as fibre assemblies, powder flows, processing of polymers and also the durability of polymeric products. In addition, the subject of polymer tribology is considered from a fundamental view, both as a system approach and also as a combination of unit processes which include the origins of friction, the nature of damage processes and the phenomena of wear. The latter are achieved by adopting now well-established simplifications. The final parts of the paper deals briefly with lubrication and environmental effects before a concluding summary is provided.

Scope

If one chooses to sub-divide the subject of tribology by divisions according to the generic material class, then by most admissions the tribology of organic polymer would provide the broadest and most comprehensive part of the subject. Divisions in tribology have not always gone according to the material class and sometimes focus on such areas as friction, contact mechanics, lubrication and so on. The argument is that fundamental knowledge acquired amongst one material class can usually and wisely applied to other materials; this view is largely followed here. To begin to outline the breadth or potential breadth of the subject it is convenient to think in the first instance of two types of tribological systems. By tribology here we mean the general subject which deals with the interactions between solid bodies in relative motion. This encompasses such familiar subjects as adhesion, friction, damage, wear and lubrication. There are issues of semantics here, which are not developed in the

present review, associated with what is meant by such terms as “friction”, “damage” and so on if one considers the broader context of the subject.

Table 1 provides a listing of some commonly encountered tribological contacts and the table is divided into two parts; Table 1A deals and with what are called “primary members” and Table 1B “secondary examples”. It is probably because the subject of tribology was largely developed by mechanical engineers that the primary examples reflect those cases which will be addressed by mechanical engineers. Here for example, we will be dealing with such things as journal bearings and slideways where it is often desirable to reduce both friction and wear and also to maintain continuous motion. The Table lists examples such as airframe bearings and various types of hinges, bearings in clocks and motors and so on and provides a few comments. In addition, the Table includes three headings under “requirement” which are termed F, D and W; F is friction, D is damage and W is wear. The Table legend describes the significance of the symbols. Although not now widely practiced as research areas, the primary areas might also include friction devices such as tyres, clutches and brakes where such things as high friction and friction stability and heat dissipation are the key issues. Similarly, in traction drives such as rollers and belts where elastomeric materials are widely used. Although it would not be common to include in this area the traction of shoes and floors, they are arguably of the same class. Finally, amongst the primary examples we note the wide and common use of polymers, particularly PTFE-based systems, as solid lubricants in a wide variety of bearing applications. These are the most obvious examples and much of our current basic knowledge has been acquired from studies of such systems in model contacts as well as in practical situations.

Of more interest, and this is where organic polymer systems have their generic peculiarity, are those items which are described as “secondary examples”. One can make a simple division in this area to divide the subject into four parts; fibrous systems, particulate systems, surface mechanical damage suppression and processing applications. Some of these areas would not normally be included under the tribological heading for polymer systems but I will choose to do so because they provide an indication of the importance, arguably more important than the primary examples, for polymer tribology in practical applications.

Under the heading of secondary examples we note the case of ropes where the single filaments in the rope interact together to provide the mechanical response of the rope. A wide variety of requirements are often required within rope systems, not least the ability to absorb a significant amount of tensile impact energy as well as the ability to mechanically damp whilst in general movement. The rope system can be argued as a special of the yarn system and yarns are widely incorporated into fabric systems where the mechanical response and durability of such items is governed, to a significant part, by the interaction at the contacts within the fibrous assembly. These contacts are usually rather special insofar as they constitute a class of contacts, which are often described as extended line contacts (one-dimensional contact arrays). The “primary members” systems would normally be described simply as multiple asperity contacts where many particle or asperity contacts occur within the two-dimensional apparent contact area. The use of fabric conditioners is widely appreciated as a means of changing the tactile properties of such fibrous assemblies and the general belief is this is achieved by providing appropriate lubrication at the contact points within the assembly. Equally, a significant fraction of the ballistic energy capture

Table I.A: Primary members

GENERIC TYPE	EXAMPLES	REQUIREMENT			COMMENT
		F	D	W	
Journal bearings	Airframe, domestic automobile hinges, clocks, motors	-	-	-	Damping requirement, heat dissipation
Slideways	Locks, furniture, toys, switches, precision machines, marine slideways	-	-	-	Continuous motion
Friction devices	Clutches, brakes	± / +	-	-	Stability, heat dissipation
Traction drives	Rollers, belts, tyres, shoes, human tools, floors	± / +	-	-	Environmental influences, critical
Lubricants	PTFE: a common solid lubricant, sorbed films	-	-	-	Often cheap and effective

Table I.B: Secondary examples

GENERIC TYPE	EXAMPLES/NEED	REQUIREMENT			COMMENT
		F	D	W	
"Ropes"	Ropes, yarns, low wear, flexible	±	-	-	Flexible, KNDT forming
Fabrics/fibrous assemblies	Optimal tactile response, ballistic protection	±	-	-	Fabric/hair conditioner
Powders / granules	Optimal processing, low "cohesion" to facilitate flow	-	+	+	
Films	Wide range for floors and domestic goods and magnetic media, lubrication	±	-	-	Boundary/solid lubricants
"White" goods	Cabinets, surfaces, scratch resistance, key requirement	±	-	-	Also bathroom goods
Polymer processing / manufacture	Control of wall boundary conditions, (non-chip forming)	±	-		Extrusion for example
Polymer processing / manufacture	Machining (chip forming)		+	+	Cutting forming
Other processing	Interface (internal and external engineering)	±			Wide range of processing aids

Table 1 Various types of tribological polymer contacts. The Table is in two parts; "primary members" and "secondary examples" - Table 1A, Table 1B respectively. "Generic Type" indicates through a shorthand the accepted definitions of typical contacts. Some specific examples are shown. F denotes friction, D denotes damage, W denotes wear under the heading "Requirement". The various signs minus, plus, plus-minus indicates the desire for a reduction of friction etc. or an increase (plus) or an optimisation (plus and minus). Some comments are offered. The primary members describe what is generally appreciated as "tribology". The secondary examples are where tribological performance or tribological action is a significant component of the response or value of the product or system.

efficiency of ballistic fabric materials can be attributed to the dissipation of friction at the point of contact between the yarns and the filaments within the yarns themselves.

An extension of the fibre system is the fine particle system and it is now generally appreciated that a significant part of the rheological or flow behaviour and, indeed, processing response for particulate systems, can be attributed to the interparticle friction (three-dimensional contact arrays) and as well as the friction between the particles and the deforming or constraining walls (two-dimensional contact arrays). These frictional forces have a significance in hopper flows and in general process engineering, particularly as organic polymers are widely used as processing aids for a wide variety of materials such as ceramics and metals. Also, many polymeric powders, such as foods as well as synthetic polymers, are processed in powder form.

The areas described as "films" and "white goods" provide opportunities to modify and improve the interaction, often of a casual nature, between polymers and their environment. Important areas here would be the human traction, for example in the friction that would occur between a packaging film and the human hand, as well as that which occurs when the package is being transported. A certain level of friction is necessary both for comfortable handling as well as processing. There are now important new areas within the remit of magnetic media response. The area of "white goods" is primarily preoccupied with either special bearing systems which occur within the moulded body, such as switches and slides, or the preservation of the optical appeal of the body. In the latter case, the important thing is to maintain the surface reflectivity and to avoid the consequences of careless particle-polymer interaction which can occur during washing or cleaning. This is an area of particular significance in the motor car industry where high glosses are imparted to the surface of paints in order to improve their optical appeal. This may be regarded as a part of what is often termed "erosive wear".

In this section I have also added polymer processing and manufacture where the wall friction, be it a polymer melt or a polymer powder or paste, between the process material and the wall boundary has a crucial influence upon the efficiency of the processing operation. This is well accepted in metal working and is now becoming of interest in polymer processing, not only for synthetic polymers but also for foods and other natural products. The efficiency of screw extrusion devices is very much controlled by the interface wall friction and, of course, the longevity of the system is governed to some extent by the interaction of the polymer with the processing walls. These non-chip forming operations are much more common than the chip-forming operations which are widely adopted for metallic systems. Polymers have the virtue of being eminently processable into suitable forms at relatively economic costs compared with that which is often necessary for metallic systems. However, there are a number of chip-forming or machining operations which are applied to polymeric systems. The one which one often encounters is the use of chip-forming to machine ultra high molecular weight poly(ethylene) for the cup in prosthesis devices. Finally, in the generic type class for "secondary examples" I have cited other "processing operations" where additives are often included into polymeric systems to provide degrees of internal lubrication or interface modification or external lubrication to modify friction and adhesion and so on. A common example here would be in the processing of polymeric films, particularly low density

poly(ethylene), where aliphatic amides are widely used as migrating lubricant aids to modify the surface of the material to lower friction or suppress auto adhesion.

These few examples have been drawn together to demonstrate the very wide remit that is enjoyed by polymer tribology, not only their applications but also in terms of the variety of the nature of the contacts and also the consequences which are encountered in practice. There are factors associated with the scale and dimensionality of contacts. In some large bearing systems, such as civil engineering and marine slideway supports based on ultra high molecular weight poly(ethylene), the apparent contact area can be several meters. In contrast, the contact area between synthetic or natural fibres can be sub micron in dimension and also approximate to a point contact. Similarly, the loads which are imposed upon these contacts can vary from many tons in civil engineering applications to nano Newtons in particulate and fibre contacts. Equally, sliding velocities can range from the trivial, for example in civil engineering applications, to supersonic in ballistic applications. Furthermore, the engineering requirements are also various. Often it is appropriate to reduce friction, for example in the case of certain journal bearings in hydraulic struts. Excessive friction modifies the damping characteristics. Alternatively, large and stable frictions are required in automobile brake and tyre applications. Often damage must be minimised, for example in the scratching of “white goods” but in machining it must be maximised. Usually excessive wear, or loss of form (see later) is not desirable but there are applications in the polishing and machining of polymers where relatively rapid wear rates are desirable. There are also important secondary issues which are common in organic polymer systems associated with environmental sensitivity or their interactions with “lubricants”. For example, the friction in “Nylon” fabric systems is very much controlled by ambient water; water induces a type of surface plasticisation (self lubrication) which greatly contributes to the “feel” of the fabric as well as electrostatic charge dissipation. At the extreme, organic polymers find quite extensive applications as soluble additives in apolar and polar lubricating media; the so-called viscosity improvers and drag reduction agents.

In summary, we can reflect that polymeric tribological interactions occur in a very wide spectrum of contacts and the scientific challenge is to draw together the understanding and information that can be gained in one area, say journal bearings, and translate that into another area such as description of the tactile response of a fabric system. The supposition has always been that a fundamental understanding of tribological principles will provide the necessary links to improve the general understanding and allow knowledge from one area to be conveniently and properly translated to another. The present review seeks to outline the principles that have been used historically in this cause.

The Scheme

Figure 1 shows a format for describing tribological characteristics which is sometimes called “the systems approach” and was widely favoured by the late Gert Salomon and more recently by Horst Czichos [1]. It also includes the idea of evolving interfacial modification, which is now widely appreciated, but was much popularised by the late Maurice Godet [2]. The presumption is the major tribological processes are primarily mechanical responses with the incorporation of certain chemical interactions. The systems approach first proposed the idea of the

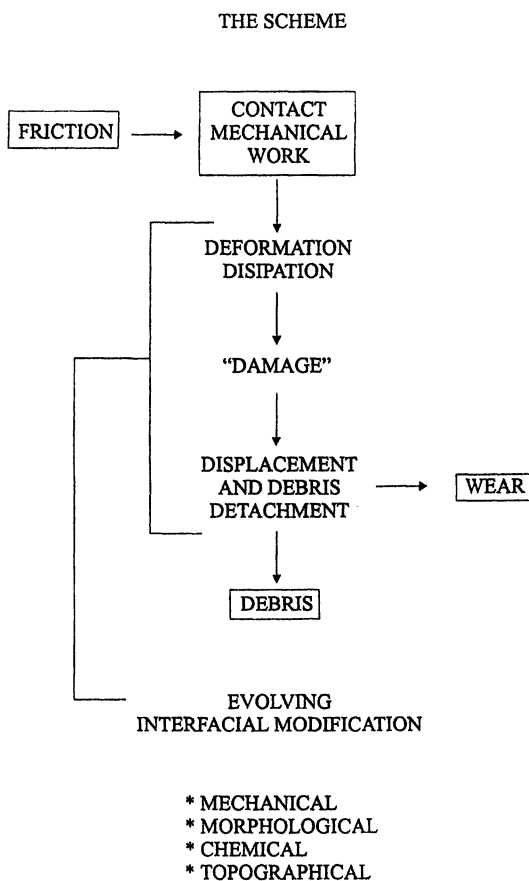


Figure 1. The scheme showing the various “units” of a tribological system as developed by Salomon and Czichos using the so-called “systems approach”. Friction arises from contact mechanical work which causes dissipation and deformation which leads to damage which produces debris and when the debris is displaced in the contact wear accrues. In the process, significant interfacial modifications, “third body formation”, occurs. The latter can be in the form mechanical, morphological chemical or topographical modifications.

introduction of contact mechanical work; basically frictional work. This process naturally led to deformation and dissipation within the contacting members and under some circumstances mechanical or chemical damage of the interface zones would accrue. In the process there will be significant mechanical, morphological chemical and topographical modification of the interface zone (third body) as well as the production of significant amounts of heat. The damage would produce debris and when the debris was eventually displaced from the contact zone the wear would be observed. Here, we are thinking in terms of wear being a process which involves the loss of mass, but see later. It has often been remarked, and it is worth noting this fact again here, that there is often a very poor correlation between the magnitude of the frictional work and the subsequent rate of wear. This fact indicates that the processes such as damage formation, interface modification and debris displacement are major factors in controlling the wear of the components. In polymeric systems, the extent of chemical wear is usually comparatively modest compared with metallic systems although in many cases there will be, because of the high energies that are introduced, a significant amount of chain scission as well as morphological modification of the polymer's structural features. Chemical wear processes may be very significant certain very high energy dissipation systems such as braking components.

If one does not adopt the "systems approach", which simply thinks in terms of friction producing debris and wear, but focuses upon what are often called the "unit processes", a term drawn from chemical engineering practice, then one may examine the various sub divisions and accord properties and features to each of them. The danger with this methodology is that the frictional process and the consequent damage and wear produce a very significant modification to the properties of the interface zone and hence simple predictions which discount this important development are likely to provide fallacious results. We have noted already the poor correlation between friction and wear which probably arises primarily because of this neglect of a key feature in the tribological process.

The so-called "unit processes" would then be the way in which friction is able to provide a means to dissipate contact mechanical work. Then how that work might produce irreversible chemical and mechanical damage. Finally, how that the damaged material could be displaced as debris from the contact zone and from without the contact to produce the wear debris and the mechanical material wear within the system. The remainder of this particular review will show what progress has been made in these areas of "unit" research.

Before moving on to those parts, one can make a comment that polymers have found wide use in bearing-practice and indeed elsewhere for a variety of reasons, not least because of what is often called their "self-lubricating capacity". What is meant here is that the interface zones that are produced by the action of sliding can often produce a weak boundary layer through thermal or strain induced restructuring effects. Essentially, the "third body" produces a self-lubricating interfacial medium which provides a weak interface and hence reduces the frictional work. Within this virtue is also the Achilles Heel of many organic polymer systems and that is the generation of these structures, particularly for polymers like PTFE, can lead to unacceptably high wear rates. In addition most polymers, particularly for the new engineering examples, are not very effective at dissipating frictional heat. Hence, they are not widely used in high speed or high energy dissipation environments. Clearly, braking systems are not of this sort and these cases tend to use cross-

linked resins which do not undergo extensive interface softening. Finally, we can also note a rather wide use of composite systems in polymer tribology. Metallic systems often use alloys and composite materials but the wide use of filled composites as well as alloy systems is wide practice. For example, it is common to include hard filler phases within PTFE journal bearing systems in order to reduce the (transfer) wear. In practice, the wear can be reduced by up to three orders of magnitude for a suitably formulated composite compared with that of the virgin polymer. Finally, a unique class of organic polymer systems are the elastomers. They have no real like within other generic material classes and not only do they have very unique mechanical properties but also extremely interesting and practical frictional properties. Polymer tribologists who have studied thermal, plastic and resonance systems have often not addressed elastomeric systems and hence in the literature one will often find that there has been no serious attempt to unify the tribology of "thermosets" and "thermoplastics" with that of the elastomeric systems. There is a different and distinctly separate literature, which describes the tribology of elastomeric systems; much of it is now rather old.

Subsequent sections will deal with simplifications, based upon "unit" processes such as friction damage, wear and so on rather independently of the polymeric material class.

Simplification

Friction Processes. Historically, it has proved both convenient and effective to consider that are just two general mechanisms whereby interface zone strain can be introduced in a sliding contact. For some polymeric systems, particularly because of the inherent self lubricating characteristics of polymers, this model appears to an attraction but in certain processing applications it serves no purpose other than to underline the gross approximations and limitations associated with such a distinction. The literature calls this approach the "two-term non-interacting model of friction". A distinction is made in that there are two ways of introducing surface strain in order to dissipate frictional work; one occurs because of the natural adhesion at the contact zones which leads to the "adhesion model of friction". The second mode is associated with gross subsurface deformation caused by geometric engagement and the gross contact mechanical displacements. Figure 2 terms the former "adhesive" and the latter "cohesive" deformation processes. The primary mechanical dissipation process, for organic polymers at least, can be either viscoelastic, as is often the case in the rolling of elastomers, or gross plastic deformation and fracture which can occur during the abrasion of ductile and glassy polymers. The majority of the deformation energy is subsequently dissipated near the contact zone as heat with a consequent important change in the mechanical properties of the system. Figure 3 shows a schematic of the distinction between the two deformation modes where the crucial geometric variable, θ , distinguishes one process from the other. When θ is zero (the adhesion mode) the adhesive stresses are responsible for transmitting the strain. When θ reaches a critical angle, which can depend upon the polymer system and the operating conditions but is typically of the order of 5 or 10°, subsurface deformations become important. There are various reviews in the literature which have dealt with the merits, or not, of this type of approximation [3,4]. For example, with rolling friction, where adhesive components are small, the dissipation energy can be very

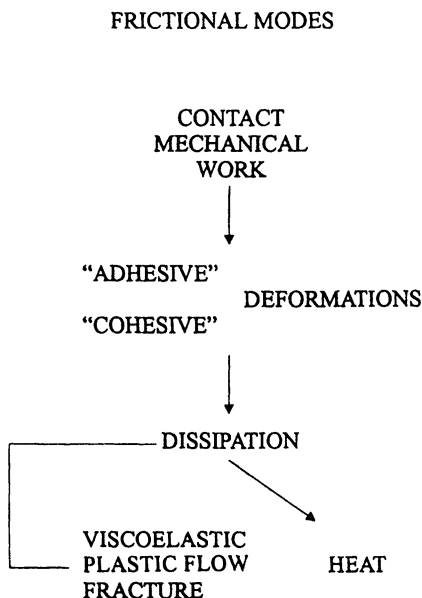


Figure 2. The classical distinction of friction modes. The contact mechanical work, or friction, leads to adhesive and cohesive deformations in the contact. This produces deformations which can be elastic, plastic or brittle in nature. Heat is produced. The scheme does not show the friction processes associated with Coloumbic (ratchet) friction or the Schallamach wave phenomena. The two-term non interaction model of friction considers the adhesive and cohesive (ploughing) to be separate and non-interacting.

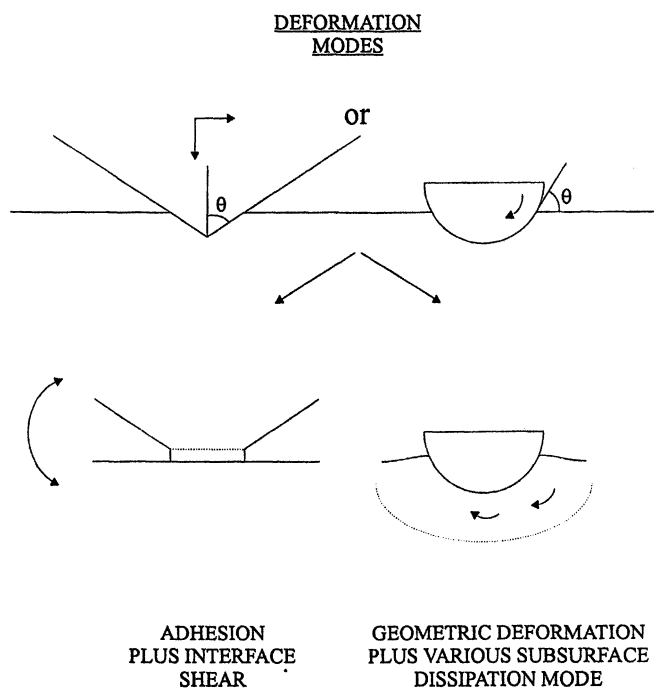


Figure 3. The schematic of the friction or deformation modes. The angle θ defines a transition from interface sliding through to the ploughing component; see text.

satisfactorily explained using contact mechanical models which suppose that the frictional energy is dissipated by viscoelastic losses in repeated deformation in the subsurface of the contact zone [5]. In the other extreme, the friction of fibres or thin films on smooth substrates can be well described in terms of an interface shear rheological term, the interface shear stress, multiplied by a contact area to describe the adhesion component [6]. For some systems "Coloumbic" or "Ratchet" friction is apparently important when the scale of the asperities approaches the contact dimensions. The differential friction effect commonly observed for natural fibres is an example.

The deformation or ploughing modes can also be well described for plastic and possibly even brittle fracture systems using modern numerical techniques. As with the elastomeric systems the models basically include geometric terms, such as θ , some load and various parameters such as an interface shear stress but more importantly a relatively accessible bulk deformation or dissipation property of the material. For the case of elastomers, an appropriate viscoelastic loss tangent is sufficient and for a ductile polymer some pressure dependent yield stress. There are many examples in the literature where good correlations have been obtained between a bulk mechanical test and a frictional response. Properly, it has been seen as the domain of others, perhaps polymer scientists, to seek to provide interrelationships between molecular structure and deformation dynamics and the consequent bulk material responses.

The interpretation of rationalisation of interface frictional modes provides a far greater challenge. Here, the prospect of numerical simulations of the sort carried out for bulk deformations has lesser means of verification. The experimental evidence is that the primary energy dissipation zone is located near to the interface and has a thickness of the order of a few molecular dimensions. It is also generally unclear as to whether or not the shear plane or shear zone is located at the original interface or within one of the sliding members. Indeed, there is evidence that both processes can occur. It is common to observe in self-lubricating polymer systems that a transfer film is formed on one of the counterfaces and that the films transfer from one surface to the other during the sliding motion. There are other cases, particularly sliding at low speeds with elastomers and glassy polymers, that indicate that the sliding plane is actually at the interface. Leaving aside for the moment the phenomena of Schallamach waves [7] which is unique to a certain type of elastomers, it would appear that there are two ways of interpreting the interface shear phenomena. One approach is to consider that the interface zone or plane is simply a region which is in continuous shear. Adhesive junctions form and break but in the process shear strain is transmitted to the narrow interface region and thereby dissipated. Based upon this approach one might suppose that the interface shear stress, that is the frictional force divided by the contact area, will be in some way a reflection of the rheological properties of the interface itself. The alternative is to seek molecular models to prescribe the way in which energy is dissipated through molecular relaxations. Both have their merits and currently there is no obvious means of accurately and satisfactorily proving the value of either. However, the macroscopic approach does have some merits. There have been a wide range of studies which have sought to quantify the interface shear stress for organic systems and to relate this to the important contact variables such as contact pressure, temperature, contact time and effective strain rate. In spite of uncertainties regarding the details of the deformation

mechanism, it would seem, based upon experimental evidence, that there is a good correlation between the interface rheology and the bulk rheology of the same polymeric systems providing that account is taken of the very different deformation conditions that exist in the interface zone as compared with those which exist in conventional mechanical testing [8]. For example, the rates of strain in the interface zone are often cited as being very high; 10^6 to 10^8 reciprocal seconds. Similarly, the contact pressures are peculiarly high and often there is transient and viscoelastic compressive loading. In particular, the pressure dependence of the bulk yield stress, as detected from contact mechanical measurements, is usually very similar to that which is obtained by bulk shear measurements in hydrostatic environments. Similarly, glass transition temperatures can be detected during the sliding of thin films which are comparable with those that can be detected in bulk dynamic mechanical measurements [9]. Thus on this basis, one can argue that the adhesion component of friction for polymeric systems follows the same sort of rules observed for metallic systems but because of the intrinsic self-lubricating capacity the interface shear stresses of the interface regions are usually somewhat less than those of the bulk material. Factors of ten are often cited as being typical.

Much has been written in recent times about the prospect of interpreting the frictional behaviour of organic layers, solids as well as fluids, based upon molecular approaches. The models have analogies with the topographical models of friction which exist in the historical literature [10]. It is interesting that the data for interface rheology (interface shear stress) often follow Eyring-type relationships and therefore it is tempting to think in terms of molecules moving past obstacles, other molecules or parts of molecules, in shear fields. The Eyring approach, which has often been applied to the interface friction model of polymers, will often provide "sensible" values for the stress and pressure volume activation units for the flow [11]. The "cobblestone models" are an example of an of Eyring approach. In the context of the molecular approaches, where it is not possible to effectively undertake structural examination *in situ*, there is evidence, from some infrared work, that the relaxations that are activated in shear fields as also sensed through infrared adsorption and emission [12].

Damage modes. It has been argued that a two-term model (two dissipation regions), if it is applicable to friction processes, may also be sensibly applied to damage processes. Figure 4 continues this theme. Damage modes can be either interfacial (localised at the interface) or cohesive which would involve a significantly greater volume of material. Models to describe these damage modes have often been developed using model contacts either studying transferred films on smooth substrates [13] or using sharp needles for scratching the surface of polymers, particularly elastomers. Schallamach pioneered this area in studying the damage processes of elastomers [14]. There are arguments as to whether these processes can be considered as unit deformation operations as opposed to fatigue deformation operations. With multiple asperity contacts, for example in abrasion, then few would doubt that there will be a significant element of repeated deformation of the surface zones and hence the generation of low or high cycle fatigue disruption processes. The details of these events will be crucial in defining the ultimate debris removal process. If one restricts oneself to the notion of only exclusive unit damage events, which can be examined through certain types of experimental simulation and also

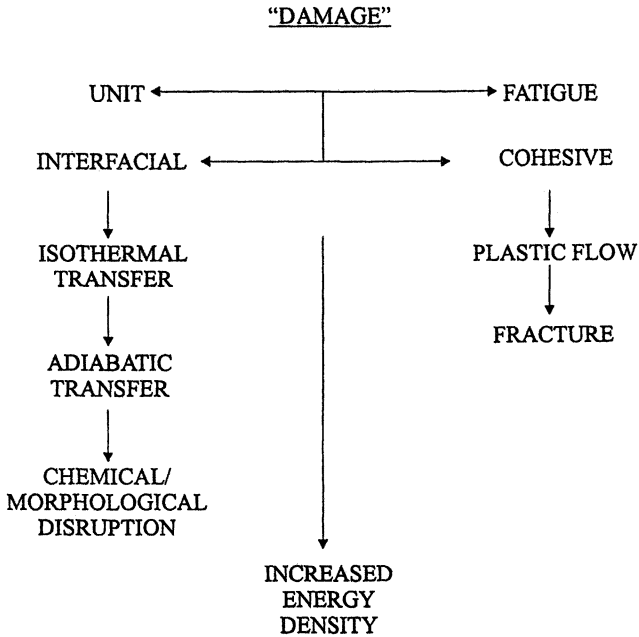


Figure 4. Damage modes. Damage is envisaged as being “unit” insofar as it occurs in one event or arising from a variety of fatigue processes. Based upon interface friction models, the damage is thought to occur at interfaces or within the cohesive zone associated with the contact. In the interfacial mode various transfer processes such as isothermal and adiabatic transfer may occur or under high energy intensities significant chemical degradation may exist. In the cohesive mode plastic flow combined with fracture are common.

adopts notion of the two zone (interfacial and cohesive) damage regimes then the Figure 4 illustrates some of the processes which might occur. In the interfacial mode certain polymers, particularly thermoplastics, will accommodate their sliding by transferring material themselves from one surface to the counterface. The literature indicates that for some systems, mainly PTFE and ultra high molecular weight poly(ethylene) (the so-called smooth molecular profile polymers), there will be transfer of an oriented film from one body to the other [15]. There are many reported studies of the structure and orientation of these films and the consequences of combined motion (linear motion plus rotation) upon the structure of these layers. Glassy polymers tend not to transfer under what are called "isothermal contact conditions" but at higher sliding velocities, and the consequent higher contact temperatures, then adiabatic or "melt" transfer can occur [16]. This can be seen in a very gross way in certain failure modes but it undoubtedly occurs at relatively slow sliding speeds where the temperatures in the contact zone heating can be significant to induce softening and flow of the polymer [17]. Highly cross-linked materials such as thermosetting resins and elastomers generally do not tend to transfer "whole polymer" to counterfaces; low molecular weight species and the products of chemical degradation may do so. They accommodate their sliding by a means which is yet to be established in detail but often, because of the fact that it is a localised energy dissipation of the interface and there is no interface self-lubrication or shear softening, high temperatures are often produced with the consequence that there is chemical erosion of the contact; some Eastern European work has suggested that the gaseous debris from such contacts may provide an aerodynamic component of lubrication.

The damage modes, in cohesive failure, are usually studied using "sharp" indentors through scratch deformation. These studies indicate that as the contact strain (the angle θ increases) one progresses from a surface smoothing, or ironing, where asperities are flattened through to plastic grooving with viscoelastic recovery to gross chip-forming followed by or combined with a variety of plastic fracture processes where material is disrupted [6.18]. A number of authors have sought to correlate, or identify, the irreversible damage with the frictional response of both elastomers and plastically deforming systems. On the face of what is available currently there are sensible correlations between bulk rupture properties and the friction and consequent damage in these operations. It is significant however that during many scratching operations, for thermoplastics, significantly high temperatures are generated and that often supposedly brittle materials will show an appreciable plastic response. The consequences of thermal heating and the potential of thermal degradation or thermally induced morphological changes becomes very important. In practical applications, the consequences of such scratching processes are greatly influenced by the environment and the prospect of interfacial lubrication. Lubrication tends to suppress the apparent consequences of scratch damage. The subject of scratch damage has seen a renewed interest in recent times because of the interest in improving the optical perception of commercial products where scratching can create an unattractive visual appearance [19]. In summary, we can conclude that the gross deformation damage modes could, in principle, be related to the established bulk material response of the system. Such material characterisation is found from simple bulk deformation tests on macroscopic specimens. In the case of transferred systems, it is not clear what the "rules" are for the formation and behaviour of these

transferred films. It would appear that systems which are capable of oriented fibre or film drawing under isothermal conditions may produce thin and highly oriented transferred films upon counterfaces. At higher temperatures the onset of transfer can be correlated with the increase of the frictional heating where the material becomes close to its glass transition temperature.

Wear modes. If we pursue the idea that there are two sorts of damage mode which are directly related to the two frictional modes then arguably there will be two sorts of generic wear processes; interface wear and cohesive wear. Moving from the idea of specific damage mechanisms into the area of wear produces a number of problems. Figure 5 provides a summary. First in practical terms, there is a matter of semantics; wear in many polymeric contacts can simply be judged a result of a loss of "clearance". This will be the case in hydraulic members where excessive wear will lead to leakage of hydraulic fluid. Such loss of form could occur through mass loss but also possibly through creep which is induced by thermal heating or protracted loading. This sort phenomena might have implications when certain displacement transducers are used to monitor wear by monitoring the change of dimension of a particular specimen. The more common definition of wear would involve a description of the loss of mass. However, even here there can be complications such as for the wear of ultra high molecular weight poly(ethylene) in aqueous media. If the polymer is not properly equilibrated with the medium prior to the introduction of the wear study, which can be very protracted, then an increase in mass can be observed [20]; the polymer absorbs water to corrupt the mass measurement.

These things apart, in the mass wear process, there are at least two special factors to be considered. First of all, the detachment of the debris which would lead to the wear can occur not only by unit, chip forming, processes but also by fatigue in the contact. Such a fatigue process could involve the repeated deformation of the surface as will be the case say in rolling contact fatigue. However, during the protracted wear process, as was mentioned earlier under Frictional Processes, there can be significant changes induced in the morphology and topography of the contact zone as the deformations progress. This might be a particularly important feature in the wear of certain composite systems where abrasive fillers are introduced to remove unwanted chemical products from the interface zone. This is common practice in certain types of poly(amide) marine bearings. The loosened debris will remain in the contact zone, possibly as a third body, and suffer repeated comminution or compaction in subsequent deformations until eventually it is expelled from the contact zone. There are many examples of significant changes in monitored wear rates simply through the changing of the contact geometry. For example, a ring of polymer sliding as a ring face bearing on a metal plate will wear significantly faster if a number of slots are cut into the bearing surface to produce what is effectively a number of pins. In certain fretting operations, if the bearing is simply inverted so that debris can fall out of the contact zone, the wear rate will significantly increase.

There does not seem to be any means of actually predicting the rate of interfacial wear processes, be they arising from transfer wear processes or through chemical degradation. This is not surprising in view of the uncertainty as to what is involved in the transfer process. However, what is not known is that if certain polymers are filled with hard or chemically active fillers then a securely bonded transfer film will attach to metal counterfaces and then the rates of wear will be reduced by several orders of

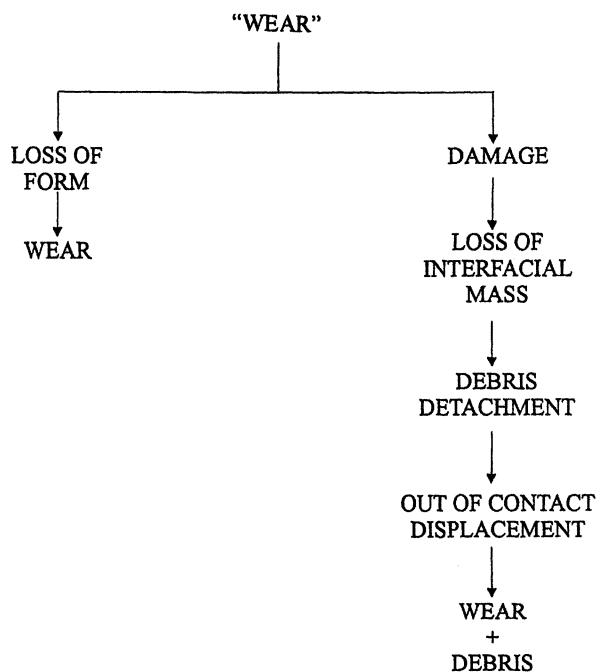


Figure 5. Wear processes. Wear processes are divided into those which result from loss of form but not mass and those which result from loss of mass. The overall wear process for the latter involves debris detachment and out-of-contact displacement before the final mass wear occurs.

magnitude [21]. For the same systems certain environmental contaminations will reverse this beneficial effect and increase the wear rates significantly [22]. The search still continues to provide a fundamental basis for understanding such things as transfer wear processes. In the extreme of abrasion, usually termed single pass abrasion, where a rough surface is driven over a polymer in one direction only, then effective correlations exist. Here we would note that repeated sliding over the same abrasive surface will cause what is known as "clogging" and a significant smoothing of the counterface. Basically, the wear debris fills-in the roughness. With repeated sliding the wear rates reduce significantly. Also, strange effects can be seen by changing the contact geometry for these types of abrasive wear processes which also indicates the fact that even in so-called single pass abrasion, where an abrasive paper is drawn over a polymer surface, there is more debris accumulated at the front of the contact than the rear. This occurs because of the way that the contact surface topography is modified by the inclusion of compacted wear debris. These difficulties apart, it does seem that under some circumstances, possibly for rather sharp abrasives, that the Ratner-Lancaster correlation provides a reasonable account of much experimental data [23]. There often appears to be an experimental correlation, sometimes of a linear form, between the abrasive wear rate and the reciprocal of the product of the stress and strain at yield for the same material in simple tension. For elastomeric systems where there is a significant element of fatigue wear, perhaps with "smoother" abrasives, then fatigue life models would appear to correlate with abrasive wear rates to some degree.

Thus, in the terms of our understanding details of wear the generalities are appreciated but the predictive capacity is not high.

Lubrication and Environmental Sensitivity

It has been noted that many polymeric systems have the capacity to induce what is called self lubrication. As a consequence it has not been a major focus of research activity, compared to metallic and ceramic systems, to study the lubrication of polymers *per se*, but more often to consider the influence of environmental sensitivity. For convenience the two are dealt with together here. We may also note that polymers are often included into polar and apolar solvents to modify the rheological behaviour as is common practice in the formulation of viscosity improvers and the development of drag reducing agents. These processes may have implications in rationalisation of environmental sensitivity.

The prospect of effective self-lubrication seems to be limited to a relatively small class of polymers, mainly ductile polymers, and it is not often seen in glassy polymers, epoxy resins and elastomeric systems. However, even though systems which have the capacity for self-lubrication can also be effectively lubricated by a number of means. It is common practice to include low molecular weight species in polymers which migrate to the surface to provide a weak lubricating boundary layer. These additives can be amides as in low density poly(ethylene), silicone based systems as in, for example, polyacetyles and poly(styrenes). Arguably, this is just a special case of boundary lubrication via internal lubrication. External boundary lubrication of polymers has generally been found to be relatively ineffective, not least because of the fact that polymer surfaces have relatively low free energy and do not readily adsorb the sorts of boundary lubricants which are commonly used for

ceramics and metals. Nor are they well wetted by common fluid lubrication media. Indeed, it is often the case that the boundary lubricants which can be used for metals can produce what is called "antiboundary lubrication" for polymer systems [24]. This is where the additive seems to induce premature failure via excessive softening of the contact. There are frequent examples in the literature where polymers, mainly PTFE based systems, are used as solid lubricants for other polymer systems. The formation of a thin polymer-rich layers, which acts as a boundary solid lubricant [25] is well established. Many patents exist to design and improve this technology and it forms an important part of composite tribology. Although this particular review has not dealt extensively with polymer composites as specific bearing materials, it has been common with many composite polymer systems to include not only soft particles but hard particles, micaceous fillers, fibres and so on. The general belief is that these hard particles might improve the thermal dissipation of the contact and also, in some cases, improve the adhesion of the so-called transfer film. In other instances they might polish the counterface to reduce the occasional damage which might occur by debris inclusion. Another useful feature of polymer systems, in terms of their overall performance, is their ability to adsorb relatively abrasive debris which might be introduced from the environment. By this route, they naturally form a reinforced composite which in some cases can be an extremely effective bearing material. In braking systems, based on phenolic resins, it is now a frequently adopted practice to include materials, such as aramides, which can operate at high temperature lubricants to stabilise a high frictional force. We may summarise all of these technologies under the heading of the attempt to deliberately form an effective third body layer at the interface by the natural consequences of the sliding process.

It is common practice to use fluids to lubricate polymeric contacts and, indeed, elastomeric systems show very effective isoviscous elasto-hydrodynamic lubrication in seal applications. One of the difficulties which is frequently encountered when using fluid lubricants with organic polymer systems is the degradation or modification of the surface through either plasticisation or the inducement of stress crazing phenomena. Elastomers frequently swell and such materials as the acrylates can be heavily surface plasticised by even modest quantities of active lubricants in concentrated contacts. It is now appreciated that in some systems, the Nylon system water was mentioned previously, that the introduction of the environment, in this case water, can effectively weaken or soften the polymer surface and thereby provide an interesting and useful third body interfacial layer. There are also examples where solvents appear to migrate into polymeric matrices and activate the migration of low molecular weight species to produce a very complicated additive filled plasticised polymer layer. These sort of "jelly-like" layers appear to be very effective in practice and indeed they may be responsible for the efficient lubrication behaviour of many natural systems. A highly concentrated and structured polymeric solution, which is loosely attached to the polymeric substrate or indeed the sliding counterface, may be formed (basically polymer solutions and see earlier). There also appears to be examples which can be identified in the literature where vapours or indeed high pressure gases can induce the modification of polymer surfaces and thereby improve or deteriorate their operating performance. These phenomena are encountered in certain types of processing plant such as the piston rings and sliders in reciprocating gas compressors.

In summary, one may reflect that the environment, or indeed lubrication deliberate or accidental, can have either a positive or negative effect upon tribological performance for polymers. It has often been remarked, but possibly it is an extreme view, that lubricating polymers is, on balance, a bad thing! This comment really only applies to the thermoplastic systems, but perhaps not ultra high molecular weight poly(ethylene) as many epoxy or elastomeric systems or indeed glassy polymers would not really survive the high heat dissipation or interface strains generated with high and unlubricated surface tractions. Nevertheless, even in the latter areas, there is a prospective of the lubricant or the environment producing significant chemical or mechanical degradation of the surface and hence undermining the operational value of the contact.

Summary

The prime purpose of this review was to provide, based upon the author's own experience, the broadest view of the tribology of polymers. The subject developed in the first instance mainly through studies of elastomeric contacts for tyre applications and also by mechanical engineers who are keen to use polymers as self-lubricating bearings (maintenance-free) in a variety of structures. In recent times it has been appreciated that there are many tribological facets associated with the performance of ordinary things such as fabrics, ropes, powder flows and more recently a significant tribology component has been identified in the processing of polymers or systems which contain relatively high concentrations of polymer additives [26].

The practical need in the various areas differs; in brakes high friction is required, journal bearings low friction, in fabrics, optimal friction. In the context of damage; for machining relatively high damage rates are required but in the durability of "white goods" a minimum perceived damage is necessary. Usually one seeks to reduce the consequences of friction and damage in terms of wear but there are cases, albeit limited ones, where high rates of effective wear in machinery are required; the polishing of contact lenses is an example.

In scientific terms, the challenge is to attempt to provide a coherent basis to account for the behaviour of all of these systems which can be easily translated from one context to the other. In the applications we have reviewed, it is clear that the contact variables such as load, apparent contact area, sliding velocity, asperity dimensions, vary over very broad scales. To rationalise requires a very detailed and comprehensive description of the subject as a whole and often practitioners have chosen to work in particular areas to develop models which would not be generally applicable within the extremes of the subject. Thus, the models which would be developed for describing the friction of fibrous assemblies would not necessarily be of great value in the description of the friction of journal bearings. The problem is compounded further because of the very wide range of mechanical response of organic polymer systems. They have extreme elastic behaviour, as seen with the elastomers, and for that reason elastomeric tribology has rather developed upon separate lines from the rest of polymer tribology. Thermoplastics and glassy polymers have similar characteristics but these are different from those of the highly cross-linked resins. In practice, it is quite rare to use a "pure" polymer and invariably the systems are filled for a variety of reasons, often ones of simple economy; polymers are relatively expensive. Finally, if one takes the view that tribology is just

the application of sensible material science, polymer deformation mechanics combined with contact mechanics, then one sees the final difficulty; that is that the mechanical response of polymer is very sensitive to the local environment. In particular, it is sensitive to strain, strain rate, temperature and indeed chemical activation from the environment itself. The interaction with environment is a particularly important feature of the behaviour of natural systems such as foods and animal tissues.

Within all of these complexities is a basis for our uncertainty as how to model, or indeed rationalise, the tribological behaviour of polymeric based contacts. There may be a secure knowledge base in one small area, which adds to the broad understanding but could not be readily transported into another context. Like the curate's egg, our understanding is "good in parts". It is the challenge of polymer tribology to provide sensible interpretations and scientific understandings of the whole subject based upon the acquisition of knowledge from the individual parts. As a subject of scientific enquiry, polymer tribology is probably no more than 70 years old. Much progress has been made in that time and the prospects for the future are exciting and provide a worthy and valuable engineering cause and challenging scientific opportunities.

References

1. Czichos, H., *Introduction to Friction and Wear*, Chapter 1 in "Friction and Wear of Polymer Composites", Ed. K. Freidrich, Elsevier, Holland 1986.
2. See "Interface Dynamics", Ed. D. Dowson, C.M. Taylor, M. Godet and D. Berthe, Tribology Series 12, Elsevier, Holland, 1998.
3. Briscoe, B.J. "Friction of Polymers" in "Fundamentals of Friction; Macroscopic Origins", Eds. E. Singer and H. Pollack, Kluwer Academic Press, Netherlands, 1992.
4. Tabor, D., "Friction, Lubrication and Wear", in *Surface and Colloid Sci*, E. Matijevic (Ed), Vol. 5, John Wiley, 1972, 245.
5. Greenwood, J.A. and Tabor, D., *Proc. Phys. Soc.* **71**, 1958, 989.
6. Amuzu, J.K.A., Briscoe, B.J. and Chaudhri, M.M., *J.Phys.D.Appl.Phys.*, **9**, 133, 1976.
7. Schallamach, A., *Wear*, **17**, 1971, 301.
8. Briscoe, B.J and Smith, A., *J.Appl.Poly.Sci.*, **28**, 1983, 3827.
9. Briscoe, B.J. and Thomas, P.S., *STLE Tribology Trans.*, **38**(2), 1995, 382.
10. Dowson, D., "History of Tribology", Longman, London 1979.
11. Briscoe, B.J., Scruton, B. and Willis, R.F., *Proc.Roy.Soc., (Lon)* **A353**, 1973, 99.
12. Briscoe, B.J., Stuart, B.H., Thomas, P.S. and Williams, D.R., *Spectrochemical Acta*, **47A**, 1991, 1299.
13. Briscoe, B.J., *Polymer Tribology: State of an Art* in "Physicochemical Aspects of Polymer Surfaces", Ed. K. Mittal, Plenum Press, New York 1983.
14. Schallamach, A., *J.Polym.Sci.*, **9**(5), 1952, 385.
15. Pooley, C.M. and Tabor, D., *Proc.Roy.Soc. (Lon)*, **A329**, 1972, 251.
16. Lancaster, J.K., "Friction and Wear" in *Polymer Science*, Ch. 14, Ed. A.D. Jenkins, North Holland, 1972.

17. Briscoe, B.J., Material Aspects of Polymer Wear, *Scripta Metallurgica*, **24**, 1990, 839.
18. Briscoe, B.J., "Isolated contact stress deformations of polymers" in *New Directions in Tribology*, Ed. I.M. Hutchings, MEP, London 1997, p.191.
19. Briscoe, B.J., Sinha, S.K., Pelillo, E. and Evans, P.D., *Wear*, **200**, 1996, 137.
20. Dowson, D., Private communication.
21. See for example *Advances in Composite Tribology*, Ed. K. Freidrich, Elsevier, 1993.
22. Pratt, G., Private communication.
23. Briscoe, B.J. and Tabor, D., The sliding wear of polymers in "Fundamentals of Tribology", Ed. N.P. Suh and K. Saka, MIT Press, Cambridge, Mass., 1980.
24. Briscoe, B.J., Davies, G.J. and Stolarski, T.A., *Tribology International*, **17**, 1984, 129.
25. See for example *Polymer Wear and its Control*, ACS Symposium Series 287, Ed. L.H. Lee, Washington, DC, 1985.
26. Briscoe, B.J., Slippery Customers; Sticky Problems, Inaugural Lecture Transcript 1994, published Imperial College Press (London), Ed. D. Pashley 1999.

Chapter 2

Contact Mechanics and Adhesion of Viscoelastic Spheres

K. L. Johnson

College of Engineering and Applied Sciences, University of Cambridge,
1 New Square, Cambridge CB1 1EY, United Kingdom

It has recently become common to use the JKR theory (Johnson, Kendall & Roberts, 1971) to extract the surface and interfacial energies of polymeric materials from adhesion tests with micro-probe instruments such as the Surface Force Apparatus and the Atomic Force Microscope. However the JKR theory strictly applies only to perfectly elastic solids. The paper will review progress in extending the JKR theory to the contact mechanics and adhesion of linear viscoelastic spheres. The observed effects of adhesion hysteresis and rate-dependent adhesion are predicted by the extended theory.

Recent years have seen an increased use of microprobe instruments to measure the surface energy and viscoelastic properties of polymeric materials. Such probes commonly comprise an effectively spherical tip pressed against a flat surface or, as in the case of the Surface Force Apparatus, two crossed cylinders of equal radii which are geometrically equivalent to a sphere in contact with a plane. A typical experiment consists of loading and subsequently unloading the contact with a controlled force, while measuring the displacement and/or contact area, until the surfaces separate. If the surfaces adhere during the compressive part of this cycle, a tensile force is required to pull them apart, which is referred to as the 'pull-off' force. Microprobe instruments are particularly advantageous for adhesion measurements for two reasons: (i) adhesion forces become increasingly significant with a decrease in the size of the contact; (ii) adhesion is strongly affected by surface roughness which is minimised by using a very small area of contact.

In order to extract values of the surface energy or viscoelastic properties of the specimens from such a test a mechanics model of the test is required. Up to the present the so-called JKR theory (1) has been used, e.g. Tirrell (2). The JKR theory, however, is derived for perfectly elastic solids and assumes reversible behaviour in both the adhesive forces and the contacting solids. But the adhesion of viscoelastic solids, notably rubber, is well known not to be reversible. More work is required to separate two surfaces than is returned when they come together, an effect known as

hysteresis'. This irreversibility may arise from the nature of the adhesive bond, e.g. Israelachvili (3) or from viscoelastic dissipation within the contacting solids (4). This latter mechanism can easily be appreciated in a qualitative way. During separation the work done by the external force has to overcome the dissipation in addition to doing work against the surface forces (surface energy). When the surfaces are coming together the surface energy is providing the driving force, which has to provide for the dissipation as well as overcoming the external load. Hence the external force on separation exceeds that on coming together by virtue of the internal viscoelastic dissipation. In common with any non-conservative system, the response is dependent upon the loading path.

Several researchers have commented on the need for a mechanics model for the adhesion of viscoelastic solids to assist in the interpretation of microprobe adhesion experiments. This paper is a progress report on work in Cambridge to extend the JKR theory to the adhesion of *viscoelastic* spheres. The present state of play will be reviewed in a predominantly qualitative way; analytical details will be presented in a separate publication.

Elastic Solids: the JKR and Maugis-Dugdale Theories.

Continuum mechanics models for the adhesion of *perfectly elastic* spheres under the action of reversible surface forces are well developed. The essential features of the JKR model are shown in Figure 1a. The surface traction acting on a contact area of radius a comprises two terms: (i) a Hertz pressure $p_1(r)$, caused by the compressive force P_1 , which flattens the spherical surfaces and (ii) an adhesive tension $p_a(r)$ which gives rise to the adhesive force P_a . The net contact force P can be expressed:

$$P = P_1 - P_a = \left(4E^* a^3 / 3R \right) - \sqrt{8\pi\Delta\gamma E^* a^3} \quad (1)$$

where E^* is the combined elastic modulus of the two solids given by

$$\frac{1}{E^*} = \frac{1 - \nu_1^2}{E_1} + \frac{1 - \nu_2^2}{E_2}$$

the relative radius of the two spheres $1/R = 1/R_1 + 1/R_2$ and the combined surface energy of the two surfaces $\Delta\gamma = \gamma_1 + \gamma_2 - \gamma_{12}$. The surfaces snap apart at a 'pull-off' force P_c given by

$$P_c = -(3/2)\pi R\Delta\gamma \quad (2)$$

We now introduce dimensionless variables: $\bar{P} = P / 3\pi R\Delta\gamma$, $\bar{a} = a / (9\pi R^2 \Delta\gamma / 4E^*)^{1/3}$ so that equations (1) and (2) become

$$\bar{P} = \bar{a}^3 - (2\bar{a}^3)^{1/2} \quad (3)$$

and
$$\bar{P}_c = -1/2 \quad (4)$$

The infinite tension at the edge of the contact in Figure 1(a) is clearly physically unrealistic and it transpires that the above results comprise an asymptotic solution to the general problem of adhesion of elastic spheres, which applies to large spheres of low elastic modulus, i.e. where the elastic deformation is large compared with the range of action of surface forces. Solutions to the general problem have been found numerically,

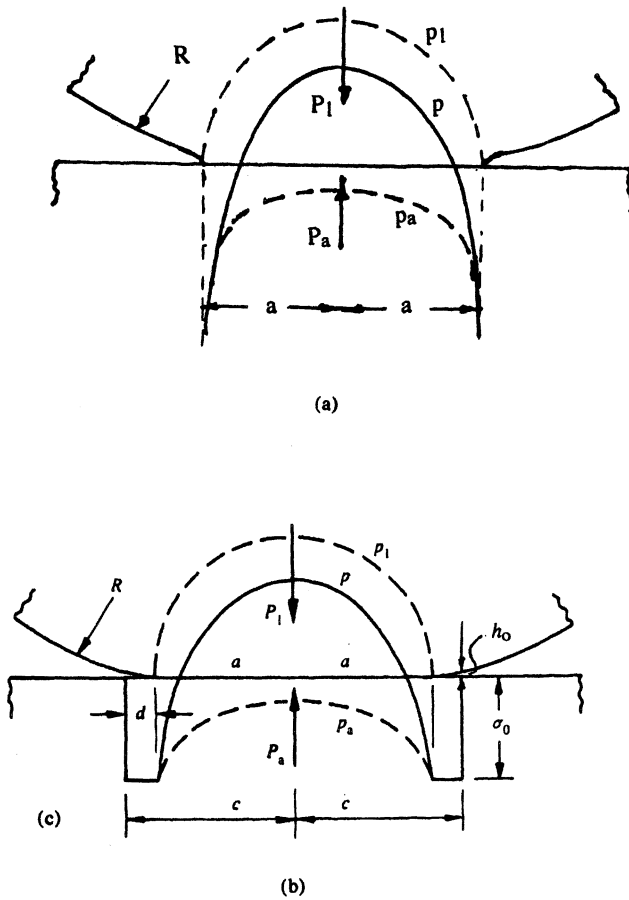


Figure 1. Adhesive contact of elastic spheres. Surface tractions comprise two terms: Hertz pressure p_1 and adhesive tension p_a . (a) JKR model has infinite tension at $r = a$. (b) Maugis model has tension σ_0 in annulus $a < r < c$.

first by Muller et al (5) and more comprehensively by Greenwood (6), but a valuable approximate solution in closed form has been presented by Maugis (7), using the analogue of a Dugdale crack. As shown in Figure 1(b), the tensile adhesive traction is taken to have a maximum finite value σ_0 which is assumed to be constant in the zone $a \leq r \leq c$ in which the separation of the surfaces $h(r) \leq h_0$, where h_0 is related to the surface energy by $\Delta\gamma = \sigma_0 h_0$. The solution is expressed in terms of a dimensionless parameter:

$$\lambda = \frac{1}{h_0} \left\{ \frac{9R\Delta\gamma^2}{2\pi E^*} \right\}^{1/3}$$

which expresses the ratio of the elastic displacement to the range of action of the surface forces. The width of the 'Dugdale zone' $d (= c - a)$ can be expressed in terms of λ by

$$\frac{d}{a} \approx \frac{3^{4/3}}{4\bar{a}\lambda^2}, \quad d/a \ll 1 \quad (5)$$

The JKR model is approached asymptotically as λ is increased and d/c becomes small. It provides a good approximation when $\lambda > 5$. For a comparison of the JKR and Maugis-Dugdale theories with numerical solutions see Johnson & Greenwood (8).

These results remain valid in the presence of frictional shear tractions interface: exactly so if $(1 + \nu_1)(1 - 2\nu_1)/E_1 = (1 + \nu_2)(1 - 2\nu_2)/E_2$ and approximately so if they differ'.

Linear Viscoelastic Solids

Material Characteristics. To be mathematically tractable analytical continuum mechanics modelling of rate-dependent materials is effectively confined to linear viscoelasticity. We shall use the simplest model which encapsulates the essential features of small strain polymer deformation: the 3-parameter model. It is represented in Figure 2 by two springs and a dashpot. At very low rates of strain the material deforms elastically with a modulus E_∞ represented by the two springs in series. At high rates of strain the deformation is again elastic, with a modulus $E = E_\infty/k$ represented by the single spring. At intermediate rates, the strain at time t after a step change in stress is given by the *creep compliance function*: $\Phi(t) = (1/E_\infty)\phi(t)$ where

$$\phi(t) = \{1 - (1 - k)\exp(t/T)\} \quad (6)$$

where $T = (1 - k)\eta/E_\infty$ is the relaxation time of the material. $\Phi(t)$ is plotted in Figure 2(a). It can be thought of as the reciprocal of a time dependent modulus $E(t)$. If such a material is subjected to cyclic strain at a frequency $\omega/2\pi$ the stress lags the strain by a phase angle δ where

$$\tan \delta = (1 - k)\omega T / (1 + k\omega^2 T^2) \quad (7)$$

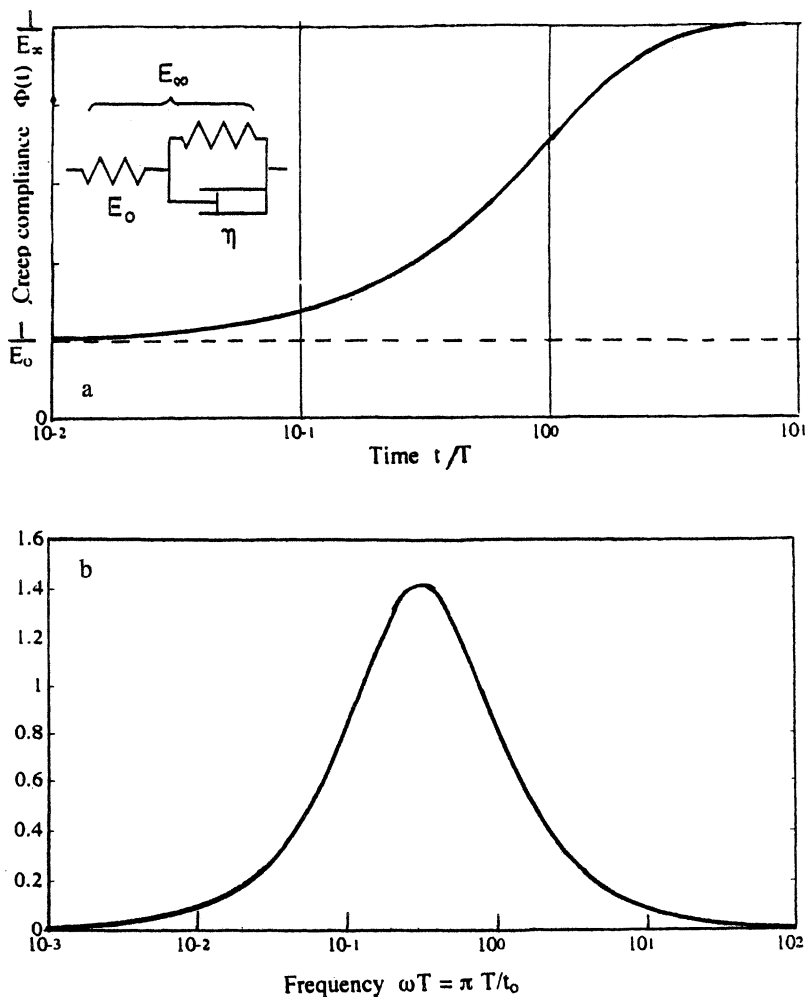


Figure 2. Three-parameter model of linear viscoelastic material: (a) Creep compliance function $\Phi(t) = (1/E_\infty)\{1 - (1 - E_\infty/E_0)\exp(t/T)\}$; (b) Phase angle δ between cyclic stress and strain gives a measure of viscoelastic energy dissipation.

Since the out-of-phase component is dissipative, $\tan \delta$ is a measure of the fractional energy dissipated during a cycle (Figure 2(b)).

An adhesion test in which the contact is first loaded and then unloaded until the surfaces separate is also cyclic. If the loading and unloading times are each t_0 the corresponding frequency is $1/2t_0$. Thus ω in equation (7) can be replaced by π/t_0 . We note that maximum dissipation occurs when $\omega T \approx 1$, when $t_0 \approx T$.

Contact cycle. We assume that an adhesion test is carried out under a controlled load and that, for simplicity, both loading and unloading take place at a uniform rate $U = P_0 / t_0$, where P_0 is the maximum compressive load. Such a *ramp cycle* is shown in Figure 3.

If we refer to the surface traction distributions in Figures 1a or 1b, it is apparent that there are two different locations of high elastic strain having very different scales of size. There is the bulk deformation of the contact arising principally from the Hertz contact pressure, whose size is characterised by the radius a of the contact. There is also an intense concentration of strain at the periphery of the contact produced by the adhesive forces, whose size is characterised by the length d of the Dugdale zone. During the cycle shown in Figure 3 the representative time for bulk deformation is t_0 , but for the strain concentration at the periphery the representative time is that for the edge of the contact to pass through the Dugdale zone, i.e. $t_d = d / \dot{a}$, where the average value of $\dot{a} = a_0 / t_0$ and a_0 is the contact size under P_0 . Hence the ratio of characteristic times governing the strain rate in the two locations is

$$t_d / t_0 = d / a_0 \quad (8)$$

It follows from equation (5) that in the JKR regime ($\lambda > 5$), $d / a_0 < 1 / \lambda^2 < 0.04$. Thus the characteristic times at which viscoelastic relaxation will influence deformation in the bulk (t_0) and at the edge of contact (t_d) are very different. Consequently we may treat the two effects independently, in the same way that crack tip stresses and bulk stresses are separated in fracture mechanics. We will consider bulk deformation first and ignore the presence of adhesion.

Viscoelastic Contact Mechanics

The contact of linear viscoelastic spheres in the absence of adhesion has been studied in detail by Ting (9) and Graham (10). (For a summary see Johnson (11)). If the two materials are different, their Poisson's ratios must be assumed equal and interfacial friction neglected. We shall examine the response to the ramp cycle of loading and unloading shown in Figure 3. The loading part of the cycle, i.e. during which the contact size a is increasing is straightforward to analyse. The viscoelastic Correspondence Principle applied to the Hertz elastic theory gives the variation of contact size $a(t)$ with load $P(t)$ to be:

$$a^3(t) = \frac{3R}{4} \int_0^t \Phi(t-t') \frac{d}{dt'} P(t') dt' \quad (9)$$

Expressing $P = Ut$ and using the creep compliance function of equation (6) gives

$$a^3(\tau) = \frac{3RUT}{4E_\infty^*} \{ \tau - (1-k)(1 - \exp(-\tau)) \} \quad (10)$$

where $\tau = t/T$. Analysis of the unloading phase, during which a is decreasing, is more difficult, in order to ensure that the surface traction is everywhere compressive. The details of the procedure are given in the references cited.

Computations have been performed for a 3-parameter solid with $k = E_\infty^* / E_o^* = 1/4$. The variation in contact radius $a(t) / a_o$ through the cycle is shown in Figure 4 for different values of cycle time t_o , where a_o is the static value of a under a load P_o . For a sufficiently slow cycle a follows the Hertz 1/3 power law with $E^* = E_\infty^*$ (shown dotted); for a fast cycle a again follows Hertz with $E^* = E_o^*$. Note that, at intermediate speeds the maximum contact size occurs after the load begins to decrease. This asymmetry in the cycle reflects the energy dissipation which is a maximum when the cycle time $2t_o$ is of the same order as the relaxation time T .

Viscoelastic Fracture Mechanics

The way in which the concepts of linear elastic fracture mechanics could be utilised to generalise the adhesion mechanics of elastic bodies of widely different shapes, including elastic spheres, was demonstrated by Maugis & Barquins (4). They then went on to show *experimentally* that the effective 'work of adhesion' G to separate unit area of a glass and polyurethane rubber interface was a unique material function of the peeling rate V , where G is defined in terms of the stress intensity factor K_I at the edge of contact by

$$G = K_I^2 / 2E_\infty^* \quad (11)$$

Their master curve of G as a function of peeling speed V for polyurethane rubber, which has a ratio of $E_o^* / E_\infty^* > 10^3$, is shown in Figure 5. The gradient of the curve in its middle range is 0.6.

The analogy between the kinetics of an adhering interface and that of a moving crack in a viscoelastic solid may be appreciated by reference to the system shown in Figure 6. Here an 'interface crack' between two semi-infinite solids is moved under steady equilibrium conditions by sliding a frictionless pin located in the mouth of the crack at a uniform velocity V , under the action of a force F . The reactions of the pin on the faces of the crack give rise to a stress intensity factor K_I at the tip. If the solids were perfectly elastic, whether the surfaces were separating or coming together, from energy considerations we can write:

$$F = K_I^2 / 2E^* = G = \Delta\gamma \quad (12)$$

If the solids are viscoelastic, there is a difference between an opening and a closing crack, due to the viscoelastic dissipation within the material. For an opening crack we shall assume that some fraction $\alpha_{op}(V)$ of the elastic energy $|G|$ is dissipated so that for an opening crack equation (12) becomes:

$$F_{op} = [K_I^2]_{op} / 2E_\infty^2 = G_{op} = \Delta\gamma + \alpha_{op}(V)G_{op}$$

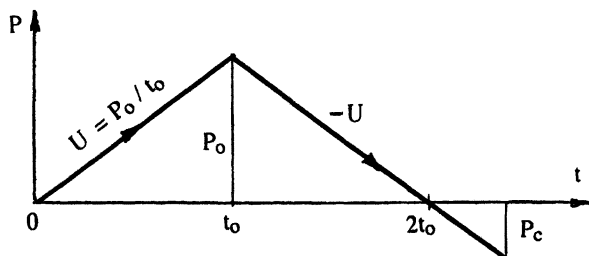


Figure 3. Ramp cycle in which the load is increased then reduced at a uniform rate. Separation occurs at the pull-off force P_c .

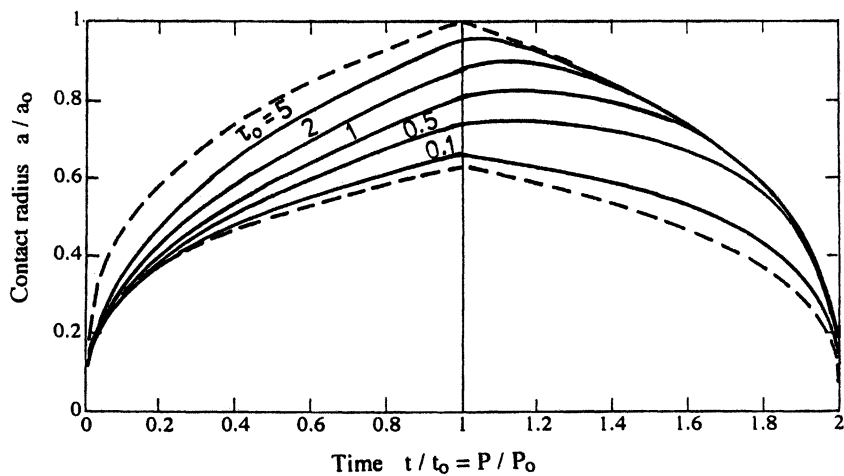


Figure 4. Variation of contact radius with load during the ramp cycle of Figure 3 without adhesion. The parameter $\tau_0 = t_0/T$.

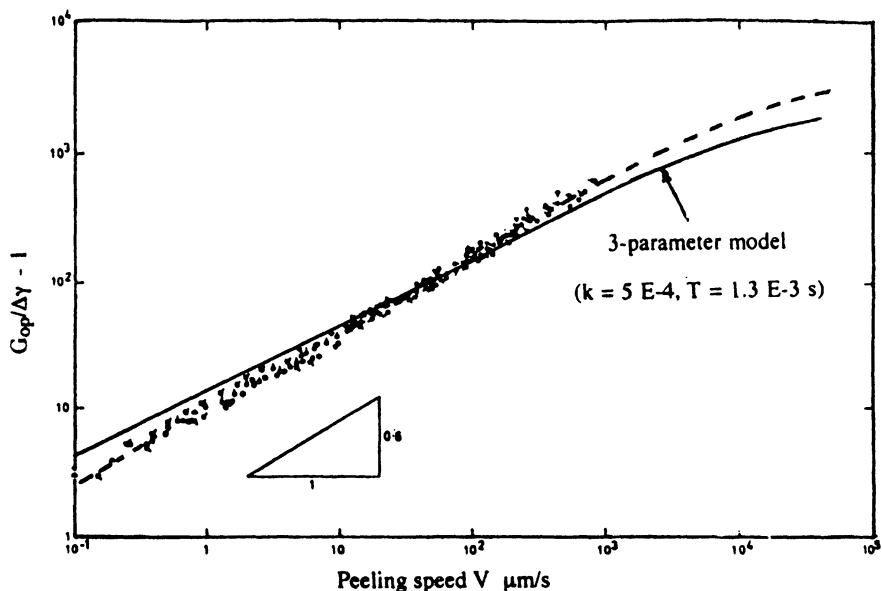


Figure 5. Measurements by Maugis & Barquins (4) of the rate dependence of the adhesion of polyurethane rubber, compared with the Schapery theory for a 3-parameter solid (equation (18)). (Reproduced with permission from reference 4. Copyright 1978 Institute of Physics.)

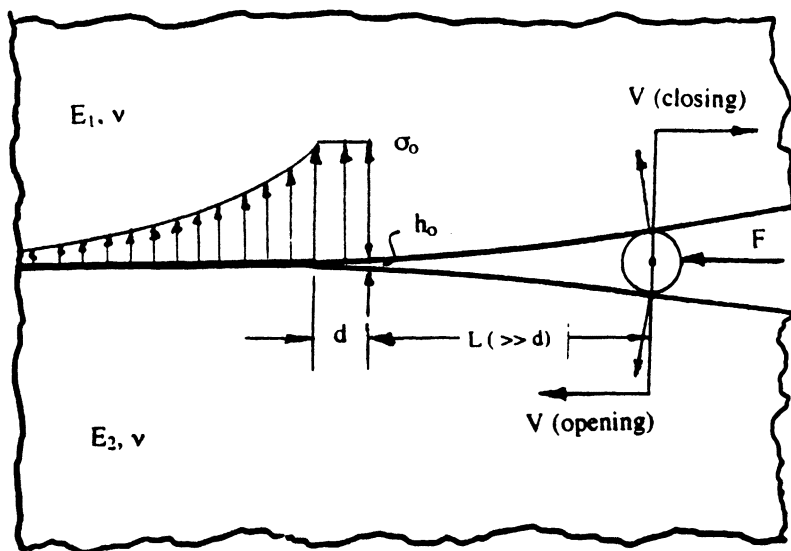


Figure 6. Representation of a steady-state moving (opening and closing) interface crack, with a Maugis-Dugdale distribution of adhesive traction.

whereupon

$$\frac{G_{op}}{\Delta\gamma} = \frac{1}{1 - \alpha_{op}(V)} = \beta_{op}(V) \quad (13)$$

which is greater than unity. With a closing crack V reverses, adhesive forces do positive work on the system and energy is extracted at the pin, so that G and $\Delta\gamma$ change sign. In this case we assume that a fraction $\alpha_{cl}(V)$ of the surface energy $\Delta\gamma$ is dissipated. Hence

$$F_{cl} = [K_I^2]_{cl} / 2E_{\infty}^* = G_{cl} = \Delta\gamma - \alpha_{cl}(V)\Delta\gamma$$

i.e.

$$\frac{G_{cl}}{\Delta\gamma} = 1 - \alpha_{cl}(V) = \beta_{cl}(V) \quad (14)$$

which is less than unity.

To determine the functions $\beta_{op}(V)$ and $\beta_{cl}(V)$ Schapery (12-13) made a fracture mechanics analysis of opening and closing viscoelastic cracks with the results summarised below. For both opening and closing cracks Schapery shows that the length d of the Dugdale zone varies approximately with the rate of peeling according to

$$d = d_o / \phi(t^*) \quad (15)$$

where d_o is the (elastic) length at zero peeling speed, given by

$$d_o = \frac{\pi E_{\infty}^* h_o^2}{4 \Delta\gamma} \quad (16)$$

and t^* is the representative time for the peeling process. In the qualitative discussion above we took this to be the time of passage through the Dugdale zone $t_d = d/V$, but Schapery suggests that $t^* = (1/3)t_d = d/3V$ is a better estimate. Thus, from equations (15) and (16), t^* can be found from

$$(t^*/T) \cdot \phi(t^*/T) = \frac{1}{3} \frac{d_o}{VT} = \frac{\pi E_{\infty}^* h_o^2}{12 \Delta\gamma VT} = \frac{1}{v} \quad (17)$$

Schapery goes on to show that for an opening crack (12) the apparent work of adhesion is given approximately by

$$\beta_{op} = \frac{G_{op}}{\Delta\gamma} = \frac{E^*(t^*)}{E_{\infty}^*} = \frac{1}{\phi(t^*/T)} \quad (18)$$

Solving equation (17) for (t^*/T) and substituting in equation (18) gives β_{op} as a function of the non-dimensional peeling velocity v .

This result has been fitted to Maugis & Barquins experimental measurements on polyurethane rubber in Figure 5, yielding values of $(E_o / E_{\infty}) = 2 \times 10^3$ and a time constant $T = 1.3 \times 10^{-3} s$. The gradient is 0.5 compared with the experimental value 0.6, but it must be remembered that a 3-parameter model is a very simple representation of a real polymer. An independent analysis of an opening viscoelastic interface crack

was made by Greenwood & Johnson (14) on the basis of an inverse cube surface force law. This led to the same results as those of Schapery presented above, except that the coefficient in the expression for $1/\nu$ in equation (17) was $1/2$ rather than $\pi/12$.

For a closing crack a different approach is required. Schapery (13) introduces a 'strain intensity factor' to replace K_I in equation (14). The length d of the Dugdale zone is still given approximately by equation (15), but the apparent work of adhesion is now given approximately by

$$\beta_{cl} = \frac{G_{cl}}{\Delta\gamma} = \frac{E_{\infty}^*}{E^*(t^*)} = \phi(t^*/T) \quad (19)$$

where t^* is still determined by equation (17).

The functions $\beta_{op}(\nu)$ and $\beta_{cl}(\nu)$ so obtained are plotted in Figure 7 for the creep compliance function of equation (6) with $k = 0.01$. It is evident that the effective work of adhesion is augmented when the surfaces are separating (opening crack) and attenuated when they are coming together (closing crack). More recently Greenwood (unpublished) has carried out a more exact analysis of opening and closing viscoelastic adhesive cracks. His values of $\beta_{op}(\nu)$ and $\beta_{cl}(\nu)$ are also plotted in Figure 7, which show what good approximations are provided by equations (18) and (19). These functions will now be used to analyse a ramp cycle of loading and unloading adhering spheres.

Viscoelastic Adhesion Cycle

We shall now attempt to model an adhesion test by considering the ramp cycle in Figure 3, with a uniform loading and unloading rate $dP/dt = \pm(P_o/t_o)$. Conditions for which the JKR theory is appropriate (Maugis' $\lambda > 5$, $d \ll a$) are assumed. In the purely elastic case the equilibrium relationship between load and contact size is given by equation (1). In the viscoelastic case the surface energy $\Delta\gamma$ is scaled by the factor β , given by equation (19) during loading and by equation (18) during unloading. In dimensionless variables equation (3) becomes

$$\bar{P} = \bar{a}^3 - \sqrt{2\beta\bar{a}^3} \quad (20)$$

from which

$$\frac{d\bar{P}}{d\bar{a}} = 3\left\{\bar{a}^2 - (\bar{a}\beta/2)^{1/2}\right\} - \left\{\frac{\bar{a}^3}{2\beta}\right\}^{1/2} \frac{d\beta}{d\bar{a}} \quad (21)$$

Now

$$\frac{d\bar{P}}{d\bar{a}} = \frac{d\bar{P}}{dt} / \frac{d\bar{a}}{dt} = \frac{\bar{P}_o}{t_o} / \left\{\frac{\bar{a}}{a} \frac{da}{dt}\right\}$$

and da/dt is the speed of the edge of the contact, which corresponds to the crack speed V in equation (17), from which

$$\frac{d\bar{P}}{d\bar{a}} = \frac{\bar{P}_o T}{t_o} \left\{ \frac{36R(\Delta\gamma)^2}{\pi h_o^3 E_{\infty}^{*2}} \right\}^{2/3} \frac{1}{\nu} = \frac{A}{\nu} \quad (22)$$

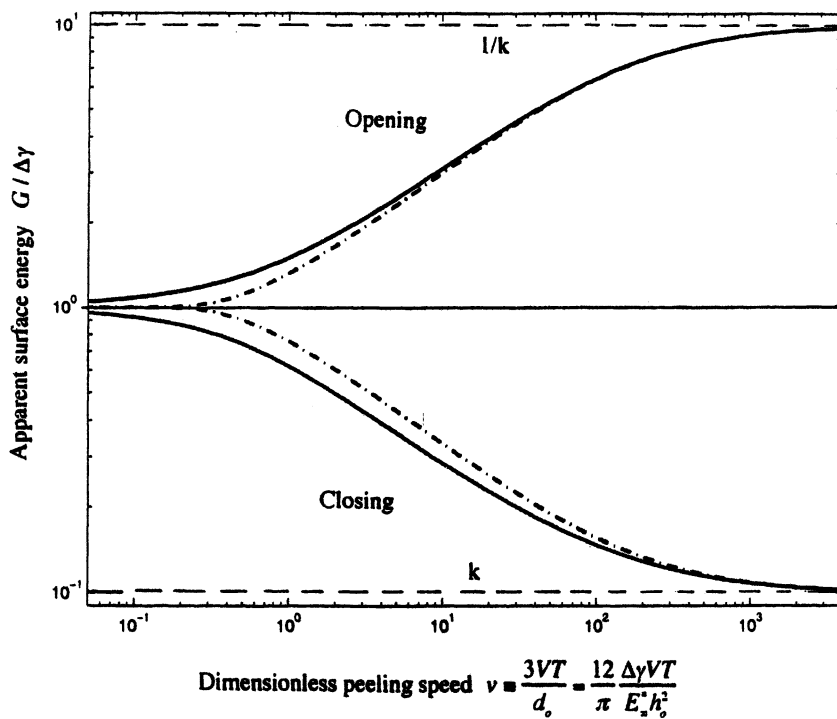


Figure 7. Apparent surface energy of a moving viscoelastic crack ($k = 0.1$).

----- Exact analysis (Greenwood, unpublished);

----- Approx. (Schapery, equations (18) & (19)).

Equating (21) and (22) gives

$$3\left\{\bar{a}^{-2} - (\bar{a}\beta / 2)^{1/2}\right\} - \left\{\frac{\bar{a}^3}{2\beta}\right\}^{1/2} \frac{d\beta}{d\bar{a}} = \frac{A}{v} \quad (23)$$

The simultaneous equations (17),(19) and (23) can be integrated step-by-step to give the variation of β with \bar{a} and hence, by equation (20), the variation of contact size with load. During loading (crack closure) $\beta = \beta_{cl}$ given by equation (19) ; during unloading (crack opening) $\beta = \beta_{op}$ given by equation (18).

Computations have been carried out using the creep compliance function in equation (6), with $k = 0.1$, for various values of the loading rate parameter A , where

$$A \equiv \frac{\bar{P}_o T}{t_o} \left\{ \frac{36R(\Delta\gamma)^2}{\pi h_o^3 E_\infty^2} \right\}^{2/3} = \frac{4\bar{P}_o T}{t_o} \lambda^2 \quad (24)$$

The results are plotted in Figure 8. The elastic (JKR) relationship is shown by the chain line. The dotted lines show the high speed limits ($A \rightarrow \infty$), for which $\beta_{cl} = k = 0.1$ on loading and $\beta_{op} = 1/k = 10$ on unloading. At finite loading rates adhesion hysteresis is clearly visible. When the surfaces first touch they snap into contact at an initial contact size. With increasing compressive load the contact grows; its size is less than the JKR value but approaches the JKR value with increasing load. When the load is first reduced, the contact size remains unchanged until the surfaces begin to separate at the higher apparent surface energy associated with an opening crack. The contact size then decreases until pull-off occurs at an enhanced pull-off force. The dimensionless pull-off force \bar{P}_c as a function of the loading rate parameter A is plotted in Figure 9. It varies from the JKR value of $-1/2$ at low speed to $-(1/2)/k = -5$ at high speed. It is apparent from Figure 8 that the contact size approaches the high speed values at the beginning and end of the cycle. This is on account of the cube root relationship between \bar{a} and \bar{P} which, for $d\bar{P}/dt$ constant, gives high value of $d\bar{a}/dt$ when \bar{a} is small.

Viscoelastic Films

Some adhesion measuring equipment, notably the Surface Force Apparatus, comprises thin films of polymer mounted on an elastic substrate. The equivalent interface fracture problem to that considered above (Figure 6) is shown in Figure 10, where each elastic solid is covered by a viscoelastic layer of thickness h . The case of the opening crack has been examined by Huntley (15). He shows that the effective work of adhesion, given for viscoelastic solids by equation (18), is modified by the thickness of the layer approximately to:

$$\beta_{op} = \frac{G_{op}}{\Delta\gamma} = \frac{\phi\{(h/d)t^*\}}{\phi(t^*)} \quad (25)$$

where the length of the Dugdale zone d is given by equations (15) and (16). Thus equation (25) may be written:

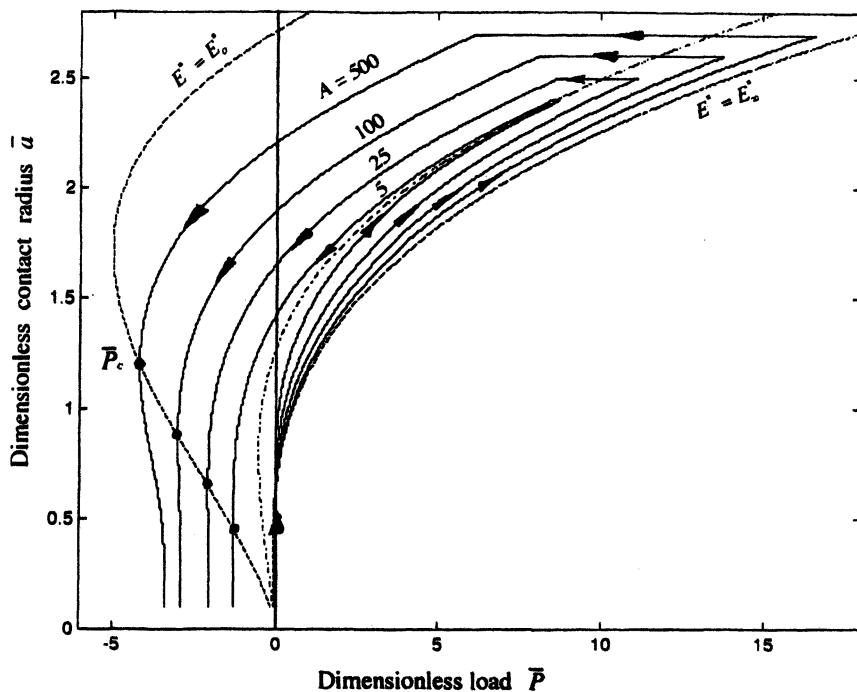


Figure 8. Simulation of a ramp loading cycle of viscoelastic spheres in contact ($k = 0.1$), showing hysteresis loops for varying values of rate parameter A .

--- JKR elastic (reversible); - - - - low and high speed limits.

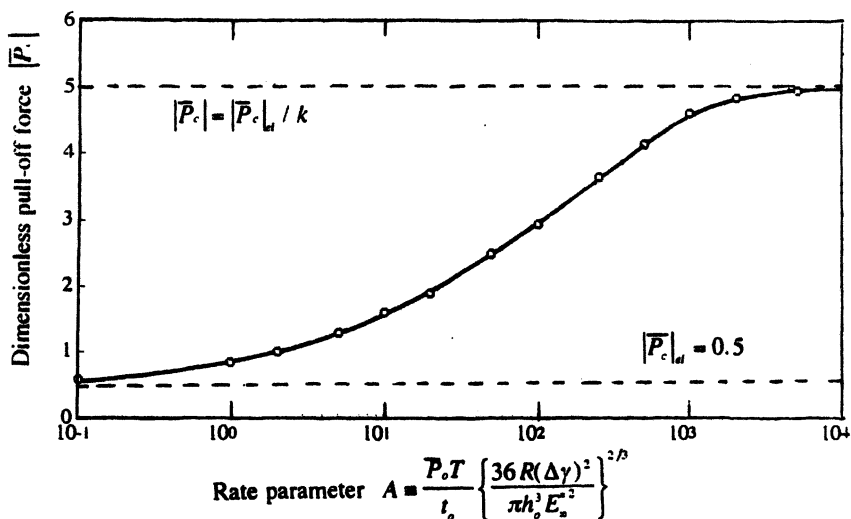


Figure 9. Dimensionless pull-off force $|\bar{P}_c|$ as a function of the rate parameter A , ($k = 0.1$).

$$\beta_{op} = \frac{G_{op}}{\Delta\gamma} = \frac{\phi\{H\phi(t^*)t^*\}}{\phi(t^*)} \quad (26)$$

where $H = h/d_o$. Using equation (17) to relate t^* to the dimensionless crack opening speed v , enables β_{op} to be plotted against v in Figure 11 for varying values of the thickness parameter H .

It is immediately apparent that reduction in the thickness of the viscoelastic layer attenuates the work of adhesion and, at high peeling speeds, causes a *decrease* of adhesion with speed. This effect may be understood when it is appreciated that increasing speed brings an increasing volume of material into the high dissipation regime shown by the curve of $\tan \delta$ in Figure 2(b). In an unlayered system this process continues until the whole of the dissipation regime is effectively contained within the solids, whereupon the work of adhesion levels off at a maximum value $1/k$. In a system comprising a thin layer backed by non-dissipative material, the dissipation regime cannot be wholly accommodated within the layer and is progressively excluded at higher speeds. The work of adhesion then decreases with speed. The range of peeling speed for which the adhesion decreases with speed is basically unstable and can lead to unsteady peeling. It is responsible for the vibration and ripping noise which frequently occurs when adhesive tape is pulled rapidly off a flexible sheet.

To apply these results to a contact cycle, it is necessary to consider the contact mechanics of the system, as discussed for the Surface Force Apparatus (SFA) by Sridhar et al.(16).

Discussion and Conclusions

To extract solid surface properties, surface energy in particular, from a contact experiment an appropriate contact mechanics model of the test is required. Under perfectly elastic reversible conditions the JKR theory of adhesion of elastic spherical surfaces has proved effective, but there are features of the adhesion of rate-dependent (viscoelastic) solids which are not modelled by the JKR theory. The most notable are: (i) the apparent surface energy (work of adhesion) is rate dependent and (ii) the work of adhesion in separating the surfaces is greater than is released when they come together (adhesion hysteresis). This paper reports progress in extending the JKR theory to *linear* viscoelastic solids. It successfully predicts both rate-dependent apparent surface energy and adhesion hysteresis.

For the purpose of exposing the *effects* of viscoelasticity, computations have been restricted to a simple 3-parameter model with a single relaxation time T and a ratio of instantaneous to relaxed modulus $E_o / E_\infty = 1/k$ (see Figure 2). It is recognised that this may be a poor model for a real polymer, but the theory is not restricted to the creep compliance function of equation (6). A simple alternative would be the power law:

$$\phi(t) = (t / T)^m \quad (29)$$

In the case of polyurethane rubber a 3-parameter model gave a reasonable fit to the Maugis & Barquins' experimental curve of $G_{op} / \Delta\gamma$ (Figure 5) by choosing $1/k = 2 E3$ and $T = 1.3 E-3$ s.

A fundamental restriction in the theory developed above is that the length d of the zone at the edge of contact where the adhesive forces act (Dugdale zone) should be small

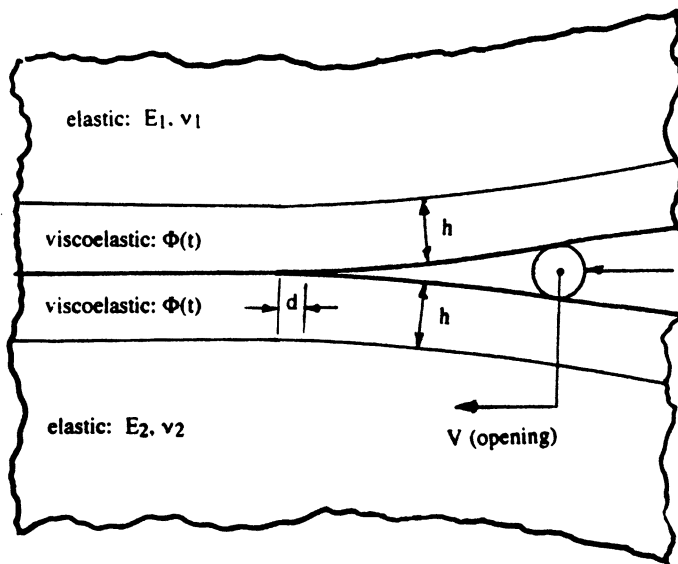


Figure 10. Interface crack between viscoelastic layers, mounted on elastic substrates.

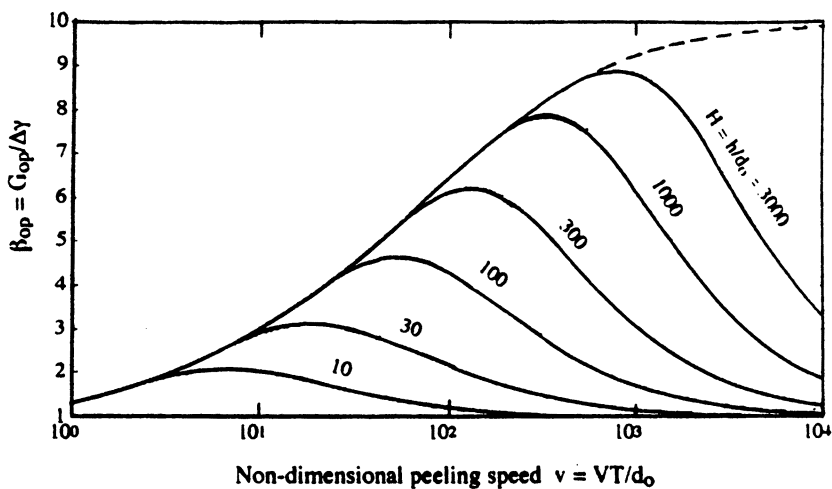


Figure 11. Effect of layer thickness h on the apparent surface energy of an opening interface crack.

compared with the radius of the contact area. As in fracture mechanics, this enables relaxation effects at the edge of contact, which govern adhesion, to be separated from effects in the bulk. Taking typical values: $E_w^* = 2 \text{ GN/m}^2$, $\Delta\gamma = 0.05 \text{ J/m}^2$, $h_o = 0.5 \text{ nm}$, equation (27) gives $d_o = 8 \text{ nm}$. Apparatus on the scale of the SFA generally has values of $a > 10 \text{ }\mu\text{m}$, so that the condition of $d \ll a$ is clearly satisfied but, with nano-probe instruments like the AFM, a may be measured in nanometres. An analysis of the situation where d is not necessarily small compared with a , when edge and bulk relaxation effects cannot be regarded as independent, is under investigation.

The contact mechanics of viscoelastic solids in the absence of adhesion is well established, but the case of a layered system calls for further work. In a loading/unloading cycle the maximum contact area is generally reached *after* the load begins to decrease, as shown in Figure 4. This feature has been demonstrated experimentally by Wahl & Unertl (17) using polyvinylethylene in a Scanning Force Microscope.

The key to analysing the adhesion of viscoelastic solids lies in Schapery's linear viscoelastic analysis of mode I fracture of an interface (12 & 13). He shows that, for an opening crack, the work of adhesion (apparent surface energy) is an increasing function of the opening (peeling) speed whereas, for a closing (healing) crack, the work of adhesion decreases with closing speed (equations (18) & (19) and Figure 7). These equations are not exact, but provide a good approximation provided that again $d \ll a$. Of course the Dugdale (uniform) variation of adhesive stress is not realistic, but an analysis by Greenwood & Johnson (14) using an inverse cube force-separation law only had the effect of changing the coefficient in equation (17) from $\pi/12$ to $1/2$. Figure 7 is plotted for a material in which $1/k = 10$; increasing this ratio extends the plot at the high speed end, but does not change the low speed end.

A loading/unloading adhesion experiment has been modelled by applying Schapery's fracture mechanics to the motion of the edge of the circular contact region between two adhering spheres. A growing contact during loading corresponds to a closing crack, while a contracting contact during unloading corresponds to an opening crack. In most experimental arrangements the load is applied through a flexible element whose stiffness is small compared with the (Hertz) stiffness of the contact itself. Thus control of the displacement of the remote end of this element leads to control of load rather than displacement of the contact. Therefore the simple ramp cycle, shown in Figure 3 is assumed, in which the load is increased and decreased at a uniform speed. The calculated variation of contact radius a with load is shown in Figure 8. Hysteresis loops are clearly revealed, which increase in width with an increase in the rate parameter A .

As shown in Figure 9, the magnitude of the pull-off force $|P_c|$ also increases monotonically with A .

The parameter A , defined in equation (24), can have a very wide range of values. It incorporates the loading rate (P_o/t_o), the viscoelastic properties of the material (k and T), the surface energy ($\Delta\gamma$) and the radius of the tip of the probe (R). For example, in the tests on polyurethane rubber shown in Figure 5, A varies between 10 and 10^4 as the peeling speed varies from 10^{-1} to $10^3 \text{ }\mu\text{m/s}$. Other things being equal, the change in tip radius from the SFA ($R = 1 \text{ cm}$) to the AFM ($R = 50 \text{ nm}$) reduces A by four orders of magnitude. It is not easy, therefore, to make useful general statements about the values of A ; each material and each experimental arrangement must be considered *ab initio*.

In experiments where a thin film of polymer is applied to an elastic substrate, the thickness of the film strongly influences the apparent surface energy, as expressed in equation (26) and shown in Figure 11. In applying this result, it must also be

recognised that the compliance of the contact is governed by the elastic modulus of the substrate. So the JKR equation (1) may be written:

$$P = (4E_e^* / 3R) - \sqrt{8\pi\beta_{op}\Delta\gamma E_e^* a^3} \quad (30)$$

where E_e^* is an 'effective modulus' of the layered system and β_{op} is given by equation (26). In general E_e^* is not constant, but is a function of the ratio of the contact radius a to the film thickness h but if this ratio is always much greater than unity, the film makes a negligible contribution to the compliance of the contact and E_e^* becomes the (constant) value for the substrate. These considerations in relation to the Surface Force Apparatus have been discussed by Sridhar et al.(16).

Acknowledgments

The author wishes to acknowledge the help of his colleagues: Dr.J.A.Greenwood for close collaboration particularly over the section on viscoelastic fracture mechanics and Dr.J.Woodhouse for assistance with the computations.

Literature cited

- (1) Johnson,K.L.; Kendall,K. & Roberts,A.D. *Proc.Roy.Soc.Lond.* **1971**, A324, 301-313.
- (2) Mangipudi,V.; Tirrell,M, & Pocius,A.V. *Langmuir* **1995**, *11*, 19-23.
- (3) Israelachvili,J In *Fundamentals of friction*; Ed.I.L.Singer & H.M.Pollock, NATO ASI Ser.E, Vol.220, Kluwer, Dordrecht, The Netherlands, pp.351.
- (4) Maugis,D. & Barquins,M. *J.Phys.D: Appl.Phys.* **1978**, *11*, 1989-2023.
- (5) Muller,V.M.; Yuschenko,V.S. & Derjaguin,B.V. *J.Coll.Interface Sci.* **1980**, *77*, 91-101.
- (6) Greenwood,J.A. *Proc.Roy.Soc.Lond.* **1997**, *453*, 1277-1297.
- (7) Maugis,D. *J.Coll.Interface Sci.* **1992**, *150*, 243-269.
- (8) Johnson,K.L. & Greenwood,J.A. *J.Coll.Interface Sci.* **1997**, *192*, 326-333.
- (9) Ting,T.C.T. *ASME, J.Appl.Mech.* **1966**, *33*, 845-854.
- (10) Graham, G.A.C. *Int.J.Eng.Sci.* **1967**, *5*, 495-514.
- (11) Johnson,K.L. *Contact Mechanics*; C.U.P. Cambridge, 1985.
- (12) Schapery,R.A. *Int.J.Fracture*, **1975**, *11*, 141-159, 369-388.
- (13) Schapery,R.A. *Int.J.Fracture*, **1989**, *39*, 163-189.
- (14) Greenwood,J.A. & Johnson,K.L. *Phil.Mag.* **1981**, *A 43*, 697-711.
- (15) Huntley,J.M. *Proc.Roy.Soc.Lond.* **1990**, *A 430*, 525-539.
- (16) Sridhar,I; Johnson,K.L. & Fleck,N.A. *J..Phys. D: Appl.Phys.* **1997**, *30*, 1710-1719.
- (17) Wahl,K.J. & Unertl,W.N. In *Tribology Issues and Opportunities in MEMS*, Ed.B.Bushan, Kluwer, Dordrecht, The Netherlands, 1998.

Chapter 3

Surface and Bulk Properties in Adherence of Elastic–Viscoelastic Solids

J. C. Charmet, D. Vallet, and M. Barquins

Laboratoire de Physique et de Mécanique des Milieux Hétérogènes,
(UMR CNRS 7636) ESPCI, 10 rue Vauquelin, 75231 Paris Cedex 05, France

The surface forces, of van der Waals type for rubber-like materials, are able to grandly modify the stress tensor provided by the contact of a blunt asperity applied against the flat and smooth surface of a rubber sample. It will be shown how the coupling of surface adhesion properties and bulk viscoelastic behavior of rubber-like material allows us to solve adherence problems. This will be illustrated through three examples: the spontaneous peeling due to the intervention of internal stresses ; the no-rebound of balls on the smooth surface of a soft elastomer and the adhesive contact and rolling of a rigid cylinder under a smooth-surfaced sheet of rubber.

When a driver jams on the brakes he thinks usually that the deceleration of the vehicle results from this action, but the true reason why the vehicle stops is in fact the great force induced by friction at the tire-road interface. It will be shown that this friction force is the direct result of the coupling of surface adhesion properties and bulk viscoelastic behavior of rubber-like materials.

It is now well-known that surface properties of solids are able to activate their bulk properties, and, as a consequence, strongly influence the mechanical behavior of the interface area of solids in contact. Our aim is to illustrate this matter through three examples: the no-rebound of balls on the smooth surface of a soft elastomer, the spontaneous peeling due to the intervention of internal stresses and the adhesive contact and rolling of a rigid cylinder under a smooth-surfaced sheet of rubber.

Preliminaries

Solving a problem of adherence requires knowledge in the fields of contact mechanics, rupture mechanics and physics of surfaces. Therefore, as a prerequisite, the main results needed for a better understanding are described below.

The friction law. The first works on friction are those of Leonardo da Vinci (1) at the beginning of the XVI century and Guillaume Amontons (2) in 1669, but the taking into account of the influence of the surface properties of solids in contact is due to Charles Augustin de Coulomb (3). In 1785 he writes the famous relationship, which is known today as Coulomb's friction law, connecting the friction resistant force T to the normal load applied N :

$$T = \mu N + A$$

In this relation the first term proportional to the applied load N is representative of the solids deformation and the coefficient μ is known today as the friction coefficient. The second term A represents the effect of the surface properties and is of great importance when the applied load N is small. This last term was introduced by Coulomb in order to explain the surprising result of previous experiments conducted by John Theophilus Desaguliers (4) in 1734. Pressing firmly together two spheres made of lead, he showed that they remained « stuck » and that a non negligible traction load was necessary to separate them.

The elastic contact. Contact mechanics was initiated by the pioneer work of Heinrich Hertz (5) in 1882. He probably realized that forces induced in the contact area of two solids pressed together are not uniformly distributed. The applied force is transmitted through a few points of contact which can be compared to spherical caps characterized by their radius of curvature. So the real size of the contact area is much lower than its apparent size. For spheres of radii R and R' of purely elastic materials, he demonstrates that the radius of the contact area a and the penetration depth δ are related to the applied load F by:

$$a^3 = FDR_{eq} \quad \text{and} \quad R_{eq}\delta = a^2 \quad \text{with} \quad D = \frac{3}{4} \left(\frac{1-\nu^2}{E} + \frac{1-\nu'^2}{E'} \right) \quad \text{and} \quad R_{eq} = \frac{RR'}{R+R'}$$

where E , E' are elastic Young's modules and ν , ν' Poisson's ratios of the constitutive material of each sphere. This well known result is of current use in mechanics, however, it didn't take into account the adhesive properties of the surfaces in contact.

In 1885 Joseph Boussinesq (6), trying to extend the validity of these results to the case of axi-symmetrical rigid convex punches indenting a flat semi-infinite elastic medium, demonstrates that, without an adequate boundary condition, the size of the contact area is generally unknown. In order to overcome this difficulty, he imposes that normal stresses vanish on the border of the contact area. In other words, the profile of the distorted medium must be tangent to the surface of the punch on the border of the contact area. Note that this condition is the same as the condition presupposed by the Hertz's theory. With this assumption, the size a_H of the contact area and the penetration depth δ_H are completely defined (Figure 1).

An observed penetration depth $\delta \neq \delta_H$ rewritten as $\delta = \delta_H + (\delta - \delta_H)$ corresponds to the addition of a vertical displacement $\delta - \delta_H$ at constant radius of contact a_H , that is to say to the addition of the vertical movement of a flat rigid axi-symmetrical punch inducing a strong divergence of the normal stresses on the border of the contact area.

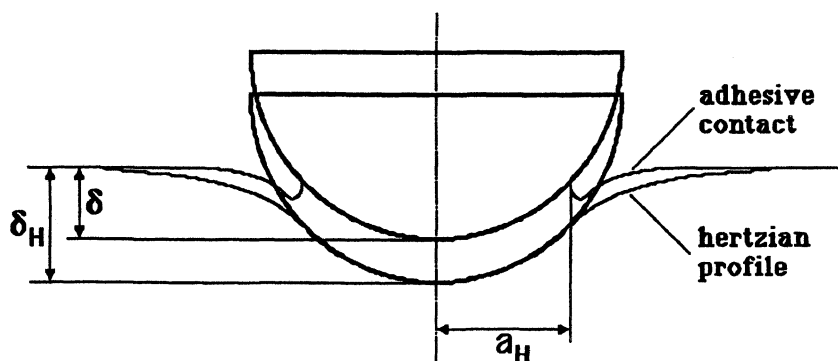


Figure 1. Comparison of distorted surface profiles of the pure elastic contact (Hertz) and of the adhesive one between a spherical punch and a flat plane and smooth surface of an highly elastic substrate for the same radius a_H of the contact area.

With a great insight, Boussinesq noticed that this singularity exists only if the solids in contact exhibit adhesion. This proposal is now interpreted in the opposite way: adhesion of solids create a singularity in the stress distribution near the border of the contact area.

Griffith's theory of brittle fracture. The connection between bulk and surface properties of solids appears for the first time in the work of Griffith (7). In 1920 he writes his famous condition of crack propagation: the work $2\gamma dA$ consumed by the creation of a new surface of crack dA is deducted from the elastic energy stored in the solid by the stresses or strains applied to it. So, in addition to the Young's modulus E and the Poisson ratio ν characterizing the behavior of intermolecular forces when the atoms are slightly displaced from their equilibrium position, we must introduce the surface energy γ which gives the work necessary to break bonds per unit area along an imaginary plan and to reversibly separate the two parts of the solid of isothermal manner. This surface energy γ is not different from the bond energy insuring the cohesion of solids. Dimensionally γ is the product of the Young's elastic modulus E by an interatomic spacing.

In order to establish the equilibrium condition of a crack, we consider a thermodynamically isolated system of constant total energy U composed by a solid containing a crack of surface A and its loading apparatus. Its energy is the sum of three terms: $U=U_P+U_E+U_S$ where U_P is the potential of the applied forces, U_E the elastic energy stored and U_S the surface energy associated to the crack. With $W_P=-U_P$, work of the applied forces, and $U_M=-W_P+U_E$ the mechanical energy of the system, the equilibrium condition $dU=0$ of the crack is given by application of the principle of virtual work:

$$G = -\left(\frac{\partial U_M}{\partial A}\right) = \frac{\partial W_P}{\partial A} - \frac{\partial U_E}{\partial A} \equiv \frac{\partial U_S}{\partial A} = 2\gamma$$

G , first letter of Griffith name, is the « strain energy release rate ». G is only a function of the solid and crack geometry and of the loading conditions. It can be calculated by solving the elastic linear equations of the problem. At the opposite, γ is a material property of the solid.

As usual, the equilibrium stability is given by the sign of the second derivative of the total energy:

$G < 2\gamma$	$G = 2\gamma$	$G > 2\gamma$
crack closing	open crack equilibrium	crack propagation at velocity V
	$\frac{\partial G}{\partial A} < 0$ stable	$\frac{\partial G}{\partial V} < 0$ controlled
	$\frac{\partial G}{\partial A} > 0$ unstable	$\frac{\partial G}{\partial V} > 0$ spontaneous

$G - 2\gamma$ is the motive energy of crack extension.

In the Griffith model (Figure 2), the surface energy vanishes on the crack and rises steeply to the value 2γ at the crack tip, inducing a singularity of the stress

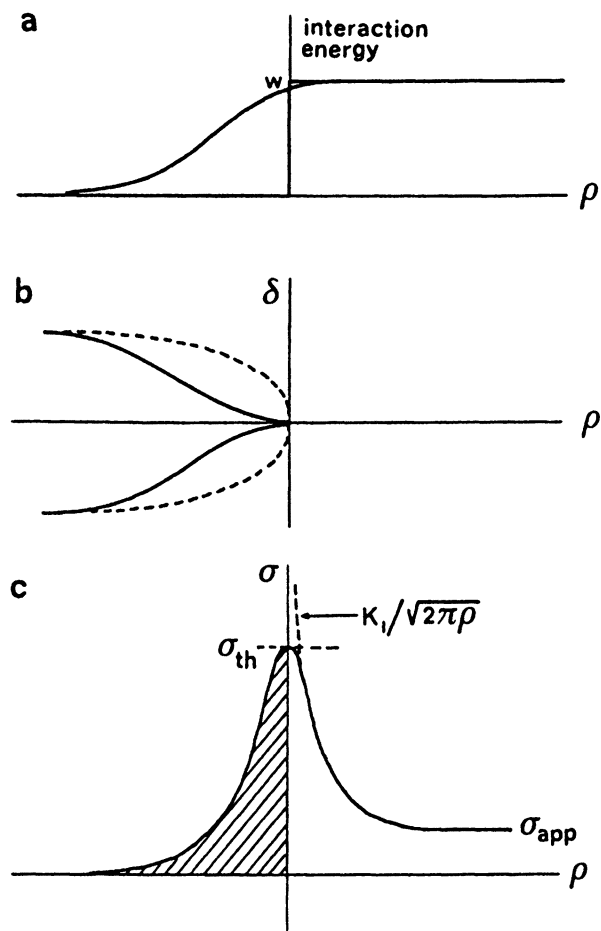


Figure 2. Interaction energy, opening displacement δ and stress distribution σ between the two sides of a crack as a function of the distance ρ from the crack tip. In Griffith's model, there is no interaction between the two sides of the crack and the surface energy $w=2\gamma$ appears as a step function (Figure a). The shape of the crack tip is parabolic (Figure b, dotted line) and the stress distribution, null inward the crack, is singular outward (Figure c, dotted line) varying as $K_I/\sqrt{2\pi\rho}$. In Barenblatt's model, the cohesive forces act on a finite but short distance inward the crack tip and the surface energy, null on the most part of the crack, increases progressively over this distance, reaching the value w at crack tip (Figure a). The sides of the crack are elastically distorted, giving the shape of the crack tip (Figure b, heavy line). There is no singularity of stress at the crack tip (Figure c, heavy line) and the maximum stress is equal to the theoretical stress σ_{th} deduced from the strength of the interatomic bond.

distribution varying as $\frac{K}{\sqrt{2\pi r}}$ where r is the distance to the crack tip. This non-physical singularity is characterized by the factor K named « stress intensity factor ». As Irwin (8) showed, in plane strain opening mode of the crack K and G are linked by the relation $\frac{E}{1-\nu^2}G=K^2$. This relation emphasizes the equivalence of the global energetic approach (rate G) and the local analysis of stress distribution (factor K).

In the sixties Barenblatt (9) and Dugdale (10) were interested in the problem of the distribution of cohesive forces in the crack tip. The Griffith equation of crack equilibrium $G=2\gamma$ don't allow us to understand the role played by the attractive molecular forces. In 1962 Barenblatt demonstrated the existence of cohesive forces acting on a short length of the crack end. In brittle solids all the resistant energy of the crack is concentrated in this small zone. Analyzed in term of stresses, this energy distribution is associated to a singular stress distribution of stress intensity factor K_m characterizing the material. Without external loading, these cohesive forces tend to close the crack. At equilibrium, this factor exactly compensates the factor K produced by the external loading, the stresses take finite values and the two surfaces of the crack join tangentially at the crack tip as physically expected (Figure 2). The stresses are recognized elastic outward from the crack tip and cohesive inward.

Adhesion and rupture. We now interpret adhesion phenomena from the point of view of the rupture mechanics. When dissimilar bodies are in intimate contact, attractive forces exist also and, trying to separate them, an energy equal to $w dA$ must be supplied to achieve their separation on an area of size dA . This energy is of the same nature as the surface energy $2\gamma dA$, however, we must take into account the elastic energy stored in the interface during the initial stage when the two solids was stucked together. So $w=\gamma_1+\gamma_2-\gamma_{12}$, called the Dupré adhesion energy, is the sum of the surface energies γ_1 and γ_2 of each solids reduced by the interfacial energy recovered γ_{12} .

The subject of adhesive contact mechanics may be said to have started when Kendall (11), solving the problem of the adhesive contact of a rigid flat cylinder punch indenting the smooth plane surface of an elastic medium, demonstrated that the border of the contact area can be considered as a crack tip. The more complex problem of a spherical punch was solved in 1971 by Johnson, Kendall and Roberts (12). The JKR theory predicts the existence of contact area greater then that given by the elastic contact Hertz's theory. The molecular attractive forces are responsible for this increase and, even in the absence of external compressive loading, the contact area has a finite size. Separating the two solids requires the application of an adherence force despite the existence of infinite normal stresses in the border of the contact area.

The energy balance of Griffith's theory cannot give information about the stability of the system that depends upon the second derivative of the total energy. That is the reason why Maugis and Barquins (13) were led to reintroduce the concepts of fracture mechanics such as the strain energy release rate G in order to study the stability according to the sign of the derivative of G . This approach has the advantage of enabling one to study the kinetics of crack propagation and to predict the evolution of the system whatever the geometry of contact and loading conditions. Therefore,

adding knowledge of contact mechanics, rupture mechanics and physics of surface is a necessity to obtain pertinent answers to solid adherence problems.

As adhesive forces are generally weak, the strains induced remain very small for most of the currently used materials. For this reason most of the experiments have been conducted on elastomers because the surface forces, of van der Waals type for these rubber-like materials, are able to greatly increase the stress tensor provided by the contact of a blunt asperity applied against the flat and smooth surface of rubber samples. As a consequence they have the great advantage of giving large visible deformations.

The viscoelastic losses. The equilibrium $G=w$ may be disrupted by a change the applied load or displacement. As soon as $G>w$ the crack supports a force $G-w$ per unit length. If the solid is purely elastic, the crack accelerates at fixed $G-w$ until its propagation speed reaches the Rayleigh velocity of the surface waves. For real bodies with internal losses the crack takes instantaneously a velocity such that the losses balance exactly the motive energy $G-w$, further evolution of the crack speed V depends upon the variation of $G-w$ with the length of the crack. In adhesive contacts, when $G>w$, the two bodies begin to separate and their separation can be seen as the propagation of a crack in the opening mode, the contact area decreasing as the crack grows. The modified energy balance can be written as $G-w=\Psi(V)$ where Ψ is the dissipation function associated to the internal losses (14).

For rubber-like materials, the viscoelastic losses vary with the strain rate and the temperature. The principle of « time-temperature » equivalence proposed in 1955 by Williams *et al.* (15) allows us to superimpose the experimental curves obtained at different temperatures through the known translation factor a_T of the WLF transformation. As a consequence, at fixed geometry, the adherence forces provoking crack extensions at different speeds V can be studied as a function of the reduced parameter a_TV .

As suggested by peeling experiments (16), it is usually assumed that viscoelastic losses are proportional to w and are only localized at the crack tip. As a consequence, Maugis and Barquins (13) have proposed in 1978 to rewrite the dissipation function $\Psi(V)$ as:

$$\Psi(V)=w\Phi(a_TV)$$

where the second term is the viscous drag resulting from the losses limited to the crack tip. $\Phi(a_TV)$ is a dimensionless function of the crack speed V and of the temperature through the shift factor a_T of the William-Landel-ferry transformation.

This function Φ is a characteristic of the viscoelastic material for the propagation in opening mode, independent of the geometry of contact and the loading system. Knowledge of the function Φ makes it possible to predict the evolution of the contact area in all circumstances. The prediction assumes only that rupture is adhesive, *i.e.*, that the crack propagates at the interface and the application of the modified energy balance $G-w=w\Phi(a_TV)$ implies that gross displacements are purely elastic, with G computed from the relaxed elastic modulus E and that the frequency dependence of E only appears at the crack tip where deformation velocities are high. Therefore the loss factor E''/E' (E' and E'' being the real and imaginary components of E) and its

frequency dependence are taken into account in the function Φ (17). The interesting feature of this balance is that surface properties (w) and viscoelastic losses (Φ) are clearly decoupled from the elastic properties, geometry, and loading conditions that only appear in G .

For elastomers, it has been shown that over a large range of speeds of propagation (10^{-1} - 10^4 $\mu\text{m/s}$), the function Φ may be represented by the power function $\Phi(a_T V) = a(T) V^n$ where $a(T)$ is a parameter depending on the temperature T and n takes the value 0.6 for polyurethane and 0.55 for natural rubber (Figure 3). Moreover, the multiplicative effect of w on viscoelastic losses, can only arise if the interface is itself capable of withstanding stress.

The spontaneous peeling

Most varnishes, paints, and coatings have the drawback of flaking and peeling off, by propagating of a crack at the interface, when the substrate is deformed, for instance, by thermal expansion. In order to better understand this behavior, we have set up a simple model, together with an experimental arrangement consisting of two transparent rubber strips in adhesive contact, in which one strip is submitted to a fixed tensile elongation or to a fixed crosshead velocity (18).

Model. Let us consider (Figure 4a) a long lap shear joint made by contacting two smooth strips of elastomer, with Young's moduli E_1 and E_2 , the same width b , and thickness h_1 and h_2 , in adhesive contact on to an area $A = bL$, without initial prestress. If an adequate tensile elongation $\epsilon = \delta/L$ is imposed to the substrate, a crack appears at the free end of the upper strip and propagate inwards along the interface (Figure 4b), the spontaneous delamination resulting in complete loss of contact. If, at a given time, x is the length of the relaxed peeled part of the upper strip, a simple application of Hooke's law to the double layer of length l and to the strained free end of the substrate allows one to calculate the force applied to the system. The derivative of the corresponding stored elastic energy $U_E = \frac{1}{2} F \delta$ allows us to calculate the strain energy release rate G which can be written as

$$G = \frac{1}{2} \delta^2 E_1 h_1 E_2 h_2 \frac{E_1 h_1 + E_2 h_2}{(L E_1 h_1 + x E_2 h_2)^2}$$

As $\left. \frac{\partial G}{\partial A} \right|_s > 0$, this equilibrium is stable, *i.e.*, if a fluctuation decreases the

contact area A , G incrementally decreases, and one has $G < w$, the crack recedes to its equilibrium position. It can only advance if the tensile elongation $\epsilon = \delta/L$ is varied bringing back G to the value w : one is dealing with the controlled rupture of an adhesive joint. As soon as an instantaneous tensile elongation greater than ϵ_{init} . given by $G = w$, with $x = 0$, is applied to the substrate, a crack is immediately initiated at the extremity of the upper strip, and propagates in the interface. Then, x increases and G continuously decreases with time. The propagation can lead to an equilibrium state if G takes the value w before the crack reaches the other extremity of the substrate, *i.e.*,

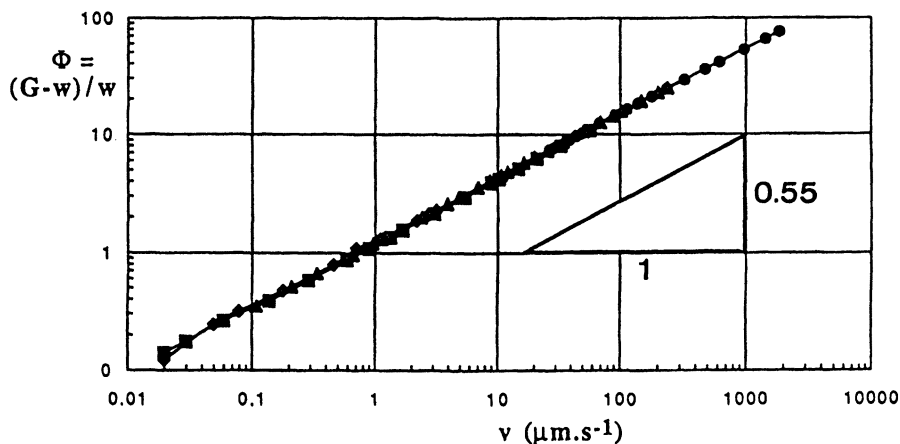


Figure 3. Dissipation function $\Phi=(G-w)/w$ versus crack speed V . Φ varies as $V^{0.55}$ in a large range of velocities. The power index 0.55 is a characteristic of the natural rubber.

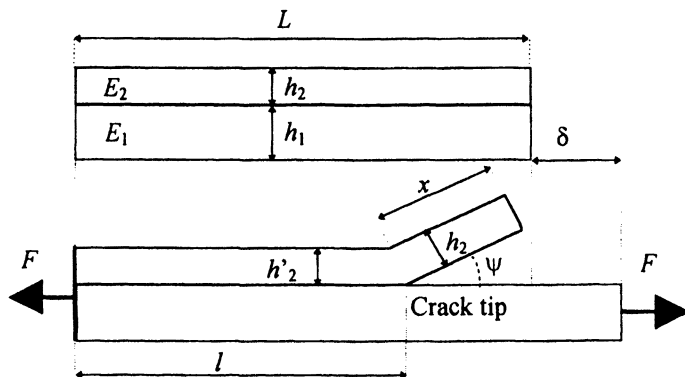


Figure 4. Geometry of the adhesive joint before (Figure a) and after (Figure b) extension δ of the substrate.

$x < L$, or to the complete rupture of the contact if $G > w$ with $x = L$. So, it is possible to define a new critical value of ϵ_{crit} corresponding to complete delamination (Figure 5).

The application of Hooke's law to the system also enables one to write the relation including all the geometrical parameters, so that the length x of the peeled strip, the resulting traction force F and the crack velocity $V = \frac{dx}{dt}$ can be deduced from the measured variation with time of the length l of the adhesive part of the joint. So, the strain energy release rate G can be experimentally related to the crack speed V given access to the exponent n of the dissipative function.

Experiments and results. The viscoelastic material chosen was an optically smooth polyurethane, recommended for dynamic studies in photoelasticity (PSM4 Vishay, with $E = 3.6$ MPa). The surfaces were wiped with an alcohol-soaked cloth, dried with warm air and left, sheltered from dust, for 30 min for the equilibrium with room temperature to be reached. Then, two strips of thickness $h = 3.175$ mm with various lengths L and widths b varying in the range 5-20 cm and 5-20 mm, respectively, were gently superimposed, and they adhered under only molecular attraction forces, without additional adhesive. In order to avoid the dwell time effect (19), strips were coupled during the same contact duration 30 min, for all experiments. Moreover, temperature (23°C) and humidity (84%) were kept constant. In these conditions, the reproducibility is better than 3%.

Experiments at fixed grips conditions and at fixed crosshead velocity were carried out using a tensile machine that enables one to impose speeds varying in the range 0.5-500 mm/min, and to measure forces up to 50 N. For a quantitative evaluation of the crack speed during the delamination, a 16-mm camera recorded the experimental arrangement at a rate varying from 10 to 50 frames/s; the frames were then enlarged and the distance l measured (Figure 4b).

Dissipation function. Corresponding values of the strain energy release rate G and its associated propagation crack speed V deduced from the measurement of $l(t)$ confirm that the dissipation function ϕ for polyurethane samples varies as the 0.6th power of the crack speed. Taking into account $a(T) = 4.75 \cdot 10^4$ SI units, corresponding to the room temperature 23°C, the mean value of Dupré's work of was found to be $w = 41$ mJ/m² (± 1 mJ/m²), a fairly low value due to the high humidity ratio (20).

Force variation. By numerical integration of the general equation for the adherence of viscoelastic materials $G - w = w\Phi$ and taking into account the variation of Φ with the 0.6th power of the crack speed, it is also possible to predict the variations of the force during the spontaneous peeling. As expected, an increase in tensile elongation provokes a proportional increase in the initial force, and the time required to observe complete delamination is shorter, with the force then remaining constant. The computed curves are in quite good agreement with experimental results.

Peeling angle. During crack propagation, the spontaneous peeling angle ψ was also measured (Figure 4b), and a slow increase with time was observed. Simple geometrical considerations associated with the incompressible character of the

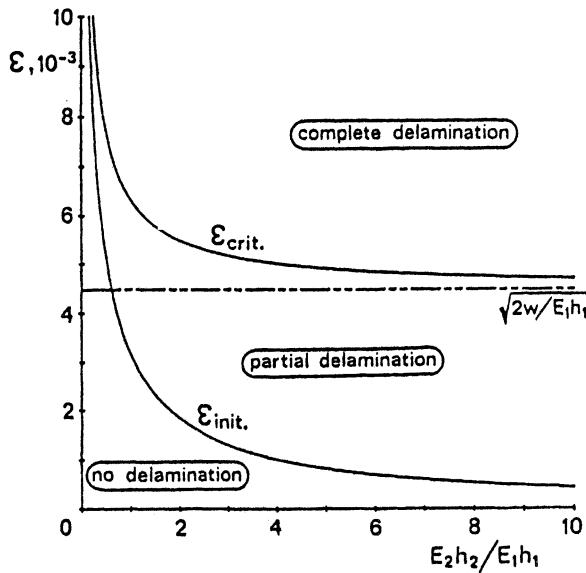


Figure 5. Range of the delamination domain as a function of the relative transversal stiffness of the peeling strip and of the substrate after its instantaneous extension δ .

tested material enable one to relate the value of angle to the uniaxial strain in the adhering upper strip. Indeed, to a first approximation, the flaking of the peeled strip can be easily ascribed to the variation of the thickness between the two adhering and relaxed states, and we can write $\cos\psi = h'/2h_2$, hence, if ϵ is not too high, $\psi \approx \sqrt{\epsilon}$. Although, the substrate is not a rigid body, and is not perfectly planar in the vicinity of contact zone due to the asymmetry of the experimental arrangement, measurements of peeling angle confirm the prediction with an accuracy of better than 8%.

As expected, the knowledge of the function Φ allows one to predict the evolution of the system, among other things, the force involved and contact duration before rupture. Due to its elementary nature and also its sound validity, this model may be suitable for solving certain practical problems such as the ability of varnishes, paints, and coatings to adhere on deformable substrates.

The bouncing ball

The rebound of rigid balls on a rubber surface is influenced by the existence of a coupling between bulk and surface properties. Starting from the observation that, under some circumstances closely related to the intervention of molecular attraction forces of van der Waals type, there is a critical release altitude below which a rigid ball sticks on a rubber sample and does not rebound at all (21), numerous experiments were carried out to measure with accuracy this critical altitude and rebound heights when molecular attraction forces act (22). A simple energy balance theory is proposed to predict correctly the rebound height of several different-sized polished stainless steel balls and projectiles, colliding with a horizontal, planar, glass-smooth and cleaned surface of a natural rubber thick sample.

Theoretical considerations. First, let us consider a rigid ball (of weight Mg) colliding with a non-adhesive plane (rubber surface contaminated with talcum powder to prevent adhesion of the ball) with a relative impact speed $V_c = \sqrt{2gh}$. The ratio $\alpha_0 = h'/h$, where h (respectively, h') the release altitude (respectively rebound height), characterizes the losses in the bulk of the viscoelastic material, without intervention of molecular attraction forces. Due to the shortness of the collision time (19) the penetration of the ball into the rubber surface occurs according to the classical theory of Hertz, even for an adhesive surface, so that maximum values of radius a_{\max} of the contact area and the elastic penetration depth δ_{\max} are closely related to the release altitude h by $a_{\max} \sim h^{1/5}$ and $\delta_{\max} \sim h^{2/5}$ through known prefactors depending upon mass M and radius of curvature R of the indenter and upon elastic properties of the substrate.

Assuming that the duration of penetration is equal to the duration of ejection from the rubber surface, each time it takes the value (23) $\tau = \delta_{\max}/V_c$ so that the ejection time of the ball can be rewritten as $\tau \sim h^{-1/10}$ with a known prefactor depending, among other things, upon $\alpha_0^{-1/5}$. The energy, W_{motor} actually available when the maximum penetration depth δ_{\max} occurs, is given by $W_{\text{motor}} = \alpha_0 Mgh$.

Assuming that molecular attraction forces act, it is obvious that they play an important role only during the ejection of the ball, due to the shortness of the collision

time. The separation never occurs as a whole but the area of contact is progressively reduced until complete separation is achieved. This reduction in contact area can be considered as resulting from the propagation of a crack, and the concepts of fracture mechanics can be used. During its propagation, the crack undergoes a drag in proportion to w and is a function of the crack velocity, $V=da/dt$, as already mentioned above. The energy dissipated by the crack propagation during the ejection of the ball can be written as kwV^n , where k and n are material dependent parameters. This energy dissipated during the separation is the sum of two terms: the interfacial energy given by wS (where S is the contact area, $S=\pi a^2$) and the energy dissipated in the immediate vicinity of the crack, W_{drag} given by the integration of the drag during the separation time. Unfortunately, the kinetics of the separation is unknown. Nevertheless, it is possible to assume (and confirm by experiments), as in the Hertz theory, that the ejection time is equal to the time of penetration τ , and to take the ratio a_{max}/τ as an estimated average of the velocity $\langle V \rangle$ of the crack, so that $\langle V \rangle$ scales as $h^{3/10}$.

Taking into account the general equation $G-w=w\phi(V)$ rewritten using the estimated speed $\langle V \rangle$ of the crack, one obtains $\langle (G-w)/w \rangle = k\langle V \rangle^n$ and the interfacial dissipation term, W_{drag} scales as $kwS\langle V \rangle^n$. Due to the large value of the coefficient k , ($k \gg 1$) (24), the interfacial energy, wS , is negligible compared with the interfacial dissipation term and the energy balance $W_{\text{motor}}=wS+W_{\text{drag}}$ reduces to $W_{\text{motor}}=W_{\text{drag}}$. This balance gives the critical release altitude hc below which sticking occurs:

$$hc = \left(\frac{A}{B} \right)^{10/(6-3n)}$$

with A scaling as $kwR^{(4+3n)/5}$ and B as $M^{(3+n)/5} \alpha_0^{(8-n)/10}$.

For $h > hc$ the rebound height is obviously provided by $h' = (W_{\text{motor}} - W_{\text{drag}})/Mg$. Using the above expression of hc it can be expressed in the reduced form:

$$\frac{\alpha_0 h - h'}{h_c} = \alpha_0 \left(\frac{h}{h_c} \right)^\beta$$

with $\beta = (4+3n)/10$ allowing the determination of the material exponent n through the elementary measurements of rebound heights.

Experiments and results. From concepts and experimental data outlined above, we have studied the rebound of a polished rigid ball (steel ball) on the flat and glass-smooth surface of a soft natural rubber sample (22). The steel ball was kept in position under a glass sheet with the help of a magnet. The vertical distance between the bottom of this ball and the cleaned surface of a thick (16mm) and soft natural rubber block was measured accurately. Six steel balls (from ball bearings) of diameter 2, 3, 4, 6, 8 and 10 mm and four indenters made from steel balls in order to obtain, on the one hand, three masses (0.173, 0.262 and 0.327 g) with the same diameter (4 mm) and, on the other hand, three radii of curvature (3, 4 and 6 mm) with the same mass (0.262 g) were employed. They were dropped onto the horizontal, plane, smooth, cleaned (with pure ethanol) and dried surface of the thick natural rubber sample.

All experiments were initiated by gently raising the magnet from the glass sheet and rebound heights were recorded with the help of a video camera coupled to a video recorder in order to make accurate measurements. The *pure latex* natural rubber soft sample tested was obtained by molding the compound against a glass smooth polished steel plate, using the following vulcanization conditions: 2.0 parts of dicumyl peroxide and a temperature of 150°C during 20 min, so that the glass transition temperature was equal to -68°C. The mechanical properties of the rubber specimen thus obtained were Young's modulus $E=0.89$ MPa and Poisson's ratio $\nu=0.5$.

Rebound heights. Curves I on Figure 6, show rebound heights h' as a function of release heights h for six balls made of stainless steel: surface effects are superimposed on bulk properties. Experimental data (symbols) verify computed predictions (heavy lines) established from the classical theory of Hertz and the general equation of the adherence previously indicated, with $\Phi \approx V^{0.55}$ for a natural rubber sample. It is only assumed that the duration of penetration of a ball is equal to the duration of ejection from the rubber surface.

The theoretical curves, I, corresponding to a non-contaminated rubber surface, are obtained by the following procedure. For each ball, the critical release altitude was accurately measured so that the mean value of the parameter $\langle kw \rangle$, product of the temperature factor and the Dupré energy of adhesion, was correctly determined: $\langle kw \rangle = 35.15 \text{ mJ} \cdot \text{m}^{-2.55} \cdot \text{s}^{0.55}$. Taking into account the value $k = 1440 \text{ m}^{-2.55} \cdot \text{s}^{0.55}$, previously assessed in similar ambient conditions (24), one deduces that Dupré's energy of adhesion is equal to $w = 24 \text{ mJ} \cdot \text{m}^{-2}$ a low value which is reasonable taking into account the shortness of the collision time (19). So, if the ambient conditions (temperature and relative humidity) are known, this rebound method offers the advantage of measuring the Dupré's energy of adhesion for short contact times.

For comparison, curve II shows rebound heights h' versus release altitudes h when the surface was dusted with talcum powder in order to prevent adhesion of the balls. These results have been used to determine the energy restitution coefficient α_0 . It was calculated as $\alpha_0 = 0.625$, which is a value commonly found on a soft natural rubber sample when molecular attraction forces do not act.

Starting from the experimentally-determined estimate of $\langle kw \rangle$, the dissipated energy W_{drag} may be theoretically evaluated as well as the computed rebound height. Figure 4 allows us to conclude that there is a very good agreement between the experimental data (symbols) and the rebound height predicted by the energy balance criterion proposed (lines).

Material exponent. From release altitudes h , corresponding rebound heights h' , critical rebound height values h_c and the resilience α_0 of the rubber-like material tested, the slope β of the rectilinear log-log curve (Figure 7) allows one to calculate the parameter n which characterizes the viscoelastic behavior. Figure 7 regroups all the experimental points measured with all the projectiles on the cleaned, adhesive natural rubber. Linear regression of all the points gives a slope $\beta = 0.564$ so that n takes the value $n = 0.546$ which is in close agreement with the value $n = 0.55$ previously deduced from recent rolling experiments on the same rubber sample (24) and used to draw computed curve on Figure 7. In fact, it is possible now to point out that the *a priori* knowledge of the exponent n was not necessary to draw computed curves on Figure 6.

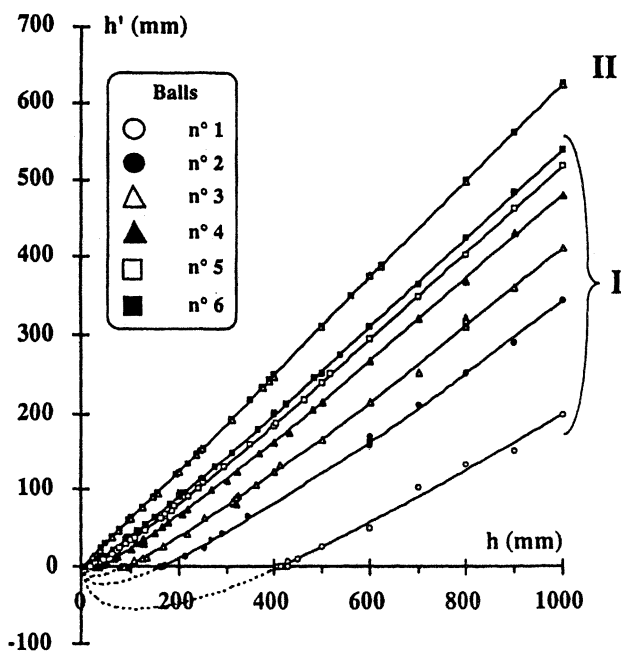


Figure 6. Rebound heights of six polished balls made of stainless steel, of diameters 2, 3, 4, 6, 8 and 10 mm, dropped on the horizontal, plane and smooth surface of a soft natural rubber sample (Young's modulus $E=0.89$ MPa and Poisson's ratio $\nu=0.5$). Curves I: the surface was cleaned with pure ethanol and dried with air, so that surface effects, due to van der Waals forces, were superimposed on bulk viscoelastic properties. Curve II: the surface was dusted with talcum powder to prevent adhesion. Experimental data (symbols) correlate quite well with computed predictions (heavy lines).

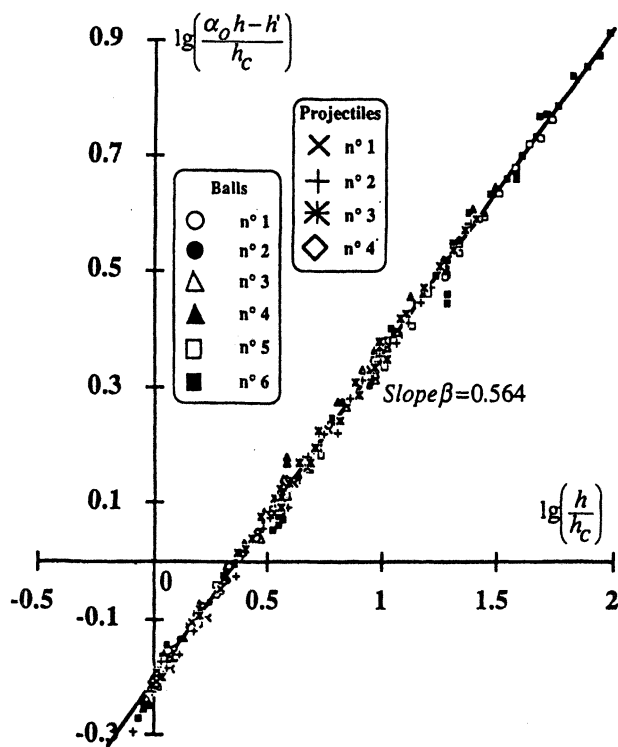


Figure 7. Master curve, in log-log coordinates, regrouping all the adhesive rebound critical heights (balls and projectiles), which allows one to determine, from its slope β , the index n characterizing the viscoelastic behavior of the natural rubber sample tested.

As a consequence, the existence of this master curve validates the model, particularly the dependence of the ratio A/B upon the curvature radius R and the mass M of the projectiles. This ratio varies as R^1 , hence, the critical release altitude hc , below which sticking occurs, varies as $(A/B)^{10/(6-3n)}$, a negative power of R which is consistent with the recent theory of Johnson and Pollock (25).

Mainly, the understanding of the bouncing process of small particles on various substrates is important for numerous applications including aerosol physics and coatings technology for which a strong adhesion is wanted. In the literature, several experiments are described and theories are proposed to explain why small particles may be captured, so that no rebound occurs (26-31). Particularly, these theories have attempted to combine both the surface effects and bulk dissipative deformation of solids.

The rolling cylinder

Again, due to the intervention of molecular attraction forces, a rigid cylinder can remain in equilibrium position under the pull of gravity on the underside of a smooth-horizontal surfaced sheet of rubber if its weight per unit axial length is lower than a critical value. Moreover, at static equilibrium under the load per unit axial length P , the length $2b$ of the contact area is larger than the value which can be deduced from the classical Hertz theory (32). For an inclined sheet, the mechanical approach of the rolling contact of a rigid cylinder under this inclined surface, if molecular attraction forces act, allows one to demonstrate, contrary to our intuition, that rolling of the cylinder occurs even if its weight per unit axial length is much greater than the critical load in static equilibrium under a horizontal surface.

Static equilibrium. Let us consider the equilibrium contact area between a long and rigid cylinder (length L and radius R) and the flat and smooth surface of an elastic half-space characterized by its Young's modulus E and its Poisson's ratio ν . Under its weight per unit axial length P , the half-width b_H of the contact area, derived from the Hertz theory, is:

$$b_H = \sqrt{\frac{4PR(1-\nu^2)}{\pi E}}$$

Of course, the length of the contact area is equal to the cylinder length. However, as it was pointed out by Johnson *et al.* (12) in 1971 for contacts of spheres, Hertz's theory do not take into account the attractive molecular forces, (van der Waals's forces in the case of elastomers) which contribute to the increase of the contact area, so that the actual half-width b of the cylinder contact is greater than b_H . But, it exists some difficulties to evaluate the elastic penetration so that the direct calculation of the strain energy release rate G , from the energy balance theory, is impossible. Conversely, as suggested by Savkoor and Briggs (33) in 1977 for spherical punches, G can be calculated from the stress intensity factor K at the edge of the contact area.

Let us assume that the actual size of b results from the action of the *apparent* Hertz load $P_1 > P$ in the absence of surface energy effects ; its value can be expressed by an equation similar to the above one. Then, at constant width, one can decrease the load per unit axial length from the fictitious value P_1 to the actual value P by increasing surface energy.

According to Boussinesq's intuition, this procedure creates normal tensile stresses at the edge of the contact area similar to these provoked by the vertical displacement of a flat punch rectangular in shape, with the same length L as that of the cylinder and a width equal to $2b$, when the flat punch is submitted to the linear force per unit axial length $P_1 - P$. Hence, the difference $P_1 - P$ is representative of the adhesion forces which play their greatest role when the actual load P tends to zero. Obviously, the previous procedure assumes that the degree of indentation of the elastomer sample by the rigid cylinder is small i.e., the width of contact area is very small with respect to the cylinder radius.

At the distance r of the longitudinal symmetry axis of the contact area, the normal tensile stress can be written (24) $\sigma = (P_1 - P) / (\pi \sqrt{b^2 - r^2})$ so that the stress intensity factor K at the edge of the contact area for crack propagating in opening mode is equal to $K = (P_1 - P) / \sqrt{\pi b}$. Like any three-dimensional crack, the edge of contact area is subjected locally to a plane strain state, so that the strain energy rate G is linked to the stress intensity factor K by the Irwin relation $G = \frac{1}{2} K^2 (1 - \nu^2) / E$, where the factor $\frac{1}{2}$ is introduced in order to take into account the punch rigidity. The equilibrium state of the contact system, defined by $G = w$, gives the equilibrium relationship :

$$P = \frac{\pi E^* b^2}{4R} - \sqrt{2\pi E^* b w} \quad \text{with} \quad E^* = \frac{E}{1 - \nu^2}$$

As expected, its right hand side is the difference of an Hertz's term and an adhesive term. This equilibrium can be stable, unstable according to the sign of $(\partial G / \partial A)_P$. The load P_C corresponding to the limit of stability $(\partial G / \partial A)_P = 0$, which may be called the elastic adherence force representing the critical tensile force for which the spontaneous rupture of the contact area just begins, and the associated half-width b_C of the ultimate contact area are equal to

$$P_C = -3P_S \quad \text{with} \quad P_S = \sqrt[3]{\frac{\pi E^* w^2 R}{16}} \quad \text{and} \quad b_C = b_S \quad \text{with} \quad b_S = \sqrt[3]{\frac{2\pi w R^2}{\pi E^*}}$$

Consequently, a rigid cylinder, of weight per unit axial length P smaller than the absolute value of P_S remains in equilibrium contact **under** the elastomer surface, due to the intervention of surface energy effect. Using the above relations and introducing the reduced force $[P] = P / |P_S|$ and lengths $[b] = b / b_S$ the equilibrium relationship takes the simple form:

$$[P] = [b^2] - 4 \sqrt{[b]}$$

For example, figure 8 shows half-width of the equilibrium contact area between smooth cylinders made of steel and PMMA cylinders in contact against the flat surfaces of an unfilled natural rubber ($E=0.9$ MPa) and of a styrene-butadiene copolymer ($E=2.2$ MPa). As expected, experimental data (35) fall in the immediate vicinity of the theoretical curve (heavy line).

Kinetic of rolling. Let us consider now the rigid circular cylinder of radius R and of weight P per unit axial length, rolling at constant speed V when the tangential force F per unit axial length is applied (Figure 9). The contact area, with width $2b$, can be seen as limited by two crack tips which propagate in the same direction (rolling direction) and with the same mean velocity: in the front part, there is a closing crack characterized by a healing mechanism and at the rear part, an opening crack, where the major part of the energy is dissipated by viscoelastic losses in a classical peeling mechanism, so that a large extension is observed at the trailing edge. This is the reason why the front and rear boundaries are not symmetrical with regard to the normal symmetrical axial plane containing the top of the cylinder (point O in figure 9).

Moreover, at the leading edge, the profile can be approximated as an equilibrium profile ($G=w$). Indeed, in spite of the short contact time, molecular attraction forces can always act, even if the rolling speed is very great, as that has been verified in previously described rebound experiments (22).

By convention, let α and β be the respective front and rear half-widths of the contact area, so that $\beta+\alpha=2b$ and $\beta-\alpha=2d$. Following the same mechanical approach as in the above static case the normal tensile stress can be written in the general case (35-36) $\sigma = \{-P/\pi + (E^*/2R)(r^2 - rd - b^2/2)\} / \sqrt{(b^2 - r^2)}$. Assuming that, as already said, the leading edge of the contact area is a crack in the equilibrium state, *i.e.* $G=w$, this last relation rewrites as:

$$P = \pi E^* b^2 / 4R - \sqrt{2\pi E^* b w} - \pi E^* b d / 2R.$$

Adding the equation of moments equilibrium with regards to the instantaneous center of rotation (point O), allow us to write the relation linking load P and tangential rolling force F as a function of characteristic lengths of the contact area (b and d):

$$P = \pi E^* b^2 / 4R - FR / d.$$

The two above relations form a system of two equations with two unknowns b and d , as a function of P and F , whose solution, taking into account the normalization by P_s and b_s , is (37):

$$\begin{aligned} d\sqrt{b} &= b_s^{3/2} \{ \sqrt{1 + F/w} - 1 \} \\ b^2 - 2b_s^{3/2} \{ \sqrt{1 + F/w} + 1 \} \sqrt{b} - Pb_s^2 / P_s &= 0 \end{aligned}$$

Let us consider the three following dimensionless variables:

$$u^3 = \frac{1}{2} \{ \sqrt{1 + F/w} + 1 \} \quad q = u \sqrt{b/b_s} \quad Q = -P / (3P_s u^4)$$

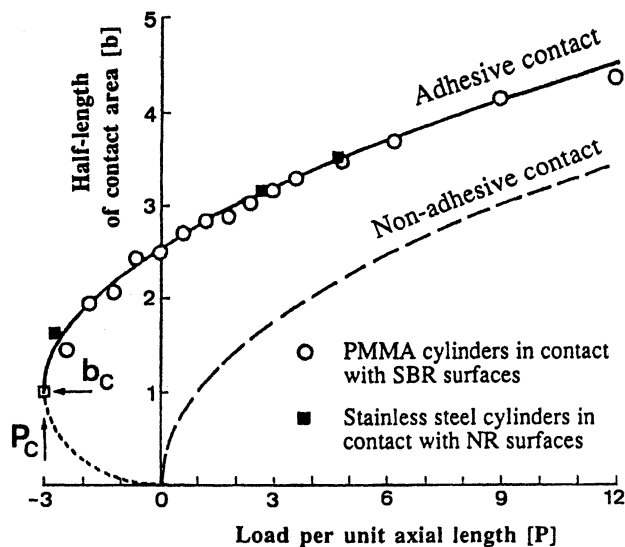


Figure 8. Half-width of the equilibrium contact area between a rigid cylinder and the smooth surface of an elastic solid as a function of the normal applied load per unit axial length, in reduced coordinates. Experimental data fall in the immediate vicinity of the theoretical curve (heavy line). The curve deduced from the classical Hertz's theory (non-adhesive elastic contact) is given for comparison.

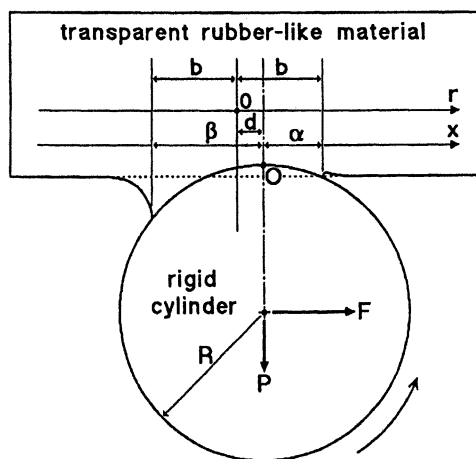


Figure 9. Asymmetrical profile of the contact of a long and rigid cylinder rolling under the flat and smooth surface of an elastic half-space. $2b$ is the total width of the contact zone whereas α represents the leading half-width and β the trailing half-width of the contact area, so that $b = (\alpha + \beta)/2$ and $d = (\alpha - \beta)/2$.

in which the variable u represents the effect of the rolling motion. Indeed, for the static condition, $F=0$, that corresponds to $u=1$. If $u=1$ and $q=Q=1$ the ultimate critical values of the static contact under a horizontal surface are found again: $b=b_C$ and $P=P_C$. Changing into variables so defined allows us to write the second solution in the following simple form:

$$q^4 - 4q + 3Q = 0 \quad \text{with } Q \leq 1 \text{ and } q \geq 1$$

With these conditions, this relation which can be represented by a master curve $q = \mathcal{A}(Q)$, always provides the critical point, under static and in rolling conditions, with the help of the double equality $q=Q=1$. The corresponding critical values b and P being these characteristic of the static case multiplied by a whole power of the rolling parameter u (with $u \geq 1$): $b_R = b_C u^2$ and $P_R = P_C u^4$, this last relation clearly showing that the rolling of a cylinder, whose weight per unit axial length is greater than the ultimate static value, can be observed. This result can seem obvious *a posteriori* because the contact area broken at the trailing edge during the rolling motion is rebuilt at the leading edge. Nevertheless, we think that it was useful to demonstrate this effect.

Rolling on and under an inclined surface. Experiments were effected with the help of simple apparatus (37). A thick (16mm) block of a soft and transparent natural rubber (Young's modulus $E=0.89$ MPa and Poisson's ratio $\nu=0.5$) with a flat, smooth and clean surface, is glued under an inclined rigid plate made of PMMA, with a slope angle θ variable from 0 to 90° with regard to the horizontal. A cylinder (radius $R = 30$ mm and length $L = 40$ mm), also made of PMMA, presenting a lateral perfectly smooth surface, is equipped with a ball-bearing system without friction where different loads can be fixed in order to change the load per unit axial length P of the cylinder for the same contact geometry. All the experiments, in which θ and P could be changed as required, were recorded with the help of a video system in order to measure more accurately the rolling speed V and the associated width $2b$ of the contact area. Taking into account that the rolling of a rigid cylinder on an elastic half-space can be seen, with regard to the dissipated energy, as a $\pi/2$ peel experiment at the trailing edge of the contact area (38) the strain energy release rate G is equal to the tangential rolling force F per unit axial length. *i.e.* the linear weight P applied to the cylinder with a correction due to the inclination θ of the surface: $G = P \sin \theta$. As expected, G varies as a power function of V in a large range of velocities:

$G = kV^n$ with $n=0.55$, which is in perfect agreement with previous kinetics of adherence of punches, rolling and rebound results obtained with the same rubber-like material (22, 24, 32, 39, 40). It should be pointed out that, as already observed, rolling upon and under the rubber surface occurs with the same speed for the same inclination, as in the case where the load per unit axial length of the cylinder is smaller than the absolute value of the elastic adherence force P_C .

The most important result that should be emphasized is the magnitude of observed rolling parameters. For instance, the cylinder is able to roll under the inclined rubber surface without falling off, even if the tensile force is 50 times greater than the critical load in static conditions (elastic adherence force P_C). This situation corresponds to a very large interfacial rupture energy of $G_{\max} = 130 \text{ J.m}^{-2}$ with an associated rolling speed $V_{\max} = 33 \text{ cm}^{-1}$, which is the maximum value that can be recorded with our

experimental system. For comparison, the equilibrium contact upon and under the horizontal rubber surface ($V=0$), corresponds to $G=w \approx 50 \text{ mJ.m}^{-2}$ for common environmental conditions in laboratory rooms (ambient temperature $T=22 \text{ }^\circ\text{C}$ and relative humidity $RH = 60\%$).

Width of the rolling contact area. The rolling speed depends on the mass per unit axial length M and on the inclination θ of the rubber surface with regard to the horizontal, this is the same for the contact width $2b$. From the following relations: $P=Mg\cos\theta$ and $F=Mg\sin\theta$, g being the intensity of the gravity, the study of variations of the parameter Q , as a function of M and V , allows us to predict the theoretical contact width of the rolling contact and to compare it with experimental data deduced from video recordings. In this case, $Q=-P/(3P_s u^4)$ can be written:

$$Q^3 = \xi^3 \chi^3 \cos^3 \theta \{ \sqrt{1 + \chi \sin \theta} + 1 \}^4 \quad \text{with } \chi = Mg/w \text{ and } \xi^3 = 256w / (27\pi E^* R)$$

Two main particular cases exist: in the first, $Q=0$, i.e. $\chi \cos \theta = 0$, that corresponds to $Mg=0$ or $\theta=\pi/2$, when rolling occurs vertically ($P=0$); in the second, $Q \neq 0$, χ (necessarily greater than one) remains proportional to $Q^3 \sin^2 \theta / (\xi^3 \cos^3 \theta)$. In this case, Q can be written in the simple form: $Q = \xi \sqrt[3]{\chi \sin \theta / \tan \theta}$ so that the contact half-width b is equal to: $b = b_s \sqrt[3]{\chi \sin \theta / 4} \mathcal{F}^2(Q)$.

If $\theta = \pi/2$, b is always proportional to $V^{n/3}$, so that it is expected that the contact area width will vary with the $n/3 = 0.55/3 = 0.183$ power function of the rolling speed V . The value of $\mathcal{F}^2(Q)$ being limited by $\mathcal{F}^2(0) = 4^{2/3}$ and $\mathcal{F}^2(1) = 1$, the widths of contact area for inclinations different from 0 must verify the proportionality to $V^{n/3}$ as soon as the rolling speed V is high enough in order that variations of $\mathcal{F}^2(Q)$ may be neglected before those of $V^{n/3}$. Figure 10 clearly shows that experimental data (symbols) are in very good agreement with computed curves drawn for the three inclinations tested: $\theta = \pi/2$, $\theta = 22.75^\circ$ and $\theta = 50.5^\circ$.

The particular case of rolling down a vertical rubber surface ($\theta = \pi/2$ and $P=0$), as the rolling speed is necessarily high, hence $F/w \gg 1$, leads to the very simple result $d_{\pi/2} = b/2$. Taking into account that the width of the contact area is divided into two unequal parts $\alpha = (b-d)/2$ and $\beta = (b+d)/2$ (Figure 9), the two particular values can be deduced: $\alpha_{\pi/2} = b/4$ and $\beta_{\pi/2} = 3b/4$, which correspond exactly to the observations and allow us to write $b_{\pi/2} = \sqrt[3]{8R^2 F_{\pi/2} / \pi E^*}$, so that the rolling force $F_{\pi/2}$ for the inclination $\theta = \pi/2$, rigorously varies as V^n , and the variation of $b_{\pi/2}$ with $V^{n/3}$ is found.

Conclusion

Due to the intervention of molecular attraction forces, the interface between a rigid solid and a rubber-like material can sustain stresses, so that bulk properties are involved. For this reason, shear delaminations are not instantaneous and kinetics are measured, also phenomena as no-rebound of balls on a rubber surface and rolling of a cylinder under a rubber sheet are observed.

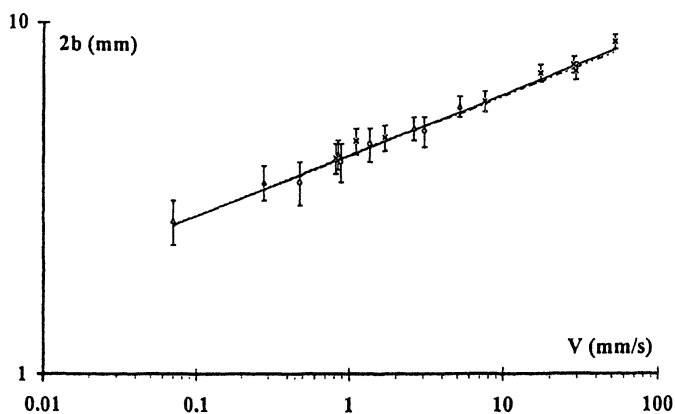


Figure 10. Width $2b$ of the rolling contact area *versus* the rolling speed V . The width $2b$ varies as $V^{0.183}$ in a large range of rolling velocities. Experimental data (symbols: \times ($\theta=90^\circ$); \circ ($\theta=50.5^\circ$); Δ ($\theta=22.75^\circ$) and theoretical curves (heavy line ($\theta=90^\circ$)).

References

1. Dowson, D. *History of Tribology*, Longman: London, 1979, 93-126.
2. Amontons, G. *Mémoires de l'Académie Royale A*, **1699**, *12*, 257-282.
3. Coulomb, C.A. *Mémoires de Mathématiques et de Physique de l'Académie Royale*, **1785**, *10*, 161-342.
4. Desaguliers, J.T. *A Course of Experimental Philosophy*, Longman: London, 1734, Vol. 1.
5. Hertz, H. *J. für die reine und angewandte Mathematik*, **1882**, *92*, 156-171.
6. Boussinesq, J. *Application des potentiels à l'étude de l'équilibre et du mouvement des solides élastiques*; Albert Blanchard: Paris, 1969, 207-211.
7. Griffith, A.A. *Phil. Trans. Roy. Soc. A*, **1920**, *221*, 163-198.
8. Irwin, G.R. *Encyclopedia of Physics, Elasticity and Plasticity*; Flüge Springer Verlag: Berlin, 1958, Vol. 4.
9. Barenblatt, G.I. *Adv. Appl. Phys.*, **1962**, *7*, 55-129.
10. Dugdale, S. *J. Mech. Phys. Solids*, **1960**, *8*, 100-104.
11. Kendall, K. *J. Phys. D: Appl. Phys.*, **1971**, *4*, 1186-1195.
12. Johnson, K.L.; Kendall, K.; Roberts, A.D. *Proc. Roy. Soc. A*, **1971**, *324*, 301-313.
13. Maugis, D.; Barquins, M. *J. Phys. D: Appl. Phys.*, **1978**, *11*, 1989-2023.
14. Andrews, E.H.; Kinloch, A. J. *Proc. Roy. Soc. A*, **1973**, *332*, 385-399.
15. Williams, M.L.; Landel, R.F.; Ferry, J.D. *J. Amer. Chem. Soc.*, **1955**, *77*, 3701-3707.
16. Gent, A.N.; Schultz, J. *J. Adhesion*, **1972**, *3*, 281-294.
17. Ramond, G.; Pastor, M.; Maugis, D.; Barquins, M. *Cahiers du GFR*, **1985**, *6*, 67-89.
18. Barquins, M. *J. Appl. Polymer Sci.*, **1984**, *29*, 3269-3282.
19. Barquins, M. *J. Adhesion*, **1982**, *14*, 63-82.
20. Roberts, A.D. *Rubber Chem. Technol.*, **1979**, *52*, 23-42.
21. Roberts, A.D.; Thomas, A.G. *Wear*, **1975**, *33*, 45-64.
22. Barquins, M.; Charmet, J.-C. *J. Adhesion*, **1996**, *57*, 5-19.
23. Leroy, B. *Amer. J. Phys.*, **1985**, *53*, 346-349.
24. Barquins, M.; Hénaux, S. *C.R. Acad. Sc. Paris*, **1993**, *317*, 1141-1147.
25. Johnson, K.L.; Pollock, H.M. *J. Adhesion Sci. Technol.*, **1994**, *8*, 1-9.
26. Dahneke, B. *J. Colloid Interface*, **1975**, *51*, 58-65.
27. Latham, R.V.; Brah, A.S.; Fok, K.; Woods, M.O. *J. Phys. D: Appl. Phys.*, **1977**, *10*, 139-150.
28. Latham, R.V.; Brah, A.S. *J. Phys. D: Appl. Phys.*, **1977**, *10*, 151-167.
29. Rogers, L.N.; Reed, J. *J. Phys. D: Appl. Phys.*, **1984**, *17*, 677-689.
30. Tsai, C.-J.; Piu, D.Y.H.; Liu, B.H.Y. *Aerosol Sci. Technol.*, **1990**, *12*, 497-507.
31. Wall, S.; John, W.; Wang, H.-C.; Goren, S. *Aerosol Sci. Technol.*, **1990**, *12*, 926-946.
32. Barquins, M. *J. Adhesion*, **1988**, *26*, 1-12.
33. Savkoor, A.R.; Briggs, G.A.D. *Proc. Roy. Soc. A*, **1977**, *356*, 103-114.
34. Muskhelishvili, N.I. *Some basic problems of the mathematical theory of elasticity*; Noordhoff International Publishing: Leyden, 1975.
35. Barquins, M.; Felder, E. *Kautsch. Gummi Kunstst.*, **1990**, *43*, 114-117.
36. Johnson, K.L. *Contact mechanics*, Cambridge University Press: Cambridge, 1985.
37. Charmet, J.-C.; Barquins, M. *Int. J. Adhesion and Adhesives*, **1996**, *16*, 249-254.
38. Kendall, K. *Wear*, **1975**, *33*, 351-358.
39. Barquins, M.; Shanahan, M.E.R. *Int. J. Adhesion and Adhesives*, **1997**, *17*, 313-317.
40. Barquins, M.; Charmet, J.-C.; Robbe-Valloire, F. *C.R. Acad. Sc. Paris*, **1998**, *326*, in press.

Chapter 4

Creep Effects in Nanometer-Scale Contacts to Linear Viscoelastic Materials

W. N. Unertl

Laboratory for Surface Science and Technology,
University of Maine, Orono, ME 04469

Nanometer-scale contacts to compliant linear viscoelastic materials can be studied experimentally with the scanning force microscope (SFM). Creep significantly modifies the formation and rupture of these contacts compared to contacts to elastic materials. Not only does the maximum contact area depend on the loading history but, unlike elastic materials, it reaches its maximum value well after the maximum load is applied. Effects due to creep are distinct from those induced at the periphery of the contact by adhesion. Creep effects dominate adhesion effects in SFM-scale contacts for a wide range of compliant viscoelastic materials. Strategies are presented to optimize experimental parameters for creep studies in SFM-scale contacts to linear viscoelastic materials.

The contributions to this book amply demonstrate the broad interest in using the scanning force microscope (SFM) to make quantitative measurements of materials properties with nanometer-scale resolution. The mechanical properties of interest include the storage and loss moduli, shear strength, and the yield strength. Knowledge of these properties is important for a broad range of applications ranging from fundamental understanding of tribological processes to the characterization of biological systems.

Continuum mechanics models from the field of contact mechanics (1,2) are widely used to analyze nanoscale SFM experiments involving elastic materials. The effects of adhesion are well-understood. Unfortunately, the appropriate analysis has not yet been carried out for viscoelastic materials. In the late 1960's, Ting (3,4) solved the creep problem for cases where adhesion can be neglected, which is generally not true for SFM contacts. Subsequently, Barquins and Maugis (5-7) incorporated viscoelastic response into the fracture mechanics approach to contact mechanics. In this approach, the increase and decrease of contact size is viewed as the opening or closing of a crack at the contact periphery. They ignored the possibility of creep. Johnson's (8) article in this volume provides an excellent overview of the present state of theoretical understanding of the contact mechanics of linear viscoelastic materials.

In this article, we apply contact mechanics to interpret dynamic SFM loading experiments on compliant linear viscoelastic materials. We start with a discussion of experimental procedures including the advantages of modulation techniques. The interpretation of typical data is then discussed using Ting's analysis. Several general conclusions are reached about data analysis and optimization of experiment design. We then examine modifications due to adhesion and conclude that they have only a small effect on the time response. Based on these results and arguments presented in Johnson's article, we conclude that creep effects should be more important than crack tip effects for SFM-scale contacts to materials with effective moduli below about 100 MPa.

The notation used to describe the contacts is shown in Figure 1. $P(t)$ is the time dependent applied load, $\delta(P,t)$ the deformation, $a(P,t)$ the contact radius, and R_1 and R_2 the radii of curvature of the two bodies at the point of contact. We consider only flat substrates so that $R_1 = R$ and $R_2 = \infty$. Each elastic material is described by its Young modulus E , Poisson ratio ν , and is assumed to be isotropic so that the shear modulus is $G = E/2(1 + \nu)$. Viscoelastic materials are assumed to be linear with stress relaxation functions $E(t)$ and creep compliance functions $J(t)$. All properties are assumed to be independent of depth.

Experimental Aspects of Dynamic Loading

This section describes typical SFM studies of the formation and rupture of contacts to a viscoelastic substrate during a single cycle of loading and unloading. Measurements are also possible under static loading conditions but will not be discussed here (9).

In analogy with bulk dynamical mechanical analysis (10,11), a small mechanical modulation can be applied to the contact and the phase and amplitude of the response measured. In SFM this modulation is either a displacement of the sample or of the base of the cantilever. In either case, the amplitude and phase of the response of the probe end of the cantilever beam are measured. The modulation can be applied either normal (12-14) to the surface or parallel to it (9,15-17). The latter is a shear modulation, shown schematically in Figure 2.

Shear modulation has an advantage over normal modulation, in that, for small modulation amplitudes, the contact area remains constant. For elastic materials, the

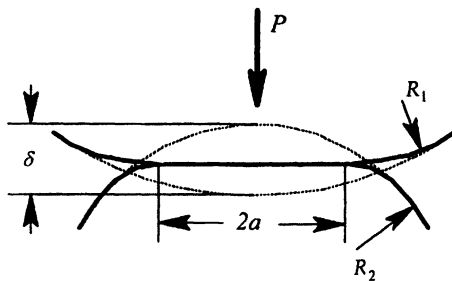


Figure 1. Geometry of a deformable contact between axially symmetric bodies.

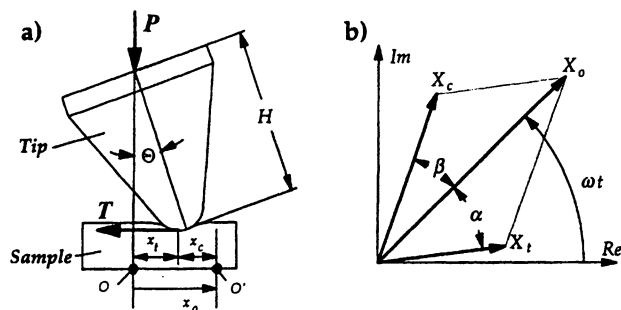


Figure 2. (a) Schematic diagram of an SFM contact with shear modulation $x_o = X_o \exp(i\omega t)$ applied to the sample. The response of the contact and tip are $x_c = X_c \exp[i(\omega t + \beta)]$ and $x_t = X_t \exp[i(\omega t + \alpha)]$, respectively. The torsional angle is typically in the range $0.001^\circ < \Theta < 0.1^\circ$ and X_o is as small as ≈ 0.1 nm. (b) Relationship between the amplitudes and phases of the drive signal (X_o), tip (X_t, α), and contact (X_c, β). (Adapted with permission from reference 9. Copyright 9 *Tribology Letters*.)

stiffness of a contact under shear is

$$\frac{dT}{dx} = 8G^* a(P) \quad (1)$$

where T is the shear force, $G^* = [(2 - \nu_1)/G_1 + (2 - \nu_2)/G_2]^{-1}$ the effective shear modulus, and x the shear displacement. The stiffness under normal modulation is

$$\frac{dP}{dz} = 2E^* a(P) \quad (2)$$

where $E^* = [(1 - \nu_1^2)/E_1 + (1 - \nu_2^2)/E_2]^{-1}$ is the effective modulus. Shear modulation is carried out in static contact at constant load or at frequencies high enough that the load is constant during a stiffness measurement. In contrast, the area must change during a normal modulation. In order not to perturb this measurement, the accompanying modulation in deformation must be small, i.e., $\Delta\delta/\delta \ll 1$. Using the Hertzian result (18) $\delta = a^2/R = (3/4E^* R^{1/2})^{2/3} P^{2/3}$ and Hooke's Law $P = \kappa_b Z$, the condition on the modulation amplitude ΔZ becomes

$$\frac{\Delta Z}{Z} \approx \frac{3}{2} \frac{\Delta\delta}{\delta} \ll 1 \quad (3)$$

where Z is the displacement required to obtain the applied load P using a cantilever

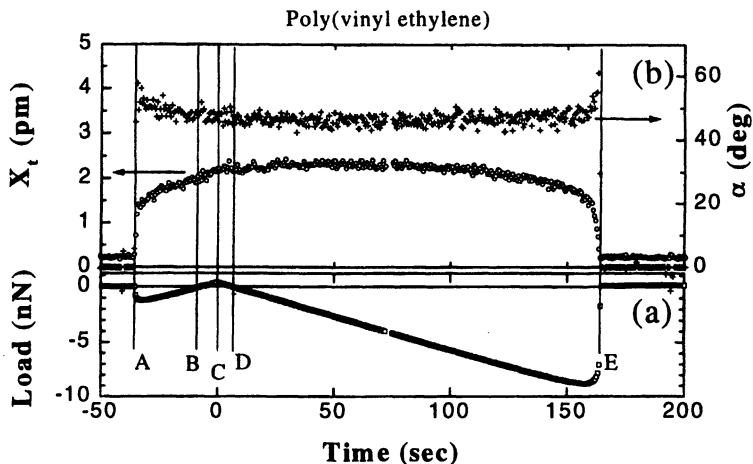


Figure 3. Dynamic contact between a silicon nitride SFM tip and a polyvinylethylene sample. (a) Force curve. (b) Amplitude X_t and phase α responses of the tip. (Adapted with permission from reference 9. Copyright 9 *Tribology Letters*.)

of bending stiffness κ_b . Equation 3 places severe restrictions on the maximum useful value of ΔZ , particularly for quantitative studies where ΔZ must be known with precision, say better than 10%. This is difficult to achieve and still properly match the stiffness of the cantilever to the stiffness of the contact as described by Burnham *et al.* (19). For example, to obtain only 10% precision in ΔZ for typical cantilevers with $0.1 < \kappa < 10$ and loads of a few nN requires the detector to have a sensitivity of better than 0.01 nm. This is at the signal-to-noise limit of many SFM instruments. The majority of studies using normal modulation reported in the literature either use ΔZ far larger than required by equation 3 or do not report a value. In the opinion of this author, these studies should be considered to be qualitative. Similar conclusions are reached if adhesion is included in the above analysis using JKR (20) or DMT (21) models. The same conclusion is reached for viscoelastic materials, but E^* and G^* in equations 1 and 2 must be replaced by the appropriate integral operators (22).

In dynamic loading, the probe is initially out of contact with the surface. Most scanning force microscopes perform dynamic loading under displacement control of the sample (but not the probe), e.g., the distance $Z(t)$ between the cantilever mount and sample is reduced at constant speed V_{in} . The probe and sample are then brought into contact, the contact is loaded, and then unloaded until it ruptures. Figure 3a shows typical loading behavior for a viscoelastic substrate, poly(vinylethylene) (9).

If the cantilever bending force constant κ_b is lower than the gradient of the probe-sample interaction force $F(z)$, *jump-to-contact* will occur at some probe-sample separation distance Z_0 (A in Figure 3a) resulting in contact. The net force acting on the contact at this point will be tensile, $F < 0$. As Z continues to decrease, the tensile

force decreases continuously until the no-load point is reached (BA in Figure 3a) after which the loading becomes compressive (BCD in Figure 3a). At some pre-set value of the load, P_{max} (C in Figure 3a) the approach is reversed. During the withdrawal at constant speed $-V_w$, the load passes through zero and become tensile. At pull-off (E in Figure 3a), the probe and sample separate and the load falls from $P_{pull-off}$ to zero. The rounding at E is characteristic of viscoelastic materials but not elastic materials (23) and its degree depends on the stiffness of the cantilever.

Small oscillatory shear forces can also be applied during dynamic loading. Figure 3b shows typical amplitude X_i and phase α response as the contact forms (A), reaches maximum load (C) and is finally ruptured (E).

For both elastic and viscoelastic materials, the response of the contact ((X_i, α) in Figure 2) is simply related to the contact radius $a(t)$. Starting from equation 1, assuming the cantilever to be perfectly elastic with torsional stiffness κ_θ , and describing the contact response by a complex shear modulus $G = G^* e^{i\delta}$,

$$a = \frac{\kappa_\theta}{G^*} \frac{X_i}{X_o} \left[1 + \left(\frac{X_i}{X_o} \right)^2 - 2 \left(\frac{X_i}{X_o} \right) \cos \alpha \right]^{-1/2} \rightarrow \frac{\kappa_\theta}{G^*} \frac{X_i}{X_o} \quad (4)$$

in the limit $X_i \ll X_o$. This is a very important result since $a(t)$ cannot be measured directly in SFM contacts. Thus, the additional information provided by a measurement of X_i is extremely valuable. This conclusion has been reached previously (9,16,22) but has not been extensively exploited by SFM researchers.

Fully quantitative measurements using shear modulation have most of the challenges encountered in other SFM experiments including determination of bending, buckling and torsional force constants of the cantilever, the true shape of the probe tip, and creep and hysteresis in piezoelectric response. Here we emphasize three essential considerations that should be made in designing shear modulation experiments for SFM.

- Do not use “sharpened” probe tips with small apex angles. These tips are easily deflected laterally by the forces encountered in shear experiments. For example, Lantz *et al.* (24) show that κ_{tip} , the bending stiffness, of sharpened commercial tips is in the range 39-84 N/m. These κ_{tip} are comparable in magnitude to the cantilever’s torsional stiffness κ_θ . Thus, quantitative analysis of the contact stiffness requires accurate knowledge of both κ_θ and κ_{tip} . At present, κ_{tip} can only be estimated using finite element analysis and require accurate measurement of the probe shape and knowledge of its modulus. Blunter tips, such as standard pyramidal tips, have much larger κ_{tip} and therefore are preferred.
- Make sure that the shear amplitude X_o is small enough. The modulation amplitude X_o must be small compared to the contact radius $a(P, t)$ to avoid non-linear response due to micro-slip and to insure that the contact does not slide. For hard elastic materials, this requires that X_o be a few angstroms or less. For more compliant materials, larger X_o can be used in some circumstances, but near pull-off X_o must remain small compared to the contact ra-

dus at pull-off, $a_{\text{pull-off}}$. X_o was only about 0.13 nm for the data in Figure 3. Yet, near pull-off, the phase lag α increases rapidly suggesting that sliding has commenced.

- For very compliant materials, use the largest probe radius R compatible with the goals of the measurement. This is primarily for convenience in analysis. The widely used analytical results of the Hertz, JKR and DMT models all assume that $a \ll R$. This assumption is easily violated for compliant materials. Consider, for example, a material with $E^* \approx 2$ MPa and a work of adhesion $W \approx 20$ mJ/m². At a load of only 2 nN, JKR analysis predicts that $a/R = 1.5$ for $R = 50$ nm, a typical value for a commercial SFM tip. This is clearly non-physical and shows that JKR analysis is not appropriate and a more realistic, non-analytical model such as that of Maugis (25) must be used. In this example, even at $R = 1000$ nm, JKR cannot be used! Unfortunately, it appears that quantitative analysis of nanometer-scale contacts to compliant elastic or viscoelastic materials will typically be non-analytical.

Contact Mechanics for Linear Viscoelastic Materials

The contact mechanics of linear viscoelastic materials is less developed than for elastic materials. In particular, the effects of adhesion have not been systematically explored. After a brief discussion of time scales, this section first considers the case of no adhesion. Then the modifications due to adhesion are discussed.

Creep in Viscoelastic Contacts in the Absence of Adhesion. Viscoelastic effects are important whenever contact dimensions change in a time interval that is comparable to a characteristic relaxation time τ of the viscoelastic material. Ting (3), following earlier work by Lee and Radok (26), Ting obtained a general solution to the Hertz contact problem for the case of a rigid axisymmetric probe and a substrate with linear viscoelastic response. He used the boundary conditions

$$\begin{aligned} u_z(r) &= \delta(t) - f(r)H(t) \text{ for } r < a(t) \\ \sigma_{zz} &= 0 \text{ on } z = 0 \text{ for } r > a(t) \\ \sigma_{rz} &= 0 \text{ on } z = 0 \text{ for all } r \end{aligned} \quad , \quad (5)$$

where u_z is the vertical displacement of the substrate surface, $H(t)$ is the Heavyside function, and $f(r)$ is the shape of the probe. Ting considered conical, parabolic, and spherical probes. This choice of boundary conditions excludes the effects of adhesion. Ting used a general form of the linear viscoelastic continuity equation

$$\sigma_{ij}(t) = \int_0^t \left[2G(t-\tau) \frac{\partial \varepsilon_{ij}(\tau)}{\partial \tau} + \delta_{ij} \lambda(t-\tau) \frac{\partial \varepsilon_{kk}(\tau)}{\partial \tau} \right] d\tau \quad (6)$$

where $\lambda(t)$ and $G(t)$ are the time dependent relaxation moduli of the substrate and the lower limit 0 allows for a possible jump in stresses at $t = 0$. If v is independent of time, $\lambda(t)$ and $\mu(t)$ are related to stress relaxation modulus $E(t)$ and the creep compliance $J(t)$ by

$$s\hat{E}(s) = \frac{1}{s\hat{J}(s)} = \frac{2s\hat{\mu}(\hat{\lambda} + \hat{\mu})}{\hat{\lambda} + 2\hat{\mu}} = \frac{s\hat{\mu}}{1 - s\hat{v}} \quad (7)$$

where $\hat{}$ represents the Laplace transformation.

The solutions depend on whether the contact radius $a(t)$ is increasing or decreasing. In the case of increasing radius, the solutions confirm the earlier results of Lee and Radok. Specifically,

$$P(t) = \frac{8}{3R} \int_0^t E(t-\tau) \frac{\partial a^3(\tau)}{\partial \tau} d\tau \quad \text{if } \frac{da(t)}{dt} \geq 0 \quad (8)$$

$$\delta(t) = \delta_e(t) \quad \text{if } \frac{da(t)}{dt} \geq 0 \quad (9)$$

where $\delta_e(t)$ is the solution to the equivalent elastic problem; e.g., $\delta_e(t) = a^2(t)/R$ for the Hertz case.

If $a(t)$ is decreasing, but still larger than its value $a(0)$,

$$P(t) = \int_0^{t_1(t)} E(t-\tau) \frac{\partial}{\partial \tau} [cP_e(\tau)] d\tau \quad \text{for } t_m \leq t \leq t' \quad (10)$$

where $t_1(t)$ is the time at which a reached the value $a(t)$ during the initial loading cycle and $cP_e(t)$ is the solution to the equivalent elastic problem; e.g., $cP_e(t) = (8/3R)a^3(t)$ for the Hertz case with $c = 2/E^*$. If $P(t)$ is known, equation 10 is used to find $t_1(t)$ and thus the value of $a(t)$. Once $a(t)$ is known, the deformation is found using

$$\delta(t) = \delta_e(t) - \int_{t_m}^{t'} J(t-\tau) \frac{\partial}{\partial \tau} \int_{t_1(\tau)}^{\tau} E(\tau-\eta) \frac{\partial \delta_e(\eta)}{\partial \eta} d\eta d\tau. \quad (11)$$

In cases where a decreases to values smaller than a_n ,

$$P(t) = E(t)cP_e(t) \quad \text{for } t' < t \leq t_n, \quad (12)$$

which is solved to find $a(t)$. The deformation is then obtained from

$$\delta(t) = \delta_e(t) - \int_{t_m}^{t-\tau} J(t-\tau) \frac{\partial}{\partial \tau} \int_{\eta_1(\tau)}^{\tau} E(\tau-\eta) \frac{\partial \delta_e(\eta)}{\partial \eta} d\eta d\tau$$

$$- \int_{t'}^t J(t-\tau) \frac{\partial}{\partial \tau} \int_{0^+}^{\tau} E(\tau-\eta) \frac{\partial \delta_e(\eta)}{\partial \eta} d\eta d\tau$$
(13)

We now illustrate these solutions for parameters typical of SFM contacts. We use mechanical models whose behavior brackets the range of response expected in real materials but are simple enough that analytical solutions can be obtained. In essentially all realistic cases, analytical solutions will not be possible. Specifically we chose the Maxwell and Voigt/Kelvin models. The Maxwell model is a series combination of an elastic spring with modulus E and dashpot with viscosity η . The relaxation functions are

$$E(t) = E^* e^{-t/\tau} \text{ and } J(t) = E^*(1+t/\tau)$$
(14)

where $\tau \equiv \eta/E^*$ is the characteristic relaxation time of the model. The Voigt/Kelvin model has the spring and dashpot in parallel with

$$E(t) = E^* [H(t) + \tau \delta(t)] \text{ and } J(t) = (1 - e^{-t/\tau})/E^*$$
(15)

The standard solid model has intermediate behavior. It consists of a spring in series with a Voigt/Kelvin model with

$$E(t) = \frac{E^*_1}{E^*_1 + E^*_2} (E^*_1 + E^*_2 e^{-t/\tau_2}) \text{ and } J(t) = \frac{1}{E^*_1} + \frac{1}{E^*_2} (1 - e^{-t/\tau_2})$$
(16)

where $\tau_1 \equiv \eta/E^*_2$ and $\tau_2 \equiv \eta/(E^*_1 + E^*_2)$. At very short times, the standard model responds like a single spring with E^*_1 and at long times like springs E^*_1 and E^*_2 in series. Johnson shows calculations for a standard solid model in his contribution in this book.

The range of behavior expected for the linear loading ramp shown in Figure 4a is illustrated in Figure 5 and Figure 6. A linear ramp mimics the load variation in a typical SFM measurement. The total time of contact between the probe and substrate is $t_{contact}$ and the time of maximum load is $yt_{contact}$ where $0 < y < 1$. The unloading time is $t_{unload} = (1-y) t_{contact}$. The slopes of the loading and unloading curves can be varied independently. In order to obtain analytical solution for the Maxwell and Voigt/Kelvin models, we also assume that the probe shape is parabolic or, equivalently, a sphere with $R \gg a$.

Figure 5 shows the major features of the Ting solution, for the Voigt/Kelvin model (Figure 5a) and the Maxwell model (Figure 5b). The elastic element has $E^* = 2$ MPa and the viscosity of the dashpot is selected to yield a relaxation time of $\tau = 50$ s. These values are similar to those of the poly(vinylethylene) sample freshly cast from

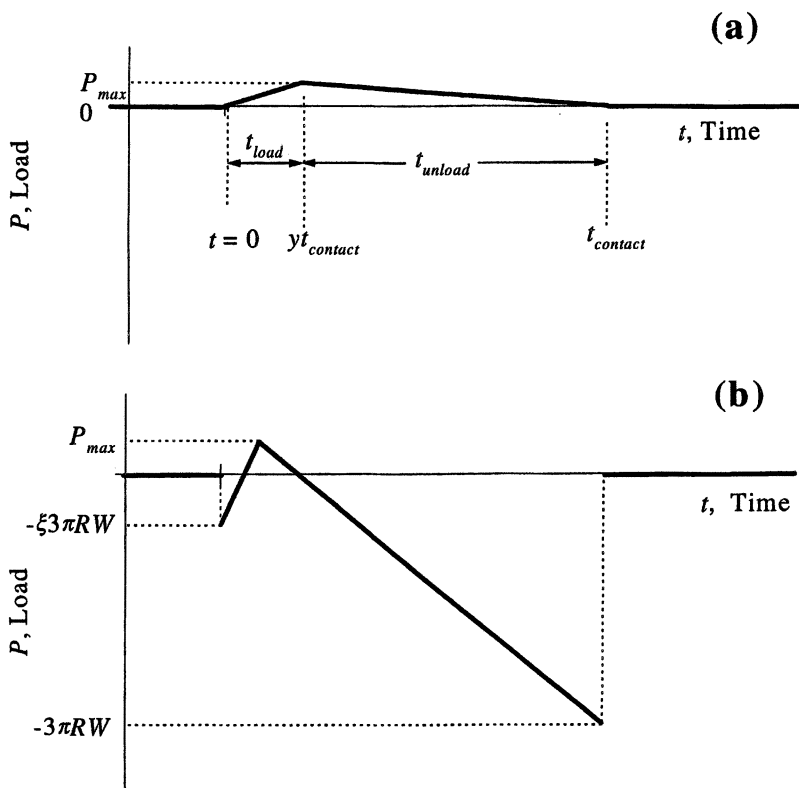


Figure 4. (a) Time dependent linear loading ramp. (b) Time dependent loading ramp with jump-to-contact and pull-off behavior.

toluene solution (Figure 3). The contact radius a is plotted as a function of $\tau/t_{contact}$, where τ is the characteristic relaxation time of the contact. Each curve is labeled by its value of $t_{contact}$. The maximum load P_{max} is 2 nN and occurs at $yt_{contact}$ where $y = 0.2$ in Figure 5. This value of y is typical of SFM force curve measurements. Also shown for reference is the response of an elastic material with the same E^* (solid lines). The most striking feature of both models shown in Figure 5 is that the time of maximum contact radius t_{peak} does *not* coincide with the time of maximum load as it does for elastic materials. Instead, maximum radius always occurs *after* the maximum load. This delay occurs because the substrate continues to respond by creep even during the unloading cycle.

Consider first the Voigt/Kelvin model (Figure 5a). The contact radius increases more slowly than in the elastic case and its maximum value is always smaller. As $t_{contact}$ goes to values much shorter than τ , t_{peak} shifts closer and closer to the end of the contact (e.g., $t_{peak} \rightarrow t_{contact}$) and farther and farther away from the time of maxi-

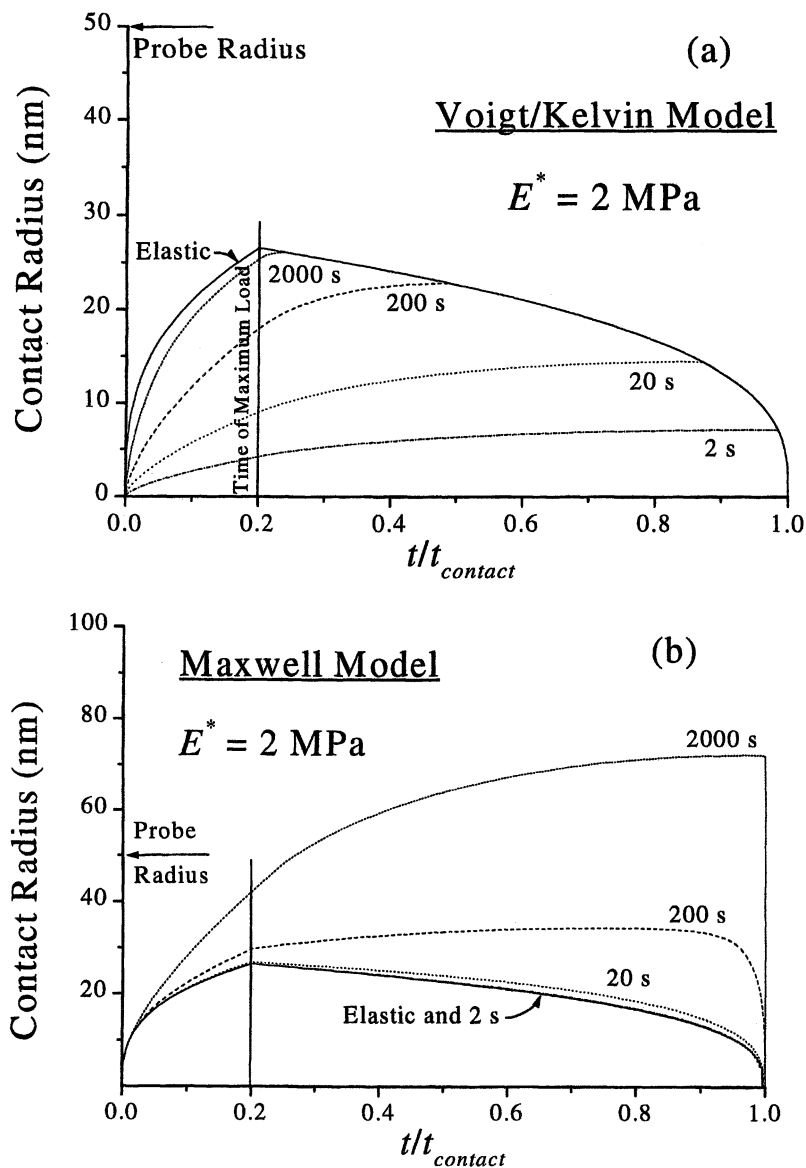


Figure 5. Solutions to the Ting model for contact of a rigid probe with a viscoelastic substrate described by (a) the Maxwell model and (b) the Voigt/Kelvin model.

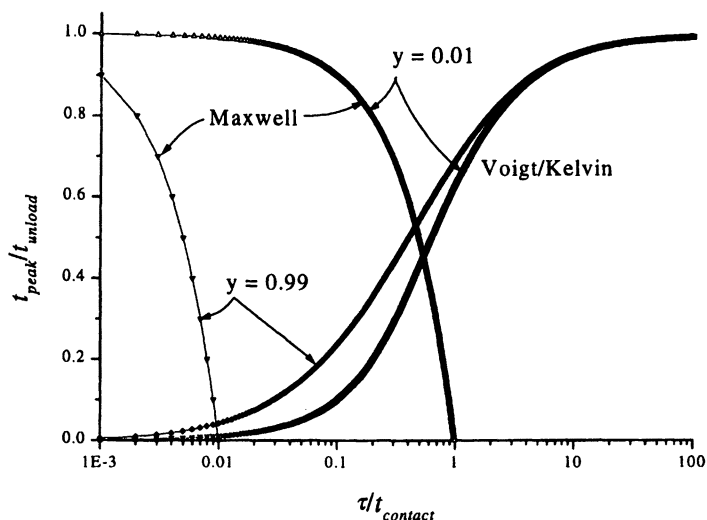


Figure 6. Time of maximum contact radius t_{peak} as a function of $\tau/t_{contact}$ for the Maxwell and Voigt/Kelvin models. Adhesion is neglected.

imum load. Conversely, as $t_{contact}$ becomes much longer than τ , t_{peak} shifts toward the time of maximum load. The expression relating t_{peak} to the other quantities is

$$\frac{t_{peak}}{t_{contact}} = y + \frac{\tau}{t_{contact}} \ln \left[\frac{1 + (y-1) \exp(-y t_{contact}/\tau)}{y} \right]. \quad (17)$$

Clearly, t_{peak} depends only on τ and is independent of both the maximum load and tip radius. Figure 6 shows equation 17 for the case $y = 0.2$. The ordinant is the time interval between maximum load and maximum contact area ($t_{peak} - y t_{contact}$) normalized to the total unloading time ($t_{contact} - y t_{contact}$); it varies between zero and unity. Extremes in behavior are indicated for $y = 0.01$ and 0.99 . Behavior for $0.01 < y < 0.99$ is intermediate. For a given τ , t_{peak} has only a weak dependence on y and the best sensitivity is found for $t_{contact}$ in the range $0.05\tau < t_{contact} < 5\tau$.

In contrast to the Voigt/Kelvin model, the contact radius for the Maxwell model (Figure 5b) is always larger than the elastic case and, the longer $t_{contact}$, the closer t_{peak} is to the end of the contact. Compared to the Voigt/Kelvin model, the Maxwell model is also much more sensitive to the relative length of the loading cycle y as shown in Figure 6. The radius becomes comparable to the probe radius early in the experiment and parabolic approximation used in the calculation is violated. Ting has given the appropriate form but it cannot be evaluated analytically. However, the qualitative trends should remain the same as shown in Figure 5b.

Based on these simple models, several important observations can be made about the response of contacts to creep. These are useful in the design and analysis of experiments to study creep.

1. The maximum value of the contact radius a always increases as the contact time t_{contact} increases.
2. The contact radius a can be either larger or smaller than elastic limit. It is larger if the viscous component dominates the response.
3. The time t_{peak} at which the maximum contact radius occurs during the unloading cycle can either increase or decrease as the total contact time t_{contact} increases. If viscous behavior dominates, t_{peak} increases.
4. Best sensitivity to creep is attained if the loading cycle is as short as possible and the unloading time comparable to the relaxation time.

The results in Figure 5 and Figure 6 assume that the load is controlled during the contact formation and rupture. This is not the case for SFM experiments where the displacement $\Delta(t)$ of the sample is usually varied linearly with time (23). Since the cantilever bends in response to the changing load, the distance between the probe and surface plane of the sample and Δ are related as follows

$$\delta(P, t) = \Delta(t) - Z(P) \quad (18)$$

where $\delta(P, t)$ is the deformation of the contact under applied load P at time t and $Z(P)$ is the deflection of the cantilever under load P . Under these conditions, the Ting analysis becomes more complicated analytically but the major conclusions reached above should not be significantly modified.

Creep in Viscoelastic Contacts with Adhesion. The contact mechanics problem for a viscoelastic material including the effects of adhesion has not been solved. To do this, the elasticity problem must be solved for the viscoelastic continuity equation, equation 6, with the boundary conditions, equation 5, on $z = 0$ replaced by (27)

$$\left. \begin{aligned} \sigma_{zz} &= -p(r) = -\frac{\partial w(D)}{\partial D(r)} \\ \sigma_{rz} &= 0 \end{aligned} \right\} \quad (19)$$

where $p(r)$ is the radial pressure distribution including contributions from non-contact adhesive forces. The Derjaguin approximation (28) is used in equation 19 to express $p(r)$ in terms of $w(D)$, the free energy of interaction between planar surfaces separated by D . This approximation is valid as long as D and the range of the interaction are much smaller than the radii of the surfaces (29). Additionally, since the actual deformation of the surfaces is assumed to be the same as would occur for flat surfaces under the same conditions, the contact radius a must also be small compared to the radii of curvature. The adhesion energy W and w are related by (27)

$$W = \int_0^{\infty} \frac{\partial w(D)}{\partial D(r)} dD, \quad (20)$$

i.e., the work per unit area required to separate the surfaces from the no-load point to $D \rightarrow -\infty$.

Barquins and Maugis (6) have approached this problem from the view point of fracture mechanics for the special case that viscoelastic losses are localized at the crack tip. They completely ignore effects of creep. Viscoelastic response is assumed to be proportional to the thermodynamic work of adhesion in analogy with the results of peel experiments. Specifically, $\Gamma - w = w\phi(a_T v)$ where Γ is the strain release rate and $\phi(a_T v)$ is assumed to be a universal function of crack speed V for a viscoelastic material and a_T is the WLF shift factor (). For macroscopic glass-polyurethane contacts ($a = 50\text{--}250 \mu\text{m}$), Maugis and Barquins showed experimentally that with $n = 0.6$ for $10^{-7} \text{ m/s} < V < 10^{-3} \text{ m/s}$ and $\alpha(T) \approx a_T^n$. Most SFM experiments are at V much smaller than this range. Greenwood and Johnson (30) showed that these results are consistent with the behavior of a crack acting under the combined effects of surface forces and applied load. Aimé and co-workers (23) have demonstrated that the Maugis-Barquins theory qualitatively describes some SFM experiments on polymers but a quantitative experimental study has not yet been made.

Effects of creep on the contact are completely ignored in the fracture mechanics approach of Barquins and Maugis. Yet, the theory of Ting and results like those in Figure 3 suggest creep effects can be significant. Comparison of the relevant time scales for the two processes provides a means to estimate the conditions for which one or the other is expected to dominate and has already been discussed by Johnson (8).

Creep effects are due to the bulk deformation whose size is characterized by a , the radius of the contact. Adhesive interactions result in large stresses that are concentrated near the contact edge. These can be characterized by the width d of the Dugdale zone over which the adhesive force with characteristic range h_o is important or, from the fracture mechanics point-of-view, by the length L of the crack at the contact edge. If the rate at which the contact size changes is $v = da/dt$, two characteristic times can be defined:

$$t_a = \frac{a}{v} \quad \text{and} \quad t_d = \frac{d}{v} \quad \text{or} \quad \frac{L}{v}. \quad (21)$$

If τ is a characteristic relaxation time of the substrate, creep will be important when $t_a \approx \tau$. However, if $t_d \approx \tau$, then adhesion (crack tip) effects at the contact periphery will dominate. Johnson (8) has shown that, in the JKR limit, these two times are very different which allows the two effects to be treated independently.

We now ask, "Do creep or crack effects dominate in SFM-scale contacts?" The JKR limit is most appropriate for compliant materials. Following Johnson (8), the width of the Dugdale zone is given by $d \approx (9^{1/3} \pi/4)(E^*/W)h_o^2$. Note that d is independent of R . Table I shows values for d and $d/a_{\text{pull-off}}$, its ratio to the contact radius at pull-off, for a range of values of E^* and W . The pull-off radius was calculated using $R = 50 \text{ nm}$ and h_o was taken as 0.5 nm . Only when E^* becomes as large as $10\text{--}100 \text{ MPa}$ does the Dugdale zone start to exceed one percent of the contact size. Clearly, creep effects should dominate the viscoelastic response of SFM contacts to most materials with effective moduli smaller than this value. Thus, the conclusions given above for

Table I

Effective Modulus, E^*	d ($d/a_{\text{pull-off}}$)	
	$W = 20 \text{ mJ/m}^2$	$W = 100 \text{ mJ/m}^2$
1 MPa	0.02 nm (0.02 %)	0.004 nm (0.002 %)
10 MPa	0.20 nm (0.4 %)	0.04 nm (0.05 %)
100 MPa	2.0 nm (9 %)	0.41 nm (1.1 %)

the Ting model should be unaffected by the neglect of adhesion in the model.

To confirm this conclusion, we incorporate the effects of adhesion into the Ting model using an empirical approach suggested by Falsafi *et al.* (31) They replaced the load P in equation 8 with an effective load P_{eff} calculated from JKR theory, i.e., $P_{\text{eff}}(t) = P(t) + 3\pi RW + \sqrt{6\pi RWP(t) + 9\pi^2 R^2 W^2}$. Assuming a modulus obtained from rheometric measurements, they solved equation 8 numerically with W as a fitting parameter. For contacts between poly(ethylene)-poly(ethylene-propylene) spheres ($R \approx 1$ mm), they obtained values of W in good agreement with previous contact angle measurements (32). This result supports the assumption made in using equation 8 that W is the thermodynamic work of adhesion.

We have extended this approach, to explore the entire range of behavior expected in dynamic contacts to linear viscoelastic materials, including contacts with decreasing area. We focus on the simple Maxwell and Voigt/Kelvin models because they represent extremes of response and also allow analytical solutions to equations 8-13. For the same reason, we assume the adhesion to be described by a DMT model. Thus, the load P is replaced by $P(t) \rightarrow P(t) + 2\pi WR$. Figure 4b shows the linear loading and unloading assumed in the calculations. Jump-to-contact occurs at $t = 0$ and its magnitude is determined relative to the pull-off load ($-3\pi RW$) by the parameter ξ . In the results presented here, $\xi = 0.2$. The other parameters are defined as in Figure 4a.

For the Maxwell model, adding adhesion has little effect except for the expected increase in the contact area. The time at which the maximum contact area occurs is not changed by inclusion of adhesion so that the results shown in Figure 6 also apply for DMT adhesion. Because the short time response of the Maxwell model is that of an elastic spring, the contact radius increases discontinuously at jump-to-contact.

In the case of the Voigt/Kelvin model, not only does the contact radius increase, it shifts slightly toward shorter times as illustrated in Figure 7. This shift is at most about ten percent. Thus, the results shown in Figure 6 are only weakly affected by adhesion.

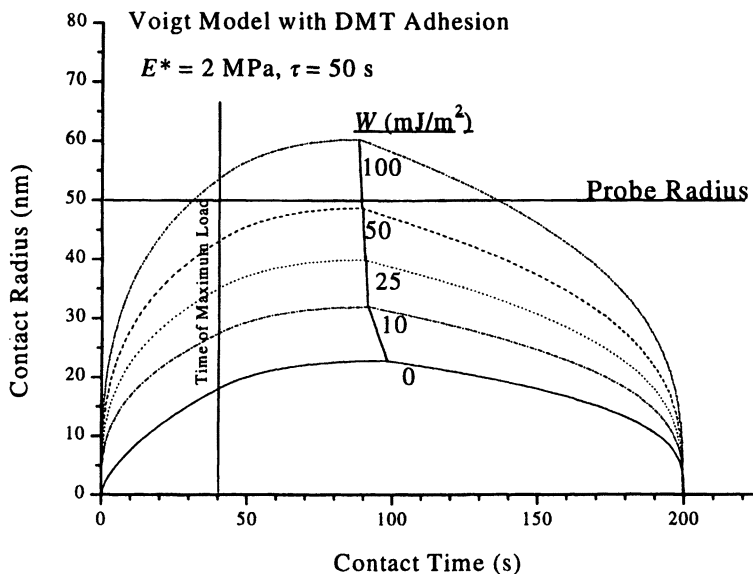


Figure 7. Effect of adhesion of the contact response of the Voigt/Kelvin model.

Conclusions

Recent SFM measurements using shear modulation techniques have increased interest in developing quantitative methods to measure viscoelastic response of nanometer-scale contacts.

We used the theory developed by Ting (3) to characterize the response of such contacts during loading and unloading. Although this theory neglects the effects of adhesion, it can be solved analytically for several simple models. The major prediction of this theory is that creep can cause the contact area to reach its maximum value well *after* the maximum load has been applied to the contact. Results for Maxwell and Voigt/Kelvin models are used to determine how to optimize experiments to study creep. Specifically, we find that, if the loading cycle is much shorter than the unloading cycle, the delayed maximum occurs in the middle of the unloading cycle if the length of the unloading cycle is about twice characteristic relaxation time of the material. For typical SFM instruments, it should be possible to study creep processes with characteristic relaxation times in the range from roughly a millisecond up to a few hundred seconds. Using an empirical approach suggested by Falsafi *et al.* (31), we also demonstrate that adhesion can be expected to have only a small effect on this conclusion.

Stated another way, this result shows clearly that quantitative characterization of compliant viscoelastic materials requires that force vs. distance curves be carried out over as wide a range of contact times as possible. This observation should be particularly relevant for many biological materials. Additionally, it suggests that studies

of pull-off behavior that have relied on rather short contact times will need to be re-evaluated.

We also show that the time dependent response of SFM-scale contacts to linear viscoelastic materials should be dominated by creep response in the bulk, rather than adhesion effects at the contact periphery even for materials with effective moduli as large as 10-100 MPa.

The analytical calculations presented here are obviously too simple to be used for quantitative analysis of experimental data. In many of the results, the assumption that the probe radius is much less than the contact radius is not satisfied. Ting describes how to do this correctly, but the calculations cannot be carried out analytically. However, we expect that the changes will be qualitative and that the major conclusions reached here will remain correct. In any case, a more rigorous analysis that correctly includes adhesion needs to be carried out. Several attempts are under way (33-35).

Acknowledgements

The author gratefully acknowledges financial support from the Department of Energy, the Office of Naval Research, the Paper Surface Science Program of the University of Maine, and the Maine Science and Technology Foundation. Discussions with K.L. Johnson and K.J. Wahl have also been invaluable.

References

1. Johnson, K.L. *Contact Mechanics*; Cambridge University Press: Cambridge, 1987.
2. Savkoor, A.B. in *Microscopic Aspects of Adhesion and Lubrication*; J.M. Georges, J.M., Ed.; Elsevier Sci. Publ. Co.: Amsterdam, 1981, p.279.
3. Ting, T.N.C. *J. Appl. Mech.* **1966**, *33*, 845.
4. Ting, T.N.C. *J. Appl. Mech.* **1968**, *353*, 248.
5. Maugis, D.; Barquins, M. *J. Phys. D* **1978**, *11*, 1989.
6. Barquins, M.; Maugis, D. *J. Adhesion* **1981**, *13*, 53.
7. Barquins, M. *J. Adhesion* **1982**, *14*, 63.
8. Johnson, K.L. this proceedings.
9. Wahl, K.L.; Stepnowski, S.V.; Unertl, W.N. *Tribology Lett.* **1998**, *5*, 103.
10. Findley, W.N.; Lai, J.S.; Onarian, K. *Creep and Relaxation of Nonlinear Viscoelastic Materials*; Dover Publications: New York, 1976.
11. McCrumm, N.G.; Read, B.E.; Williams, G. *Anelastic and Dielectric Effects in Polymeric Solids*; Dover Publications: New York, 1967.
12. Marganov, S.N.; Whangbo, M.H. *Surface Analysis with STM and AFM*; VCH Publishers: New York, 1996.
13. O'Shea, S.J.; Welland, M.E.; Pethica, J.B. *Chem. Phys. Lett.* **1994**, *223*, 336.
14. See for example; Tanaka, K.; Taura, A.; Ge, S.R.; Takahara, A.; Kajiyama, T. *Macromolecules* **1996**, *29*, 3040.
15. Yamanaka, Y.; Tomita, E. *Jpn. J. Appl. Phys.* **1995**, *34*, 2879.
16. Carpick, R.W.; Ogletree, D.F.; Salmeron, M. *Appl. Phys. Lett.* **1997**, *70*, 1548.

17. Lantz, M.A.; O'Shea, S.J.; Welland, M.E. *Phys. Rev. B* **1997**, *55*, 10776.
18. Hertz, H. *J. Reine Angew. Math.* **1882**, *92*, 156.
19. Burnham, N.A.; Gremaud, G.; Kulik, A.J.; Gallo, P.J.; Oulevey, F. *J. Vac. Sci. Technol. B* **1996**, *14*, 1308.
20. Johnson, K.L.; Kendall, K.; Roberts, A.D. *Proc. Roy. Soc. London A* **1971**, *324*, 301.
21. Derjaguin, B.V.; Muller, V.M.; Toporov, Y. *J. Colloid Interface Sci.* **1978**, *53*, 314.
22. Fretigny, C.; Basire, C.; Granier, V. *J. Appl. Phys.* **1997**, *82*, 43.
23. Aimé, J.P.; Elkaakour, Z.; Odin, C.; Bouhacina, T.; Michel, D.; Curély, J.; Dautant, A. *J. Appl. Phys.* **1994**, *76*, 754.
24. Lantz, M.A.; O'Shea, S.J.; Hoola, A.C.F.; Welland, M.E. *Appl. Phys. Lett.* **1997**, *70*, 970.
25. Maugis, D. *Langmuir* **1995**, *11*, 679.
26. Lee, E.H.; Radok, J.R.M. *J. Appl. Mech.* **1960**, *27*, 438.
27. Barthel, E. *J. Colloid Interface Sci.* **1998**, *200*, 7.
28. Derjaguin, B.V. *Kolloid-Z.* **1934**, *69*, 155.
29. Hunter, R.J. *Foundations of Colloid Science*; Oxford Univ. Press: Oxford, 1995; Vol. I, pp. 191.
30. Greenwood, J.A.; Johnson, K.L. *Phil. Mag. A* **1981**, *43*, 697.
31. Falsafi, A.; Deprez, P.; Bates, F.S.; Tirrell, M. *J. Rheol.* **1997**, *41*, 1349.
32. Zhao, W.; Rafailovich, M.H.; Sokolov, J.; Fetters, L.J.; Plano, R.; Sanyal, M.K.; Sinha, S.K.; and Sauer, B.B. *Phys. Rev. Lett.* **1993**, *70*, 1453.
33. K.L. Johnson, private communication.
34. P. Kleban, private communication.
35. A. Falsafi, private communication.

Chapter 5

The Role of Interfacial Slippage in Adhesive Release

K. Vorvolakos and M. K. Chaudhury

Department of Chemical Engineering, Lehigh University, Bethlehem, PA 18015

The peeling of a viscoelastic adhesive from various silicone polymers allowed us to examine the roles of surface energy and interfacial friction in adhesion and release. Surface energies of the polymers as inferred from contact angle and contact mechanics studies do not correlate with their adhesive release behavior. Fluorescent particle velocimetry showed that the adhesive undergoes significant slippage on surfaces at and near the crack tip region. Slippage is high on the surfaces that exhibit excellent release. These studies strongly suggest that the release properties of surfaces are governed by interfacial friction, which gained further support from the direct measurement of interfacial shear stress at the adhesive/polymer interfaces.

Polydimethylsiloxane (PDMS) based coatings fall in a unique class of materials that are known to facilitate release of biological and non-biological adhesives. Despite its tremendous technological implications, the fundamental science behind the release mechanism is still poorly understood. Based on the conventional theories of adhesion¹⁻⁶, one may assume that the release property of a material is controlled by its surface free energy, of the type that gives rise to water repellency. Recent studies from our laboratory, however, pointed out that although the surface free energy serves as a useful guide, it is not a sufficient indicator to the release performance of a material. For example, it has been found that PDMS, the surface energy of which is higher than that of a fluorocarbon, provides better release to adhesives than the fluorocarbon surfaces⁷. It has been stipulated that the reason for this discrepancy is the differences in the interfacial dynamics -- not equilibrium surface energetics. The detailed answer to this question lies in the mechanics of fracture.

There are two common modes⁸ of fracture seen in an adhesive interface -- opening mode and shear mode. In the opening mode fracture, the applied load needs

to overcome only the intermolecular forces. The shear mode failure, on the other hand, involves energy dissipative frictional processes. In terms of energetics, the shear mode fracture depends on the relaxation time of the molecules at the interface, which varies exponentially with the activation energy of bond dissociation⁹. The activation energy of bond dissociation may not necessarily correlate with the energy of bond dissociation.

Fracture of a real interface generally involves a mixed-mode failure. Let us consider the case of a viscoelastic adhesive tape separating from a surface. When the tape is peeled, the adhesive stretches in the direction perpendicular to the surface. In order to preserve the volume, however, the adhesive contracts laterally, and thus a shear stress is developed parallel to the interface (Fig. 1). If the interfacial shear stress

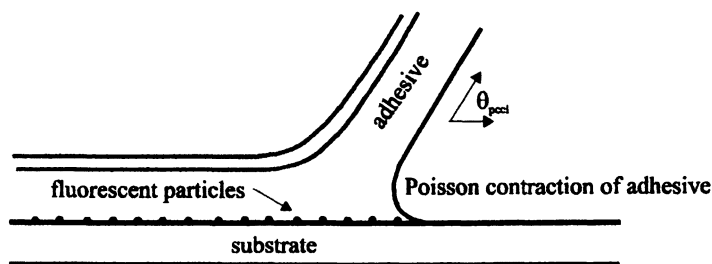


Fig.1. Simplified sketch showing the release of an adhesive from a surface. The slippage of the adhesive can be studied by fluorescent particle velocimetry.

between the adhesive and the substrate is relieved by interfacial slippage, the deformation of the adhesive, and thus the corresponding viscoelastic energy dissipation, decreases. These findings have recently been summarized in some recent publications^{10,11}. Here, we extend the previous study by examining the release characteristics of an acrylic adhesive on various commercially available silicone coatings, the surface energetics of which have been inferred from contact angles and contact mechanics studies. These results provide further support to our previous findings that release behavior of a coating cannot be predicted by surface energetics alone, and highlight the need to consider the dynamic properties of interfaces, such as friction.

Release Profiles of Silicone Coatings

Several silicone based commercial coatings, bearing the following trade names were obtained from Dow Corning Corporation: Dow Corning Silicone Plus High Performance, Dow Corning Q3-7246, Dow Corning 236 Dispersion, 3140 MIL-A-46146 RTV, Hempel Release Coating, and Dow Corning 1-0570. We will denote the above commercial coatings with the symbols A, B, C, D, E and F, respectively. Glass slides, coated with thin films (~ 15 - $20 \mu\text{m}$) of these polymers, were used for the adhesion and contact angle analysis. All of these coatings exhibited similar contact angles with water, indicating comparable surface energetics (Table 1).

Table 1. Contact Angles of Water

	A	B	C	D	E	F
θ_A (degrees)	114	110	114	111	115	116
θ_R (degrees)	93	97	72	93	***	81

The advancing and receding contact angles of water on various silicone elastomers. *** indicates that the contact line of the water drop was pinned on this surface.

The adhesion strengths of an acrylic adhesive to these surfaces were measured by a peel test at a 40° peel configuration, according to a method described previously^{7,10,11}. The peeling was started by hanging dead loads on one end of the tape. The delamination of the adhesive was examined under a microscope, which allowed accurate estimation of the crack growth rates. The adhesive fracture energy (G) was estimated from the peel force (F) values according to equation (1)¹²:

$$G = F(1 - \cos\theta) \quad (1)$$

Where, F is the peel force per unit width of the adhesive, and θ (40°) is the peel angle. The fracture energies exhibited a pronounced dependence on the peel velocity V (Fig. 2), which is typical of a viscoelastic adhesive.

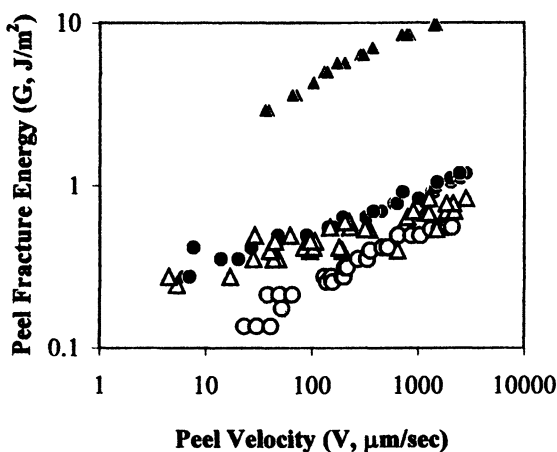


Fig. 2. Relationship between peel fracture energy (G) and velocity (V) of crack propagation. The adhesion strengths on these coatings decrease according to the following trend: $F > C > D > E > A \sim B$. For clarity, the data are shown only for A(O), C(●), D(△), and F(▲).

The release forces of the acrylic adhesive varied markedly from substrate to substrate, even though the surface energies of these coatings, as inferred from the contact angles of water, do not vary in a remarkable way. There was also no obvious correlation between the release forces and the contact angle hysteresis on these surfaces.

Direct Measurement of Surface Energetics of PDMS Coatings by Contact Mechanics

Although the surface energies of the silicone coatings could be inferred from the contact angles, we estimated their surface energetics more directly by contact mechanics. The method of contact mechanics, pioneered by Johnson et al.¹³, measures the deformations produced on bringing a hemispherical material into contact with another flat or hemispherical object. A mechanical calibration of the contact deformation using equation (2) yields the elastic stiffness and the adhesion energy of the system.

$$a^3 = \frac{R}{K} \left\{ P + 3\pi WR + \left[6\pi WRP + (3\pi WR)^2 \right]^{1/2} \right\} \quad (2)$$

where a is the contact radius, R is the radius of curvature of the hemisphere, K is the elastic stiffness, W is the work of adhesion, and P is the applied force. For a graphical analysis of the data, equation (2) can be rearranged as follows:

$$\frac{a^{3/2}}{R} = \frac{1}{K} \frac{P}{a^{3/2}} + \left(\frac{6\pi W}{K} \right)^{1/2} \quad (3)$$

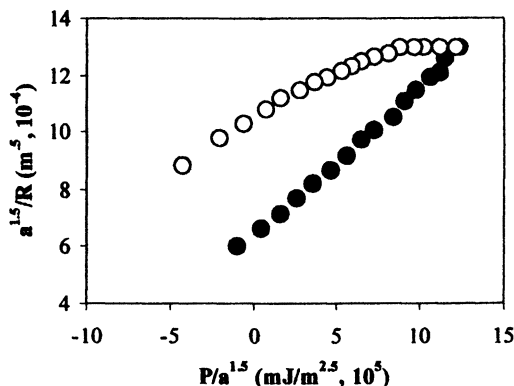


Fig.3. A typical plot of $a^{1.5}/R$ vs. $P/a^{1.5}$ for a hemisphere made of polymer C on a film of polymethylmethacrylate. Closed circles (●) represent the data obtained from the loading experiments, whereas the open circles (○) represent the data obtained from the unloading experiments.

According to equation (3), a plot of $a^{3/2}/R$ versus $P/a^{3/2}$ should yield a straight line (Fig. 3), the slope and intercept of which give the elastic stiffness (K) and the work of adhesion (W). Using the JKR methodology, we have examined the surface characteristics of the silicone elastomers by contacting hemispherical lenses of the elastomers with a polar (polymethylmethacrylate) and a nonpolar (polystyrene) surface, first increasing the loads and then decreasing the loads. The works of adhesion from these loading (W_L) and unloading (W_U) experiments are summarized in Table 2.

Table 2. Adhesion Energies of Silicone Coatings

	A	B	C	D	E	F
W_L^{PMMA} (mJ/m ²)	27	41	41	27	40	35
W_U^{PMMA} (mJ/m ²)	82	71	162	108	134	83
W_L^{PS} (mJ/m ²)	32	38	45	26	40	22
W_U^{PS} (mJ/m ²)	86	66	69	86	79	43
K (MPa)	1.73	0.97	1.9	1.05	0.63	1.96

Loading (W_L) and unloading (W_U) works of adhesion (mJ/m²) of various silicone polymers on PMMA and PS as obtained from contact mechanics. The elastic stiffness of the coatings as obtained from the loading part of these measurements are reported. Note that the coatings C and F were quite non-compliant and thus were not suitable for the JKR measurements. The adhesion energies of C and F were measured by supporting thin films of these coatings on a deformable PDMS lens. (See reference 14 for details).

The W_L values of the polymers are in the range of 40-45 mJ/m². In some cases, unusually low values of W_L were observed (22-27 mJ/m²). We suspect that these are influenced by surface roughness or other imperfections.

All the surfaces exhibit adhesion hysteresis (i.e., $W_U > W_L$) to various degrees. The hysteresis, in general, is lower on PS than on PMMA, which may reflect that the silicone polymers engage in polar interactions with the latter substrate. We take the adhesion of the silicone polymers on polymethylmethacrylate as an indicator of the interaction between the silicone polymers and the acrylic adhesive. The trends of these adhesive energies, like the contact angles, are not consistent with the trend of the release profiles of the elastomers shown in Fig. 2. We next investigated whether there is any correlation between the release profiles of the various silicone elastomers and their interfacial slip characteristics based on the methodology described by Newby and Chaudhury¹⁰.

Investigation of Interfacial Slippage

The adhesive tapes used for the slip experiments were prepared by sparingly coating their surfaces with small (.5 μ m) fluorescent latex (polystyrene) particles. After these adhesive tapes were placed on the test substrates, they were peeled at a 40° peel

angle under a fluorescent microscope. The slippage of the adhesive was ascertained from the lateral displacement of the latex particles, as the crack tip approached towards them. The slippage patterns are shown in Fig.4.

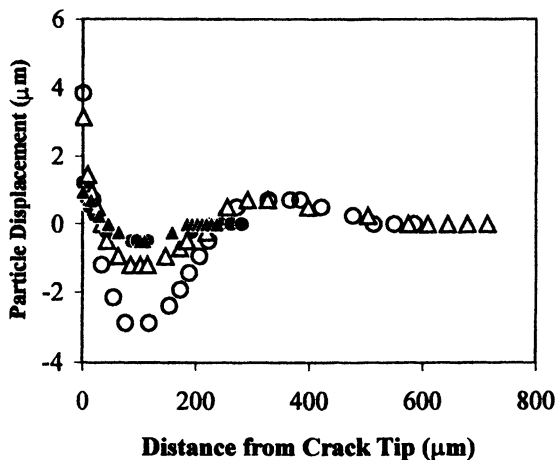


Fig.4. Oscillatory motion of fluorescent particles at the adhesive-polymer interfaces. Positive displacement indicates that the particles move away from the crack tip. The interfacial slippage close to the crack tip decreases as follows: A~B>E>D>C>F. This trend is consistent with the peel force data shown in Fig.2. For clarity, the data are shown only for A(O), C(●), D(Δ), and F(▲).

All the particles exhibited oscillatory motion on the PDMS surfaces. The particles first moved when they were as far away as 600 μm from the crack tip, then moved toward and finally away from the crack tip before being carried away by the separated adhesive.

From the slip profiles, it is evident that coating F, which exhibits the poorest release of the acrylic adhesive, exhibits smallest amount of interfacial slippage. In this case, the net displacement of the particles is only about 1 μm . On the other hand, the slippage of the adhesive is highest (4 μm) on coatings A and B, which exhibit the best release characteristics. These results strongly suggest that there is a direct relationship between the adhesive release behavior of a surface and its ability to relieve shear stress by interfacial slippage. This point is more strongly emphasized by the direct measurement of the shear stress that was obtained by sliding the adhesive on the silicone-coated glass slides at different velocities. Fig. 5 summarizes these results. The shear stress is clearly highest on coating F and lowest on coating A. The sequence (F>C>D>E>B~A) of the shear stress values, as well as that of interfacial slippage near the crack tip, is the same as that obtained from the peel tests (Fig. 2).

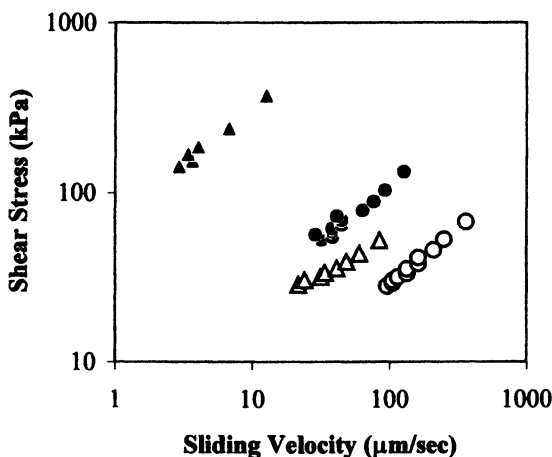


Fig.5. The interfacial shear stress of an acrylic adhesive on silicone coatings as a function of shear velocity. Interfacial shear stress decreases as follows: F>C>D>E>B~A, which is in complete agreement the trends of the peel fracture energy and interfacial slippage. For clarity, the data are shown for the coatings A(O), C(●), D(Δ), and F(▲).

These agreements reconfirm our previous finding¹⁰ that the release properties of surfaces are controlled to a significant extent by interfacial friction.

Summary and General Comments

The adhesion of an acrylate adhesive to the silicone coatings does not correlate in any simple way with the energetics of the surfaces as inferred from the contact angle and contact mechanics. Direct velocimetry using fluorescent particles shows that the adhesive undergoes significant slippage on surfaces, which allows easy release of the adhesive. It is likely that, as a result of slippage at the crack tip, the adhesive deformation, and thus the fracture energy, is minimized. There are, however, several issues that will require careful attention in the future. For example, it will be important to understand the precise relationship between the deformations and flow fields in the bulk of the adhesive and near the crack tip region. There are clearly cases where slippage is so extensive that it penetrates deeply into the interface from the crack tip⁷. In many cases, however, slippage is limited to the crack tip region. This latter problem may be of greater importance than the one of extensive slippage and requires careful analysis. In a general way, the slippage at the crack tip would control the dynamic contact angle θ_d , thus affecting the shape of the adhesive in the crack tip region, and consequently, the energy dissipation due to viscoelastic flow⁷.

The general picture is perhaps clear. However, predicting the dynamic contact angle of a viscoelastic material on a solid surface poses a formidable challenge.

Acknowledgements

We thank the Office of Naval Research (Grant N00014-97-1-0162) for financial support of this work. We also thank Greg Bauch of Dow Corning Corporation for supplying us with the silicone coatings used in this research.

References

1. Gent, A. N.; Schultz, J. *Journal of Adhesion* **1972**, *3*, 281
2. Gent, A. N.; Kinloch, A. J. *Journal of Polymer Science* **1971**, *A2(9)*, 659
3. Andrews, E. H.; Kinloch, A. J. *Proceedings of the Royal Society* **1973**, *A332*, 385.
4. Kinloch, A. J. *Adhesion and Adhesives (Science and Technology)*; Chapman and Hall, London, **1987**
5. Good, R. J.; Gupta, R. K. *Journal of Adhesion* **1988**, *26*, 13
6. Lee, L. H.(Eds) *Adhesive Bonding*; Plenum Press, New York, **1991**
7. Zhang Newby, B-m; Chaudhury, M. K.; Brown, H. R. *Science* **1995**, *269*, 1407
8. Hutchinson, J. W.; Suo, Z. *Advances in Applied Mechanics* **1992**, *29*, 63
9. Schallamach, A. *Wear* **1963**, *6*, 375
10. Zhang Newby, B-m; Chaudhury, M. K. *Langmuir* **1997**, *13*, 1805
11. Zhang Newby, B-m; Chaudhury, M. K. *Langmuir* **1998**, *14*, 4865
12. Kendall, K. J. *Physics D: Applied Physics* **1975**, *8*, 1449
13. Johnson, K. L.; Kendall, K.; Roberts, A. D. *Proceedings of the Royal Society of London*, **1971**, *A324*, 301
14. Mangipudi, V. S.; Huang, E; Tirrel, M.; Pocius, A. V. *Macromolecules Symposium* **1996** *102* 131

Chapter 6

Response of Thin Oligomer Films to Steady and Transient Shear

Mark O. Robbins¹ and Arlette R. C. Baljon²

¹Department of Physics and Astronomy, Johns Hopkins University,
Baltimore, MD 21218

²Chemistry Department, Cornell University, Ithaca, NY 14853

Molecular dynamics simulations are used to examine the shear response of atomically thin films of simple short-chain molecules. A wide variety of behavior is observed including steady sliding, oscillatory motion, stick-slip motion and transient ordering. The steady-state response reveals a glass transition as pressure increases or film thickness or temperature decreases. The changes in dynamics are independent of how the glass transition is approached, and all results for the shear-rate dependent viscosity collapse onto a universal curve using a generalization of time-temperature scaling. When the yield stress of glassy films is exceeded they exhibit stick-slip motion. Slip occurs through melting of the film, or interfacial sliding at the wall or within the film. Long term memory effects are observed due to ordering at the wall/film interface.

Experiments with the Surface Force Apparatus have revealed a fascinating range of dynamic behavior when oligomers are confined between two parallel surfaces separated by less than a few nanometers (1-14). As the film thickness decreases, the relaxation times and viscosities of simple fluids increase by 10 or more orders of magnitude. At small enough thicknesses, films enter a solid state that is capable of resisting static shear forces (1,3,11,12,14). When the yield stress of these films is exceeded, motion occurs through intermittent stick-slip events rather than smooth sliding (3-5,8,9). Stop/start experiments (3,5) and the response to oscillatory shear (10) reveal that films store memory of their previous sliding history for very long times.

In this chapter we describe some molecular dynamics (MD) simulation studies (15-23) of this rich experimental system. After describing the simulation methods, we consider the origin of long relaxation times. Experiments and simulation results are consistent with the onset of a glass transition as the spacing between the confining

walls decreases. We compare results for decreasing wall spacing to results for decreasing temperature in a bulk system. The same changes in dynamic response occur in the two cases. Moreover, the results for all thicknesses and temperatures collapse onto a single universal curve when viscosities are renormalized by the low shear rate value and shear rates are scaled by the relaxation rate. This indicates that confinement does not produce a new type of glass transition. Instead it shifts the glass transition temperature in much the same way as an increase in bulk pressure.

If the thickness or temperature is decreased below the glass transition, one observes very non-linear response to an applied stress. The films are solid-like at low stresses and shear when a yield stress is exceeded. In experiments, an alternating or constant displacement is applied through a system with some intrinsic elasticity. We illustrate the types of non-steady or "stick-slip" motion that results in these two cases and discuss the effect of system compliance. We also describe how molecules move when the film yields. In some cases the film transforms to a liquid-like state, and in other cases yield occurs at an interface between the film and a wall.

The stick-slip events exhibit memory over extremely long times (3,5,10). The origin of this memory must be some structure stored in the glassy film, but experiments can not determine the nature of this structure. The paper concludes with a study of the onset of sliding that shows how order in the film increases as it shears. It had been suggested, by analogy with bulk polymers under shear, that order might be stored through alignment of molecules along the shear direction. However, for our systems memory is stored through alignment of monomers in channels between lines of wall atoms that allows easy shear at the wall/film interface. This alignment allows memory of past sliding to be stored for arbitrarily long times in glassy films. Experimental tests of this mechanism are suggested.

Simulation Method

Potentials and Geometry. We will describe results for films containing linear short-chain molecules. These are modeled using a simple bead-spring potential that has been used extensively in studies of polymer structure and dynamics (24). Each spherical monomer within the molecule interacts with all other monomers through a Lennard-Jones (LJ) potential V_{LJ} that is truncated beyond r_c . For monomers separated by a distance $r < r_c$,

$$V_{LJ}(r) = 4\epsilon[(\sigma/r)^{12} - (\sigma/r)^6 - (\sigma/r_c)^{12} + (\sigma/r_c)^6] , \quad (1)$$

where ϵ and σ are characteristic energy and length scales of the potential, respectively.

The cutoff at r_c is introduced to speed the calculations. It has two major effects on the results. One is a trivial shift upwards in the pressure at a given density. The second is an increase in the viscosity or shear strength of the film. For one value used below, $r_c = 2.2\sigma$, both effects are small. Both effects are large for the other value used, $r_c = 2^{1/6}\sigma$, but the same trends in structure and dynamics are observed with substantial savings in computer time.

Adjacent monomers within the same molecule are connected by an additional anharmonic potential

$$V^{\text{CH}}(r) = -\frac{1}{2} \kappa R_0^2 \ln[1 - (r/R_0)^2] \quad , \quad (2)$$

that is strongly attractive. We used values of $R_0 = 1.5\sigma$ and $\kappa = 30\epsilon\sigma^{-2}$ that have been shown to prevent unphysical bond crossing and breaking in polymer melts at comparable densities and temperatures (17,21,24). The results presented below are for linear chains of $n=6$ or 16 monomers. Qualitatively similar results (17,20,21,25,26) are obtained for chains with n between 4 and 16. For comparison, the entanglement length of these model molecules (24) is between 30 and 35.

Each of the walls confining the film contains two (111) layers of an fcc crystal. The axes are chosen so that the layers lie in the x - y plane and the film thickness is measured along the z -axis. Periodic boundary conditions are imposed in the x - y plane. Each wall atom is tied to a lattice site with a spring. These are stiff enough that thermal displacements are less than the Lindemann criterion for melting (20,27).

Wall atoms and fluid monomers interact with a LJ potential that has different energy and length scales, ϵ_w , σ_w , and r_{cw} , than the monomer-monomer interaction. These parameters play an important role in determining the interfacial shear strength at the wall/film interface (27). Another important factor is the nearest-neighbor spacing d_{nn} between wall atoms (27). When d_{nn} is comparable to the spacing between monomers in the film, the monomers can easily lock into registry with the wall, and the shear strength is high. The mean spacing was chosen to suppress such epitaxial order in the simulations presented below.

Units. All quantities will be expressed in terms of ϵ , σ , and the characteristic time $\tau = \sigma(m/\epsilon)^{1/2}$, where m is the monomer mass. Appropriate values for real materials are in the range of tens of meV, a fraction of a nanometer, and a few picoseconds, respectively.

Method of Imposing Shear. The magnitude of the frictional force that is measured in an experiment or simulation can be strongly influenced by the way in which sliding is imposed. Most experiments impose a constant normal load (1-9,14), while simulations have often fixed the separation between the walls. This can produce dramatically different results. For example, as discussed below, the power law relating viscosity and velocity in thin films is changed when simulations are done at fixed thickness rather than fixed load (17,20,25,26). Unless otherwise noted our simulations mimic experiments by imposing a constant load on the walls. Since the area A in the x - y plane is constant, this is equivalent to fixing the pressure P_{\perp} normal to the walls. The constant pressure constraint is implemented by fixing the bottom wall and moving the top wall in response to any imbalance between the instantaneous internal pressure and the external pressure P_{\perp} (20).

The frictional force may also depend on the direction of sliding, and the relative orientation and registry of the two walls. The situation is illustrated in Figure 1 which shows a representative contour plot of the energy as a function of position as a single monomer moves over a (111) surface. The maximum energy positions (circles)

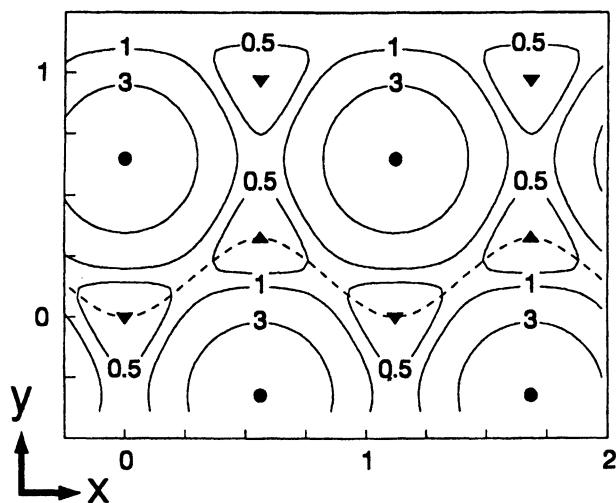


Figure 1. Schematic energy contours (in ϵ) for motion of a monomer over the (111) surface of an fcc crystal. Circles indicate locations directly above surface atoms and triangles indicate hollows between surface atoms. The zero is chosen to coincide with the energy at hollow sites, and the energy above surface atoms is about 6. The dashed line shows the lowest energy path for motion along x . (Reproduced with permission from Ref. 22.)

lie directly over atoms in the wall. The minimum energy positions (triangles) lie in the hollows between wall atoms. Most sliding directions eventually cause the monomer to pass directly over the high-energy positions, but there are low energy paths along the x-axis and at 60° and 120° to it. This leads to lower frictional forces in these directions.

A dashed line that weaves between energy minima indicates the most energetically favorable path for motion along the x-axis. Whether the monomer can follow this path depends on the rigidity of the measurement apparatus and film. If the monomer were attached to the tip of a very stiff cantilever on an atomic force microscope, it could be forced to trace out a straight line at fixed y . For some values of y the monomer would pass directly over energy maxima. The energy would then vary by about 6ϵ vs. about 0.6ϵ on the dashed line. Since the energy change sets the scale for the amount of energy that can be dissipated through friction, the measured friction depends strongly on y . As the measurement apparatus and film become less stiff, the y component of the force from the wall is able to displace the monomer to more energetically favorable values of y . In the limit of a very compliant apparatus or computer program, the monomer can always follow the dashed line.

The SFA is very compliant on the atomic scale. For thin films, we modeled this compliance by coupling the displacement of the top wall to two springs that controlled motion in the directions normal and parallel to the average sliding direction. The springs were weak enough to allow the wall to be displaced relatively easily by a lattice constant, but strong enough to prevent displacements that were comparable to the dimensions of our simulation cell. For runs with thicker films ($h > 6\sigma$), the internal compliance of the film was sufficient to allow lateral displacements.

Maintaining Constant Temperature. The work done in order to slide the walls past each other is converted into random thermal motions. This heat will cause the temperature of the simulation cell to rise indefinitely, unless the cell is coupled to an outside heat bath.

There are several strategies that are used to maintain constant temperature in equilibrium systems. All of them define an instantaneous effective temperature based on the instantaneous kinetic energy of the atoms and equipartition. The equations of motion for atoms are then modified so that the kinetic energy will maintain a value consistent with the temperature of the heat bath.

Non-equilibrium simulations require a modified approach. One change is that there are average velocities of the atoms that contribute to the kinetic energy, but are not random thermal motions. These must be subtracted from the instantaneous velocities of each atom to define the local temperature (28-30). A second issue is that heat may be generated at different rates in different regions of space. Some thermostats, including the Nose-Hoover method, remove heat from all regions of space uniformly. This can lead to overcooling of regions where less heat is generated. We have chosen to use a local Langevin method where a damping and noise term are added to the equations of motion of individual atoms (20,31). In most cases, the thermostat was only coupled to the random component of the velocities of wall atoms. This represents a physically reasonable model for flow of heat generated in the film through the wall layers that are treated explicitly in our simulation and then on into the

subsequent wall layers that are not treated explicitly. Good temperature control is provided for the system sizes and shear rates described below. However care should be exercised, since the temperature rise in the center of the film increases roughly quadratically with both system size and shear rate (32).

For some simulations, including Figure 6, the wall atoms were fixed to lattice sites and thus had no random velocities. In such cases, constant temperature was maintained by coupling one component of the fluid velocity to a Langevin heat bath. This component was chosen to be perpendicular to both the z-axis and to the direction of wall motion so that there was no flow of atoms along the thermostated direction. Our tests and previous work (27) show that thermostating the walls or the atoms gives equivalent results for the range of system thicknesses and velocities of interest here. Experiments are typically performed at much lower velocities where heating is completely irrelevant.

Phase Transitions and the Steady State Shear Response

The phase of the film is affected by the temperature T , normal pressure P_{\perp} , film thickness h , wall structure, and also the imposed shear stress or shear rate. Entropy tends to dominate at high T and h , and at low P_{\perp} . In these limits unsheared films are in a simple liquid state. The film thickness is important because walls decrease the entropic degrees of freedom of adjacent molecules and thus favor a solid state. Shear favors the disordered liquid state at the shear rates of interest here, but may favor ordered states at much higher shear rates (30,33).

The film enters a solid state as T or h decrease or P_{\perp} increases. Bulk films of spherical molecules tend to crystallize (27,34,35). Walls may frustrate or enhance crystalline order in molecularly thin films, depending on the relative size of wall and fluid atoms and the relative orientation of the crystalline axes of the walls. Recent simulations of rigid short-chain alkanes indicate that they also crystallize when confined between hydrocarbon walls (36) although crystallization is not observed with metal wall potentials (37-39). The more flexible linear molecules used here enter a glassy state. As we now illustrate, the nature of the changes in the dynamical response near the glass transition is the same whether T , h , or P_{\perp} is varied.

To quantify the response of a system to shear, a tribologist would normally plot the frictional force per unit area f , or shear stress, as a function of the sliding velocity v . A rheologist would plot the viscosity of the film $\mu=f/\dot{\gamma}$ as a function of shear rate $\dot{\gamma}=du_x/dz$, where u_x is the local velocity at a given value of z . The actual shear rate in the center of the film is readily determined in simulations, but not in experiments. Experimental measurements are normally presented in terms of an effective mean shear rate across both the film and the wall/film interface $\dot{\gamma}_{\text{eff}}\equiv v/h$. The effective viscosity is then $\mu_{\text{eff}}\equiv f/\dot{\gamma}_{\text{eff}}$.

Figure 2 shows the temperature dependence of f and μ_{eff} at $P_{\perp}=0$ in a film that is thick enough to exhibit bulk behavior. The high temperature behavior is typical of a simple fluid. At low shear rates the response is Newtonian: The shear stress rises linearly and the viscosity is constant. At high shear rates the fluid can not relax as rapidly as it is sheared, and the viscosity begins to drop. The crossover shear rate is

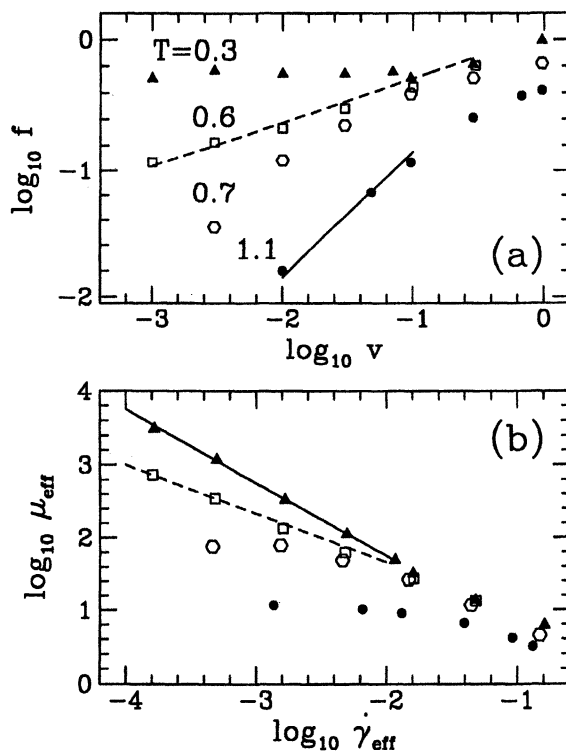


Figure 2. The frictional force f per unit wall area for chains of length 16 is plotted against wall velocity for the indicated values of T in (a). Dashed and solid lines have slope 1/3 and 1, respectively. The effective viscosity μ_{eff} vs. shear rate $\dot{\gamma}_{\text{eff}}$ at the same values of T is shown in (b). Here the dotted and solid lines have slopes -2/3 and -1. Data are for films containing 512 monomers at $P_{\perp}=0$ with 200 atoms in each wall and $\epsilon_w=2\epsilon$, $\sigma_w=0.9\sigma$, $d_{\text{nn}}=0.963\sigma$, $r_c=2.2\sigma$, and $r_{\text{cw}}=2.2\sigma_w$. (Reproduced with permission from Ref. 22.)

$\sim 0.03 \tau^{-1}$ at $T=1.1\epsilon/k_B$ in Figure 2. As for simple fluids (40,41), this is about an order of magnitude smaller than the thermal velocity divided by a molecular dimension, and indicates that motion is relatively unhindered. As T decreases, the limiting low shear rate viscosity μ_0 begins to rise, and non-Newtonian behavior (changing μ_{eff}) sets in at progressively lower shear rates. A characteristic relaxation time τ_r can be identified with the inverse of the shear rate $\dot{\gamma}_r$ where μ_{eff} begins to drop. Both μ_0 and τ_r rise rapidly as T decreases. By $T=0.6\epsilon/k_B$, the value of μ_{eff} continues to rise at the lowest shear rates that we have been able to consider. The friction and viscosity follow power laws, $f \propto v^{1/3}$ and $\mu_{\text{eff}} \propto \dot{\gamma}_{\text{eff}}^{-2/3}$, over a wide range

The exact nature of glass transitions is still a matter of debate. Some argue that the relaxation time diverges at a finite temperature T_g , while others argue that it merely increases so rapidly that it can not be observed below T_g . Our goal is not to resolve this issue, but we do observe a qualitatively different shear response once τ_r becomes too long for us to measure. As illustrated by the data for $T=0.3\epsilon/k_B$, the kinetic friction or shear stress becomes independent of velocity and μ_{eff} decreases as the inverse of $\dot{\gamma}$. This is typical of the frictional force between macroscopic solid surfaces (42,43) and is consistent with solidification of the film.

The same changes in f and μ are observed when h is decreased or P_{\perp} is increased at fixed T in either experiments (3,7-9,13) or simulations (17-20). Figure 3 shows the behavior for one system. In (a) the thickness was varied by changing the number of fluid layers m_l between the walls at fixed P_{\perp} , and in (b) the pressure was varied with a fixed number of layers. Newtonian behavior with the bulk viscosity is seen for thick films ($m_l \geq 6$) and at low pressures in thin films (e.g. $P_{\perp}=2$ for $m_l=4$). As pressure rises or thickness decreases, μ_0 and τ_r rise rapidly. For the extreme cases shown in Figure 3, τ_r is too long for us to observe and the viscosity follows a power law $\mu_{\text{eff}} \propto \dot{\gamma}_{\text{eff}}^{-2/3}$ over the entire range of shear rates. At higher pressures or for fewer layers than shown here (20), we observe the solid-like behavior seen for $T=0.3$ in Figure 2: The shear stress becomes constant and $\mu_{\text{eff}} \propto \dot{\gamma}_{\text{eff}}^{-1}$.

The trends can be understood in terms of the free volume picture that is often applied to glass transitions (44). The idea is that the molecules in a glass are too tightly packed to move past each other. Increasing the volume of the material adds "free volume" V_f . The more free volume, the more likely a molecule is to find a gap that it can move through to a new position. The diffusion constant and relaxation rate $\dot{\gamma}_r$ are predicted to vary as $\exp(-V_0/V_f)$, and Figure 4 shows that results for confined films (18,20) can be fit to this form with $V_f \propto h-h_c$. Increasing pressure clearly decreases the amount of free volume and favors the glassy state. Confining walls limit the freedom of molecules to move and may also increase the density if wall fluid interactions are attractive. Both effects limit the free volume and lead to a glassy state. Decreasing temperature leads to thermal contraction, and thus decreases free volume. For the case of Figure 2, the volume per monomer decreases from $1.15\sigma^3$ at $T=1.1 \epsilon/k_B$ to $0.98\sigma^3$ at $T=0.6\epsilon/k_B$ to $0.94\sigma^3$ at $T=0.3 \epsilon/k_B$.

Scaling Near the Glass Transition. It is important to note that while the behavior shown in Figure 3 is very similar to that seen in experiments, the time scales probed by the two techniques are very different. Experiments are usually performed at

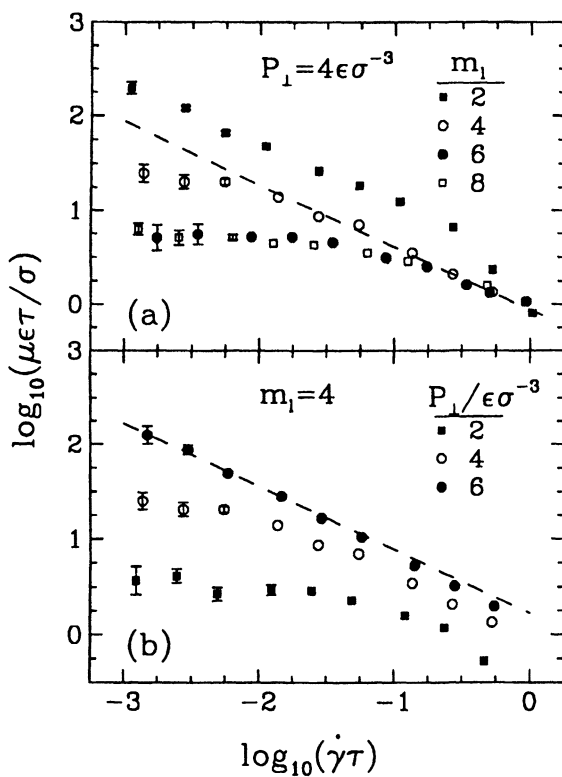


Figure 3. Plots of μ vs. shear rate from Ref. 17 for 6-mers at (a) fixed $P_{\perp} = 4\epsilon\sigma^{-3}$ and varying m_1 , and (b) fixed m_1 and varying P_{\perp} . Dashed lines have slope $-2/3$. Both panels show the same behavior as Figure 2 as the glass transition is approached. Other parameters were $\epsilon_w = 3\epsilon$, $r_{cw} = 2.2\sigma$, $r_c = 2^{1/6}\sigma$, $d_{nn} = \sigma$, and $k_B T = 1.1\epsilon$. (Reproduced with permission from Ref. 17.)

velocities less than 10^{-5} m/s, while simulations on current computers have been limited to velocities greater than 10^{-1} m/s. The duration of experiments and simulations differ by an even larger number of orders of magnitude. Thus one may wonder whether the two methods are really probing the same phenomenon. While the only way to prove the connection would be to extend the methods to overlapping time scales, scaling behavior near other glass transitions covers even more decades of time scale than the above experiments and simulations combined. There are many cases where two or more experimental methods that probe different ranges of time scales can be compared quantitatively using time-temperature scaling. Results from all methods and temperatures for a quantity like viscosity fall on to a universal curve when normalized by the low frequency value at each temperature and plotted against the shear rate normalized by the characteristic relaxation rate at that T.

In the case of interest here, the film thickness may play the role of temperature. Demirel and Granick (13) have studied the real and imaginary parts of the elasticity, which can be related to the viscosity. They found that results for different thicknesses of OMCTS could be collapsed onto a universal curve like those used in time-temperature scaling. Although the data at each thickness only covered three or four decades in frequency, the final curve spanned 7 decades.

Figure 5 shows a similar collapse of simulation results for the viscosity. Each curve is normalized by the low frequency viscosity μ_0 . Then the shear rate is normalized by the shear rate where the viscosity has dropped to $\mu_0/2$. Results for different temperatures in bulk films of 16-mers (Figure 2) and for thin films of 6-mers with different interactions (Figure 3a, b and other cases from Ref. 20) all collapse on to a universal curve. Viscosities were typically measured over three decades at any given set of parameters, but the combined curve spans five decades. The collapse of many different, overlapping observations indicates that there is a universal response function present at all temperatures and thicknesses that moves to lower shear rates as one approaches the glass transition. As in experiments, different parts of this universal curve fall into the observable range of shear rates at different thickness and temperatures. Although the observable ranges of our simulations and experiment are very different, the close similarity between the observed variations in viscosity, and the observation of universal scaling in both sets of data, suggests that the same phenomena are being observed.

The universal curve in Figure 5 helps to clarify one of the robust features in previous simulations (17-20,25,26). For a wide range of parameters, the viscosity at constant load is observed to decrease as $\dot{\gamma}^{-x}$ with x near 2/3. The high shear rate tail of the universal curve is best fit by a slope of 0.69 ± 0.03 . As long as one is close enough to the glass transition to observe a substantial region of the tail, and thus a substantial decrease in viscosity, one will conclude that the exponent x is near 2/3. Simulations with short alkanes between hydrocarbon surfaces were kept from accessing this region because the chains crystallized (36). They sampled the crossover region where the apparent exponent is smaller and the total change in viscosity is also small. Similar variations in the effective slope with the distance from the crossover shear rate have been seen in experimental data (7,45).

While several analytic theories for the exponent relating μ and $\dot{\gamma}$ at constant load have been presented (46-48), none seem able to account for the wide range of shear profiles and molecular geometries where it is observed. Thompson et al. (20) explored a variety of systems to determine what factors might change the power law describing the drop in viscosity. They found that all simulations at constant load gave a power law consistent with Figure 5. However, simulations (17,20,25,26) at fixed h yielded an exponent of $-1/2$ instead of $-2/3$. An exponent of $-1/2$ is also found in bulk simulations for the same chain molecules at fixed volume (49). It would be interesting to determine whether results for constant volume could be collapsed onto a universal curve like that in Figure 5, but with a different power law shear thinning at large shear rates.

In the following we will focus on the low temperature, small h limit where the films have entered a glassy state. Two types of SFA experiments have been done in this limit. Granick and coworkers have applied an oscillatory shear and studied the dependence on amplitude and frequency (6-12). Israelachvili and coworkers have generally studied steady sliding (1-5). Both types of motion are discussed below.

Unsteady Motion

Response to oscillatory shear. Figure 6 shows the response of a glassy film to an oscillatory shear force. To mimic the SFA experiments, the top wall was pulled by a spring ($k/A = 7.94\epsilon/\sigma^3$) coupled to a translational stage. The stage was displaced sinusoidally, and its position is shown by dashed lines in panels (a) and (c). A solid line shows the position of the top wall. The force f_x on the wall is just the difference in wall and stage positions multiplied by the spring constant (panels (b) and (d)).

For low amplitudes the film responds like an elastic solid. The displacement of the top wall (Figure 6(a)) is in phase with the applied force (Figure 6(b)). Except for a small transient during the first period, both force and displacement are sinusoidal. The two quantities grow linearly with stage displacement and their ratio gives the total elastic shear modulus of the system. This modulus reflects the stiffness of both the wall/film interface and the film itself.

As the displacement of the stage increases, the force on the top wall grows. Eventually it exceeds the yield stress of the system and produces a highly non-linear response. As shown in Figure 6(c), the top wall slips rapidly each time the yield stress is exceeded. The absolute values of the yield stresses for forward and backward slips are roughly equal, but both fluctuate from cycle to cycle.

Similar behavior has been observed in SFA experiments. There is a sharp transition from elastic response to slip as the drive amplitude increases. Experiments can not determine whether slip occurs at the wall/film interface or within the film itself. For the case shown in Figure 6, we find that slip is localized at one of the wall/film interfaces. However, we have also found cases where slip occurs within the film, and cases where both types of slip occur. The size of the slip and the number of slips per period vary with the size of the displacement and the spring constant. For the case shown, the spring is stiff and the system only slips to the nearest low energy state. Much larger slips are observed when the spring stiffness is decreased.

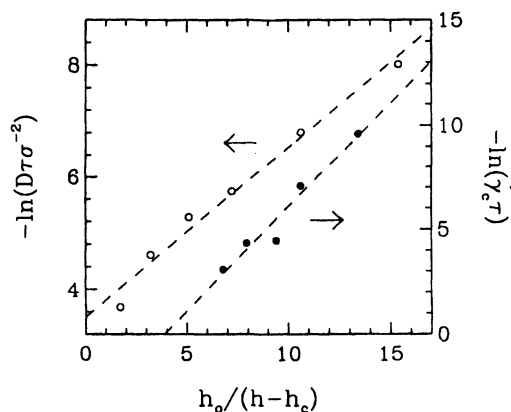


Figure 4. Fit of the variation of diffusion constant D and relaxation rate $\dot{\gamma}_c$ for 6-mers to free volume theory. The logarithms of the two quantities should be proportional to $h_0/(h_c-h)$ where h_c is the thickness at the glass transition. In the fit $h_0=1.58\sigma$ and $h_c=1.57\sigma$. Other parameters were $\epsilon_w=\epsilon$, $r_{cw}=r_c=2^{1/6}\sigma$, $d_{nn}=1.2\sigma$, $m_1=2$ and $k_B T=1.1\epsilon$. (Reproduced with permission from Ref. 20. Copyright 1995 Laser Pages Publishing Ltd.)

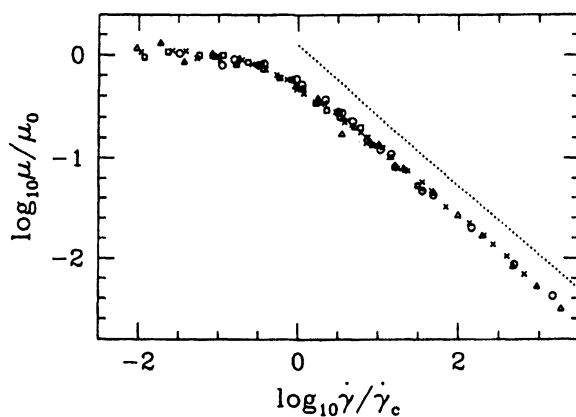


Figure 5. Collapse of data from Figures 2 and 3 and for other cases reported in Ref. 20 onto a universal curve. Each data set was normalized by the low shear rate viscosity μ_0 . Then the shear rate was normalized by the value at which the viscosity had dropped to $\mu_0/2$. Circles represent data from Figure 2, squares from Figure 3(a), triangles from Figure 3(b), and crosses are from simulations with the parameters of Figure 4 or with $\epsilon_w=\epsilon$, $r_{cw}=r_c=2.2\sigma$, $d_{nn}=1.2\sigma$, $m_1=4$ and $k_B T=1.1\epsilon$. The dashed line has slope -0.69 .

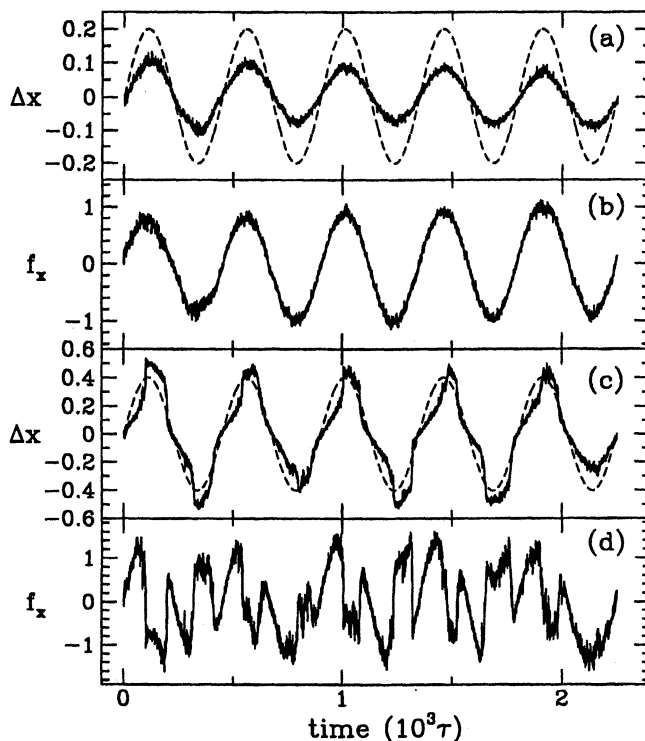


Figure 6. Oscillatory response of a glassy film with two layers of chain molecules of length $n=6$. Panels (a) and (c) show the x component of the displacement of the stage (dashed lines) and top wall (solid lines) at two different amplitudes for a period of 450τ . Panels (b) and (d) show the x component of the corresponding forces on the top wall f_x . There were 288 monomers and 288 atoms in each wall, $\epsilon_w=\epsilon$, $r_{cw}=r_c=2^{1/6}\sigma$, $d_{nn}=1.2\sigma$, $k_B T=1.1\epsilon$, and $P_{\perp}=16\epsilon/\sigma^3$. (Reproduced with permission from Ref. 22.

Copyright 1997 Kluwer.)

One of the most striking experimental observations is that the amplitude and phase of the slip vary in a well-defined pattern over many thousands of cycles (10). This indicates that the film remembers its previous motion over extremely long times. A similar conclusion comes from intermittent sliding experiments (3,5) as we discuss in the next section.

Stick-Slip Motion. Figure 7 shows the response of a glassy system when the translation stage is advanced at constant velocity. Similar behavior is observed in experiments (1-3). Initially the film resists shear and the top wall remains stuck. The force on the wall grows linearly with time as the translation stage advances. When the stress exceeds the static friction f_s , the wall begins to slip forward rapidly. This causes a decrease in the force. Once the force drops below another threshold value, f_t , the top wall sticks, the force rises, and the process repeats.

Oscillatory stick-slip motion of this type is common in everyday life, and leads to the squeak of hinges and the music of violins. Note that in these contexts, and in Figure 7, the distance slipped is roughly equal to the difference between f_s and f_t divided by the translation stage's spring constant. This is very different from the atomic-scale stick-slip observed with atomic force microscopes. In the latter case, the slip distance is tied to a spacing between atoms on the surface and is independent of the spring constant. The potential energy of the tip varies periodically with position, and the tip advances rapidly by a period when the corresponding maximum force is exceeded. This ratcheting motion is well described by Tomlinson's simple model of a particle in a periodic potential (50-52). The behavior of thin films can be much richer. When the spring constant is very large, the slip may be reduced to a single lattice constant. This is the case in Figures 6 and 8. For the weaker springs of Figure 7 and SFA experiments, the slip distance may increase to several or thousands of lattice constants.

The fact that the top wall doesn't stop after advancing by a lattice constant is one indication of memory. The state of the system must have changed or the fact that the force had dropped slightly below f_s would lead the wall to stick once more. A trivial change in the state of the system is its stored kinetic energy. This can provide enough inertia to carry the wall over a potential energy barrier that would pin a stuck wall. However, simulations indicate that structural changes in the system provide longer term memory.

One pronounced change is an increase in the spacing between walls during sliding at constant load. This increase in film thickness was first seen in simulations (15) and has recently been observed in oscillatory shear experiments (10). The thickness changes slowly compared to the time for the top wall to move laterally by a lattice constant and helps to maintain the system in the sliding state.

Two types of structural change occur within the film, depending on the mechanism of sliding. In some cases, slip occurs at the wall/film interface and causes the monomers at the interface to reorder. For Figure 7, all the shear occurs at the interface with the bottom wall. This type of behavior is discussed further in the next section. In many other cases, the entire film undergoes a transition from a static glassy or crystalline state to a shearing liquid state when sliding starts (15,16,20). This transition is induced by the shear and not by an increase in temperature. The random

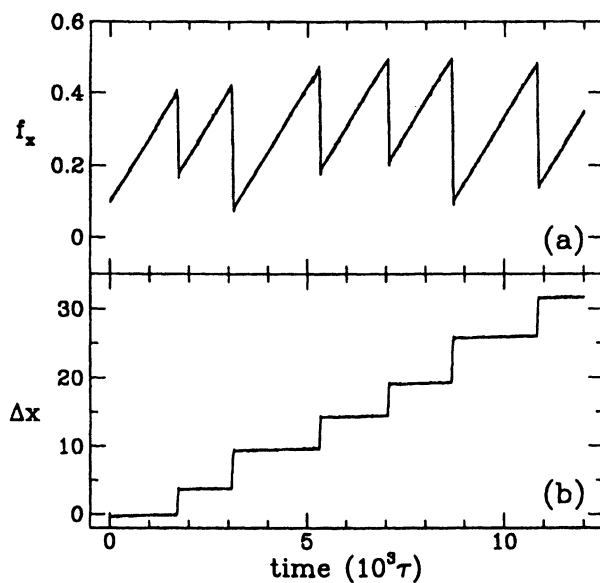


Figure 7. Stick-slip motion of a glassy film at $T=0.3 \epsilon/k_B$ and $v=0.003 \sigma/\tau$ with the parameters of Figure 2 and a spring constant of $k/A=0.0622 \epsilon\sigma^3$. (Reproduced with permission from Ref. 22. Copyright 1997 Kluwer.)

component of the kinetic energy of atoms in our simulations does not increase substantially, and heating effects are even smaller at the much lower velocities used in experiments. Shear-melting transitions at constant temperature have been observed in both theoretical and experimental studies of bulk systems (30,33,53-55). The solid state is stabilized at low temperatures because atoms stay in a structure that minimizes the energy. When a bulk solid is forced to shear, it must sample structures with higher energy. Thus it becomes less stable and may melt. A similar transition can occur in thin films

When sliding starts, or the wall sticks, the film must undergo a transition from one state to another. This time period is generally very short compared to the period of stick-slip motion or of the oscillatory drive. However, the film remembers its past motion for much longer times. As mentioned above, orderly progressions in the yield stress are observed over thousands of oscillations (10). Evidence of memory also comes from intermittent sliding experiments (3,5). In these experiments the stage was moved at a high enough velocity that stick-slip motion was suppressed, and the friction reached a steady state kinetic value f_k . The stage was then stopped suddenly. The force did not relax much below f_k while the stage was stopped, indicating that the film rapidly returned to a glassy state that resisted shear. After an interval Δt , the velocity of the stage was brought back to its initial value. If Δt was small, the frictional force remained at f_k , and the top wall began to slide almost immediately -- it remembered its previous sliding state. However, if Δt was large, the top wall remained stuck until the force increased by Δf to a yield stress. Then it slipped forward rapidly until the force dropped back to f_k . For most films studied, the value of Δf increased rapidly from zero to $f_s - f_k$ after a well-defined waiting time. The conclusion was that films remembered the direction of sliding and moved more easily in that direction until enough time had passed that the film relaxed to its initial state and threshold force f_s . The measured waiting time was a few to many seconds -- much larger than the time required for films to start or stop moving during stick-slip motion, and immensely longer than typical relaxation times in bulk films. The open question is how information about the direction of sliding is stored in the structure of the film for such long times. A possible answer to this question comes from the following simulations of the onset of sliding in glassy films.

Transient Behavior During Yield and Memory Storage.

Figure 8 shows the time dependence of various properties of a film as the top wall was moved forward and then backwards along the x-axis. The initial state was created by cooling an equilibrated state at $T=1.1 \text{ } \epsilon / k_B$ down to $T=0.3 \text{ } \epsilon / k_B$ with $P_{\perp}=0$ over a time interval of 500τ . Similar results were obtained with different initial states. No spring was used between the translation stage and top wall, so the y-coordinate of the top wall was constant.

One of the characteristics of a glassy system is that it can become trapped in any of a large number of metastable states. As the film cooled from 1.1 to 0.3 ϵ / k_B , the film thickness h decreased, but the area in the x-y plane remained fixed. This anisotropy led to stress in the film. When the stress exceeded a local yield stress, the

film became unstable, and rearranged into the nearest metastable state. The stress in the film never relaxed completely, and the film remained somewhat thicker than the lowest energy state. For the case of Figure 8, the film also built up a small stress in the -x direction (see $t=0$ in panel (b)).

The top wall was given a velocity of $0.003 \sigma/\tau$ at time $t=0$, and the velocity was reversed after 6000τ . The potential from the walls induces well-defined layers in the adjacent fluid (56-60). The distribution of shear displacements in the film can be determined from the variation in the mean position of the top and bottom layers as a function of time. In the simulation of Figure 8(a), the top layer remained stuck to the top wall at all times and advanced at a constant speed. During the first 1000τ , the bottom layer was also locked to the bottom wall, and the film sheared internally to a total strain of about 1/2. For $1000\tau < t < 6000\tau$ the bottom layer slid over the bottom wall. The entire film advanced at the mean velocity of the top wall, but the bottom wall ratcheted forward in a series of atomic-scale stick-slip events. There was no external spring attached to the top wall, but the film was thick enough to provide the necessary elasticity for this ratcheting motion. At $t=6000\tau$ the direction of sliding was reversed. The top layer remained locked to the top wall, and the bottom layer ratcheted in the opposite direction over the bottom wall. At $t=7000\tau$ the bottom layer stuck once more. The film sheared internally until $t=8000\tau$ where the net displacement of top and bottom layers was nearly equal. For the remainder of the run, the bottom layer ratcheted over the bottom wall and there was no internal shear.

The changes in the mode of sliding are reflected in the internal properties of the film. Figure 8(b) shows the stress in the film. For the first $\sim 100\tau$ the film remains locked in a metastable state and responds elastically. The force reaches a maximum of about 0.6 before the film begins to shear internally between metastable states. The stress increases while the film is stuck in each metastable state, and there are sudden drops when a state becomes unstable and the system jumps to a new state.

As monomers move over each other to reach new metastable configurations, there are fluctuations in packing density. These show up as variations in h . The size of the peaks in the stress gradually increases because the system can only get locked into a new state if that state resists more stress. At $t=1000\tau$, the stress reaches a maximum value of about unity. The film has now become stiff enough that sliding can occur most easily at the wall/film interface, and the mode of sliding changes to slip at the bottom wall. The bottom layer ratchets over many lattice spacings of the bottom wall. During this time there are small internal rearrangements that cause the ratcheting motion to become more pronounced, and the average film thickness to decrease.

One way that the film might store memory of the sliding direction is through orientational order. This phenomenon is common when bulk polymers are forced to shear. The polymer chains are distorted from random walks with spherical symmetry to an average elliptical shape. If the shear velocity is in the x-direction and the velocity increases along the z-axis, then the major axis of the ellipse is in the x-z plane and its angle depends on shear rate. The degree of order can be quantified by the xz component of an orientational tensor

$$\sigma_{ij} = \langle 3R_i R_j / R^2 - \delta_{ij} \rangle / 2 \quad , \quad (3)$$

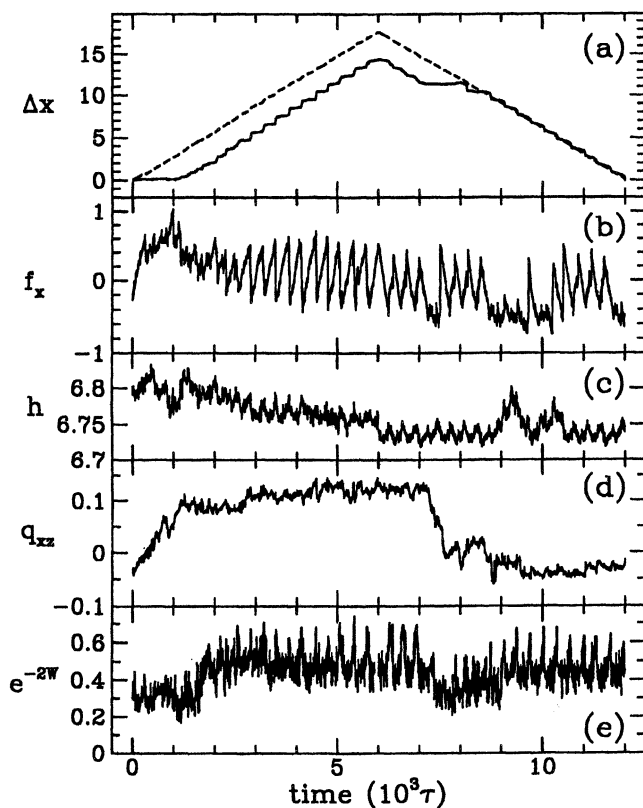


Figure 8. Time dependence of (a) the displacement Δx along the x-axis of the layers of monomers nearest to the top (dashed) and bottom (solid) walls, (b) the x component of the frictional force on the top wall f_x , (c) the wall separation h , (d) the xz component of the orientational tensor q , and (e) the Debye-Waller factor of the bottom layer of monomers e^{-2W} . The top wall was moved with velocity $0.003\sigma/\tau$ in the x direction for the first 6000 τ and then moved back to its original position at the same speed. All parameters were the same as for Figure 2. (Reproduced with permission from Ref. 22. Copyright 1997 Kluwer.)

where i and j indicate Cartesian coordinates, \bar{R} connects the endpoints of a chain, and the brackets indicate an average over chains. When the chains are randomly oriented, q_{ij} vanishes. The maximum value of $q_{xz}=3/4$ occurs when the chains are stretched along the line $x=z$ ($R_x=R_z=R/\sqrt{2}$). As a bulk polymer melt is sheared along the x -direction, the end-to-end vectors are stretched and tilted toward the line $x=z$, and q_{xz} increases (61). The stretching produces elastic stresses and the polymers rearrange to relax this stress and lower q_{xz} . The steady-state value of q_{xz} is determined by a competition between the rate of shear and the rate of relaxation.

Confinement limits the value of R_z and suppresses q_{xz} . Simulations of films confined to only two to four layers found no significant orientational order (20,25,26). In particular, R_x^2 and R_y^2 approached the same value at long times even if anisotropy was imposed on the initial state (20). The film considered here is closer to a bulk system because h is greater than the typical value of R . As shown in Figure 8(d), there is a build up of orientational order during the period ($t < 1000\tau$) where the film shears internally. If the layers slipped past each other with no relaxation of the chains, the change in q_{xz} would equal 0.3 times the imposed strain. The observed increase is roughly equal to this value, indicating that there is little relaxation as the film moves between metastable states. The value of q_{xz} saturates at a small fraction of the maximum order.

The orientational order does not relax on the time scale of our simulations if the velocity of the top wall is stopped. Thus it does represent one type of memory that can be stored in a sufficiently thick film. However, orientation does not appear to be related to the waiting time needed to return the system to its unsheared state and initial yield stress. When the velocity of the top wall is inverted, the orientation should shift to the $-x$ direction. However, the film slides at the bottom wall from 6000τ to 7000τ with no change in orientation. There are three clear ratcheting steps. The peak stress before each step is equal in magnitude, but opposite in sign, to the peak stress before the direction of motion was inverted. The film does shear internally from $t = 7000\tau$ to 8000τ . However, this only returns q_{xz} to its initial random value, instead of building up orientation along the new sliding direction. The film then continues to slide at the bottom wall as before.

Given that sliding is mostly localized at the bottom wall, it is natural that memory is stored in the order at that interface. Figure 9 shows snapshots of the wall and monomer atoms at the bottom of the film. Before sliding starts (Figure 9(a)), the monomers are poorly aligned with wall atoms. If they were displaced in the x -direction, many would pass directly over wall atoms. As illustrated in Figure 1, there is a high energy barrier that blocks such displacements. It is difficult for monomers to displace around wall atoms, because they are locked together in a glassy structure. Thus the barrier for sliding between wall and film is high.

After sliding has occurred (Figure 9(b)), monomers are aligned into horizontal channels between lines of wall atoms. This lowers the barrier for sliding in the x -direction. The degree of order can be quantified by calculating the Fourier component of the monomer density at a wavelength equal to the spacing between lines of wall atoms along the y -axis. When squared and normalized by the mean density, this

quantity gives the Debye-Waller factor e^{-2W} . The Debye-Waller factor varies from zero for a random monomer distribution to unity for perfect periodic order.

As shown in Figure 8(e), there is a sharp rise in the Debye-Waller factor at the point where slip begins to localize at the wall/film interface. At this point the film has rearranged internally to a configuration with a relatively high yield stress of about unity. This applied stress is strong enough to force some of the monomers in the bottom layer to move around wall atoms. They are then likely to get trapped in the low energy channels between wall atoms. The increased order lowers the threshold for sliding at the wall/film interface, and the shear and reorientation within the film stops. As the Debye-Waller factor grows, the stick-slip peaks in f become more regular. Note also that there are peaks in e^{-2W} during each slip. The monomers are most likely to avoid the locations of lines of wall atoms while they are sliding. The peak values of e^{-2W} actually exceed the value of 0.6 found in equilibrium crystals near their melting temperature (36).

In contrast to orientational order, the preferred channeling of monomers is the same for $\pm v$. When the velocity is reversed at $t=6000\tau$ there is no change in the preferred order of monomers and sliding at the wall/film interface is not affected. There is a small drop in order during the internal shear from $t = 7000\tau$ to 8000τ , and then e^{-2W} returns to a high value.

To verify that the Debye-Waller factor could be the origin of long term memory, we set $v=0$ after sliding at the wall had occurred. As expected, there was no noticeable decay in e^{-2W} over the longest times studied ($10^4\tau$). As long as the order remained, the film sheared easily along the bottom wall when sliding was re-initiated.

A more dramatic illustration of memory is shown in Figure 10. The run began from the state at time $t=6000\tau$ in Figure 8. Instead of reversing velocity, the top wall was moved at 60° from the x -axis. This direction is symmetrically equivalent to the x -axis, and simulations for random initial states produce data like that at the start of Figure 8. However, Figure 10 shows very different behavior because the bottom interface remembers its previous sliding direction. The structure of the bottom layer at the start of the run (Figure 9(b)) allows easy sliding along x , but sliding at 60° would bring monomers on top of wall atoms.

Figure 10 shows that the top layer of the film remains stuck to the top wall for $t < 3000\tau$ and thus moves at 60° to the x -axis. The bottom layer of the film slides easily along the channels parallel to the x -axis, but can not slide along the y -axis. This leads to shear in the y -direction within the film, and a corresponding increase in the y component of the shear stress. The stress becomes strong enough to order the top layer of the film at about 3000τ , and slip then occurs between the top layer and the wall. Snapshots like Figure 9 show that the monomers in the top layer are channeled along the sliding direction. Sliding continues to occur at the top wall until about 8000τ . The bottom layer ratchets over the bottom wall for the next few thousand τ , and then slip returns to the top wall/film interface for the remainder of the run. Ratcheting is also visible when sliding occurs at the top wall, but the stuck regions have a slope given by the wall velocity rather than being horizontal.

The channeling observed in our simulations may explain the memory effects seen in SFA experiments. The confining walls of the SFA are generally not aligned

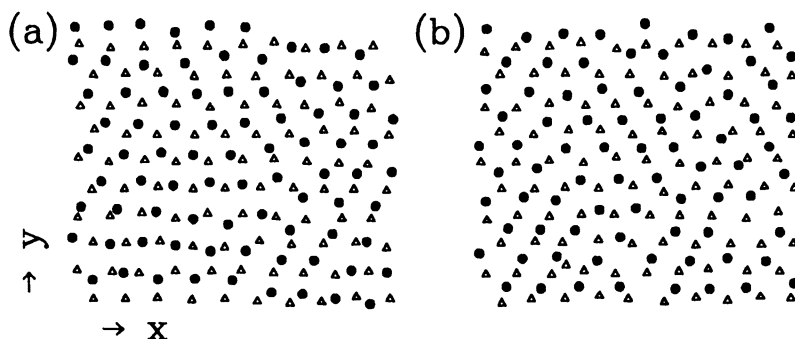


Figure 9. Snapshots of the relative positions of the bottom layer of monomers (circles) and the adjacent layer of wall atoms (triangles) projected onto the x-y plane. Panel (a) shows a configuration before sliding had occurred and (b) shows the configuration at $t=6000\tau$ in Figure 8, when sliding takes place between the bottom layer and the wall. Note that sliding has aligned the monomers in horizontal lines parallel to the direction of motion. (Reproduced with permission from Ref. 22. Copyright 1997 Kluwer.)

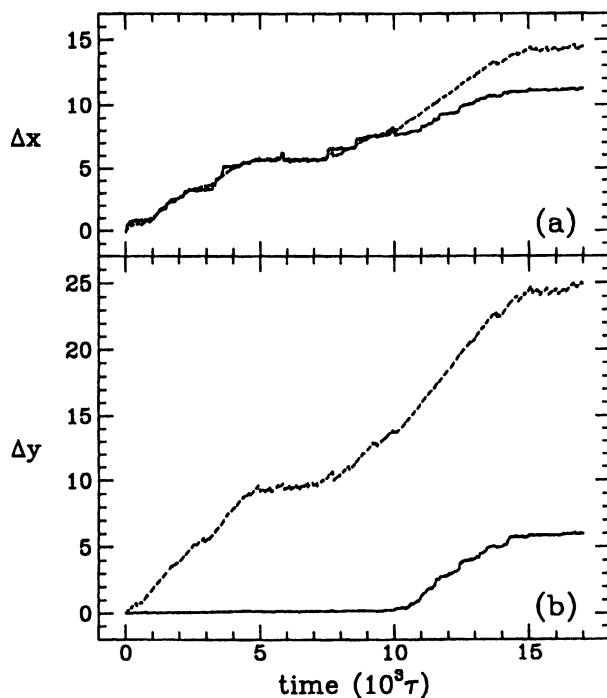


Figure 10. Time dependence of the translation along (a) x and (b) y of the layers of monomers nearest the top (dashed) and bottom (solid) walls. The top wall was displaced at 60° to the x-axis starting from the state at 6000τ in Figure 8. (Reproduced with permission from Ref. 22. Copyright 1997 Kluwer.)

with each other, or with the direction of sliding. However, an easy channeling direction along each wall is no more than 30° away from the applied velocity. When motion starts, a large static stress f_s would be needed to order each interface for sliding along the closest channel direction. Once the order is imposed, sliding can occur at a lower f_k without internal shear of the film. The channeling would persist for a long time after sliding stopped, allowing motion to restart with the lower force f_k . However, if one waits long enough for the interface to forget the order imposed by shear, the threshold force for starting motion will return to f_s .

It is difficult to test this scenario with direct experimental measurements of the location of slip. However, if the channels are not aligned along the sliding direction there will tend to be forces normal to the sliding direction. A study of these forces and their memory effects as a function of wall alignment could provide evidence for channeling.

Concluding Remarks

The simulations described here establish a closer connection between the glass transition induced by confinement and ordinary thermal glass transitions (Figure 2). Indeed Figure 5 indicates that the dynamic behavior near the glass transition is surprisingly universal. Whether thickness, pressure or temperature is varied, the changes in viscosity can be collapsed onto the same universal curve. This curve describes results for different chain lengths ($n=6$ to 16) and for interaction potentials that produce shear only at the wall/film interface, only at an interface in the center of the film, or spread uniformly throughout the system.

The high shear rate tail of the universal response function in Figure 5 follows a power law $\mu=\dot{\gamma}^{-x}$ over three decades in shear rate. The observed exponent is about $-2/3$ with a best fit value of $x=-0.69(3)$. As long as the system can be taken close enough to the glass transition that one sees a substantial drop in viscosity, this exponent should be observable. If one can only observe part of the curve near the beginning of the drop in μ , the apparent exponent will be smaller. This may have been the situation in Ref. 36 where crystallization occurred before the relaxation rate had slowed substantially relative to the bulk value.

Once the film has transformed to a glassy state, it behaves like a solid. The response to small shear stresses is elastic (Figure 6). Above a yield stress the film rearranges and flows. In some cases the film enters a liquidlike state (15,16), and in others it "cracks" at the wall or in the center of the film and shears along the resulting interface. The two situations are difficult to identify in experiments, which do not yet provide direct structural information.

Experiments do reveal dramatic memory effects that should reflect structural changes. It is tempting to draw analogies to bulk polymers and assume that the chains become aligned along the shear direction. Some amount of alignment is found in our simulations of thicker films (Figure 8) during the initial work hardening of the film. However, channeling of monomers between lines of wall atoms provides a more important source of structural memory in these films (Figure 8-10). This type of memory should be easy to distinguish from chain alignment. If the direction of sliding is reversed, the chain alignment must reverse but channeling remains unchanged. The

waiting time experiment of Refs. 3 and 5 could be redone with the direction of motion changed after the waiting time. If this experiment still showed a memory effect, it would be clear evidence for channeling rather than chain alignment. Other information could be obtained by changing the direction of motion by less than 180° .

One of the interesting features in glassy films is the presence of a static friction f_s (Figure 7) and a lower, velocity independent, sliding friction f_k (Figure 2). This is typical of the friction between macroscopic solids (42,43), but surprisingly rare in simple model calculations (50,51,62-64), simulations (65-67), and experimental studies (68,69) of solid-on-solid friction at the molecular scale. Most molecular scale calculations consider ideal crystalline solids with atomically flat interfaces. Unless the lattice constants of the solids and the alignment of their crystalline axes is exactly right, the two solids will be incommensurate, i.e. they will not share any common periodicity. There is then no preferred registry between the solids, and no force is needed to initiate motion. It is very unusual for contacting surfaces to be intrinsically commensurate. Even two identical surfaces are only commensurate when they are aligned exactly at one of a discrete set of angles. Thus one would expect that static friction would be a very rare phenomenon rather than nearly universal.

One of the possible origins of static friction in macroscopic systems is the presence of "third bodies" between the solids (67). These typically include wear debris, adsorbed atmospheric molecules, dust, and thin lubricant films. Like the thin films considered here, third bodies have more degrees of freedom than crystalline surfaces. This allows the combined system of bounding surfaces and third bodies to lock into local energy minima, and can produce static friction. Chemical heterogeneity, surface roughness and length scale can also lead to static friction (67), and more work is needed to establish which effects dominate in different limits.

Acknowledgements. We thank G. S. Grest, E. D. Smith, and P. A. Thompson for many helpful discussions, and S. Granick, J. N. Israelachvili and P. M. McGuiggan for sharing their thoughts and data with us. Support from NSF Grant no. DMR-9634131 and the Pittsburgh Supercomputing Center is gratefully acknowledged.

Literature Cited

1. Israelachvili, J. N.; McGuiggan, P. M.; Homola, A. M. *Science* **1988**, *240*, 189.
2. Homola, A. M.; Israelachvili, J. N.; McGuiggan, P.M.; Gee, M. L. *Wear* **1990**, *136*, 65.
3. Gee, M. L.; McGuiggan, P. M.; Israelachvili, J. N.; Homola, A. M. *J. Chem. Phys.* **1990**, *93*, 1895.
4. Yoshizawa, H.; McGuiggan, P. M.; Israelachvili, J. N. *Science* **1993**, *259*, 1305.
5. Yoshizawa, H.; Chen, Y.-L.; Israelachvili, J. N. *J. Phys. Chem.* **1993**, *97*, 4128.
6. Granick, S. *Science* **1992**, *253*, 1374 (1992).
7. Hu, H.-W.; Carson, G. A.; Granick, S. *Phys. Rev. Lett.* **1991**, *66*, 2758.
8. Reiter, G.; Demirel, A. L.; Granick, S. *Science* **1994**, *263*, 1741.
9. Reiter, G.; Demirel, A. L.; Peanasky, J.; Cai, L. L.; Granick, S. *J. Chem. Phys.* **1994**, *101*, 2606.
10. Demirel, A. L.; Granick, S. *Phys. Rev. Lett.* **1996**, *77*, 4330.

11. Alsten, J. V., Granick, S. *Phys. Rev. Lett.* **1988**, *61*, 2570.
12. Alsten, J. V., Granick, S. *Macromolecules* **1990**, *23*, 4856.
13. Demirel, A. L.; Granick, S. *Phys. Rev. Lett.* **1996**, *77*, 2261.
14. Klein, J.; Kumacheva, J. *Science* **1995**, *269*, 816.
15. Thompson, P. A.; Robbins, M. O. *Science* **1990**, *250*, 792.
16. Robbins, M. O.; Thompson, P. A. *Science* **1991**, *253*, 916.
17. Thompson, P. A.; Grest, G. S.; Robbins, M. O. *Phys. Rev. Lett.* **1992**, *68*, 3448.
18. Thompson, P. A.; Robbins, M. O.; Grest, G. S. In *Thin Films in Tribology*; Dowson, D.; Taylor, C. M.; Childs, T. H. C.; Godet, M.; Dalmaz, G., Eds.; Elsevier: Amsterdam, Holland, 1993; pp 347-360.
19. Robbins, M. O.; Thompson, P. A.; Grest, G. S. *MRS Bulletin* **1993**, *18*, 45.
20. Thompson, P. A.; Robbins, M. O.; Grest, G. S. *Israel J. of Chem.* **1995**, *35*, 93.
21. Baljon, A. R. C.; Robbins, M. O. *Science* **1996**, *271*, 482.
22. Baljon, A. R. C.; Robbins, M. O. In *Micro/Nanotribology and its Applications*; Bhushan B., Ed.; Kluwer Academic Publishers, Amsterdam, Holland, 1997; pp 533-553.
23. Baljon, A. R. C.; Robbins, M. O. *MRS Bulletin*, **1997**, *22(1)*, 22.
24. Kremer, K.; Grest, G. S. *J. Chem. Phys.* **1990**, *92*, 5057.
25. Manias, E.; Hadziioannou, G.; Bitsanis, I.; ten Brinke, G. *Europhys. Lett.* **1993**, *24*, 99.
26. Manias, E.; Hadziioannou, G.; ten Brinke, G. *J. Chem. Phys.* **1994**, *101*, 1721.
27. Thompson, P. A.; Robbins, M. O. *Phys. Rev. A* **1990**, *41*, 6830.
28. Evans, D. J.; Morris, G. P. *Phys. Rev. Lett.* **1986**, *56*, 2172.
29. Loose, W.; Ciccotti, G. *Phys. Rev. A* **1992**, *45*, 3859.
30. Stevens, M. J.; Robbins, M. O. *Phys. Rev. E* **1993**, *48*, 3778.
31. Grest, G. S.; Kremer, K. *Phys. Rev. A* **1986**, *33*, 3628.
32. Khare, R.; de Pablo, J. J.; Yethiraj, A. *Macromolecules* **1996**, *29*, 7910.
33. Stevens, M. S.; Robbins, M. O.; Belak, J. F. *Phys. Rev. Lett.* **1991**, *66*, 3004.
34. Schoen, M.; Cushman, J. H.; Diestler, D. J.; Rhykerd, C. L. *J. Chem. Phys.* **1988**, *88*, 394.
35. Schoen, M.; Rhykerd, C. L.; Diestler, D. J.; Cushman, J. H. *Science* **1989**, *245*, 1223.
36. Stevens, M. J.; Mondello, M.; Grest, G. S.; Chui, S. T.; Cochran, H. D.; Cummings, P. T. *J. Chem. Phys.* (to be published).
37. Ribarsky, M. W.; Landman, U. *J. Chem. Phys.* **1992**, *97*, 1937.
38. Xia, T. K.; Ouyang, J.; Ribarsky, M. W.; Landman, U. *Phys. Rev. Lett.* **1995**, *69*, 1967.
39. Gao, J.; Luedtke, W. D.; Landman, U. *Science* **1995**, *270*, 605.
40. Loose, W.; Hess, S. In *Microscopic Simulations of Complex Flows*; Mareschal, M., Ed.; Plenum Press, New York, New York, 1990; p. 267.
41. Hansen, J. P.; MacDonald, I. *Theory of Simple Liquids*; Academic Press: London, England, 1990.
42. Rabinowicz, E. *Friction and Wear of Materials*; Wiley: New York, New York, 1965.
43. Bowen, F. P.; Tabor, D. *Friction and Lubrication*; Oxford: Oxford, England, 1958.
44. Grest, G. S.; Cohen, M. H. In *Advances in Chemical Physics*, Prigogine, E.; Rice, S. A., Eds., Wiley, New York, New York, 1981; p. 455.
45. Carson, G. A. *Ph.D. thesis*, University of Illinois, 1992.
46. Rabin, Y.; Hersht, I., *Physica A* **1993**, *200*, 708.
47. Urbakh, M.; Daikhin, L.; Klafter, J. *Phys. Rev. E* **1995**, *51*, 2137.
48. DeGennes, P. G. (unpublished).
49. Kröger, M.; Loose, W.; Hess, S. *J. Rheology* **1993**, *37*, 1057.
50. Tomlinson, G. A. *Phil. Mag. Series* **1929**, *7*, 905.
51. McClelland, G. M. In *Adhesion and Friction*, Grunze, M.; Kreuzer, H. J., Eds., Springer Verlag, Berlin, Germany, 1990, Vol. 17; p. 1.

52. Glosli, J. N.; McClelland, G. *Phys. Rev. Lett.* **1993**, *70*, 453.
53. Chaikin, P. M.; di Meglio, J. M.; Dozier, W. D.; Lindsay, H. M.; Weitz, D. A. In *Physics of Complex and Supramolecular Fluids*, Safran, S.; Clark, N. A., Eds.; Wiley-Interscience, New York, New York, 1987; p. 65.
54. Ackerson, B. J.; Clark, N. A. *Phys. Rev. Lett.* **1981**, *46*, 123.
55. Ackerson, B. J.; Hayter, J. B.; Clark, N. A.; Cotter, L. *J. Chem. Phys.* **1986**, *84*, 2344.
56. Rowley, L. A.; Nicholson, D.; Parsonage, N. G. *Mol. Phys.* **1976**, *31*, 365.
57. Lane, J. E.; Spurling, T. H. *Aust. J. Chem.* **1980**, *29*, 2103.
58. Snook, J. K.; van Megen, W. *J. Chem. Phys.* **1980**, *72*, 2907.
59. Abraham, F. F. *J. Chem. Phys.* **1978**, *68*, 3713.
60. Toxvaerd, S. *J. Chem. Phys.* **1981**, *74*, 1998.
61. Doi, M.; Edwards, S. F.; *The Theory of Polymer Dynamics*; Oxford: Oxford, England, 1986.
62. Sokoloff, J. B. *Phys. Rev. B* **1990**, *42*, 760.
63. Hirano, M.; Shinjo, K. *Phys. Rev. B* **1984**, *41*, 11837.
64. Frenkel, Y. I.; Kontorova, T., *Zh. Eksp. Teor. Fiz.* **1938**, *8*, 1340.
65. Cieplak, M.; Smith, E. D.; Robbins, M. O. *Science* **1994**, *26*, 1209.
66. Persson, B. N. J. *Phys. Rev. B* **1993**, *48*, 18140.
67. Robbins, M. O.; Smith, E. D. *Langmuir* **1996**, *12*, 4543.
68. Krim, J.; Watts, E. T.; Digel, J. *J. Vac. Sci. Technol. A* **1990**, *8*, 3417.
69. J. Krim, D.-H. Solina, and R. Chiarello, *Phys. Rev. Lett.* **1991**, *66*, 181.

Chapter 7

Micromechanics and Microtribology of Polymer Films

F. Oulevey¹, D. Gourdon¹, E. Dupas¹, M. Liley², C. Duschl³, A. J. Kulik¹,
G. Gremaud¹, and N. A. Burnham^{1,4}

¹ Department of Physics, Swiss Federal Institute of Technology, CH-1015
Lausanne, Switzerland

² Advanced Microsystems, CSEM SA, CH-2007, Neuchâtel, Switzerland

³ Department of Chemistry, Swiss Federal Institute of Technology, CH-1015
Lausanne, Switzerland

⁴ Nanomechanics LLC, P.O. Box 700, Pittsford, NY 14534-0700

Mechanical properties of a polymer blend change as a function of temperature, particularly near phase transitions. Normally, the modulus and damping of a blend are recorded for the entire sample. Here, we present atomic force microscopy results from local measurements of the individual components of a polymer blend. The data are collected either as images at a set temperature, or spectra of a small area on the surface as a function of temperature.

Using lateral force microscopy on Langmuir-Blodgett films, we found unexpected friction anisotropies and asymmetries in the frictional behavior. The data were found not to be related to the hexagonal packing of the molecules, but rather related to a small molecular tilt.

New instrumentation allows access to new length scales. Here, we summarize results obtained using two techniques based on atomic force microscopy. The first [1] is a nanoscale equivalent of DMA, dynamic mechanical analysis; the second is a small-scale version of a tribometer [2].

Micromechanics

In the nano-DMA, a sinusoidal mechanical oscillation is applied to the sample by the transducer shown in Fig.1. The tip of an atomic force microscope is placed in contact with the sample, and the amplitude and phase of the cantilever's response is recorded as a function of position on the sample's surface, forming images related to the sample's elastic modulus and damping. Lateral resolution is of the order of a few tens of nanometers. The microscope may also be operated in spectroscopy mode, where the tip remains nominally on the same point of the surface, and the temperature of the sample is ramped.

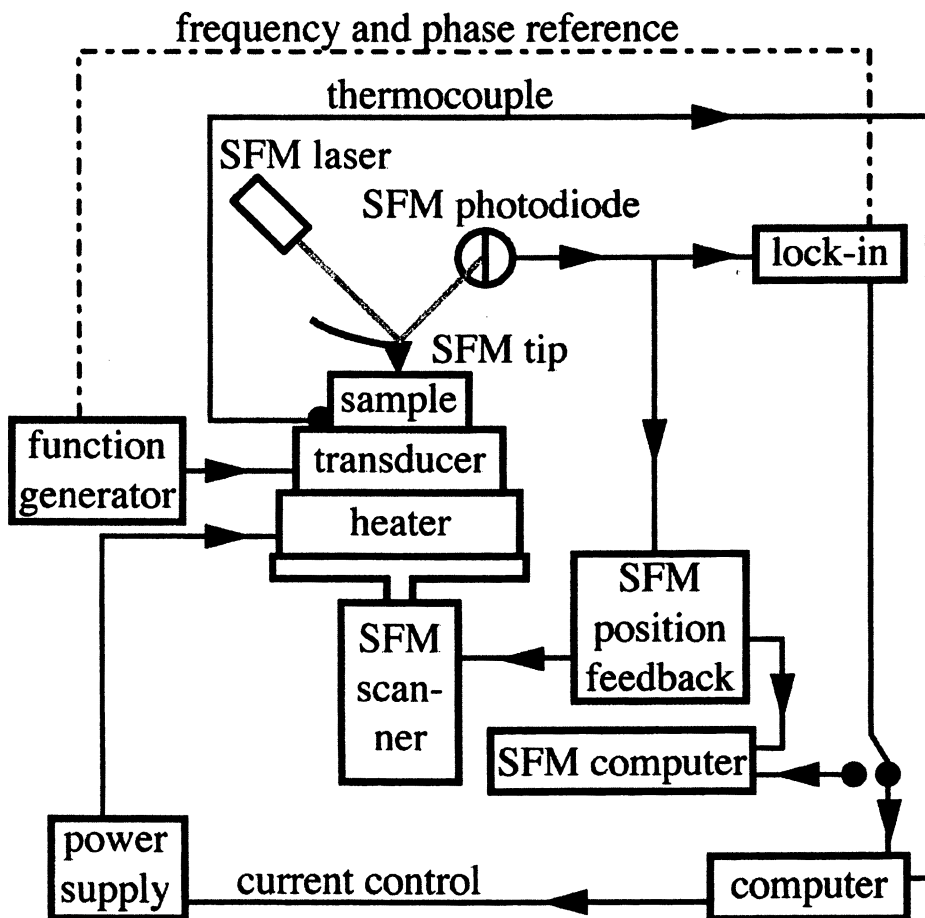


Fig.1. Schematic diagram of the nano-DMA.

Micromechanical measurements are far from easy. There are two technical hurdles that must be overcome. The first is to understand and control the cantilever response [3]. For example, if the stiffness of the cantilever is 0.1 N/m, and that of the interaction 10 N/m, the cantilever bends 99% of the applied displacement. If the interaction stiffens to 100 N/m, then the cantilever effectively moves 100% of the applied displacement. Not many detection systems are sensitive enough to resolve a difference of less than one percent of an applied displacement of a few Ångströms. Naturally, many researchers increase the excitation amplitude in order to work above the detection limits of their microscopes. This induces sliding of the cantilever along the surface of the sample because cantilevers are typically placed at an angle of 15 degrees to the surface plane. A modulation amplitude of 10 nm causes 2.2 nm of sliding. This incorporates frictional effects into the modulation images [4].

One way to avoid the problems of frictional effects and low sensitivity to stiffness is to drive the cantilever into the inertial regime using frequencies above the contact resonance, instead of exciting the system at a few kilohertz—the usual approach. This stems from the inherent response time and thus inherent response frequency of the cantilever-sample system. If the modulation frequency is higher than the response frequency, the tip of the cantilever cannot move quickly enough to keep up with the motion of the sample and transducer, and the sample is compressed underneath the mass of the tip. The relationship between applied displacement and cantilever response now becomes, to first order, linearly dependent on stiffness [3,5]. Large modulation amplitudes are no longer necessary in order to discern changes in contact stiffness. This in turn reduces the coupling between friction and the modulation images.

The second technical problem is thermal drift. Materials can have thermal expansion coefficients ranging from negative values up to, typically, $10^{-5}/^{\circ}\text{C}$. A change of 100°C causes a 1 cm bar to expand $10\ \mu\text{m}$ —many force microscopes' scan range. The instrument should be constructed with low-expansion materials in a design as concentric as possible, with the tip centered. A corollary to the mechanics of thermal drift is the detection sensitivity to temperature, which should be compensated for temperature.

Figure 2 shows a blend of polyvinylchloride (PVC) and polybutadiene (PB) at various temperatures above and below the glass transition of the PVC. The images in the upper row are atomic force microscope images representing topography. (Bright means high.) In the lower row are the rigidity images (cantilever modulation amplitude), related to the elastic modulus, where bright means stiff. We have also succeeded in collecting data at a single point (nominally) as a function of temperature, and the plots show good correlation with global DMA-style measurements [1].

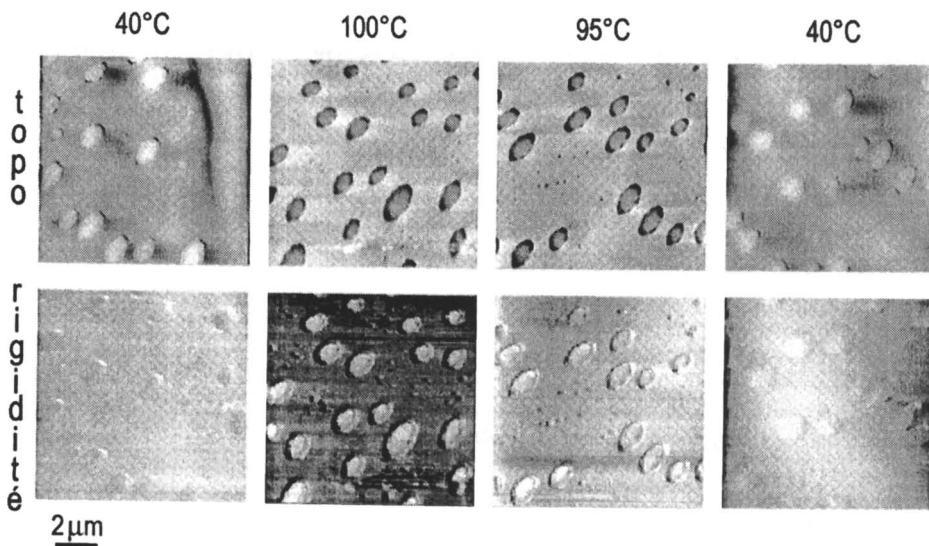


Fig.2. Force microscope (top row) and rigidity images (= cantilever response amplitude, bottom row) as a function of temperature. The gray scale remains the same for each row. The excitation frequency was 820 kHz. PVC ($T_g = 95^{\circ}$) forms the continuous matrix of this 60/40% compound.

Microtribology

The tip of an atomic force microscope makes a single point contact with a surface. Consequently, understanding tribological behavior becomes intellectually simpler. Friction has been shown to be correlated not with the magnitude of the adhesion between two bodies, but rather with the adhesion hysteresis [6]. Our recent study of a model system, a Langmuir-Blodgett film on mica [7], shows no dependence on adhesion hysteresis, but rather a dependence on molecular orientation [2].

Raw Friction Data

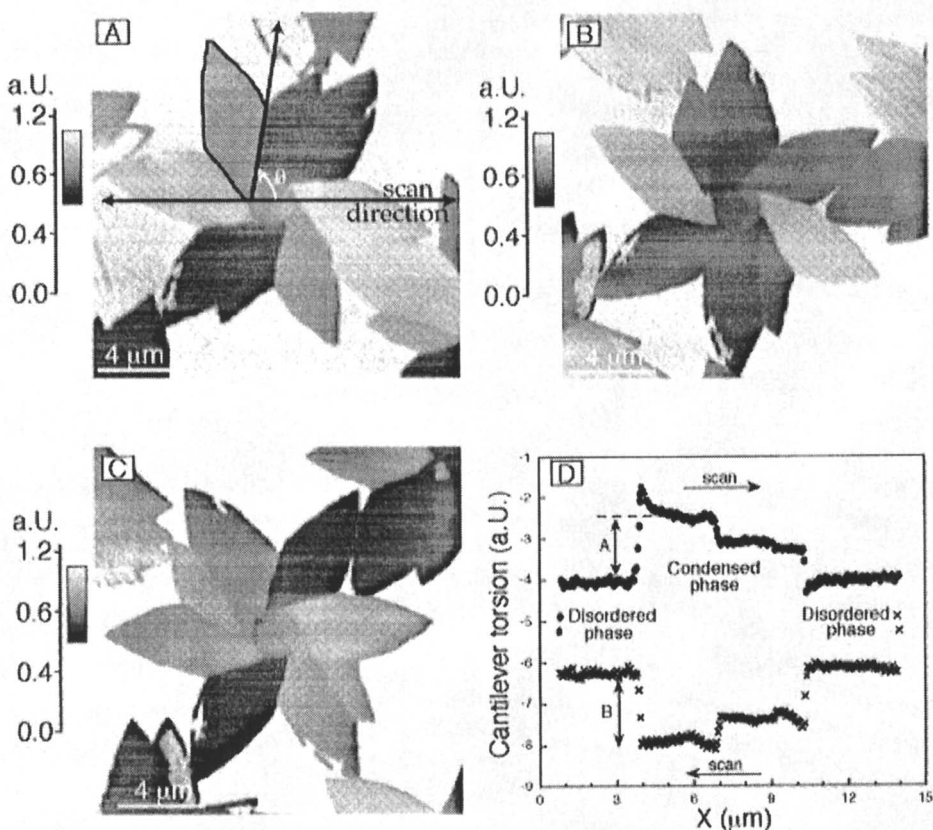


Fig.3. A series of lateral force images. Dark means more torsion, that is, higher friction. For each image, the scan direction was from left to right. a), b), and c) show the same flower-shaped domain in different orientations after rotation of the sample underneath the cantilever. In d), the cantilever torsion is plotted as a function of position along a line through the bottom half of the flower in c) for both the left-to-right and right-to-left scans. The use of 'A' and 'B', indicated in d), is explained in the text.

We observed the effect presented in Fig.3. A Langmuir-Blodgett monolayer deposited on mica forms flower-shaped domains. The molecules within a flower are in the condensed state. The matrix surrounding the flowers is a disordered phase. The condensed domains are comprised of subdomains. Upon rotation underneath the cantilever, the contrast of the subdomains changes in a systematic way. The cantilever torsions marked 'A' and 'B' in Fig.3d were added to ascertain the total friction A+B and subtracted for the friction difference A-B. Upon 360° rotation of the sample, the total friction behaved with C_2 symmetry, whereas C_1 symmetry was discerned for the friction difference A-B. We denote the C_2 behavior by the term "anisotropy" and the C_1 behavior by "asymmetry". The anisotropy provides most of the contrast between the subdomains (petals). The small contribution from the asymmetry can be seen in the horizontal petals of Fig.3c. There, the petals have similar orientations with respect to the scan direction, yet exhibit slightly different contrast.

Are the anisotropy and asymmetry related to molecular orientation? Electron diffraction demonstrated that the condensed molecules are hexagonally packed, and the upper limit for the tilt from the normal was fifteen degrees. Brewster angle microscopy determined that the tilt from the normal was approximately ten degrees, and the azimuthal tilt direction was along the subdomain boundary, as sketched in Fig.4.

Anisotropy and asymmetry

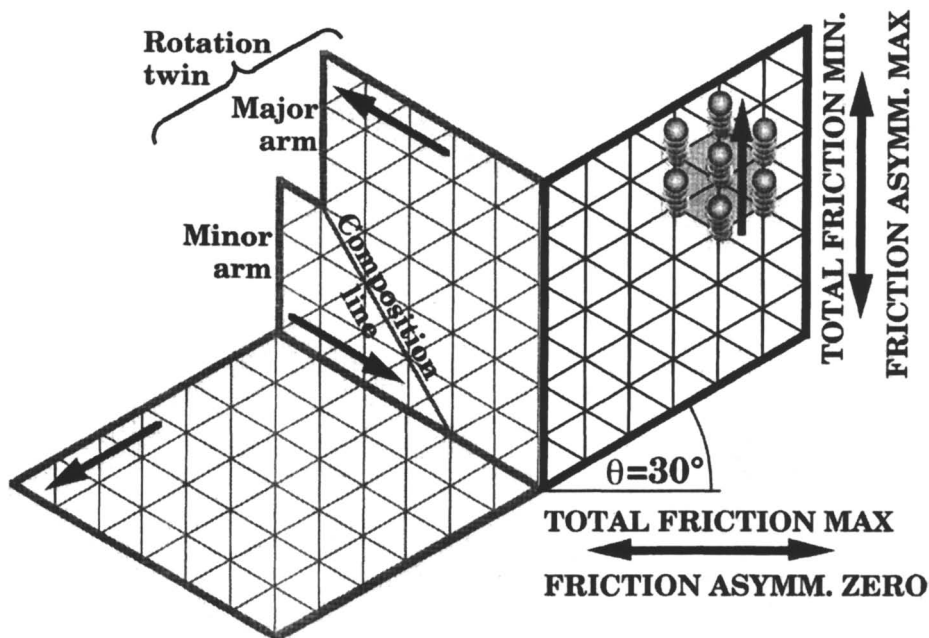


Fig.4. Schematic of the frictional and structural results.

The anisotropy (total friction) and asymmetry maxima and minima are depicted with the double-ended arrows. The hexagonal packing of the molecules does not correlate with the frictional behavior, but the molecular tilt does. The anisotropy corresponds to moving across or along the molecular tilt direction, whereas the asymmetry corresponds to moving against or with the nap of the molecules. Interestingly, the friction scanning against the nap was lower than with the nap. Adhesion hysteresis is an isotropic phenomenon and cannot account for the effects summarized here and elaborated in Ref. [2]. The orientation of molecules tilted less than 15 degrees strongly contributed to the friction behavior.

Closing words

Technical advances in force microscopy permit investigations of the micromechanical and microtribological properties of polymers. Insights into the fundamental processes of friction have already been gleaned, and soon phase transitions in polymer blends will be systematically studied at the nanoscale.

Acknowledgement

We are indebted to H. Pollock and M. Song of Lancaster University for the PVC/PB sample, and to the British Council/Swiss National Fund, who supported our work.

References

1. Oulevey, F.; Gremaud, G.; Semoroz, A.; Kulik, A.J.; Burnham, N.A.; Dupas, E.; Gourdon, D.; *Rev. Sci. Instruments* **1998**, *69*, 2085.
2. Liley, M.; Gourdon, D.; Stamou, D.; Meseth, U.; Fisher, T.M.; Lautz, C.; Stahlberg, H.; Vogel, H.; Burnham, N.A.; Duschl, C.; *Science* **1998**, *280*, 273.
3. Burnham, N.A.; Kulik, A.J.; Gremaud, G.; Gallo, P.-J.; Oulevey, F.; *J. Vac. Sci. Technol.* **1996**, *14*, 794.
4. Mazeran, P.E.; Loubet, J.-L.; *Tribol. Lett.* **1997**, *3*, 125.
5. U. Rabe and W. Arnold; *Appl. Phys. Lett.* **1994**, *64*, 1493.
6. J.N. Israelachvili, Y.-L. Chen and H. Yoshizawa; *J. Adhesion Sci. Technol.* **1994**, *8*, 1231.
7. We used the amphiphile bis[8-(1,2-dipalmitoyl-sn-glycero-3-phosphoryl)-3,6-dioxaocetyl] disulfide that consists of two chiral phospholipids linked by a hydrophilic spacer.

Chapter 8

Physics and Physical Chemistry at the Nanotip Scale

Fundamental Investigation of the Mechanical Response of Soft Materials with an Atomic Force Microscope

S. Kopp-Marsaudon, L. Nony, D. Michel, and J. P. Aimé

CPMOH–Université de Bordeaux, I–351, Cours de la Libération, 33405
Talence Cedex, France

In the local microscopy's field, a large effort is dedicated to study the mechanical properties which can be accessed with a nanotip. Within this context, soft materials are well adapted to probe mechanical response at the nanometer scale. After a discussion of some experimental and technical key points, we present three different types of experiments done on one model polymer : polystyrene films with different molecular weights. In the experiments, the tip may scan the sample surface (friction loops), or move upward and downward in the vicinity of the sample –in contact mode (force curve) or in an oscillating mode (approach-retract curves)-. The comparison of the results shows the sensitiveness of the tip to local mechanical properties. New routes to explore mechanical properties without touching the sample are proposed.

Since the last few years, the study of soft materials with an atomic force microscope (AFM) has shown that it gives much more than just topography. The idea is either to put the tip in contact with the sample and measure the cantilever deflection variations or to vibrate the tip in the vicinity of the sample and to measure changes of the oscillating behavior.

The contact experiments allow probing of friction processes at the nanometer scale, thus providing new information for the tribology field (1-6). Bulk mechanical properties of soft materials can be accessed in contact experiments through the force curve analysis (7-9) and with force modulation (10).

The more recent development concerns the use of the oscillating behavior of the tip-cantilever (CL) system when brought close to the sample surface. Two modes can be used in dynamic force microscopy. With one mode, commonly called tapping,

the tip-CL oscillations are done at a fixed drive frequency and a fixed drive amplitude. In that case oscillation amplitude and phase variations are recorded. In the other mode commonly called non contact AFM (11), the oscillation amplitude is kept constant and the recorded quantity is the shift in resonance frequency. Note that the name "tapping" as opposed to "non contact" mode is confusing, as it is possible to work in non contact in the tapping mode. A large effort has been made to understand the oscillating behavior both theoretically and experimentally (see refs (12-18) for the tapping, (19-27) for the non contact). Theoretical and experimental development in the field of dynamical force microscopy allow the measurement to be more quantitative. In particular, phase images is now understood as mechanical as shown on the model samples provided by the copolymers (28-30). For non contact experiments, their main result is the possibility to reach contrast at the atomic scale, which is started to be understood through the study of the oscillating behavior of the tip-CL system.

In this paper we will compare different experiments in contact and with an oscillating tip to show their contribution for the study of soft material. In static contact mode, force curves and friction loops are recorded while in tapping a systematic investigation of approach-retract curves is presented. A model sample is used: monodisperse polystyrene films of different molecular weights (M_w): bulk mechanical properties and molecular weight dependence of the glass transition temperature. In order to emphasize the inherent difficulties encountered with an AFM, we begin with a detailed discussion of the technical conditions.

Technical Section.

A Presentation. In an AFM experiment, a nanotip is attached to the end of a compliant cantilever. Two types of experiments can be performed, one in which the tip is brought in contact with the sample, and throughout the experiment the tip remains in contact, rubbing the surface. In that case change of the cantilever deflection or torsion is recorded and the study belongs to the field of tribology, the domain of science devoted to the study of friction processes. In a second type of experiment, the tip-cantilever is kept vibrating at or near its resonance frequency and during most of the oscillation period the tip does not touch the sample or even never touches the sample. This second method provides additional information, and for very soft materials, as liquid polymers are, becomes the unique way to probe mechanical properties at the nanometer scale.

B AFM Key Issues. In both cases, several parameters are not accurately known, making quantitative measurements difficult to achieve. In this section is given a short list of these parameters. The key issues are force calibration, tip characterization with estimation of the contact area between the tip and the sample, and effects of the experimental environments. The behavior of the contact area, either stationary or fluctuating, is a key parameter to have at least robust, reproducible experimental data. We arbitrarily focus on the attempts to design in situ experiments that allow the measurements to be more quantitative. Most of these key issues are far from being resolved or standardized. They still appear to be very dependent of the scale at which the required signal has to be obtained. The experimental constraints will not be the

same for a signal measured at the molecular or mesoscopic scale. Also the chosen experimental strategy is very dependent of the mechanical properties of the surface or object analyzed. The following is a list of works aiming to calibrate AFM. There are in many cases attempts that are indicative of the difficulties encountered and cannot be considered as a definite route to make routinely quantitative measurement with an AFM.

1 Deflection and Force Calibration. Deflection measurement of the end of the cantilever is achieved by optical detection as described in Figure 1a. Care must be taken to avoid spurious signal due to interference between sample and cantilever and misalignment of the photodiodes. Calibration of the deflection is easily obtained by performing a force curve (Figure 2a) or an approach-retract curve (Figure 2b). Such an operation requires a good calibration of the relationship between the applied voltage on the piezo actuator holding the sample and the vertical displacement. For a good correspondence between the cantilever displacement and the sample one requires that the contact stiffness is much larger than that of the cantilever stiffness, and therefore requires the use of hard materials.

Force calibration is much more difficult to achieve. One way to estimate cantilever force constants is to use formulae for the force constants of simple beam geometry (31). For any of these calculations, all the cantilever dimensions and the relevant moduli must be known. The knowledge of the cantilever dimension is a tricky problem, even for a simple geometry as a beam with a rectangular section. The most important parameter is the thickness, typically half a micron, which cannot be accurately controlled during microfabrication. Because the force constants follow a cubic law as a function of the thickness, dispersion in thickness values induces sizable dispersion in force constant (32). Several experimental attempts have been performed (32, 33), which are in many cases time consuming and cannot be easily standardized. In situ evaluation should obviously be more easy, attempts using power spectrum analysis of thermal fluctuations is quite promising., This approach requires a good estimation of the effective mass and geometrical properties and also that the thermal fluctuations can be easily discriminate from other noise sources (34-36). Note also that calibration with an optical beam detection, is dependent of the laser spot location, thus may vary from one measurement to another if optical adjustment takes place. Here again, there are a few simple ways to overcome this difficulty, the most obvious being to have an experimental set allowing to make various measurements still keeping the same optical realignment.

2 Tip Characterization. The tip is the central parameter of any scanning probe microscope, and an accurate knowledge of the size and of the shape of the tip should normally be a necessary requirement to get a quantitative measurement. The nanometer size, or atomic size, of the tip makes scanning probe microscopy attractive, but results in the relevant part of the tip responsible for the interaction to be unknown. Therefore, reproducible experimental data accompanied with a theoretical description will be required to have a robust interpretation of the experimental data. Nevertheless, numerous attempts have been made to estimate the shape and size of the tip, here we

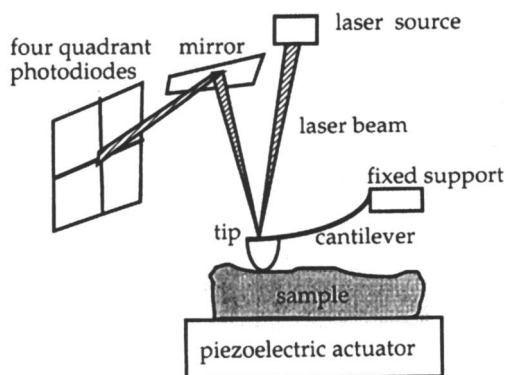


Figure 1: AFM optical detection method sketches.

Figure 1a: a laser beam is centered on the cantilever free end where the tip is attached. It then reflects on a mirror towards the photodiodes (here four quadrants photodiodes). As the sample moves (we will always in the following consider that the piezo actuator -which induces the relative tip-sample movement- is under the sample), the tip deflection or torsion variations are measured through voltage vertical or horizontal difference of the photodiodes signals.

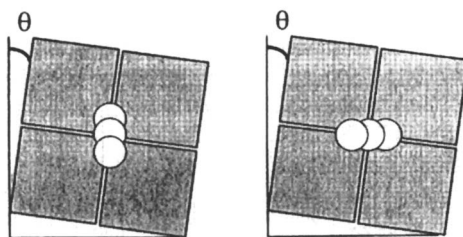


Figure 1b: effect of the orientation of the photodiode four quadrants on the measurement of the output signals of the vertical or lateral voltage difference.

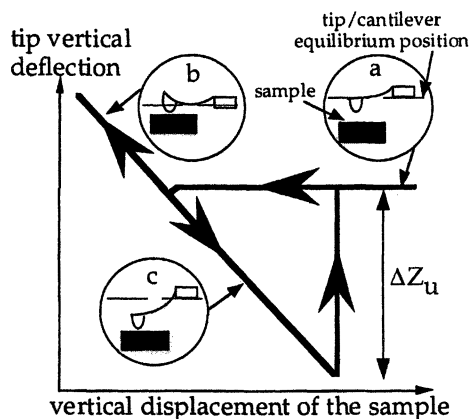


Figure 2a: Idealized force curve performed in contact AFM: plot of the tip deflection variations with the vertical displacement of the sample. In part a, the tip is far from the sample, the cantilever rests at its equilibrium position. In part b, the tip is in contact with the sample, the cantilever is compressed. The vertical displacement is then reversed. The cantilever deflection reaches then its initial value and continues to decrease while the tip sticks on the sample. If the sample is hard (like for example mica or silica surface), the slope of part b and c should be equal to 1, allowing to transform the photodiodes vertical signal difference from voltage to distance. At the end of part c, the force due to the extended cantilever equals the adhesive force, it snaps back to its equilibrium position. The vertical displacement ΔZ_u necessary to unstuck the tip from the sample is noted in gray.

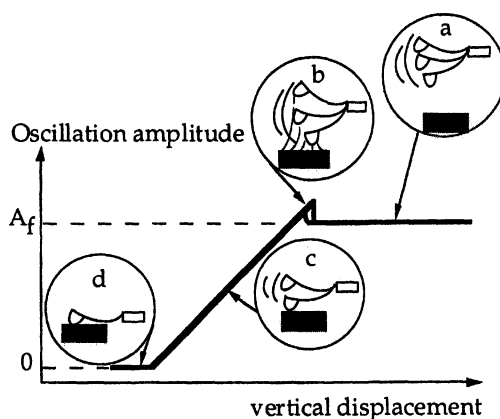


Figure 2b: Idealized approach-retract curve: plot of the oscillation amplitude variation with the tip-sample distance during the approach and retraction of a sample toward an oscillating tip-cantilever system. First, when the tip is far from the sample, it oscillates with its free amplitude A_f as depicted in part a. In part b, the tip-CL system interacts with the surface through an attractive field. If the drive frequency is slightly below the resonance one, the oscillation amplitude increases. Part c corresponds to the so-called AFM tapping mode where the tip comes in intermittent contact with the sample. In this part, the oscillatory amplitude A decreases linearly with the CL-surface distance d with a slope equal to 1 if the sample is hard, that is if $d < A_f$, $A(d) = d$. In part d, the tip is stuck on the sample with an oscillation amplitude down to zero. The tip might be damaged; this part is usually avoided.

focus on in situ experimental estimation regardless of possible tip shape measurement with TEM or use of sophisticated numerical calculation producing image reconstruction from a tip shape and size estimation (37, 38). The main aim is to give a quick and easy rough estimation of the tip structure. This choice is governed by the fact that the authors are fully convinced, if not able to rigorously prove the statement, that any attempts to very accurately measure the tip parameters is not only very time consuming but in most cases useless. The main reason is that the most important parameter is the contact area between the tip and the sample which is not a measurable quantity. The contact area depends of several factors which are not uniquely dependent of the tip structure itself. Knowledge of the contact area requires having first an exact knowledge of the mechanical response of the sample at the nanometer scale, a problem which is at the origin of numerous efforts and is currently under investigation. Secondly, a perfect description of the chemical composition of the surface and of the tip requires a good control of the sample environment and of the tip treatment and third that the tip does not vary during the experiment either due to mechanical deformation or tip modification due to a chemical deposition during the raster scan.

The in situ tip structure determination is obtained by scanning an area of calibrated objects, then the images are reconstructed with simple geometrical models providing estimation of the tip structure. The most direct and simple way would be to scan infinitely sharp Dirac like object (38) or steep object such that the image reproduces accurately the tip structure (39). Unfortunately very thin columns are also flexible. For example, the force constant of a cylindrical column is $k_{\text{col}} \sim E d_{\text{col}}^4 / L_{\text{col}}^3$, where E is the elastic modulus, d_{col} the diameter and L_{col} the height of the column. A Dirac like object is obtained for $d_{\text{col}} \ll L_{\text{col}}$, so that the column stiffness falls within the range of the lateral stiffness k_l of usual cantilevers (3, 31, 40). (The lateral stiffness scales as $k_l \sim k_v 2L/3h$, where k_v is the usual vertical CL stiffness, L its length and h the tip height.) For $k_{\text{col}} \sim k_l$, the elastic displacement of the column is half the imposed displacement monitored by the piezoactuator (9) and the image integrates both the tip shape and the elastic response of the column (38). Increasing the width of the column increases the spring constant, but the edges of the columns become loosely defined. Thus, the scan of such structures (like cusp steps (39)) does not produce precise information about the apex of the tip. The alternative is to scan a two-dimensional area of latex spheres (41). Scanning an array of objects of high symmetry allows the geometrical arguments to be very simple, multiple tip effects, tip asymmetry and rough estimation of the tip size can be deduced. Nevertheless, care must be taken due to the influence of the lateral force and an accurate description of the role of the force of friction must be included particularly when curved surfaces are scanned (28, 41).

Another strategy is to chemically modify the tip. Thin film coatings applied to the microfabricated lever can provide robust, smooth, structure with desirable properties (42, 43). Further work in this direction would be useful, so as to provide a wider array of dependable tip structures and materials.

3 Experimental Environment. The question of the sample environment addresses the simple question of what interaction is really taking place between the tip and the surface or object investigated. Influence of contaminants and capillary forces

due to a film of water may produce an undesirable mechanical response of the cantilever. The sample environment constraints depend of the samples investigated and the scale at which variation of the contrast must be obtained.

The most drastic constraints are required when the goal is to achieve contrast at the atomic scale, either with the contact mode, atomic stick-slip (44-46), or using the resonant non contact mode (23-26). The necessary requirement is that the driving interaction between the tip and sample must vary at the angström scale. Such a constraint implies that the surface must be properly prepared. It seems that uniquely ultra high vacuum (UHV) and low temperature conditions can meet this requirement. As noted in reference (24) a tip preparation may also be needed. The tip was sputtered in situ with Argon ions to remove the oxide layer from the tip. Cleaning the tip was found to be of importance to achieve stable atomic resolution.

At a larger scale, it was found that tribological investigation of grafted silica surfaces with organosilane molecules and polymers requires working under a controlled atmosphere (47, 48). If not, water adsorbed on the treated silica surface renders the measurement of the shear force randomly distributed particularly when the velocity dependence of the shear force is investigated (48). On the opposite, as shown below, it does appear that tribological investigation of polystyrene film does not need such a constraint.

C Experimental Conditions.

1 Reference Sample. When soft materials are investigated, modification of the tip may occur during the experiment. To estimate a tip modification three simple experimental protocols can be set using a reference sample, for example a flat silica surface or a mica surface.

One way to check the tip is to compare the force curve results on the reference sample before and after each experiment, and between each sample. This operation is usually only sensitive to drastic tip changes, which appear most of the time after an accidental break of the tip, and is a way to rapidly test important tip coating.

A more sensible way for a tribological experiment, is to routinely perform a friction loop (Figure 3) on the reference surface. If the magnitude of the friction loop remains constant at any stage of the experiment, this means that even if any molecules or polymers have been stuck on the apex there are only few and unable to produce a significant additional cantilever deflection within the range of the available sensitivity.

In the case of experiment using the tapping mode, a good test is to perform multiple approach-retract curves at different driving amplitudes and limited to the area b circled in Figure 2b. It has been shown that the size of the cycle of hysteresis of the amplitude is not only a function of the tip size (20, 28), but also shows sizable variations when polymers remain stuck on the apex. Such an example is given in Figure 4. Another good test is to check the variation of the phase during the approach-retract curve because, as shown by recent results (29, 49 and 50), it is rich in information. In the future, many studies will be devoted to the phase variations. Here again, one gets an in situ experiment which is able to provide information about tip change during the experiment.

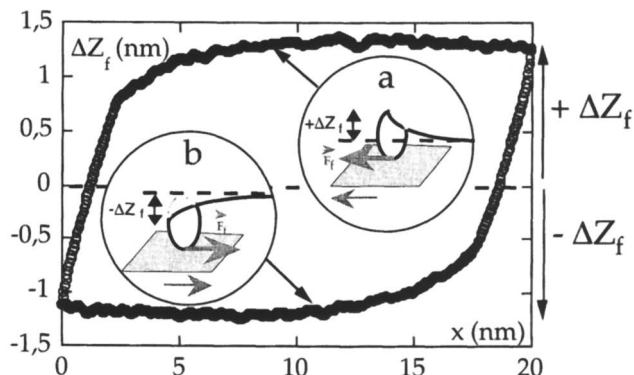


Figure 3: Friction loop: tip friction deflection ΔZ_f variation during the scan of a flat sample parallel to the cantilever symmetry axis for a fixed tip-sample vertical position. The dashed line gives the tip-CL equilibrium position. When the flat sample moves to the left (trace, part a), the tip deflection ΔZ_f due to friction is positive, whereas it is negative when the sample moves to the right (retrace, part b). Between part a and b, when the scan way changes, the tip remains glued on the sample, it is called static friction contrarily to part a or b where dynamic friction takes place. The static friction may be masked when larger scans are done, like for the following friction experiments. Experimental friction loop obtained on a $M_w = 94500$ PS sample, with a 20nm scan.

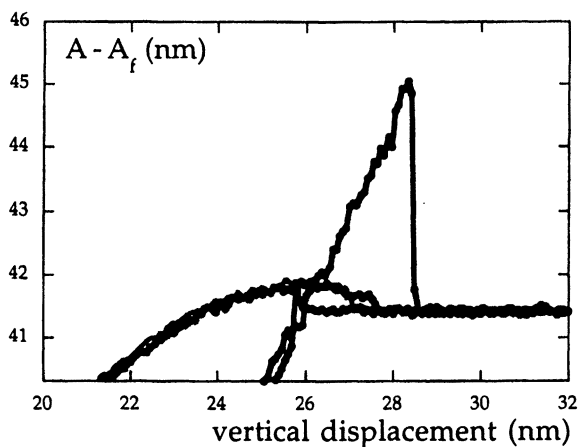


Figure 4: Approach -retract experimental curve (corresponding to part b of figure 2b) change during the experimentation provoked by a damage of the tip apex. At a given driving amplitude, the approach-retract curve first showed the usual hysteresis cycle. After the damage was done during the experimentation, at the same conditions for the first approach-retract curve, the hysteresis disappears interpreted in this case by a larger curvature radius of the tip apex due to the breaking. Those particular approach-retract curves were obtained on mica, with an amplitude of 20nm.

2 Tribological Experiments. For tribological measurements, the lateral force lying in the plan of contact between the tip and the surface produces the additional vertical deflection (Figure 2b) or cantilever torsion. Lateral forces arise not only from friction but also from the local surface slope (31, 51). If the sample surface is not flat, the surface normal force will have a component directed laterally and will result in contrast in lateral image. These complications can be avoided by using flat samples whenever possible.

Furthermore, the magnitude of the lateral force can be a function of the contact area, therefore keeping constant the contact area during a measurement is of great importance. One way seems to switch off the feedback loop, that is to work with the so-called constant height mode (47, 48, 52). This additional constraint requires not only a flat surface but also that the surface makes almost a perfectly horizontal plane. If not, since the feedback loop is not used, the deflection varies during the scan of a line thus the applied normal force. Furthermore, by using the constant height mode, the cantilever deflection is directly measured, that is the quantity of interest, and not the corresponding vertical displacement of the piezoactuator holding the sample.

Three important and related technical points remain which are not standardized but central for tribological experiments; they are related to the optical detection method used for most of the AFM. First, the laser beam must be centered on the cantilever end. The centring can easily be checked by scanning parallel and perpendicular to the cantilever symmetry axis. Secondly, for each apparatus, the four photodiodes quadrants orientation must be carefully checked (one method is described in fig 1b). Lastly, one has to work within the linear response domain of the photodiodes, which implies a limited variation domain for the vertical movement of the sample when the vertical difference from the photodiodes signal is used. This constraint can be detoured by using horizontal difference signal, see ref (28, 52).

3 Tapping Experiments. The first test implies an analysis of the resonance curve of the cantilever (CL). The oscillating tip-CL system must exhibit a unique resonance curve with a well-defined Lorentzian shape. As shown below and in numerous theoretical and experimental work (20, 27), the oscillating properties at a proximity of a surface are mainly driven by non linear dynamic behavior, so that multiple resonance will make things not understandable because of the coupling between the different modes. The resonance curve helps to discriminate some defective cantilevers or to adjust the cantilever holder right in its place, allowing a good transmission of the oscillatory movement from the piezo-actuator to the tip-CL system.

The second step is to check the tip quality through the measurement of the cycle of hysteresis during an approach-retract curve (20) as shown in figure 2b and 4.

Local Mechanical Responses of Polymeric Films.

We discuss two examples of sample response different from the bulk one in AFM experiments. All the experimental results deal with varying the molecular weight (M_w) of polystyrene films (weights from 1890 to 1 million, polydispersity varying from 1.02 to 1.07 from Fluka).

We divide this part into three sections: contact experiments implying tribology and force curves, oscillating tip experiments with approach-retract curves, and lastly the discussion.

A Contact AFM

1 Friction Coefficient. As stated above, recording of the friction data was done without using the feedback loop. The friction coefficient μ was obtained by performing friction loops for different applied forces in a range limited from the equilibrium position to smaller forces up to the minimal one when the tip snaps back to its equilibrium position (between c and a in Figure 2a). The friction deflection is then plotted against the vertical tip-sample position like in Figure 5, showing a clear linear relationship. Note that other routes can be taken to measure the friction coefficient (53, 54).

Figure 6 gives the results obtained on polystyrene films of different M_w (52). A clear dependence of the friction coefficient with M_w is shown. The friction coefficient of the lowest molecular weights polystyrene is around $\mu = 0.25$, then, starting for molecular weights close to the entanglement weight ($M_e = 10000$), μ increases up to a larger value ($\mu = 0.4$ for higher molecular weights).

2 Force Curve Cycles. Multiple force curve cycles have been done at one place of the sample, avoiding deliberately the compressive (part b in Figure 2a) where the tip is more likely to damage the sample surface. For the lowest molecular weights, the vertical displacement ΔZ_u necessary to separate the tip from the sample (arrow in Figure 2a) decreases with the number of cycles (or with time as a cycle duration was 1s).

An example of this vertical displacement normalized variation is given in Figure 7 for three molecular weights. An exponential law can fit the variations with one characteristic parameter which can be converted to a characteristic time. The experimental results show again a clear different response for the different molecular weights.

3 Discussion of the Molecular Weight Dependence. The variation of the vertical displacement ΔZ_u needed to separate the tip from the sample is striking: the vertical displacement needed to separate the tip from the sample is closely related to the adhesive force between the tip and the PS sample. As an organic material interacts with the tip uniquely through the Van der Waals London dispersive force, the strength of the attractive interaction is simply given by the product of the radius of the tip and the Hamaker constant. The Hamaker constant is a function of the chemical composition and of the density of the two interacting materials (55), it thus does not depend of the molecular weight. Consequently, by using the same tip to investigate samples of various molecular weights, thus keeping the same radius of curvature of the tip, the strength of the attractive interaction between the tip and the surface should remain constant. It therefore has no reason to change with the number of force curve cycles done (or with time) for one specific sample.

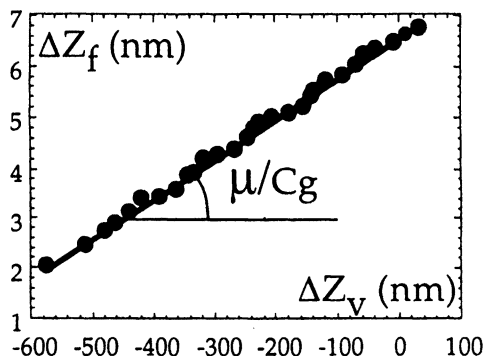


Figure 5: Variation of the friction deflection ΔZ_f with the tip-sample distance variation ΔZ_v . The friction coefficient μ is given by: $F_f = \mu P$ with F_f the friction force, P the applied effective load, in this case $F_f = k_l \Delta Z_f$ and $P = k_v \Delta Z_u + k_v \Delta Z_v$ with ΔZ_u a constant throughout the experiment and k_l , k_v are the lateral and vertical cantilever stiffness respectively, giving $\Delta Z_f = \mu \frac{3h}{2L} \Delta Z_v + C$, with h the tip height and L the cantilever length.

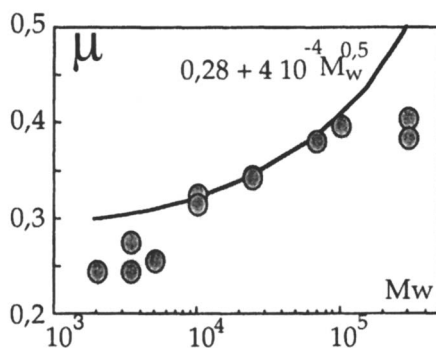


Figure 6: Variation of the friction coefficient μ of PS samples with the sample molecular weight M_w . Explanations for the fit are given in the last part, paragraph A4.

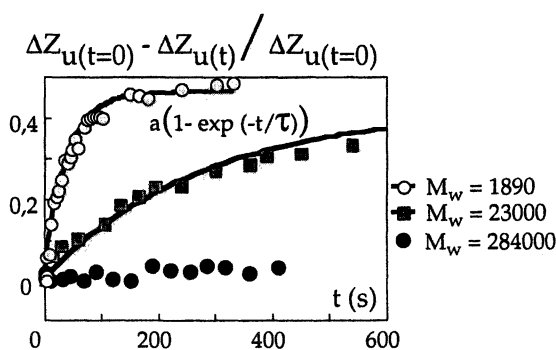


Figure 7: Force curve experiments on PS films: normalized variation of the vertical displacement ΔZ_u needed to unstick the tip from the sample with time for three M_w samples: 1890 - 23000 - 284000. The variation with time is obtained by the number of cycles multiplied by the duration of one cycle. Whereas for the 284000 M_w sample ΔZ_u is quite constant, its changes for the smaller M_w PS: its normalized variation can be fitted by an exponential law, enabling to extract a characteristic time for the smaller M_w samples.

The general molecular weight dependence of the friction coefficient is also surprising except for the highest M_w values that give a friction coefficient close to the value obtained previously with macroscopic vitreous samples (56, 57). Note that the macroscopic values were obtained for larger speeds, but no evidence of speed influence was found in the AFM study (52).

To understand this variation, one can look for the answer with variations of bulk properties with M_w . For this purpose the Fox and Flory law (58, 59) which gives a equivalence between M_w and glass transition temperature as given in Figure 8a can be used and applied to the variation of PS mechanical dynamic modulus with temperature determined by Pérez (60) (Figure 8b), supposing that this M_w -temperature equivalence doesn't affect the variation of the dynamic modulus. The maximal variation of the dynamical modulus with M_w is about 15% from the smallest to the highest M_w samples. It is thus insufficient to explain a variation of the friction coefficient of about a factor of two.

Therefore, the origin of μ and ΔZ_u variation with M_w has to be found elsewhere.

4 Analogy with Crazes and Fractures. The observed variations of the friction and orce curve data as a function of M_w will be discussed at a qualitative level, most of the ideas being borrowed from the mechanical description of fracture in vitreous polymer. The variation with time of the force curves suggests an aging effect, which in itself gives a new route to understand the friction results through a disentanglement effect. Following this idea, an analogy with crazes (the precursors of fractures) in vitreous polymers as described by Kramer (61) or de Gennes (62) is used.

In the vitreous polymers craze model (Figure 9), there is an active zone at the interface between the vitreous bulk polymer and the fibrils of the craze. Depending on M_w , failure may take place by two ways: either by chain scission of the fibrils (fragile fracture, for the high molecular weights) or by disentanglements in the active zone (ductile fracture by plastic flow, at intermediate M_w). Thus, depending on M_w , a fragile or ductile fracture can occur in conditions depending on the active zone thickness Δ . If Δ is smaller than the maximum size of the distorted coil size ($\lambda_m R_g$ with λ_m the maximal extension coefficient and R_g the gyration radius), the active zone will be liquid like, it cannot support load and plastic flow will occur. Whereas if the thickness Δ is larger than $\lambda_m R_g$, the active zone behaves like a rubber: it will support load and the failure will occur in fibrils. An important fact for the following is that the size of the distorted coil varies with $M_w^{0.5}$.

For the AFM experiments, an alternative way is to suppose the existence of an active viscoelastic zone at the tip-sample interface induced by the shear. For the intermediary M_w , the response of the polymeric films will be governed by a disentanglement process, giving a friction force scaling as:

$$F_f \propto \Delta$$

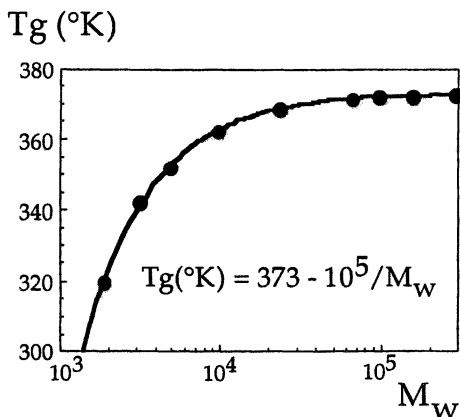


Figure 8a: Variation of the glass transition temperature T_g of PS samples with their molecular weight M_w as given by the Fox and Flory law (57, 58). The circles correspond to the molecular weight samples used in those studies.

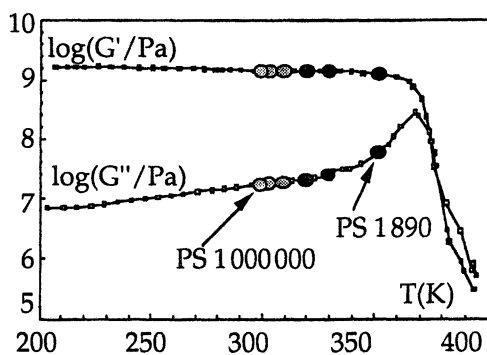


Figure 8b: Variation of the dynamic modulus values of one PS sample with temperature as adapted from (59). Using Fox and Flory equivalence between temperature and weight given in figure 9a, circles are pointed corresponding to the sample used for those studies.

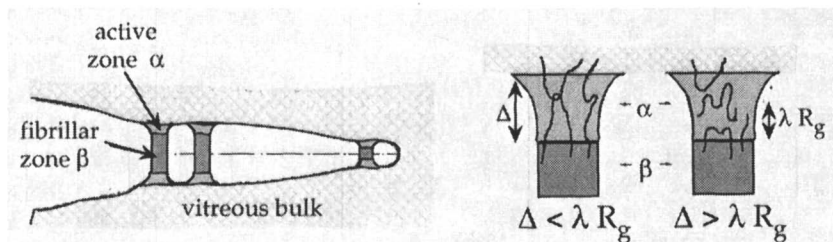


Figure 9: Sketch of a craze preceding a crack in vitreous polymer. There are two regimes for the active zone α : when $\Delta < \lambda_m R_g$, the active zone behaves like a rubber and can sustain load, whereas if $\Delta > \lambda_m R_g$, the active zone behaves like a fluid and fails under stress. Adapted from (61).

Δ being the size of the viscoelastic zone. As the maximum Δ above which the active zone is liquid is proportional to R_g , the expected limiting size Δ scales as R_g and therefore as $M_w^{0.5}$.

This formulation gives a direct dependence for μ upon Δ and thus a variation of μ scaling as $M_w^{0.5}$. The data of Figure 6 are fitted with the law $\mu = 0.28 + 4 \cdot 10^{-4} M_w^{0.5}$. The fit is satisfactory in the limited molecular weight domain of five different M_w .

The assumption that disentanglement controls the friction process for intermediary M_w is also coherent with the lower μ values for the lower molecular weights: they cannot support load, and thus fail (by failing we mean the point where friction changes from static to dynamic) at a smaller force threshold, they behave as liquid. One way to evaluate the friction force F_f for those chains not entangled is given by:

$$F_f = N \zeta_m v_m$$

where v_m is the relative sliding speed between monomer units, ζ the monomeric friction coefficient and N the number of monomeric units involved in the friction process. One can take $N = 10^4$, corresponding to a volume of about 5 nm^3 . The scanning speed was $20 \cdot 10^{-6} \text{ ms}^{-1}$. To evaluate ζ_m , we can consider it as thermally activated, with an activation enthalpy for flow or diffusion of PS at temperature well above T_g , and use the experimental values obtained for PS in crazing experiments, Kramer and Berger give (60):

$$\zeta_m = 1.7 \cdot 10^{-28} \exp\left(\frac{+19000}{T}\right)$$

With $T = 400^\circ\text{K}$ (for the melt), one obtain $\zeta_m = 7.2 \cdot 10^{-8} \text{ J s m}^{-2}$ and thus $F_f = 15 \text{ nN}$.

An evaluation of the experimental order of magnitude is obtained by the typical friction vertical deflection (2 nm) multiplied by the cantilever lateral stiffness (around 4 Nm^{-1}), giving $F_{f\text{exp}} = 8 \text{ nN}$, thus the same order of magnitude.

B Oscillating Tip. In these experiments, the sample was approached towards the vibrating tip at a fixed position of the plane surface. It was then retracted when the tip is near the surface. During the experiment, the fixed drive frequency is at a value slightly below the resonance frequency, such that the vibrating amplitude is below the resonant one. With this condition, the amplitude of the vibrating cantilever increases when the attractive force field between the tip and the surface becomes large enough. Then, as soon as an increase of the amplitude is observed, the sample is retracted. To understand the specificity of the results obtained on PS films, we present first typical results obtained with a reference hard sample.

1 Typical Approach-Retract Curve. All the results presented for the following are focused in Figure 2b part b, at the spot where the oscillation amplitude just starts to change from the free one. Figure 10a shows typical results obtained on a hard surface (PS high molecular weight ($M_w=284000$) sample).

When the tip-CL system vibrates far from the surface, it oscillates with its “ free ” amplitude A_f . When the attractive force field becomes large enough (typically for distances between the tip and the surface smaller than 2nm), if the drive frequency is slightly below the resonant one, the oscillation amplitude increases. At this point the sample is retracted. For its retraction, the oscillation amplitude takes a new route than for the approach: the variation of the oscillation amplitude shows an hysteresis between the approach and the retraction of the tip from the sample. The retraction route depends on the drive amplitude as shown in Figure 10b which represents only retractions for clarity purposes. The smaller the drive amplitude the smaller the hysteresis cycle, to a point where no hysteresis cycle can be detected.

All those experimental results can be satisfactorily described by the study (with analytical expressions or simulations) of the oscillating behavior of the tip-cantilever system in interaction with the sample through an attractive force field (20, 28). When the tip is close to the sample, the non linear dynamical behaviour of the oscillator gives a bifurcation from a monostable to a bistable state. Theoretical work shows that it is very informative to follow not only the variations of the amplitude during the approach and retraction but also the phase variations (20, 29, 63).

2 Mechanical Response of PS Films. In the following, we will present results obtained on lower M_w PS which have a higher mechanical susceptibility. The lower M_w samples show an atypical response during the retraction as represented in Figures 11a ($M_w = 95000$) and b ($M_w = 1890$).

As for $M_w = 95000$ sample, the amplitude variation is comparable to the previous hard reference sample for the larger driving amplitude only (44 nm for this particular case). For other driving amplitudes, changes occur which become marked for the smaller A_f ; the amplitude decreases in a non ambiguous way. For the lower $M_w= 1890$, this behavior is even more pronounced despite the higher A_f values.

Figure 12 compares the results obtained on three different M_w for the same free amplitude. For the same free amplitude, the $M_w=150000$ shows a typical hard sample response whereas the lower M_w give atypical results, with specifically an amplitude decrease at the beginning of the retraction more marked for the lower M_w sample.

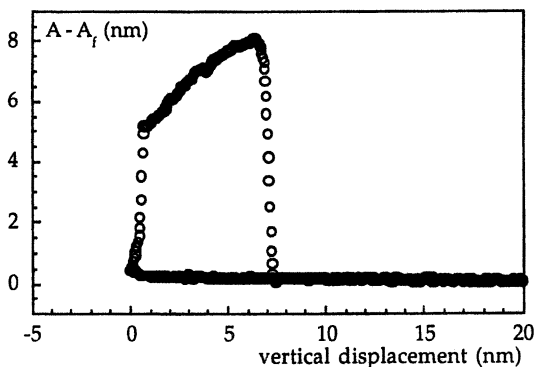


Figure 10: Approach-retract curves on PS samples.

Figure 10a : Approach-retract curves (focused in part b of figure2b) obtained on a $M_w=284000$ sample, for a free amplitude of 42nm, at a frequency of 292.47kHz below the resonance one ($\nu_r=293.18$ kHz). Similar results have been obtained on other hard surfaces like silica.

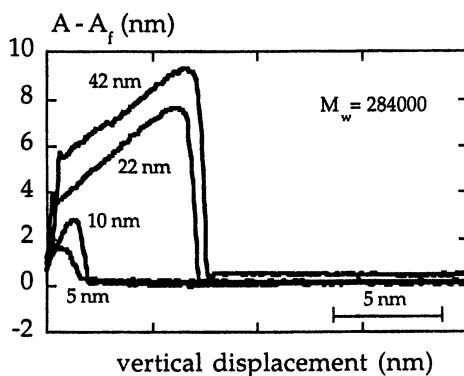


Figure 10b : Retract parts of the variation of the tip oscillation amplitude during the approach and retract of a hard sample: $M_w = 284000$ PS for multiple A_f values. As given by the theory (20), the hysteresis cycle size decreases with decreasing A_f values.

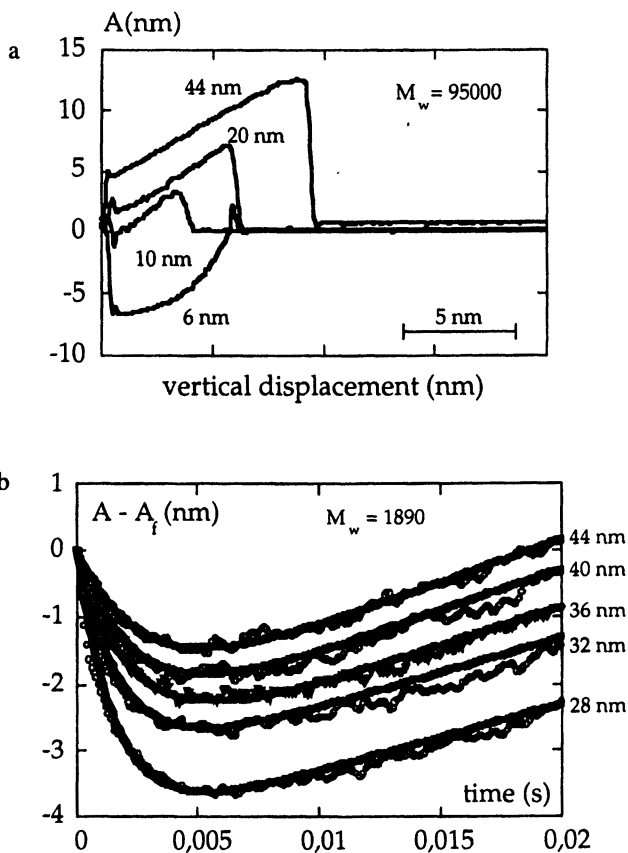


Figure 11: variation of the vibrating tip oscillation amplitude during the retract for $M_w = 95000$ (figure 11a: variation of A_f with the displacement) and $M_w = 1890$ (figure 11b: variation of A_f with time. The time was obtained from the displacement by taking into account the piezo-actuator displacement speed). The gray lines in figure 11b are fit from equation 11 (see last part, # B 3).

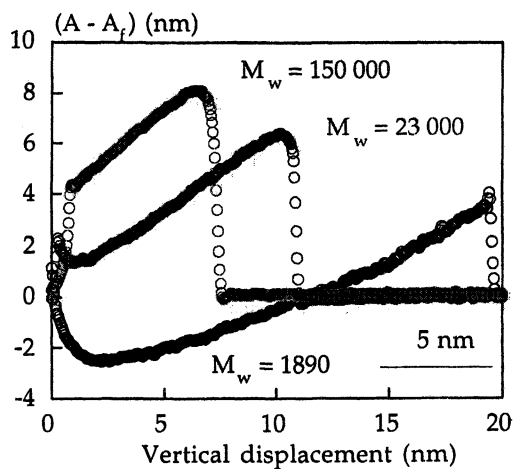


Figure 12: Variation of the oscillation amplitude of vibrating tip during the retract for three molecular weights with the same driving amplitude ($A_f = 40$ nm): $M_w = 150000$, $M_w = 23000$ and $M_w = 1890$ as noted.

Thus, by oscillating the tip close to the surface, a clear molecular weight dependence is again found, despite the intrinsic difference with the previous AFM experiments where the tip is in contact with the sample.

3 Interpretation of the Results. The results can be understood by the growth of a PS nanoprotuberance under the action of the tip as sketched in Figure 13 (64). The model includes two parts:

- (i) the action of the tip: during one oscillation, the tip is most of the time far from the sample, meaning that most of the time, the tip doesn't interact with the surface. The tip action is therefore modeled through a periodic rectangular function force. The force acts only when the distance between the tip and the sample is smaller than a critical distance d_c . It attracts the sample through a sphere/plan interaction ($F_{\text{ext}} = \frac{HR}{6d_c^2}$, with H the Hamaker constant, R the tip radius and d the distance between the tip and the sample). The rectangular function force thus acts only during a finite time called the residence time τ_{res} as given below :

$$\tau_{\text{res}} = \frac{T}{\pi} \cos^{-1} \left(1 - \frac{d_c}{A_f} \right) \quad (1)$$

The Fourier series of the force is:

$$F_{\text{ext}}(t) = F_{\text{ext}} \left(\frac{\tau_{\text{res}}}{T} + \sum_n \frac{1}{\pi n} \sin(n \omega \tau_{\text{res}}) \cos(n \omega t) \right) \quad (2)$$

Here, we will focus uniquely on the static component part. Such an assumption leads to a description of the tip action as a step like function as sketched in Figure 14 and an effective static force F_{stat} :

$$F_{\text{stat}} = F_{\text{ext}} \frac{\tau_{\text{res}}}{T} \quad (3)$$

- (ii) the PS mechanical response which is taken as viscoelastic for intermediate and low molecular weights. Thus, exactly as for the tribologic experiments, the existence of an active viscoelastic zone is considered.

During the oscillation, when the tip is far from the sample, the nanoprotuberance is taken to relax with one unique relaxation time τ_N , its mechanical susceptibility $J(t)$ is then given by:

$$J(t) = J_0 (1 - \exp(-t/\tau_N)) \quad (4)$$

where J_0 is the compliance of the nanoprotuberance, given by :

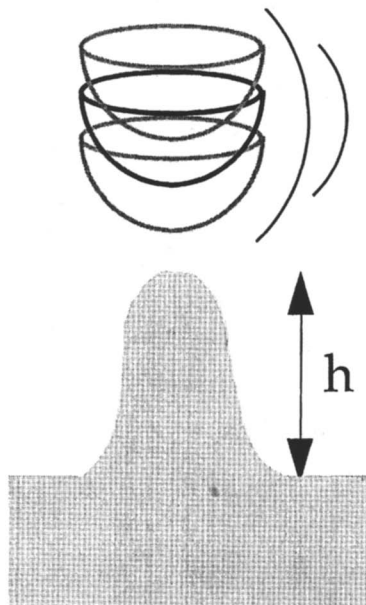


Figure 13: sketch of the PS nanoprotruberance growing with a height h during the vibration of the tip in its vicinity.

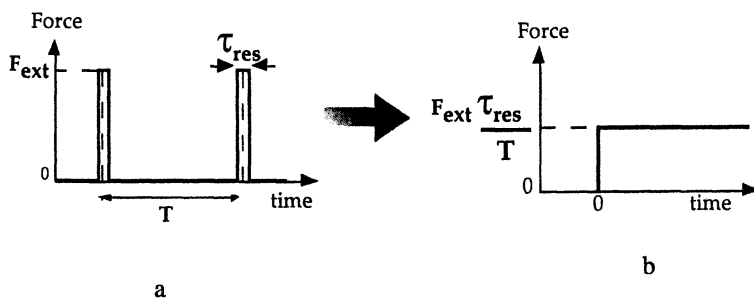


Figure 14: Modeling of the tip action:

Figure 14a: periodic rectangular force of magnitude F_{ext} developed in fourier series.

Figure 14b : focus on the static component part of the force which has now the magnitude $F_{\text{ext}} \frac{\tau_{\text{res}}}{T}$, and starts at $t=0$ corresponding to the time when the nanoprotruberance starts to grow.

$$J_0 = \frac{1}{G_0 \Phi}$$

with G_0 the elastic modulus at zero frequency, and Φ the protuberance diameter. The nanoprotuberance height seen as an elastic displacement is then given by:

$$h(t) = \int_{-\infty}^t J(t-t') \dot{F}(t) dt \quad (5)$$

To compare this expression with our experimental results (which are the oscillation amplitudes $A(t)$), one assumes that the tip vibrating amplitude $A(t)$ is:

$$A(t) = A_f - z(t)$$

where the vertical location of the sample $z(t)$ is given by:

$$z(t) = h(t) - v_p t \quad (6)$$

where v_p is the speed of the piezoelectric vertical displacement.

With a step function for the force (expression (3)), equation (5) gives the simple result:

$$h(t) = J_0 F_{\text{ext}} \frac{\tau_{\text{res}}}{T} (1 - \exp(-t/\tau_N)) \quad (7)$$

In most cases, despite the simple expression of equation (7), $h(t)$ is non linear and needs to be solved numerically because of an avalanche effect due to the variation of the tip residence time τ_{res} when the nanoprotuberance height varies (64). Meanwhile, in the specific cases when the nanoprotuberance height can be neglected with regard to the oscillation amplitude (meaning high initial oscillation amplitudes) one can use expression (6) and a Taylor development of the expression (1) of τ_{res} :

$$\tau_{\text{res}} = \frac{T}{\pi} \cos^{-1} \left(1 - \frac{d_c}{A_f - (h(t) - V_p(t))} \right)$$

$$\tau_{\text{res}} = \frac{T}{\pi} \sqrt{\frac{2d_c}{A_f}} \left(1 + \frac{1}{2} \frac{(h(t) - V_p(t))}{A_f} \right) + O \left\{ \frac{T}{\pi} \sqrt{\frac{2d_c}{A_f}} \left(1 + \frac{3}{2} \frac{(h(t) - V_p(t))}{A_f} \right) \right\}^3 \quad (8)$$

Introducing equation (8) in the expression of the elastic displacement, equation (5) can be solved through a Laplace transform. After some calculation, one obtains:

$$h(t) = S_e (1 - \exp(-\beta_e t)) - \frac{J_0 F_{ext}}{\pi 2 A_f} \sqrt{\frac{2 d_c}{A_f}} \frac{\beta}{\beta_e} V_p t \quad (9)$$

with the normalized source term S_e and relaxation term β_e coming from the Laplace transform:

$$\beta_e = \beta \left(1 - \frac{J_0 F_{ext}}{\pi 2 A_f} \sqrt{\frac{2 d_c}{A_f}} \right), \quad \text{with } \beta = \frac{1}{\tau_n}$$

$$\text{and } S_e = \frac{J_0 F_{ext}}{\pi} \sqrt{\frac{2 d_c}{A_f}} \frac{\beta}{\beta_e} \left(1 + \frac{V_p}{2 A_f \beta_e} \right)$$

Because of the softness of the protuberance, there is a slope α different from 1 between the amplitude variation and the piezo actuator vertical displacement. It gives the final expression for the sample vertical position:

$$z(t) = h(t) - V_p t = (1 - \exp(-\beta_e t)) - \alpha \left(1 + \frac{J_0 F_{ext}}{\pi 2 A_f} \sqrt{\frac{2 d_c}{A_f}} \frac{\beta}{\beta_e} \right) V_p t \quad (10)$$

Expression (10) has been used to fit the data shown in Figure 11b, with three fit parameters: the product $\frac{J_0 F_{ext}}{\pi} \sqrt{\frac{2 d_c}{A_f}}$, β and α . It has been also possible to fit the experimental variations of the amplitude for $M_w = 23000$ and $M_w = 3250$ samples. Those successful different fits enable comparison of the parameters used for each M_w as represented in Figure 15 a and b. Even though the parameters vary with A_f (which they shouldn't because the parameters represent intrinsic polymer properties), there is a marked trend to differentiate the 1890 M_w values from the 3250 and 95000 M_w ones.

C Discussion. If we consider the three experiments, the experimental results have all been found to exhibit variation of the mechanical properties with the PS molecular weight. Those variations can be interpreted with the existence of a local PS active viscoelastic area at the tip-sample interface.

Nevertheless, the three studies' interpretations cannot be compared at the same level.

For example, the force curve experimental procedure is not as controlled as the tribological and approach-retract ones for two major reasons:

- the cantilever built-in 12° tilt which induces a lateral movement together with the imposed vertical displacement (for example, a vertical movement of 100 nm, will induce a 20 nm lateral deviation). The measurement thus includes shear.

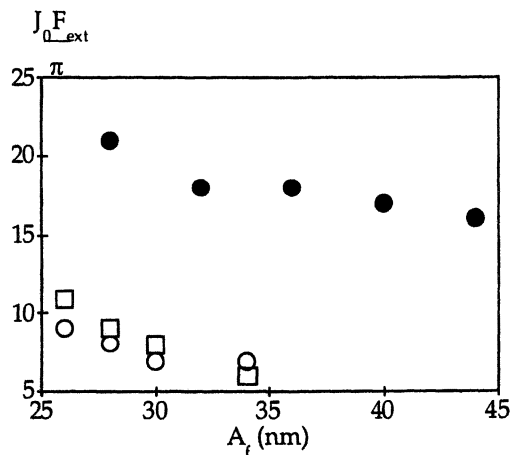


Figure 15 : Variation with the oscillation free amplitude A_f of the two parameters used for the fits of the amplitude variation with distance for three molecular weights.

Figure 15 a: variation of the product $J_0 F_{ext} / \pi$ with A_f .

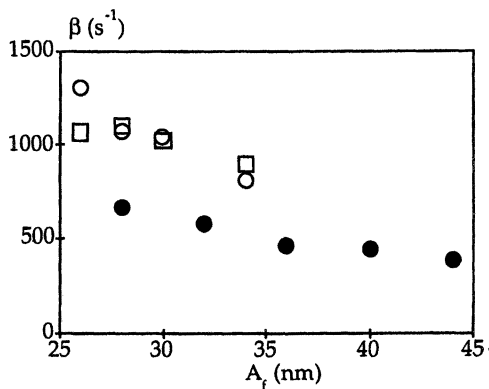


Figure 15 b : variation of the relaxation time $\tau_n = 1/\beta$ with A_f .

- moreover, even if care was done not to compress the cantilever during the experiments, plastic deformations occurred during the cycles, which could be seen afterwards. Those results indicate aging effects due to repetitive cycles.

For those reasons, the force curve results are presented only to reinforce the M_w dependence aspect of the mechanical properties that can be probed with an AFM on PS films.

For the tribological experiments, the procedure is robust: the same quantitative results can be obtained with other tip-CL systems, each μ value results from several hundred measurements. Nevertheless, the cost to pay is the heavy technical constraint.

The analogy with the fracture model gives a power law, which fits the data. Meanwhile, the power law fit concerns only five experimental points for practical reasons. This limited application domain thus doesn't enable us to determine unambiguously the physical origin of the friction coefficient evolution with the molecular weight.

In our case, the oscillating tip experiments were done without or with only slightly touching the surface. A promising extension of this study would be to probe mechanical properties of soft samples without touching them at all. A mechanical study avoiding the contact between the tip and the sample has several advantages:

- there is no contact area, therefore no assumptions needed to evaluate it
- there is no need to borrow concepts coming from fracture mechanics
- contrary to the contact measurement, it does not depend on the stiffness of the machine
- the sample is less perturbed.

Nevertheless the main difficulty of the oscillating tip results concerns an accurate description of the viscoelastic response of the nanoprotuberance under the action of the attractive force between the sample and the tip. Many points remain open for the interpretation of the atypical variations of the amplitude. They are mostly linked to the multiple crude assumptions made with the model : it is difficult to evaluate a local response when both the tip shape and effective force are unknown. One could discuss for example the sphere-plane surface interaction used, or ask about the local stiffness of the polymer, or question the unique relaxation time which is a to simple polymer viscoelastic response. Among our fit parameters, the sample properties should be independent of the drive amplitudes used. The variations reported in figure 15 indicate that a simple rheological model is unable to describe the whole growth process of the nanoprotuberances.

Meanwhile, the interpretation helps to link the origin of the non linearity with the way the experiments are performed. It has also shown that the action of an oscillating tip can be simply described by considering uniquely the static component of the force. This incidentally induces a possibility to adjust and finely tune the strength of the attractive interaction to varied samples by simply changing the free oscillation amplitude (this changes the residence time of the tip near the sample and thus the force).

TABLE of symbols

General	
CL	cantilever
E	Elastic modulus
H	Hamaker constant
M_e	Entanglement molecular weight
M_w	Molecular weight
PS	Polystyrene
T_g	Polymer glass temperature
Tip-Cantilever constants	
L	Cantilever length
h	Tip height
R	Tip apex radius
k_l	Cantilever lateral stiffness
k_v	Cantilever vertical stiffness
ω	Oscillating pulsation
ν	Oscillating frequency
ν_r	Resonance oscillating frequency
A	Oscillation amplitude of the tip-cantilever system
A_f	Free oscillation amplitude: when no interaction occur between the sample and the surface
A_r	Resonance oscillation amplitude
T	Periodicity of the tip oscillation
Friction : contact AFM experiments	
μ	Friction coefficient
F_f	Friction force (lateral force) on the tip apex
ΔZ_v	Tip-sample vertical distance variation
ΔZ_f	Friction deflection
ΔZ_u	Vertical displacement needed to unstick the tip from the sample in a force curve experiment
λ_m	Maximal extension coefficient of a distorted polymer coil
Δ	Active zone thickness for a craze
R_g	Polymeric gyration radius
Nanoprotuberance :oscillating tip experiments	
d_c	Critical distance where the tip stops or starts to interact with the sample
F_{ext}	Attraction force between the sample and the tip modeled by a rectangular function
J_n	Nanoprotuberance compliance
ν_p	Piezoactuator vertical displacement during the force curve experiment
α	Slope of the amplitude variation with the piezoactuator vertical displacement
Φ	Nanoprotuberance diameter
τ_{res}	Residential time during which the tip interacts with the sample in an approach-retract curve
$\tau_e = 1/\beta$	Relaxation time of the protuberance for a static force applied
β_e	Normalized relaxation term (linked to β) coming from the Laplace transform

Conclusion

We have discussed three essentially different AFM studies performed on a series of PS films of different molecular weights. In two experiments, the tip is brought into contact with the polymer film. The third experiment deals with the analyze of the oscillating behavior of the tip-CL system in the vicinity of the sample.

The experiments described follow the basic general AFM studies law based on the intrinsic technical AFM unknowns: to follow relative evolution of some properties as a function of one unique parameter, in the present case the molecular weight. However, in some specific cases, it is possible to reach quantitative results with an AFM. An example is given with the friction coefficient measurement experiments which shows the technical and experimental constraints needed to achieve such a goal. Some general technical clues are given to control and adapt the experimental procedure to the type of sample and measure one wants to obtain with an AFM, specifically when dealing with soft material.

The three experiments results show variations with the molecular weight which cannot be explained in terms of bulk properties variations. The same basic assumption was done to understand those experimental results : the existence of a local area with homogeneous viscoelastic properties. Thus in the cases related here, the AFM tip is sensitive to local properties.

Those three studies put together are convincing that different mechanical properties can be probed with an AFM at the nanometer scale and that AFM studies give new routes to explore soft samples mechanical properties.

From the discussion held ahead, we have shown the tribology experiments for their robustness. As for the vibrating tip experiments, the studies of the amplitude variation are attractive for their increased sensitivity. Moreover, the ability to describe the polymer response with the static component part of the force, allows the experimentalist to vary the effective force strength through the variation of the time during which the tip is close to the sample. This residence time can be simply adjusted by the change of the oscillation free amplitude. Therefore, varying the drive oscillation amplitude of the tip-cantilever system becomes a fine tune button which can be used to probe many soft samples with different tip-cantilever systems and adapt the attraction strength. Finally, we would like to emphasize the natural extension of those vibrating tip experiments which is the possibility of probing mechanical properties of high susceptibility samples without touching them with the tip.

Literature cited

- (1) *Fundamentals of friction*, Singer I. L., Pollock H. M. Eds.; NATO advanced Study Institute Series E : Applied Sciences; Plenum, New York ,1992, 220.
- (2) Overney R. M. , Meyer E., Frommer J., Brodbeck D., Lüthi R., Howald L., Güntherodt H.J., Fujihira M., Tanako H., and Gotoh Y.; *Nature* 1994, 359, 133.
- (3) Radmacher M., Tillman R. W., Fritz M. and Gaub H. E.; *Science* 1992, 257, 1900.
- (4) Singer I. L.; *J. Vac. Sci. Technol.* 1994, B12, 2605.
- (5) Schwarz U.D., Köster P., Wiesendanger R.; *Rev. Sci. Instrum.* 1996, 67 (7), 2560.

- (6) Tsukruk V. V., *Rubber Chemistry and Technology*, 1997, 70(3), 430.
- (7) Landman U., Luedtke W. D., Burnham N. A. and Colton R. J.; *Science* 1990, 248, 454.
- (8) Burnham N. A. and Colton R.; *J. Vac. Sci. Technol.* 1989, A 7 (4), 2906.
- (9) Aimé J.P., Elkaakour Z., Odin C., Bouhacina T., Michel D., Curély J., Dautant A.; *J. Appl. Phys.* 1994., 76, 754.
- (10) Mazeran P. E. and Loubet J. L., *Tribology Letters* 1997, 3, 125.
- (11) Albrecht T. R., Grütter P., Horne D., Rugar D., *J. App. Phys.* 1991, 69 (2), 668.
- (12) Gleyzes P., Kuo P.K., Boccara A.C., *Appl. Phys. Lett.* 1991, 58 (25), 2989.
- (13) Tamayo J., Garcia R., *Langmuir* 1996, 12, 4430.
- (14) Magonov S. N., Elings V., Whangbo M. H., *Surface Science* 1997, 389, 201.
- (15) Leclère Ph., R. Lazzaroni, J. L. Brédas,, J. M. Yu, Ph. Dubois, R. Jérôme; *Langmuir* 1996, 12(18), 4317.
- (16) Stocker W., Beckmann J., Stadler R., Rabe J. P.; *Macromolecules* 1996, 29, 7502.
- (17) Anczykowski B., Krüger D., Fuchs H., *Phys. Rev. B* 1996, 53, 15485.
- (18) de Weger J., Binks D., Moleriaar J., Water W., *Phys. Rev. Lett.* 1996, 76 21, 3951.
- (19) Bachelot R., Gleyzes P., Boccara ; *A.C. Probe Microscopy* 1997, 1 ,89.
- (20) Boisgard R., Michel D., Aimé J. P. ; *Surf. Science* 1998, 401, 199.
- (21) Giessibl F. J.; *Sciences* 1995, 267, 68.
- (22) Sasaki N et al, *Jpn. J. Appl. Phys.* 1998, 37,L533.
- (23) F. J. Giessibl ; *Phys. Rev. B* 1997, 56, 16010.
- (24) Sugarawa Y., Otha M., Ueyama H., Morita S.; *Sciences* 1995, 270, 1646.
- (25) Kitamura S., Iwatsuki M.; *Jpn J. Appl. Phys;* 1996, 35, L668-L672, 3954.
- (26) Bammerlin M., Lüthi R., Meyer E., Baratoff A., Lü J., Guggisberg M ;, Berger Ch., Howald L., Güntherodt H.J.; *Probe Microscopy* 1997, 1,3.
- (27) 1st International Workshop on NC-AFM, NC-AFM'98 July 1998 Osaka. Prof. S. Morita Osaka University (Japan).
- (28) Michel D., PHD of Université Bordeaux I, 1997, n°1812.
- (29) Nony L., Boisgard R., Aimé J.P., submitted to *J. Chem. Phys.*
- (30) Marsaudon S., Lazzaroni R., Leclère. Ph, Aimé J. P., submitted to *European Journal of Physics*.
- (31) Warmack R. J., Zheng X. Y., Thundat T. and Allison D.P.; *Rev. Sci. Instrum.* 1994, 65, 394.
- (32) Cleveland J. P., Manne S., Bocek D., Hansma P.K.; *Rev. Sci. Instrum.* 1993, 64, 403.
- (33) Florin E. L., Moy V. T. Gaub H. E., *Science* 1994, 264, 415.
- (34) Hutter J. L. and Bechhoefer J., *Rev. Sci. Instr.*, 1993, 64, 1868
- (35) Lüthi R., Meyer E., Haefke H., Howald H. Gutmannsbauer W., Guggisberg M., Bammerlin M., Güntherodt H.J.; *Surf. Sci.* 1995, 338, 247.
- (36) Butt H. J., Jaschke M.; *Nanotechnology* 1995, 6, 1.

- (37) Dongmo S., Troyon M., Vautrot P., Delain E., Bonnet N.; *J. Vac. Sci. Techn. Part B* 1996, 14(2), 1552.
- (38) Montélénius L. and Tegenfeld J. O., *Appl. Phys. Lett.* 1993, 62.
- (39) Griffith J. E., Grigg D. A., Vasile M. J., Russel P. E. and Fitzgerald E. A.; *J. Vac. Sci. Technol.* 1992, A 10, 674.
- (40) Griffith J. E., Grigg D.A.; *J. Appl. Phys.* 1993, 74, R83.
- (41) Odin C., Aimé J.P., Elkaakour Z., Bouhacina T.; *Surf. Sciences* 1994, 317, 321.
- (42) Frisbie C. D., Rozsnyai F. F., Noy A., Wrighton M. S. and Lieber C. M., *Science* 1994, 265, 2071.
- (43) Wilbur J.L., Biebeck H. A., MacDonald J.C., and Whitesides; *Langmuir* 1996, 12, 5126.
- (44) Takano H., Fujihira M; *J. Vac. Sci. Technol. B* 1996, 14, 1272.
- (45) Morita S., Fujisawa S., Sugawara Y.; *Surf. Sci.Rep.* 1996, 23, 3.
- (46) Hölscher H., Schwarz U.D., Zwörner O., Wiesendanger R.; *Phys. Rev. B* 1998, 57 (4), 2477.
- (47) Gauthier S., Aimé J.P., Bouhacina T., Attias A.J., Desbat B.; *Langmuir* 1996, 12, 4840.
- (48) Bouhacina T., Aimé J.P, Gauthier S., Michel D. ; *Phys. Rev. B* 1997, 56, 7694.
- (49) Haugstad G.D., Hammerschmidt J.A., Gladfelter W. L.; Poster 536, Boston MA, august 1998, ACS 216th meeting, Microstructure and Tribology of Polymer Surfaces Symposium.
- (50) Haugstad G., *Ultramicroscopy*, in press.
- (51) J.P. Aimé, Z. Elkaakour, S. Gauthier, D. Michel, T. Bouhacina, J. Curély, *Surface Science*, 1995, 329, 149.
- (52) Michel D., Kopp - Marsaudon S., Aimé J. P.; *Tribology Letter* 1998, 4, 75.
- (53) Schwarz U.D., Köster P., Wiesendanger R.; *Rev. Sci. Instrum.* 1996, 67 (7), 2560.
- (54) Meyer E., Lüthi R., Howald L., Bammerlin M., Guggisberg M., Güntherodt H.J., Scandella L., Gobercht J., Schumacher A., Prins R. in *Physics of Sliding Friction*; Person B.N.J. and Tosatti E.Ed; NATO ASI Series E: Applied Science; Kluwer Academic Publishers Dordrecht/Boston/London, 1996, 311, 349-367.
- (55) Israelachvili J., *"Intermolecular and surface forces"*; Academic Press: New York, 1992.
- (56) McLaren K.G., Tabor D. ; *Nature* 1963, 197, 856.
- (57) Grosch K.A., *Proc. R. Soc. London* 1963, A274, 21.
- (58) Fox T.G., Flory P.J. ; *J. Appl. Phys.* 1950, 21, 581.
- (59) Rudd J.F.; *Handbook of polymers* 1989, V, 81.
- (60) Pérez J., *Physique et Mécanique des Polymères Amorphes*, Tec-Doc, Paris, 1991.
- (61) E. Kramer, L. Berger, *Adv. Polym. Sci.* 1990, 91.
- (62) P.G. de Gennes, *Europhys. Lett.* 1991 ; 15, 191.
- (63) Aimé J.P., Couturier G., Boisgard R., Nony L., *Appl. Surf. Sci.* in press.
- (64) Aimé J.P., Michel D., Boisgard R., Nony L.; *Phys. Rev.B*, in press.

Chapter 9

Disentanglement in Ultrathin Polymer Films, Surface Strain, and Auto-Dewetting

R. M. Overney¹, C. Buenviaje¹, S. Ge², M. Rafailovich², and J. Sokolov²

¹ Department of Chemical Engineering, University of Washington,
Seattle, WA 98195

² Department of Materials Science, State University of New York at Stony Brook,
Stony Brook, NY 11794-2275

In this paper, we emphasize the importance of the film preparation on the mechanical properties of polymer thin films. With shear and adhesion measurements, conducted with scanning force microscopy (SFM), we discuss the effect of spin casting on the degree of disentanglement of polymer chains in the boundary regime to the substrate surface. The thickness of the mechanically strained boundary layer is measured, and its unexpected far-field effect discussed with a two-fluid model. The surface interaction and mechanical properties, which were obtained from unannealed polyethylene copropylene (PEP) films, are compared to annealed PEP films and to auto-dewetting occurrences in strained systems. The measurements show that spin coating together with the interaction strength of the substrate surface can cause autophobicity.

The mechanical properties of a polymer film depends, in a complex manner, on interfacial interactions (1-9). Interfacial interactions determine polymer chain conformation, dynamics, and reactivity. Designing polymer films with well-defined specific shear mechanical properties and surface properties requires, not only a detailed understanding of the physics, but also the ability to control interfacial interaction parameters. This paper will discuss, based on lateral force and force modulated scanning force microscopy (SFM) measurements, the effect of the sample preparation in conjunction with the interaction strength of the interface on the mechanical properties of thin polymer films. We will introduce the lateral disentanglement strength, P , of the unstressed bulk elastomer, measure the effect of interfacial stresses on P , relate P to the lateral strain induced during the spin-coating process, and introduce a two-fluid model to describe mechanical properties of the interfacial boundary layer in order to justify the far-field effect of the interface as previously reported (1). Finally, we will discuss the outcome of interfacial constraints on the dewetting process of binary systems.

³ Corresponding author.

Equilibrium Theories and the Extent of Interfacial Confinement

Based on thermodynamic bulk theories (e.g., free volume theory (10-13)) or flow theories of melts (e.g., Rouse Theory (14)) material properties, such as visco-elastic material constants or transition temperatures are related to molecular parameters. Bulk properties are theoretically described by structural models, for instance, the basic statistical coil model or the meander model (15). Such scaling theories work well because interaction lengths that have to be considered are rather short short-range in nature (16-18). Existing classical mean-field theories or molecular dynamic simulations assume that, for instance, interfacial interactions are completely screened within a distance corresponding to the persistence length of the polymer (16,19). Thus, confinement effects because of interfacial interaction, like pinning of polymers at substrate surfaces, are only considered up to 0.6 to 1 nm distance (19).

Effects of Film Coating Procedures. Not considered in such scaling theories are "pre-historical" effects that occurred during the film coating process, for instance, in the case of fast solvent evaporation. In technologically highly relevant polymer coating procedures, such as spin casting, film preparation effects may cause long-term changes in the polymer viscoelastic properties that do not anneal within the characteristic diffusion times used for scaling theories (1,3). Hence, interfacial effects may be noticeable up to a distance that exceeds the polymer's persistence length by orders of magnitude. Long-term polymer viscoelastic frustration has been recently observed in a dewetting study of a binary homopolymer system (1,9).

Shear Mechanical Measurements by SFM Recent research efforts are strongly focusing on static (mechanical) and kinematic (diffusion) properties of polymeric materials in the vicinity to interfaces (1-9,20-26). Particularly one technique, the scanning probe microscopy (SPM), has been found to be very suitable in determining surface shear and viscoelastic properties on the submicrometer scale (20,27-41). In previous studies on polyethylene-copropylene (PEP) and polystyrene (PS) films annealed above their respective T_g , we found that the properties of the films change in the vicinity of interactive substrate such as silicon (1). For PS, the tracer diffusion coefficients, which are inversely proportional to the zero shear viscosity, were found to gradually decrease by more than two orders of magnitude with decreasing film thickness (3). Simple surface pinning was ruled out since the onset of the effect appeared at approximately 200 nm, or at least $10-R_g$ -distance from the interface where the probability of direct surface contact was nearly zero. A similar effect was observed for PEP in dewetting experiments where the velocity of the dewetting film was inversely proportional to the viscosity (1). Surface mechanical measurements of PEP films showed a similar trend (1). As the film thickness decreased from approximately 200 nm, the film surface became more elastic and less viscous, approaching the characteristics of a completely solid surface for films of 200 nm. The present

reological data (as outlined in detail below) is consistent with these findings and provide an explanation for the long-range effects of the interactive surface.

Experimental

Materials used in this Study. The effect of spin casting on mechanical properties of polymers in the boundary regime to interactive interfaces was studied with the monodisperse homopolymer, polyethylene-copropylene (PEP) ($M_w=374,000$, $M_w/M_n<1.1$, $T_g = -62$ °C). PEP polymer films, of varying thickness between 20-520 nm, were made by spin casting from toluene solution onto HF etched (hydrogen passivated) silicon wafer (42). The bulk radius of gyration R_g of the polymers was determined to be 24.3 nm. Film thicknesses were determined by ellipsometry (autoEl, Rudolph). The films were dried for approximately one week at room temperature under atmospheric pressure and intentionally left unannealed prior to scanning.

Samples to Test Wetting Compatibility. The wetting compatibility of chemically identical, but strained, polymer surfaces was investigated between homopolymer films of deuterated poly(ethyl acrylate) (dPEA) and graft copolymers of dPEA backbone and pendant polystyrene (PS) chains, dPEA-g-xPS, as listed in Table 1 ("x" represents the grafting density). The backbone of the graft copolymer and the homopolymer, dPEA, was synthesized by free-radical polymerization with a polydispersity index of M_w/M_n of 2.5. The graft-copolymers have pendant monodisperse PS chains ($M_w=15,000$) which are randomly grafted along the dPEA backbone. dPEA-g-xPS and dPEA films were spin cast on HF treated silicon and fused glass surfaces, respectively. The dPEA-g-xPS films (~40-100 nm) were annealed at 450 K for 24 hours in a vacuum of 10^{-4} Torr. The dPEA films (~50 nm) were then peeled off the glass surfaces and floated from water onto the graft copolymer surfaces. The binary system, dPEA/dPEA-g-xPS, was annealed again under the same conditions. Finally, the films were quenched to room temperature.

Table 1: List of Graft Copolymers

dPEA-g-xPS	Average grafts/chain	$M_{w,PS}$	wt. % PS	$M_{w,dPEA}/\text{graft}$
dPEA-g-1PS	0.9	15,000	9.3	146,000
dPEA-g-3PS	2.8	15,000	28.4	38,000
dPEA-g-5PS	4.8	15,000	48.0	16,000

The "wetting-autophobicity" (also called auto-dewetting (43-46)) of dPEA/dPEA-g-xPS was compared to the dewetting behavior of two incompatible polymer film surfaces with negative spreading coefficient, PS/dPEA-g-xPS. The PS

top layer (Mw=90k) was transferred and floated from fused quartz glass onto dPEA-g-xPS as the dPEA films above.

Substrate. Cut silicon wafers (001) were used as lateral force calibration standards. The silicon wafers were cleaned via sequential sonication in acetone (15 minutes) and methanol (30 minutes) (HPLC grade from commercial sources), rinsed with ultra-pure water (MilliQ systems), and transferred in the last cleaning solvent into an environmental chamber under zero humidity. In the low humidity environment, the silicon friction standard surfaces were heated above 100°C to remove excess water. The sample surfaces provide reproducible lateral force values over a time period of two hours.

Instrumentation. Commercial atomic force microscopes (*Explorer* from Topometrix Inc., *Nanoscope IIIa*, Digital Instruments Co. Ltd.) which are based on the laser beam deflection detection scheme were used in conjunction with digital oscilloscopes of very stable low frequency (1-20 Hz) trigger system for lateral force (friction) measurements, and dual-phase lock-in amplifiers and function generators for force modulation measurements. Various triangular silicon nitride cantilevers were used. The lateral spring constants were determined with the "blind" torsional calibration method discussed in more detail in the Appendix.

Lateral Force Calibration. The following equation was applied to calibrate the lateral force, F_T , measured from the torque of the cantilever:

$$\Delta F_T = (0.18 \pm 0.02) \frac{\Delta I_T}{\mu^*}. \quad (1)$$

I_T is the lateral force signal of the detection scheme and corresponds to the photo diode current taken from the friction loop (47). $\mu^* = \Delta I_T^{\text{cal}} / \Delta F_N^{\text{cal}}$ is attained, with the same cantilever, from lateral force measurements on a silicon calibration sample (c.f., silicon surface treatment in Appendix). Note that there are no cantilever length dimensions necessary for the lateral force calibration.

In order to determine the calibration friction coefficient for the "blind" calibration method, $\mu_{\text{cal}} = 0.18 \pm 0.02$, a bare rectangular cantilever (without gold coating) (Nanosensors GmbH) was used and its length dimensions carefully measured by scanning electron microscopy. Particular care was taken in measuring the cantilever thickness by avoiding shadow effects due to tilt and electron surface charging. Silicon rectangular cantilevers have several advantage over the common silicon nitride gold coated triangular cantilevers:

- After determination of length dimensions, the spring constants and the normal and lateral forces can analytically be easily calculated,
- the cantilever homogeneous material without gold coating makes the sensor very precise without any bimetallic bending effects due to temperature variations, and
- the cantilever is basically a single crystal of well defined elastic moduli with an oxide layer of a few ångstrom thickness.

The cantilever used for calibration had a length of 441 μm , a width of 69 μm , a thickness of 1.4 μm , and a tip length of 16.2 μm . The cantilevers was a (110) etched silicon bar with a Young's modulus of 169.3 GPa. A Poisson's ratio of 0.41 was provided by the manufacturer which provides a shear modulus of 60 GPa. A sample heating/cooling system (MMR Techn.) which is based on rapid gas evaporation was used for removing excess water from the silicon friction standard surfaces to keep the temperature constant at 20 $^{\circ}\text{C}$. Calibration measurements were conducted in a dry nitrogen flow chamber at zero humidity.

Results and Discussion

Lateral Disentanglement Strength. Friction is measured as function of the normal load between a silicon nitride tip and an unannealed 520 nm PEP film over a distance of 20 μm at 1 Hz, Figure 1. The normal load regime, F_N , includes the applied positive load and the negative adhesive load. Three distinct regimes are recognizable:

- (i) a parabolic shaped friction regime at low loads ($F_N < 12.5$ nN),
- (ii) a linear friction regime with a slope (i.e., friction coefficient μ_1) of 2.1 in the intermediate load regime ($12.5 < F_N < 33$ nN), and
- (iii) a linear friction regime with a very low friction coefficient, μ_2 , of 0.3 in the high loading regime ($F_N > 33$ nN).

Parabolic Friction Regime. The parabolic shaped friction regime is due to the low load hemispherical-contact of the cantilever as discussed in detail by Pittenger and co-workers (48). At higher loads than 12.5 nN, it is the shaft (or cone) of the cantilever tip that governs the contact area. Considering the sample's liquid-like nature, we can assume that the cantilever is fully plastically indenting the sample surface for loads exceeding 12.5 nN. If the yield pressure of the polymer material is reached, the friction coefficient is determined by the location of the maximum pressure.

The Young's modulus of the film can be obtained from the tangential traction for a sphere-plane contact given by the Hertz theory and Amontons' law of friction (49):

$$q(r) = \mu p(r) = \frac{3\mu F_N}{2\pi a^3} \sqrt{a^2 - r^2} \quad (2a)$$

$$p(r=0) = \frac{3F_N}{2\pi a^2} = \left(\frac{6F_N E^2}{\pi^3 R^2} \right)^{1/3} \quad (2b)$$

where $q(r)$ and $p(r)$ are the distributions of traction and pressure, respectively, and πa^2 is the contact area. The Young's modulus, E , can be determined, if the contact radius, a , and the radius of curvature, R , are known. Using scanning electron microscopy we measured the radius of curvature of the tip to be approximately 10 nm which we confirmed by adhesion measurements (see below). It is reasonable to assume that the maximum contact radius of the spherical hemisphere is reached for

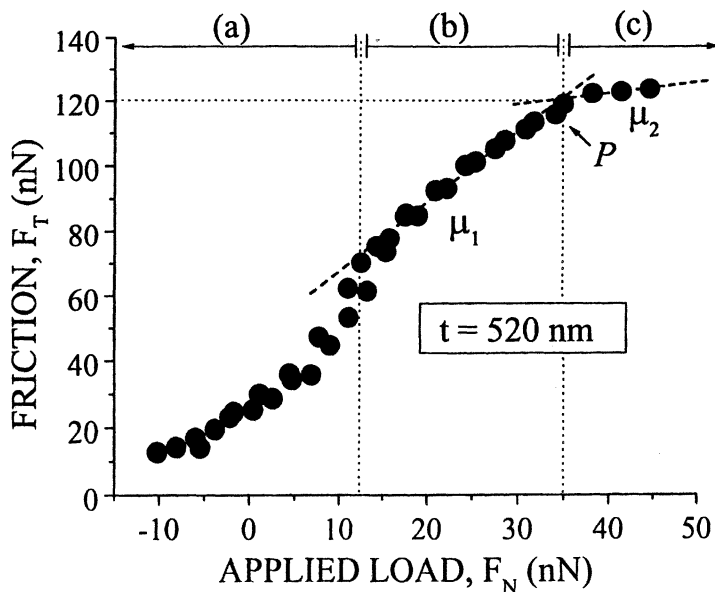


Figure 1. Lateral force (friction) measurements as function of the applied load on PEP with thickness, t . (a) The parabolic force regime is dominated by the spherical shape of the cantilever tip. (b) In the intermediate load regime the friction coefficient is $\mu_1 = 2.1$. (c) In the high load regime the friction-load ratio is $\mu_2 = 0.3$. P indicates the location of the transition point.

an applied load of 12.5 nN. Any further changes in the contact area with increasing load are due to the truncated cone, and significantly less dependent on load than it is the case for the spherical hemisphere. Hence the measured curvature of the tip, 10 nm, correspond to the radius of maximum contact at a load of 12.5 nN which leads to a contact area of 314 nm². Substituting these values into equation (3), we obtain a Young's modulus which is in good agreement with the bulk value in literature of 15 MPa (50).

Viscous Plug Flow Regime. At loads between 12.5 and 33 nN the maximum pressure is found, based on contact mechanical considerations of plastic indentation (49), below the contact interface causing the polymer to flow during the scanning process. In this regime, the contact area is changing linearly with load. Thus, a three-dimensional viscous plug flow behavior in the intermediate load regime is responsible for the high friction coefficient of 2.1.

Sliding or Lubrication Regime. Above a load of $F_N = 33$ nN, the friction coefficient is found to decrease significantly (Figure 1). At the intercept, P , three-dimensional viscous shear is replaced by a two-dimensional sliding process. This transition point is the surface or interfacial analogue to a phase transition in the polymer. For lower loads the polymer, which is a viscous fluid at room temperature, exerts a drag force on the moving tip and undergoes plug flow. As the load is increased the tip plows deeper into the liquid and the drag increases with increasing load. In addition to viscous drag, some of the frictional energy is also dissipated in stretching the polymer chains. At point P , a cross-over occurs where most of the additional shear energy is now dissipated in chain stretching as opposed to penetrating deeper into the sample. Above point P , which defines the disentanglement strength of the elastomer, the shear process is basically occurring two-dimensionally. This leads to the analogue of a phase transition of decreased entropy. Further increase in load will eventually lead to chain scission and removal of the film from the substrate.

Boundary Layer Thickness and Disentanglement Strength. In Figure 2 friction-load curves are presented between 20 nm to 520 nm film thickness of PEP. It is found that the polymer bulk shear properties remains constant down to a film thickness of around 200 nm. This is in correspondence with previous friction measurements of temperature annealed PEP films (1). For films thinner than 200 nm the absolute friction value is decreasing, and the transition from viscous flow to shear sliding occurs at lower load, Figure 2. At a film thickness of 20 nm, which is on the order of the bulk radius of gyration of the PEP sample, no transition point is recognizable, and thus only a single friction coefficient of 0.3 can be obtained. This friction coefficient corresponds to slopes obtained for loads above P_t for films with thickness $t > 20$ nm. In Figure 3, the transition loads, P , are plotted as function of the film thickness, t . The following linear relationship is found:

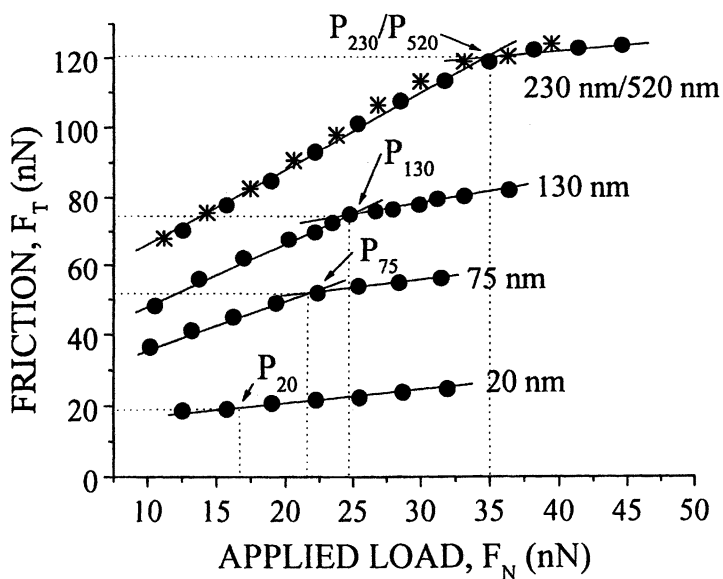


Figure 2. Lateral force vs. load measurements of 20-520 nm thick PEP films. Critical loads at the transition loads, P_t , are shifted towards lower loads for thinner films. The transition points are the same for 230 nm and 510 nm (bulk regime). No transition point is found for $t = 20$ nm. P_{20} is found from interpolation in Figure 3.

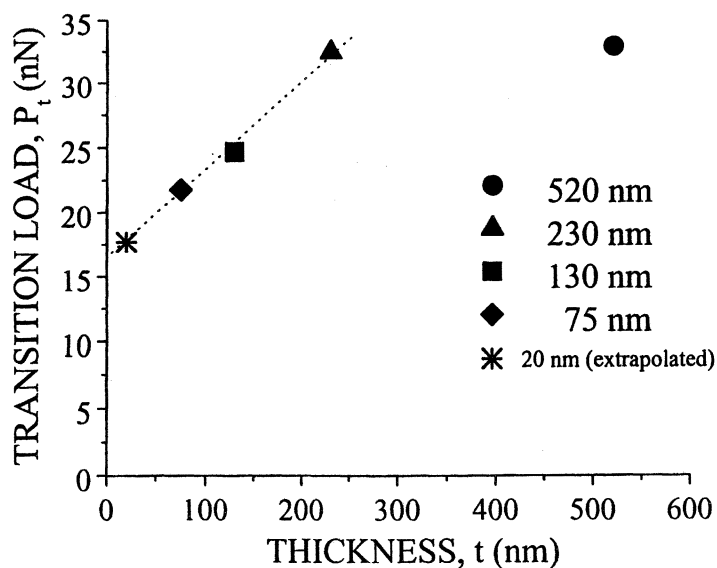


Figure 3. Transition loads, P_t , of PEP are plotted as function of the film thickness, t . A linear relationship is found up to a film thickness of about 230 nm which defines the extension of the interfacially constraint boundary regime. No film thickness dependence of the transition load is found above 230 nm (bulk regime).

$$P = 0.48 \frac{N}{m} t + 9.4 \text{ nN}; \quad t \leq 230 \text{ nm} . \quad (3)$$

The extrapolation of this to $t=20$ nm leads to a transition load of 19 nN which is well within the experimental range studied. Hence, the 20 nm thick material appears to be laterally as much disentangled as a thicker film is after a lateral shear process at a load above P .

Two trends became apparent: First, for films with $t < 230$ nm, the overall frictional force decreases rapidly with the film thickness. This effect is very surprising since the film is at least 7-10 R_g thick at the onset. Second, the plug flow regime (i.e., the intermediate friction regime) becomes smaller and finally disappears completely for films of $t=20$ nm (approximately R_g). For films thicker than 230 nm, the polymer is able to flow freely and the buried interface is not felt. As the films become thinner, free plug flow is now impeded by the confining interface and the transition point occurs earlier. Finally for films around R_g , interactions with the surface make all flow impossible, the material becomes "solid like" and no transition point is observed because shear sliding occurs at any load at the interface.

Spin-Coating Induced Strain and Density Gradient. The transition load, P , measured for different t , is presented in Figure 4 as function of the pull-off adhesion force, F_{adh} , which was obtained from force-displacement curves using maximum indentation loads equal or higher than P . The linear relationship signifies that the plug flow-sliding transition occurs independent of the film thickness at a constant transition pressure P/A , where A is the contact area. Hence the contact area is also increased with increasing film thickness. On the other hand, high resolution X-ray reflectivity data were obtained at the Cu-wavelength and showed a decreasing density of 10 % for thin films (40 nm) prior to annealing compared to thick films (500 nm) (51). The density defect disappeared upon annealing in agreement with recent published neutron reflectivity measurements (52). The observed increase in the adhesive properties are an indication for an enhanced molecular mobility in thicker films as expected from unstrained bulk liquid-like elastomers. The decrease in density for thinner films is, on the other hand, an evidence that spin coated interfacial PEP boundary layers are strained and filled with voids. The formation of voids is very likely in a spun cast film where evaporation occurs fast and the polymer mobility is constrained by the interfacial interaction.

Based on the discussed observations we can conclude that the spin casting process induced a strain in the polymer films which is frozen in as the solvent is rapidly evaporated. Since the glass transition of PEP is well below room temperature, annealing and relaxation of the chains occurs under ambient conditions. Voids which are left behind by the solvent are removed and the melt density is recovered.

Structural Model. Based on the above presented surface mechanical data obtained from unannealed ultrathin PEP films, and previous studies of thin annealed

PEP (1) and annealed and unannealed PS (3) films, we suggest the following structural model, Figure 5:

- (i) The layer immediately adjacent to the silicon substrate is pinned to the surface. Consequently, the large spin-casting-induced deformation of the chains cannot be relaxed. The pinning strength (or the interfacial interaction strength) determines whether or not this interfacial sublayer remains constraint (1,3). Furthermore, as it was demonstrated by Sauer et al. (26), the voids left behind by the solvent decrease the entanglements of the polymer. This results in the formation of a porous sub-layer with much slower kinetics than the layers above it. The strained interfacial porous sublayer can be pictured as highly disentangled and laterally anisotropic with a thickness on the order of the polymer's radius of gyration.
- (ii) The polymers adjacent to the surface immobilized sublayer can diffuse through the sublayer's pores forming a two-fluid-system, as previously observed in a PS system (3). A boundary layer is formed between the interfacial sublayer and the polymer bulk phase which is structurally and mechanically different from the bulk. The boundary layer thickness for PEP is found to extend over a distance of 7-10 R_g . Similar far-field effects were found also in PS systems (3). SFM strain experiments let us conclude that the polymers are less disentangled in the boundary layer than in the interfacial sublayer, and gradually reach the entanglement of the polymer melt for an increasing distance from the substrate. It is important to note that the normal diffusion into the pores of the interfacial sublayer causes an additional anisotropy in the boundary layer in normal direction. We believe that it is this normal anisotropic component paired with film properties (e.g., molecular weight) and spin casting conditions which are responsible for the observed far-field effects of interfacial confinement.
- (iii) Finally, at a distance of about 7-10 R_g apart from the substrate, the polymer behaves like the bulk elastomer and loses any memory of the presence of the silicon surface and the spin-coated induced interfacial alignment.

Flow and Sliding Properties Based on Structural Model. Flow and sliding properties of different thickness regions have been studied by SFM. In thick films, the flow is unhindered and classical plug flow occurs. A rapid increase in friction with load is observed as expected if the contact area (and with it the "jump-off" adhesion) is loading dependent. A surface transition point from three-dimensional viscous flow to two-dimensional interfacial sliding is observed at high pressure. This transition could illustratively be presented as the "barrier height for disentanglement" which would be the phase transition analog from a melt to a gel. The thinner the film (or the closer the material is probed to the sublayer), the faster the transition to a gel-like material occurs, as the flow is hindered by the altered mechanical and structural properties in the boundary layer. Finally, when the film thickness is comparable to the immobilized sublayer no flow occurs only sliding. Hence, the porous sublayer is already in a gel-like state.

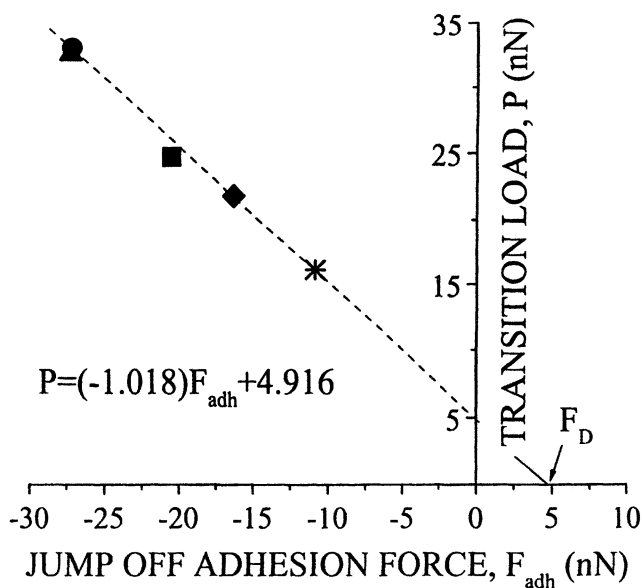


Figure 4. The jump off adhesion forces taken from force displacement curves are plotted as function of the transition loads for film thicknesses between 75-520 nm (see Figure 2 and 3). * indicates the value at a film thickness of 20 nm which has been extrapolated. The Dupré's force of adhesion, F_D , is extrapolated to be 5 nN.

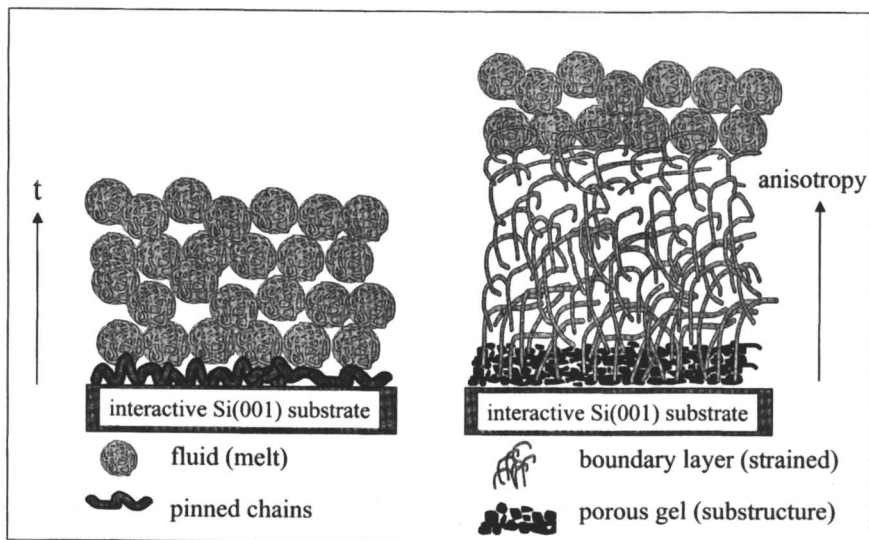


Figure 5. Two-fluid model of the interfacially constraint PEP film. The strained boundary layer consist of (a) a porous gel-like sublayer which is strained in lateral direction due to spin casting and trapped by the interfacial interaction, and (b) a top layer which is partially diffused into the porous sublayer, and thus distorted in normal direction. Adjacent to the boundary layer is the unstrained bulk polymer phase.

Surface Free Energy of Strained Homopolymer Elastomer Films. Force-displacement measurements are often used for the determination of the interfacial interaction strength or the surface free energy. It is however important to note that the instability adhesion or "jump-off" adhesion, F_{adh} , alone is insufficient for a discussion of interfacial interactions because F_{adh} is a convoluted result of interfacial interactions and contact deformations (e.g., contact area). In a first step, it is necessary to extrapolate the adhesive pull-off force to zero maximum-applied-load, P_{max} , which is only theoretically possible for contact measurements. This is shown in Figure 4. A negative slope of about 1 and an adhesive force intercept, the Dupré adhesion force F_D , of 5 nN are found in Figure 4. The corresponding Dupré's work of adhesion (per unit area of contact) is defined as:

$$\gamma_D = \gamma_1 + \gamma_2 - W_{12}; \quad W_{12} = 2\gamma_{12}, \quad (4)$$

where γ_1 and γ_2 are the surface free energies of the two bodies and γ_{12} is the interfacial energy per unit area, and W_{12} represents the work of adhesion required to separate two solid surfaces, excluding any energy of deformation (53-55). In a next step the adhesion force has to be related to the work of adhesion. The JKR-theory (49,56) connects the "pull-off" adhesion force with the work of adhesion by $F_{adh}(P_{max}) = 3\pi R\gamma(P_{max})$, assuming a sphere-plane contact at the maximum applied force, P_{max} , during an adhesion measurement. P_{max} is important as it takes strain into account. The load, P , corresponding to the transition point, P , fulfills the criteria of a maximum load because no further strain occurs at higher load. Hence the load independent work of adhesion (per unit contact area), γ_D , is given by:

$$\gamma_D = \frac{1}{3\pi R} \lim_{P_{max} \rightarrow 0} F_{adh}(P_{max}) = \frac{F_D}{3\pi R} \quad (5)$$

γ_D is calculated to be 53 dyn/cm for a radius of curvature of 10 nm (see above) and a Dupré adhesion force of 5 nN. This is in excellent agreement with the following set of interfacial and surface energies: $\gamma_{Si-nitride} = 92$ dyn/cm, $\gamma_{PEP} = 30.9$ dyn/cm (9), and $\gamma_{12} = 35$ dyn/cm. Only dispersion forces were considered for the interfacial tension; i.e., $\gamma_{12} \approx \sqrt{\gamma_{PEP}^d \gamma_{Si}^d}$ (57), with $\gamma_{PEP}^d = 30.0$ dyn/cm (9), $\gamma_{Si}^d = 40$ dyn/cm (the surface tension of the silicon-nitride surface is reasonably well approximated by a silicon-oxide surface) (26).

Note that for thin PEP films surface and interfacial energies were not found to depend on the amount the films are strained.

Interfacial Energy of Graft-Copolymers and the Effect on Wetting Autophobicity. Recently we reported a significant effect on friction forces and adhesion depending on the grafting density of dPEA-g-xPS graft copolymer films (1). The graft copolymers, are "macromolecular combs" composed of a linear backbone of dPEA with grafted pendant side chains of PS. SIMS measurements identified micelle-like superstructures, lamellar and cylindrical in shape, at a grafting density $x = 3$ and 5, respectively (1). The side chains, PS, form the core of the superstructure while the backbones, dPEA, create the surface. It was found that the

dPEA backbone layer thickness is thinner than what would be expected from Gaussian chains (58). This indicates that the backbone layers of such micelle-like superstructures are distorted from polymer melts. We found that the lateral force and adhesion force of graft copolymer films decrease with increasing grafting density (1), and concluded that the strain in the dPEA backbone increases and surface molecular mobility decreases with higher number of grafts per chain.

The Effect of Grafting Density on Dewetting of Compatible Polymers. Our interest here was to study the effect of strained surfaces on the wetting compatibility of dPEA homopolymer on the chemically identical surface of dPEA-g-xPS graft copolymer films ($x=1,3,5$). In the case of a low grafting density ($x=1$) no dewetting occurred during temperature annealing within the polymer system. Different was the result however for higher grafting densities ($x=3,5$), Figure 6. SFM measurements reveal that dewetting occurs, and the dewetting velocity increases with increasing grafting density as expected. Interdiffusion between the homopolymer and the graft copolymer surface is reduced with increased surface strain. This is in contrast to simple liquids that always spread on a chemically identical free surface. Strain induced polymeric systems can however autodewet.

The interfacial tension of the graft copolymer system can be determined by measuring the contact angle of the dewetting homopolymer (29). For small contact angle, as measured, the interfacial tension, ΔF , can be approximated by (6):

$$\Delta F = \frac{1}{2} \theta_e^2 \gamma_{dPEA}, \quad (6)$$

where θ_e is the equilibrium contact angle and γ_{dPEA} is the surface tension of dPEA. In order to achieve highest accuracy friction, force modulation and topography line scans were considered to determine the contact angles. As expected the interfacial tension increases with increasing grafting density, Figure 7, and is responsible for the wetting autophobicity.

The Effect of Grafting Density on Dewetting of Incompatible Polymers. Finally, we illustrate how different autodewetting is from dewetting of incompatible polymer systems, i.e., systems with negative spreading coefficient, $S = \gamma_2 - (\gamma_{12} + \gamma_1)$. We replaced the homopolymer dPEA with PS and found that the dewetting velocity decreases as the grafting density of a thick film of dPEA-g-xPS increases, Figure 8. It is known that on a rigid surface (or well defined interface with zero diffusion zone) the wetting dynamics is controlled by the viscous drag forces of the excess surface energy in the wedge of the spreading droplet (59,60). If the substrate is the material of lower viscosity, as it is here the case, then the drag force is determined by the substrate viscosity. The functional relationship between dewetting velocity, v , and substrate viscosity, η , is given by (61):

$$v = \frac{\gamma}{\eta} \theta_e^2, \quad (7)$$

which explains why the dewetting velocity decreases with increasing grafting density of a binary system with negative spreading coefficient.

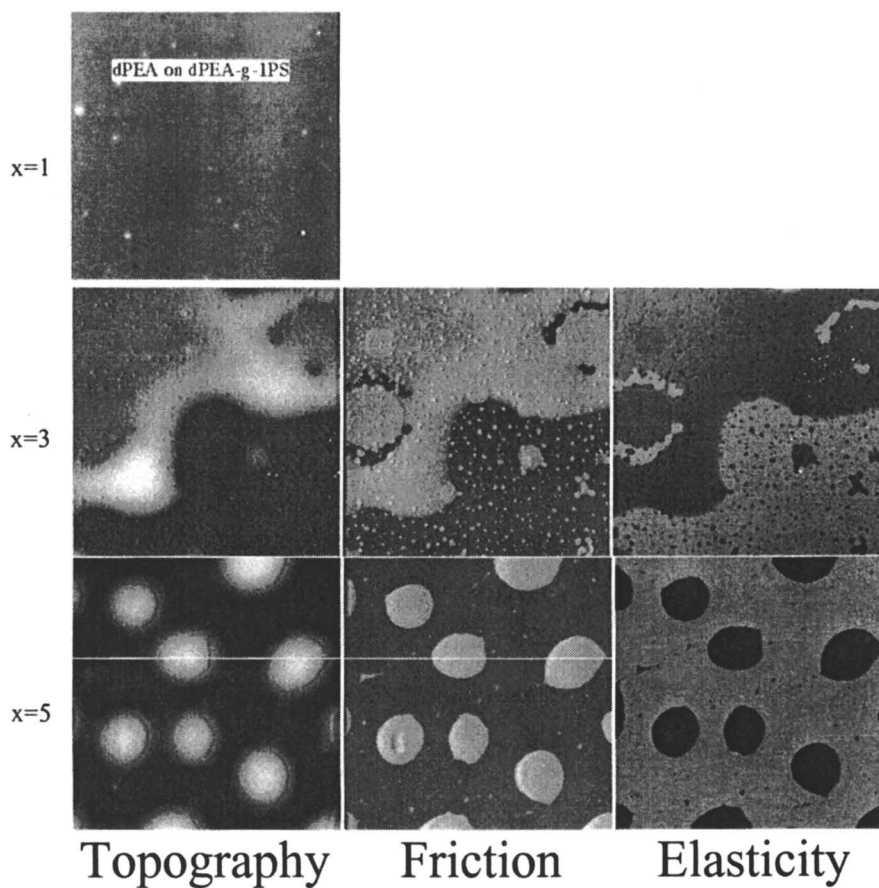


Figure 6. Increasing dewetting velocity (autophobicity) with increasing grafting density is observed on binary homopolymer/graft-copolymer systems, PEA/PEA-g-xPS (x ; grafting density). (50 μm scan images)

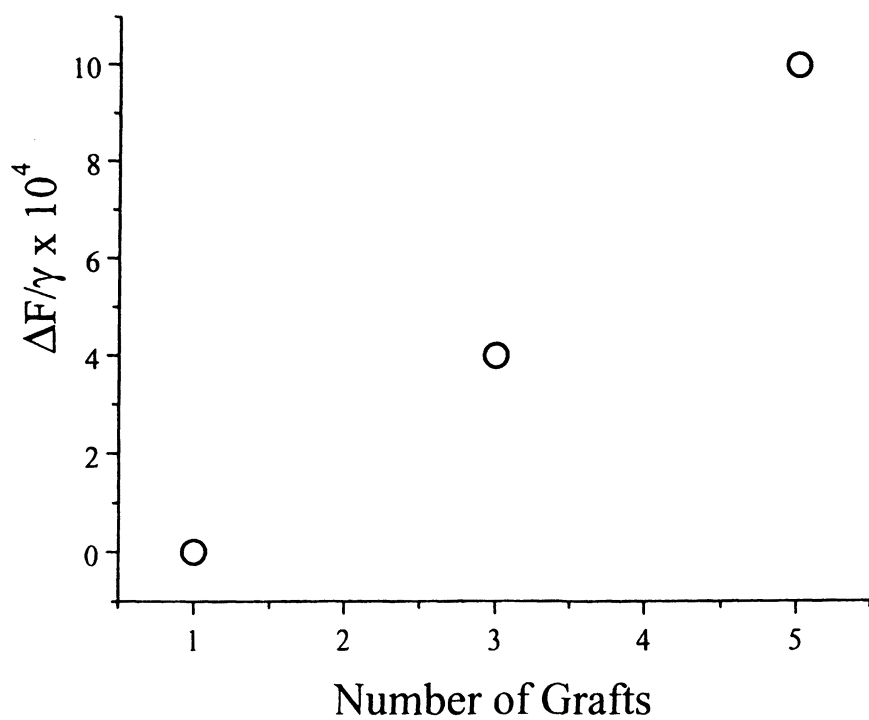


Figure 7. Increase in interfacial tension between dPEA homopolymer and dPEA-g-xPS graft copolymer with grafting density, x.

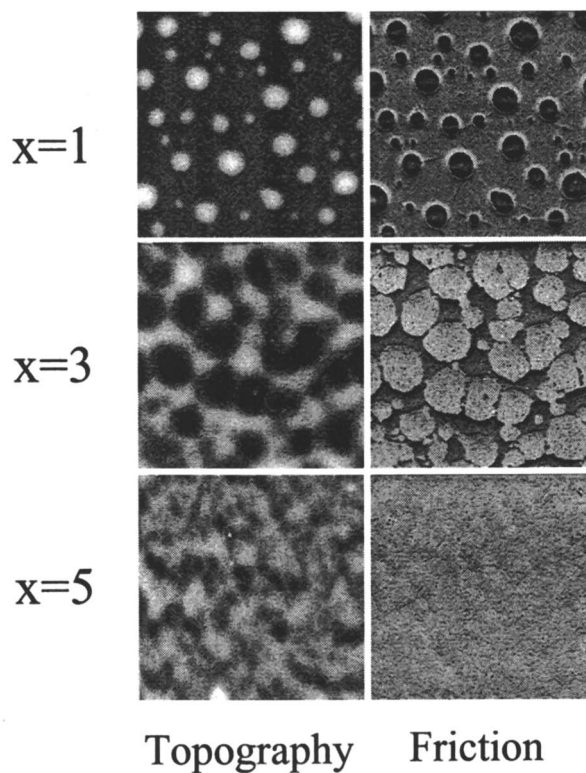


Figure 8. Decreasing dewetting velocity with increasing grafting density is observed on non-compatible binary homopolymer/graft-copolymer systems, PS/PEA-g-xPS. (50 μm scan images)

Conclusion and Summary

Effects of Spin Coating and Substrate Interaction. Effects of spin coating and interactive interfaces on shear mechanical properties of ultrathin unannealed PEP elastomer films were discussed. It was found that a stressed boundary layer is formed, 7-10 R_g thick. This unexpected far-field effect for a polymer has recently also been observed for annealed PEP films (1). The degree of disentanglement depends strongly on the distance towards the interactive interface. Strained film surfaces were found to determine the film stability, and thus, can be responsible for spontaneous autophobicity.

Two-Fluid Model. A two-fluid model was presented to explain the far-field effect and is based on shear transition properties of films thicker than the polymer's radius of gyration. A high friction viscous shear plug flow regime at intermediate load, and a low friction shear sliding regime at high load were found. The transition between the two regime was interpreted as the polymer's disentanglement strength. At the solid interface a gel-like, laterally strained, and molecular disentangled PEP sublayer is formed. The model suggests that this porous sublayer serves as an "anchor place" for the polymer melt to diffuse partially in, and to create anisotropy in normal direction to the surface. This anisotropic effect is suggested to be the reason for the far-field effect. Recent neutron reflectivity measurements confirm the two fluid model and find no significant change in the gel-like structure of the sublayer after temperature annealing (3). This explains why in annealed PEP films, the reported 7-10 R_g thick, mechanically strained, boundary layer (1) still exists.

Surface Energy of Interfacially Confined Films. Pull-off adhesion measurements and transition loads provided the possibility to determine the surface energies of thickness dependent, differently strained, polymer surfaces. The surface energy of PEP films was found to be constant, i.e., independent of the thickness, and hence independent of the lateral surface strain. This result was used in auto-dewetting studies of PEA homopolymers and mechanically surface strained graft-copolymer systems of identical chemical species. The strain on the surface of dPEA-g-xPS was found to increase dependent the interfacial free energy, and to enhance the possibility of auto-dewetting for increasing grafting density. SFM studies on dewetting of a chemically incompatible binary system PS/dPEA-g-xPS demonstrated the uniqueness of the auto-dewetting process.

Appendix

The normal load, F_N , which corresponds to the applied load when positive, and to the adhesive load when negative, is determined as follows:

$$\Delta F_N = \frac{k_N}{S} \Delta I_N; \quad k_N = \frac{EWT^3}{4L^3}, \quad (8)$$

where k_N is the normal spring constant, S is the sensitivity of the photodiode, ΔI_N is the normal deflection signal of the cantilever measured by the photo diode, E is the Young's modulus and W , T , and L are the width, thickness, and length of the cantilever, respectively. A torque on the cantilever causes a lateral force, F_T , with

$$\Delta F_T = \frac{3}{2} \frac{k_T R}{SL} \Delta I_T; \quad k_T = \frac{GWT^3}{3LR^2}, \quad (9)$$

where k_T is the torsional spring constant, R is the length of the cantilever tip, ΔI_T is the signal from the detection scheme of the torsional deflection of the cantilever, and G is the shear modulus.

Using a well defined cantilever, the friction coefficient for the calibration standard is defined as

$$\mu_{cal} = \frac{\Delta F_T}{\Delta F_N} \quad (10)$$

and found to be 0.18 ± 0.02 .

A cantilever of unknown torsional spring constant is calibrated as follows:

First, determine the cantilever's normal spring constant, and then the ratio, α , between the photodiode signal in lateral direction and the applied load in dimensions of Ampere or Volt as provided by the SFM system; i.e.:

$$\alpha = \frac{\Delta I_T}{\Delta I_N}. \quad (11)$$

Next, use the normal spring constant and the photodiode sensitivity (slope of the force-displacement curve) that leads to the non-dimensionless friction coefficient

$$\mu^* = \frac{\Delta I_T}{\Delta F_N} = \frac{I_T}{k_N I_N} = \frac{\alpha S}{k_N}. \quad (12)$$

With the the ratio between μ^* and $\mu_{cal} = 0.18 \pm 0.02$ the lateral force is quantified. It is

$$\frac{\mu_{cal}}{\mu^*} = \frac{\Delta F_N}{\Delta I_T} = \frac{\Delta F_T}{\Delta I_T}. \quad (13)$$

Thus the quantified friction force based on the "blind-calibration" method is

$$\Delta F_T = (0.18 \pm 0.02) \frac{\Delta I_T}{\mu^*}. \quad (14)$$

This calibration procedure on the silicon calibration standard works well for loads above 5 nN where the 2/3 power law that is obtained from sphere-plane contacts can be approximated by Amonton's linear relationship.

Acknowledgments

The authors of this paper would like to thank the Exxon Educational Foundation, the Shell Foundation's Faculty Career Initiation Fund, and the Royalty Research

Fund of the University of Washington for financial support of this research. This research was also supported by the NSF MRSEC (DMR96325235).

Literature Cited

- (1) Overney, R. M.; Guo, L.; Totsuka, H.; Rafailovich, M.; Sokolov, J.; Schwarz, S. A. *Mat. Res. Soc. Symp. Proc.* **1997**, *464*, 133-144.
- (2) Tolan, M.; Vacca, G.; Wang, J.; Sinha, S. K.; Li, Z.; Rafailovich, M. H.; Sokolov, J.; Gibaud, A.; Lorenz, H.; Kotthaus, J. P. *Physica B* **1996**, *221*, 53-9.
- (3) Zheng, X.; Rafailovich, M. H.; Sokolov, J.; Strzhemechny, Y.; Schwarz, S. A.; Sauer, B. B.; Rubinstein, M. *Phys. Rev. Lett.* **1997**, *79*, 241-244.
- (4) Zheng, X.; Sauer, B. B.; Van Alsten, J. G.; Schwarz, S. A.; Rafailovich, M. H.; Sokolov, J.; Rubinstein, M. *Phys. Rev. Lett.* **1995**, *74*, 407.
- (5) Liu, Y.; Russell, T. P.; Samant, M. G.; Stohr, J.; Brown, H. R.; CossyFavre, A.; Diaz, J. *Macromolecules* **1997**, *30*, 7768-7771.
- (6) Liu, Y.; Rafailovich, M. H.; Sokolov, J.; Schwarz, S. A.; Zhong, X.; Eisenberg, A.; Kramer, E. J.; Sauer, B. B.; Satija, S. *Phys. Rev. Lett.* **1994**, *73*, 440-3.
- (7) Frank, B.; Gast, A. P.; Russel, T. P.; Brown, H. R.; Hawker, C. *Macromolecules* **1996**, *29*, 6531-6534.
- (8) Buenviaje, C.; Shouren, G.; Rafailovich, M.; Sokolov, J.; Drake, J. M.; Overney, R. M. *Macromolecules* **1998**, work submitted.
- (9) Overney, R. M.; Leta, D. P.; Fetters, L. J.; Liu, Y.; Rafailovich, M. H.; Sokolov, J. *J. Vac. Sci. Technol.* **1996**, *B 14*, 1276-1279.
- (10) Fox, T. G.; Flory, P. J. *J. Appl. Phys.* **1950**, *21*, 581.
- (11) Doolittle, A. K. *J. Appl. Phys.* **1951**, *22*, 1471.
- (12) Williams, M. L.; Landel, R. F.; Ferry, J. D. *J. Amer. Chem. Soc.* **1955**, *77*, 3701.
- (13) Boyer, R. F. *J. Polym. Sci.* **1975**, *30*, 189.
- (14) Rouse, P. E. *J. Chem. Phys.* **1953**, *21*, 1272.
- (15) Pechhold, W. R.; Grossmann, H. P. *Faraday Disc. Chem. Soc.* **1979**, *68*, 58-77.
- (16) de Gennes, P. G. *Scaling Concepts in Polymer Physics*; Cornell Univ. Press: Ithaca, NY, 1979.
- (17) Kausch, H. H. *Scattering, Deformation, and Fracture in Polymers Symposium*, Mater. Res. Soc., Boston, MA, 1987; p 379-86.
- (18) Hall, C. K. *J. Chem. Phys.* **1980**, *73*, 1446-51.
- (19) Brogley, M.; Bistac, S.; Schultz, J. *Macromol. Theor. Simul.* **1998**, *7*, 65-68.
- (20) Kajiyama, T.; Tanaka, K.; Takahara, A. *Macromolecules* **1997**, *30*, 280-285.
- (21) Rabeony, M.; Pfeiffer, D. G.; Behal, S. K.; Disko, M.; Dozier, W. D.; Thiagarajan, P.; Lin, M. Y. *J. Chem. Soc. Faraday Trans.* **1995**, *91*, 2855-61.
- (22) Green, P. F.; Christensen, T. M.; Russel, T. P.; Jérôme, J. J. *J. Chem. Phys.* **1990**, *92*, 1478.
- (23) Russel, T. P.; Menelle, A.; Anastasiadis, S. H.; Satija, S. K.; Majkrzak, C. F. *Macromolecules* **1991**, *24*, 6263.

- (24) Granick, S. *MRS Bulletin* **1996**, *21*, 33-6.
- (25) Georges, J.-M.; Tonck, A.; Loubet, J.-L.; Mazuyer, D.; Georges, E.; Sidoroff, F. *J. Phys. II France* **1996**, *6*, 57-76.
- (26) Sauer, B. B.; Walsh, D. J. *Macromolecules* **1994**, *27*, 432-440.
- (27) Overney, R. M.; Meyer, E.; Frommer, J.; Brodbeck, D.; Luethi, R.; Howald, L.; Guentherodt, H. J.; Fujihira, M.; Takano, H.; Gotoh, Y. *Nature (London)* **1992**, *359*, 133-5.
- (28) Overney, R. M.; Meyer, E.; Frommer, J.; Guentherodt, H.-J.; Fujihira, M.; Takano, H.; Gotoh, Y. *Langmuir* **1994**, *10*, 1281-1286.
- (29) Overney, R. M.; Guentherodt, H. J.; Hild, S. *J Appl Phys* **1994**, *75*, 1401-1404.
- (30) Overney, R. M.; Takano, H.; Fujihira, M. *Europhys Lett* **1994**, *26*, 443-447.
- (31) Overney, R. M. *TRIP* **1995**, *3*, 359-364.
- (32) Overney, R. M.; Leta, D. P.; Pictroski, C. F.; Rafailovich, M. H.; Liu, Y.; Quinn, J.; Sokolov, J.; Eisenberg, A.; Overney, G. *Phys. Rev. Lett.* **1996**, *76*, 1272-1275.
- (33) Overney, R. M.; Leta, D. P. *Tribology Letters* **1996**, *1*, 247-52.
- (34) Carpick, R. W.; Salmeron, M. *Chem. Rev.* **1997**, *97*, 1163-1194.
- (35) Salmeron, M. B. *Mrs Bull* **1993**, *18*, 20-5.
- (36) Salmeron, M.; Neubauer, G.; Folch, A.; Tomitori, M.; Ogletree, D. F.; Sautet, P. *Langmuir* **1993**, *9*, 3600-11.
- (37) Haugstad, G. *TRIP* **1995**, *3*, 353-59.
- (38) Haugstad, G.; Gladfelter, W. L.; Jones, R. R. *J. Vac. Sci. Technol. A* **1996**, *14*, 1864-8.
- (39) Kajiyama, T.; Tanaka, K.; Takahara, A. *Macromolecules* **1995**, *28*, 3482-3484.
- (40) Gracias, D. H.; Zhang, D.; Shen, Y. R.; Somorjai, G. A. *Tribology Letters* **1998**, *4*, 231-5.
- (41) Oulevey, F.; Gremaud, G.; Semoroz, A.; Kulik, A. J.; Burnham, N. A.; Dupas, E.; Gourdon, D. *Rev. Sci. Instr.* **1998**, *69*, 2085-94.
- (42) Cheremisinoff, N. P. *J. Macromol. Sci. Chem.* **1989**, *A26*, 1231-1259.
- (43) Long, D.; Ajdari, A.; Leibler, L. *Langmuir* **1996**, *12*, 1675.
- (44) Shull, K. *Faraday Soc. Discuss.* **1994**, *84*, 203.
- (45) Shull, K. R. *Macromolecules* **1996**, *29*, 8487.
- (46) Gay, C. *Macromolecules* **1997**, *30*, 5939.
- (47) Overney, R.; Meyer, M. *Mater. Res. Soc. Bulletin* **1993**, *18*, 26-34.
- (48) Pittenger, B.; Cook, D. J.; Slaughterbeck, C. R.; Fain, S. C. *J. Vac. Sci. Techn. A* **1998**, *16*, 1832-1837.
- (49) Johnson, K. L. *Contact Mechanics*; Cambridge University Press: Cambridge, 1987.
- (50) Gotro, J. T.; Graessley, W. W. *Macromolecules* **1984**, *17*, 2767.
- (51) Wu, L. W., work to be published.
- (52) Wallace, W. E.; Tan, N. C. B.; Wu, W. L. *J. Chem. Phys.* **1998**, *108*, 3798-3804.
- (53) Israelachvili, J. *Intermolecular & Surface Forces*; Academic Press Inc.: London, 1991.

- (54) Maugis, D.; Pollock, H. M. *Acta metall.* **1984**, *32*, 1323-1334.
- (55) Pollock, H. M.; Maugis, D.; Barquins, M. *App. Phys. Lett.* **1978**, *33*, 798-799.
- (56) Johnson, K. L.; Kendall, K.; Roberts, A. D. *Proc. R. Soc. A* **1971**, *324*, 301-313.
- (57) Adamson, A. W. *Physical Chemistry of Surfaces*; 3rd ed.; Wiley: New York and London, 1976.
- (58) Ge, S.; Gue.L.; Rafailovich, M. H.; Sokolov, J.; Pfeiffer, D. G.; Schwarz, S. A.; Colby, R. H.; Dozier, W. D. *Langmuir submitted*. **1998**.
- (59) de Gennes, P.-G. *Rev. Mod. Phys.* **1985**, *57*, 827.
- (60) Leger, L.; Joanny, J.-F. *Rep. Prog. Phys.* **1992**, 431.
- (61) Brochad-Wyart, F.; Martin, P.; Redon, C. *Langmuir* **1993**, *9*, 3682.

Chapter 10

Scanning Force Microscopy of Micromechanical Properties of Polymers

Z. Huang¹, S. A. Chizhik², V. V. Gorbunov², N. K. Myshkin²,
and V. V. Tsukruk^{1,3}

¹ College of Engineering and Applied Sciences, Western Michigan University,
Kalamazoo, MI 49008–5062

² Metal–Polymer Institute, National Academy of Science, Gomel, 246550, Belarus

Scanning force microscopy (SFM) was used for probing micromechanical properties of polymeric materials. Classic models of elastic contacts, Sneddon's, Hertzian, and JKR, were tested for polyisoprene rubbers, polyurethanes, polystyrene, and polyvinylchloride. Applicability of commercial cantilevers is analyzed and presented as a convenient plot for quick evaluation of optimal spring constants. We demonstrate that both Sneddon's and Hertzian elastic models gave consistent and reliable results, which are close to JKR solution. For all polymeric materials studied, *correlation* is observed between absolute values of elastic moduli determined by SFM and measured for bulk materials. For rubber, we obtained similar elastic modulus from tensile and compression SFM measurements.

Mapping of surface mechanical properties with a submicron resolution became a reality after the introduction of scanning force microscopy (SFM) technique.¹ However, the quantitative characterization of the micromechanical properties is still a challenge for SFM.^{2,3} Quantitative measurements require the knowledge of tip shape and cantilever

³ Corresponding author.

spring constants. Optimal scanning conditions for the retrieval of reliable micromechanical data are difficult to define. The types of micromechanical contact should be clarified and appropriate models of elastic contact should be chosen. These and other problems complicate SFM application to micromechanical studies of polymer surfaces.

In the present communication, we report the results from studies of micromechanical properties on polymeric materials interpreted using classic theories of elastic contacts, Sneddon's, Hertzian, and Johnson-Kendall-Roberts (JKR). These models are tested for a set of polymeric materials with known Young's modulus, E , from 1 MPa to 3 GPa. Special attention is paid to the elucidation of applicability of different contact models and optimization of experimental probing procedures.

Experimental.

The samples for investigation were selected to represent a variety of polymeric materials with a wide range of elastic properties. Polyisoprene rubber had a nominal Young's modulus of about 2 MPa.⁴ Polyurethanes (PUs) were polyester-based Elastollan (BASF) and Dyreflex PU (Bayer). Polyvinylchloride (PVC) was Selectophore from Fluka. Polystyrene (PS) was obtained from Janssen Chimica. Young's moduli for cast polymeric films were measured by tensile testing at the Instron 4301 instrument at elongation speeds from 2 to 300 mm/min. The Dimension 3000 (Digital Instruments, Inc.) was used to characterize surfaces of spin-coated polymer films according to the well-established procedure.⁵ To evaluate the micromechanical properties, we analyzed 10 - 20 force-distance curves measured at 3 - 6 randomly selected locations, using an approach-retract frequency in the range from 0.02 to 183 Hz.

We used a set of silicon and silicon nitride V-shaped cantilevers with nominal spring constants, k_n , from 0.06 to 47 N/m, stiffer cantilevers were applied to harder materials. Actual values of spring constants were determined the fundamental resonant frequency calibration proposed earlier⁶, and cross-checked by both cantilever-against-cantilever technique and added mass technique (see review of different approaches in Ref. 6). Tip radii were measured using mixed gold nanoparticles. Measured radii were in the range of 20 - 60 nm. Shape of the tip ends at a nanometer scale was virtually symmetrical and for most tips, spherical approximation could be used.

To check mechanical and piezoelement creep contribution we conducted separate measurements of force-distance curves at similar scanning conditions on silicon wafers. As we observed, significant creep related hysteresis between approaching and retracing modes was recorded in the case of strong adhesive interaction between the SFM tip and a surface. This hysteresis was significant in air where strong capillary forces contributed and at higher speeds of scanning and probing. Therefore, we paid special attention to selection of optimal parameters for scanning. The elimination of the strong capillary forces was achieved by scanning in fluid (MilliQ water and/or absolute alcohol). This approach also reduced otherwise significant uncontrolled indentation at initial contact point. To assure elastic response of polymeric materials studied, we limited frequency

range to keep viscous contribution very small. We did not compensate for the 10° inclination of our cantilever because of its insignificance for this analysis.

Analysis of a full cycle of approaching-retracing measurements cannot be done correctly in most cases due to the presence of strong piezoelement hysteresis. Therefore, we separated approaching and retracing parts and analyzed incremental changes for the approaching part of force distance curves during intimate repulsive contact (see the designations in Figure 1). As we observed for stiff silicon surfaces, a single approaching part shows virtually linear displacement for relatively soft cantilevers used here. For this "calibration" experiment, the measured vertical deflection is exactly equal to the piezoelement displacement and, hence, can be used for testing the linearity of the piezoelement displacement in one direction. Our results indicate a minor contribution (less 3%) of system creep for the one-directional displacement. As we concluded, switching direction of piezoelement motion (changing voltage) causes usually observed strong hysteresis but steady motion in one direction (e.g., approaching) displays very small non-linearity which can be neglected for incremental analysis used in our data processing.

Results and discussion.

Recently, commercial cantilevers have been considered for optimal probing tools and provide reasonable indentation conditions for wide range of polymers.^{7,8} We address the question of reliability of SFM measurements for probing micromechanical properties of polymeric materials by estimating acceptable range of spring parameters and performing measurements for a wide range of commercially available cantilevers.

The limits of detection of surface deformation are determined by the ratio of materials elasticity and spring constant of cantilevers. If cantilever stiffness is too high then the vertical deflection of the SFM cantilever, z_{defl} , is very small as compared to z_{pos} , the vertical displacement of the piezoelement. In this case, the ratio, T , of indentation depth, $h = z_{pos} - z_{defl}$, to total displacement reaches upper measurable limit:

$$T = h / z_{pos} \rightarrow 1 \quad (1)$$

On the other hand, if material is much harder the cantilever stiffness, then $z_{pos} \approx z_{defl}$, which results in lower limit of observation:

$$T = h / z_{pos} \rightarrow 0 \quad (2)$$

Apparently, unambiguous measurements of materials properties are possible only far from these limits. For further estimations, we take an assumption that the ratio of indentation depth and cantilever deflection should not be outside of 1:10 and 10:1. This condition, in our opinion, takes into account a usual level of noise and nonlinearities of commercial mechanical system and provides an acceptable signal level (10% above system contribution), which can be clearly separated from background. We should mention that this is a very safe estimate. For many polymeric materials, we observed that

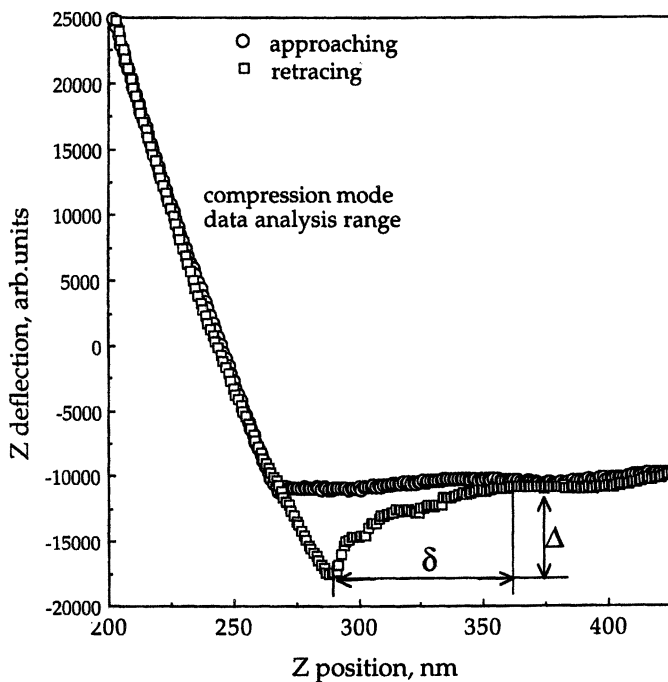


Figure 1. Force distance data for polyisoprene rubber in an approaching-retracing cycle, vertical scale is cantilever deflection in arbitrary units, horizontal axis is vertical displacement with an arbitrary zero point. Designations are shown as used in equations.

even exceeding signal of 3 - 5% is enough to get a reasonable estimation of elastic properties.

Using this deflection/indentation conditions, we estimated the range of ratios between elastic modulus of materials and cantilever spring constants, which satisfies measurable limits discussed above (Figure 2). For these estimations, we used Hertzian model of elastic contact and a two-spring model as discussed below (Figure 3). As clear from the plot presented, choosing optimal spring constant within the range 0.01 to 100 N/m should allow measurements of elastic moduli from as low as MPa to as high as tens of GPa. This range of elastic moduli spans the vast majority of polymeric materials ranging from gels to hard plastics excepting some advanced polymers with extremely high modulus.⁴

To test the validity of the proposed plot, we used a variety of commercially available cantilevers to probe elastic properties and estimated reliability of the limits proposed. As can be seen from the data points for various cantilevers tested here, we obtained reliable results within the predicted area and unstable results (significant scattering of data points to be analyzed) or surface damage beyond the defined limits in some cases (Figure 2). In Table 1, we summarized data on available cantilevers with their nominal spring constants, which were successfully applied to different polymeric materials in this work.

Table 1. Distribution of applicability of cantilevers with different nominal stiffness towards various materials (cantilevers are manufactured by Park Scientific, Digital Instruments, and NT-DMT)

Spring constant, N/m	Rubber (E=2.4 Mpa)	Polyurethanes (E =18-40 Mpa)	PVC, PS (E = 1-3 Gpa)
0.06	stable		
0.2	stable	unstable	
0.25	stable	unstable	
0.38	stable	stable	
0.5	stable	stable	unstable
2.9	~ damage	stable	unstable
47.0	damage	~ damage	stable

After optimizing cantilever selection, we developed the SFM data processing procedure. The equations for calculation of Young's modulus from cantilever deflection data can be derived by using a two-spring linear model of interacting cantilever spring and elastic surface (Figure 3). Conditions for quasi-static equilibrium for this model are presented as equality of cantilever spring forces exerted and elastic surface response (Figure 3). By using known relationships between normal load $P(h)$ and indentation parameters offered in elastic contact models, one can obtain analytical expressions of

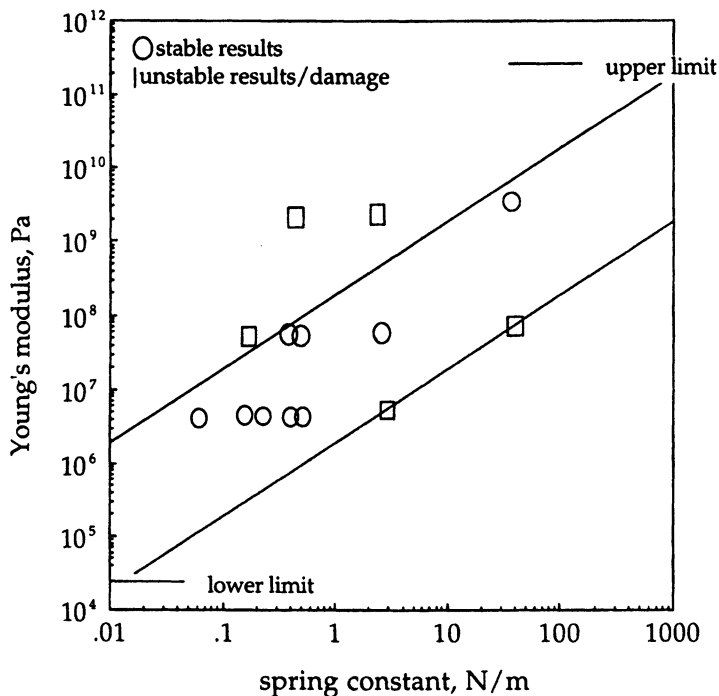


Figure 2. Range of the applicability of cantilevers with different spring constants with limits $h/z_{defl} = 0.1$ (upper limit) and $h/z_{defl} = 10$ (lower limit) and tested cantilevers for various materials (marks).

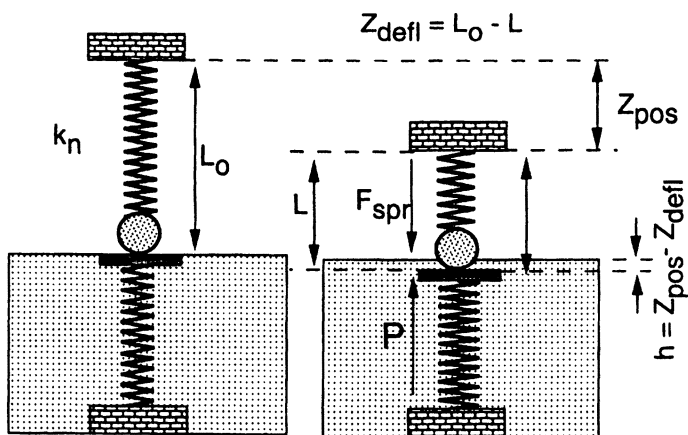


Figure 3. Double-spring model of elastic contact and major designations used in this work.

Young's modulus evaluation for each model.^{9, 10} For the polymer systems considered here, we assume $E_{\text{tip}} \gg E_{\text{polymer}}$ and, therefore, $E = E_{\text{polymer}}$ (elastic modulus of silicon tip is 160 GPa versus 0.01 - 3 GPa for polymers). Then, with a good accuracy, we take Poisson's ratio $\nu = 0.5$ for all elastomers, $\nu = 0.38$ for PVC, and $\nu = 0.33$ for PS.¹¹

After manipulation with Sneddon's equations¹² for this model we obtain:

$$\text{pyramid indenter shape} \quad E_i = \frac{\sqrt{\pi}}{2\sqrt{2}\beta \tan \alpha} (1 - \nu^2) k_n \frac{\Delta z_{\text{defl}, i, i-1}}{h \Delta h_{i, i-1}} \quad (3a)$$

$$\text{parabolic indenter shape} \quad E_i = \frac{1}{2\sqrt{R}\beta} (1 - \nu^2) k_n \frac{\Delta z_{\text{defl}, i, i-1}}{\sqrt{h} \Delta h_{i, i-1}} \quad (3b)$$

where $\beta = A_{\text{cross}}/A$, A_{cross} is cross-sectional indenter area at indentation depth h from the apex, β is equal to 2 for elastic deformation of sphere and $(\pi/2)^2$ for pyramid and conic shapes^{10, 13}; α is half of pyramid angle of the indenter (we took $\alpha = 35^\circ$ for typical SFM pyramid tip); R is tip radius; and $i, i-1$ refers to the adjacent indenter (tip) displacements.

Derivation of Young's modulus from the Hertzian model gives:

$$E_i = \frac{3}{4} (1 - \nu^2) \frac{k_n}{R^{1/2}} \frac{z_{\text{defl}}}{h^{3/2}} \quad (4)$$

with JKR model giving:

$$E_i = \frac{9}{4} (1 - \nu^2) R k_n \Delta \left[\frac{P_1}{3Rh} \right]^{3/2} \quad (5)$$

where $P_1 = (3P_2 - 1) \left[\frac{1}{9} (P_2 + 1) \right]^{1/3}$, $P_2 = (z_{\text{defl}}/\Delta + 1)^{1/2}$, and Δ is cantilever deflection at point where the tip loses contact with the surface.⁹

We use Sneddon's, Hertzian, and JKR approaches to process the force-distance data and calculate Young's modulus at different penetration depths for rubber material (Figure 4). Young's modulus changes monotonically at indentation depths larger than 10-20 nm. Below 20 nm indentation depth, unstable results are frequently obtained (Figure 4). This phenomenon is caused by the attractive force gradient near surfaces and irregular initial contact of uneven tip end and surface.¹⁴ All three approaches give convergent results at larger indentation depths. However, difference in absolute values of elastic modulus determined from different models is within 50-100% (see Figure 4, pay attention to log y-scale). This is due to wrong assumptions of the tip shape for non-spherical models. In addition, as is known, both Hertzian and JKR models cannot be applied for indentation depth larger than tip radius. These models show significant deviations in this range and, therefore, pyramid or cone models should be used if large indentation depth is required.

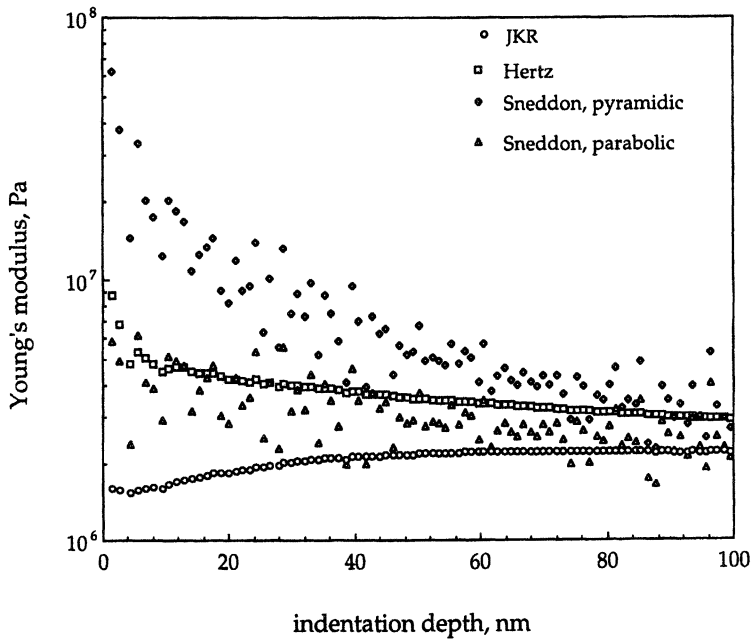


Figure 4. Comparison of different models for the evaluation of elastic modulus.

The calculated Young's modulus for rubber is 2.9 ± 0.6 MPa and 2.4 ± 0.5 MPa as determined by the Hertzian model and JKR models, respectively. Both values are very close to elastic bulk modulus for polyisoprene measured from tensile experiment (1.6 – 2.5 MPa). For further calculations, we selected the Hertzian model, which is relatively simple, gives reliable results, and does not require additional speculations or measurements of interfacial energies needed to be known in the JKR theory.

The Hertzian model was used to calculate depth dependencies of elastic moduli for a set of polymeric materials (Figure 5). Data are presented here at 0.5Hz frequency of contact. Additional measurements at various frequencies showed very strong frequency dependence for polymeric materials as will be discussed in a separate publication.¹³

The most important feature of the summary plot in Figure 5 is the close correlation between elastic moduli determined from SFM and bulk values. For four different types of materials, bulk elastic moduli differ by four orders of magnitude ranging from units of MPa for rubber to several GPas for PS. SFM data shows four distinctive ranges of elastic response of different materials at indentation depth in the range of 20 - 100 nm. These data are shown in comparison with bulk elastic moduli measured by tensile experiment (Figure 5). As clear from this comparison, the absolute value of elastic modulus determined from SFM data *correlates with bulk moduli for all materials*. Deviation of absolute values measured by these two methods does not usually exceed 30-50%. Taking into account all assumptions and simplifications behind model calculations (Hertzian model, non-linear contributions, elastic limit), differences in sample preparation (spin-coated films versus cast films), dispersion of experimental measurements for different samples and different speeds of deformation (tensile experiment), and different surface locations (SFM) the correlation observed is reasonably good.

All data discussed above are based on measurements of elastic modulus in compression mode. However, for compliant materials with strong adhesion between surface and the SFM tip, probing of elastic modulus in a tensile mode is also possible. Here, we discuss some preliminary results of application of this approach to very compliant rubber material. To facilitate this evaluation we made two basic suggestions about system behavior at the pull-off point. First, we assume that the distance between "contact point" and pull-off point on the force-distance curve corresponds to the formation of a polymer neck with the length δ (Figure 1). Direct reading of δ can be taken from the force-distance curve. Maximum force, F_c , at pull-off point should be equal to tensile spring forces generated by the cantilever deflection, Δ , and at conditions for breaking adhesive contact provided by the JKR model:

$$F_c = k_n \Delta = 3\pi R\Delta\gamma/2 \quad (6)$$

where $\Delta\gamma$ is surface energy.

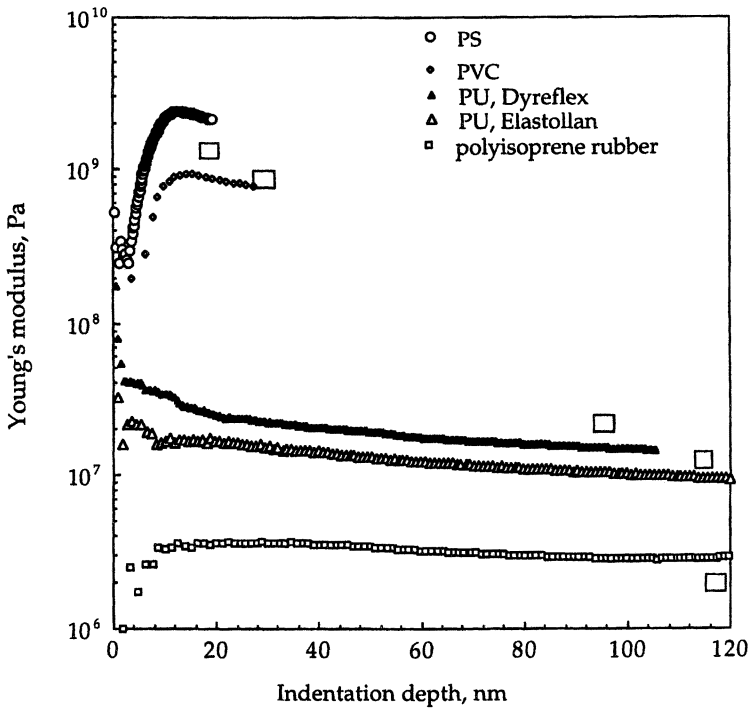


Figure 5. Summarized data for depth variation of elastic modulus for rubber, two different PUs, PVC, and PS. Bars demonstrate values of elastic bulk modulus measured from tensile experiments.

On the other hand, neck behavior under tensile stress is described by elastic theory at small elongations as^{10, 15, 16}:

$$\delta = (9F_c R(1-\nu^2)/4E)^{2/3}/3R \quad (7)$$

An expression for elastic modulus evaluation from force-distance data can be derived from (7) taking into account condition (6):

$$E = 9(1-\nu^2)Rk_n \Delta / 4(3R\delta)^{3/2} \quad (8)$$

Using the relationship (8) we calculated elastic moduli from the retracing part of force-distance curves for rubber material and compared with results obtained from approaching part according to the Hertzian model (Figure 6). We found a good correlation between these two independent measurements for this very elastic material. Vast majority of measurements gave absolute values between 2 – 3 MPa with deviations within 30%.

Conclusions

By combining optimal cantilever parameters and experimental conditions one can obtain reliable force distance data which is appropriate for further contact mechanics analysis for a wide selection of polymeric materials. Both Sneddon's and Hertzian models of elastic contact give consistent results in the range of indentation depth up to 100 nm. *Close correlation* is observed between elastic moduli determined by SFM in compression mode (approaching cycle) and measured values for bulk materials. As shown, for elastic materials force-distance curves can be used for evaluation of tensile elastic moduli from retracing cycle. For rubber material, the latest is in a good agreement with measurements in compression mode.

Through proper selection of the SFM cantilevers, a very wide range of polymeric materials can be tested by the SFM technique. Elastic moduli can be measured as low as MPa for rubbers to as high as several tens of GPa for hard plastics if selection of cantilever spring constants from 0.05 to 100 N/m is available. A probe plot selection for quick evaluation of optimal SFM cantilevers for polymeric materials with various elastic properties is proposed and verified.

Acknowledgments

This work and international collaboration are supported by The National Science Foundation, The Surface Engineering and Tribology Program, CMS-9409431 and CMS-9610408 Grants and Becton Dickinson Co. Donation of polyurethane materials by BASF and Bayer is highly appreciated. The authors thank J. Hazel and other members of our group for helpful discussion.

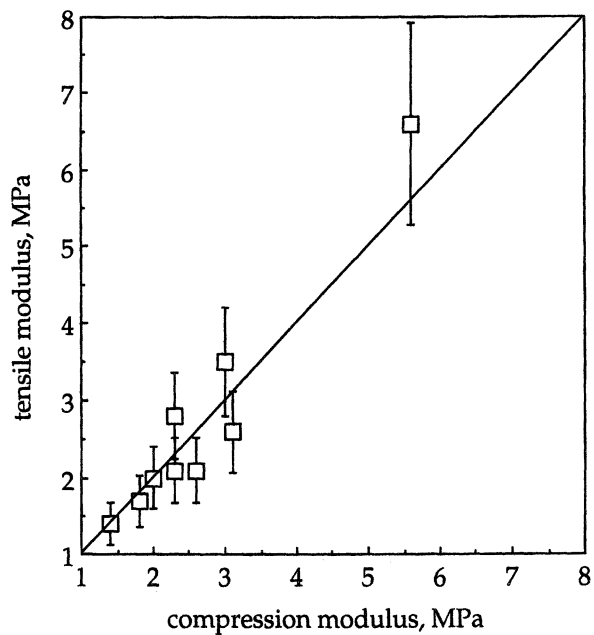


Figure 6. Correlation between elastic modulus values obtained in compression mode (x-axis) and retracing mode (y-axis).

References

1. Binnig, G.; Quate, C. F.; Gerber, Ch. *Phys. Rev. Lett.* **1986**, *12*, 930. Sarid, D. *Scanning Force Microscopy*, Oxford University Press, New York, 1991.
2. *Scanning Probe Microscopy of Polymers*, Ratner, B.; Tsukruk, V. V., Eds., ACS Symposium Series, 1998, v. 694.
3. Burnham, N. A.; Colton, R. J. *J. Vac. Sci. Technol.*, **1989**, *A7*, 2906. *Micro/Nanotribology and Its Applications*, Bhushan, B., Ed., NATO ASI Series, Kluwer Acad. Publ., Dordrecht, 1997.
4. Aklonis, J. J.; MacKnight, W. J. *Introduction to Polymer Viscoelasticity*, J. Wiley & Sons: NY, 1983.
5. Tsukruk, V. V. *Rubber Chem. & Techn.*, **1997**, *70(3)*, 430.
6. Hazel, J.; Tsukruk, V. V. *J. Tribology*, **1998**, *120*, 814.
7. Vanlandingham, M. R.; McKnight, S. H.; Palmese, G. R.; Ellings, J. R.; Huang, X.; Bogetti, T. A.; Eduljee, R. F.; Gillespie, J. W. *J. Adhesion*, **1997**, *64*, 31.
8. Vanlandingham, M. R.; McKnight, S. H.; Palmese, G. R.; Eduljee, R. F.; Gillespie, J. W.; McCulough, R. J. *J. Mat. Sci. Lett.*, **1997**, *16*, 117.
9. Johnson, K. L.; Kendall, K.; Roberts, A. D. *Proc. R. Soc., London*, **1971**, *A324*, 301.
10. Sviridenok, A. I.; Chizhik, S. A.; Petrokovets, M. I. *Mechanics of A Discreet Friction Contact*, Nauka I Tekhnika, Minsk, 1990.
11. *Polymer Handbook*, Brandrup, J.; Immergut, E. H.; Eds., Wiley&Sons, NY, 1975.
12. Phart, G. M.; Oliver, W. C.; Brotzen, F. B. *J. Mater. Res.*, **1992**, *7*, 613.
13. Tsukruk V. V.; Huang, Z.; Chizhik, S. A.; Gorbunov, V. V. *J. Materials Science*, **1998**, *33*, 4905. Tsukruk, V. V., Gorbunov, V. V., Huang, Z., Chizhik, S. A., *Polymer J.*, **1998**, submitted.
14. Hues, S. M.; Colton, R. J.; Meyer, E.; Guntherodt, H.-J. *MRS Bull.*, **1993**, *18(1)*, 41.
15. Tabor, D. H. *J. Colloid. Interface Sci.*, **1977**, *58*, 2.
16. Muller, B. M., Yuschenko, V. S. *Colloid. J. USSR*, **1980**, *42*, 500.

Chapter 11

Probing Adhesive, Mechanical, and Thermal Properties of Polymer Surfaces Using Scanning Probe Microscopy

**Gregory F. Meyers¹, Benjamin M. DeKoven^{1,3}, Michael T. Dineen¹,
Andrew Strandjord^{1,4}, Paul J. O'Connor¹, Terry Hu¹, Yi-Hung Chiao¹,
Hubert M. Pollock², and Azzedine Hammiche²**

¹ The Dow Chemical Company, Corporate R&D, Midland, MI 48667

² School of Physics and Chemistry, University of Lancaster,
Lancaster LA1 4YB, United Kingdom

The use of scanned probe microscopy (SPM) to study adhesion and mechanics of polymer surfaces has been investigated at Dow since 1992 (1,2) and, since 1997, studies of thermal properties at polymer surfaces have begun. Our goal has been to combine the imaging capabilities of SPM with surface property measurements. Initial work used contact mode atomic force microscopy with soft silicon nitride cantilevers to generate force vs. distance (F-d) curves (Figure 1). Operating in an unscanned mode, the sample is pushed into a tip mounted on the end of a soft cantilever, leading to deflection of the cantilever (loading). On retraction of the sample, the lever deflection is also monitored (unloading). During loading, the tip may penetrate into the material, providing information about the mechanical properties of the surface. On unloading, the tip may adhere to the surface, leading to information about tip-surface adhesion.

The pull-off portion of the F-d curves is used as a means to provide qualitative information about the chemical nature of the surface, provided there is no plastic deformation resulting from the contact. The loading portion of the curve is used to provide qualitative understanding of the mechanical nature of the contact. The latter illustrates the limitations of beam bending approaches to nanoscale mechanical property measurements using static deflection AFM. The use of resonant AFM techniques with stiffer cantilevers to provide evidence of both chemical adhesion and mechanical deformation was further investigated. Mechanical property measurements of surfaces can be made quantitative using depth sensing nanoindentation, but for soft polymers this approach also has limitations. Finally, scanning thermal microscopy (SThM) was used to identify the presence or absence of thin polymer films on metal surfaces.

³ Current address: Intevac, Santa Clara, CA 95054-2704

⁴ Current address: IC Interconnects, Colorado Springs, CO

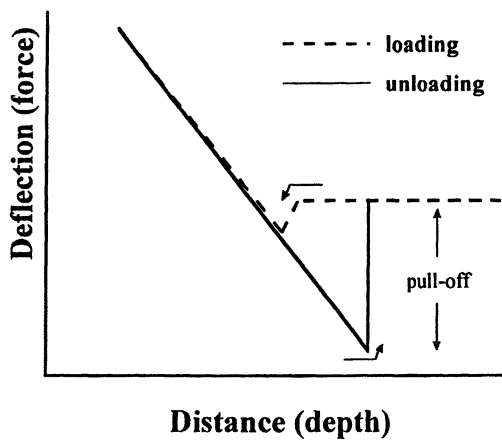


Figure 1. Schematic of deflection vs. distance curve. Deflection can be converted to force using the spring constant. Distance can be converted to depth by removal of the compliance.

Experimental

F-d curves were made using a "G" head scanner on either a Nanoscope II (small sample AFM) or Nanoscope III (MultiMode AFM) manufactured by Digital Instruments, Inc. The z response of the G head scanning piezo as a function of DC offset voltage and frequency (1 or 11 Hz) was measured using interferometry for 50V sweeps. The functional fit of this response was used as a correction to measured displacements. With the Nanoscope II, silicon nitride cantilevers were used with nominal force constants of 0.58 N/m or 3.1 N/m. Silicon cantilevers were used with the Nanoscope III. In this case the spring constant was measured directly from the peak resonance frequency. In both cases the lever deflection was converted to force using deflection from a sapphire single crystal which is assumed to be non-deformable under the specified conditions. The lever deflection calibration was $1V = 15 \text{ nN}$ for the silicon nitride cantilevers with $k = 0.58 \text{ N/m}$. Approximately forty tips were used during the study. Tip radii were measured from scanning electron microscopy images of selected tips. Force curves were collected in air at room temperature by disabling the x and y scanning, and cycling the z piezo a specified distance at a frequency of 12.5 Hz for calibrated loads up to 200 nN.

Tapping Mode (trademark of Digital Instruments, Inc.) and phase images were obtained on a Nanoscope III (S/N NS3-519) using a Dimension 3000 Large Sample AFM (S/N 3000-1/225, Digital Instruments, Inc., Santa Barbara, CA.) and "G" scanner head (S/N DMLS-288). The system is also equipped with a Phase Extender Module (Model EX-1, S/N 505). In Tapping Mode the lever is oscillated at resonance and the feedback control adjusts for constant tapping amplitude. This is still a contact mode of AFM; however, the normal forces and shear forces are greatly reduced over conventional static deflection contact mode AFM. All images were recorded in constant force mode where the sample z position was adjusted during scanning to keep the r.m.s. (root mean squared) lever deflection constant. The tapping lever has a phase component that can change depending on the interaction of the tip with the surface. The phase image plots the phase lag as a function of position and is collected at the same time as the topography. Scanning was carried out in air using commercially available silicon cantilevers and tips with nominal force constants of 48 N/m.

Tapping conditions were controlled by zeroing the phase signal (90 degrees) with the tip engaged but not tracking the surface. The setpoint voltage was then reduced and the voltage at which the phase signal was first observed to shift was noted (this is the set-point voltage, A_0). The setpoint was further decreased to improved tracking while noting the direction (sign) of the phase signal until the desired operating setpoint voltage (A_{sp}) was achieved. The ratio (r_{sp}) of A_{sp}/A_0 determines the degree of tapping.

Quantitative nanoindentation was achieved using the Tribometer Micromechanical Testing Instrument (trademark of Hysitron, Inc., Minneapolis, MN) directly coupled

to a Nanoscope III Scanned Probe Microscope (Digital Instruments, Inc., Santa Barbara, CA). The indenter tip was a Berkovich diamond with a nominal radius of 40 nm. The tip was driven electrostatically following a pre-determined loading (25 sec.)- hold (10 sec) - unloading (25 sec.) profile and the displacement of the surface is measured independently using capacitive detection of the actual indenter displacement. Typical loads accessible for this experiment range from 50 μ N to about 5000 μ N. The indenter tip can be used for imaging under the control of the SPM operating in contact mode with a minimum load of about 1 μ N. The imaging capability is useful for finding a particular feature to indent or for imaging the resulting indent. The calibration and analysis of load-displacement data was based on a published method (3).

SThM was carried out in the laboratory of H. Pollock and A. Hammiche in the Physics Department of the University of Lancaster, Lancaster, UK using a modified Topometrix Explorer SPM (Topometrix Corporation, Santa Clara, CA). The microscope uses a small Wollaston wire, bent and etched to form a contact mode AFM tip with a nominal radius of about 200 nm. The tip is used both as a heat source and a heat sensor. A second, reference, tip is held in air in close proximity to the sample for differential measurements. The heat to the tip can be modulated and the material response to the modulated heating can be monitored during imaging via lock-in techniques. For the work described here the microscope was operated in three imaging modes: (1) constant deflection (for topography); (2) constant temperature (DC); and (3) modulated temperature (AC). In an unscanned mode, the tip can be positioned on the surface for local differential thermal analysis (DTA) or local modulated temperature-DTA and local thermomechanical (TMA) measurements (4,22).

Several surfaces were used for the current work. For the F-d curves we used polystyrene (monodisperse materials and a commercial Styron 685D grade from Dow Chemical) films spun from toluene onto silicon wafers; commercial low density polyethylene film (LDPE, commercial grades 530I and 760C from Dow Chemical); thin film silicon nitride as found on the underside of the cantilever substrates; cleaved mica (Electron Microscopy Supplies); sapphire single crystal (Meller Optics); evaporated gold film (0.2 micron); cleaved highly oriented pyrolytic graphite (HOPG, XYA grade, Union Carbide); polydimethylsiloxane elastomers (PDMS, M. Chaudhury of Dow Corning Corporation); and rubber from a rubber band.

The crosslinkable epoxy thermoplastic modified with 5 wt % grafted rubber concentrate (CET-GRC) was prepared according to published procedure (5). The rubber domains are nominally 0.1 micron in diameter and consist of a core-shell structure with a 0.03 micron diameter polystyrene seed. Blocks of the CET-GRC were cryo-polished at -90°C using a diamond knife to provide a smooth face for SPM imaging. Some of these surfaces were post stained in OsO₄ vapors by suspending the polished blocks in sealed containers over an aqueous solution of

OsO₄ for several minutes. The stain selectively reacts with unsaturated groups in the polymer surface region, in this case the rubber containing phases.

Photodefineable benzocyclobutene (PhotoBCB) is a highly cross-linkable low dielectric polymer made from Diels-Alder addition of vinyl and cyclobutane groups between monomer units consisting of divinyl siloxane bis-benzocyclobutene (6). The partially cross-linked material was spun cast as a 5 micron film onto copper coated silicon wafers. The photoBCB was then patterned using a proximity mask and I-line (365 nm) radiation. The material is negatively defined, i.e., exposed areas are further cross-linked and the unreacted material is then removed during development. The mask leaves circular vias ranging from 5 to 50 microns. Following development and hard thermal cure the vias contain polymer residue ("scum"), which is removed in an oxygen containing plasma step.

Results and Discussion

Adhesion Using Pull-Off Force

In order to make sense of pull-off force data it is important to demonstrate that the measurements are made in the absence of plastic deformation during contact. Comparison of topview contact mode images after contact at low peak loads (15 nN) and high peak loads (150 nN) were used to check for plastic deformation (Figure 2). With the exception of polystyrene, these surfaces showed no evidence of plastic deformation. Polystyrene showed unique patterning during scanning which was found to depend on the polymer molecular weight [1, 7]. It is useful to compare typical deflection vs. distance curves for four surfaces which have been subjected to a peak load of 45nN (Figure 3). All exhibit a large hysteresis in unloading due to adhesion, as the force required to break the contact is at least 10X that necessary to form the contact. Note that the pull-off force and pull-off areas are very different for the materials at the same applied load. Also note that slopes of the loading portion of the curves are similar for all surfaces with the exception of the rubber surface which is lower. The LDPE surface exhibited a large pull-off force, but these types of surfaces gave variable results as discussed later.

The pull-off force is plotted against applied load for each surface in air (Figure 4). Note that the pull-off forces are independent of load over the range studied. Based on JKR theory (8,9) the pull-off force can be related to surface energy via equation 1:

$$F = 3\pi R \sqrt{(\gamma_{\text{tip}} \gamma_{\text{surface}})} \quad (1)$$

where R is the radius of the tip (40 nm by scanning electron microscopy), γ_{tip} and γ_{surface} represent the surface energies of the tip and surface, respectively. The surface energy of the tip can be estimated by measuring the pull-off force between the silicon nitride tip and the silicon nitride thin film on the underside of the cantilever substrate and solving for equation 1. This gave a calculated surface energy for silicon nitride of 225 mJ/m². Using this value for the tip allowed for the

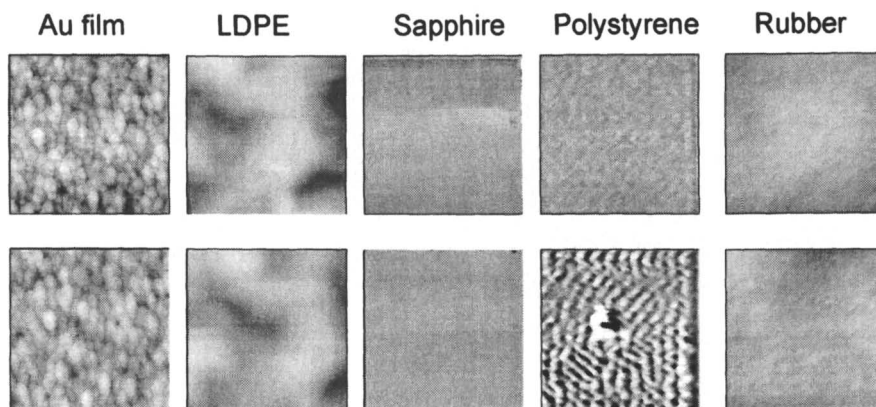


Figure 2. Contact mode AFM images of surfaces after contact at 15 nN (top row) and 150 nN (bottom row). Images are at $1\mu\text{m} \times 1\mu\text{m}$ and obtained with a silicon nitride cantilever, $k = 0.58 \text{ N/m}$.

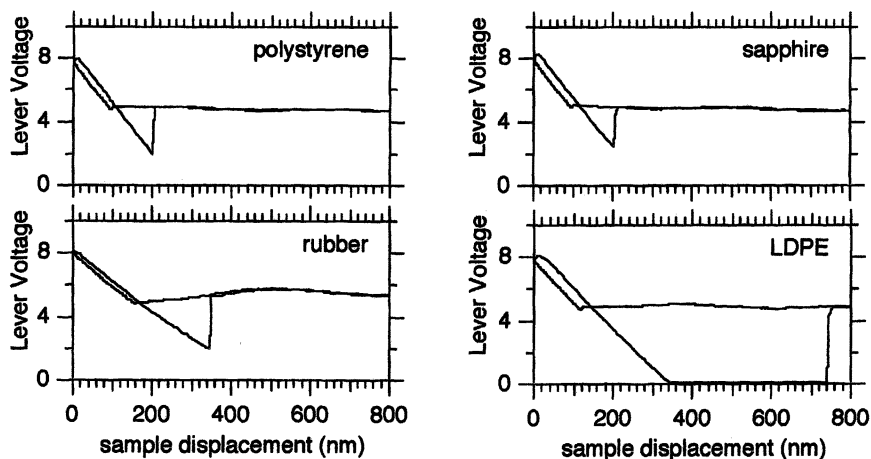


Figure 3. Representative deflection vs. distance curves for polystyrene thin film, sapphire single crystal, rubber and low density polyethylene film obtained with a silicon nitride cantilever ($k = 0.58 \text{ N/m}$). The calibration for lever deflection is $1\text{V} = 15 \text{ nN}$.

calculation of surface energies for each material, shown on the right Y axis of Figure 4 and given in Table I. We have used a nominal value of the tip radius (40 nm) in these calculations. Tip-to-tip variations will add additional errors in these estimates. The lowest values were obtained for hydrocarbon surfaces (PS, LDPE, graphite, and rubber); next higher was for metal oxides (silicon nitride, mica, and sapphire), and the highest was for gold metal. The estimated surface energies are consistent with those derived from more macroscopic methods, such as contact angle measurements. Reported values for the surface energies of polystyrene and cleaved mica are 33 mJ/m^2 and 300 mJ/m^2 , respectively (10).

Table I. Calculated surface energies from pull-off data over the applied load range of 20 nN to 75 nN (silicon nitride cantilever, $k = 0.58 \text{ N/m}$, and tip with radius $R = 40 \text{ nm}$).

Material	surface energy (mJ/m^2)
polystyrene	12 ± 1
graphite	29 ± 2
polyethylene	53 ± 8
rubber	71 ± 5
sapphire	109 ± 5
silicon nitride	226 ± 11
mica	244 ± 27
gold	287 ± 4

The reproducibility and accuracy of the pull-off measurements depended on many factors, such as surface and tip cleanliness, the relative curvature of surface features to the curvature of the tip (i.e. roughness and contact area), and variations in tip shape. Examples are shown for sapphire and LDPE surfaces (Figure 5). The pull-off force from a sapphire surface left open in the laboratory for several months gave an initially high pull-off force at low applied load and then low pull-off forces for subsequently higher loads. Contact mode AFM images revealed a surface layer 3-4 nm thick that could be altered during scanning. If the sapphire surface was cleaned for several minutes in a UV-ozone chamber, the surface gave consistent pull-off values at all loads. The high initial pull-off force on the contaminated surface was probably due to necking while the lower pull-off forces at higher loads probably resulted from pull-off between the lower surface energy contaminant on both the tip and surface. Variations in pull-off forces were also noted for LDPE films. In this case variations were found to be related to surface roughness and, therefore, contact area. Measurements were obtained on two films with local roughness that was either less than or greater than the tip radius (Figure 5). When the roughness is less than the tip radius in the vicinity of contact, the pull-off forces are consistently lower.

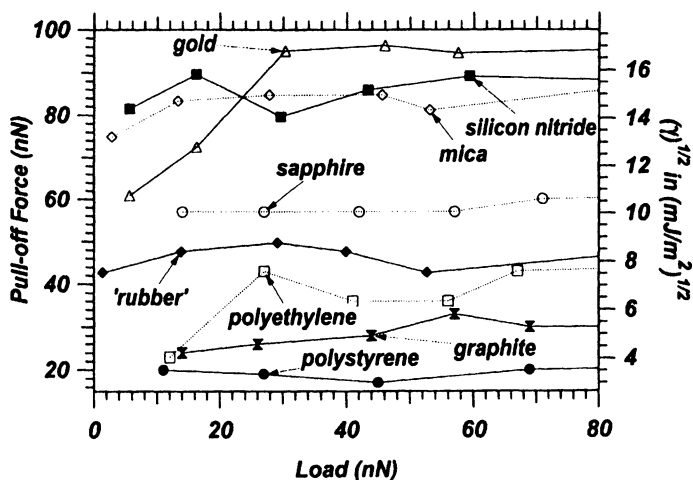


Figure 4. Pull-off force vs. maximum applied load during contact for each surface using a silicon nitride cantilever ($k = 0.58 \text{ N/m}$). The surface energy scaling is based on JKR theory as described in the text.

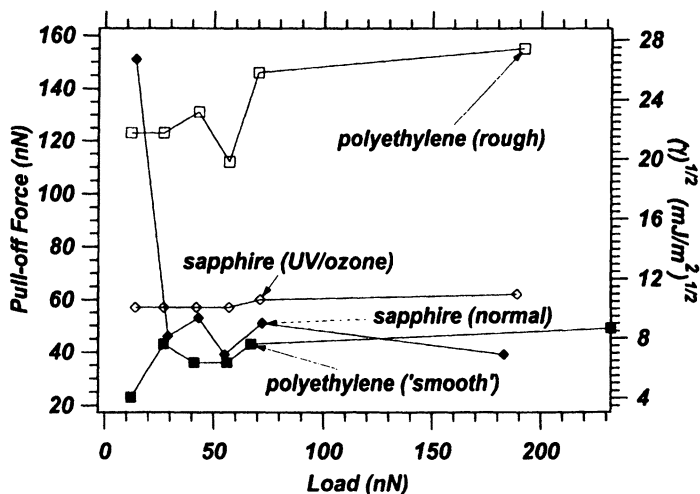


Figure 5. Pull-off force vs. maximum applied load during contact demonstrating the effect of surface contamination (sapphire) and roughness (LDPE) on measurement accuracy.

This summarized our understanding of pull-off forces circa 1992 (2). Despite these problems we were encouraged by the *potential* for SPM to provide measures of local surface energy on polymers. Other groups have made much progress in this area since 1992 and these measurements can be made quantitatively for specific systems (e.g. using chemically functionalized tips and surfaces) and under specific conditions (e.g. in liquids) (11). Further understanding of the nature of tip-surface contacts on polymers is necessary before the technique can be made for general use.

Qualitative information regarding relative differences in surface adhesion can now be obtained routinely while imaging using, for example, phase detection in Tapping Mode AFM (TMAFM) (12). In this technique the cantilever is driven to resonance and the phase lag of the lever interacting with the surface is measured as a function of position during scanning. Adhesive interactions can dominate phase image contrast when the lever is operated in a low amplitude and light tapping regime, where sample deformation is minimized, as described later.

Mechanical Properties Based on Lever Deflection of Soft Cantilevers

The lever deflection is plotted against sample displacement for all surfaces (Figure 6). The slopes of these curves during loading were similar despite the fact that the nominal moduli of the materials varied by three orders of magnitude. We were surprised to find, for example, that LDPE and sapphire had similar mechanical behavior under experimental conditions. Only at the highest applied loads (ca 200 nN) do the slopes begin to change and distinguish between materials. Surface displacements for loads up to 150 nN are less than 2 nm with the exception of elastomers. Using soft cantilevers ($k = 0.58 \text{ N/m}$) our experiments could only distinguish rubbers or polydimethylsiloxane (PDMS) elastomers from other polymers, metals, and metal oxide surfaces. This observation is readily explained by the relative differences in stiffness between the cantilevers used and the stiffness of the surfaces under investigation. Using Hertzian contact mechanics, Radmacher et al. (13) derived equations for calculating surface stiffness (k_s) and tip penetration depths (d) during contact, as shown below:

$$d = [(9\pi^2 / 16)[F^2 / E^* R]^2]^{1/3} \quad (2)$$

$$k_s = \delta F / \delta d = [(6 / \pi^2)(E^* R F_0)]^{1/3} \quad (3)$$

$$E^* = (\pi E) / (1 - \nu^2) \quad (4)$$

Equation 2 gives the penetration depth, equation 3 gives the surface stiffness and equation 4 is the calculated effective modulus based on bulk modulus, E , and Poisson's ratio, ν . We have applied this analysis to our materials to calculate the surface penetration and surface stiffness using the measured radius of our tip and the known bulk mechanical constants of the materials at an applied load of 50 nN (Table II).

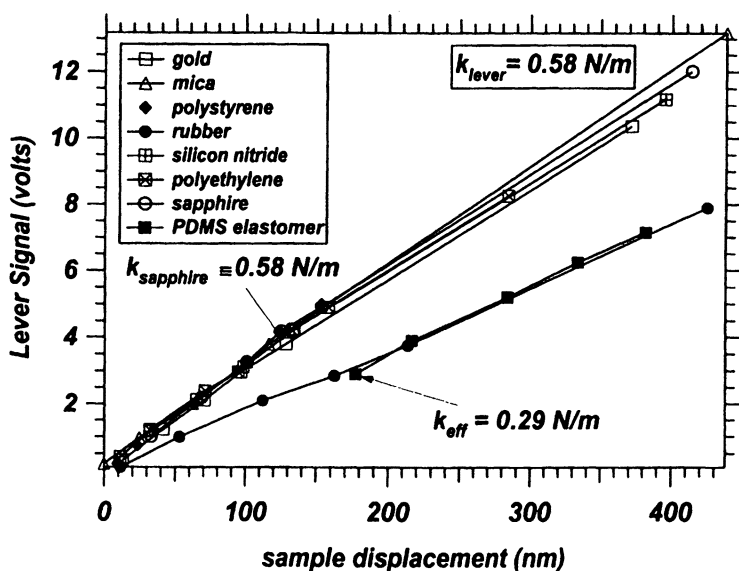


Figure 6. Lever deflection vs. sample displacement for all surfaces (1V deflection = 15 nN force, silicon nitride cantilever $k=0.58 \text{ N/m}$). Measured surface penetration is less than 2 nm for all surfaces up to loads of 150 nN with the exception of elastomers.

Table II. Calculated surface stiffness and tip penetration depths for several materials using a silicon nitride cantilever ($k=0.58\text{N/m}$, tip radius= 40 nm) and a 50nN contact force.

material	$E(\text{N/m}^2)$	ν	penetration depth (nm)	k_s (N/m)
PDMS	10^6	0.5	270	0.28
polyethylene	10^9	0.4	2.9	26
polystyrene	3×10^9	0.33	1.4	54
sapphire	4×10^{11}	0.2	0.06	1300

Only for the PDMS elastomer is the stiffness of the surface on the order of the cantilever stiffness used to probe the mechanical properties. All other surfaces show negligible penetration. The sensitivity to measure mechanical properties of polymer surfaces using AFM under static deflection depends on the relative stiffness of the cantilever and surface (14). The soft ($k < 1\text{N/m}$) contact mode cantilevers were not able to distinguish between materials with bulk modulus in excess of 1GPa (2).

This finding has practical consequences for imaging. For example, contact mode AFM imaging of a cryo-polished surface of a rubber modified epoxy reveals what appear to be holes where the rubber should be (Figure 7, top). However, exposure of the surface to osmium tetroxide vapor causes the rubber to swell, crosslink, and harden (15). The rubber can now be imaged under the same conditions (Figure 7, bottom). Prior to staining, the rubber was compressed under the load of the tip. Applying the equations 2, 3, and 4 to this case we can determine the surface stiffness and penetration depths of the two phases in the CET-GRC material (Table III).

Table III. Calculated surface stiffness and tip penetration depths for the epoxy (CET)-rubber (GRC) composite surface using a silicon nitride cantilever ($k=0.58\text{ N/m}$, tip radius= 40 nm) and a 50 nN contact force.

phase	$E(\text{N/m}^2)$	ν	depth (nm)	k_s (N/m)
CET (epoxy)	3.1×10^9	0.38	0.6	35.4
GRC (rubber)	6.9×10^6	0.50	74.7	0.66

The calculations indicate that under our scanning conditions the $<100\text{ nm}$ rubber particles (due to polishing) should be nearly completely compressed and the epoxy phase should be unaffected, consistent with what was observed. Careful inspection of the image at the top of Figure 7 shows small ridges on one side of the holes,

**cryo-polish @ -90°C,
unstained**

**cryo-polish @ -90°C,
OsO₄ vapor stained**

Figure 7. Contact mode AFM of CET-GRC (5 wt% rubber, 0.1 μm diameter) after cryo-polishing (top) and after staining in OsO₄ vapor (bottom).

presumably as a result of rubber being squeezed up the side of the epoxy hole in the scan direction.

Recently, a resonant imaging mode, TappingMode, with phase detection has been applied to the study of both adhesion and mechanical deformation on this sample. The phase change of the oscillating tip in contact with the sample surface has recently been shown to be proportional to changes in tip-sample energy dissipation (16). By carefully controlling the tapping parameters reproducible phase images can be obtained in which the rubber phase contrast can invert relative to the phase signal of the epoxy matrix (Figure 8). As noted in the Experimental section, controlling the free amplitude of vibration near the surface and noting the attenuation of this free amplitude while the tip is in contact with the surface can control the tapping conditions. For a given free amplitude, the degree of tapping is the ratio of the set-point amplitude to the free amplitude. As this ratio approaches 1 the degree of tapping is lighter; as it approaches 0 the degree of tapping is harder. In all cases, the instantaneous force is sufficient to compress the rubber phase so that the rubber still appears as holes in the height images. The depth of the holes varies by only 5% with slightly deeper holes noted for the hardest tapping conditions (left hand side of Figure 8). The phase angle of the tapping tip will be sensitive to the tapping conditions. Under light tapping conditions the tip-surface interaction can become trapped in the adhesive state. As the set-point ratio is decreased and the tapping becomes harder, the tip-surface interaction becomes repulsive. The phase contrast observed is consistent with this understanding. The rubber exhibits positive contrast relative to the epoxy when tapping conditions are trapped in the adhesive regime (top three phase images of Figure 8), but exhibits negative contrast relative to the epoxy when conditions are in the repulsive regime (bottom five phase images of Figure 8). The energy dissipation represented by the phase images show a transition from adhesion (seeing the rubber) to mechanical deformation (not seeing the rubber). Other, more subtle details in the contrast of the phase images can be seen (e.g., substructures in the rubber particles) which require further study.

Mechanical Properties Using Depth Sensing Nanoindentation

An alternative approach to making surface mechanical measurements combines contact mode AFM imaging and depth sensing nanoindentation (17). This approach replaces the flexible cantilever beam with a stiff diamond indenter. The diamond indenter can be driven into a surface and retracted while the surface displacement is measured independently and continuously to generate a load vs. displacement curve. The same indenter tip can be used for contact mode imaging before and after indenting under the control of our Nanoscope III SPM. These measurements are quantitative based on published methods (3) where the tip shape and system compliance are calibrated using fused silica and aluminum surfaces, respectively. Measuring the stiffness of the contact at the onset of unloading provides a means to determine a modulus and hardness of the test surface.

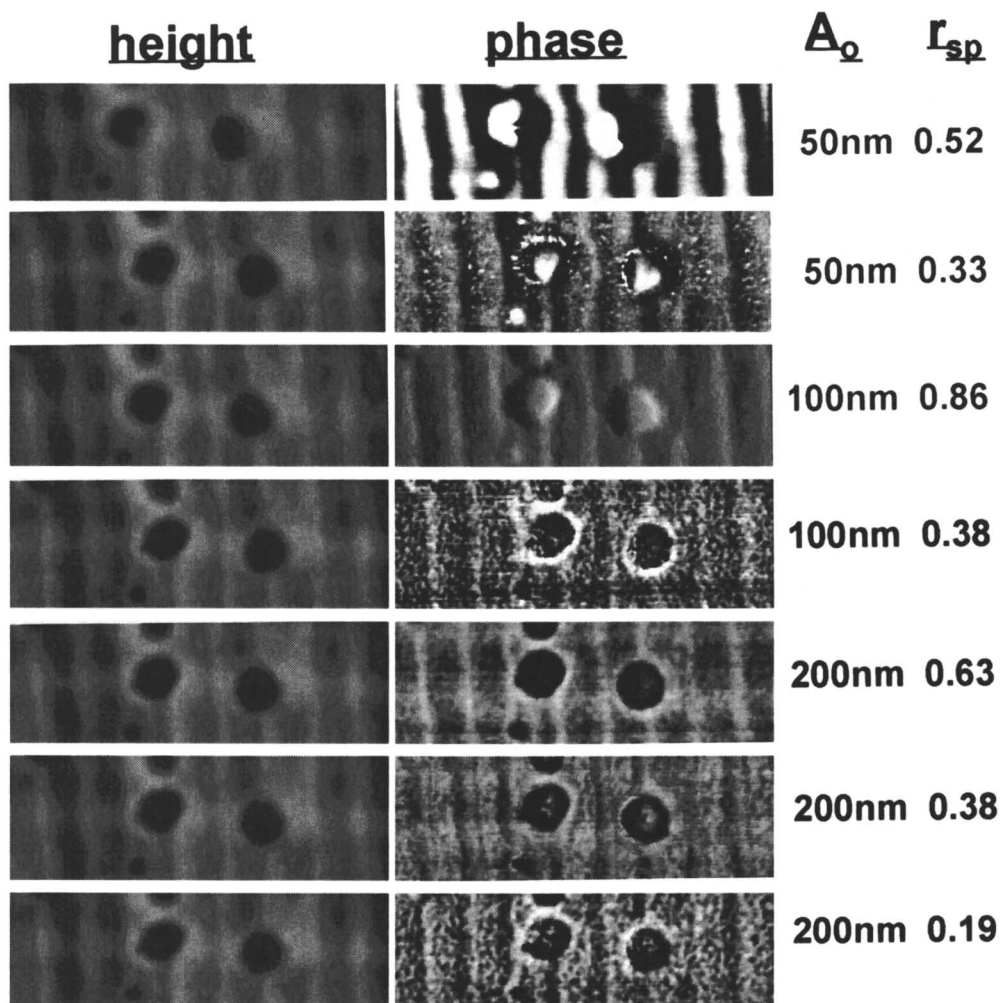


Figure 8. TappingMode AFM height and phase images of CET-GRC (5wt% rubber, 0.1 μm diameter) after cryo-polishing (images are 1 μm x 0.3 μm). Table at far right indicates tapping parameters used to generate each pair of images as described in the text.

Nanoindentation can be used to demonstrate the performance of abrasion resistant coatings such as Vitrinite (trademark of Metroline Surfaces, Inc.) Protective Coating on polycarbonate. This coating is a unique inorganic-organic hybrid material produced via plasma polymerization of siloxane and oxygen (18). A 500 μN load indent penetrates 350 nm into the surface and leaves a 165 nm impression in the uncoated polycarbonate (Figure 9, top). For the Vitrinite Protective Coating a dramatically different mechanical response is observed. At a load of 1000 μN , the Vitrinite Protective Coating surface is penetrated 250 nm and only a 2 nm impression remains after the load is removed (Figure 10, top). The ability to image is useful in identifying areas for indentation which are free of defects or, as in this case, for characterizing the surface morphology of the coating. Load vs. depth plots reveal the nature of the contacts. For the uncoated polycarbonate the deformation is elastic-plastic, while the Vitrinite coating is wholly elastic in its response. The analysis of the unloading curves can be obtained in the absence of any plastic deformation in the surface. The reduced modulus and hardness of the polycarbonate were 3.1 and 0.2 GPa, respectively. The reduced modulus and hardness of the Vitrinite coating were 7.2 and 1.5 GPa, respectively. The mechanical properties of polycarbonate using depth sensing nanoindentation agree with bulk values. However, these mechanical properties are obtained at a cost of surface sensitivity due to the large penetration depths. The unique mechanical properties of the Vitrinite coating (2X higher modulus and 7X higher hardness) compared with the polycarbonate substrate contribute to an effective abrasion resistant coating.

The quantitative basis on which the depth sensing nanoindentation measurements are made fills a current need in the cantilever beam bending methods. As previously discussed, beam bending methods must start with an understanding of cantilever beam stiffness. Beyond this the AFM based methods have yet to deal experimentally with the tip shape issue, i.e., researchers tend to rely on idealized tip shapes in order to estimate contact areas for extracting mechanical data (19,20). Our experience with the calibration of sharp Berkovich indenters is that the area calibration deviates the most from ideal shapes near the end of the tip, and the deviation becomes less the further up the tip one goes, consistent with published results (21). On the other hand, the depth sensing nanoindentation technique is also lacking in surface sensitivity for soft materials like polymers. The starting point for measurement is with the tip in contact with the surface at a load approaching 1 μN , almost 20-200X higher than conventional AFM using soft cantilevers. Thus, the tip could either damage or penetrate the surface of the material before the measurement is made. An approach that combines the best elements of both approaches is still needed.

Thermal Properties

The potential of scanning thermal microscopy (S_{Th}M) to provide new property information regarding polymer surfaces has been investigated over the past year with the Pollock group in the UK. In the S_{Th}M experiment a small Wollaston wire

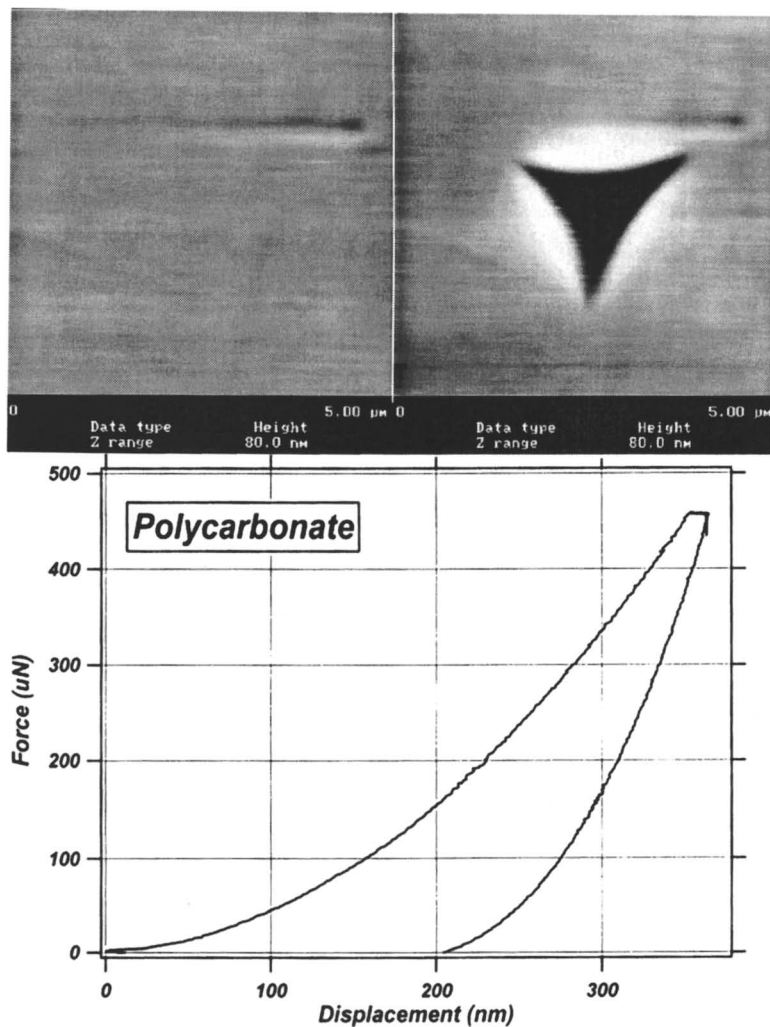


Figure 9. Nanoindentation of a commercial polycarbonate surface using a Berkovich diamond indenter (40 nm radius).

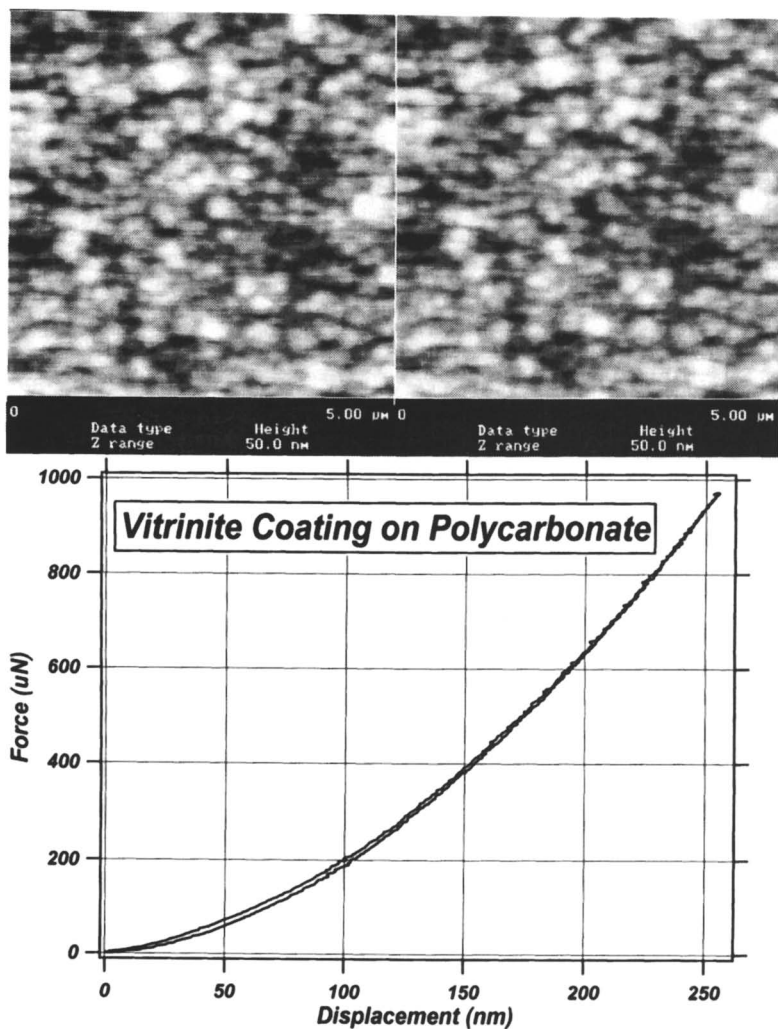


Figure 10. Nanoindentation of a commercial polycarbonate coated with a 2 μm thick Vitrinite (trademark of Metroline Surfaces, Inc.) Protective Coating surface using a Berkovich diamond indenter (40 nm radius).

is used as a contact mode AFM tip. The tip is used both as a heat source and a heat sensor. The heat to the tip can be modulated and the material response to modulated heating can be monitored during imaging via lock-in techniques. The frequency of the modulation will affect the penetration depth of the thermal wave (e.g., higher frequencies giving shallower sampling depths). We have taken advantage of this capability to study the processing of 5 μm photoBCB dielectric films to make vias to conductive copper substrates. Development of the photodefined material leaves polymer residues ("scum") in the via holes. This material is removed after hard thermal cure by brief exposure to an oxygen containing plasma. Perspective view TappingMode AFM images of 30 μm holes before and after the plasma "de-scum" treatment are shown (Figure 11). Clearly, the via hole is better defined following the plasma treatment.

Topview SThM images before "de-scum" are shown (Figure 12). The DC images (Figure 12, left) provide an indication of thermal conductivity where the brighter areas are more conductive. The contrast is generated by the current necessary to balance the temperature between the scanning and reference tip at a constant 40 $^{\circ}\text{C}$. Regions of higher thermal conductivity are clearly localized over the copper pads. The AC phase images (Figure 12, right) are the result of a ± 5 $^{\circ}\text{C}$ modulation on the 40 $^{\circ}\text{C}$ DC signal at 1 kHz (top) or 30 kHz (bottom) frequency. The frequency of the modulation is used to control the penetration depth of the evanescent thermal wave (22). The low frequency modulation (1 kHz) identifies the copper in the via while the high frequency modulation (30 kHz) identifies only the polymer residues. The penetration of the thermal wave is about 5X shallower for the 30 kHz case. Similar images for the via hole after "descum" were recorded (not shown). In this case the high frequency AC image shows little evidence of polymer residue.

Conclusions and Perspectives

Static deflection AFM can be used to probe adhesion of polymer surfaces in air using soft cantilevers ($k < 1$ N/m). The measurements can be made in air under ambient conditions in the absence of plastic deformation. The calibrated pull-off force can be used in conjunction with JKR theory and an estimation of tip radius from electron microscopy to provide a local estimate of surface energy. The accuracy of the measurement depends on surface contamination, surface roughness (relative to the curvature of the tip), and tip shape uniformity.

Static deflection AFM can be used to measure local mechanical properties of polymer surfaces, but only after consideration of the relative stiffness of the cantilever and the surface under study. Cantilevers with stiffness in excess of 50 N/m are necessary to indent materials with a bulk modulus in excess of 1 GPa (10^9 N/m²). Soft levers with a spring constant less than 1 N/m are sufficient to indent elastomers. Conventional staining techniques used in electron microscopy provide a viable way to harden unsaturated, hydrocarbon elastomers for imaging with soft cantilevers. Alternatively, low bulk modulus polymers ($E < 1$ MPa or 10^6 N/m²) require resonant imaging techniques such as Tapping Mode for direct imaging.

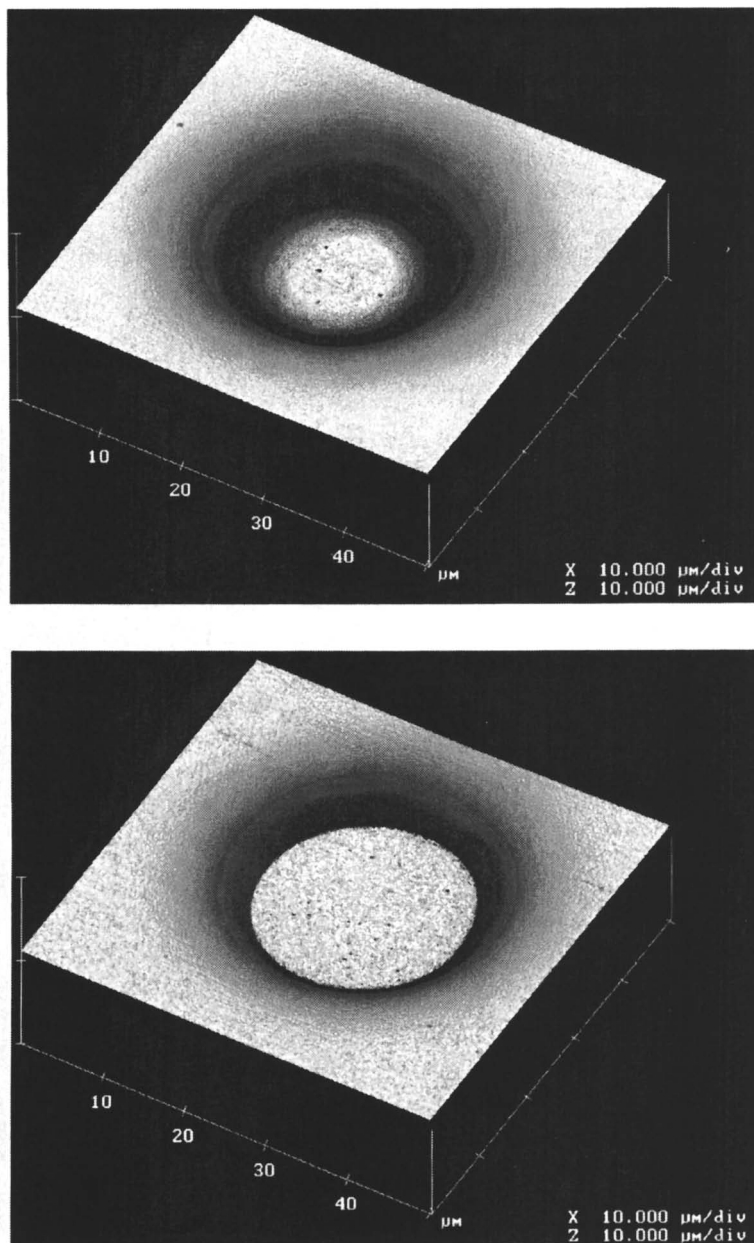
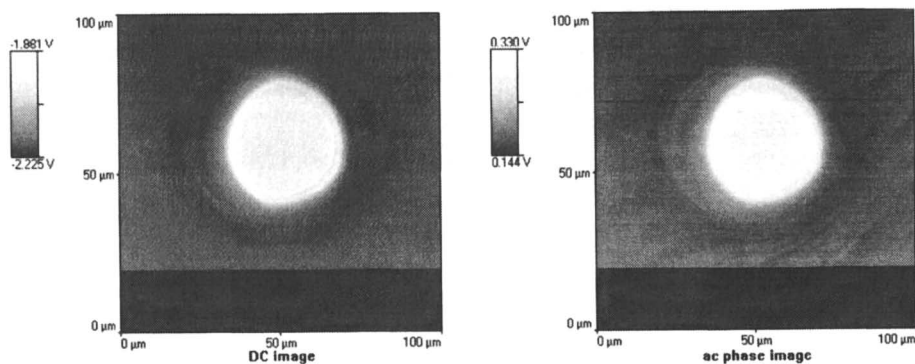


Figure 11. Tapping Mode AFM image of 35 μm via holes patterned in a photoBCB thin film over a copper substrate before plasma treatment to remove polymer residues ("scum", top) and after plasma treatment (bottom).

1 kHz modulation frequency



30 kHz modulation frequency

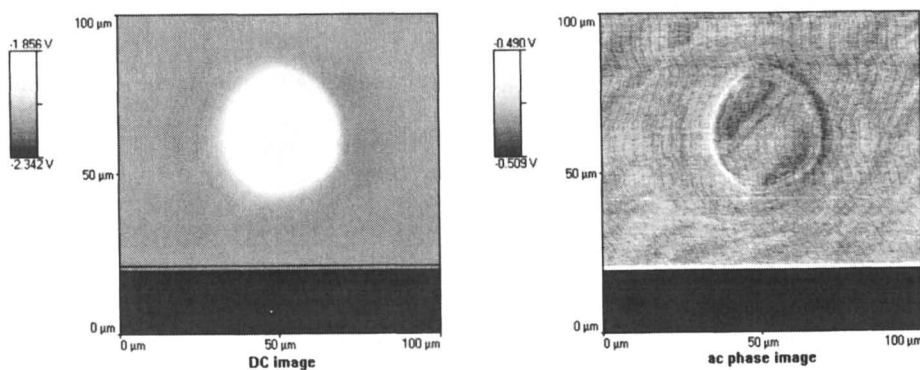


Figure 12. SThM images of 35 μm via holes patterned in a photoBCB thin film over a copper substrate before plasma treatment to remove polymer residues. DC thermal images (left) and AC phase images (right) are shown for frequencies of 1 kHz (top) and 30 kHz (bottom).

Further information regarding adhesion and deformation can be obtained using phase detection in conjunction with Tapping Mode on multiphase polymer surfaces.

Depth sensing nanoindentation is a viable alternative to AFM beam bending for mechanical property measurements on polymer surfaces. The technique provides quantitative results owing to careful calibration of the system compliance and tip area/shape. It suffers from the high minimum load (about 1 μN) necessary for imaging prior to indenting. A new approach, which combines the best elements of both approaches, is still needed.

Scanning thermal microscopy based on thermal diffusion represents an exciting new SPM tool to probe the thickness of thin polymer layers on conductive substrates.

Acknowledgments

The authors would like to thank The Dow Chemical Company for internal funding. We thank Manoj Chaudhury of Dow Corning Corporation for preparing the PDMS samples. We also thank Craig Garrison and Joan Marshall of Dow Chemical for the preparation of the rubber modified epoxy samples. We also acknowledge Sean Corcoran of Hysitron, Sergei Magonov of Digital Instruments, and Edgar Andrews of Queens College, London, for helpful insights. GFM would like to thank Deborah Meyers for careful reading of this manuscript.

Literature Cited

- (1) Meyers, G. F.; DeKoven, B. M.; Seitz, J. T. *Langmuir* **1992**, *9*, 2330.
- (2) DeKoven, B. M.; Meyers, G. F. American Vacuum Society 39th National Meeting, Chicago, IL, November 9-13, 1992.
- (3) Oliver, W. C.; Pharr, G. M. *J. Mater. Res.*, **1992**, *7*, 1564.
- (4) Hammiche, A.; Reading, M.; Pollock, H. M.; Song, M.; Hourston, D. J. *Rev. Sci. Instrum.* **1996**, *67*(12), 4268.
- (5) Sue, H.-J.; Bertram, J. L.; Garcia-Meitin, E. I.; Wilchester, J. W.; Walker, L. L. *Colloid & Polym. Sci.* **1994**, *272*(4), 456.
- (6) Moyer, E.S.; Becker, G. S.; Rutter Jr., E. W.; Radler, M.; Bremmer, J. N.; Bernius, M. T.; Castillo, D.; Strandjord, A. J.; Heistand, R. *Mater. Res. Soc. Symp. Proc.* **1994**, *323*, 267.
- (7) Woodland, D. D.; Unertl, W. N. *Wear* **1997**, *203-4*, 685.
- (8) Johnson, K. L.; Kendall, K.; Roberts, A.D. *Proc. R. Soc. London* **1971**, *A324*, 301.
- (9) Chaudhury, M. K.; Whitesides, G. M. *Langmuir* **1991**, *7*, 1013. (See equation 13).
- (10) Israelachvili, J. *Intermolecular & Surface Forces* (2nd Edition); Academic Press: San Diego, 1992.
- (11) Noy, A.; Vezenov, D. V.; Lieber, C. M. *Annu. Rev. Mater. Sci.* **1997**, *27*, 381.
- (12) Whangbo, M-H; Magonov, S. N.; Bengel, H. *Probe Microscopy*, **1997**, *1*, 23.

- (13) Radmacher, M.; Tillmann, R. W.; Fritz, M.; Gaub, H. E. *Science*, **1992**, *257*, 5078.
- (14) VanLandingham, M. R.; McKnight, S. H.; Palmese, G. R.; Elings, J. R.; Huang, X.; Bogetti, T. A.; Eduljee, R. F.; Gillespie Jr., J. W. *J. Adhesion*, **1997**, *64*, 31.
- (15) Sawyer, L. *Polymer Microscopy*; Chapman and Hall: New York, 1992, p. 93-109.
- (16) Cleveland, J. P.; Anczykowski, B.; Schmid, A. E.; Elings, V. B. *Appl. Phys. Lett.* **1998**, *72(20)*, 2613.
- (17) Hysitron, Inc., Edina, MN.
- (18) Dykhouse, R.J.; Dykhouse, J.R.; O'Connor, P.J.; Hu, T. *Proceedings of the 40th Technical Conference of the Society of Vacuum Coaters* **1997**, 40.
- (19) Weisenhorn, A. L.; Khorsandi, M.; Kasas, S.; Gotzos, V.; Butt, H.-J. *Nanotechnology* **1993**, *4*, 106.
- (20) Chzhik, S. A.; Huang, Z.; Gorbunov, V. V.; Myshkin N. K.; Tsukruk, V. V. *Langmuir* **1998**, *14(10)*, 2606.
- (21) Doerner, M. F.; Nix, W. D. *J Mater. Res.* **1986**, *1(4)*, 601.
- (22) Hammiche, A.; Pollock, H. M.; Hourston, D. J.; Reading, M.; Song, M. *J. Vac. Sci. Technol. B* **1996**, *14*, 1486.

Chapter 12

Temperature-Dependent Surface Properties of Thin Polystyrene Films Determined by Scanning Force Microscopy

Othmar Marti and Sabine Hild

Experimental Physics, University of Ulm, D-89069 Ulm, Germany

Variable temperature Scanning Force Microscopy of mixed polystyrene (2000 - 100000 g/mol) and poly(methylmethacrylate) (100000 g/mol) thin films was used to probe mechanical properties such as surface stiffness and pull-off forces. Adhesion data can be explained by the molecular properties of the constituents. The adhesion of Polystyrene samples was measured by force distance curves and using the Pulsed Force Mode. It can be shown that surface tension is not the dominant part of the tip-surface interaction, but the mechanical properties of the material will influence the measured adhesive force. Wetting of the tip by polymer molecules at higher temperatures due to increasing mobility is one possible model.

It is well known that the mechanical properties of polymers vary with temperature. Amorphous polymers like polymethylmetacrylate (PMMA) exhibit glass-like properties under mechanical load if their temperature below the glass transition temperature T_g . Above T_g they demonstrate a rubber-like behaviour. On a macroscopic scale these changes in mechanical behaviour can be used to determine phase transitions by thermal mechanical analysis. During the last few years the determination of elastic properties of surfaces or thin films by Scanning Force Microscopy (SFM) have become increasingly important. Dynamical techniques such as force modulation can especially be used to characterize heterogeneous surfaces [1]. Combining these dynamical techniques with a temperature variation allows to perform thermal analysis [2] or thermal mechanical analysis on a microscopic scale [3]. Although good qualitative characterization of heterogeneous surfaces on a

small scale is possible, the quantitative estimation of material constants, e.g. the Young's modulus, is difficult due to the adhesive properties of soft materials which influence their mechanical behavior on microscopic scale [4,5]. Therefore it is necessary to investigate also the adhesive properties of materials and their variation on a microscopic scale as a function of temperature.

Conventionally, adhesive properties of materials are characterized by their surface energy or by the surface tension γ . A wide range of investigations have been performed especially for polymers [6]. It is known that the surface tension in homologous series tends to increase with increasing molecular weight. For example, polystyrene (PS) with a molecular weight (MW) of 1600 g/mol [6] has a surface tension γ of 39.3 N/m [6], whereas PS with a MW of 44000 g/mol has a γ of 40.7 N/m [6]. The influence of temperature has been investigated as well. It has been found that the surface tension of polymers varies linearly with temperature [6]. The typical value for the temperature coefficient $C = -(d\gamma/dT)$ is 0.05 N/m, which means the surface tension decreases 0.05 N/m per 1 °C of increasing temperature [7]. For PS a decrease from $\gamma = 40.7$ N/m at 20 °C to $\gamma = 32.1$ N/m at 140 °C has been found [8]. It must be mentioned, however, that the temperature coefficient will change if the phase of the polymer changes [6]. C_g below the glass transition temperature T_g is related to C_r above T_g , at which point the polymer is in a rubbery state, by the following equation:

$$C_g = \frac{\alpha_g}{\alpha_r} C_r$$

with α the isobaric thermal expansion coefficient. Thus, the γ versus T plot will be continuous but with a change in slope at T_g . For PS the α_g is smaller than α_r by a factor of about 2.5 [9]. This should lead to a stronger decrease in surface tension above T_g than below.

On a microscopic scale adhesive properties of a material can be determined using a scanning force microscope (SFM) obtaining force vs. distance curves (FDC) and measuring the adhesive forces between the tip and the surface [10]. The adhesive force is correlated to the measured pull off force when the tip is retracted from the surface. To obtain a two-dimensional image of the adhesive force FDC's have to be taken line-by-line [11]. This method has some disadvantages: a) The scanning times are much longer than for normal contact mode measurements because no more than 100 FDCs can be acquired per second, higher frequencies will excite disturbing resonances. b) A high amount of data must be recorded; and c) The curves must be digitized since the minimum force value, i. e. the pull-off force, can not determined exactly. Due to these disadvantages a new technique called Pulsed Force Mode has been developed in which force curves can be acquired with frequencies ranging from 100 Hz up to several kHz. The amount of data is reduced by recording only specific points of the curve using sample&hold or peak picker cir-

cuits. A detailed description of this technique is given in [12]. It has been shown that analog recording of the pull off force will increase the accuracy by a factor of 50 % [13] compared to the conventional technique.

Although it is known that interactions between tip and surface are determined by the chemical nature of the interacting materials, the responsible molecular interactions are not clearly understood yet. The commonly used silicon or silicon nitride tips both have SiO_2 groups at the surface. Such tips show higher adhesive forces on hydrophilic surfaces than on hydrophobic ones [14,15]. Berger et al. [16] have shown that for two different low molecular weight molecules, the measured adhesive force can be correlated to the surface tension. The ratio of the two measured adhesive forces is equal to the ratio of the surface tension. Nevertheless, the correlation between surface tension and adhesive force for long-chain materials is not yet well understood. Due to the fact that PS and PMMA have different chemical compositions, they have different surface energies and should show different interactions with a chemically neutral SFM tip. However, it is also possible that the mechanical properties of the chains, i. e. the chain length and the chain mobility, can influence the interaction of the silicon tip with a polymeric surface, thus demonstrating that polymeric materials with similar surface tension values can exhibit different adhesive behavior in a SFM experiment.

Experimental

Sample. Three PS samples with different molecular weights and glass transition temperatures were investigated (Table 1). A blend of PMMA and PS was used to obtain adhesive force images. These polymers show phase separation due to their chemical difference. A PMMA with a molecular weight of 100000 g/mol and a glass transition temperature T_g of 109 °C was chosen as second component for the blend. T_g has been estimate by DSC measurements.

Table 1. Sample Data

	PS 2	PS 6	PS 100
Molecular weight	2.4 k	6.5 k	100 k
Glass transition T_g	55 °C	67 °C	104 °C

Polymer solutions of 10 mg polymer in 1 ml toluene were prepared. For the polymer blends, 75 % PMMA solution and 25 % PS with different molecular weights were mixed. The solutions were spin-coated on silicon substrates, freshly cleaned in a solution of 50 % H_2SO_4 and 50 % H_2O_2 . Using a speed of 2000 rpm for the spin coating process, homogeneous films with thickness of about 150 nm were produced.

For experimentation the samples (PS100, PS6, PS2) were mounted on the same support to guarantee the same thermal history. The samples were initially heated

from 25 °C to 70 °C in 5 °C increments, measured and then cooled to room temperature and measured once again to test the influence of an annealing effect. To ensure that the measured adhesive forces were not influenced by tip contamination, a bare silicon substrate, cleaned as described above, was also mounted on the same support as the polymeric samples. At the end of each polymer surface measurement, the pull-off force on the silicon samples was measured.

Heating device. The heating table consists of a small copper block with a diameter of 20 mm and thickness of 5 mm (Figure 1). A heating foil is used as a heater and a PT100 is used as a heat sensor [17-19]. The temperature is sensed with a PT100 resistor, mounted in a hole drilled in the side of the sample holder. This resistor is monitored by a temperature controller to regulate the input power to the heater foil. This set-up works within 20 °C and 150 °C. The temperature can be controlled to an accuracy of 0.1 °C during the measurement. Since the temperature sensor is between the sample and the heater, the sample temperature will in actuality be lower than the temperature indicated by the sensor.

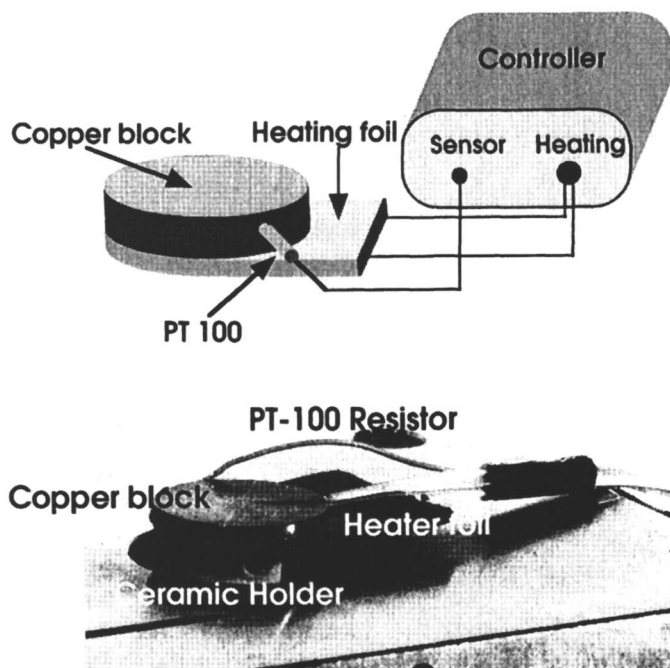


Figure 1. Heating device for combination with a scanning force microscope.

We estimated the temperature difference between a sample surface (silicon) and the PT100 by a calibration measurement, in which the temperature on top of the silicon substrate is measured by a second, calibrated temperature sensor. Each 5 °C

increment was separated by a 10 min wait period in order to allow for equilibration to a thermally balanced state at the surface of the silicon sample. After this wait period the sample temperature is 5 °C lower than the indicated temperature at the stage. This difference has been noted for the entire investigation temperature range between 20 °C and 150 °C. All measurements are subsequently corrected by this value.

The small size allows combination of the table with a scanning force microscope. It was found that sample temperatures up to 150 °C have negligible influence on the temperature of the microscope and its piezo. For the experiments we used a scanning force microscope of stand-alone type (Topometrix Explorer). Due to the large available z-range (10 μm) the thermal expansion during heating can be compensated by the z-piezo of the SFM. After the heating table is in thermal equilibrium, no thermal drift in the x-y direction can be detected. No thermal drift in the scanning or in the detection unit of our set-up was observed during heating of the table to 150°C, bored an examination of a drawn net print. For SFM measurements at variable temperature, non-coated silicon cantilevers have been used to avoid cantilever bending. The entire set-up is installed in a flow box in order to control humidity during measurements.

Scanning Force Microscopy. All measurements were performed under a constant humidity of 45 %. For recording the Force Curves, silicon cantilevers with a spring constant of 1.2 N/m were used. Curves were taken with frequency of 1 Hz. To get Force versus Distance Curves (FDC)'s from the measured Force versus Piezo Displacement Curves, these curves were transformed by a standard calibration procedure. Reduced cantilever stiffness is taken into account when calculating the FDCs of the thin polymer films at different temperatures. Pull-off forces estimated from 10 curves have a standard deviation of about 3 nN.

It has been shown that the cantilever sensitivity is influenced by temperature variations, and these changes have been taken into account for the calibration measurements in that all FDC's were obtained from measurements on a silicon substrate.

The adhesive force images were performed by Pulsed Force Mode (PFM) using a modulation frequency of 1 kHz and an amplitude of 400 nm. Uncoated silicon cantilevers with 2.8 N/m were used as force sensors. The force values measured by PFM are recorded in volts. To convert this value into force values the following equation was used:

$$F_{adh}[nN] = S[V] \cdot \frac{1}{A} \cdot C \left[\frac{nA}{V} \right] \cdot \frac{1}{s} \left[\frac{nm}{nA} \right] \cdot f \left[\frac{nN}{nm} \right]$$

where F_{adh} is the measured pull-off force, S is the detected force in volts, A is an amplifying factor, which can be adjusted in the PFM-box, C = 6.57 is a conversion factor given by the SFM system, s* is the sensitivity of the detection unit,

which must be estimated from FDC, and f is the spring constant of the cantilever. To estimate force values from the adhesive force images the histogram technique can be used. The accuracy of the determined force values is ± 5 nN.

Results and Discussion

Calibration. To investigate the influence of thermal treatment in cantilever properties, FDCs at different temperatures on a silicon substrate were recorded. No change in the characteristic shape of the curve could be observed, but a reduction in the slope occurred. This reduction is equal to a 10% decrease of cantilever stiffness from heating to 67 °C. The adhesive forces show a decrease in the pull-off force with increasing temperature to approximately 50 °C (Figure 2). At higher temperatures the measured forces are constant. This behaviour can be explained by the removal of the water layer at higher temperatures, which in turn reduces the capillary forces. It is obvious that the part of the water layer most responsible for capillary forces is removed at about 50 °C. At higher temperatures any change in adhesive force caused by capillary forces is negligible. Similar adhesive and mechanical properties are observed upon cooling to room temperature.

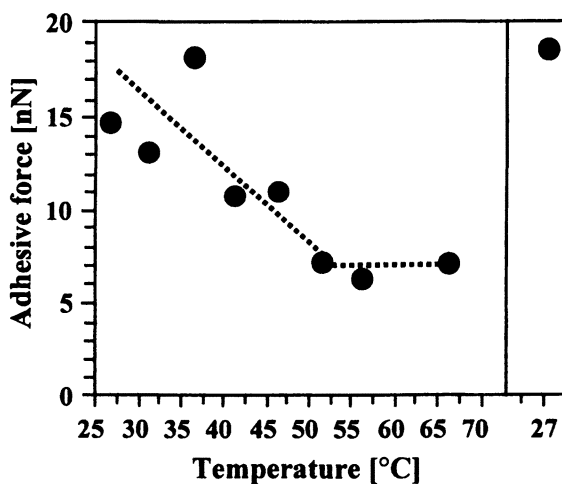


Figure 2. Temperature induced changes in adhesive force of a bare silicon substrate. The adhesive forces decrease because the majority of the water layer is evaporated at higher temperatures.

Force versus Distance Curves. Figure 3 shows representative curves for different polymer films at room temperature (27 °C) and at 67 °C. Changes in penetration depth and in the slope of the retraction segment of these curves are summarized in Table 2. The slope of the curves reflect the elastic properties of the film, where a larger slope is correlated to a higher local stiffness. As expected, the local stiffness

of the PS100 does not change within the experimental precision because it remains always in the glassy state.

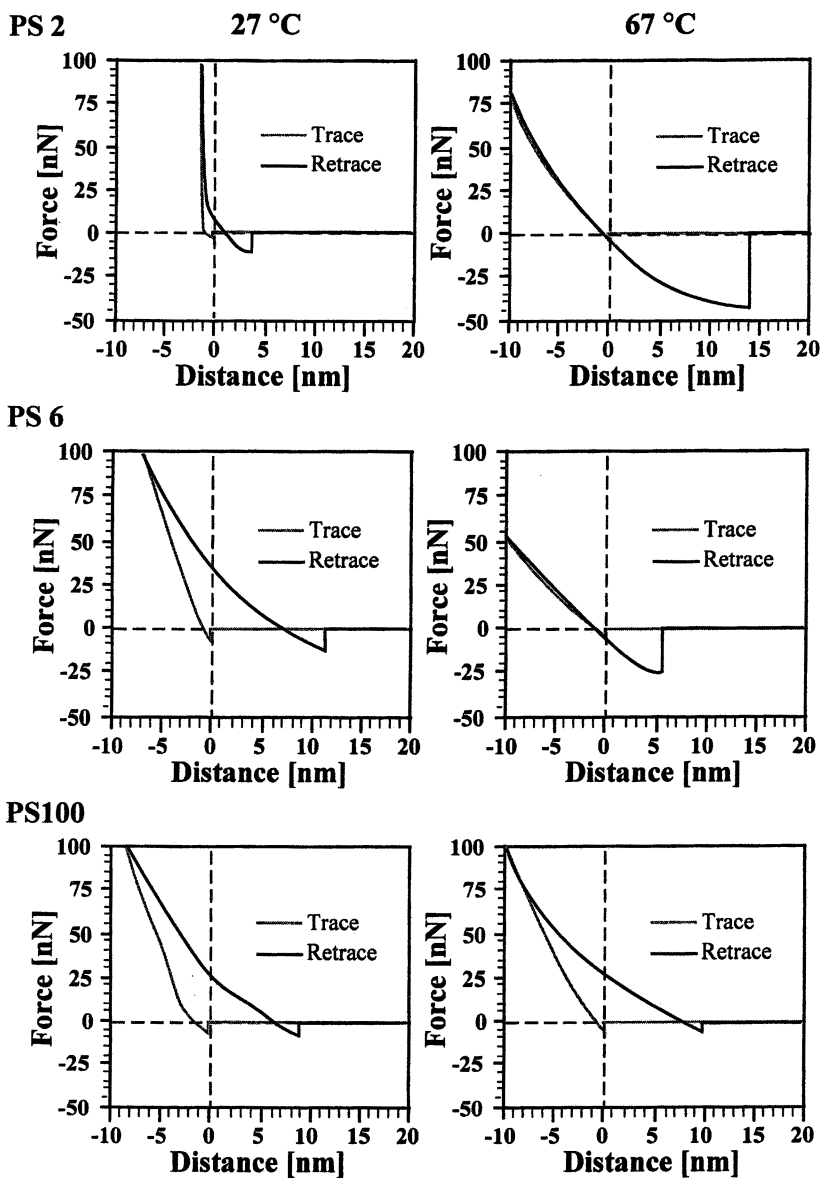


Figure 3. Force vs. Distance Curves of PS films with various molecular weights taken at different temperature show variation in mechanical and adhesive properties.

At room temperature the largest local stiffness is found for the low molecular-weight sample PS2. Heating the samples to 67 °C results in a decrease of the force curve slopes for PS6 and PS2, thus indicating a softening of the polymeric material when it is heated above the glass transition temperature T_g . Additionally, this behaviour shows that the high local stiffness detected at room temperature can not be caused by substrate stiffness. If the substrate properties dominates the measured stiffness, no softening of the polymeric layer at higher temperatures would occur. To present, no conclusive explanation of increasing local stiffness with decreasing molecular weight can be given, although it is possible that low molecular weight polymers may be arranged in a more ordered state than their high molecular weight analogues.

Table 2. Mechanical Data Obtained from Force Curve Analysis

	PS 2	PS 6	PS 100
Penetration depth at 20 nN load			
27 °C	2.4 nm	2.0 nm	3.4 nm
67 °C	3.4 nm	3.5 nm	3.2 nm
Slope [nN/nm]			
27 °C	-20	-15	-11
67 °C	-9	-8	-10

Comparing trace and retrace curves, an elastic recovery of the PS2 film can be seen at all times, whereas for PS6 and PS100 irreversible deformation is observed at room temperature. If PS6 is heated above the glass transition then its behaviour also becomes elastic. This effect can be explained by the increasing mobility of the chains.

For all samples the penetration depth is determined at 27 °C and 67 °C at a given load of 20 nN. PS2 and PS6 at 27 °C exhibited similar values of about 2.5 nm. For the PS100 sample, the tip indentation is 3.5 nm. Assuming a spherical tip with a radius of 20 nm, the difference in penetration depth is equal to a difference in contact area of about 30 %. Comparable penetration depths of 3 to 3.5 nm have been found for all samples upon heating to 67 °C. The change in contact radius can influence the measured adhesive force and must be taken into account for the following discussion.

The adhesive properties of the polymeric films have been characterized by analyzing the pull-off force (Table 3). At 27 °C an increase of the adhesive force with decreasing molecular weight has been found, although surface tension data would imply a decrease in adhesive force with decreasing molecular weight.

Table 3. Adhesion Forces Obtained from Force Curve Analysis

	PS 2	PS 6	PS 100
Pull off force [nN]			
27 °C	12	11	6
67 °C	50	26	5

This demonstrates that surface tension is not the dominant part of the tip-surface interaction. A variation in adhesive force is also not due to a variation of the contact radius. This is shown by the fact that the contact radius estimated from the penetration depth of PS100 is larger than that of PS2, which would indicate that the adhesive forces should be larger. At 67 °C the contact radius is equal for all samples and even then there is a large difference between the measured adhesive forces. The adhesive forces of PS2 and PS6 increase with increasing temperature, whereas for PS100 no change in adhesive force was found.

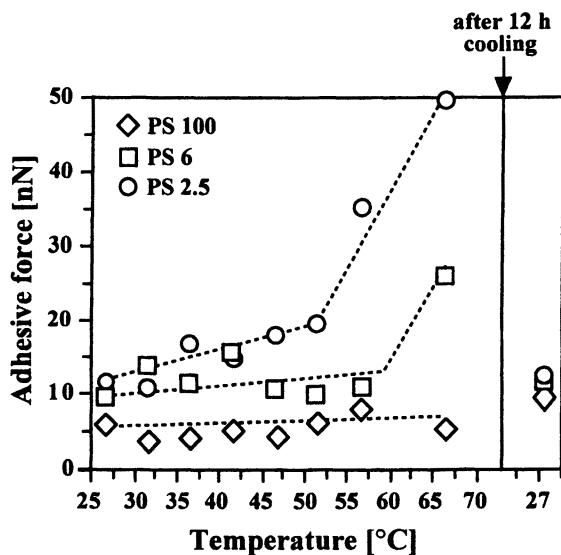


Figure 4. Variations of the adhesive force of thin PS films during heating to 67 °C. Whereas the high molecular weight sample (PS100) shows constant adhesive forces, the lower molecular weight samples (PS2 and PS6) exhibit an increase in adhesive force beyond the glass transition temperature.

One possible explanation for this behaviour is that the number of free chain ends, available to interact with the tip are responsible for the measured adhesive force. The small PS chain ends are not entangled and therefore more mobile, allowing for better adherence to the tip. This results in higher adhesive force for the

PS2 sample at room temperature. At higher temperatures the mobility of the chains is increment, and thus the possibility of interacting with the tip is higher.

The temperature-induced changes of the pull-off force over the entire experimental temperature range are shown in Figure 4. Adhesive forces similar to those found at the outset of the measurement samples can be detected with subsequent cooling of the samples. Due to this, an influence from film annealing can be neglected. For PS100 below its glass transition temperature, no specific variation in the pull-off force with increasing temperature can be observed. This also indicates that an influence of the water layer, which has been found for the bare silicon substrate, and the resulting capillary forces can be neglected for the investigated system. In contrast to PS100, PS6 and PS2 show a strong dependence of the adhesive force with increasing temperature: Below T_g an increase in temperature causes only a small linear increase of adhesive force. When T_g is reached, the adhesive force begins to increase more rapidly with increasing temperature. The rate of adhesive force increase of the PS2 is larger than that of the PS6. A similar linear behavior has been found for the surface tension [6], but a decrease in adhesive force for all PS samples would be expected from the literature.

Hence, increased in mobility of the chains may be a possible explanation. Above the glass transition temperature the polymer chains form a viscous liquid. Because of this, molecules can wet the tip in a manner similar to the capillary forces in the water layer, thus causing the pull-off force to increase. Below, T_g they are more or less pinned to their reptation channel. Our data confirms this model of the polymer mobility.

Adhesive force images. For the comparison of two polymers with different T_g , a blend of PS and PMMA is used because phase separation occurs. First, a phase separated film of 75 % PMMA and 25 % PS2 was investigated at increasing temperatures using the Pulsed Force Mode. In the topography image taken at room temperature (25 °C) (Figure 5) PS areas marked by circles appear to be elevated. In the adhesive force image a contrast between the PS and PMMA areas can be seen. In the hydrophobic PS areas lower adhesive forces have been detected than in the surrounding hydrophilic PMMA region. The adhesive force histograms (AFH) from this image shows two pronounced peaks with one maximum at 70 nN and the other at 87 nN. The peak at lower adhesive force corresponds to the PS areas and the second to the PMMA matrix. The adhesive behavior can be explained by the differences in chemical composition: the interaction between the SiO_2 groups of the tip is stronger with the polar PMMA than with non-polar PS (Figure 5, lighter areas).

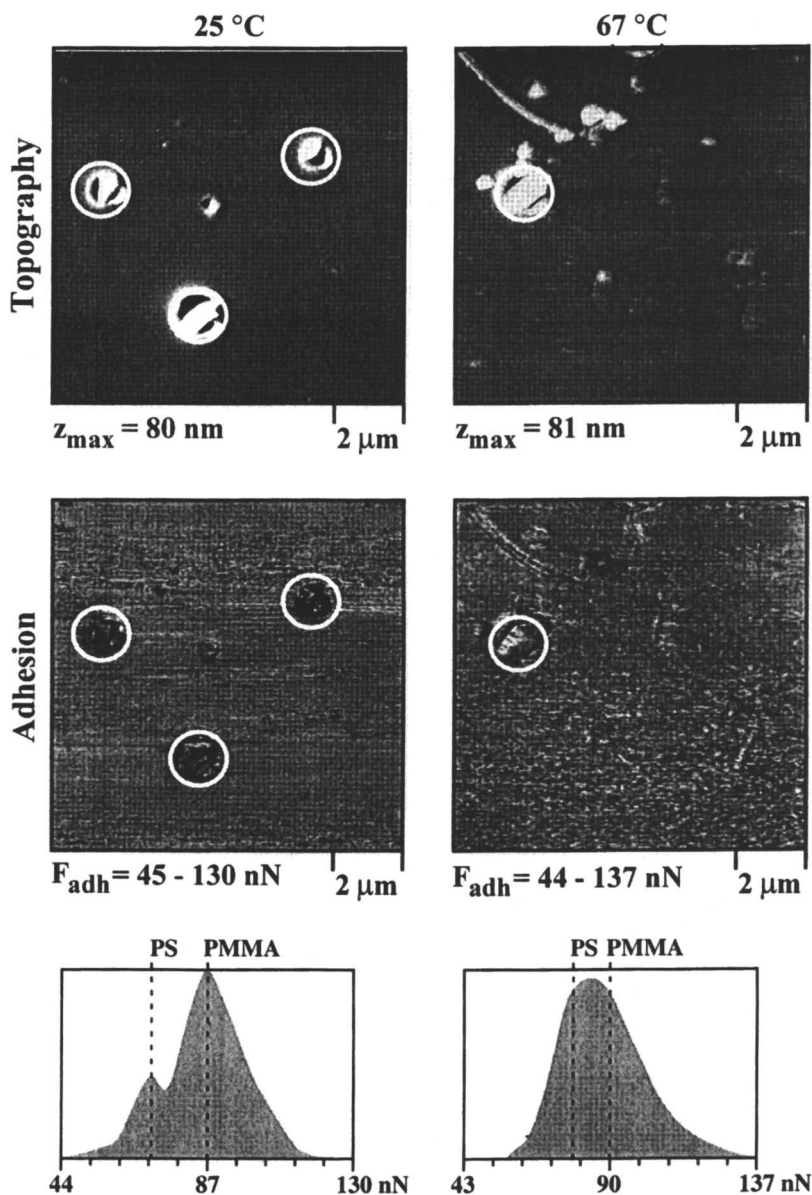


Figure 5. Scanning force images of a blend of PMMA and PS2 taken at room temperature and 67 °C. At 27 °C the PS2 areas (marked by circles) have lower adhesive force (darker color) than the surrounding PMMA. Heating causes significant change in the adhesive force images. The adhesive force histogram (AFH) taken from the adhesive force image at 27 °C shows two pronounced peaks. In the AFH taken at 67 °C only one peak can be observed.

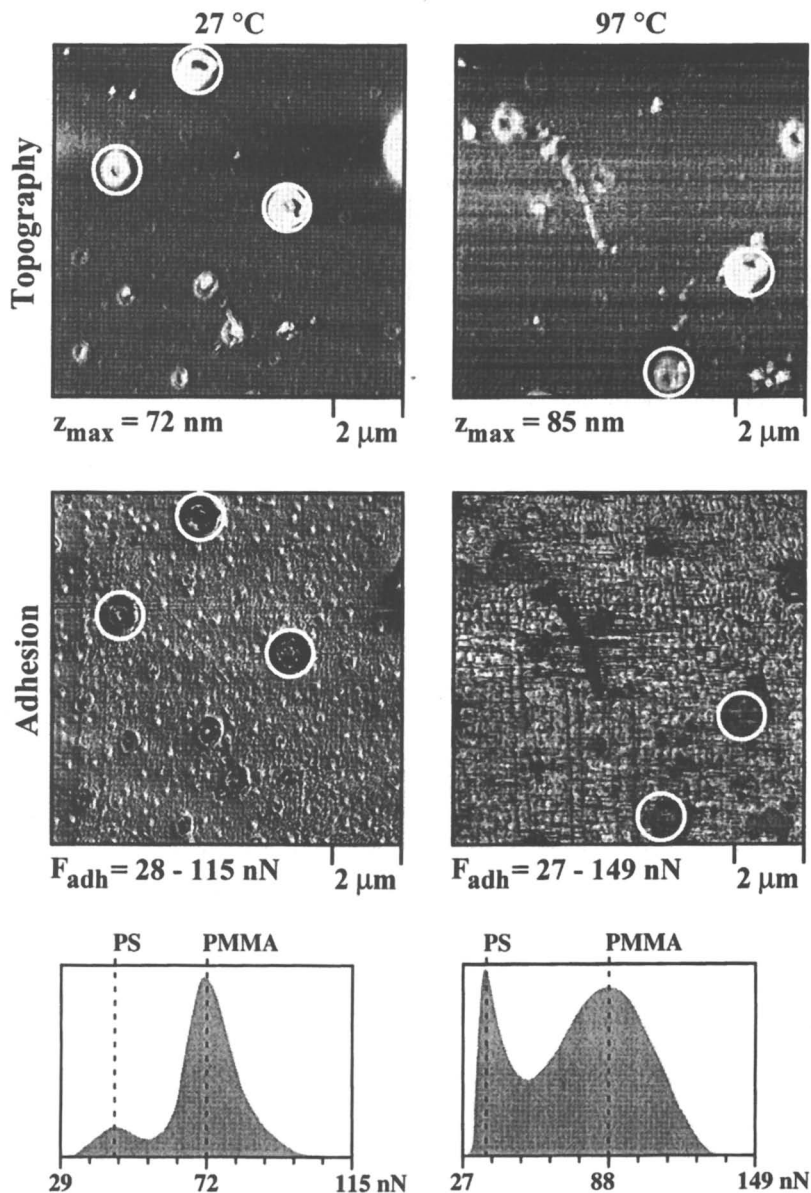


Figure 6. Scanning force images of a blend of 75 % PMMA and 25 % PS100 at room temperature and 97 °C. Adhesive force histograms taken from adhesive force images show two pronounced peaks at 27 °C and 97 °C, which indicates no change in adhesive forces during heating. The PS100 areas (marked by circles) have lower adhesives force (darker) than the surrounding PMMA. Additional smaller droplets with a diameter of about 300 nm are visible.

In the topography image, no significant change can be observed after heating the sample to 67 °C, which is 12 °C above the glass transition temperature of PS2. As expected from the FDC measurements, the contrast in the adhesive force images decreases (Figure 5) due to increasing of adhesive force of PS2 when it is heated above T_g . The PS2 areas can only be detected by the sudden change in adhesive force [20] at the edge of the droplets. At 67 °C only one broad peak in the AFH can be observed with a maximum at 85 nN.

In Figure 6 phase-separated film of 75 % PMMA and 25 % PS100 at room temperature and at 97 °C are shown. The (raised) PS areas are marked by circles. Again due to chemical differences the adhesive force of these areas is lower than the adhesive force of the surrounding PMMA. Up to 97 °C there is no change in adhesive contrast in the marked areas. In the AFH two peaks are observed, which do not change significantly with increasing temperature. The peak of a maximum at 80 nN correspond to the determined adhesive force for PMMA. For PS100 we find an adhesive force of about 50 nN, which again is smaller than the value observed for PS2.

Also of note in the adhesive force images, small droplets with a diameter of about 300 nm can be seen where the adhesive force appears to be different. This difference in adhesive force is due to a topography effect [20]. Heating the sample up to 97 °C, the adhesive force of the droplet structure decreases. A possible explanation for this may be that in these areas small droplets of PS are covered by PMMA. The spin-coated films are not in thermodynamical equilibrium but in a frozen state. Due to the evaporation of the solvent, it is also possible that PMMA remains at the surface because it is less soluble in toluene than PS. Heating the sample close to its glass transition temperature increases the mobility of the chains and the PS droplet becomes visible by a second-phase separation step which is thermally induced. In this case the sample is in thermodynamic equilibrium.

Conclusions

In this work we have shown that quantitative measurements of adhesive forces are possible using FDC. Thin films of PS with different molecular weight are investigated at various temperatures. For all temperatures a decrease in adhesive force with increasing molecular weight has been found. When the polymeric material is heated above its glass transition temperature, a dramatic increase in adhesive force is observed. This behaviour can not be explained by variations in surface tension. We were able to measure not only the pull off force but also the penetration depth and the slope of the load curve. It has been found that a variation in contact radius can be neglected for further interpretations. The decrease in slope of the load curve at higher temperatures demonstrates also that the mechanical properties of a polymer will influence the detected adhesive force. Wetting of the tip by polymer molecules at higher temperatures is one possible explanation for this observation.

While the FDC has been mainly used for local probing of the surface adhesive force, images have been obtained using the PFM. This enables also the determina-

tion of temperature-induced changes from adhesive force contrasts. At room temperature, a chemical contrast in the polymer blend consisting of PS and PMMA can be observed, which demonstrates the material sensitivity of the method. Above T_g the adhesion force contrast of PS decreases with increasing temperature. This observations confirms the model we proposed from FDC measurements.

Since the absolute contact radius of commercial SFM cantilevers is rather ill-defined, the data is reliable as long as one discusses relations. Absolute quantities would require well-defined wear-resistant tips, for instance these made of diamond. The influence of the tip material can be neglected in these experiments, since silicon or silicon nitride has a much higher Young's modulus than the polymer samples. For quantitative measurements at different temperatures the influence of temperature induced changes in detection sensitivity must be mentioned.

For most quantities measured by scanning probe microscopes a comparison of bulk material properties and SFM-measured properties is lacking. We believe that the Pulsed Force Mode measurement technique together with an accurate characterization and control of the tip size and surface composition will enable a correlation. The technique also lends itself to comparisons with measurements of surface tension. The variation in contact time may lead to new insights in the dynamics of nanoscale wetting.

Acknowledgments

The authors gratefully acknowledge many invaluable discussions with S. Minko, M. Pietralla, W. Wilke, G. Krausch. We would like to thank L. Weiss, C. Mayer and G. Volswinkler for much experimental help, as well as H. Waschipky, U. Krotil, Th. Stifter and R. Brunner for discussions. This work is funded by the German Science Foundation through the grant SFB 239, project C10. One of us (S. Hild) gratefully acknowledges the Margarete-von-Wrangell foundation for the fellowship from Land Baden-Württemberg.

References

1. M. Radmacher, R. W. Tillmann, H. E. Gaub, *Biophys. J.*, **1993**, *64*, 735
2. Hammiche, A.; Hourston, D.J.; Pollock, H.M.; Reading, M.; Song, M., *Journal of Vacuum Science & Technology B (Microelectronics and Nanometer Structures)*, **1996**, *14*, 1486
3. Oulevey, F.; Gremaud, G.; Sémoroz, A.; Kulik, A.; Burnham, N. A.; Dupas, E., Gourdaon, *Rev. Sci. Instrum.*, **1998**, *69*, 2085
4. Johnson, K. L.; Kendall, K.; Roberts, A. D. *Proc. R. Soc. London*, **1971**, *A 324*, 301
5. Derjaguin, B. V.; Muller, V. M., Toporov, Y. P., *Colloid Interface Sci.*, **1978**, *53*, 378
6. Wu, S. *Polymer Interface and Adhesion*, Marcel Dekker, Inc., **1982**, 88
7. Wu, S., *Polymer blends, Vol. 1*, D. R. Paul, S. Newman, ed., Academic Press, New York, **1978**, 243
8. Wu, S., *J. Macromol. Sci.*, **1974**, *C10*, 1
9. Müller, J., Pietralla, M., private communications

10. Mizes, H. A.; Loh, K.-G.; Miller, R. J. D.; Ahuja, S. K.; Grabowski, E. F. *Appl. Phys. Lett.*, **1991**, *59*, 2901
11. van der Werf, K. O.; Putman, C. A.; de Grooth, B. G.; Greve, *J. Appl. Phys. Letter*, **1994**, *65*, 1195
12. Rosa-Zeiser, A.; Weilandt, E.; Hild, S.; Marti, O., *Meas. Sci. Technol.* **1997**, *8*, 1333
13. Förstner, J. , private communications
14. Frisbie, C. D.; Rosznay, L. F.; Noy, A.; Wrighton, M. S.; Lieber, C. M., *Science*, **1994**, *265*, 2071
15. Akari, S.; Horn, D.; H. Keller, H., *Adv. Materials*, **1995**, *7*, 594
16. C. E. H. Berger, K. O. van der Werf, R. P. H. Kooyman, B. G. de Grooth, J. Greve, *Langmuir*, **1995**, *11*, 4188,
17. O. Marti, S. Hild, J. Staud, A. Rosa, and B. Zink, in *Micro/Nanotribology and its applications*, edited by B. Bhushan, Kluwer Scientific Publishers, Dordrecht, **1996**, Vol. E:330, 455-456.
18. W. J. Kulnis, Jr. and W. N. Unertl, A thermal stage for nanoscale structure studies with the scanning force microscope ., Conference "Determining Nanoscale Physical Properties of Materials by Microscopy and Spectroscopy.", Boston, United States (1994).
19. I. Musevic, G. Slak, and R. Blinc, *Rev. Sci. Instrum.*, **1996**, *67*, 2554-2556
20. T. Stifter, E. Weilandt, S. Hild, and O. Marti, "Influence of the topography on adhesion measured by SFM," *Appl. Phys.*, **1998**, *A 66*, 597-605

Chapter 13

Viscoelastic Measurements in Thin Polystyrene Melts as Derived from Scanning Force Microscopy-Induced Nanoflow Patterns

Ronald H. Schmidt¹, Wayne L. Gladfelter¹, and Greg Haugstad²

¹ Department of Chemistry and ² Center for Interfacial Engineering,
University of Minnesota, Minneapolis, MN 55455

The response of a thin-film polystyrene melt to a raster-scanned SFM tip was investigated. At high temperatures the scanning process induced intricate pattern formation whose quantitative characteristics were compared as a function of tip trajectory, temperature, and scan rate. Analysis of the images revealed that the features are strongly correlated with the geometry of the raster scan pattern. The dependence of the patterns on temperature and scan rate was consistent with time-temperature superposition as described by the Williams-Landel-Ferry (WLF) equation. WLF analysis implies an increased glass transition temperature derived from elevated pressure beneath the tip. The latter provides an estimate of the radius of the affected film region near the tip.

Tremendous interest has arisen in recent years regarding the issues of chain mobility and glass transition at polymer surfaces (1-4). Keddie *et al* used ellipsometric measurements of thermal expansivity to study T_g of polystyrene on silicon as a function of film thickness (1). The observed T_g asymptotically approached the bulk value of 100°C as thickness was increased, but for thinner films (≤ 10 's of nm), T_g was significantly depressed. Clearly, such effects are of critical importance in the application of ultrathin polymer films as lubricants and protective coatings in magnetic data storage devices and micromechanical systems (5). Until recently, however, direct mechanical measurements of polymer behavior at the nanoscopic scale (which is necessary for mechanical analysis of ultrathin films) and at elevated temperatures has not been possible.

SFM has proven to be a powerful tool for measuring time-dependent mechanical properties of polymer films at ambient temperatures. Because piezoelectric scanners are incompatible with substantial temperature elevation, however, the SFM community has only begun to examine the role of temperature in

material response. Fundamentally, the response of “soft” materials to external forces is often dominated by entropic (i.e., temperature-dependent) effects (6,7). The approach to thermodynamic equilibrium for polymeric systems is typically slow, so that the response to mechanical perturbation is a function of both temperature and rate (i.e., is viscoelastic). Rigorous studies of thin-film polymer nanotribology therefore must include methodologies to quantify the interrelated roles of these two parameters.

Methodology

In order to access sample temperatures significantly different from ambient conditions without affecting the performance of the scanner, the SFM's piezo transducer and accompanying electronics must remain completely isolated from the sample. The SFM used for this study was designed and constructed by Molecular Imaging to meet this stringent requirement, thereby allowing us to resistively heat the sample. An aluminum-coated silicon cantilever, manufactured by Nanotechnology-MDT, with a spring constant of 3.8 N/m and a tip radius of <10 nm was used for this study. The sample was prepared by spin coating a 0.5% solution of polystyrene ((Aldrich; $M_w = 110,000$; $M_w/M_n = 1.1$) in toluene onto a cleaned silicon (100) substrate (with native oxide present) at 2000 rpm, resulting in a 20 nm film. A feedback loop was used during imaging to adjust the cantilever height in order to maintain a constant cantilever deflection— and hence a constant load— when sample tilt or variations in the surface topography were encountered.

Description of Scan-Induced Patterning

Several researchers have reported that “bundles” commonly form in a variety of thin polymer films when they are raster scanned by a sharp, slow-moving tip (8-13). All previously reported studies were performed at room temperature, and the bundles were observed to align perpendicular to the tip trajectory. Elkaakour et al found that the velocity dependence of the repeat distance of the scan-induced features correlates with the frequency-dependent storage modulus (11).

The width and height of scan-induced bundles were observed to be strongly dependent upon the temperature and scan velocity, yet the orientation of the features remained constant over a wide temperature range (20°C to approximately 140°C). At temperatures above 140°C the pattern of the scan-induced features changed dramatically. Figure 1a is a topographical image acquired at 151°C while raster scanning from top-to-bottom, and 1b is the subsequent scan taken while rastering from bottom-to-top. Brighter features correspond to higher surface elevations. The bundles are widest at the center of the image and tend to orient themselves vertically (i.e., perpendicular to the tip trajectory); towards the left and right edges of the scan area, these wide features branch off into narrower ones which orient themselves at an angle less than 90° relative to the tip trajectory. Continued scanning over the same region results in cumulative damage to the film, resulting in the buildup of polymer at the center of the scanned region and bare silicon at the left and right edges (Figures

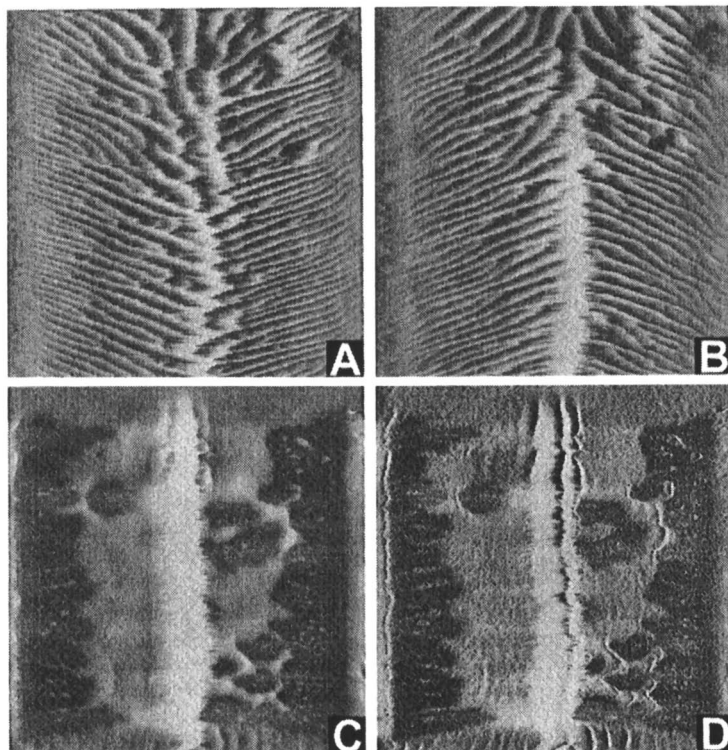


Figure 1 (A). 10 μm SFM image of topography acquired at 151 $^{\circ}\text{C}$ while scanning from top-to-bottom. Lighter shades represent higher topography, and the height difference between the lightest and darkest features is 20 nm. (B) was acquired during the following scan, during which the tip rastered from bottom-to-top. Note that the topography at the center of the scanned region is higher compared to the previous image. (C) and (D) are 12.5 μm topography and friction images, respectively, of the 22nd consecutive scan of the same region. The film has ruptured, and most of the polymer has accumulated at the center of the scanned region. The lowest topographical features exhibit reduced friction (darker colors) and are thought to correspond to the bare silicon substrate.

1c and d). Figure 1d shows contrast in the tip-sample frictional force between the polymer melt (high friction) and the bare substrate (low friction).

Varying the Raster Geometry. To understand the morphologies seen in Figure 1, we examined the effect that variations in tip trajectory have on the observed morphologies. The SFM tip was raster scanned in a triangular wave pattern over the sample surface as depicted on the left side of Figure 2; the departure from strictly horizontal scans is exaggerated in Figure 2 for clarity. The angle of the tip trajectory relative to the X-axis (i.e., ϕ in the left of Figure 2) was varied by changing the number of scan lines executed during the acquisition of an image from 128 to 512 fast-scan cycles per image. The topography images in the right side of Figure 2 display the scan-induced patterns corresponding to the three different scan angles. We measured the angles that the bundles form with the X-axis at the left (θ_L) and right (θ_R) edges of each image. The values of θ_L and θ_R shown in Figure 2 are averages determined from ten different bundles in each image. The angles ϕ and θ differ by two orders of magnitude, yet they are directly proportional over the range examined.

Deriving a Mathematical Description of Bundle Orientation. Surrounding each scan line is a region of finite width over which the polymer film is perturbed by shear stresses (light gray regions in Figure 2Left). Because of slow relaxations, the effects of this tip-induced perturbation are cumulative for successive scans. Note that whenever an overlap with the previous scan occurs (as represented by the dark gray regions in the left of Figure 2), the tip is moving towards the center of the scan area (i.e., towards the vertical line represented by $X = 5 \mu\text{m}$). The result is a net movement of polymer towards the center of the raster-scanned region. The overlap with the previous scan is greatest near the *edges* of the imaged region, increasing the efficiency with which polymer is swept inward. This accounts for the more nearly horizontal orientation of polymer bundles near the edges of the scanned area.

The location of a particular point on a bundle is defined with the coordinates (X,Y). For brevity, we only discuss the left half of the scanned region. Results presented in Figure 2 indicate that the slope of a bundle with respect to the fast-scan axis at some value of X is

$$\left. \frac{dY}{dX} \right|_{X=0} = a_1 \Delta Y_{t,t} \quad (1)$$

where a_1 is a constant and $\Delta Y_{t,t}$ is the vertical distance between successive “trace” (left-to-right) scan lines. Clearly $\frac{dY}{dX}$ is not constant across the entire X axis. A more general expression is:

$$\frac{dY}{dX} = a_1 \Delta Y_{t,t} + f(X), \text{ with } f(0) = 0 \quad (2)$$

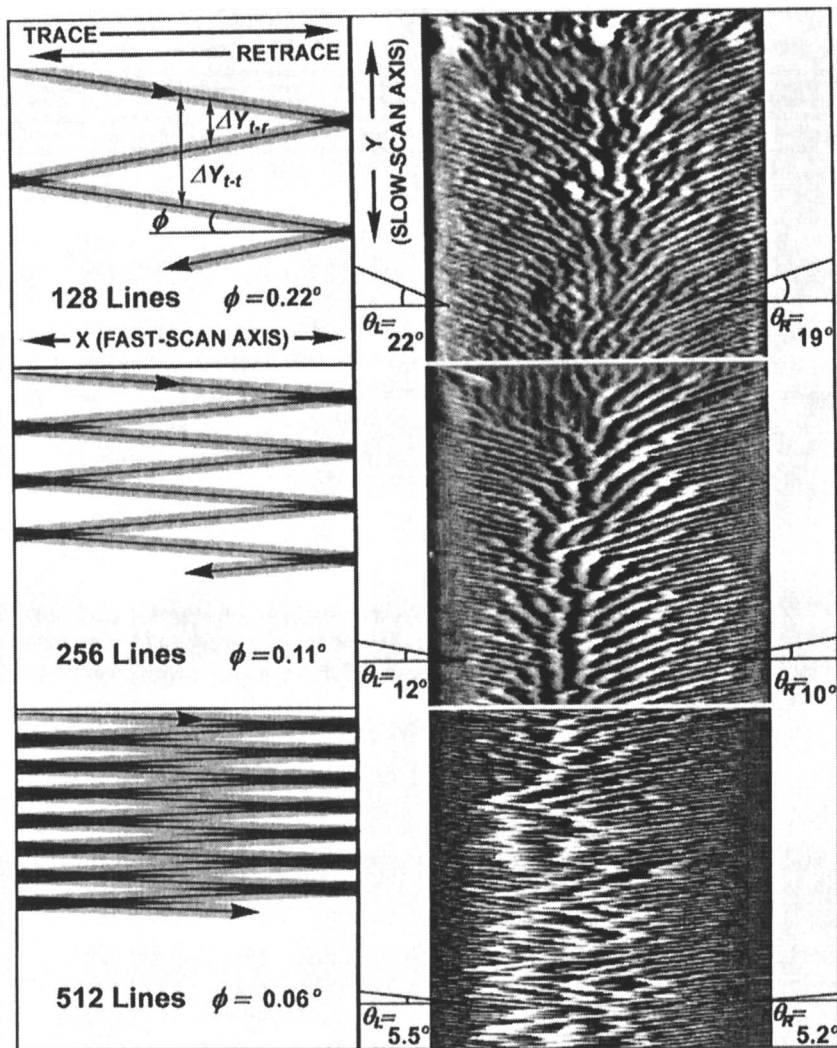


Figure 2 (left). Schematic of the tip trajectory for 128 (top), 256 (middle), and 512 (bottom) fast-scan cycles per image. The angle of the tip's trajectory (ϕ) relative to the fast-scan axis is greatly exaggerated for clarity. The light gray regions are areas that are perturbed by the tip. Overlap of perturbed regions occurs at the left and right edges of the scan area (dark gray triangles), at which time the tip is moving towards the center of the scan area. Decreasing ϕ results in the overlapping perturbed regions extending further from the edges of the scan area. The corresponding topography images are shown on the right. θ , as defined in the figure, is proportional to, but much larger than, ϕ .

Whereas ΔY_{t-t} is constant across the entire fast-scan axis, ΔY_{r-t} (the vertical distance between a retrace and the subsequent trace scan line) varies linearly from zero at the left edge of the imaged region to a maximum equal to ΔY_{t-t} at the right edge:

$$\Delta Y_{r-t} = \frac{X}{X_{\max}} \Delta Y_{t-t} \quad (3)$$

Assuming that the functional dependence of the bundle slope on ΔY_{r-t} at position X is the same as it is for ΔY_{t-t} at the image edge (i.e., it is linear), we can write:

$$\frac{dY}{dX} = a_1 \Delta Y_{t-t} + a_2 \Delta Y_{r-t} = \Delta Y_{t-t} \left(a_1 + \frac{a_2}{X_{\max}} X \right) \quad (4)$$

Integration yields:

$$Y = \left(\frac{a_2 \Delta Y_{t-t}}{2 X_{\max}} \right) X^2 + (a_1 \Delta Y_{t-t}) X + a_3 \quad (5)$$

We tested Equation 5 by tracing three bundles on each side of an image, plotting the data to a common curve (Figure 3, solid and open symbols), and performing a quadratic fit (solid lines) with fitting parameters a_1 , a_2 , and a_3 . The ratio of the second derivatives for the 128-, 256-, and 512-line images is expected to be 4:2:1 (reflecting the ratio of the slopes of the dark triangles in Figure 2). The empirical ratio (from the quadratic fit) is 4.7 : 2.4 : 1. Thus, the agreement of the quadratic fits and the experimental results suggest the validity of our model. This model does not, however, account for the *branching* of wide, perpendicularly-oriented bundles near the center of the raster scanned region to narrower, more horizontally-oriented bundles at the left and right edges of the scan area.

Molecular Interpretation. Stresses in a polymer melt may lead to alignment of the polymer chains along the direction of the imposed stress vector. A reduction in entanglements accompanies this orientation, so that translational motion of the polymer is enhanced. The tip is thought to behave as a “molecular comb” which orients the polymer chains parallel to the tip trajectory. Successive visits of the tip to the same polymer chains result in greater net orientation of the chains and hence enhanced translational mobility.

The parameters a_1 and a_2 in Equation 5 measure the tendency of the scanning tip to orient the polymer chains and move them towards the center of the scan area. Presumably, a_1 and a_2 are functions of the *width* of the perturbed region surrounding a scan line, the *magnitude* of the tip-polymer interaction, and the *relaxation time* of the polymer's (viscoelastic) response to this perturbation. By changing these parameters one can manipulate the morphology of the scan-induced pattern. One way to modify the viscoelastic response of the polymer is to vary the temperature and fast-scan frequency at which images are acquired. Extrinsic

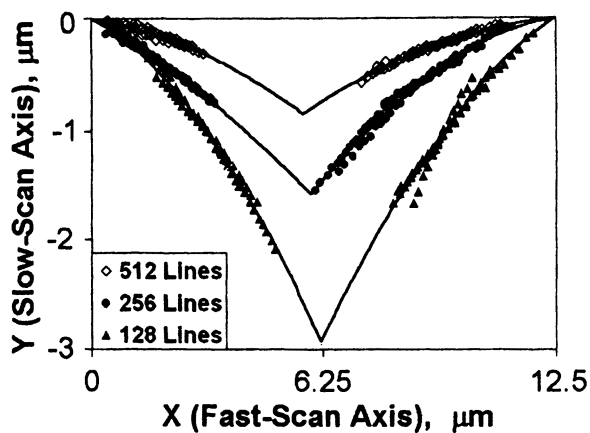


Figure 3. Three bundles on each side of 128-, 256-, and 512-line images were traced and plotted onto common curves (solid and open symbols). The lines represent a quadratic fit to the symbols. The quality of the fit and the dependence of the fitting parameters on the relative distances between scan line perturbations suggest the validity of Equation 5.

parameters of further importance would be the magnitude of shear (and tensile) forces applied as well as the tip-sample contact area (in turn a function of tip shape). In collecting the images shown in Figure 4, the extrinsic parameters were held approximately constant by using a single, stable tip at constant load, while the intrinsic parameters of temperature and rate were varied. We must caution, however, that variation of the (experimentally accessible) scanning rate necessarily convolves two distinct elapsed times of importance: (1) the time during which perturbative forces act on a polymer conformer during a single scan (velocity dependence), and (2) the time between repeated applications of perturbative forces to adjacent regions of the film (successive trace/retrace scans).

Studying the Viscoelastic Response. The 10 X 10 μm topography images of Figure 4 demonstrate the temperature and frequency dependence of scan-induced patterning. (Images were acquired at five different temperatures and over a greater frequency range than depicted in Figure 4.) At higher fast-scan frequencies for a given temperature—or at lower temperatures for a given frequency—the bundles tend to align nearly perpendicular to the tip trajectory. This type of morphology is similar to what has been reported in the past and is thought to be characteristic of elastic/plastic behavior. Decreasing the scanning frequency or increasing the temperature causes the bundles to align more efficiently with the tip trajectory, representing a viscous response of the polymer to the tip-induced shearing forces.

The images in Figure 4 were quantified by measuring the slopes of the bundles near the left and right edges of the scan area. Twenty measurements were performed for each image (ten on each side), and the results plotted in Figure 5A as

$\left| \frac{dY}{dX} \right|$ vs. the fast-scan frequency for five temperatures varying from 142 to 160°C.

Note that a given slope is reached at a *higher* frequency (shorter relaxation time) as the temperature *increases*. This observation is consistent with the time-temperature superposition principle which describes viscoelastic behavior. Recognizing the similarity in the curve shapes for each of the data sets in Figure 5a, we determined an empirical shift factor for each temperature (a_T) which, when applied to the frequency scale for each curve in Figure 5a, shift the data to a chosen reference temperature ($T_0 = 142^\circ\text{C}$). The shifted data are shown in Figure 5b.

Interpretation of Empirical Shift Factors. The linearity of $\frac{(T - T_0)}{\log a_T}$ vs. ($T - T_0$) (where a_T is the empirical shift factor and T_0 is the reference temperature to which the data are shifted), shown in the inset, implies that the results are consistent with the Williams-Landel-Ferry (WLF) equation, known to describe viscoelastic behavior in many amorphous polymers (14):

$$\frac{(T - T_0)}{\log a_T} = -\frac{C_2}{C_1} - \frac{1}{C_1}(T - T_0)$$

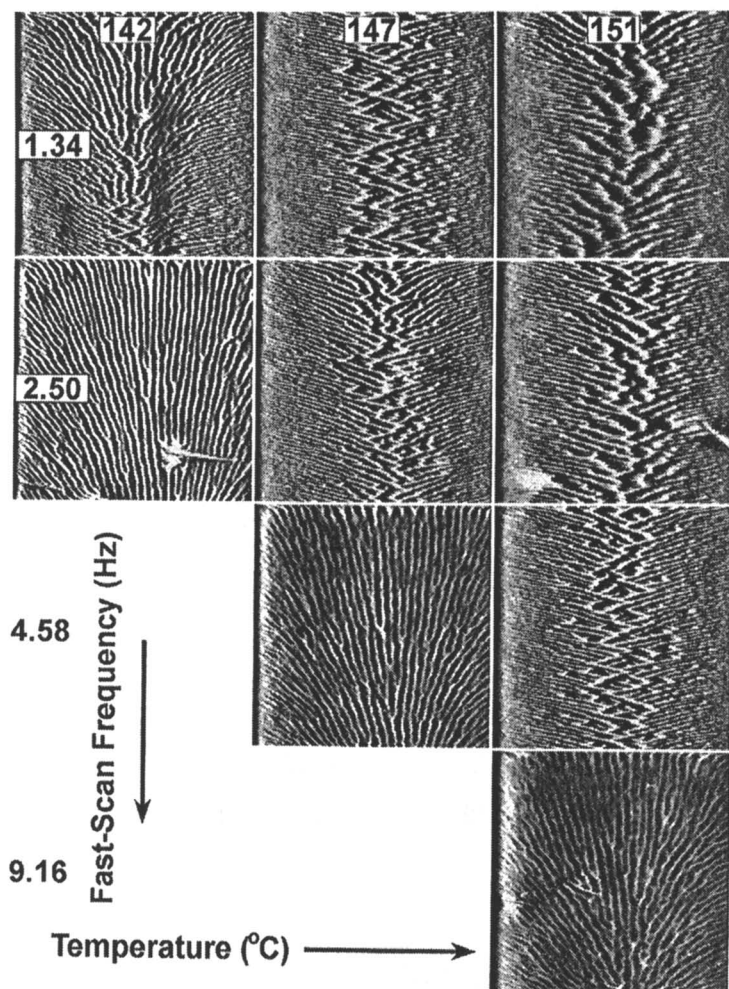


Figure 4. 10 μm images acquired at different temperatures and fast-scan frequencies. Decreasing the fast-scan frequency has a similar effect on the scan-induced pattern as increasing the temperature.

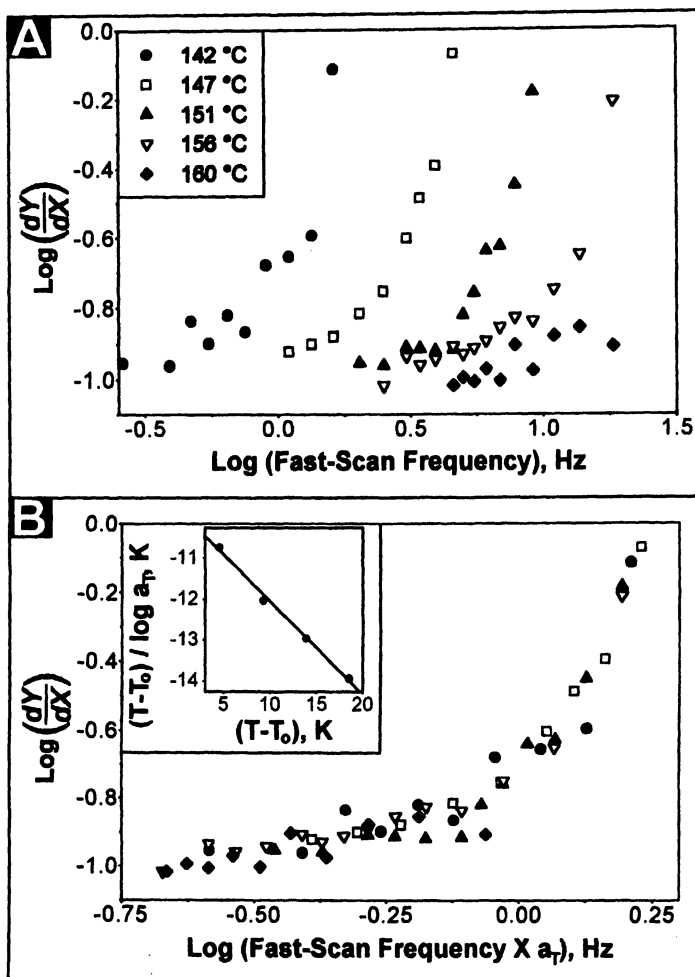


Figure 5 (top). The images in Fig. 4. were quantified by measuring the slope of the scan-induced bundles at the left and right edges of the scan area. Each point represents the average of twenty measurements from many more images than shown in Fig. 4. Empirical factors were determined which, when applied to the frequency axis, shift the data taken at different temperatures to 142°C (bottom). The linearity of the plot in the inset suggests that the shift factors are described by the WLF equation.

Here C_1 and C_2 are constants evaluated from the slope and intercept and depend on the value chosen for the reference temperature, T_0 . If the master curve is referenced to the glass transition temperature (T_g), then $(2.303 C_1)^{-1}$ is theoretically understood to be the fractional free volume at the glass transition (f_g) (6,7,14).

For the glass transition to occur, a critical free volume, f_g , must be reached. At $f < f_g$, the polymer is hard and brittle, while $f > f_g$ results in rubbery or fluid-like behavior. As shown in Table 1, $f_g = 0.032$ for PS. Using this value of f_g , we fixed the value of C_1 in order to estimate an effective glass transition temperature of 113°C from our measurements. In interpreting this result, we must consider two complications in SFM of ultrathin films: interfacial effects and elevated pressure. Several studies have demonstrated that as the thickness of a polystyrene film approaches the polymer coil dimensions, T_g decreases significantly below the bulk value of 100°C (1-3). In a system similar to what we investigated (i.e., 20 nm PS film on a Si substrate), Keddie *et al* measured a T_g of 87°C. On the other hand, substantial *increases* in T_g have been reported in bulk PS when the sample was subjected to elevated hydrostatic pressure (15). Assuming that the 26°C increase in T_g is exclusively due to pressure effects, we estimate—based on the effect of hydrostatic pressure on the T_g of bulk PS—that the *effective tip pressure* on the surface is 84 MPa (15). Given the effective pressure and the applied load (110 nN), we can calculate an *effective perturbation radius* of 20 nm, which is remarkably close to the tip's radius of curvature (approximately 10 nm).

T_0 (°C)	$(2.303 C_1)^{-1}$	C_2 (°C)
142	0.10	43
100 (bulk T_g (14)) *	$0.032 = f_g$ *	51 *
100	0.014	7.6
113	0.032	14

Table 1. Comparison of WLF analysis to literature values for bulk polystyrene. * indicates literature values (14).

Summary. Both temperature and scan frequency affect the patterns created by movement of a nanoscopic tip in contact with a polymer surface. At experimental time scales which are faster than the relaxation time associated with the elongation of a polymer coil, the polymer's response to the tip-induced shearing forces is elastic. Experimental time scales slower than the characteristic relaxation time results in alignment of the polymer with the tip trajectory and net translational movement of polymer towards the center of the scan area. The time-temperature dependence of the patterns are well-described by the WLF equation which is typically used to describe viscoelastic behavior. Analysis of our data further suggests that the T_g of the polymer is elevated in the region confined between the tip and the substrate.

Acknowledgments. This work was supported by grants from the Center for Interfacial Engineering and the donors of the Petroleum Research Fund, administered

by the American Chemical Society. We also wish to thank Molecular Imaging for their technical support and instrument development.

Literature Cited

- (1) Keddie, J. L.; Jones, R. A. L.; Cory, R. A. *Europhys. Lett.* **1994**, *27*, 59-64.
- (2) Forrest, J. A.; Dalnoki-Veress, K.; Stevens, J. R.; Dutcher, J. R. *Phys. Rev. Lett.* **1996**, *77*, 2002-2005.
- (3) Forrest, J. A.; Dalnoki-Veress, K.; Dutcher, J. R. *Phys. Rev. E.* **1997**, *56*, 5705-5716.
- (4) Mayes, A. M. *Macromolecules* **1994**, *27*, 3114-3115.
- (5) Bhushan, B. *Handbook of Micro/Nanotribology*; CRC Press: Boca Raton, 1995.
- (6) Tant, M. R.; Wilkes, G. L. *Polymer Engineering and Science* **1981**, *21*, 874-895.
- (7) Matsuoka, S. *Polymer Engineering and Science* **1981**, *21*, 907-921.
- (8) Leung, O. M.; Goh, M. C. *Science* **1992**, *255*, 64-67.
- (9) Lea, A. S.; Pungor, A.; Hlady, V.; Andrade, J. D.; Herron, J. N.; Voss Jr., E. W. *Langmuir* **1992**, *8*, 68-73.
- (10) Meyers, G. F.; DeKoven, B. M.; Seitz, J. T. *Langmuir* **1992**, *8*, 2330-2335.
- (11) Elkaakour, Z.; Aime, J. P.; Bouhacina, T.; Odin, C.; Masuda, T. *Phys. Rev. Lett.* **1994**, *73*, 3231-3234.
- (12) Jing, J.; Henriksen, P. N.; Wang, H.; Marteny, P. *J. Mat. Sci.* **1995**, *30*, 5700-5704.
- (13) Woodland, D. D.; Unertl, W. N. *Wear* **1997**, *203-204*, 685-691.
- (14) Ferry, J. D. *Viscoelastic Properties of Polymers*; Wiley & Sons: New York, 1980.
- (15) Stevens, J. R.; Coakley, R. W.; Chau, K. W.; Hunt, J. L. *J. Chem. Phys.* **1985**, *84*, 1006-1014.

Chapter 14

Experimental Study of the Friction Regimes on Viscoelastic Materials

C. Basire and C. Fretigny

ESPCI, Laboratoire de Physique Quantique, CNRS ESA 7069,
Systèmes Interfaciaux à l'Echelle Nanométrique,
10 rue Vauquelin, F-75231 Paris Cedex 05, France

An atomic force microscope is used to study friction on polymers which are in a viscoelastic state at the temperature of experiment. It is shown that, during the preliminary phase of friction and before the transition to the sliding regime, the contact area remains nearly constant. This allows for a determination of the relaxation and of the complex modulus of the material. A good agreement is found between moduli measured by this method and macroscopically determined ones. The position of the transition is seen to scale with the characteristic size of the contact area but it does not depend on the displacement velocity. Finally, a transient stick-slip regime is observed before the sliding steady state is reached.

Although frictional forces play a vital role in daily life, the fundamental mechanisms of friction are yet poorly understood. Many physical phenomena contribute to the complexity of this problem - most macroscopically measurable frictional effects are dominated by the influence of wear, adhesion, elastic and plastic deformations, boundary lubrication (1-2)... Moreover, roughness of surfaces usually makes difficult the interpretation of experimental studies of friction at a macroscopic scale. Recently however, it has become possible to investigate friction at an atomic scale or at a mesoscopic one using an atomic force microscope. The contact area is usually much smaller than typical roughness scales, and the method leads to more fundamental interpretations (3). We present here an experimental investigation of friction between a nano-tip and a polymeric material. The preliminary phase of friction and the transition to the sliding regime are analysed.

Materials and method

The polymers used in this study are styrene-isoprene and styrene-butadiene copolymer, which glass-transition temperature are imposed by the proportion of each monomer. Their degree of cross-linking are controlled during polymerisation by the proportion of transfer agent. They present a glassy modulus of about 10^9 Pa and a relaxed one of typically 10^5 Pa. At room temperature they are in a viscoelastic state. Samples are obtained through the evaporation of the aqueous phase on polyethylene terephthalate substrates. Thickness of the films is about ten micrometers. Samples of centimetric size were also prepared and mechanically characterised using dynamic mechanical analysis.

Experiments are performed under ambient conditions (about 30°C) with an unmodified commercial instrument (4) using V shaped cantilevers (nominal stiffness of 0.12 and 0.6 N m^{-1}) with square-based pyramidal silicon nitride tip. Tip end radius is estimated to be about a few tens of nanometers. Since AFM is not used as a tool for determining topographic profiles, but for performing displacement and measuring forces, an accurate calibration method was followed (5) to convert the signal from the photodiodes, due to the torsion and the deflection of the cantilever into forces.

In order to investigate the tribological behaviour of the tip, it is important to define precisely the initial conditions of the contact. For that purpose, the surface of the sample is scanned in contact mode, at constant deflection (in order to maintain the deflection constant, the vertical position of the sample is adjusted by a servo-loop). Then the position of the tip is kept constant during a given dwell time. This procedure allows the point on the surface to be chosen where the analysis will be made. During the dwell time adhesion forces cause the tip to penetrate into the material at constant normal load (6). Indentation depth can be measured using the feed-back loop of the AFM. For the materials studied here, after about one hour the tip is deeply intruded in the sample (the indentation depth is almost constant about several hundreds of nanometers). Analysis of this phase has been presented elsewhere (6). From this initial state, the sample is displaced at constant velocity in its plane and perpendicularly to the cantilever axis (7). A typical evolution of the tangential force (proportional to the torsion of the cantilever) with the displacement is plotted on Figure 1. This experiment is done at a constant normal load because the servo-loop maintains the deflection of the cantilever constant (presented results correspond to zero normal load). In a first stage the friction force is seen to increase, which corresponds to the static friction zone. Then it remains nearly constant, before an abrupt transition occurs into a regime where the intensity of the tangential force remains low and almost constant. In this part of the curve, the tip slides on the surface (it is the usual situation in which the images are taken), which corresponds to the sliding friction regime. This curve is characteristic of the so-called "stiction" effect : friction changes from a static to a sliding state (8).

The effects of dwell time on the stiction curve are shown on Figure 2 : in the static friction regime, at constant velocity and under zero applied normal load, the increasing rate of the amplitude of the friction force increases when the dwell time is longer. The position of the transition is also shifted towards the higher displacements. Several stiction curves corresponding to experiment realised at different velocity and

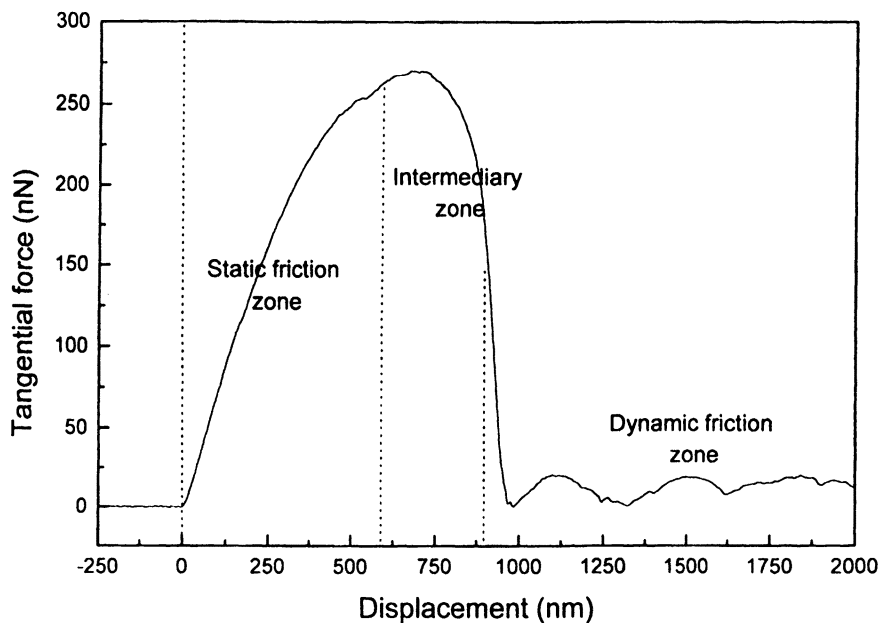


Figure 1. Evolution of the tangential force during the displacement of the sample at constant velocity ($v = 400 \text{ nm} \cdot \text{s}^{-1}$): Stiction effect.

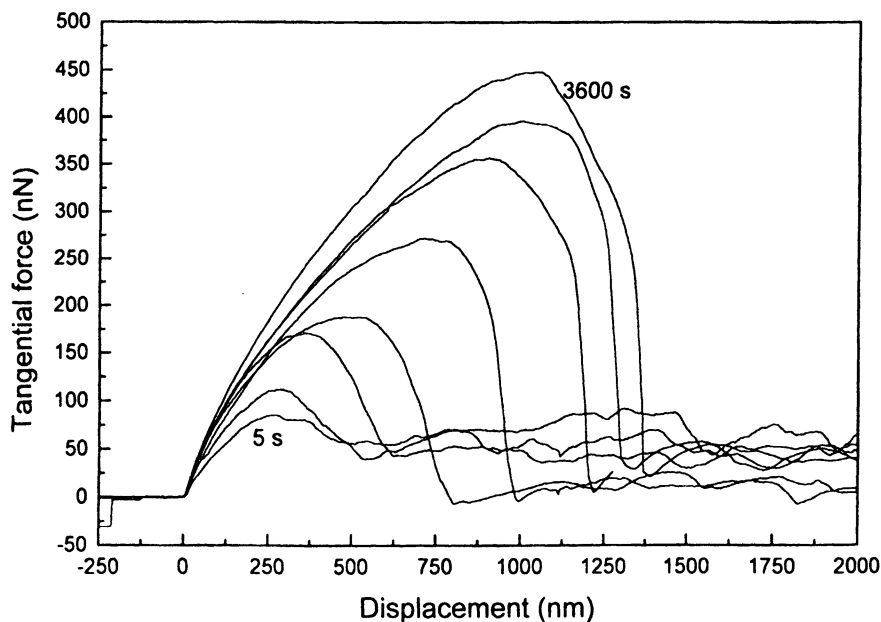


Figure 2. Stiction curves obtained at $80 \text{ nm} \cdot \text{s}^{-1}$ after several dwell times ($5 \text{ s} < \tau < 1 \text{ h}$) corresponding to penetration depths ranging from 45 to 345 nm.

after a constant dwell time are presented on Figure 3. In the static part of the curve, the friction force is seen to be very sensitive to the velocity of the displacement while the displacement threshold appears to be unaffected. In the following, a discussion of the static region is presented. It is shown to allow for a quantitative determination of the complex moduli of polymeric, few micrometers thick films. Then the transition from static to sliding friction and the sliding friction regime are analysed.

Static friction

In the frame of elastic material contact mechanics, static friction of a sphere has been analysed by several authors. Mindlin (9) consider the non-adhesive case, assuming a friction law under the slider in an annulus surrounding a region where interfacial slip has not occurred. Using fracture mechanics concepts, Savkoor and Briggs (10) have given a description of the adhesive case. More recently, in the Maugis-Dugdale description of adhesion, Johnson (11) modified and extended the Savkoor and Briggs approach. In these models and for small displacements, contact radius remains nearly constant. In the limit of the small displacements the material is submitted to a tangential force, T , which is proportional to the radius of the contact area, a and to the elastic modulus E :

$$T = \frac{16}{9} Eay$$

where a Poisson ratio of $\frac{1}{2}$ has been assumed (In this case, the normal and lateral problems are de-coupled (9-10). This relation then expresses the tangential force necessary to the displacement y of a disk of radius a , at the surface of a semi-infinite elastic domain). The lateral contact stiffness is then $\frac{16}{9} Ea$.

In the case of viscoelastic materials, very few studies have been done, because of the complexity of their formulation. The situation is much simpler when the principle of correspondence (12) applies, that is when the domain where the boundary conditions apply, does not depend on time. Thus, for sufficiently small displacements, leading to constant dimension of the contact area, the previous equation can be generalised for viscoelastic materials.

For the displacement y of a disk at constant velocity v , it can be written as :

$$T(t) = \frac{16}{9} a \int_0^t E(t-t') \frac{dy}{dt'} dt' = \frac{16}{9} a v \int_0^t E(t') dt'$$

In the present experiments, after the initial dwell time, the penetration of the tip is much larger than the tip end radius. It is then possible to approximate the tip to a perfect pyramidal punch. The contact area has thus a square shape. We assume in the following that the previous expression remains valid if a represents a characteristic length of the contact area. Then, in the beginning of the stiction curve, the tangential force is expected to be proportional to the characteristic length of the contact area and to the velocity of the displacement. In previous studies, we have shown that during the indentation of the tip, penetration depth and characteristic length of the contact area remain proportional to one another (6,13). This can be explained as follows. Considering the geometrical similarities existing between a pyramid and a cone, it has been shown that in non-adhesive contact mechanics the contact size is proportional to

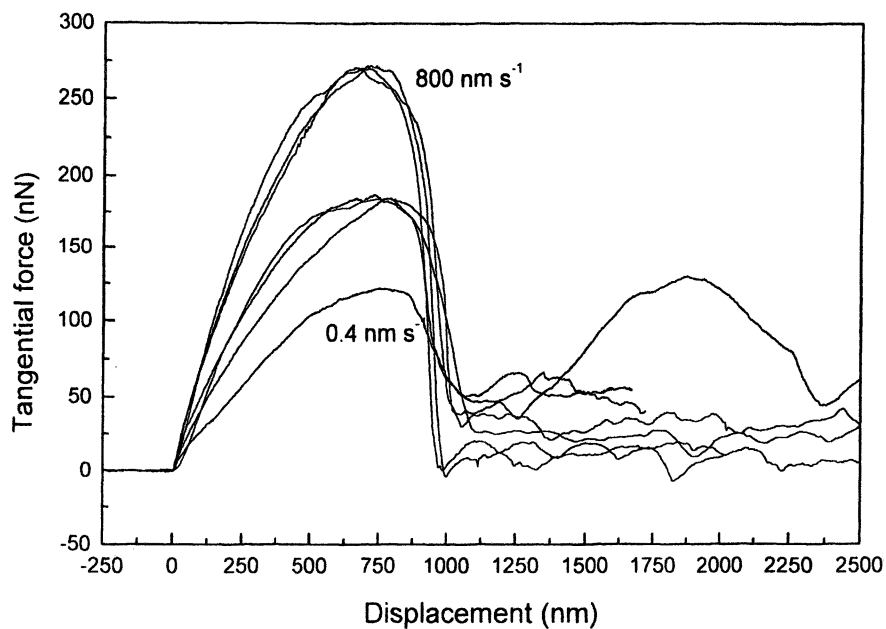


Figure 3. Stiction curves obtained at several velocities ($0.4 < v < 800 \text{ nm s}^{-1}$) after a constant dwell time ($\tau = 30 \text{ min.}$).

the indentation depth (14). This proportionality is kept in the description of the adhesive contact of a conical punch (15) under zero normal load, as it is the case in our experiments. Finally, since the lateral stiffness of the cantilever is much larger than the lateral contact stiffness, the test can then be thought of as a fixed grips.

By normalising the curves of Figure 2 in dividing the amplitude of the tangential force in the static friction state by the indentation depth measured at the end of the indentation, it is clear that all the curves are almost superimposed (Figure 4). The evolution of the tangential force normalised to the penetration depth and by the displacement velocity, deduced from the results of Figure 3, are plotted on Figure 5. It can be noted that all the curves strongly overlap during the phase of growth of the tangential force. Both results confirm the expected proportionality of the tangential force on the contact size and on the displacement rate.

Since the overlapping curve of figure 5 is characteristic of $\int_0^t E(t) dt$, it is

possible to obtain the relaxation modulus of the polymer by differentiation. Results so obtained are plotted on Figure 6 together with the result of a macroscopic dynamic mechanical analysis on a sample of centimetric size. The values of the contact characteristic size a we have used, are deduced from the equilibrium expression describing the adhesive contact of a cone on an elastic material under zero normal load (15) : $a = 4/\pi \delta \tan \gamma$. δ is the penetration depth and γ is the cone half-angle. To represent the pyramidal tip, we have taken a value of $\pi/4$ for this angle. The relaxation modulus deduced from the stiction data is in good agreement with the determined one macroscopically. It should be noted that the geometrical approximations made above should not affect very much the accuracy of this determination.

These results confirm the presented description of the preliminary phase of friction and give a method for the determination of the relaxation modulus of polymeric materials at a local scale. We applied it to a range of viscoelastic samples (5). In each case agreement between macro- and microscopic determinations was good. The materials tested have typical relaxed moduli ranging from 0.01 MPa to 10 MPa. Resolution of the measurements is imposed by the characteristic length of the contact area : the volume participating to the mechanical response to the excitation can be estimated to have a size representing several times the characteristic length of the contact area. For the presented experiment, the resolution of the method can be estimated to be about one micrometer.

As another illustration of the interpretation of the preliminary phase of friction, a method is presented for determining the complex moduli of these polymeric materials. After indentation, a lateral cyclic displacement is imposed to the sample, perpendicularly to the axis of the cantilever. The amplitude of the measured tangential force is proportional to the amplitude of the excitation and depends on the frequency of the solicitation. Here again, this situation can be analysed using the correspondence principle, by Fourier analysis of the periodic excitation. Detailed analysis can be found in ref. (16) and in a forth coming paper. From the data it is possible to extract the local complex modulus of the material. Values of the storage and loss moduli so obtained are plotted on Figure 7, for a styrene-isoprene copolymer of glass-transition temperature of about 9°C. For comparison we have reported the macroscopically

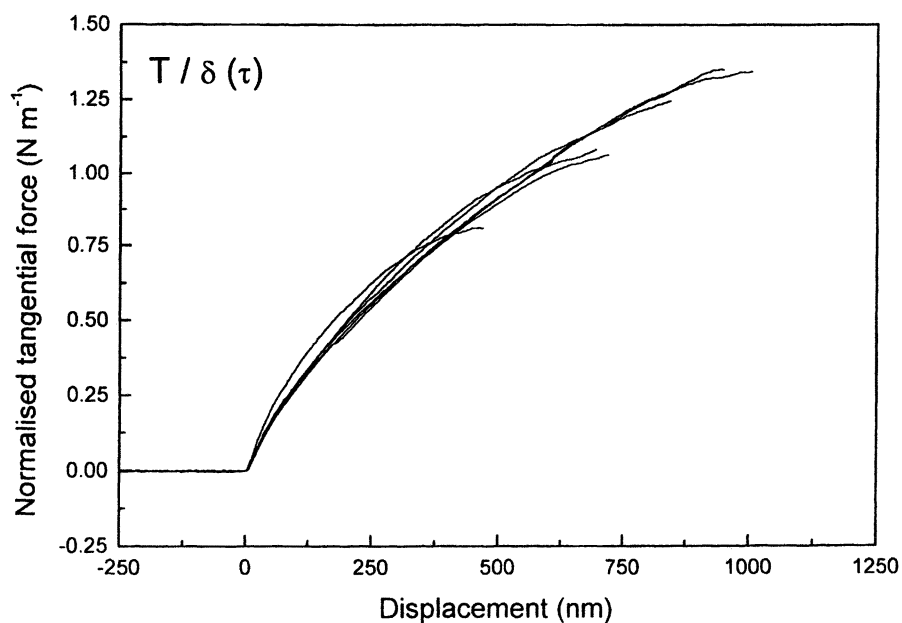


Figure 4. Normalised tangential force in the static zone. The tangential force has been divided by the indentation depth measured at the end of the indentation process.

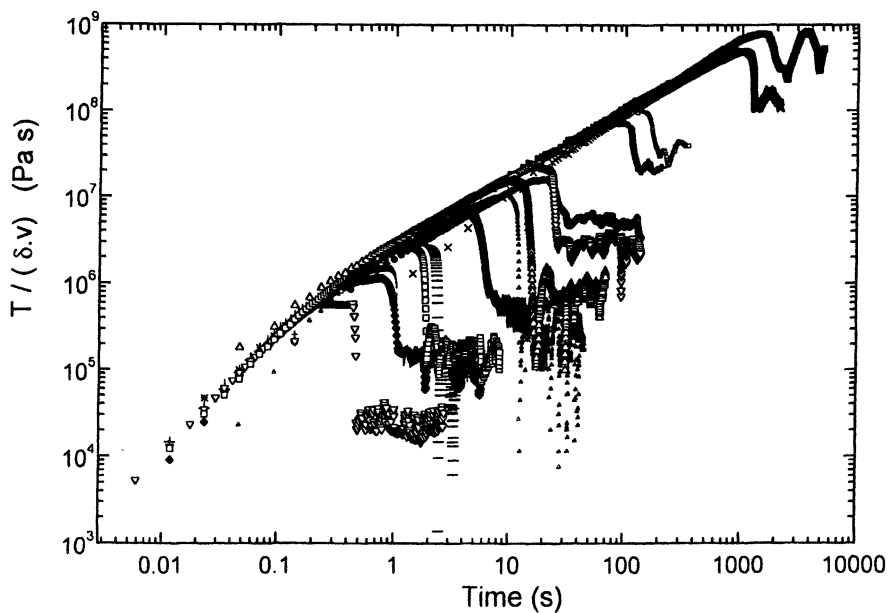


Figure 5. Tangential force normalised to the velocity and to the indentation depth, $T / (\delta v)$, plotted against time, after a constant dwell time ($\tau = 30$ min.) and for several velocities ($0.4 \text{ nm s}^{-1} < v < 4 \text{ } \mu\text{m s}^{-1}$).

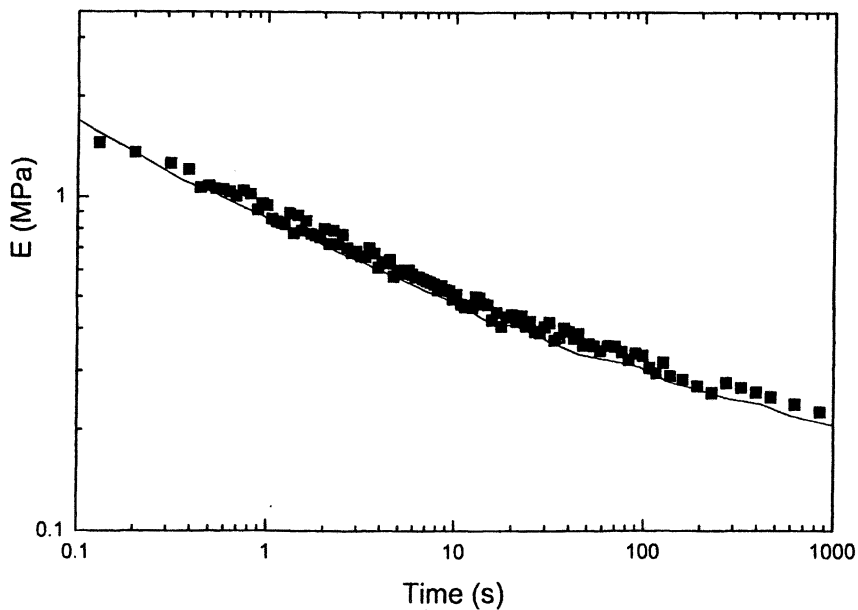


Figure 6. Relaxation modulus obtained by derivating the overlapping curve of Figure 5 (■) for the styrene-butadiene sample. Comparison with the relaxed modulus determined on a macroscopic sample (—).

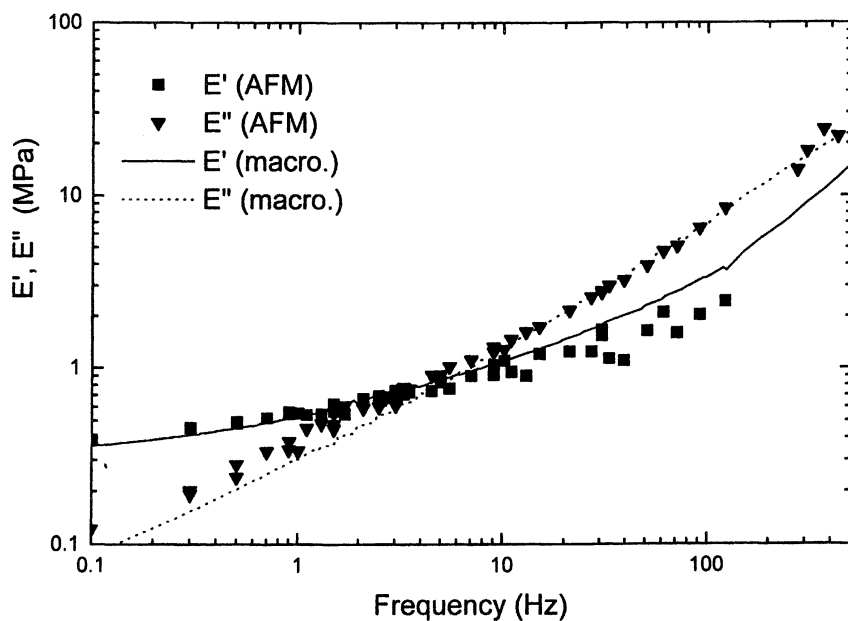


Figure 7. Variations of the storage and loss moduli with frequency obtained from the analysis of the response of the material to a periodic modulation, for the styrene-isoprene sample. Comparison with the macroscopically determined ones.

determined moduli. We observe that both determinations are in good agreement from 0.1 Hz to typically 100 Hz.

In the superimposed stiction curves of Figure 5, it is clear that the tangential force is proportional to the characteristic length of the contact area not only for small displacements but also for larger values. This observation can be easily understood if the dimension of the contact area remains nearly constant in the static friction zone. To confirm this hypothesis, a small periodic lateral displacement (few nanometers) is superimposed to the displacement at constant velocity, in order to test the contact stiffness, which is proportional to the characteristic length of the contact area. A typical response is plotted on Figure 8A. We have verified that the small modulation of the position of the sample does not modify the overall shape of the stiction curve. The response can be analysed as the sum of a contribution due to the displacement at constant velocity (continuous tangential force) and of a contribution linked to the periodic solicitation, characteristic of the lateral stiffness. The amplitude of the pseudo-periodic contribution reflects the variations of the characteristic length of the contact area. These data are plotted on Figure 8B together with the continuous tangential force. Stability of this amplitude confirms that the dimension of the contact area remains nearly constant during the increasing phase of the tangential force in the static friction zone. An abrupt drop of the contact area is then observed : it can be attributed to the transition from static to dynamic friction regimes. In the following a discussion of the position of this transition is presented.

Transition - sliding friction

As it can be noticed on Figure 2, the position of the transition increases with the indentation depth. On Figure 9 this position is plotted versus the indentation depth for a given velocity displacement : the transition occurs at a displacement which represents about 3.4 times the indentation depth. Moreover, it is nearly independent of the velocity of the displacement in a range of about 4 decades in velocity (Figure 3). The reason for such a large value of the threshold and of this quasi velocity-independence is not clear, but seems to be linked to a critical deformation in these viscoelastic materials.

From the scaling properties noted above, the work necessary to cause the tip to slide can be defined per unit of contact area by integration of the stiction curve and normalisation. The dependence of this energy with the velocity is shown to follow a power law (Figure 10). This effective separation energy is larger than the expected thermodynamic work of adhesion (several tens of mJ m^{-2}) by one or two order of magnitude. This is to be attributed to the dissipative character of the materials. The exponent is similar to the one which describes the frequency dependence of the complex modulus.

After the transition and before a steady regime is reached, a transient stick-slip behaviour is apparent in a certain range of velocities. To study this regime, experiments have been carried out after a zero dwell time (displacement velocity is suddenly reduced). This procedure avoids the effects of the mechanical history of the material. The tangential force is seen to fluctuate in a characteristic manner under zero normal load (Figure 11). A simultaneous measurement of the height of the

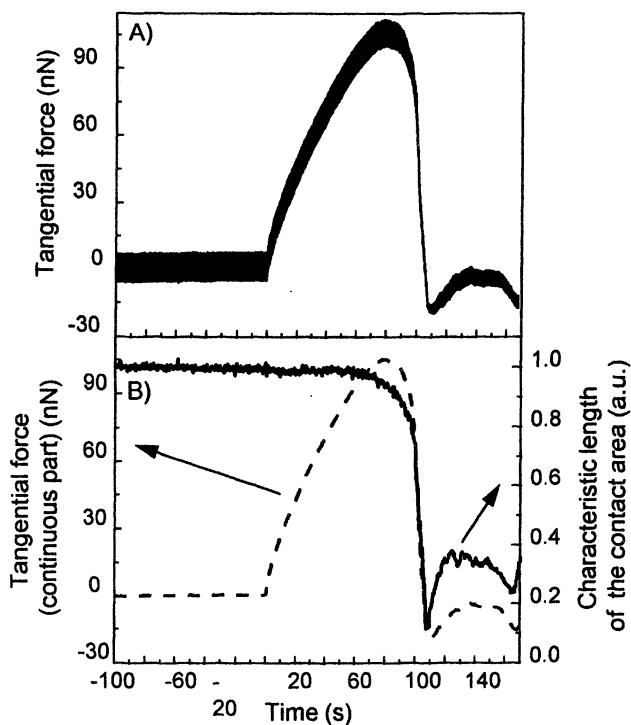


Figure 8. A) Tangential force during the displacement of the sample at a constant velocity of $5 \text{ nm}\cdot\text{s}^{-1}$ and a periodic sollicitation with an amplitude of $\pm 2.5 \text{ nm}$ at 4 Hz. B) Variation of the characteristic length of the contact area and of the continuous part of the tangential force obtained from response A).

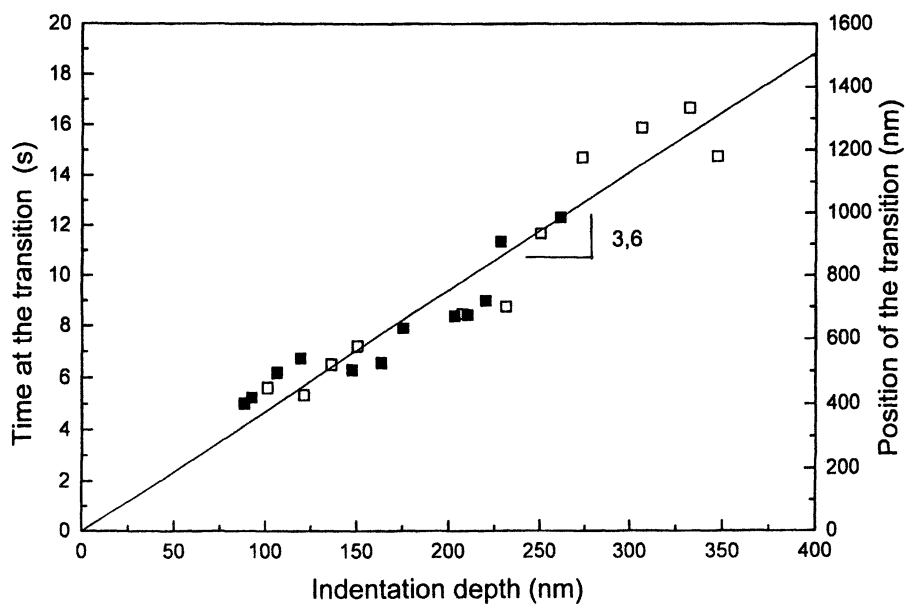


Figure 9. Position of the transition from static to dynamic friction plotted versus the indentation depth. The symbols (□) and (■) represent data obtained with two cantilevers whose normal nominal stiffness is respectively 0.12 and 0.6 N m^{-1} .

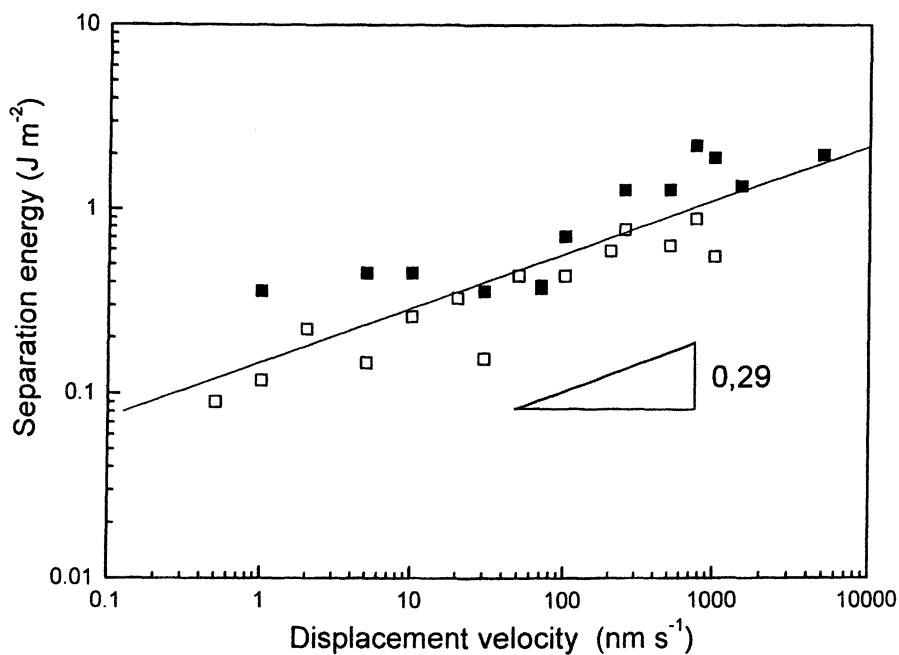


Figure 10. Variation of the effective energy of separation between the tip and the viscoelastic material plotted against the displacement velocity. The symbols (\square) and (\blacksquare) represent the data obtained with two cantilevers as in Figure 9.

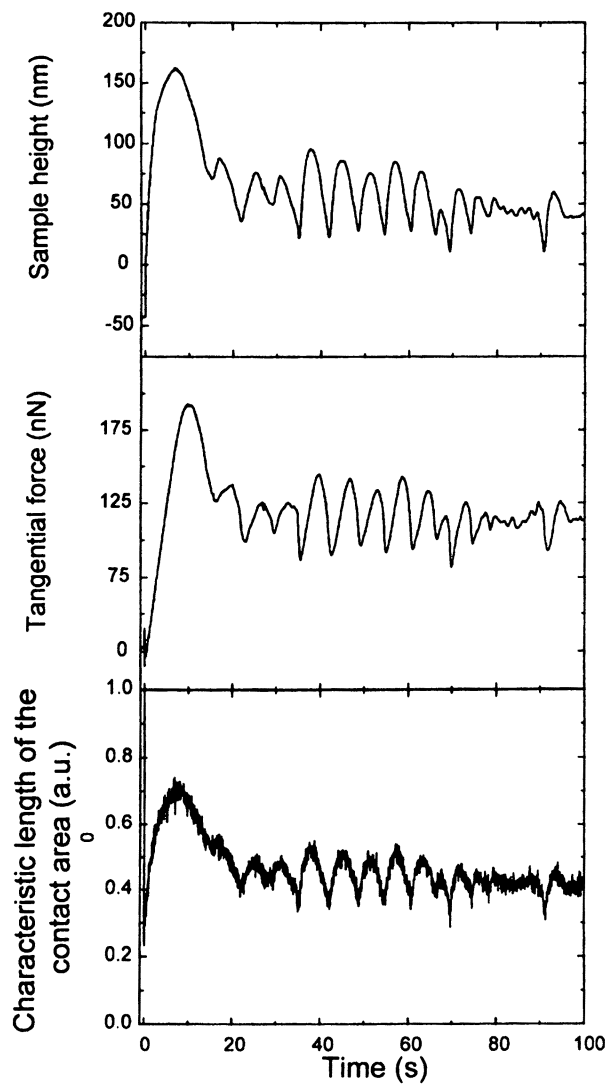


Figure 11. Stick-slip experiment.

sample and of the characteristic contact size obtained from a small lateral modulation of the position are also plotted on Figure 11. It is clear from the Figure that the tip penetrates into the material and the contact size increases when the tangential force increases. Conversely, decreasing of the tangential force coincides with phases of diminution of the contact area and of penetration depth. The amplitudes of these oscillations of the tangential force, of the indentation depth and of the contact area decrease at longer times though this damping is not very reproducible. This regime is a transitory phenomenon, which converges to the steady friction state after several cycles. A typical image obtained immediately after such an experiment is shown on Figure 12 : sequences of holes and bumps are observed. (As expected, this imprint disappears slowly with time). Then the phenomenon of stick-slip can be seen as a competition between the indentation process under interfacial forces and the sliding process due to the displacement. Moreover the period of the phenomenon decreases when the displacement velocity is increased : this effect can be related to the difference between an effective contact time between the tip and the surface and the time necessary for the tip to penetrate into the material because of interfacial forces. Damping of the phenomenon can be explained by assuming that, after a sliding phase, the tip penetrates into a material which has already suffered deformation. Periodic plastic deformations of polymers under an AFM tip have been observed by several groups (17). The experiments presented here could contribute to help understanding that kind of stick-slip. A detailed analysis of this part of the curve will be presented elsewhere.

When a steady friction regime is reached, the tangential force is measured for different normal load ($-50 \text{ nN} < P < 250 \text{ nN}$). The friction force varies linearly with the normal load but does vanish at zero load. The slope of the curve allows a dynamic coefficient of friction to be defined. This friction coefficient is observed to decrease when the velocity increases (Figure 13). This effect is to be linked to the existence of the stick-slip motion (18).

Conclusion

This analysis of the behaviour of a single contact between the tip of an AFM and a viscoelastic material under shear has revealed that the contact size remains almost constant until the transition. This permits measurements of the viscoelastic moduli of material : relaxation modulus and complex modulus are determined by deforming the surface of the material respectively at a constant speed or periodically. The resolution of the experiment presented here is about one micrometer. It is related to the indentation depth. It could be improved by using chemically modified tip or sharper tip. This method can be applied to composite materials, thin films, polymer blends.... It is not too sensitive to the precise shape of the tip end because of the large indentation depth. In these experiments normal load and displacement are controlled during the experiment, contrary to the "force curve" method generally proposed (19). The "fixed grips" experiment used here permits a simpler analysis of viscoelastic properties of polymers. The initial sliding regime has been shown to be accompanied by a transitory stick-slip phenomenon, resulting in the competition between indentation and sliding.

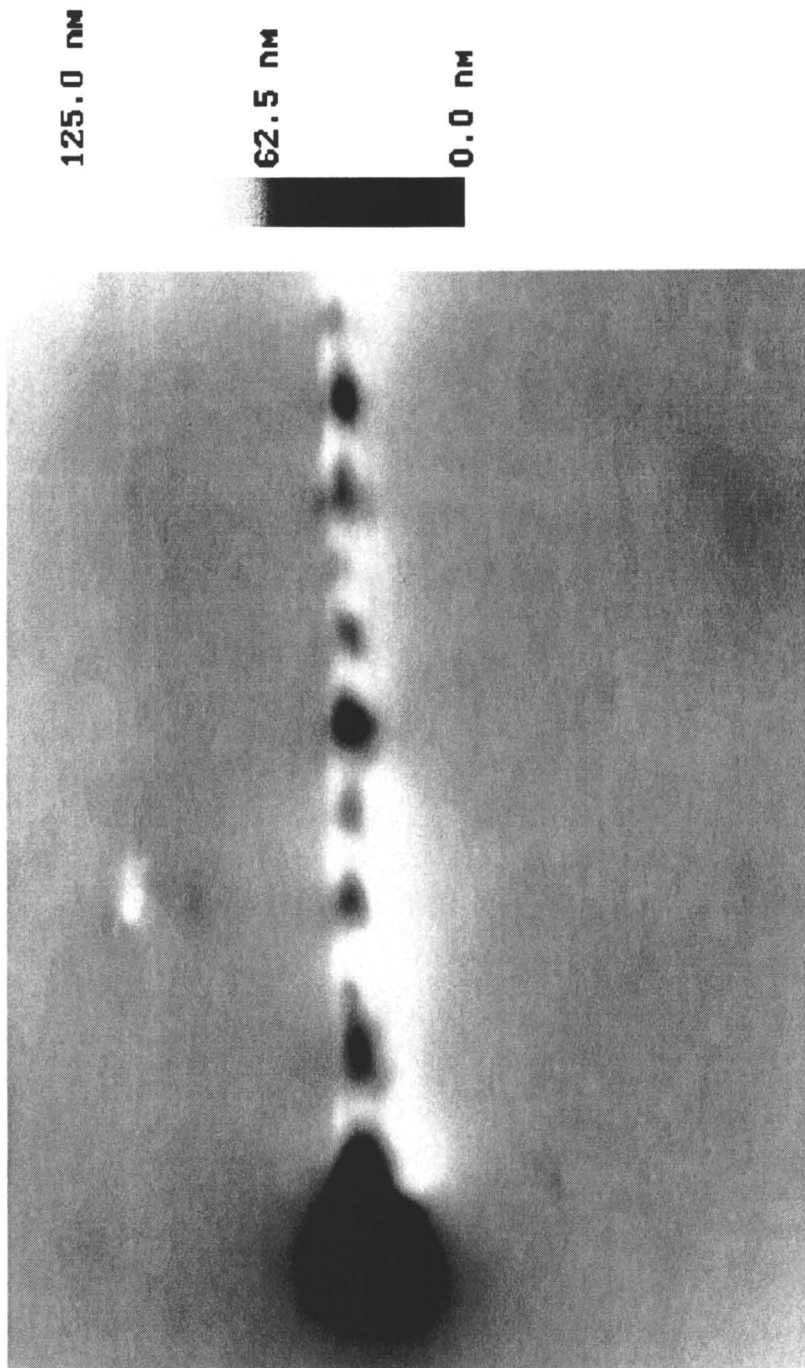


Figure 12. Image ($8 \mu\text{m} \times 4 \mu\text{m}$) of the polymeric surface after a stick-slip experiment realised at 25 nm s^{-1} . The grey scale represents the topography.

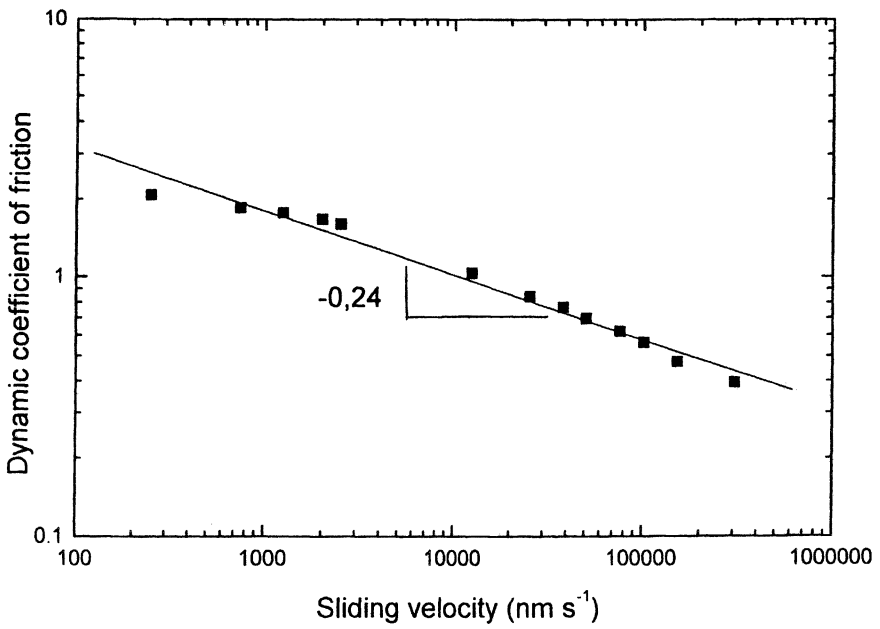


Figure 13. Variation of the dynamic friction coefficient with the velocity.

References

1. "Workshop of friction, arching, contact dynamics", Wolf, D.E. and Grassberger, P. Eds., World Scientific publishing Co. Pte. Ltd. Singapore, 1996.
2. "Fundamentals of Friction : Macroscopic and Microscopic Processes", Singer, I.L.; Pollock, H.M. Eds; NATO ASI Series 220, 1992.
3. Johnson, K.L. *Proc Roy. Soc. Lond. A*, 1997, 453, 163.
4. Nanoscope IIIa, Digital Instruments, Santa Barbara, California USA.
5. Basire, C. thesis Université Pierre et Marie Curie, Paris VI, 1998.
6. Basire, C.; Fretigny, C. *C.R. Acad. Sci. Paris*, IIb, 1997, 325, 211.
7. Basire, C.; Fretigny, C. in "Polymers and Surfaces, a versatile combination", Hommel, H. ed., research Signpost, Trivandrum, India, 1998.
8. Israelachvili, J.N. in ref (2), 351. Yoshizawa, H.; Chen, Y.; Israelachvili, J.N. *J. Phys. Chem.*, 1993, 97, 4128. Göddenhenrich, T.; Müller, S.; Heiden, C. *Rev. Sci. Instrum.*, 1994, 65, 2870.
9. Mindlin, R.D. *J. Appl. Mech.*, 1949, 259. Mindlin, R.D.; Deredsiewick, H. *J. Appl. Mech.*, 1953, 327.
10. Savkoor, A.R.; Briggs, G.A.D. *Proc. R. Soc. Lond.*, 1977, A356, 103.
11. Johnson, K.L. *Proc. R. Soc. Lond.*, 1997, A453, 163.
12. Graham, G.A.C. *Q. Appl. Math.*, 1968, 26, 167.
13. Basire, C.; Fretigny, C. *to be published*.
14. Johnson, K.L. *J. Mech. Phys. Solids*, 1970, 18, 115. King, R.B. *Int. J. Solids Structures*, 1987, 23, 1657. Beck, S.; Tonck, A.; Georges, J.M.; Loubet, J.L. *Philosophical Magazine A*, 1996, 74, 1061.
15. Maugis, D.; Barquins, M. *C. R. Acad. Sc. Paris*, 1980, t.291 - série B, 161.
16. Fretigny, C.; Basire, C.; Granier, V. *J. Appl. Phys.*, 1997, 82, 43.
17. Leung, O.M.; Goh, M.C. *Science*, 1992, 255, 64. Meyers, G.F.; DeKoven, B.M.; Seitz, J.T. *Langmuir*, 1992, 8, 2330. Jin, X.; Unertl W.N. *Appl. Phys. Lett.*, 1992, 61, 657. Elkaakour, Z.; Aimé, J.P.; Bouhacina, T.; Odin, C.; Masuda, T. *Phys. Rev. Lett.*, 1994, 73, 3231.
18. Rabinowicz, E. in ref (2), 25.
19. *see for example* Vanlandingham, M.R.; McKnight, S.H.; Palmese, G.R.; Eduljee, R.F.; Gillespie, J.W.; McCulough, J.R.R.L. *J. Mat. Sci. Lett.*, 1997, 16, 117. Nakajima, K.; Yamaguchi, H.; Lee, J.C.; Kageshima, M.; Ikehara, T.; Nishi, T. *Jpn. J. Appl. Phys.*, 1997, 36, 3850. Mareanukroh, M.; Hamed, G.R.; Eby, R.K. *Rubber Chem. Technol.*, 1996, 69, 801.

Chapter 15

Micro- and Nano-Wear of Polymeric Materials

G. S. Blackman¹, L. Lin², and R. R. Matheson³

¹ DuPont CRD, Experimental Station E323/110B, Wilmington, DE 19880

² DuPont Automotive, Marshall Research Laboratory, 3500 Grays Ferry Avenue, Philadelphia, PA 19146

³ DuPont Automotive, 950 Stephenson Highway, Troy, MI 48007

Industrial automotive polymers are exposed to harsh environmental conditions yet they are expected to maintain a pleasing high gloss finish for at least five years. The automobile manufacturers demand improvements in mar (abrasion) and etch resistance for all new coatings. The combination of a precision large stage AFM with a high-resolution microscratch device has allowed us to directly measure wear rates and has led to the beginning of a fundamental understanding of the micro-wear mechanisms of polymers. We have discovered a subsurface crazing phenomenon in topcoats that occurs in all of the commercial coatings we have studied. The presence of subsurface voids has a profound effect on the visibility of the scratch as well as on subsequent healing and the inevitable degradation of the coating upon environmental exposure. The thresholds for plastic deformation, fracture and the scratch morphology are very sensitive to changes in the chemistry or formulation conditions of the coating. The AFM/microscratch techniques have been successfully applied to many other classes of industrial coatings.

One of the primary functions of industrial polymers and coatings is to protect the underlying material. The coatings are subjected to daily and seasonal fluctuations of temperature and humidity and exposed to environmental contaminants such as acid rain and salt. Automotive coatings are subjected to additional hazards including car washes, road grit, gravel, and keys. Despite the harsh treatment, automotive coatings are expected to maintain a pleasing high gloss finish for at least five years. The present work is focussed on mar or abrasion resistance of automotive topcoats; however, the techniques have been successfully applied to other classes of industrial coatings.

Mar resistance depends on a complex interplay between visco-elastic or thermal recovery, yield or plastic flow, and fracture. Environmental exposure affects

these relationships further complicating their interaction. Polymers are challenging because they exhibit a range of mechanical properties from near liquid through rubbery materials to brittle solids. The mechanical properties are rate and temperature dependent and visco-elastic recovery can cause scratches to change with time.

Many standard tests of mar resistance have been developed over the years (1). We have investigated several of the most common tests with the Atomic Force Microscope (AFM), including wet and dry rub tests, the crockmeter test, and bench top, laboratory scale and full-size commercial car wash tests. All of the tests suffer from two major flaws: (1) the damage is caused by complex uncontrolled multi-asperity contacts and (2) the damage is evaluated optically. Typical optical measurements such as gloss reduction, or changes in gray level of an optical micrograph, give only a qualitative measure of wear with little information about the mar mechanisms.

Single indenter scratch tests abound, but most were designed to study scratch adhesion and are not sensitive or stable enough for studies of mar of polymers. Briscoe et al. (2) have used indentors of various shapes to study polymer wear; however, the indenter radii were too large to produce the characteristic mar damage observed on automobiles. Wu developed a very sensitive micro-scratch instrument that he used to study wear of hard coatings as well as polystyrene (3). The samples were generally quite smooth and the scratches short (<100 μm). Automotive topcoat surfaces can be rough, especially after environmental exposure, and the stability to make centimeter long scratches for appearance correlation studies is necessary (4). An AFM probe can be used to produce and measure scratches on polymer surfaces (5), but quantitative mechanical measurements are very difficult to obtain. Imaging the scratches with the tip that produced them often causes tip artifacts.

Careful integration of a sensitive micro-mechanical instrument with an AFM provides the best of both worlds: quantitative measurement of the mechanical response of the polymer and three-dimensional images of the resulting scratch morphology.

Experimental

We have coupled our own high-resolution microscratch device with a large stage AFM (4). The microscratch instrument produces a scratch and measures the mechanical response of the polymer with micro-Newton sensitivity. (Figure 1) The sample is transferred to the AFM for detailed measurements of scratch morphology. Both systems have precision XY stages and integrated high-resolution optical microscopes and are cross calibrated to ensure registry. Reference indents produced at the time of the scratch experiment or unique features of the scratch morphology make it possible to return to the same location with the AFM (within +/- 100 nm in some cases). Repeated AFM images of the same area provide definitive measurements of the evolution of the scratches after exposure to heat, the environment, or accelerated weathering (7).

The Microscratch instrument uses a 1 μm radius indenter to produce the scratches. The normal force on the indenter is ramped under fast feedback control at 20 $\mu\text{N}/\text{sec}$ as the sample is translated with a velocity of 25 $\mu\text{m}/\text{sec}$. The noise level on the force sensors is better than 5 μN (peak to peak) and the uncertainty on the

displacement measurement is ~ 0.2 nm (4). The Microscratch instrument can also be used as a stylus profilometer due to its exceptional sensitivity. Height profiles before and after the scratch are collected. The penetration depth during the scratch is calculated by subtracting the profile of the undamaged coating from the displacement measured during the scratch. The permanent damage is calculated by subtracting the profile of the undamaged surface from the profile just after the scratch.

The stage travel and reproducibility is periodically checked with a NIST traceable Geller Standard over a distance of millimeters. The AFM piezoelectric translators are calibrated prior to each experiment with a NIST traceable VLSI standard. The AFM probe shape is periodically checked with a silicon nano-edge, a 293 nm Moxtek standard, or an NT-MDT tip calibrator.

The detailed scratch morphology was determined by obtaining high resolution AFM images every few hundred microns for the entire length of the scratch. The numbered vertical lines in Figure 1 indicate the locations of the AFM images. Selected images are collected in Figure 2. Each scan line of each image was statistically analyzed and a variety of scratch morphology parameters (e.g. width, depth, average sidewall angle) was calculated.

Because commercial software for roughness and image analysis was inadequate for detailed statistical measurements of scratch morphology, we developed our own methods. Surface roughness statistics, such as RMS and Ra, cannot describe discrete defects such as scratches. Techniques based on averaging multiple scan lines work well for the uniform features in a microelectronic circuit, but the detail in a complex scratch is lost. In our method, the critical points for the scratch are located for each AFM scan line and scratch morphology parameters are calculated. The results are analyzed over the image to yield parameters such as width and depth, and their statistical variation along the scratch.

Figure 3 illustrates the scratch morphology calculation for Image 9 where heavy and sustained fracture occurs. Scan size is adjusted so that the damaged portion takes up the center third of the image. Feedback parameters and scan speed are adjusted until the left and right scans are as identical as possible over the steep slopes in the image. In each scan line a left and a right inflection point are defined as the first points where the local standard deviation of the height is sixteen times that of the undamaged area. The first and last sixteen points in each scan line are used as the undamaged reference. The local height variation is calculated in a window of sixteen consecutive points which is moved towards the center of the scan line until each inflection point is located. The other critical points are the two highest points on opposite sides of the scratch and the lowest point near the middle of the scan line. The locations of the critical points become less certain as the scratch gets smaller or the coating becomes rougher. Error conditions eliminate any scan line from the statistical calculations if the critical points are ill defined. The two component isocyanate is an exceptionally smooth coating (~ 2 nm RMS) and the scratch morphology parameters are well defined until the scratch depth is below ~ 10 nm.

Once the critical points for each scan line have been located it is a simple matter to calculate the relevant scratch morphology parameters. In Figure 3a the critical points for each scan line are indicated. Figure 3b is the first scan line of the image. The width is defined as the lateral distance between left and right inflection points and is a measure of the total extent of the damaged area. The depth is

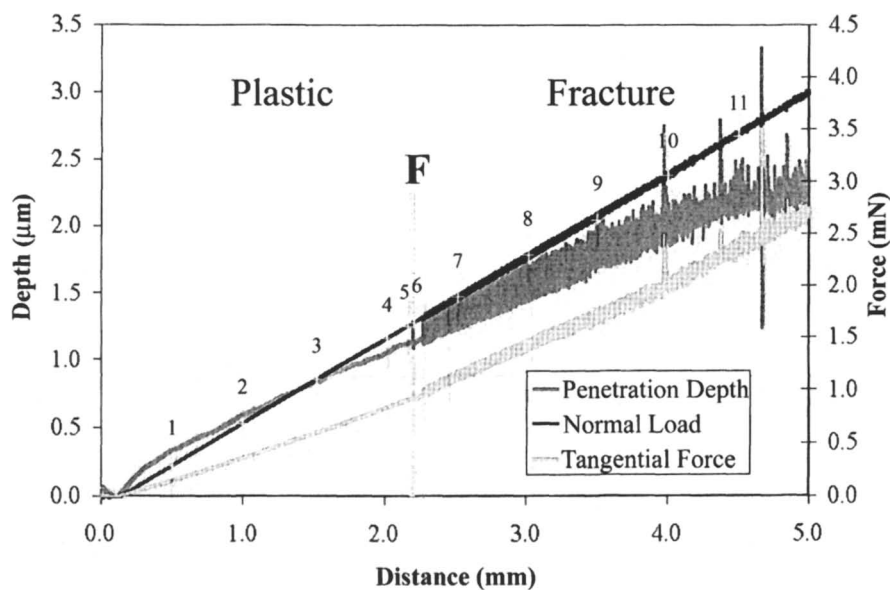


Figure 1. Penetration depth and tangential force measured as the normal force is ramped during a microscratch experiment. The sample is a commercial two component isocyanate topcoat. Note the fracture threshold labeled F and the numbered vertical lines indicating location of AFM images.

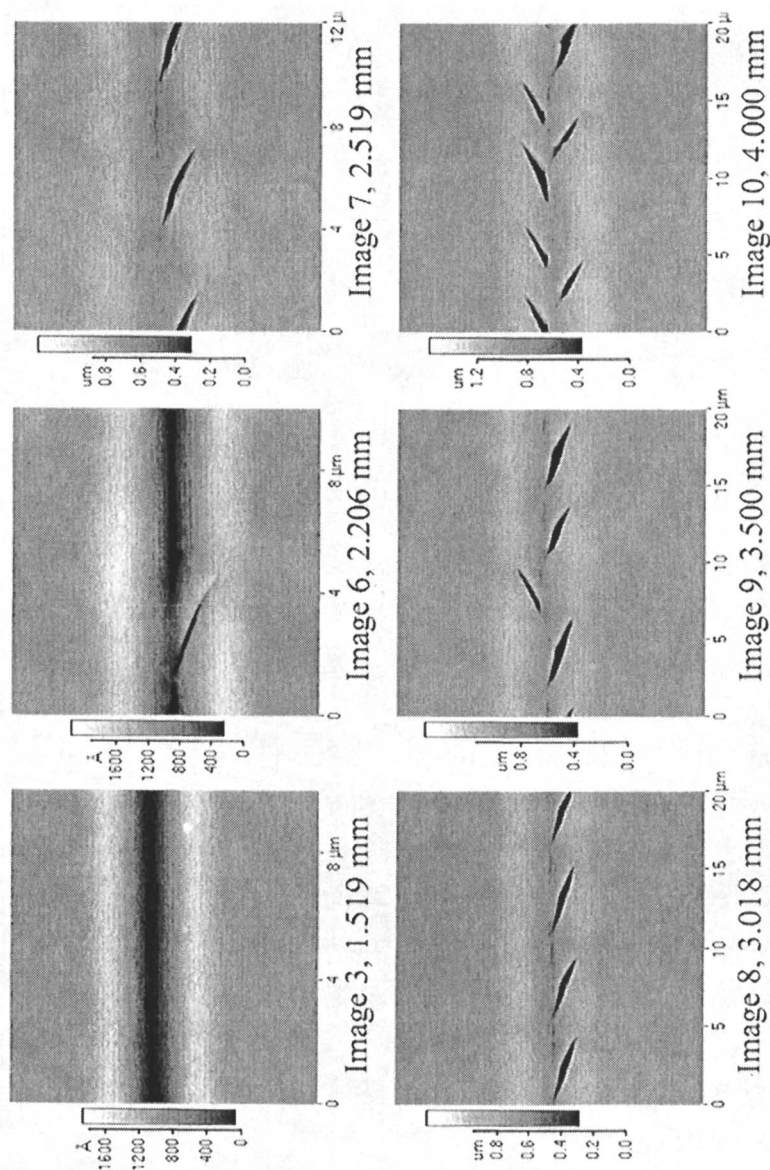


Figure 2. Selected AFM images numbered for reference to other figures. Note different lateral and height scales included with each image.

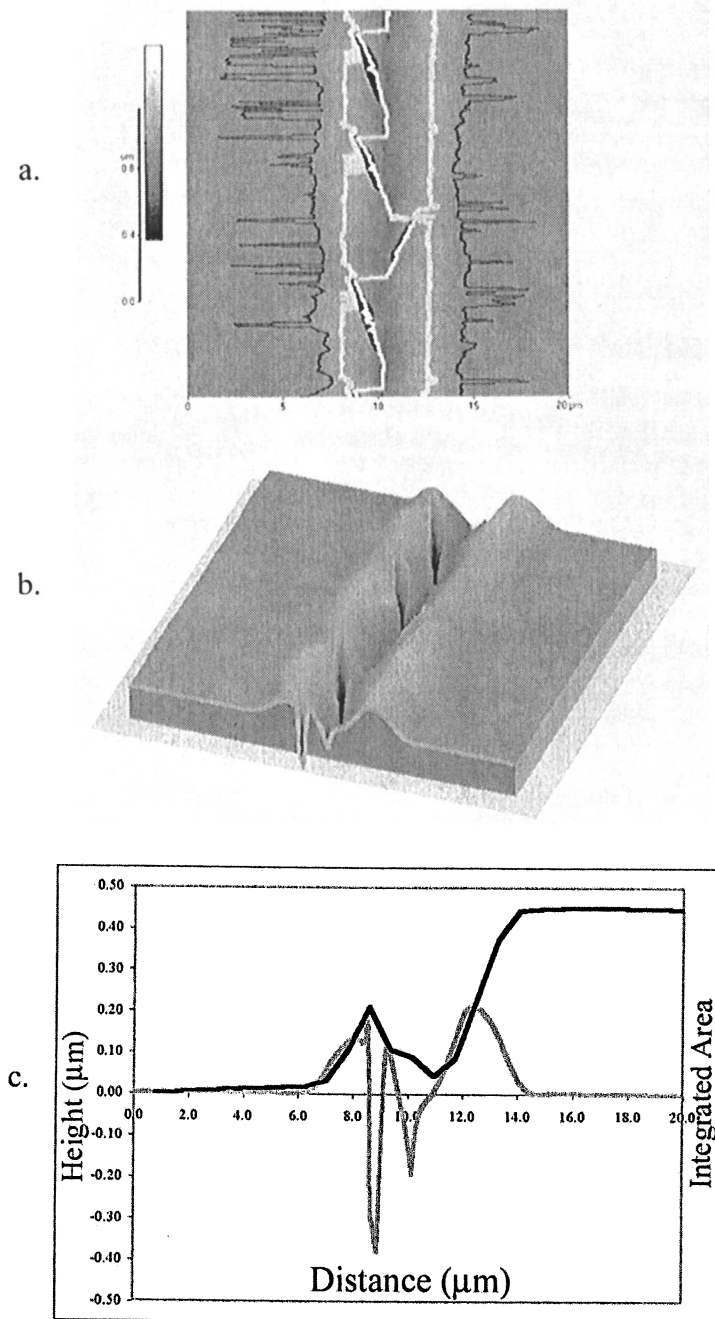


Figure 3. Scratch morphology calculations performed on Image 9. a) Plot of critical points from automated analysis. b) Three dimensional image highlighting scan line used in c) for area integration.

calculated by subtracting the height at the minimum in the scan line from the mean height of the undamaged area. Note that the location of the minimum is not always in the center of the damaged area, especially when fracture occurs. Height measurements from a single scan line or from a stylus profilometer cannot capture this important variation and would be misleading at best. Average widths and depths are calculated from the 256 individual measurements in each image. The standard deviation of the depth (scratch roughness) is also calculated and is a sensitive marker for when fracture begins.

The wear volume is calculated by integrating the deformed area for each scan line (Figure 3c) and summing over the full image. The undamaged area to either side of the scratch again sets the reference height. Any material above that level is defined as positive and compressed, displaced or removed material is negative. Wear rate is the wear volume divided by the length of the scratch in the image. The units for wear rate are cubic microns per micron.

The sample described herein is a typical steel substrate painted using standard automotive spray equipment. There are four paint layers: first the e-coat, then primer, basecoat and finally the top or clear coat. The topcoat is a commercial two component isocyanate (2k-iso) ~30 μm thick.

Results and Discussion

A polymeric coating can respond to forces exerted during a scratch in one of three ways: elastic or visco-elastic deformation, plastic deformation or fracture. The combination of sensitive mechanical measurements and high resolution three-dimensional AFM images gives information about the onset and extent of each mode of deformation as coating chemistry and formulation conditions are varied. Not only are the thresholds for initial deformation and fracture very sensitive to changes in the coating, but the morphology of the scratch and the resulting appearance change as well.

The visibility of a scratch depends on many things including the size of the plastic zone and the detailed morphology of fracture. Harder more brittle coatings tend to have smaller zones of plastic deformation that are difficult to see, but fracture occurs at lower loads and causes a step change in the visibility. Softer coatings tend to dissipate more energy before fracture, generally leading to higher fracture thresholds, but they yield much earlier and the larger size of the plastic zone makes the scratch more visible (6). For certain coatings, as the normal force increases debris is generated which also contributes to the visibility. The 2k-iso topcoat is relatively soft and shows large and distinct plastic deformation. Fracture is regular and periodic and debris generation is minimal.

There are two distinct regimes in both the micromechanical measurements and in the scratch morphology plots.(Figure 4) The transition point is unambiguously and precisely determined from either the microscratch force and displacement curves or from the AFM scratch morphology measurements. The transition point, labeled F in the figures, is at a scratch distance of 2.201 mm which corresponds to a normal force of 1.64 mN. During the creation of the scratch there is an abrupt fluctuation of the displacement and the tangential force (Figure 1) and at precisely the same scratch distance the AFM images show the first rupture or fracture of the coating.(Figure 2,

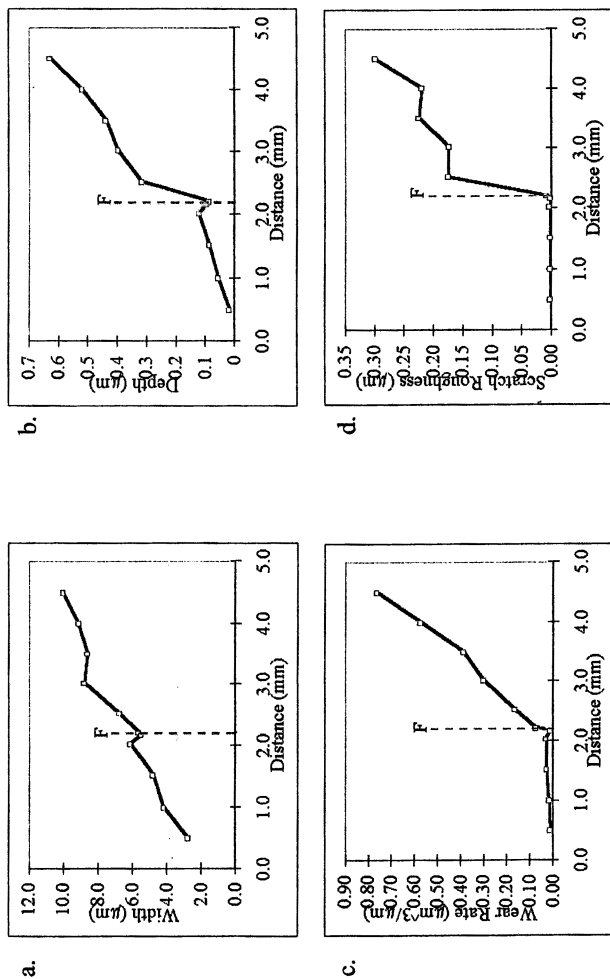


Figure 4. Scratch morphology parameters plotted as a function of scratch distance. Note abrupt change in depth, scratch roughness and wear rate at point labeled F (2.201 mm).

Image 6) All the images collected from before the transition point have smooth regular sidewalls, similar to Image 3, characteristic of pure plastic deformation. The scratch size, width and depth calculated from the AFM images (Figure 4a and b), exhibits a monotonic increase throughout this plastic region. The wear rates are small and positive, and the error bars on the measurement are less than the size of the data points. The exact reason for the positive wear rate in the plastic region is unknown, but may be due to large visco-elastic relaxation that occurs with this coating or perhaps even to incipient cracks or crazes that occur at low stresses. Scratch roughness, the variation of the depth, is steady at 1-2 nm in the plastic regime equal to or slightly below the roughness of the coating itself.

Above point F fracture occurs in a regular and periodic manner. Figure 5 is an expanded region from around the transition point in Figure 1. The locations of images 5, 6, and 7 are also indicated on the figure. Larger scale AFM images show the precise registry between the AFM measurements and the Microscratch measurements.

The wear volume calculation provides insight into the nature of the fracture event. Figure 2 is a collection of AFM images from along the scratch. The morphology evolves from smooth plastic deformation in image 3 to a single fracture event in image 6. As the applied normal load increases, the rate of fracture increases. The rate of fluctuations of the tangential force and penetration depth in Figure 1 continues to increase until they appear almost sinusoidal. At a scratch distance of 2.5 mm (Image 7) there are two complete fracture events, each one is slightly larger than the one in image six. By Image 9 (3.5 mm) crevices appear on both sides of the scratch and each opening is larger and deeper. Eventually the fracture is so rapid that the regularity of the force and displacement fluctuations is lost.

The trend towards deeper and more gaping crevices as the normal load increases (Figure 2) is due to ever larger subsurface defects and to increasing residual stress in the coating surface. The effect of residual stress is to hold open each crevice. Gentle heating above T_g of the polymer will relax the surface and AFM images show the collapse of the periodic ruptures in the film (6). The scratch roughness (variation in depth) in Figure 4d captures some of this aspect of the change in morphology. However, it is very likely that the AFM probe is not penetrating to the deepest point in each crevice, therefore the true depth of fracture is larger than the AFM measurements suggest.

Some of this "missing" information is captured by the integrated area for each scan line used in the wear rate calculation. Figure 6 is a plot of the integrated area as a function of distance for selected images. The periodic nature of the fracture events is apparent through images 7 and 8, as is the loss of regularity as the fracture events overlap in images 9 and 10. The wear rate for image 3 is $0.028 \mu\text{m}^3/\mu\text{m}$ and every scan line has approximately the same integrated area. The wear rate calculated from just prior to the fracture event is $0.013 \mu\text{m}^3/\mu\text{m}$, but just 40 μm later the wear rate jumps to $0.076 \mu\text{m}^3/\mu\text{m}$. The AFM image of the first fracture event (Image 6) shows a single crevice opening in one sidewall which extends 108 nm deep. The sidewall on the opposite side bulges out because the indenter plunges deeper into the coating as the feedback control attempts to maintain the normal force. Some fluctuation in normal force occurs due to the rapid onset of each rupture. When this first fracture event occurs there is an increase in the integrated area in the region prior to and along the visible crevice. (Compare Figure 2 and 6 for Image 6) This suggests that the

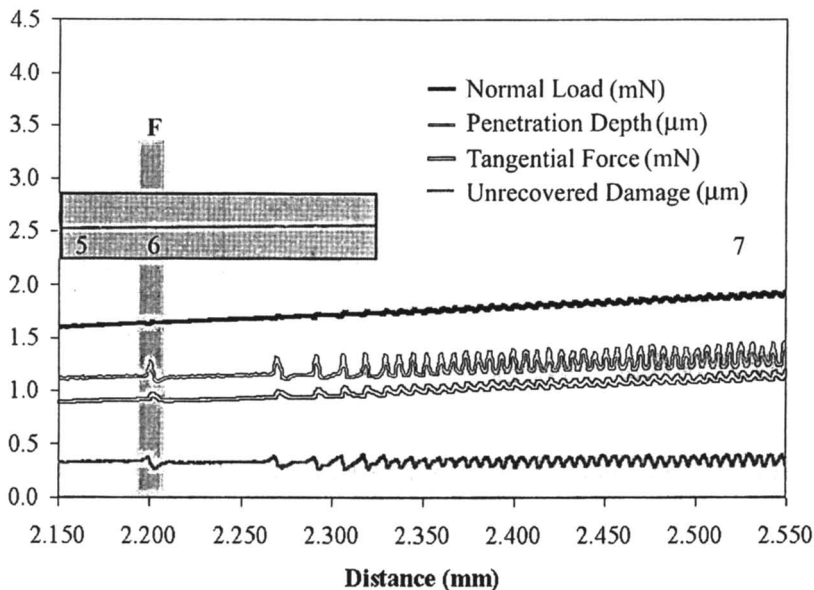


Figure 5. Expanded region around the fracture threshold from Figure 1. Fragments from Lower resolution AFM images are included to highlight precise correlation between AFM and Microscratch Instrument.

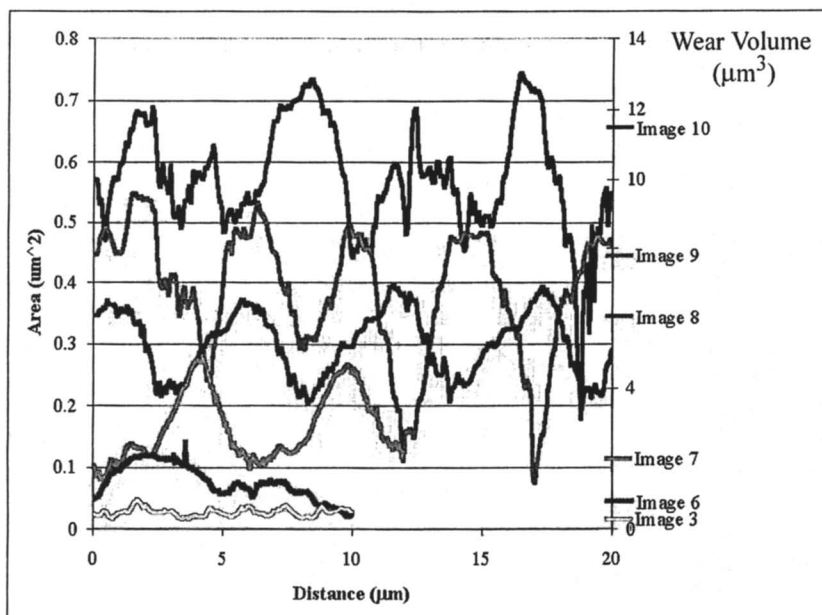


Figure 6 Integrated areas from AFM scan lines plotted vs. distance. Total wear volume for each image plotted on secondary axis.

additional volume is from a pore which extends beneath the surface towards the beginning of the scratch.

A positive wear rate during an abrasion experiment is certainly a surprising result! Material is moved by the ploughing action of the indenter, but over the small AFM image the net transfer (in vs. out of the ten micron region of the scratch) is not enough to account for the observed volume change. Each crevice in the AFM image is the opening to a much larger pore that extends microns deep into the coating. The excess volume in the image of the first fracture event (Image 6) is on the order of one cubic micron ($0.076 \mu\text{m}^3/\mu\text{m} \times 10 \mu\text{m}$ image) but can increase to over fifteen cubic microns at higher loads. The crevice in the AFM image is $2.9 \mu\text{m}$ long and $0.25 \mu\text{m}$ wide (Figure 2) and is consistent with an oblate sphere shaped pore of 1-2 μm radius. Ultramicrotomy/TEM of the scratch confirms the presence of football shaped openings beneath the surface (4).

In a two-component isocyanate topcoat, the fracture is generally even and periodic and the wear rate increases monotonically up to 20 mN.(Figure 1) The amplitude of the force fluctuations and the regularity of the fracture event is lost at the higher loads (4). The chemistry of other topcoats e.g., acrylic melamine, exhibit the same abrupt transition from plastic to fracture and the same rapid positive increase in the wear rate (4, 6). However, the increase in wear rate is neither smooth nor monotonic. Large swings in magnitude have been observed, and the wear rate eventually begins to decrease back towards zero as the load increases. When a scratch is produced on an acrylic melamine, debris is generated which clings to the indenter and the surface. On the more brittle melamine systems the fracture events are random and quickly overlap in the force measurements. As the cracks get larger and closer together, they eventually meet under the surface and a loose chip is created. The AFM images and the calculated scratch morphology parameters reflect the loss of material. Debris generation and chipping are more severe failure modes that create easily visible scratches.

Conclusions

The combination of a precision, large-stage AFM with a high-resolution microscratch device has allowed us to directly measure wear rates and has led to the beginning of a fundamental understanding of the micro-wear mechanisms of polymers. AFM confirms that each force and displacement fluctuation observed during the scratch are a direct result of a fracture event. We have discovered a subsurface crazing phenomenon in topcoats that occurs in all of the commercial coatings we have studied. The presence of subsurface voids has a profound effect on the visibility of the scratch (4) as well as on subsequent healing and on the inevitable degradation of the coating upon environmental exposure (7). The thresholds for plastic deformation, fracture and the scratch morphology are very sensitive to changes in the chemistry or formulation conditions of the coating. Even subtle changes with aging can be monitored with the new scratch techniques. Information from our studies is critical to the development of the next generation of automotive topcoats.

Acknowledgments

The authors would like to acknowledge B.V. Gregorovich for helpful conversations and S.A. Riggs for her AFM contributions.

Literature Cited

1. Gregorovich, B.; Mcgonigal, P.J. *SME technical paper*, **1993**.
2. Briscoe, B.J.; Evans, P.D. *Composites Science and Technology* **1989**, *34*, 73.
3. Yang, A.C.-M.; Wu, T.W. *J. Materials Sci.* **1993**, *28*, 955.
4. Lin, L.; Blackman, G.S.; Matheson, R.R. *Microstructure and Tribology of Polymer Surfaces*; ACS Symposium Series **1999**.
5. Bhushan, B.; Israelachvili, J.N.; Landman, U. *Nature* **1995**, *374*, 607.
6. Lin, L.; Blackman, G.S.; Matheson, R.R. *to be published*.
7. Lin, L.; Blackman, G.S.; Adamsons, K.A. *to be published*.

Chapter 16

Surface Nanochemical Studies of Polymers and Other Organic Surfaces by Scanning Force Microscopy

Kirill Feldman, Georg Hähner, and Nicholas D. Spencer

**Laboratory for Surface Science and Technology, Department of Materials,
ETH-Zürich, Switzerland**

The nanochemical characterization of organic/polymer surfaces is an increasing technological need that cannot be met by current ultrahigh vacuum, charged particle analytical approaches. The high spatial resolution of scanning force microscopy offers the possibility of making measurements on a nanometer scale relatively simply. In the case of species displaying different pK_a values that are within a reasonable range, electrostatic contrast may be used in order to distinguish between surface species (such as COOH and CH₃, for example), when the sample is examined by lateral force microscopy. In the case of most polymers, however, a more promising approach is to obtain contrast by measuring a combination of van der Waals forces and (for polar polymers) H-bonding and polar effects. This can be used to distinguish components of certain polymer blends, for example. In the case of distinguishing between non-polar polymers, the pull-off forces measured by AFM can be calculated by applying the appropriate contact mechanical model, provided that this series of polymers exhibits similar mechanical properties. Under this condition, the pull-off force is proportional to the work of adhesion, which can also be calculated from Israelachvili's approximation to the Lifshitz theory of van der Waals interactions, leading to the observation that pull-off force increases with refractive index of the polymer.

Chemical differences between organic surfaces can frequently be distinguished by AFM approaches, provided that the situation is not dominated by the effects of mechanical properties.

In many high technologies, the trend towards submicron morphological and chemical structures continues apace. The need to be able to characterize such systems on the nanometer scale is therefore of increasing importance. For metals and semiconductors, this has been achieved by means of well-developed ultrahigh vacuum surface science methods, such as field-emission scanning Auger spectroscopy, which is now virtually commonplace on chip-fabrication lines. In the case of insulating systems, such as oxides or organic surfaces, there remains a considerable gap between our ability to characterize a surface morphologically and our capabilities for analyzing the nanochemical structures on a surface. This is chiefly due to the reliance of most traditional surface analytical approaches on the use of charged particles in ultrahigh vacuum.

In the case of many systems in the areas of biosensors and implants, surface nanochemical imaging of organic surfaces (and often polymers and especially polymer blends) is becoming a critical need that needs to be met by new approaches. One of the most promising directions seems to be the application of scanning probe methods, such as atomic and lateral force microscopy (AFM and LFM) to distinguish between (and image) chemically different areas on an organic surface. Much research in this area has focussed on functionalizing AFM tips, in order to be able to monitor particular surface species via a characteristic interaction between the surface and the immobilized functionality. The vast majority of such studies has involved the characterization of flat, organic surfaces, frequently prepared by self-assembled monolayer (SAM) techniques (1-8). SAMs represent ideal model systems for investigating organic surfaces. Their relevance as models for polymers is questionable, however, since, as generally prepared, they present a concentrated plane of functionality with restricted mobility that is rarely found on a polymer surface.

In this article, we describe the use of chemical imaging methods that rely on physical interactions (such as electrostatic and van der Waals) between chemically defined tips and organic surfaces, and focus on some of the problems that are specific to the nanochemical characterization of polymer surfaces.

Experimental

Experimental details have been described at length in references (9), (10), and (11). Force-distance measurements and lateral-force imaging were performed with a scanning probe microscope (Nanoscope III Multimode, Digital Instruments, USA) equipped with a liquid cell and enclosed in a thermally equilibrated environment. Silica-coated tips were prepared by oxygen-plasma treating Si_3N_4 Microlevers (Park Scientific Instruments, USA).

Isotactic polypropylene (i-PP), poly(vinylidene fluoride) (PVDF), and poly(tetrafluoroethylene-co-hexafluoropropylene) (FEP) films were first prepared from foils made by pressing powders between aluminum sheets above their corresponding melting temperatures. The films obtained were then pressed between plasma-cleaned silicon wafers (once again, above their melting temperatures) to achieve low surface roughness. Thin films of the other polymers were prepared by spin casting 2 wt. % solutions onto plasma-cleaned silicon wafers followed by drying

in a vacuum oven at 120°C for 24 hours. The thicknesses of the produced films were on the order of 50-100 nm, as measured by ellipsometry. The measured surface roughness of all films was close to that of the silicon substrates.

Microcontact printing (12-14) of self-assembled monolayers was carried out using a patterned polydimethylsiloxane stamp to print a 2mM ethanolic solution of the relevant thiol onto gold-coated silicon substrates.

Tip-Surface Interactions

Electrostatic Forces—The AFM Tip. The most frequently used commercial AFM tip consists of microfabricated silicon nitride. Under normal laboratory conditions, this is, in reality, an ill-defined, hydroxylated melange of silicon oxynitride and silicon dioxide, the precise composition of which depends on a combination of manufacturing conditions and tip history. An isoelectric point of around pH=5 has been frequently observed in force-distance measurements under electrolyte in our laboratory (15), suggesting the oxidized oxynitride composition mentioned above. In order to achieve a better reproducibility, however, we have adopted an oxygen plasma-treatment procedure, which leaves the tip coated with hydroxylated silica, as evidenced by an isoelectric point of around pH=3 (16), as measured by force titration (15).

Electrostatic Forces—Organic Surfaces. The characteristic amphoteric behavior of oxide surfaces with pH has been exploited by Marti et al (9,15) in order to distinguish between different oxides on an inorganic surface with submicron resolution. In this approach, charge-charge interactions between the oxidic surfaces of tip and sample under electrolytes lead to a modification of the total normal force between the surfaces and thus to a frictional contrast between areas on the surface of different charge.

A similar effect can also be observed with some organic surface species, where the pK_a of the surface-bound molecule leads to a characteristic acquisition of surface charge at a particular pH (17). Such an effect is particularly useful in cases such as that displayed in Figure 1, where a species with a moderate pK_a (-COOH-terminated hexadecane thiol) can be readily distinguished from a species that only dissociates under extreme conditions (methyl-terminated hexadecane thiol). In order to exploit this effect, however, the chemical species to be distinguished must display appropriate dissociative behavior, which is, of course, not necessarily the case. The convenient spectrum of isoelectric points that can be used for identification purposes in oxide systems (15) is not mirrored in the organic world, where amphoteric behavior is the exception rather than the rule.

Although many polymer surfaces tend to acquire charge in an aqueous environment (18), the same technique is not readily applicable for polymers, since polymer films are in general not as smooth and flat as films made from SAMs such as thiols. Roughness and degree of crystallinity contribute to the observed signal for nearly all modes of AFM operation, such as LFM and pull-off force measurement. The signal due to mechanical effects hence, in general, overwhelms the chemical signal.

Care must always be exercised in ascribing observed contrast to purely chemical effects. Significant contrast in a patterned CH_3-COOH system can be observed in

ambient air due to different capillary forces sensed by the tip on the hydrophilic and hydrophobic areas (14).

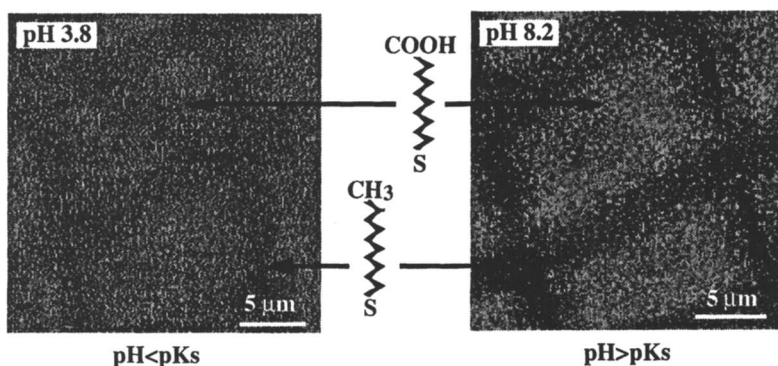


Figure 1. Lateral force images of a monolayer of alkanethiols with differently functionalized endgroups (produced by microcontact printing). Images were recorded in 1mM NaCl solution for different pH values. A change in friction contrast due to the deprotonation of the acid groups is clearly visible.

More subtle factors may also lead to contrast in LFM images, which might erroneously be interpreted as being due to chemical effects. This is illustrated by the following example: A chemically homogeneous film was prepared by microcontact printing a pattern of CH_3 -terminated thiols and subsequently “filling in” the non-printed areas by immersion in the same thiol solution (11,19). Despite the chemical uniformity, the stamped pattern contrasted distinctly with the immersed region in LFM images (Figure 2).

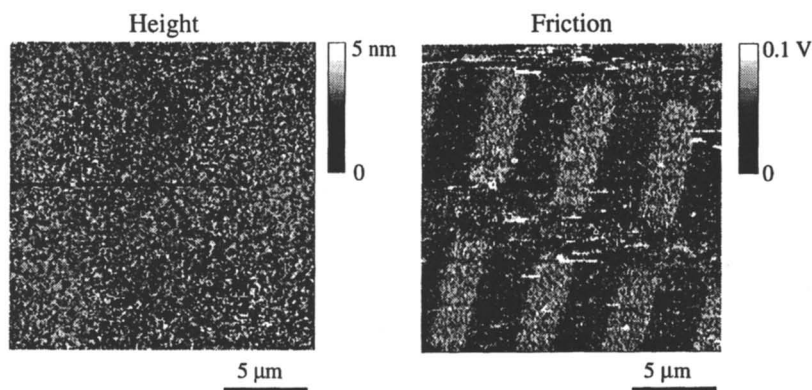


Figure 2 Height (left) and friction-force (right) images for a sample that was prepared by microcontact printing with a 2-mM solution of hexadecanethiol in ethanol, followed by immersion into a 2-mM solution. Regions that are darker in the friction image were prepared by microcontact printing. Reproduced from ref. (11), © 1997 American Vacuum Society.

NEXAFS measurements showed, however, that the order and orientation of the differently prepared areas shown in Figure 2 were very similar (9). The contrast seen in LFM between the stamped and immersed regions was interpreted as resulting from slightly different domain sizes (i.e. different concentrations of domain walls) in the differently prepared areas, since the domains are in the same size range as the contact area between tip and surface. In this case, contrast results from the different *mechanical* properties of the differently prepared areas of the film.

Van der Waals Forces. In addition to electrostatic forces, an important set of interactions to be considered in an AFM experiment comprises the van der Waals forces, which, although not as strong as coulombic interactions, are always present. The work of adhesion per unit area, W , may be calculated from the following equation (20):

$$W = A_{total}/12\pi D_0^2 \quad (1)$$

where $D_0 = 0.165$ nm is the commonly used value for the cutoff separation (20), and A_{total} is the non-retarded Hamaker constant, which can be estimated for two macroscopic dielectric bodies interacting across a medium using Israelachvili's (20) approximation to the Lifshitz (21) theory of van der Waals forces (I-L theory). This approximation utilizes bulk dielectric properties, namely refractive indices and static dielectric constants of the interacting bodies and the medium, to calculate the dispersion (London), and combined dipole/dipole (Keesom) and dipole/induced-dipole (Debye) contributions to the overall Hamaker constant. The I-L theory has several important consequences for AFM measurements:

1. The strongest attractive dispersion interaction is anticipated in vacuum or air. However, force-distance measurements in air are dominated by capillary forces (22) due to the presence of contaminant layers on the surfaces of probe and sample. For this reason, force-distance measurements with SPM techniques are often performed in vacuum or under liquids.
2. If the refractive index of the medium falls between that of the tip and surface, the van der Waals force becomes repulsive—this effect can be utilized for reducing the potentially damaging force exerted by the AFM tip on delicate biological samples, such as DNA (23). Manipulation of the sign of the van der Waals force is also described in (24).

It must be borne in mind that the observed overall resulting force will be a superposition of many different types of interaction, including electrostatic and van der Waals forces, as well as others, such as hydrophobic interactions and steric repulsion.

Force Measurements on Polymers

Non-Polar Polymers. The ability to distinguish between polymers of differing refractive index was tested (10) by measuring pull-off forces between a silica tip and a series of four non-polar polymer samples in perfluorodecalin (a non-polar, low-refractive-index liquid, $n=1.317$): polystyrene (PS, $n=1.582$), isotactic polypropylene

(iPP, $n=1.501$), poly(vinylidene fluoride) (PVDF, $n=1.407$), and poly(tetrafluoroethylene-co-hexafluoropropylene) (FEP, $n=1.348$). Using the same tip, some 1000 force curves were obtained for each polymer, and a histogram plotted (Figure 3).

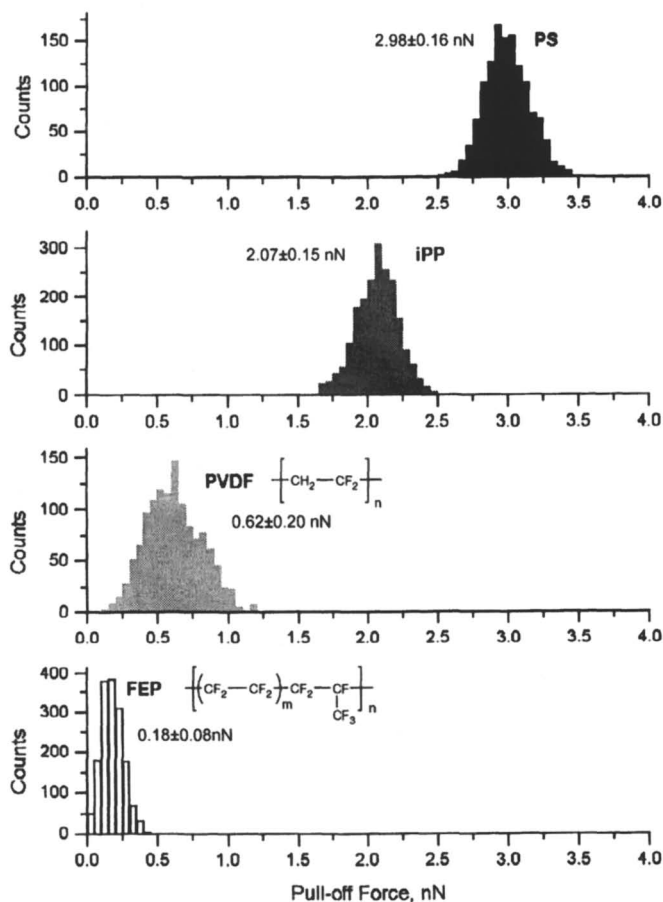


Figure 3 Histograms of pull-off forces measured between a SiO_x probe and PS, i-PP, PVDF, and FEP surfaces in perfluorodecalin. Reproduced from ref. (10) © 1998 American Chemical Society.

For non-polar polymers interacting with a silica probe under perfluorodecalin the Hamaker constant scales with the refractive index. This leads to the observation that the polymer with the highest refractive index shows the largest pull-off force. In fact, calculating the work of adhesion, W , from Eq. 1, and plotting the measured pull-off forces against this quantity, one sees a reasonable correlation (Figure 4), as would be expected from the appropriate contact mechanical models (25).

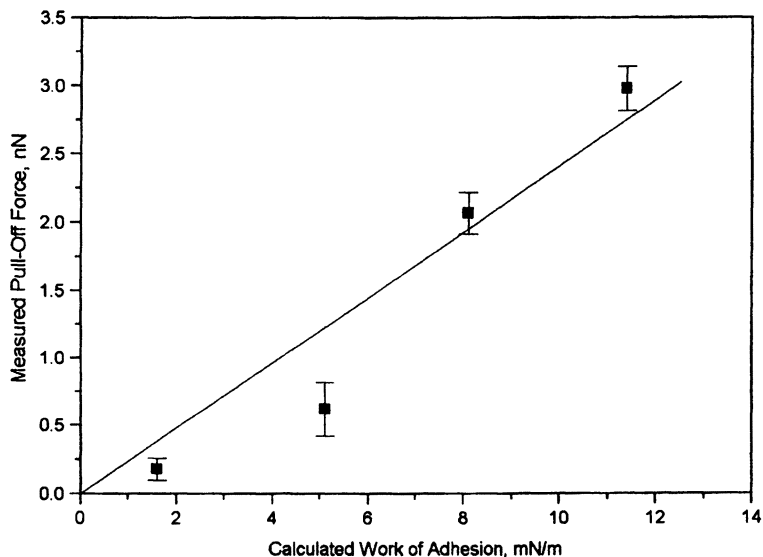


Figure 4. Comparison of measured pull-off forces and calculated work of adhesion for interactions between a SiO_x probe and PS, i-PP, PVDF, and FEP surfaces in perfluorodecalin. Reproduced from ref. (10) © 1998 American Chemical Society.

Polar Polymers: the Involvement of H-Bonding and other Effects. In the case of polar polymers, the situation is more complicated, since the I-L theory is no longer applicable. This is due to the fact that the theory concerns bulk properties that are no longer relevant when surface effects, such as the rearrangement of surface polar groups, are present.

In addition, hydrogen bonding between the -OH groups and bound water on the silica tip and the polymer surface may occur, which is not included in the approximation described above. The results can nevertheless be useful in a semiquantitative way, especially if one compares the interaction between a given polymer sample and tips of differing polarity.

This was demonstrated for the series of polymers: polystyrene (PS), poly(acrylonitrile) (PAN), poly(methyl methacrylate) (PMMA), and polyacrylic acid (PAA) using silica-coated and clean gold tips. The histograms of the pull-off forces (10) are shown in Figure 5, indicating that polymers with different functionalities can be chemically distinguished, provided that the mechanical properties are similar.

In the case of PMMA, it is possible that surface rearrangement could be taking place (placing either methyl or methacrylate groups towards the surface) in order to maximize the interaction with both polar and non-polar probes. The breadth of some peaks (e.g. PAN) compared to others can be ascribed to partial crystallinity of the material.

Nanochemical Imaging of Polymers and Organic Films

In general, mechanical and chemical contributions are jointly responsible for the contrast observed in images of heterogeneous systems recorded with the atomic force microscope for nearly all different modes of operation (lateral, TappingMode, force mapping, phase imaging, etc.). These contributions are convoluted, and there is no standard way to separate them unambiguously. While on ultrathin, especially monolayer, films a distinction between chemically different regions can often be made by functionalizing the tip or changing the medium of the environment, the same is not generally valid for polymers. However, in cases where the mechanical properties of polymers are comparable a chemical distinction is possible.

Due to the convolution problem described above, the quantitative AFM nanochemical imaging of polymers is difficult. Nevertheless, the approach can be used to *distinguish* between polymers in a blend. Examination of the histograms in Figure 5 shows that in the case of the polymers PS and PMMA, for example, the ranking of pull-off forces is reversed between gold and silica-coated tips. Since frictional forces often tend to vary monotonically with pull-off force, these rankings might be expected to translate into a reversal of contrast between PS and PMMA, when comparing lateral (frictional) force images obtained by a silica or a gold tip. This is indeed what is observed: In Figure 6, AFM and LFM images of a spin-coated PS-PMMA (1:10 w/w) blend (zero applied load, under perfluorodecalin) are shown. In the case of gold tips, greater friction is observed on the (non-polar) PS regions, whereas in the case of silica tips, the situation is reversed. The edge resolution of the PS islands is much better than 100nm—a result unobtainable by current charged-particle-based UHV surface analytical methods.

In summary, there is no standard recipe for extracting chemical information for polymer surfaces on a nanometer scale: Each case has to be examined on its own merits. The choice of medium or the chemical modification of the tip may in some cases greatly facilitate extraction of chemical information. In general, mechanical properties will contribute to the observed signal when imaging and it is difficult to separate these contributions from those due to chemical effects, for nearly all modes of AFM operation. While a chemical distinction has been achieved in several cases, *identification* of organic surfaces has yet to be achieved by AFM methods.

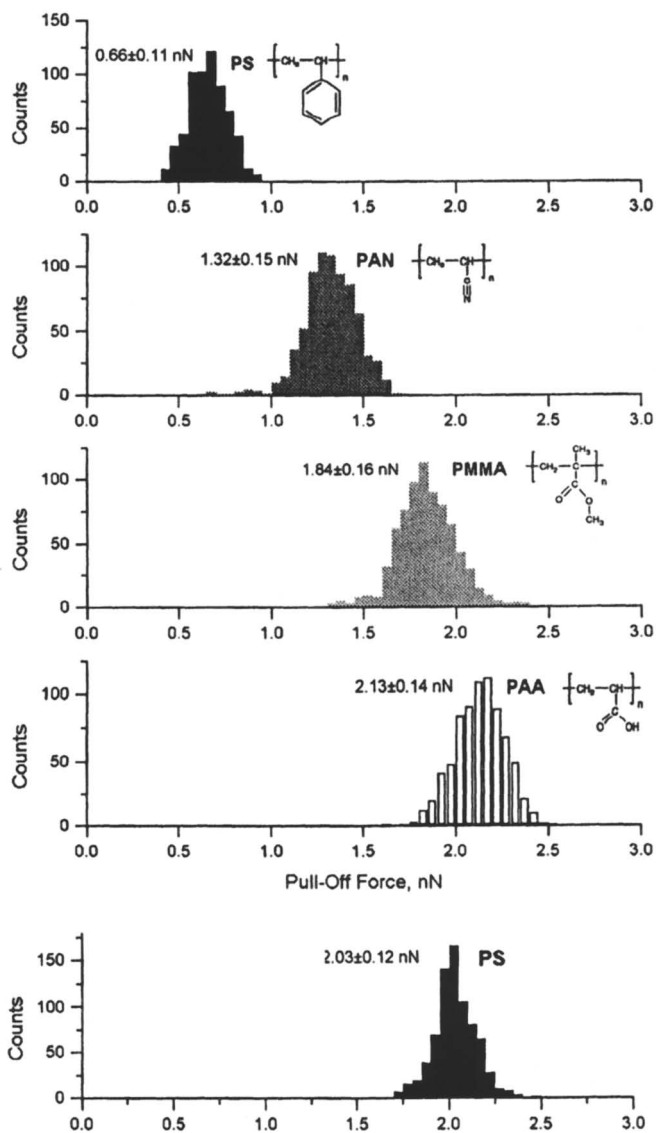


Figure 5 Histograms of pull-off forces measured between a SiO_x probe (top) and gold probe (bottom) with PS, PAN, PMMA, and PAA surfaces in perfluorodecalin. Reproduced from ref. (10) © 1998 American Chemical Society.

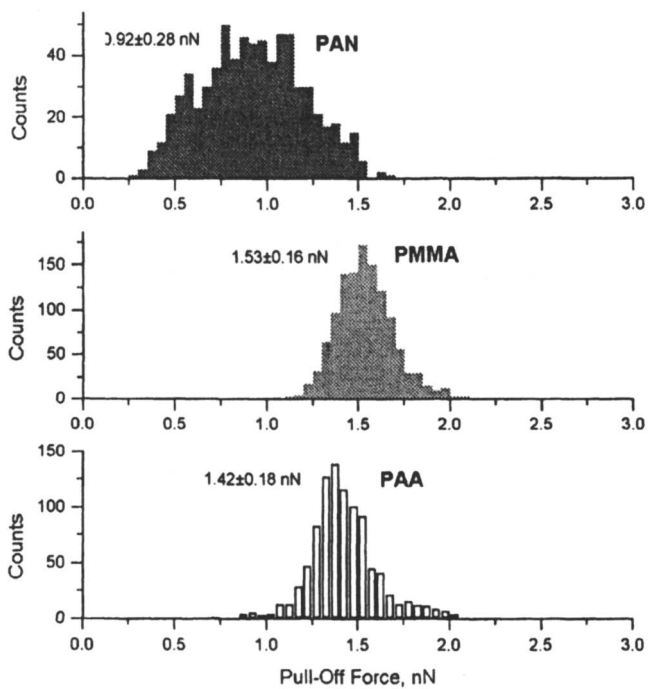


Figure 5. Continued.

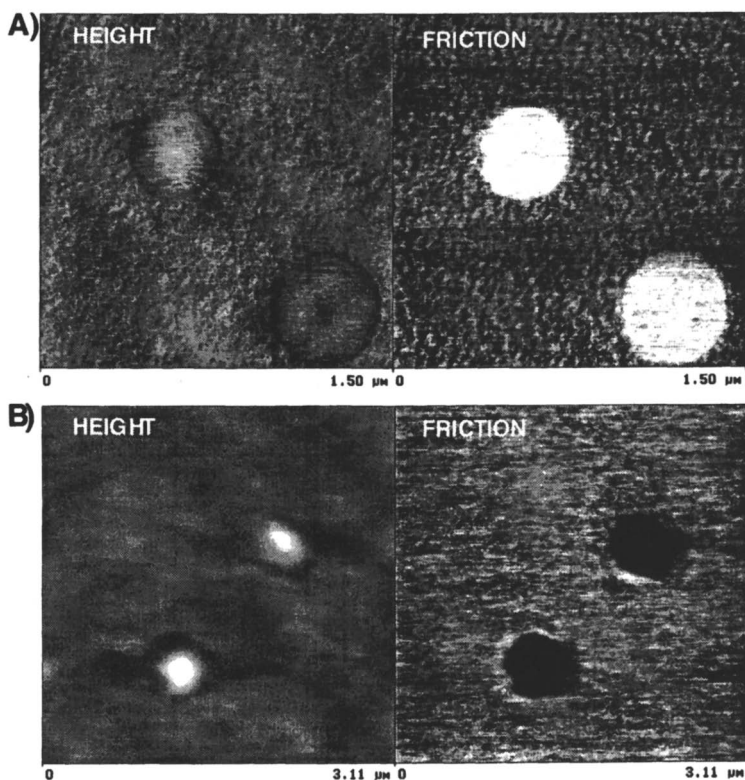


Figure 6 Height (AFM) and friction (LFM) images of a spin-cast polystyrene:poly(methyl methacrylate) polymer blend [PS:PMMA (1:10 w:w)], obtained with a) Gold-coated and b) SiO_x tips under perfluorodecalin. Reproduced from ref. (10) © 1998 American Chemical Society.

Conclusions and Outlook

Scanning force microscopy seems to be a promising approach for studying organic and polymer surfaces, both morphologically and chemically, with high spatial resolution. A number of different forces, such as electrostatic and van der Waals, can be capitalized upon for analysis and/or imaging purposes, but the choice depends critically on the system under study. Of prime importance is the interplay between chemical effects and mechanical properties. In many systems, the latter dominate the situation. In cases where mechanical effects are minimal, chemical contrast can be utilized to provide high-resolution AFM images of heterogeneous organic surfaces.

Acknowledgments

NDS and KF are grateful for funding from the Council of the Swiss Federal Institute of Technology through their Priority Program on Materials and MINAST program.

References

1. Frisbie, C. D.; Rozsnyai, L. F.; Noy, A., Wrighton, M. S.; Lieber, C. M. *Science* **1994**, *265*, 2071.
2. Lee, G. U.; Kidwell, D. A.; Colton, R. J. *Langmuir* **1994**, *10*, 354.
3. Akari, S.; Horn, D.; Keller, H.; Schrepp, W. *Adv. Mater.* **1995**, *7*, 549.
4. Sinniah, S. K.; Steel, A. B.; Miller, C. J.; Reutt-Robey, J. E. *J. Am. Chem. Soc.* **1996**, *118*, 8925.
5. Green, J.-B. D.; McDermott, M. T.; Porter, M. D.; Siperko, L. M. *J. Phys. Chem.* **1995**, *99*, 10960.
6. Han, T.; Williams, J. M.; and Beebe, T. P. *Analytica Chimica Acta*, **1995**, *307*, 365.
7. Lio, A.; Charych, D.H.; Salmeron, M. *J. Phys. Chem.*, **1997**, *101*, 3800.
8. Fujihira, M. In *Micro/Nanotribology and Its Applications*; Bhushan, B., Ed.; NATO ASI Series E: Applied Sciences; Kluwer Academic Publishers: Dordrecht, 1997; Vol. 330, p 239.
9. Hähner, G.; Marti, A.; Spencer, N. D. *Tribology Letters* **1997**, *3*, 359.
10. Feldman, K.; Tervoort, T.; Smith, P.; Spencer, N.D., *Langmuir* **1998**, *14*, 372.
11. Fischer, D.; Marti, A.; Hähner, G. *J. Vac. Sci. Technol.* **1997**, *A15*, 2173.
12. Kumar, A.; Whitesides, G.M. *Appl. Phys. Lett.* **1993**, *63*, 2002.
13. Kumar, A.; Biebuyck, H.A.; Whitesides, G.M. *Langmuir* **1994**, *10*, 1498.
14. Wilbur, J.L.; Kumar, A.; Kim, E.; Whitesides, G.M. *Adv. Mater.* **1994**, *6*, 600.
15. Marti, A.; Hähner, G.; Spencer, N. D. *Langmuir* **1995**, *11*, 4632.
16. Iler, R.K. *The Chemistry of Silica*; Wiley-Interscience: New York, 1979.
17. Vezenov, D. V.; Noy, A.; Rozsnyai, L. F.; Lieber, C. M. *J. Am. Chem. Soc.* **1997**, *119*, 2006.
18. Garbassi, F.; Morra, M.; Occhiello, E. *Polymer Surfaces: From Physics to Technology*, John Wiley & Sons Ltd: Chichester, **1994**; Chapter 1.
19. Bar, G.; Rubin, S.; Parikh, A.N.; Swanson, B.I.; Zawodzinski, T.A.; Whangbo, M.H. *Langmuir* **1997**, *13*, 373.
20. Israelachvili, J. *Intermolecular and Surface Forces*, 2nd ed.; Academic Press: London, 1992; Chapter 11.
21. Lifshitz, E. M. *Sov. Phys.* **1956**, *JETP* *2*, 73.
22. Grigg, D. A.; Russel, P. E.; Griffith, J. E. *J. Vac. Sci. Tech. A.* **1992**, *10*, 680.
23. Hansma, H. G.; Sinsheimer, R. L.; Li, M.-Q.; Hansma, P. K. *Nucleic Acids Research* **1992**, *20*, 3585.
24. Hutter, J.L.; Bechhoefer, J. *J Appl. Phys.* **1993**, *73*, 4123.
25. Maugis, D. *J. Coll. Interface Sci.* **1992**, *150*, 243.

Chapter 17

Molecular Relaxations in Polymer Films Studied by Temperature-Controlled Friction-Force Microscopy

Jon A. Hammerschmidt¹, Greg Haugstad², and Wayne L. Gladfelter¹

¹ Department of Chemistry and ² Center for Interfacial Engineering, University of Minnesota, Minneapolis, MN 55455

Temperature-controlled friction force microscopy (FFM), has been developed to determine the frictional (dissipative) character of thin polymer films. Using FFM variations in friction can be sampled over micron-scale regions and reduced to "friction histograms," yielding the distribution of frictional forces on the surface. The temperature dependence of the mean value of the frictional distribution was correlated to the known α -relaxation (glass-to-rubber transition) and/or secondary relaxation mechanisms of polymer films. The dominant contribution to friction, on polymer films, was attributed to viscoelastic mechanical loss. Using equivalent time scales, measured α -relaxations were found to occur at lower temperatures than bulk polymer values. The frictional response of PMMA displayed time-temperature equivalency upon variation of scan-velocity and temperature. The rate dependence of the hindered rotation of the $-\text{COOCH}_3$ group (β relaxation) in PMMA was consistent with Arrhenius type behavior, allowing calculation of an activation energy. The activation energy was found to be lower than measured bulk energies.

The tribological properties, in particular friction, of polymers are known to have a large, even dominant contribution from internal viscoelastic dissipation (1), which ultimately is derived from molecular relaxation. Traditionally this has been characterized by macroscopic measurements of rolling friction as a function of velocity and/or temperature (1,2). These rolling friction experiments mapped out a response similar to bulk viscoelastic loss tangent ($\tan\delta$) data, an expected result considering the thick ($>100\ \mu\text{m}$) polymer films and large probing depths employed. Dynamic techniques which measure $\tan\delta$ as a function of temperature, where δ is the

complex phase of the viscoelastic moduli, generally display several broad peaks corresponding to different classes of molecular relaxation (3,4). With each class of relaxation encompassing a sizable range of relaxation times (3,4). Typically three broad relaxational peaks are observed, prior to the melting transitions, in polymer viscoelastic loss tangent measurements as a function of increasing temperature or time (4). Secondary relaxations, which can be chain rotations, torsions, or local mode relaxations, are conventionally labeled γ and β , whereas the glass transition (T_g), reflecting rubbery behavior, is commonly assigned as the α relaxation.

With the emergence of friction force microscopy (FFM) (5), a type of scanning probe microscopy (SPM) that measures the lateral force on a probe caused by sliding friction, the ability to probe frictional processes at the nanometer scale is possible. Because the probe has a radius of curvature of tens of nanometers, and applied loads are on the nanonewton scale, the true surface layer can be studied under wearless sliding contact. Several studies have made use of this ability, determining the velocity dependence of friction and its relationship to polymer molecular motion on thin films (6-9). Gelatin, polyvinyl alcohol (PVOH), polyvinyl acetate (PVAc), polyethylene terephthalate (PET), and polystyrene (PS) thin films exhibited peaks in the velocity dependence of friction, attributed to the glass-transition or secondary relaxations (reflecting movement of functional groups on polymer chains). The velocity dependence of friction on nominally dry gelatin films displayed a peak in the friction-velocity relationship, which was attributed to the glass-to-rubber transition (T_g) (6). Subsequently, the peak was shifted to higher velocity for increasingly perturbative scanning. Variations in frictional distributions were also recorded. Friction histogram breadth and symmetry reflected the energy dispersion of relaxations characteristic of glassy or rubbery behavior. In another study, an estimated contact diameter of the probe tip as a velocity-to-frequency conversion length scale allowed comparison to tabulated frequency-dependent $\tan\delta$ data (7). This enabled the assignment of the α and/or β relaxation processes for PET, PVOH, PVAc, and gelatin thin films. Kajiyama et al. investigated the rate dependence of friction by varying the molecular weight of polystyrene (8). A transition from glassy to rubber-like behavior with decreased molecular weight was demonstrated, and attributed to excess free volume at the surface induced by surface segregation of chain end groups.

One obstacle of the above experiments was the limited velocity range available in commercial FFM, typically 4 orders of magnitude. It is well known that both the time scale and the temperature affect the overall viscoelastic behavior of a polymer system (10). To date the limitations of *piezoelectric* scanners have restricted the range of temperatures examined to a narrow range near ambient conditions. With newly-designed force microscopes a broader range of temperature variation is now accessible.

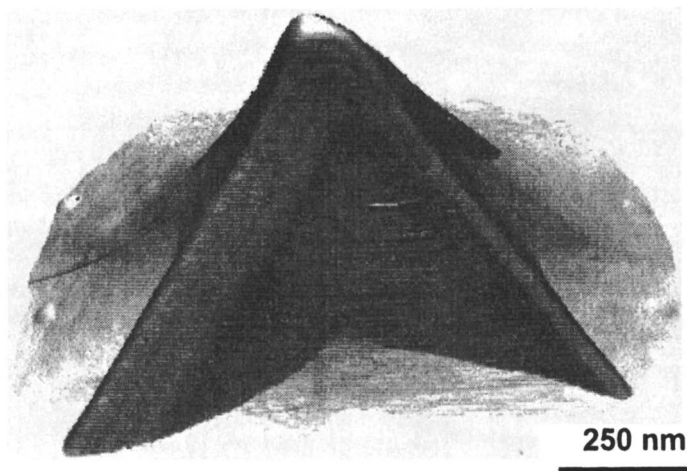
In this chapter we will describe a quantitative methodology allowing determination of the frictional distribution of a polymer surface. We will develop an understanding of friction on polymer film surfaces by examining temperature-dependent behavior, as well as the interplay between time (velocity) and temperature.

Experimental Measurements using Friction Force Microscopy

All film characterization was performed with a Molecular Imaging PicoSPM scanning probe microscope in conjunction with a Digital Instruments Nanoscope III controller. The design of the PicoSPM isolates the sample stage from the piezoelectric scanner and associated electronics, thus allowing for a wide variation in sample temperature, humidity, and atmosphere. Temperature variation is accomplished via a resistive heating stage (temperature range = ambient temperature to 170°C). The temperature stage was calibrated using a k-type micro-thermocouple attached to a bare Si(100) wafer. The sample area was enclosed within an o-ring-sealed glass chamber. A CaSO₄ column in conjunction with a hygrometer and feedback-controlled airflow were used to control the relative humidity (RH) for all experiments between 2-8%, limiting the effect of adsorbed water on the surfaces. Polymer films were equilibrated at these humidities for several hours before collecting images. Park Scientific Instruments uncoated 85- μm silicon cantilevers (spring constant ≈ 0.5 N/m) with integrated sharpened tips were used to characterize the frictional behavior of the polymer films. Reflective coatings were precluded in order to eliminate cantilever bending due to the difference in thermal expansivity of the cantilever and coating material. The probe tip radius of curvature was characterized through the use of a calibration grating (NTMDT). The grating is composed of silicon needles with a radius of curvature of <10 nm. Figure 1a displays a topographic image of one grating needle acquired in contact mode, and rendered as a surface plot. Figure 1b shows a profile of the tip apex from Figure 1a. The topographic profile obtained is a convolution of the grating and probe tip radius of curvatures (r_c) (11,12). From the image profile $r_c=26.8$ nm, containing the sum of tip and grating radii of curvatures. The nominal radius of curvature from the manufacture was approximately 20 nm, in agreement with our measurement attributing for <10 nm contribution from the calibration grating. The radius of curvature for the probe tip used our experiments was therefore estimated at ≈ 20 nm.

Materials. PMMA (Polysciences, MW=60,000, Mw/Mn=1.10), PS (Aldrich, MW=44,000, Mw/Mn=1.10), and PET (Aldrich) films were prepared by spin coating (2000 rpm) 0.25 wt % polymer/solvent solutions onto silicon (100) wafers, which had a native oxide layer. Toluene was used as the solvent for PMMA and PS, and 2-chlorophenol was used for PET. Films were annealed at 100°C under vacuum (≈ 0.01 torr) for 2 hours and allowed to cool under vacuum. Experiments were performed within days of film coating, and 1 day or less after annealing. Film thicknesses were measured using ellipsometry (Sopra) and found to be approximately 21, 12, and 20 nm (± 5 nm), for PMMA, PET, and PS, respectively. Film surfaces were homogeneous with rms roughnesses ≤ 1 nm.

a



b

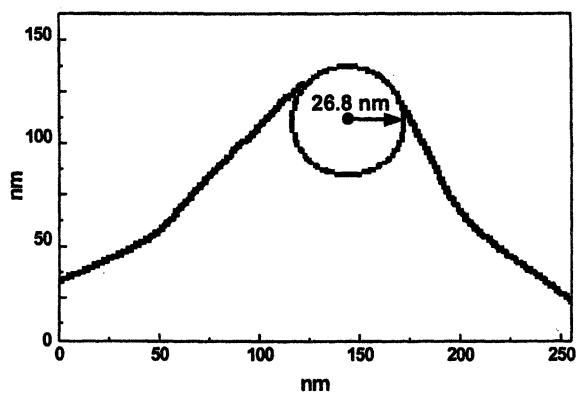


Figure 1. (a) Surface rendered topographic AFM image of calibration grating displaying tip geometry. (b) Profile of calibration grating and radius of curvature measurement.

Experimental Methodology

Figure 2 top displays 3 images which were acquired simultaneously, topography (height), friction (trace), and friction (retrace) on a PMMA surface. Height images were acquired to determine surface roughness, wear, and to gauge any topographic contributions to the lateral force. Forces remained sufficiently low to preclude changes in the measured topography over the course of an experiment, i.e. no discernible wear or roughening occurred. Applied forces were $\approx 10\text{--}15$ nN, and tip-sample adhesive forces were $\approx 15\text{--}30$ nN. The exact values of contact forces were evaluated for each experiment and used in the results and discussion sections.

The frictional force was determined from (one half) the difference of trace (left-to-right) and retrace (right-to-left) 512×512 pixel lateral force images, as indicated in Figure 2. Topographic contributions to the overall lateral force were independent of scanning direction, and thus were removed by the subtraction process. Hysteresis in the scanning position (from trace to retrace images) also was removed by invoking a 1-2 pixel shift between trace and retrace images, yielding a more precise removal of topographic contributions. Image subtraction and shifting was accomplished using customized image processing algorithms. The frictional force was quantified by creating "friction histograms" of the subtracted friction images, i.e. number of image pixels within incremental friction-force intervals (6). This reduces 512 individual scan lines to a "spectroscopic" line shape, as shown in Figure 2, including information on the *distribution* of frictional forces. Images were collected with offset and planefit functions disabled, thereby retaining the zero of lateral force and thus the offset of the frictional peak on the friction force axis. All friction peaks were fit to a Gaussian distribution, as shown (Figure 2), to determine the mean value of the frictional force distribution. Numerous methods of friction force calibration exist (6,13-15), absolute friction forces in our study were determined by utilizing the coefficient of friction for silicon on silicon as a standard (16). All temperature and velocity-dependent frictional data reported herein use one subtracted friction image (512×512 -pixel trace-retrace) per data point. All images, except those used for the velocity/frequency variation study, used a scan size of 4×4 μm and scan frequency of 5 Hz, implying a scan velocity ($2 \times (\text{scan width}) \times (\text{scan frequency})$) = 40 $\mu\text{m}/\text{sec}$.

Figure 3 displays mean friction force as a function of temperature for a Si(100) wafer covered with native oxide. These data were collected as a control and exhibit no substantial temperature dependence within our experimental range. All reported variations in friction, on polymers, as a function of temperature are thus attributed to the properties of the material, or its interaction with the SFM tip.

Temperature Dependence of Friction on PMMA, PET, PS.

The temperature dependence of friction on a PMMA film is shown in Figure 4. "Friction difference" (trace – retrace) images are displayed for 3 temperatures 50°C , 90°C , and 110°C (Figure 4a). All three images have the same Z (friction) scale and

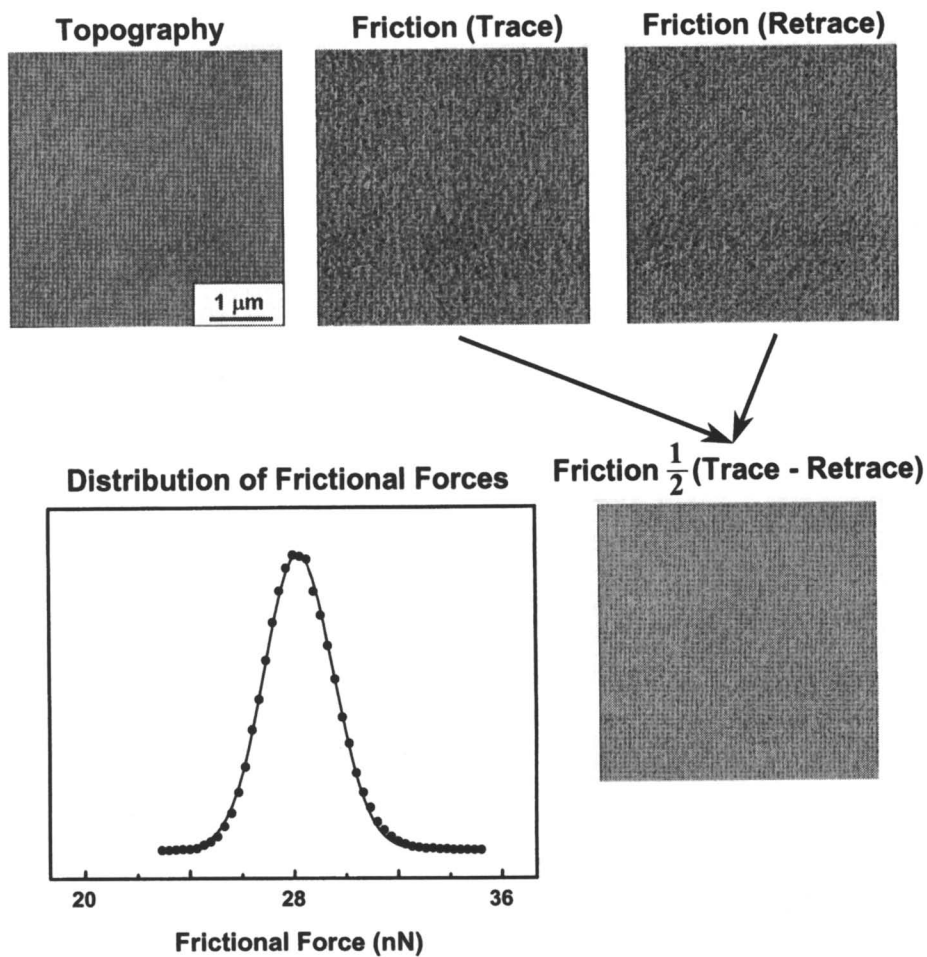


Figure 2. $4\mu\text{m} \times 4\mu\text{m}$ topography, friction (trace), friction (retrace), and friction difference images of PMMA film surface. Histogram of friction difference image, fit to Gaussian distribution, displaying the distribution of frictional forces.

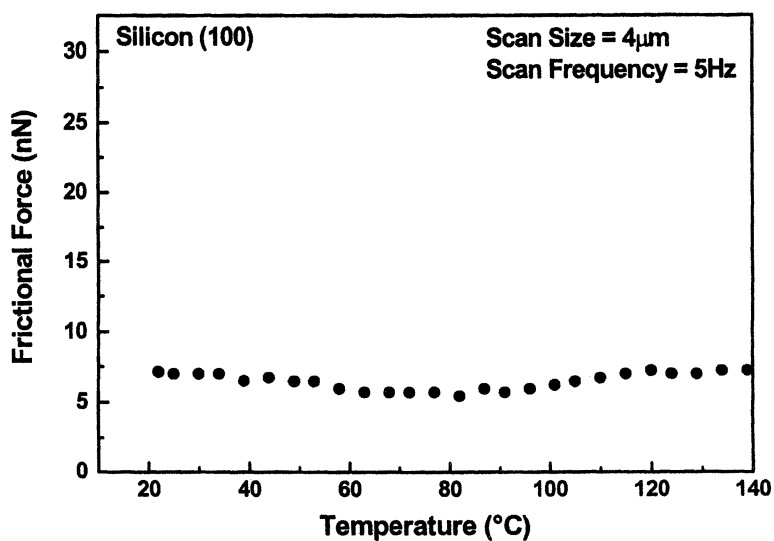


Figure 3. Mean frictional force versus temperature for a silicon(100) wafer with native oxide.

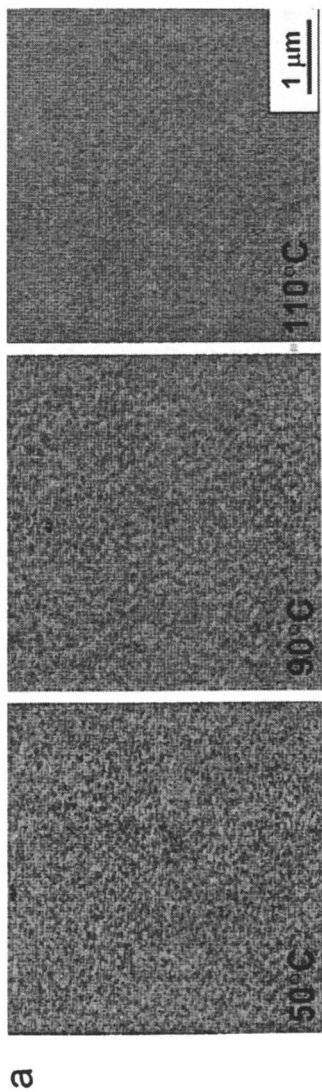
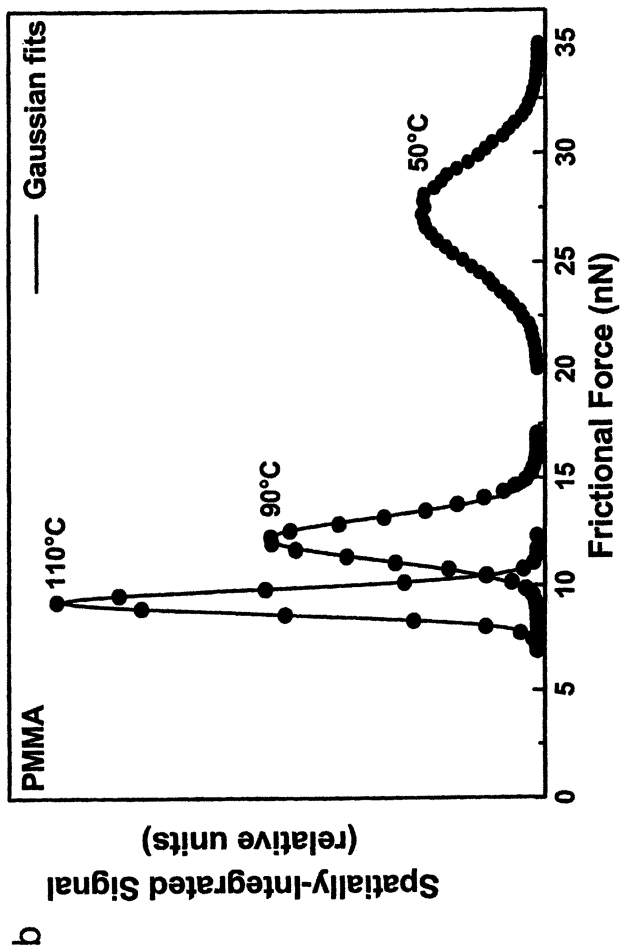


Figure 4. (a) Friction difference images at 50°C, 90°C, and 110°C of a PMMA film surface.



(b) Histograms of friction difference images, at different temperatures, fit to Gaussian distribution.

exhibit a “granular” frictional nanostructure. No noticeable change in nanostructure occurred in the topography with increasing temperature. Quantitative histograms of these images (Figure 4b) are symmetric and are effectively reproduced by a Gaussian function. The mean value of the distribution shifts dramatically as a function of temperature. The breadth or dispersion increases with increasing mean value. Figure 5 shows the statistical nature of friction whereby a linear relationship between the dispersion (histogram width) and the mean value of friction is present. The points are derived by varying temperature from 25 to 120°C and recording dispersions and mean values of friction. Certainly some probability exists for small, discrete lossy events (relaxations) at each pixel location on a friction image. The more likely each event (at certain temperatures), the greater the number of events occur. These sum to the measured mean value at a given pixel. The more individual lossy events, the greater their sum, and also the greater the variation in their sum. The addition of these events produces a Gaussian distribution. The Gaussian distribution, eq. 1, where F_f is friction, \bar{F}_f is the mean value, σ is the dispersion, A is the area, and y the magnitude, describes this behavior.

$$y = \frac{A}{\sigma\sqrt{\pi/2}} e^{-\frac{2(F_f - \bar{F}_f)^2}{\sigma^2}} \quad (1)$$

For the case of increasing the mean value of friction and the dispersion in frictional force, both increase linearly and the overall magnitude (y) will decrease. The statistics in Figure 5 support this description of frictional force.

The mean values from representative friction histograms for PMMA, PET, and PS are plotted as a function of temperature in Figure 6a-c. For each polymer there is a characteristic, reproducible dependence on temperature. Friction data for PMMA displays a broad peak centered at $\approx 50^\circ\text{C}$ and another smaller peak is centered at $\approx 90^\circ\text{C}$. In bulk viscoelastic studies the maximum of the secondary β molecular relaxation occurs at 50°C at ≈ 2000 Hz (4). The β mechanism is assigned to the hindered rotation of the $-\text{COOCH}_3$ group about the C-C bond linking it to the main polymer chain (4). The glass to rubber transition (T_g), measured from bulk studies, for PMMA, PET, and PS at 2000Hz are approximately 125°C , 95°C , and 125°C respectively (4). In Figure 6a-c literature $\tan\delta$ data at 2000Hz are included for comparison and are shown as solid lines (4). For each polymer there is good agreement with the overall shape of the measured friction and $\tan\delta$ curves (Figure 6a-c). In particular, the breadth of the relaxation peaks (FWHH) are well correlated, except in the case of PS where the explored temperature interval includes only a monotonic rise of dissipation.

The pull-off force (a measure of adhesion) of the probe tip was measured for PMMA, PET, and PS at each temperature (Figure 7a-c) prior to collecting friction images. A frequency of 5 Hz with a maximum applied load of ≈ 20 nN was used for these force versus distance measurements. Figure 7a displays no temperature dependence on adhesion for PMMA until a temperature of 80°C where a

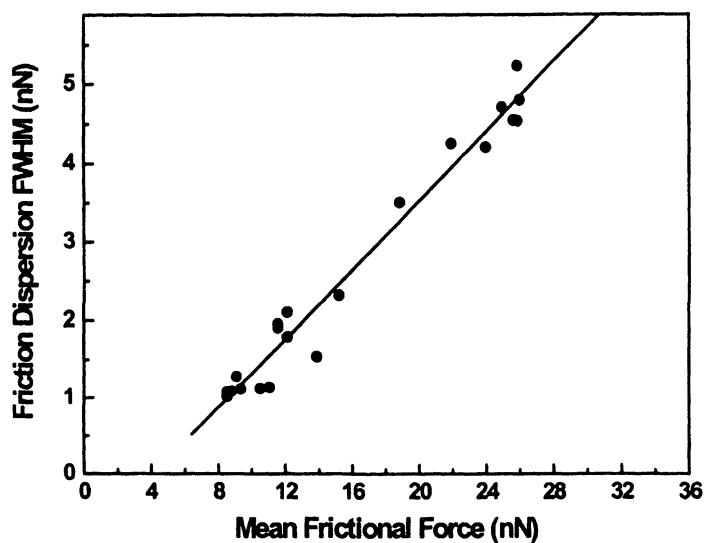


Figure 5. Friction histogram dispersion versus mean frictional force for a PMMA film surface.

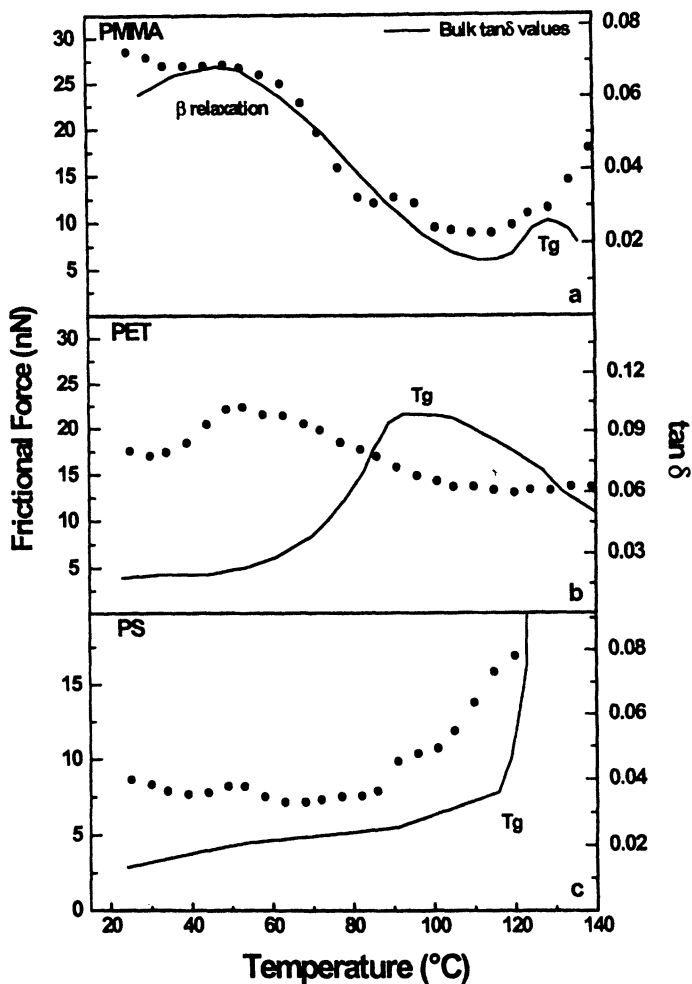


Figure 6. (a) Frictional force versus temperature for a PMMA film. (b) Frictional force versus temperature for a PET film. (c) Frictional force versus temperature for a PS film. Figures a-c overlaid with literature bulk viscoelastic data.

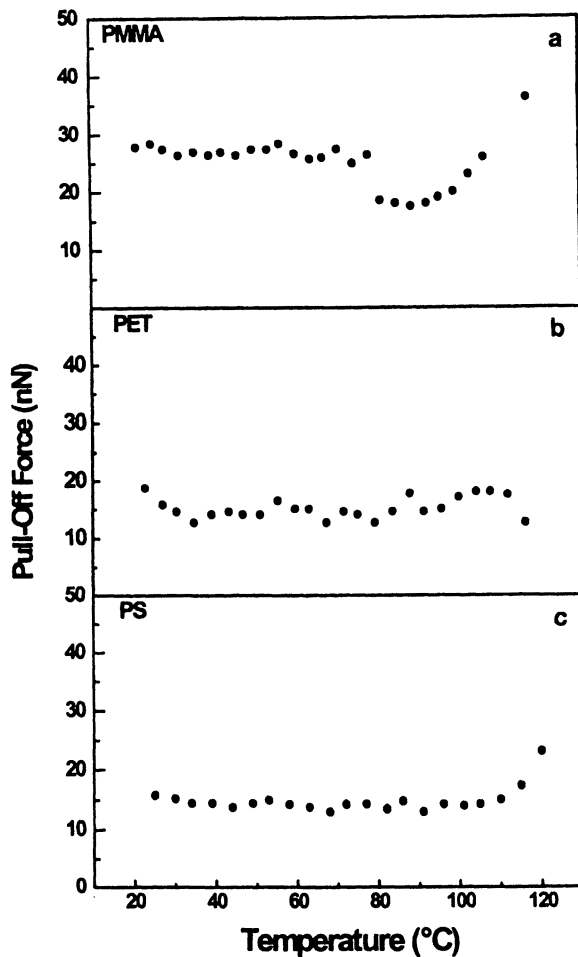


Figure 7. (a) Pull-off force (adhesive) versus temperature for a PMMA film (b) Pull-off force (adhesive) versus temperature for a PET film. (c) Pull-off force (adhesive) versus temperature for a PS film. Obtained during Figure 6 friction data collection.

discontinuity results, most likely from a change in tip state, then a steady increase in pull-off force results as the temperature increases well into the rubbery regime. PET displays no temperature dependence in pull-off force throughout the full temperature range explored (Figure 7b). Figure 7c shows a steady increase in pull-off force beginning at 120°C, which is above the glass-transition temperature of PS.

Time-Temperature Dependence on Friction

The interplay between relaxation time and temperature, i.e. time-temperature superposition, is well-established in polymer studies (10). In this investigation we focus upon PMMA to compare the dependencies of friction on scan velocity and temperature, and to relate the findings to molecular relaxations at the polymer surface. In Figure 8 the temperature dependence of friction is plotted with different symbols at four scanning velocities ranging from 2 to 220 $\mu\text{m}/\text{sec}$ as indicated. Velocities of 220, 50, 20, and 2 $\mu\text{m}/\text{sec}$ are achieved through increasing scan frequency and scan size. Data were acquired at all four velocities prior to ramping to the next temperature of interest. As rate decreases, the β relaxation peak (at 40°C for 220 $\mu\text{m}/\text{sec}$) apparently shifts to lower temperatures. This is consistent with the idea that the same molecular relaxation requires longer time at lower temperatures. Figure 9 is the same PMMA data from Figure 8, but it is plotted as friction versus velocity at discrete temperatures. Figure 10 shows a “master curve” constructed from the velocity study data (Figure 9). Here each set of data (at a given temperature) is multiplied by a shift factor a_T , such that the data sets overlie each other.

The Arrhenius relationship (Eq. 2) between shift factor a_T , and temperature T is commonly used for secondary relaxation phenomena (4). T_0 is the reference temperature and E_a is the activation energy.

$$\ln a_T = \frac{E_a}{R} \left(\frac{1}{T} - \frac{1}{T_0} \right) \quad (2)$$

In Figure 10 the velocities at different temperatures were shifted to a common temperature of 60°C. The Arrhenius plot is shown in Figure 11. From the slope of the Arrhenius plot, an activation energy of ≈ 12 kcal/mole was calculated for the hindered rotation of the $-\text{COOCH}_3$ in PMMA.

Discussion of Friction Force Results

Friction commonly is described with two coupled terms, interfacial (chemical) forces and ploughing (mechanical loss) forces. It is important to consider both when interpreting results to assign a mechanism of friction. Figure 7 shows no pull-off (adhesive) dependence on temperature except when the temperature is sufficiently into the rubbery regime. Above T_g the contact zone will increase due to a decrease in polymer modulus. In the case of PMMA this increase in contact zone did not

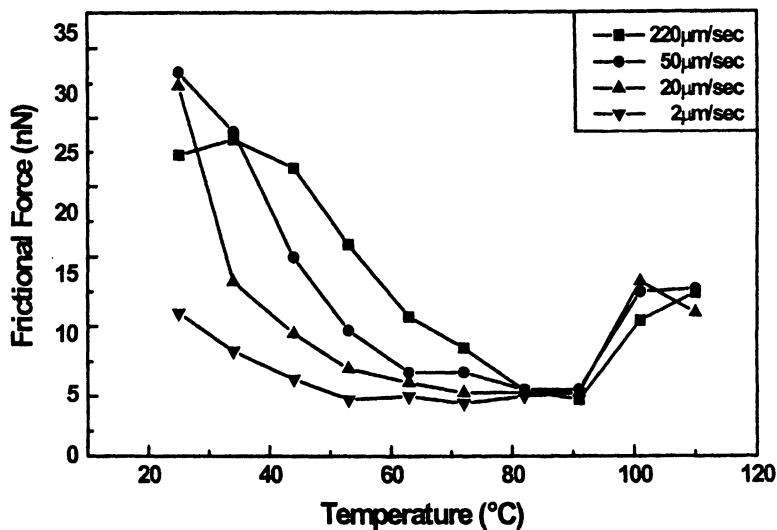


Figure 8. Frictional force versus temperature taken at 2, 20, 50, and 220 $\mu\text{m}/\text{sec}$. scan velocities for a PMMA film.

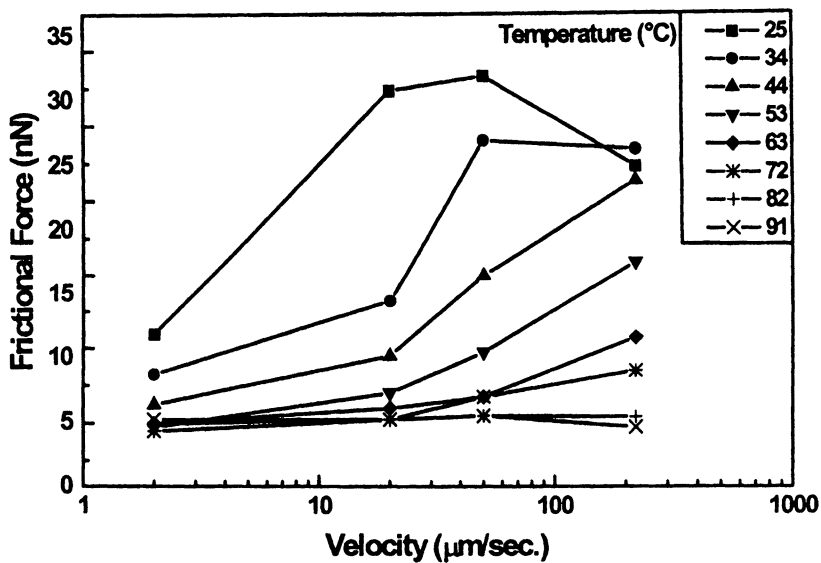


Figure 9. Frictional force versus scan velocity at several temperatures for a PMMA film.

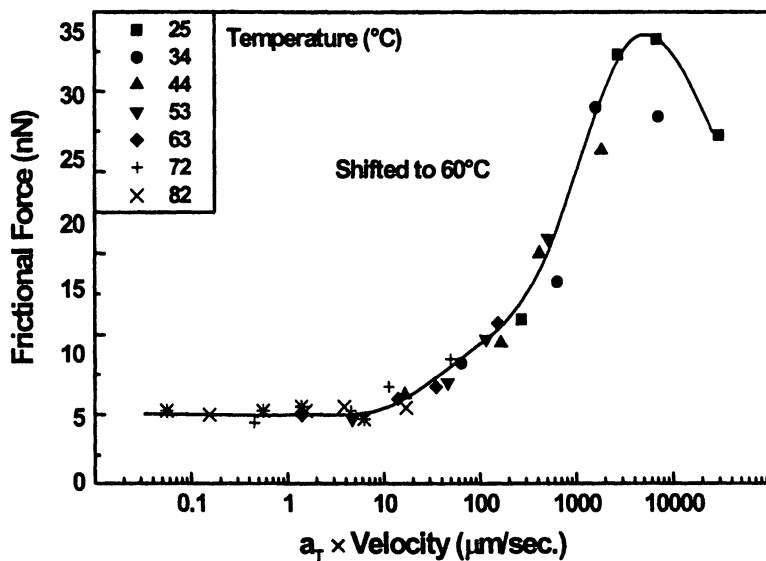


Figure 10. "Master curve" of frictional force versus velocity data shifted to 60°C.

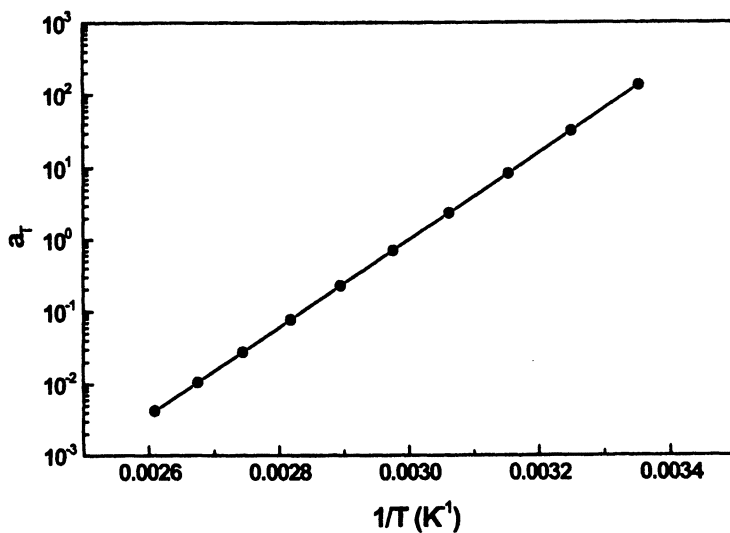


Figure 11. Arrhenius plot of shift factor a_T versus inverse temperature, with linear fit.

occur until well into the rubbery regime and very near the bulk glass transition temperature. PS displayed an increase very near the bulk T_g as well. PET showed no dependence of adhesion on temperature, but most likely at much higher elevated temperatures would display a similar increase in pull-off force. In our case of a hard tip on a polymer film, the dominant source of friction is derived from mechanical viscoelastic loss. Thus knowing our dependence of friction on adhesion, our interpretations will be discussed in terms of mechanical energy dissipation, and not tip-polymer interfacial phenomena.

Velocity / Frequency Relationship. The characteristic temperature-dependent line shapes for each polymer, as determined by bulk dynamic mechanical or dielectric experiments from literature (4), were used as a comparison to our frictional measurements. For the comparison to be valid the literature data must be adjusted to match the same frequency (time-scale) of the friction experiment. The conversion procedure of scan velocity to frequency has been described in previously (7), whereby a contact diameter was calculated to convert the scan velocity to a frequency by simple division. The contact diameter thus allows a gauge for the time the probe tip affects a point on the polymer surface. For the given radius of curvature of 20 nm, applied load=10 nN, adhesive load=15 nN, and assuming a bulk storage modulus, the contact diameter can be estimated by JKR theory to be 18.7 nm. Thus for a scan velocity of 40 $\mu\text{m}/\text{sec}$ the equivalent frequency of measurement is ≈ 2000 Hz and all tabulated $\tan\delta$ data used are scaled accordingly to this frequency for comparison.

It is important to consider possible errors in the comparison of time scales for $\tan\delta$ and friction measurements. A potential difficulty of this analysis is its reliance upon knowing the contact zone of the tip on the polymer surface. Measurement of the radius of curvature of the tip, assuming spherical contact, involves either a calibration grating, as in our case, or using SEM images. If the radius measured was under/over-estimated by a factor of 2 the frequency calculated would change by $\approx 10^{0.1}$ Hz. In the case of the polymers studied, in order to shift a relaxation 5°C a change of an order of magnitude in frequency would be necessary. Thus our methodology should be within $\approx 1^\circ\text{C}$. Furthermore, to account for the 35°C and 50°C differences between measurement types our rate conversion methodology would have to produce errors of 7 orders of magnitude in frequency for PMMA, and 10 orders of magnitude in frequency for PET using 5°C per order of magnitude shift in temperature for the time-temperature conversion for both these polymers (4). Although approximations certainly yield some error in our rate conversion, clearly they alone cannot account for such egregious differences in T_g .

Thin Film / Bulk Comparison. In all surface friction studies we observe the position of the glass-transition temperature lowered somewhat compared to bulk dynamic mechanical measurements. This type of thin polymer film behavior is not surprising since thin films are known to vary considerably from bulk polymer (17). This is a result of chain conformation differences (8), confinement effects (18), as well

as air-polymer and substrate-polymer interfaces dominating a large portion of the films (19-21). Differences in free volume due to surface chain-end concentration can also impact polymer surface properties (21-23). The combined thin film and surface effects have been shown to affect the polymer viscoelastic relaxation properties, and therefore would also effect the tribological properties.

The friction data for PMMA and PET contain peaks corresponding to $\tan\delta$ peaks, but shifted 35°C and 50°C lower, respectively. Furthermore the activation energy of ≈ 12 kcal/mole calculated for the hindered rotation of the $-\text{COOCH}_3$ in PMMA was lower than the previously measured value (17-23 kcal/mole) using bulk mechanical and dielectric methods (4). Although the position of the β relaxation in PMMA (Figure 6a) corresponds to the bulk value, this lowered activation energy would suggest otherwise. Most likely the discrepancy arises from the previously discussed underestimated contact zone which would lower the comparison frequency of the measurement.

The lowered T_g and activation energy measurements may be indicative of a greater free volume at the polymer surface. Depression of the glass transition has been observed for films similar in thickness to ours (<100 nm) (17,19,20). The effect has been attributed to an increase in free volume in the polymer due to the effects of constraining surfaces. This affects the polymer conformations and such effects could account for the drastic departure from bulk behavior observed in the present study. It is also known that elevated pressure under the probe could *increase* the glass transition temperature (24-26), but the magnitude of such an effect may be quite small under the relatively low contact forces (≈ 20 nN) examined in this work.

Conclusions

A quantitative method, using temperature controlled FFM and "friction histograms," has been developed to determine the frictional (dissipative) character of polymer surfaces. The use of friction images encompassing 512 surface raster scans as opposed to a single friction loop allowed efficient data collection and determination of the distribution of frictional forces. It was shown that there is a distribution of frictional forces which varies with temperature, thus it is important to have an adequate sampling of the surface to determine the frictional characteristics. The method utilized has allowed us to correlate frictional response in films of PMMA, PET, and PS with their known α and/or β relaxation mechanisms. With every polymer systems we observed a marked shift of the glass-transition temperature to lower temperatures as observed in bulk systems. The temperature of the β relaxation in PMMA was consistent with bulk measurements, which could reflect the rotations of the side group $-\text{COOCH}_3$ were not hindered any less in the thin film than the bulk. Whereas the cooperative relaxation of the glass transition was less hindered than the bulk due to increased free volume of the free polymer surface.

The rate dependence of the hindered rotation of the $-\text{COOCH}_3$ group in PMMA was consistent with Arrhenius time-temperature behavior allowing calculation of an activation energy. The activation energy was lower than measured

bulk values, suggesting a greater mobility at the polymer surface. This study presented the strong dependence of time and temperature on friction, which must be taken into account for any friction measurement on polymer surfaces.

Acknowledgements

This work was supported by grants from the Center for Interfacial Engineering and the donors of the Petroleum Research Fund, administered by the American Chemical Society. We also wish to thank Molecular Imaging for their technical support.

References

- (1) Grosch, K. A. *Proc. R. Soc. London* **1963**, *274*, 21.
- (2) Ludema, K. C.; Tabor, D. *Wear* **1966**, *9*, 329.
- (3) Aklonis, J. J.; MacKnight, W. J. *Introduction to Polymer Viscoelasticity*; 2nd ed.; Wiley: New York, 1983.
- (4) McCrum, N. G.; Read, B. E.; Williams, G. *Anelastic and Dielectric Effects in Polymeric Solids*; Wiley: London, 1967.
- (5) Overney, R. M.; Meyer, E.; Frommer, J.; Brodbeck, D.; Lüthi, R.; Howald, L.; Güntherodt, H.-J.; Fujihira, M.; Takano, H.; Gotoh, Y. *Nature* **1992**, *359*, 133.
- (6) Haugstad, G.; Gladfelter, W. L.; Weberg, E. B.; Weberg, R. T.; Jones, R. R. *Langmuir* **1995**, *11*, 3473.
- (7) Hammerschmidt, J. A.; Moasser, B.; Gladfelter, W. L.; Haugstad, G.; Jones, R. R. *Macromolecules* **1996**, *29*, 8996.
- (8) Kajiyama, T.; Tanaka, K.; Takahara, A. *Macromolecules* **1997**, *30*, 280.
- (9) Tanaka, K.; Takahara, A.; Kajiyama, T. *Macromolecules* **1997**, *30*, 6626.
- (10) Ferry, J. D. *Viscoelastic Properties of Polymers*; Wiley & Sons: New York, 1980.
- (11) Bustamante, C.; Keller, D. J. *J. Phys. Today* **1995**, *48*, 32.
- (12) Biscarini, F.; Levy, P. *Appl. Phys. Lett.* **1997**, *71*, 888.
- (13) Noy, A.; Frisbie, C. D.; Rozsnyai, L. F.; Wrighton, M. S.; Leiber, C. M. *J. Am. Chem. Soc.* **1995**, *117*, 7943.
- (14) Putman, C.; Igarashi, M.; Kaneko, R. *Jpn. J. Appl. Phys.* **1995**, *34*, L264.
- (15) Ogletree, D. F.; Carpick, R. W.; Salmeron, M. *Rev. Sci. Instrum.* **1996**, *67*, 3298.
- (16) Overney, R. M. *Polymer Preprints* **1998**, *39*, 1100.
- (17) Keddie, J. L.; Jones, R. A. L.; Cory, R. A. *Europhys. Lett.* **1994**, *27*, 59.
- (18) Forrest, J. A.; Dalnoki-Veress, K.; Dutcher, J. R. *Phys. Rev. E.* **1997**, *56*, 5705.
- (19) Forrest, J. A.; Dalnoki-Veress, K.; Stevens, J. R.; Dutcher, J. R. *Phys. Rev. Lett.* **1996**, *77*, 2002.
- (20) Keddie, J. L.; Jones, R. A. L.; Cory, R. A. *Faraday Discuss.* **1994**, *98*, 219.
- (21) DeMaggio, G. B.; Frieze, W. E.; Gidley, D. W.; Zhu, M.; Hristov, H. A.; Yee, A. F. *Phys. Rev. Lett.* **1997**, *78*, 1524.

- (22) Mayes, A. M. *Macromolecules* **1994**, *27*, 3114.
- (23) Affrossman, S.; Hartshorne, M.; Jermone, R.; Pethrick, R. A.; Petitjean, S.; Vilar, M. R. *Macromolecules* **1993**, *26*, 6251.
- (24) Billingham, P. R.; Tabor, D. *Polymer (GB)* **1971**, *12*, 101.
- (25) Parry, E. J.; Tabor, D. *Polymer (GB)* **1973**, *14*, 617.
- (26) Stevens, J. R.; Coakley, R. W.; Chau, K. W.; Hunt, J. L. *J. Chem. Phys.* **1985**, *84*, 1006.

Chapter 18

Polypropylene/(Ethylene-Propylene) Copolymer Blends

Surface Morphology and Elasticity as Measured by AFM and FMM

B. Nysten, C. Meerman, and E. Tomasetti

Unité de chimie et de physique des hauts polymères, Université catholique de Louvain, place Croix du Sud, 1, B-1348 Louvain-la-Neuve, Belgium

Quantitative and qualitative methods were developed to measure the surface mechanical properties of polymers by atomic force microscopies. They were used to study the effects of molding processes and of viscosity on the surface morphology of polypropylene / (ethylene-propylene) copolymer blends (PP/EP). On compression-molded "physical blends", EP nodules are present at the outermost surface while, on injection-molded "reactor blends", they are covered by a PP layer. Resins with high viscosity ratio between EP and PP present heterogeneous surface elastic properties corresponding to the dispersion of spherical EP nodules below the surface. The low viscosity ratio resins have homogeneous surface elastic properties comparable to those measured above EP nodules on high viscosity ratio resins. This is compatible with a fine dispersion of plate-like shaped EP nodules below the surface

The surface content and the distribution of (ethylene-propylene) copolymer (EP) in toughened polypropylene (PP) resins (PP/EP) have important impact on a lot of properties such as gloss, paint adhesion, hardness, ... These surface properties are more and more important in the multiple applications of these resins, for instance for paint adhesion in the automotive industry. It has already been shown that the introduction of EP in PP provides better paint adhesion but its role remains speculative (1-4). A major drawback to the understanding of the EP influence on PP/EP surface properties is the lack of knowledge concerning the blends surface morphology (EP content, EP lateral distribution, ...). This is essentially due to the similar chemical composition of both polymers that prevents surface analysis by classical chemical surface spectroscopies.

It was previously shown that atomic force microscopy, AFM, and force modulation microscopy, FMM, can bring novel informations concerning the elastic and the viscoelastic properties of PP/EP resins at the microscopic level. They enabled the mapping of EP rubbery nodules distribution and the explanation of the macroscopic behavior of these resins (e.g. differences in the impact resistance) (5). Moreover, recent works showed that the use of AFM techniques (force-curves and force-modulation measurement, FMM cartography) can be used to characterize the surface elastic properties of PP/EP blends (6). Especially, these studies demonstrated that FMM can map the surface and the subsurface distribution of EP nodules.

In the present paper, the techniques used to measure the surface elastic properties will be briefly described. Then, the application of these techniques to the study of PP/EP surfaces will be presented. First, the surface distribution and morphology of EP nodules at the surface of PP/EP compression-molded "physical blends" and of injection-molded "reactor blends" will be compared. Second, the effect of EP vs PP viscosity ratio on the surface distribution and morphology of EP in injection-molded PP/EP will be studied.

Theoretical

Force-Curves Measurements. In force curve measurements, a vertical displacement of the sample, z , is imposed and the subsequent tip displacement, d , is measured. The tip-sample interaction force, F , is deduced by means of the Hooke's relation, $F = -k_c d$, where k_c is the cantilever stiffness. Force curves are generally divided into different regions (7). If the part where the electrostatic repulsion forces are dominant is only considered, with silicon tips much stiffer than polymers, tips penetrate the sample surface and an indentation depth, δ , equal to $z - d$, can be measured. The lower the sample elastic modulus, the greater will be the indentation depth. By using the Hertz mechanical model adapted to the geometry of the tip-sample system (8,9) surface elastic modulus could be deduced from the following equations corresponding respectively to a spherical, a paraboloid and a conical tip:

$$F = \frac{4}{3} K \sqrt{R} \delta^{3/2} \quad (1.1)$$

$$F = \frac{4}{3} K \sqrt{2k} \delta^{3/2} \quad (1.2)$$

$$F = \frac{2}{\pi} K \tan \alpha \delta^2 \quad (1.3)$$

where $K = E / (1 - \nu^2)$ is the surface elastic modulus, E is the Young's modulus and ν the Poisson's ratio of the material. R is the tip radius of curvature, k , the coefficient describing the paraboloid tip, and α , the opening angle of a conical tip. When the geometry and the size of the tip is determined, it is possible to quantitatively measure the surface modulus from the force-indentation curve using the appropriate model according to the ratio between the tip dimensions and the maximum indentation depth reached during the force-curve experiment.

The elastic model was modified by taking into account the adhesion force acting between the tip and the surface using the Johnson, Kendall and Roberts theory (JKR model) (10). This leads to the following relations for the different tip geometries (spherical, paraboloid and conical):

$$F = \frac{4}{3} K \sqrt{R} \delta^{3/2} - \left(8\pi K R^{3/2} W_{adh} \delta^{3/2} \right)^{1/2} \quad (2.1)$$

$$F = \frac{4}{3} K \sqrt{2k} \delta^{3/2} - \left(8\pi K (2k)^{3/2} W_{adh} \delta^{3/2} \right)^{1/2} \quad (2.2)$$

$$F = \frac{2}{\pi} K \tan \alpha \delta^2 - \frac{8}{\pi} \sqrt{K W_{adh}} (\tan \alpha)^{3/2} \delta^{3/2} \quad (2.3)$$

where W_{adh} is the work of adhesion that can be determined by measuring the pull-off force on the force-indentation curves (10).

Force-Modulation. In force modulation, the sample and the tip are previously placed in contact with a interaction force kept constant (F_0). A modulation of the sample vertical position is added to its contact equilibrium position and the subsequent modulation movement of the cantilever deflection is measured by means of a lock-in amplifier. The amplitude and the phase shift of the cantilever response are influenced by the viscoelastic properties of the surface. In FMM, the sample vertical position is modulated during the sample scanning and simultaneous acquisition of topographical and viscoelastic maps of the surface can be realized.

The sample-tip-cantilever system can be modeled as a mechanical system with springs and dash-pots (11,12). Solving the motion equations of this model at low frequency (i.e. below the cantilever resonance frequency) and neglecting the damping constants (i.e. neglecting viscoelastic effects in polymers) leads to the following relation for the ratio between the sample modulation amplitude, z_1 , and the tip response amplitude, d_1 , also called the dynamic elastic response:

$$\frac{d_1}{z_1} \equiv \frac{k_i}{k_i + k_c} \quad (3)$$

In this relation, k_c is the cantilever stiffness and k_i is the tip-surface effective stiffness given by $\partial F / \partial \delta$. From the relations (1.1 to 1.3), it can be seen that k_i depends on the static contact force, the tip geometry and the surface elastic modulus. Knowing the cantilever stiffness, the static contact force and the tip geometry and dimensions, it is thus theoretically possible to determine the surface elastic modulus from the dynamic response.

Experimental

Materials. For the calibration of force-curves and force-modulation measurements, experiments were performed on various standard homopolymers (polycarbonate, PP, polyethylene and EP) with Young's modulus ranging between 10 and 3000 MPa. Plates (50x30x2 mm³) of these polymers were compression-molded on polyimide (Kapton, Du Pont de Nemours) during 3 min under a pressure of 2 MPa. For the measurement of the bulk elastic modulus, rods (50x5x2 mm³) were cut in these plates. For AFM experiments, small sample pieces were fixed with cyanoacrylate glue (Ara glue, Sodiema) on AFM sample holders.

The main characteristics of the PP/EP resins studied here are listed in table I. The PP/EP "physical blend" (PPEP1) was obtained by mixing pellets of PP (LY from Shell, $E = 1500$ MPa) and of EP (Vistalon 805 from Exxon, $E = 20$ MPa) in a Brabender mixer at 60 rpm and 180°C during 5 min. The materials was ground in liquid nitrogen and then compression-molded on polyimide (Kapton, Du Pont de Nemours) during 2.5 min at 220°C under a pressure of 450 kPa. The PP/EP "reactor blend" (PPEP2) (Hifax SP179) was supplied by Montell (Ferrara, Italy). Plates of 10 x 15 cm² were injected with a DK300T Codim by Renault (Rueil-Malmaison, France). The material at a temperature of 270°C was injected in a mould at 30°C with an injection speed of 20 mm sec⁻¹ and a holding pressure of 270 bars.

Table I: Main characteristics of the resin used in the present study: elastomer content, resin viscosity in the melt (Melt Flow Index) and viscosity ratio between the xylene soluble and the xylene insoluble fractions.

Resin	Type	EP wt. %	MFI (g/10 min)	η_{sol}/η_{ins}
PPEP1	Physical blend	20.0		
PPEP2	Reactor blend	23.0		3.2
PPEP3	Reactor blend	13.8	4.7	1.63
PPEP4	Reactor blend	12.1	5.2	0.76

The resins used to study the influence of EP/PP viscosity ratio were provided by SOLVAY. Samples, PPEP3 and PPEP4, are "reactor blends" produced in gas-phase by a two-stage polymerization process. They differ by the viscosity ratio between the EP and the PP phases which corresponds to the ratio of the solution intrinsic viscosities of the xylene-soluble fraction (mainly EP) and the xylene-insoluble fraction (mainly crystalline PP). Disks of these resins were injection molded and analyzed by TEM and by AFM and FMM.

DMA Measurements. Elastic tensile modulus, E' , of the standard polymers was measured by dynamic mechanical analysis, DMA, on a Rheometrics RSAII DMTA apparatus. Measurements were done at 1 Hz. The deformation amplitude was limited to 0.02% for the stiffer polymers and to 0.1% for the softer ones.

AFM Analyses. Force curves, local force modulation, AFM and FMM images were realized in air with an Autoprobe CP from Park Scientific Instruments (Sunnyvale, CA) using a 100 μm scanner. The cantilevers were triangular (180 μm length, 25 μm wide and 2 μm -thick) silicon Ultralevers (Park Scientific Instruments) with k_c ranging between 10 and 20 N m^{-1} . The apex geometry and dimensions of the tips were determined by high resolution FEG-SEM. Measured radius of curvature, R , ranged between 10 and 30 nm and cone opening angles, α , varied between 10 and 20°. The cantilevers stiffness was determined within 10% by the measurement of the free resonance frequency of the cantilever in air (13).

The conversion factor of the voltage measured on the photodetectors into tip displacement was calibrated by performing a force-curve measurement on a rigid sample (silicon) and by assuming that, in this case, the tip displacement is equal to the sample displacement. This calibration procedure was repeated each time the cantilever was changed or the laser beam refocused on the cantilever.

For force modulation measurements and imaging, the sample vertical position was modulated by adding a sinusoidal signal to the z -voltage applied to the piezoelectric scanner. Unless specified otherwise, the modulation amplitude, z_1 , was equal to 7 Å and the frequency was equal to 2 kHz, i.e. at least two order of magnitude lower than the cantilevers resonance frequency. The deflection signal of the cantilever, d_1 , was measured with a dual phase lock-in amplifier (EG&G Princeton Applied Research, Model 5210). The static force, F_0 , varied between 10 and 200 nN. The cut-off frequency of the feedback loop was maintained below 300 Hz. For AFM and FMM imaging, the scanning frequency was equal to 0.4 lines sec^{-1} . The fast-scan direction was always perpendicular to the cantilever long axis.

To measure force-curves or to perform quantitative measurements of the dynamic elastic response in force modulation the sample raster scan was stopped and the tip was positioned at various location at the sample surface.

TEM Analyses. For the TEM analyses, the samples were stained with $\text{RuCl}_3 \cdot x\text{H}_2\text{O}$ in NaClO . 90-nm-thick sections were then cut at low temperature (-40°C). For both resins, transverse sections parallel to the injection direction were studied. For the PPEP4 resin, additional sections were made perpendicular to the injection direction.

Results and Discussion

Force-Curves and Force-Modulation Calibration. In figure 1(a & b), typical force-indentation curves obtained respectively on a rigid ($E = 610$ MPa) and a soft ($E = 27$ MPa) polymer are presented. The elastic modulus derived from the analysis of the force-indentation curves is compared to the bulk elastic modulus measured by DMA in figure 1(c). For this analysis, the used tip geometry was adapted to the maximum indentation depth reached during the experiment, δ_{max} . For $\delta_{max} \ll R$, the spherical geometry was considered while, for $\delta_{max} \gg R$, the conical one was used. For intermediate values, the paraboloid model was used.

Using the Hertz model, a good quantitative agreement is obtained for stiffer polymers ($E > 500$ MPa). For the softer polymers, the elastic modulus is systematically underestimated. The results of the analysis performed on polymers

with Young's modulus ranging between 10 and 500 MPa show that taking into account the adhesion force improves the quantitative measurement of the surface modulus on "soft" polymers (Fig. 1(c)). Surprisingly, on stiffer polymers, the results are better with the Hertz model than with the JKR model. This could be in agreement with the fact that this second model is better suited for soft materials (14).

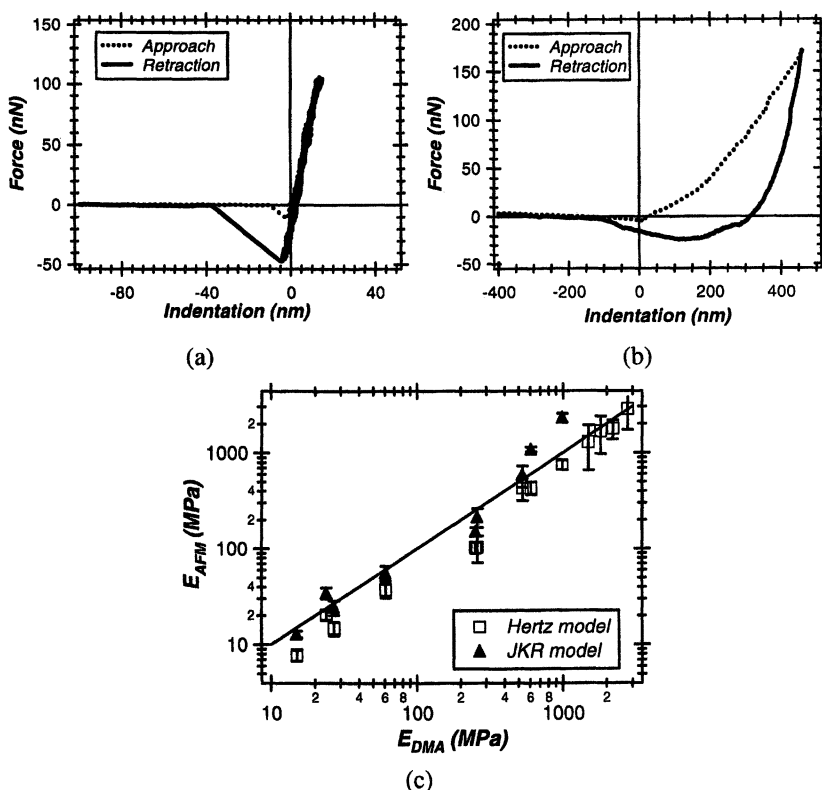


Figure 1. Typical force-indentation curves obtained respectively (a) on a rigid polymer ($E = 610$ MPa) and (b) on a soft one ($E = 27$ MPa). (c) Comparison between the surface Young's modulus deduced from the analysis of the force-indentation curves and the volume modulus measured by dynamic mechanical analysis, DMA, using the Hertz elastic model (□) and using the JKR model (▲).

In figure 2, the results obtained in force modulation on various polymers are presented. As expected, the elastic response increases with the bulk modulus. Using Hertz models, the elastic modulus has been derived. For rigid polymers, the agreement between the surface modulus and the bulk modulus is quantitatively good. For softer polymers, a large discrepancy is observed, probably due to the fact that the adhesion force and the viscoelasticity are neglected. This could also be explained by

the well known fact that, in AFM experiments, the assumption of pure vertical indentation is not valid. Lateral deformation should normally be taken into account in the models (Mazeran, P.E.; Loubet, J.-L. *Tribology Lett.* in press). However, the results show that the dynamic response measured by force modulation is qualitatively correlated to the Young's modulus and may be used to evaluate and compare the elastic properties of polymer surfaces.

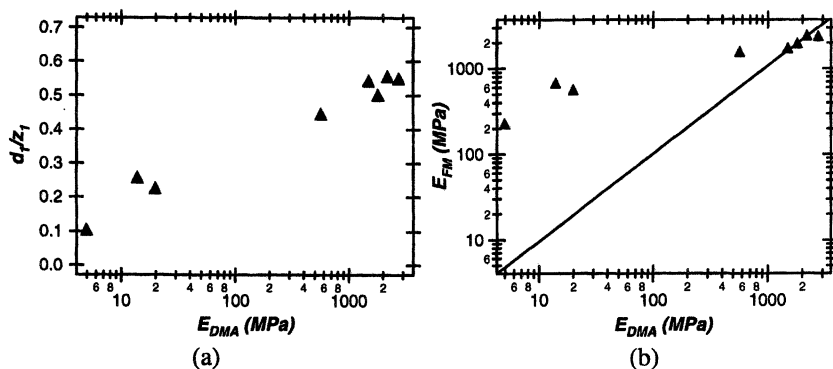


Figure 2. (a) Variation of the dynamic elastic response, d_1/z_1 , measured by local force modulation as a function of the bulk elastic modulus. (b) Comparison between the surface Young's modulus deduced from force modulation experiments and the volume modulus calculated using Hertz model.

Compression-Molding vs Injection-Molding. The FMM elastic images obtained on the surface of the PP/EP "physical blend" and in the volume and at the surface of the "reactor blend" are presented in figure 3. The volume analyses were performed on 5 μm thick cut realized at -40°C . The FMM image reveals soft regions in dark (EP nodules) embedded in a rigid matrix in bright (PP). The results of local measurements of the dynamic response on the PP matrix and on the EP nodules are given in table II.

Table II: Elastic response measured on the pure PP & EP, on the PPEP1 sample, in the volume and at the surface of PPEP2 resin.

	Dynamic elastic response	
	PP	EP
Pure components	0.60 ± 0.04	0.25 ± 0.02
« Physical blend » surface	0.60 ± 0.04	0.25 ± 0.01
« Reactor blend » volume	0.60 ± 0.04	0.38 ± 0.04
« Reactor blend » surface	0.60 ± 0.04	0.43 ± 0.09

These measurements reveal that the PP matrix and EP nodules of the "physical blend" surface have the same elastic properties as the surface of the respective pure

samples. This interpretation is confirmed by studying the histogram of the dynamic response (Fig. 4(a)) where two peaks are observed at 0.25 and 0.6. These ratios are very close to the values obtained by local measurements on EP and PP respectively (Tabl. II). These results suggest that, in this case, EP is present at the outermost surface.

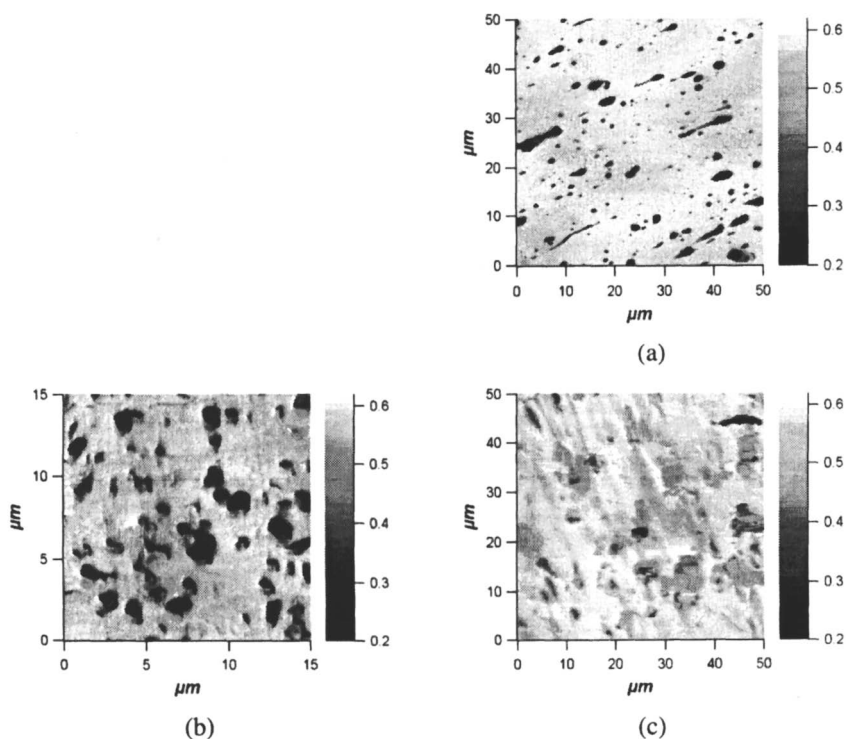


Figure 3. Elastic response FMM images obtained on the surface of the compression-molded "physical blend" PPEP1 (a) and in the volume (b) and at the surface (c) of the injection-molded "reactor blend" PPEP2. Gray scales are calibrated in d_1/z_1 units.

For the injection-molded "reactor blend", comparison between figures 3(b) and 3(c) reveals that, in the bulk, a large contrast exists between the elastic response on the EP nodules and on the PP matrix while, at the surface, this contrast is weaker and nodules with various gray levels are observed. This qualitative analysis is confirmed by the quantitative local measurements of the d_1/z_1 ratio on the PP matrix and on the EP nodules in the bulk and at the surface (Tabl. II). These measurements show that PP has the same elastic properties in the bulk and at the surface. They also suggest that surface EP nodules have higher stiffness values than bulk nodules. Finally, the

elastic response values measured on the surface nodules are more spread than on the bulk nodules.

The histograms of the dynamic responses (Fig. 4(b & c)) confirm these observations.

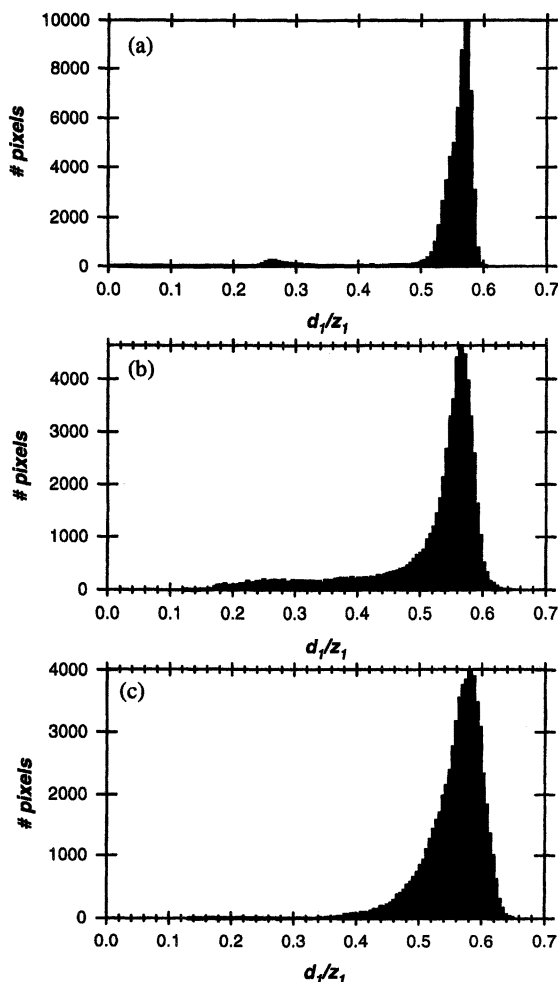


Figure 4. Histograms of the dynamic elastic response corresponding to the FMM images (Fig. 3). (a) Surface of the PPEP1 sample. (b) Volume and (c) surface of the PPEP2 sample.

In the bulk, a sharp peak corresponding to PP is observed close to 0.6 and a broad one between 0.15 and 0.4. This broad peak can be explained by the complex microstructure of EP nodules of "reactor blends" leading to inhomogeneous

mechanical properties (5). At the surface, a single peak appears close to 0.6 with a shoulder extending towards the low d_1/z_1 values. These observations can be explained by the presence of a surface PP skin with varying thickness covering the EP nodules close to the surface. The presence of the PP skin at the surface of injection molded PP/EP blends have been already proposed in the literature (3,15,16). It can be explain by the fact that the injection molding process induces high shear rate at the surface; the phase having the lower viscosity (PP) tends thus to go to the surface in order to minimize friction forces during molding process (17).

Effect of EP/PP Viscosity Ratio. TEM images obtained on the PPEP3 and PPEP4 samples are presented in figure 5.

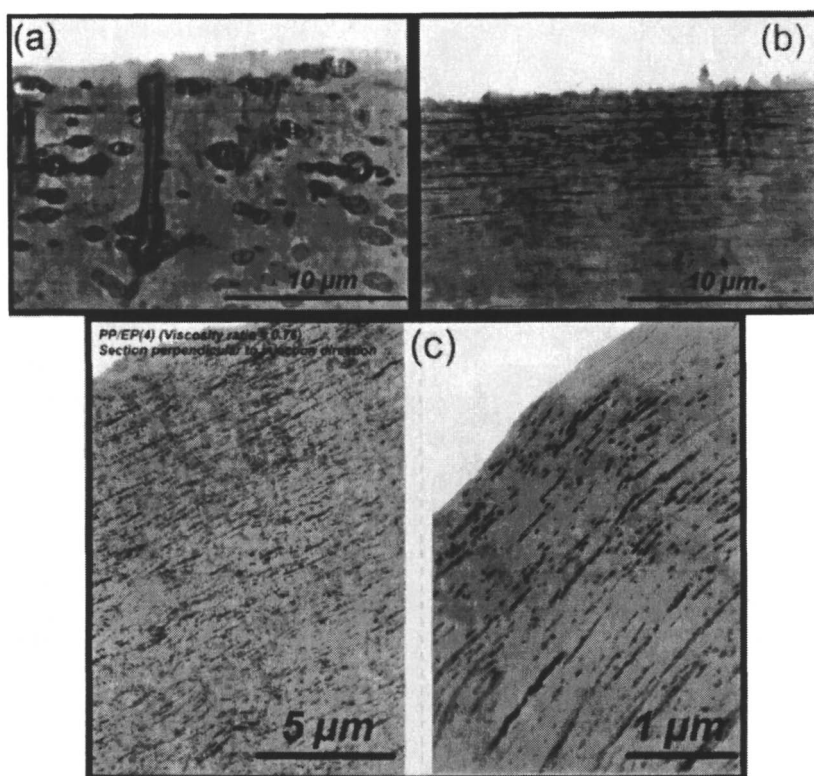


Figure 5. TEM images obtained on sections parallel to the injection direction of the PPEP3 resin (a) and of the PPEP4 resin (b) and on sections perpendicular to the injection direction of the PPEP4 sample (c).

An increased deformation of the EP nodules in the injection direction with the decrease of the viscosity ratio is observed. For the PPEP3 resin (Fig. 5(a)), the EP nodules are almost spherical, even close to the surface, while, for the PPEP4 resin

(Fig. 5(b)), the EP nodules are elongated in the injection direction. The deformation is more important close to the surface where the shear rate during injection is more pronounced. A higher concentration of EP nodules near the surface also seems to appear when the viscosity ratio decreases. TEM images of sections perpendicular to the injection direction (Fig. 5(c)) reveal that the EP nodules below the surface are in fact plate-like shaped. Very few rod-like shaped EP nodules can be observed. These observations confirm that the EP vs PP viscosity ratio strongly influences the EP nodules morphology close to the surface. At high viscosity ratio, the nodules are almost not deformed. At low viscosity ratio, the high shear rate close to the mould surface strongly deforms and orients the nodules in the injection direction. The TEM observations also reveal that the outermost surface is composed of a more or less thin pure PP skin in all cases which confirms the hypothesis made for the PPEP2 sample.

On the PPEP3 resin, the surface morphology appears slightly oriented in the injection direction (Fig. 6(a&b)). The EP nodules that appear in the FMM images are

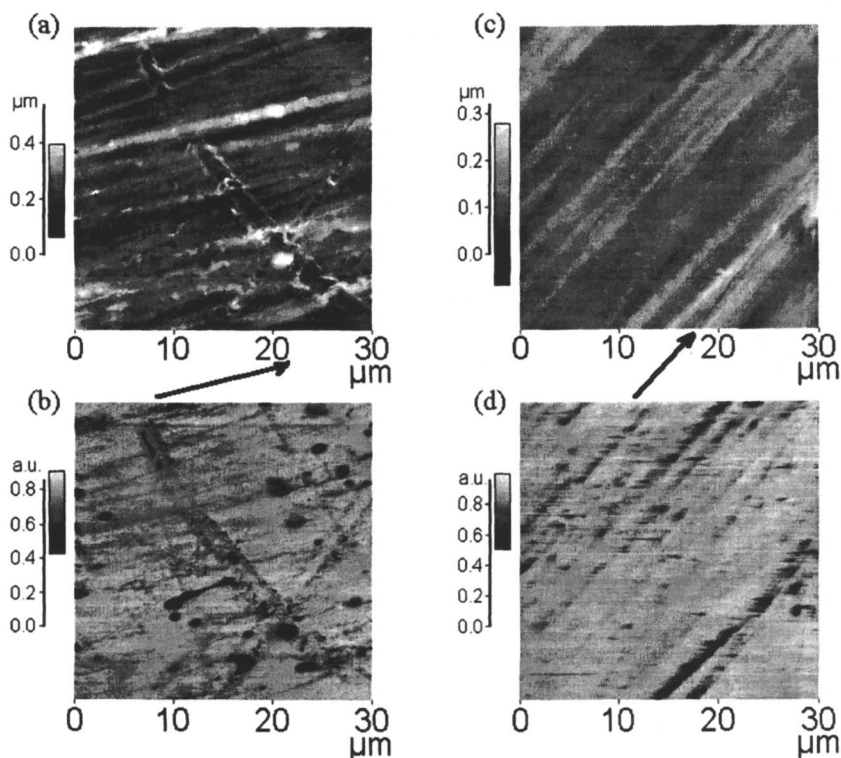


Figure 6. AFM and FMM images obtained on the PPEP3 and the PPEP4 samples: PPEP3 topography (a) and FM elastic response (b), PPEP4 topography (c) and FM elastic response (d). The injection directions for both samples are indicated by the arrows.

almost not deformed. On the PPEP4 sample, the surface morphology is clearly oriented in the injection direction (Fig. 6(c&d)). However, few EP nodules or even not could be observed at or below the surface as revealed by the weak contrast on the FMM images.

The measured values of the elastic modulus and of the dynamic elastic response measured at different spots on the surface of both samples are summarized in table III. The value of the surface elastic modulus of the matrix is of the order of 100 MPa. Surprisingly, this value is one order of magnitude lower than what is expected for pure PP (approximately 1000 MPa). The very rapid crystallization conditions near the surface "freezing" both PP and EP amorphous phases in disorganized micro-domains could perhaps explain this observation. The calculated modulus for EP is around 25 MPa, i.e. almost one order of magnitude lower than that measured on the matrix. The surface elastic modulus of the low viscosity ratio resin is estimated to vary between 20 and 35 MPa, i.e. around the value measured above EP nodules on the high viscosity ratio resin. While for the high viscosity ratio, the elastic dynamic response is very different on the matrix and on the nodules, for the low viscosity ratio resin, it is almost the same everywhere on the surface and its value varies around that measured above the EP nodules of the PPEP3 resin.

These results combined with those obtained by TEM show that the resin with the highest EP/PP viscosity ratio present heterogeneous surface elastic properties corresponding to the rough dispersion of almost spherical EP nodules below the surface. On the contrary, the low viscosity ratio resin presents homogeneous surface elastic properties at the resolution of our measurements (> 100 nm). The measured surface rigidity is comparable to that measured above EP nodules on the high viscosity ratio resin. This could be explained by the easier deformation of the EP nodules into platelets and by their fine dispersion below the thin PP surface layer.

Table III: Elastic modulus and dynamic elastic response measured on the PP matrix and the EP nodules of the PPEP3 resin and on the surface of the PPEP4 sample.

	Elastic modulus (MPa)	Dynamic elastic response
PP matrix on PPEP3	100	0.71
EP nodules on PPEP3	25	0.32
Surface of PPEP4	20 to 35	0.21 to 0.42

Conclusions

The use of a simple elastic model taking into account adhesion forces enables the quantitative measurement by AFM of the elastic modulus of polymer surfaces. Local force-modulation measurement also permits to qualitatively compare the local stiffness of polymers. These techniques associated to the imaging abilities of AFM

and FMM could be thus used as powerful tools to characterize the surface morphology (EP nodules shape and distribution) of PP/EP blends.

The analysis of the effect of the molding process show that, at the surface of compression-molded "physical blends", the EP nodules are present at the outermost surface. On the contrary, FM measurements reveal that the surface EP nodules in injection-molded "reactor blends" are covered by a thin PP surface layer.

The EP/PP viscosity ratio also strongly influences the surface morphology and elasticity of injection-molded blends. TEM and FMM show that the resin with the higher viscosity ratio presents heterogeneous surface elastic properties corresponding to the rough dispersion of almost spherical EP nodules below the surface PP skin. The low viscosity ratio resin has homogeneous surface elastic properties at the scale of the FMM resolution. The measured rigidity is comparable to that measured above EP nodules on the high viscosity ratio resin. This is compatible with a fine dispersion of plate-like shaped EP nodules below the thin surface PP layer.

Acknowledgments

B.N. is Research Associate of the Belgian National Funds for Scientific Research (F.N.R.S.). E.T. thanks the Belgian Funds for Industrial and Agricultural Research (F.R.I.A.) for its financial support. The authors also gratefully acknowledge the Department of Scientific Policy (P.A.I.), Montell, Renault and Solvay for their support.

References

1. Bonnerup, C.; Gatenholm, P. *J. Adhesion Sci. Technol.* **1993**, *7*, 247
2. Clemens, R. J.; Batts, G. N.; Lawniczak, J. E.; Middleton, K. P.; Sass, C. *Progress in Organic Coatings* **1994**, *24*, 43
3. Prater, T. J.; Kaberline, S. L.; Holubka, J. W.; Ryntz, R. A. *J. Coatings Technol.* **1996**, *68*, 83
4. Ryntz, R. A.; Xie, Q.; Ramamurthy, A. C. *J. Coatings Technol.* **1995**, *67*, 45
5. Nysten, B.; Legras, R.; Costa, J.-L. *J. Appl. Phys.* **1995**, *78*, 5953
6. Tomasetti, E.; Nysten, B.; Legras, R. *Nanotechnology* **1998**, *9*, 305
7. Burnham, N. A.; Colton, R. J.; Pollock, H. M. *Nanotechnology* **1993**, *4*, 64
8. Hertz, H. *J. Reine Angew. Math.* **1882**, *92*, 156
9. Sneddon, I. N. *Int. J. Eng. Sci.* **1965**, *3*, 47
10. Johnson, K.L.; Kendall, K.; Roberts, A.D. *Proc. Roy. Soc. London A* **1971**, *324*, 301
11. Burnham, N. A.; Kulik, A. J.; Gremaud, G.; Gallo, P. J.; Oulevey, F. *J. Vacuum Sci. Technol. B* **1996**, *14*, 794
12. Burnham, N. A.; Gremaud, G.; Kulik, A. J.; Gallo, P. J.; Oulevey, F. *J. Vacuum Sci. Technol. B* **1996**, *14*, 1308
13. Cleveland, J. P.; Manne, S.; Bocek, D.; Hansma, P. K. *Rev. Sci. Instrum.* **1993**, *64*, 403
14. Dejarguin, B.V.; Müller, V.M.; Toporov, Y.P. *J. Coll. Interf. Sci.* **1975**, *53*, 314
15. Ryntz, R. A.; Ramamurthy, A. C.; Mihora, D. J. *J. Coatings Technol.* **1995**, *67*, 35
16. Ryntz, R. A.; McNeight, A.; Ford, A. *Plastics Engineering* **1996**, *52*, 35
17. Bhatia, Q. S.; Burell, M. C.; Chera, J. J. *J. Appl. Polym. Sci.* **1992**, *46*, 1915

Chapter 19

Molecular Alignment and Nanotribology of Polymeric Solids Studied by Lateral Force Microscopy

G. Julius Vancso and Holger Schönherr

Faculty of Chemical Technology, Polymer Materials Science and Technology,
University of Twente, P.O. Box 217, 7500 AE Enschede, Netherlands

Lateral force microscopy (LFM) was used to study the tribological behavior of polymer surfaces exhibiting morphological order. Anisotropic friction was observed (a) on extended-chain crystals obtained either by channel die compression or by friction transfer deposition (HDPE, PTFE); (b) on lamellar crystals (HDPE); and (c) on PEO obtained by transcrystallization. For extended-chain crystals the friction was investigated at various relative scan angles with respect to the polymer chain direction. Maximum friction was observed perpendicular to and minimum friction for scans parallel to the chain direction, respectively. The anisotropic friction for lamellar crystals was explained by the occurrence of chain-folding oriented preferentially in planes parallel to the corresponding crystal face. The magnitude of the friction force, as well as the friction anisotropy, increased with scan velocity. For all polymer systems discussed in this paper, the friction anisotropy can be rationalized in terms of the cobblestone model (interlocking asperity model) of interfacial friction described e.g. by Israelachvili and coworkers.

Friction and lubrication are phenomena which play a crucial role in various aspects of our daily life (*J*). Despite its importance the physics of friction is only partly

understood. Even conceptually simple systems, such as highly ordered monolayers, are often too complicated to allow one to predict the magnitude of friction, and to identify which parameter (e.g. molecular conformation, dispersion, packing arrangement, and chemical composition) is most important for the corresponding tribological behavior (2). Friction measurements on the *nanometer* scale have only recently become possible with the invention of the atomic force microscope (3). By scanning the specimen perpendicular to the long axis of the AFM cantilever, the lever will be twisted around its long axis as result of the friction forces acting between surface and tip (lateral force microscopy, LFM). Thereby LFM allows one to investigate the wear and frictional behavior of polymer surfaces from the 100 μm to the submicrometer scales.

In recent years it has been demonstrated that also adhesion (or adhesion hysteresis) plays an important role in friction. Israelachvili and coworkers could show that friction and adhesion hystereses are, in general, directly correlated if certain assumptions are fulfilled. These authors have proposed models based on data obtained by surface forces apparatus (SFA) experiments, e. g. the cobblestone model of interfacial friction (4). In addition, several groups described the application of continuum contact mechanics (e.g. Johnson-Kendall-Roberts (JKR) theory (5)) to describe friction data measured between flat surfaces and nanometer sized contacts (6).

Much effort is being recently devoted to bridge the gap between macroscopic (multiple asperities) and microscopic (single asperity) friction studies. In general, nanometer scale studies of friction (nanotribology) by LFM, combined with adhesion measurements (e. g. by measuring the pull-off force curves with an AFM), can be helpful to develop microscopic models of friction and to establish relationships between friction and adhesion (adhesion hysteresis) (7). Nanotribological studies resulted in a number of interesting observations such as molecular scale stick-slip motions on graphite (8), or dependence of friction on adhesion due to different functional groups exposed in highly ordered monolayers (9).

For polymers, anisotropic friction (10) was observed on lamellar crystals (11 - 13), as well as on extended-chain crystals obtained by friction transfer deposition (14). The anisotropic friction for lamellar crystals was explained by the occurrence of chain-folding oriented preferentially in planes parallel to the corresponding crystal face. For extended-chain crystals friction anisotropy observed parallel and perpendicular to the chain direction was interpreted by the interlocking asperity model. In this paper we give an overview regarding our nanotribological observations on oriented high density polyethylene (HDPE), poly(tetrafluoroethylene) (PTFE) and on crystals of polyethylene (PE) and transcrystallized poly(ethylene oxide) (PEO).

Experimental

Materials and Orientation. The HDPE samples used in this study were obtained by (a) compression in a channel die (15, 16) and (b) by orienting a slider (17) in friction transfer (18). PTFE surfaces were unidirectionally oriented by sliding a block of

polymer over a heated (220°C) glass slide (17). In our study the worn surface of the slider (rather than the transferred film) (14) was investigated. The specimen orientation was adjusted manually in the force microscope such that SFM scans could be performed at preselected angles with respect to the orientation direction which coincides with the polymer chain axis. Single crystals of PE (Polysciences, $M_w = 52000$ g/mol, $M_w/M_n = 2.9$) were grown as reported earlier (11 - 13). The PEO samples were prepared by electrospinning of 1% aqueous solutions of PEO (average molar mass 2×10^6 g/mol, Aldrich) onto glass substrates as described previously (19). Onto the electrospun fibers small droplets of aqueous PEO solution were placed. Crystallization of PEO took place at room temperature during the evaporation of the solvent.

Scanning Force Microscopy / Lateral Force Microscopy. The SFM experiments were performed on a NanoScope III (Digital Instruments, (DI) Santa Barbara, CA) using triangular shaped cantilevers (DI) with a nominal spring constant of 0.12 N/m and 0.38 N/m, respectively. The torsional spring constant was calibrated as described in reference (20). In addition to unmodified tips, chemically modified tips were also used. The procedure for self-assembled monolayer deposition for the chemical modification of the tips is described in reference (20).

Results and Discussion

Anisotropic friction was observed for all samples discussed in this paper. The anisotropy is directly correlated with the directionality of the polymer molecules at the surface of the specimens. The directionality was either confirmed experimentally by AFM (for uniaxially oriented polymers and the transcrystallized PEO) or reported in the literature in numerous diffraction studies for extended-chain polymer single crystals. The existence of regularly packed folds at the surface of lamellar polymer crystals is still a matter of discussions.

Uniaxially Oriented Polymer Fibers. For the crystal facets of PTFE and HDPE imaged, the uniaxially oriented arrangement of the polymer chains results in anisotropic friction. In Figure 1, a typical SFM image of the morphology of oriented PTFE is shown. The fibril orientation coincides with the macroscopic orientation direction. Figure 2 shows an LFM image of PTFE with molecular resolution. The image was acquired on top of one of the fibrils exposed at the surface of the oriented specimen depicted in Figure 1. The interchain distance of 5.6 Å corresponds well with the reported literature value of 5.55 Å of the phase IV hexagonal structure of PTFE (21). The mismatch between fibril and polymer chain orientation was found to be smaller than 10°. Therefore the polymer chain direction with respect to the fixed scanning direction of the LFM (90° with respect to the cantilever's long axis) could be easily adjusted manually by turning the specimen (22). These images were acquired in a liquid cell, filled with ethanol, using -CF₃ modified tips.

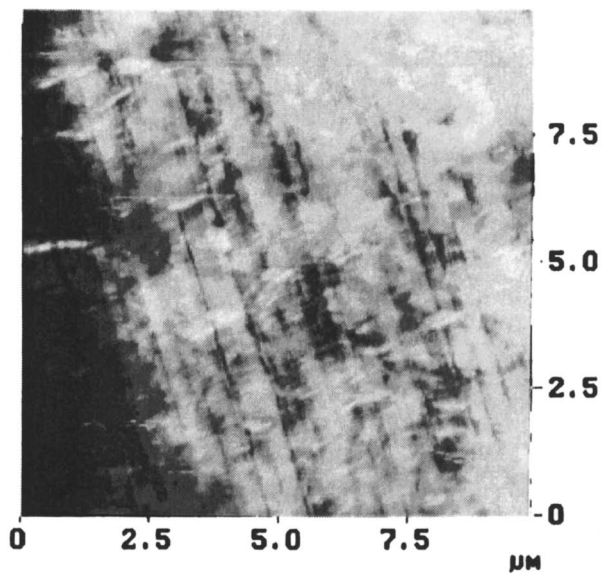


Figure 1. AFM height image of oriented PTFE with a $-\text{CF}_3$ tip in ethanol ($z = 250 \text{ nm}$).



Figure 2. LFM image of oriented PTFE obtained with a $-\text{CF}_3$ tip in ethanol ($z = 0.1 \text{ V}$). Molecular resolution is a result of a stick-slip process.

The anisotropy of the friction force as measured by LFM with unmodified tips is shown in Figure 3a (ethanol) and Figure 3b (air). The magnitude of friction is significantly higher for scans performed perpendicular to the polymer chain direction as compared to the parallel direction. Furthermore, the friction force vs. normal force dependence is not always linear. Linearity was reported earlier (23) although a *single* asperity contact is predicted to show a non-linear dependence (6). In contrast to our previous results, the ratio of friction measured at an angle with the polymer chain direction to friction measured parallel to the polymer chain direction was found to be higher than that for HDPE (*vide infra*). This discrepancy with data reported earlier can be attributed (a) to a lower degree of perfection of the oriented PTFE crystal surface (*e.g.* occurrence of chain ends and entanglements) and (b) inaccuracies in the adjustment of the specimen for LFM measurements performed parallel to the exposed polymer chains. The degree of structural perfection is not accessible by AFM as we obtain only lattice resolution. Careful analysis of the crystal facet orientation in the angle-dependent measurements shown in Figure 3 can minimize the error in relative scan direction. As seen in Figures 3a and 3b, the friction force measured in scans parallel to the PTFE chains is almost constant and its magnitude is close to the noise level of our experiment. A small change in relative scan angle of 7°, however, leads to a significant increase of friction (Figure 3a). Similar results could be obtained on the HDPE specimens (Figure 4). With reference to the HDPE images it is worthwhile mentioning that the repeat distances observed in the LFM scans correspond very well with the known repeat length in the (bc) facet of (orthorhombic) PE.

For measurements in air, we observed a reduction in pull-off forces for -CF₃ tips as compared to unmodified, or differently modified tips. The friction anisotropy observed on HDPE is summarized in Figure 5a. For the -CF₃ terminated tip a smaller magnitude of friction is measured than that for a -COOH tip. The ratio of friction ($F[\text{perpendicular/parallel}] \approx 4$) is lower than that for PTFE (*vide supra*). The friction anisotropy was measured for HDPE with unmodified tips in air as a function of relative scan angle (Figure 5b). Similar to PTFE (*vide supra*) the magnitude of the friction force was smallest for scans parallel to the polymer chain direction and increased with increasing relative scan angle.

Polymer Lamellar Crystals Grown from Solution. Similarly to the regular array of polymer chains exposed at extended-chain fibrillar crystals, the folded sections of polymer molecules at the fold plane of solution-grown “single” crystals can cause anisotropy of friction (Figures 6). This has been observed for a variety of materials, such as POM, PE, and poly(4-methyl-1-pentene) (11 - 13). The explanation proposed for this observation is based on the presence of oriented folds at the surface of the fold plane.

In the present study, solution grown lamellar crystals of PE on mica were studied by LFM in air, as well as in water. The friction anisotropy shown in the corresponding micrographs was well pronounced. The relative friction measured by LFM on PE crystals in different orientations, as well for the same crystal after

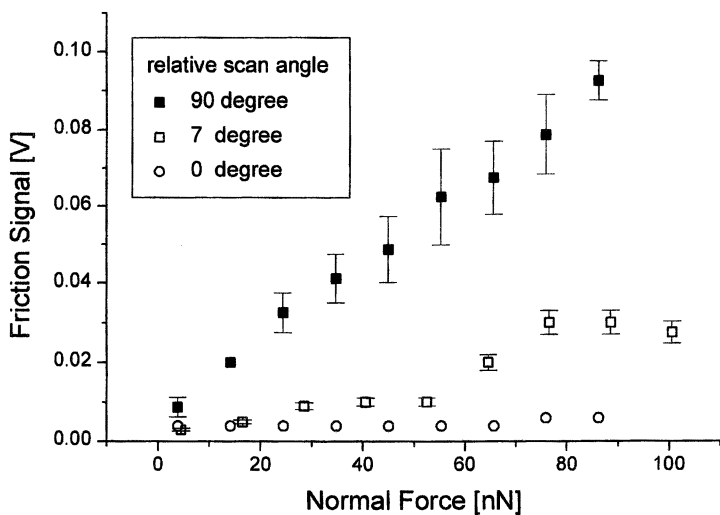


Figure 3a. Friction vs. relative scan angle for oriented PTFE measured with a Si_3N_4 tip in ethanol.

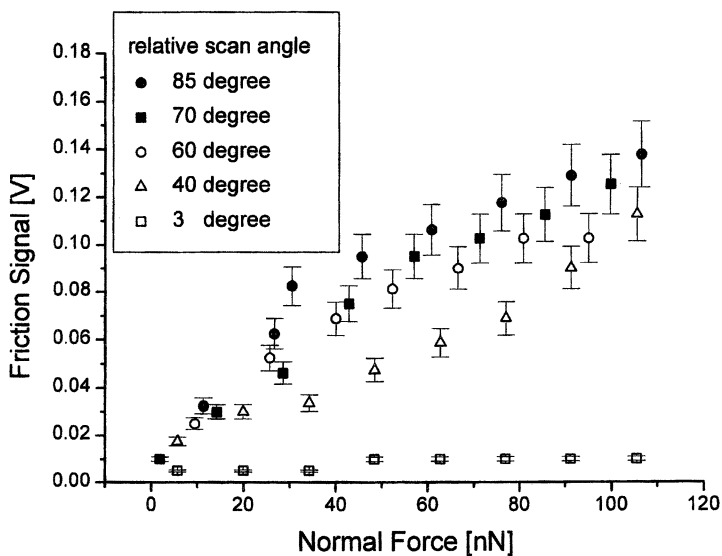


Figure 3b. Friction vs. relative scan angle for oriented PTFE measured with a Si_3N_4 tip in air.

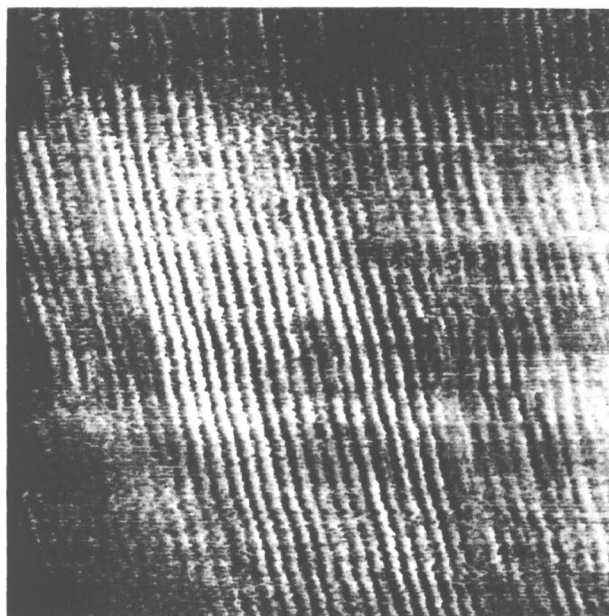


Figure 4. LFM image of HDPE (scan size: 17.3 nm x 17.3 nm) obtained with a $-\text{CF}_3$ tip in air (image reproduced with permission from reference 20 Copyright 1997 American Chemical Society.)

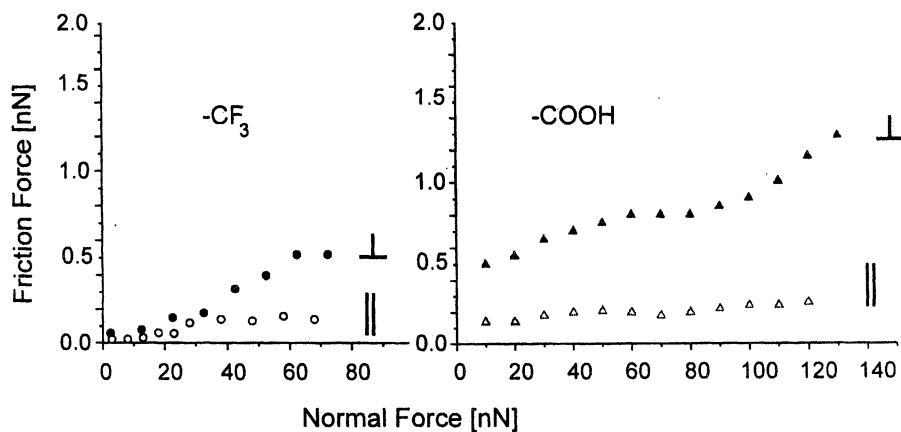


Figure 5a. Friction force vs. normal force plot for HDPE measured with modified tips in air (plots reproduced with permission from reference 20 Copyright 1997 American Chemical Society.)

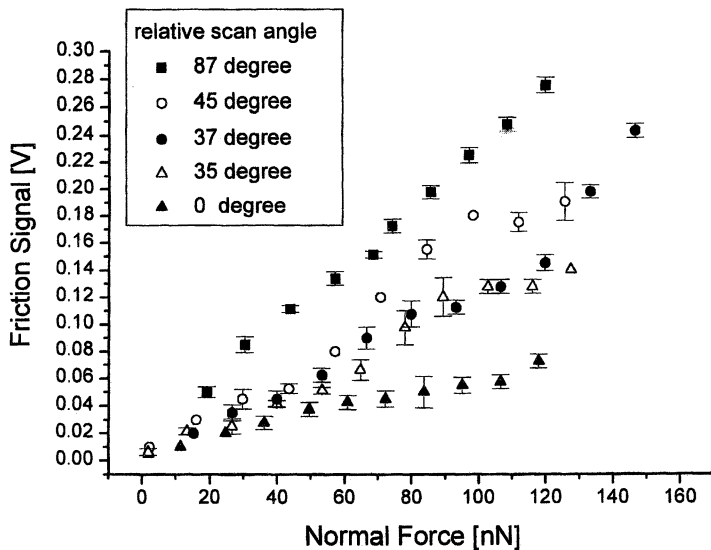


Figure 5b. Friction force vs. normal force plot for HDPE measured for different relative scan directions, obtained with a Si_3N_4 tip in air.

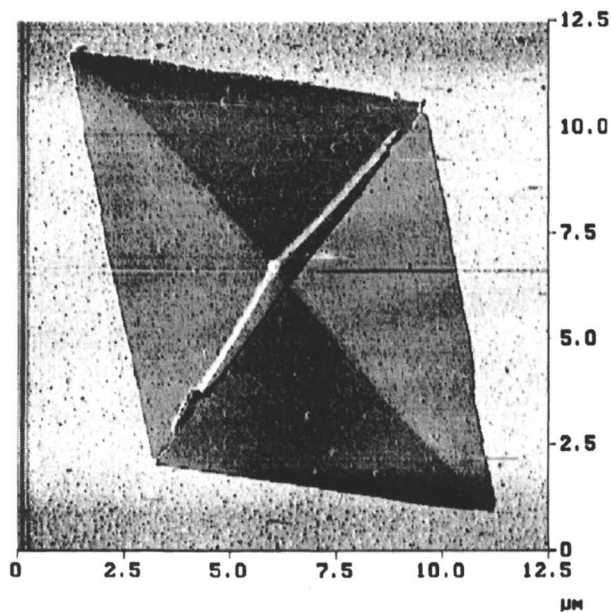


Figure 6a. LFM image of a solution grown PE lamellar crystal obtained in air ($z = 0.2$ V).

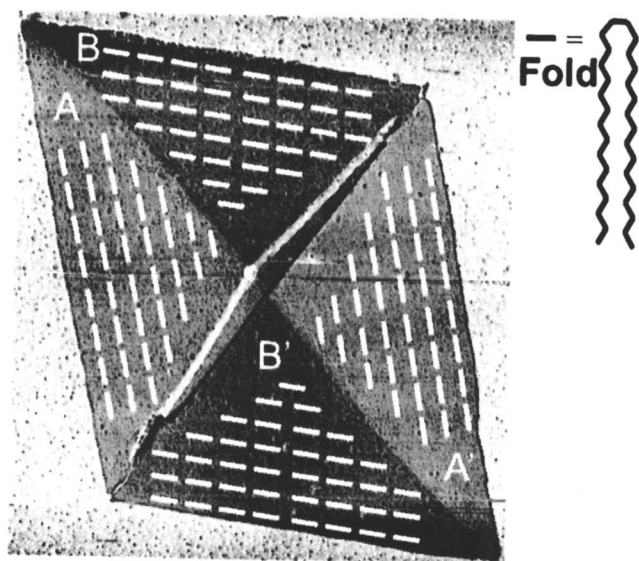


Figure 6b. The directions of the chain folds are schematically indicated in the LFM image of the solution grown PE lamellar crystal shown in Figure 6a (not to scale).

manual rotation of the specimen, was in all cases related to the orientation of the crystal edges (which coincide with the fold directions as depicted in Figure 6b) with respect to the fixed scan direction. By performing line scans in dependence on the normal force (24) and the scan velocity on the crystal shown in Figures 6, we could construct a friction "phase diagram" (4) between silicon nitride and PE lamellar crystals (Figure 7).

Friction is found to be higher in the sectors denoted with A in Figure 6a which have the growth edge predominantly parallel to the scan direction. The difference in friction between low and high friction sectors (A and B, respectively), was found to increase with normal force and scan velocity. The adhesion, however, is the same on all different sectors on the sample (Figure 8). The observed friction behavior can be described in first approximation assuming a time (or sliding velocity) dependence of the friction signal similar to linear polymer viscoelasticity. The relative values of the dissipative and the conservative energy contributions during sliding friction vary as a function of scan velocity. According to the time-temperature superposition principle, increasing velocity corresponds to decreasing temperature. The friction forces observed in our experiments increase with increasing sliding velocity. This increase corresponds, for the given materials, to an increase of dissipative energy loss (related in the first approximation to the loss tangent, $\tan \delta$, of the polymer surface). In other words, the polymer surface behaves more "solid-like" with increasing sliding velocity. The friction force (similar to $\tan \delta$) according to this model should possess a maximum if either the temperature is decreased, or the sliding velocity is increased. This surface "solidification" temperature is below ambient for the PE lamellar crystals for the sliding velocities and load values one can reach in the LFM experiments.

The friction and adhesion of PE in air have lower values compared to mica (high capillary forces on the hydrophilic mica dominate), while in water the friction and adhesion values are higher (hydrophobic force on PE is dominant). In Figure 9 the corresponding images of single crystals in water are shown.

Transcrystallized Polymer Crystals. A third example of friction anisotropy that is caused by the regular arrangement of polymer molecules was observed in transcrystallized samples of PEO grown on PEO fibers, as shown in Figure 10. Two electrospun fibers (19), which make an angle of ca. 90° , can be seen. Lamellae of PEO grown from aqueous solution, which was deposited on the fibers, exhibit sectorized growth. Growth starts simultaneously and proceeds only until the lamellar features impinge. This process leads to sectors of the crystallizing material. As can be concluded from the lateral force image (right), the friction is clearly different in the sectors with different orientation.

Discussion with Respect to the Cobblestone Model of Interfacial Friction (4). Let us first discuss the friction problem of the fold plane of lamellar crystals and the AFM tip asperity, as described by the Cobblestone model of interfacial friction (4). Ideally, in adhesional contact at rest, the outermost atom(s) of the tip fit snugly into

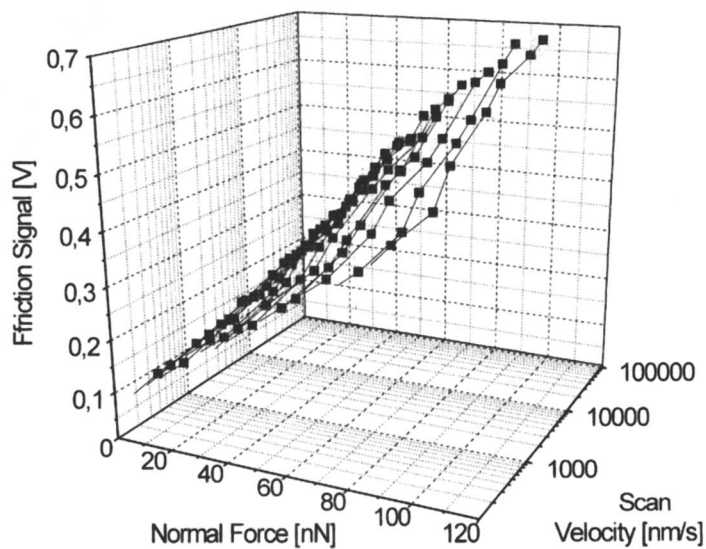
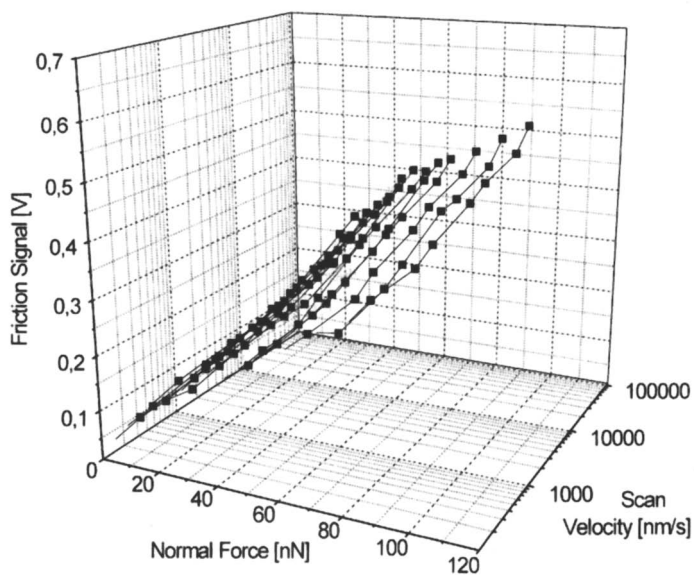
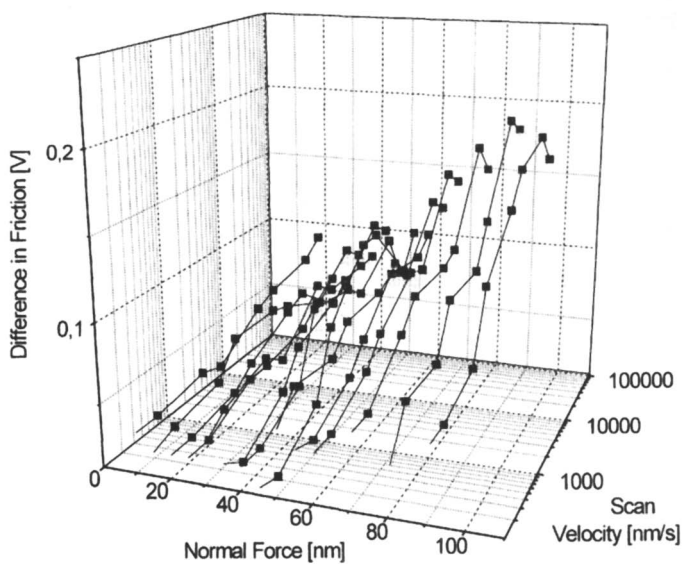


Figure 7. Friction vs. normal force vs. scan velocity for (a) high friction sector,



(b) low friction sector,



(c) difference in friction between sectors measured on PE lamellar crystal in air.

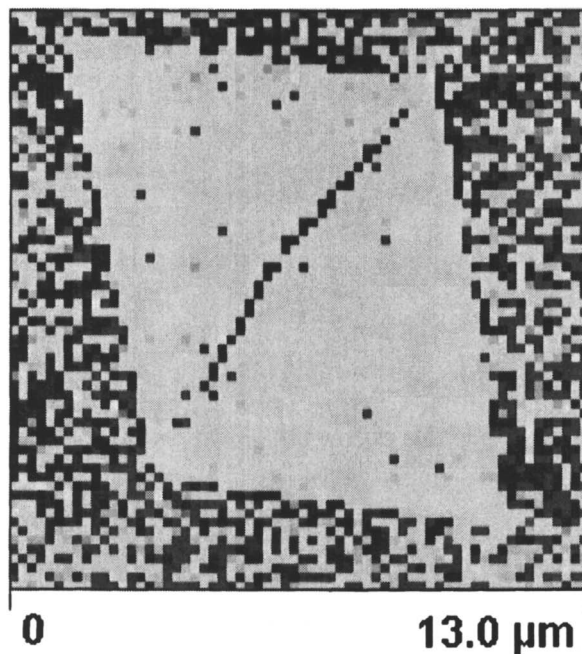


Figure 8. Adhesion image of the lamellar PE crystal shown in Figure 6. Bright tones corresponds to low adhesion (50 nN), dark tones to high adhesion (80 nN). The contrast in the adhesion images is defined on the basis of the convention that attractive forces are negative.

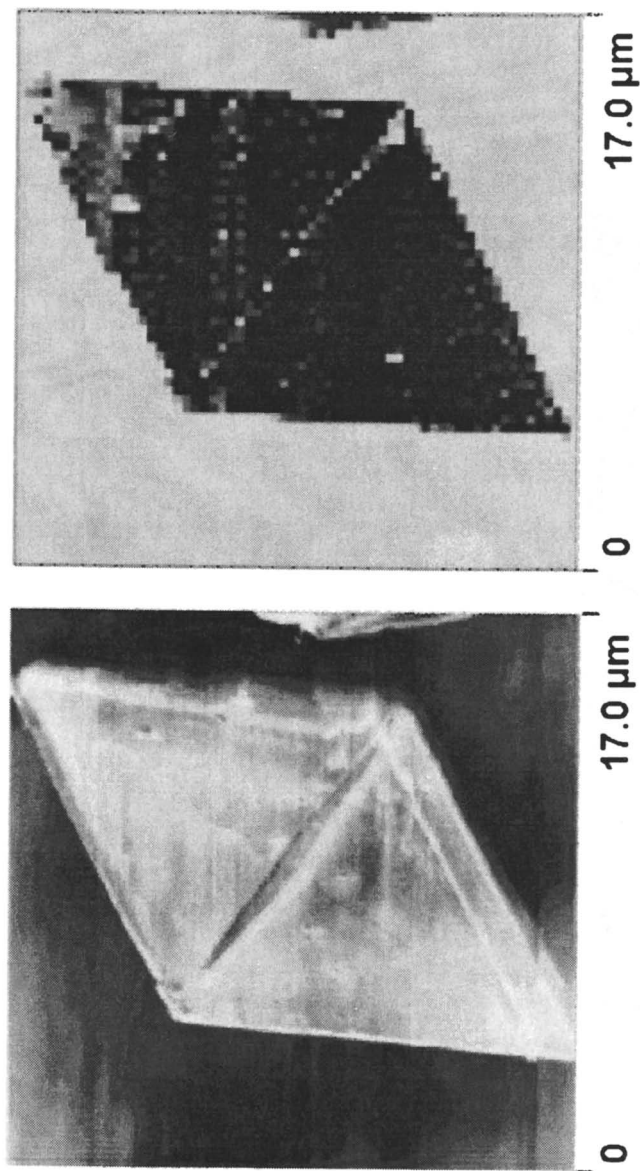


Figure 9. Friction force image (left, z-scale: dark 0.0 V - bright 0.5 V) and adhesion force image (right, z-scale: bright 1 nN - dark 60 nN) on PE lamellar crystal obtained in water. The contrast in the adhesion images is defined on the basis of the convention that attractive forces are negative.

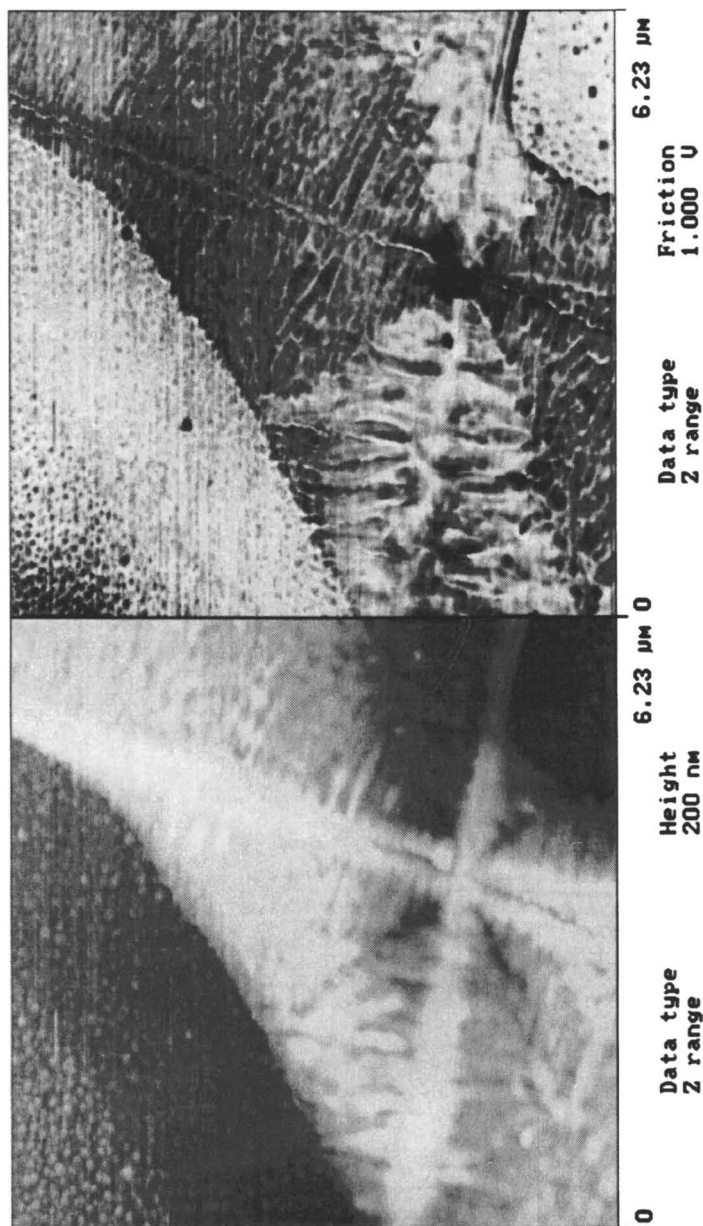


Figure 10. Dual height (left) and friction (right) image of PEO transcrystallized on electrospun PEO fibers.

the grooves defined by the folds of the polymer crystal. Upon applying a lateral force on the tip, it will move laterally and in the normal direction by the small distances d_0 and d , respectively, as shown in Figure 11. The general equation for both static and kinetic friction force F can be given in the following form:

$$F = \epsilon (2E_0A/D + L) d/d_0 \quad (1)$$

where ϵ is the energy fraction dissipated during the kinetic friction process, E_0 is the energy per unit area needed to separate the tip from contact to infinity, A is the contact area, and L is the load on the tip. For the fold surface of the solution-grown lamellar crystal the ratio of d/d_0 , and thus the friction force, will depend on the direction of the lateral movement of the sample under the tip. The effective d in the fold direction is expected to be lower as compared to the value of the effective d in the fold-perpendicular direction as the outermost atom(s) of the tip can "slide" in the grooves defined by the chain folds. During the friction process, which occurs perpendicular to the folds, the tip apex will "bump" into the folds (provided that the chain folds are predominantly directional within each sector, compare Figure 6).

In the case of the uniaxially oriented HDPE and PTFE surfaces consisting of fibrillar extended-chain crystals, the ratio of d/d_0 and thus the friction force, is expected to depend on the relative angle between chains and fixed scan direction. For the highly oriented fibers depicted in Figures 1, 2, and 4, rough estimates for d_0 values can be given. The value of d_0 in the chain-perpendicular direction is equal to the known van der Waals radius of the polymer chains. The quantity d_0 depends on the relative scan angle γ (angle between fast scan axis and polymer chain direction) while d can be assumed to be constant. From geometrical considerations it can be shown that:

$$d_0(\gamma) = d_0(90^\circ) / \sin \gamma \quad (2)$$

Thus, if we assume that E_0 , A , and ϵ are independent of the relative scan direction and L is constant, the friction should vary systematically with the scan angle. The friction data measured for PTFE and HDPE (*vide supra*) can be reasonably well described by a $\sin \gamma / d_0(90^\circ)$ dependency as predicted by equations 1 and 2. In Figure 12 an example for PTFE measured in air is shown.

In the chain-parallel direction, only the HDPE showed a periodic stick slip behavior with a repeat distance of ca. 2.5 Å. This distance is equal to the repeat unit of polyethylene (16, 20). For PTFE the LFM friction loops in our experiments did not reveal any stick slip behavior. Thus, in this case, we cannot determine the value of d_0 in the chain-parallel direction. In this case we can, however, assume that the value of d is close to 0. Based on equation 1, the friction anisotropy is therefore expected to be larger for PTFE, than that for HDPE. For a semi-quantitative comparison of friction forces predicted by equation (1) on one hand and experimental results obtained on highly oriented polymer surfaces on the other hand, one should be

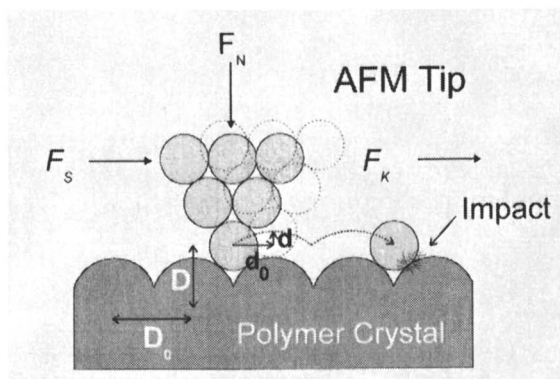


Figure 11. Schematic representation of the events occurring during sliding motion of the AFM tip over an ordered surface (Adapted from ref. 4).

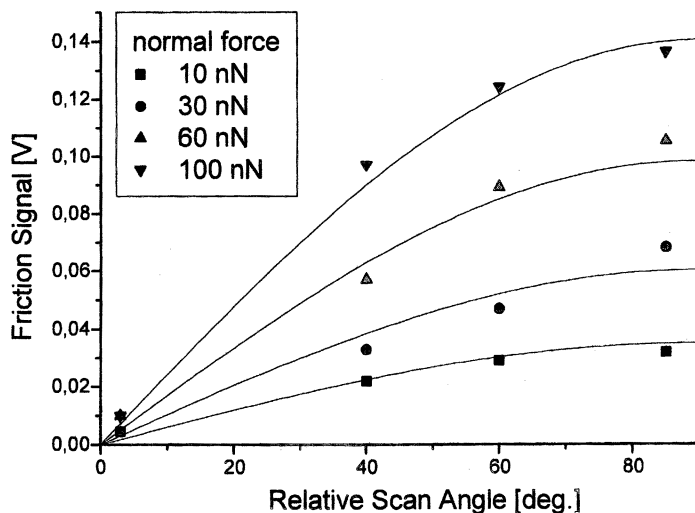


Figure 12. Experimentally determined friction force vs. relative scan angle for PTFE. The corresponding fits are based on equations 1 and 2. For details see text.

able to measure or calculate the adhesion energy, as well as the contact area from AFM data. Corresponding research is currently in progress in our laboratory.

Conclusions

Anisotropic friction and molecular stick-slip friction were observed on a number of polymer systems by LFM using non-functionalized and functionalized tips. The observations described in this paper can be understood within the frame of the cobblestone (interlocking asperity) model. For a quantitative description, however, important parameters such as the energy fraction dissipated during the kinetic friction process (ϵ) are still lacking.

Acknowledgment

The authors thank Dr. Rob Pearce for the donation of the PE lamellar crystal sample. This work has been supported by the Council for Chemical Sciences of the Netherlands Organization for Scientific Research (CW-NWO) in the priority program materials (PPM).

References

1. *Fundamentals of Friction*; Singer, I. L.; Pollock, H. M., Eds.; Kluwer: The Netherlands, 1992.
2. Kim, H. I.; Koini, T.; Lee, T. R.; Perry, S. S. *Langmuir* **1997**, *13*, 7192.
3. For a recent review see: Magonov, S. N.; Whangbo, M.-H. *Surface Analysis with STM and AFM*; VHC: Weinheim 1996.
4. Israelachvili, J. N.; Chen, Y.-L.; Yoshizawa, H. In *Fundamentals of Adhesion and Interfaces*; Rimai, D. S.; DeMejo, L. P.; Mittal, K. L., Eds.; VSP, 1995, pp. 261 - 279.
5. Johnson, K. L.; Kendall, K.; Roberts, A. D. *Proc. R. Soc. London, A* **1971**, *324*, 301.
6. Carpick, R. W.; Agraït, N.; Ogletree, D. F.; Salmeron, M. *Langmuir* **1996**, *12*, 3334.
7. For a recent review see: Carpick, R. W.; Salmeron, M. *Chem. Rev.* **1997**, *97*, 1163.
8. Mate, C. M.; McClelland, G. M.; Erlandsson, R.; Chiang, S. *Phys. Rev. Lett.* **1987**, *59*, 1942.
9. Frisbie, C. D.; Rozsnyai, L. F.; Noy, A.; Wrighton, M. S.; Lieber, C. M. *Science* **1994**, *265*, 2071.
10. Examples of anisotropic friction were reported for a variety of systems, see reference 7, and: Schönherr, H.; Kenis, P. J. A.; Engbersen, J. F. J.; Harkema, S.; Hulst, R.; Reinhoudt, D. N.; Vancso, G. J. *Langmuir* **1998**, *14*, 2801 and references therein.
11. Nisman, R.; Smith, P. F.; Vancso, G. J. *Langmuir* **1994**, *10*, 1667.
12. Smith, P. F.; Nisman, R.; Ng, C.; Vancso, G. J. *Polym. Bull.* **1994**, *33*, 459.
13. Pearce, R.; Vancso, G. J. *Polymer* **1998**, *39*, 6743.
14. Vancso, G. J.; Förster, S.; Leist, H. *Macromolecules* **1996**, *29*, 2158.
15. Galeski, A.; Bartczak, Z.; Argon, A. S.; Cohen, R. E. *Macromolecules* **1992**, *25*, 5705.

16. Schönherr, H.; Vancso, G. J.; Argon, A. S. *Polymer* **1995**, *36*, 2115.
17. Schönherr, H.; Vancso, G. J. *Polymer* **1998**, *39*, 5705.
18. Wittmann, J. C.; Smith, P. *Nature* **1991**, *352*, 414.
19. Jaeger, R.; Schönherr, H.; Vancso, G. J. *Macromolecules* **1996**, *29*, 7634.
20. Schönherr, H.; Vancso, G. J. *Macromolecules* **1997**, *30*, 6391.
21. *Polymer Handbook*; Brandrup, J.; Immergut, E. H., Eds.; 3rd ed.; Wiley: New York, 1989; p V/37.
22. The accurate determination of the angle (error ca. $\pm 2^\circ$) was based on the orientation of the crystal facet as measured by *in situ* LFM scans (see Figure 2).
23. Koutsous, V. Ph.D. Thesis, State University of Groningen, The Netherlands, 1997.
24. Normal force is defined as the sum of experimentally determined pull-off force and external load.

Chapter 20

Scanning Force Microscopic Study of Polyethylene Single Crystals Prepared by a Self-Seeding Method

Tomokazu Fujii, Atsushi Takahara, and Tisato Kajiyama

Department of Materials Physics and Chemistry, Graduate School of Engineering,
Kyushu University, 6-10-1 Hakozaki, Higashi-ku, Fukuoka 812-8581, Japan

The surface structures of high-density polyethylene (HDPE) single crystals with weight average molecular weight, $M_w=32k$, $120k$ and $520k$ prepared by a self-seeding method were investigated by atomic force microscopy (AFM) and lateral force microscopy (LFM). A characteristic lozenge shape lamellar crystal of ca. 12 nm thick was observed with AFM. The contrast of lateral force of the HDPE single crystal in LFM images was observed between adjacent sectors, which means that the chain folding directions were different. The magnitude of lateral force in LFM measurement increased with scanning angle, θ , which was defined as the angle between scanning direction of the cantilever and $\{110\}$, that is the growth face of the HDPE single crystal. These results indicate that the surfaces of the HDPE single crystals prepared by a self-seeding method exhibit regular sharp chain folding along $\{110\}$ at the surface. Furthermore, it was suggested that the folding structure of the HDPE single crystal surface might depend on the crystallization methods, such as isothermal crystallization or self-seeding one.

Since polyethylene (PE) single crystal prepared by isothermal crystallization method from a dilute xylene solution was discovered by Keller et al. (1), several chain folding models on the PE single crystal surface have been proposed (2-4). As the thickness of lamellar crystal is much shorter than the length of a PE chain, a PE molecular chain should fold at the lamellar surface with an appropriate conformation. However, since direct experimental evidence on the chain folding structure have not been found out yet, various possibilities on the chain folding structure have been proposed for the past three decades (3,4). It is reasonable to consider that the chain folding structure of the single crystal strongly depends on the crystallization temperature, the cooling rate, the molecular weight and its distribution (4).

¹ Corresponding author.

Scanning force microscopy (SFM) is one of the new scanning probe microscopic (SPM) techniques for investigating the surface topology or the surface properties of solid materials with spatial resolution on a molecular level. SFM can image the surface morphology on the basis of the various types of forces acting between sharp microcantilever tip and sample surface, such as van der Waals, electrostatic, frictional, and magnetic forces. Moreover, it has been proved that the molecular resolution image of lipid monolayer can be observed by atomic force microscopy (AFM) (5) and lateral force microscopy (LFM) (6). The molecular resolution image can be observed because the stick-slip motions of the cantilever and tip occur on an molecular scale in LFM measurement. The direct observation of chain folding on the PE single crystal surface was attempted by using AFM (7). However, since the molecular motion of the chain folding part might be active at room temperature (293 K) that is higher than the glass transition temperature of the PE, the direct observation of the chain folding part at room temperature is very difficult by using AFM or LFM.

Anisotropic LFM measurement can reveal the properties of sample (8). It has been indicated that the LFM can distinguish the different molecular tilt angle of the thiolipid monolayer based on friction anisotropic and asymmetric measurements using frictional loop (9). Anisotropic lateral forces on the single crystal surface of polyoxymethylene and PE have been revealed by LFM (10-12). In our previous report (12), the LFM measurement of the isothermally crystallized fractionated high-density polyethylene (HDPE) single crystals with weight average molecular weight, $M_w=10k$ and $45k$ revealed that the lateral force on the single crystal surface was dependent on the scanning direction against the $\{110\}$ growth face. On the other hand, the lateral force was independent of the scanning direction for the HDPE single crystal surface of unfractionated HDPE with $M_w=520k$. These LFM results indicate the sharp regular fold for the fractionated HDPE single crystals with $M_w=10k$ and $45k$, whereas the loose loop with randomly reentry chain folding for the unfractionated HDPE single crystal with $M_w=520k$. In this study, the AFM observation and the LFM measurement were carried out for the HDPE single crystals prepared by a self-seeding method (13) in order to discuss the effect of crystallization conditions on the chain folding structure of the HDPE single crystals.

Experimental Method.

Sample Preparation. HDPEs used were unfractionated HDPE (Marlex 9, $M_w=520k$) with a broad molecular weight distribution and fractionated HDPEs ($M_w=32k$ and $120k$) with a narrow molecular weight distribution. The HDPE single crystals were prepared by a self-seeding technique (13). Table I shows the crystallization conditions used in this study. The HDPEs ($M_w=32k$, $120k$ and $520k$) were dissolved in *p*-xylene at T_{d1} K to obtain a 0.01 wt% solution. The solutions were kept at the first crystallization temperature, T_{c1} K for 30 min. Then, the solution was heated again to T_{d2} K and the solutions were kept again for crystallization at the second crystallization temperature, T_{c2} K for 48 hrs. Finally, the solution was cooled to 293 K. A small amount of solution with the suspended HDPE single crystals was dropped onto a cleaned silicon wafer substrate and allowed to air-dry at 293 K for the AFM observation and the LFM measurement.

AFM observation and LFM measurement. The AFM and the LFM images of the HDPE single crystals were obtained with SPA300 (Seiko Instruments Industries, Co. Ltd., Japan). The cantilever used in this study was a rectangular-shaped one with a quadrangular pyramid of silicon nitride (Si_3N_4) microtip (Olympus, Co. Ltd., Japan). The bending spring constant of the cantilever was 0.09 N m^{-1} . In the AFM observations and the LFM measurements, the distance between tip and sample surface was kept constant by a feedback loop, moving the sample surface (the sample position) up and down with the piezoelectric scanner (topography mode). The images were taken with $20 \mu\text{m} \times 20 \mu\text{m}$ scanner. The AFM observations and the LFM measurements were carried out under a reference force of -0.022 nN (repulsive force) at 298 K in air. Figure 1 shows the definition of the scanning angle, θ , in the LFM measurement. In the LFM measurement, the magnitude of anisotropic lateral force was measured by changing the scanning direction of cantilever from 0° (the scanning direction is parallel to the $\{110\}$ growth face) to 90° (the scanning direction is perpendicular to the $\{110\}$ growth face) against the $\{110\}$ growth face of the HDPE single crystal. Since the scanning direction was perpendicular to the long axis of the cantilever, the degree of cantilever torsion reflected the magnitude of lateral force between microtip and sample surface. The magnitude of lateral force was determined based on the measurement under bidirectional scanning.

Results and Discussion.

AFM observation and LFM measurement. Figures 2, 3 and 4 show the AFM topographical (a), the LFM (b) images for the $M_w=32\text{k}$, 120k and 520k HDPE single crystal prepared by a self-seeding method and the schematic representation of sharp chain folding on the HDPE single crystal surface and the scanning direction of cantilever in LFM measurement. In the cases of AFM observation and the LFM measurement shown in Figures 2, 3 and 4, the scanning direction of the cantilever was from left to right and the images were captured during scanning without any filter treatments. Characteristic lozenge shaped lamellar crystals with ca. 12 nm thick were observed for any molecular weight used in this study. The thickness and dimension of a single crystal agreed well with those obtained from small-angle X-ray scattering measurement and transmission electron microscopic observation (4), respectively. The LFM images showed a different contrast corresponding to the different lateral force between adjacent sectors, when the scanning direction was parallel to the $\{110\}$ growth face. This means that the fold domain boundaries are clearly distinguishable on the basis of LFM measurement. Since a disordered fold surface composed of random irregular chain folds or physically adsorbed polymer chains in a random coil state on single crystal surface would not exhibit such a lateral force anisotropy, it seems reasonable to consider that the regular chain folding is formed on the single crystal surface, even in the case that the unfractionated HDPE single crystal with high M_w of 520k was prepared by the self-seeding method. This conclusion is quite different from that the switchboard type chain folding was formed for the single crystal of the same HDPE prepared by an isothermal crystallization (12). Since the self-seeding technique means that higher molecular weight components crystallize in a solution and lower ones dissolve in solvent, the fractionation based on molecular weights proceeds during a crystallization process. Therefore, it seems reasonable to consider that the fractionation of molecular weights in the self-seeding process affects the surface structure of the HDPE single crystal. Also, it should be noticed that in the case that the diagonal axis of the single crystal

Table I. Crystallization conditions of HDPE single crystals in self-seeding method.

Mw	Mw/Mn	T _{d1} /K	T _{c1} /K	T _{d2} /K	T _{c2} /K
32k	1.11	411	339	368	343
120k	1.19	411	338	370	343
520k	large	411	338	374	343

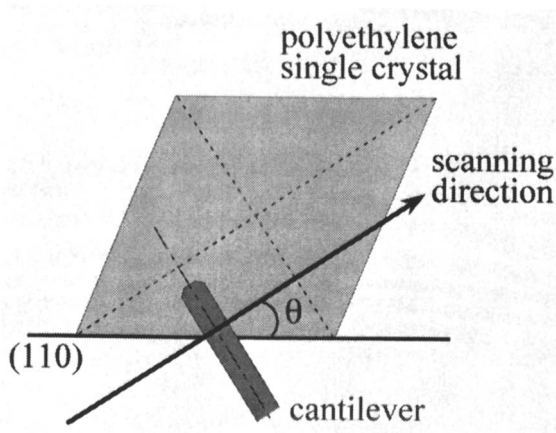


Figure 1. Schematic representation of the definition of the scanning angle, θ , in the lateral force measurement.

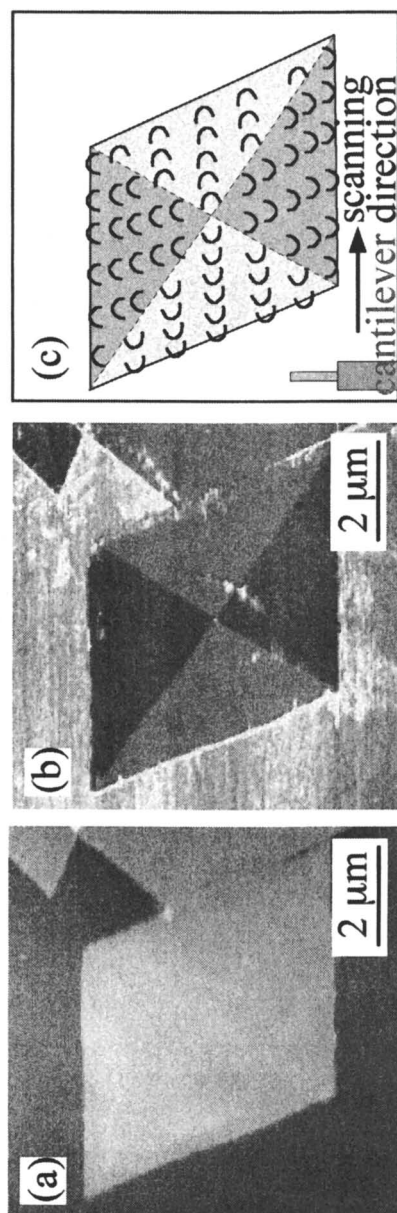


Figure 2. AFM (a), LFM (b) images and relationship between scanning direction of cantilever and chain folding direction (c) of single crystals of the fractionated HDPE ($M_w=32k$)

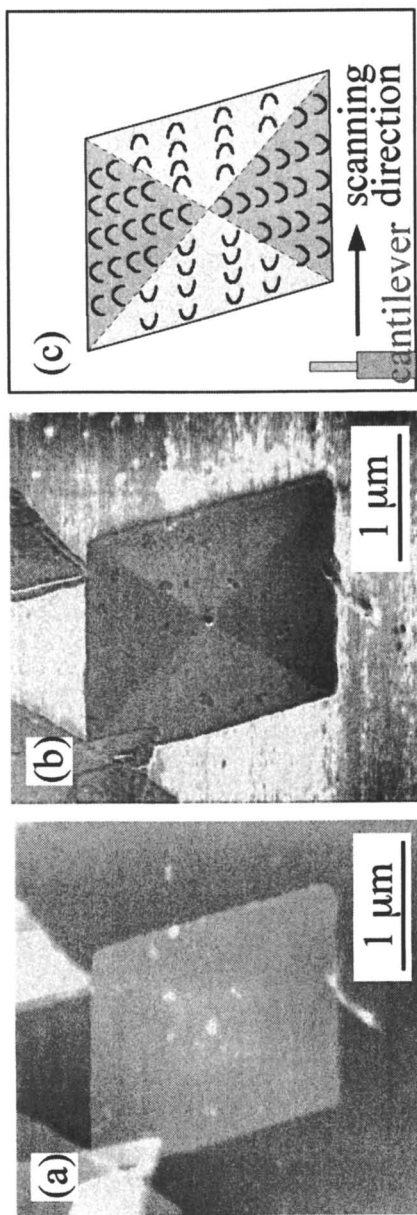


Figure 3. AFM (a), LFM (b) images and relationship between scanning direction of cantilever and chain folding direction (c) of single crystals of the fractionated HDPE ($M_w=120k$) single crystals.

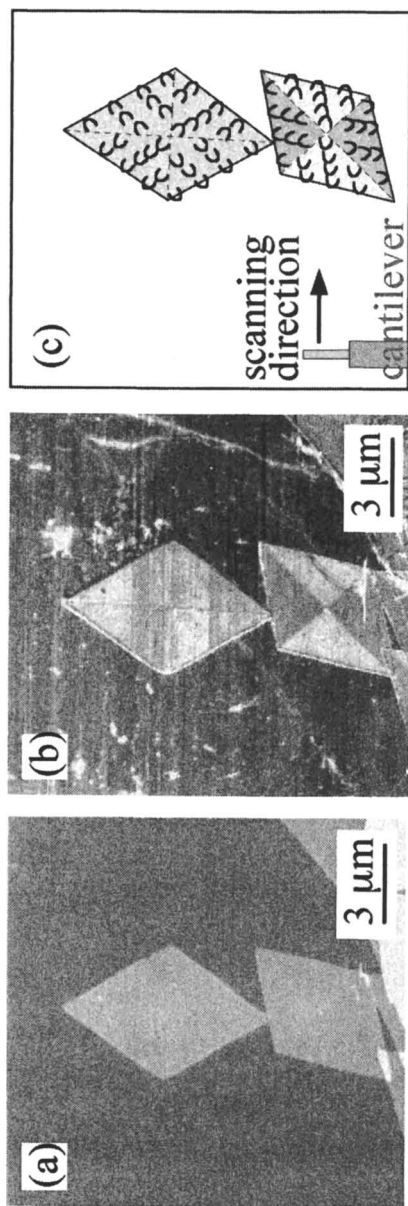


Figure 4. AFM (a), LFM (b) images and relationship between scanning direction of cantilever and chain folding direction (c) of single crystals of the unfractionated HDPE ($M_w=520k$) single crystal.

was parallel to the scanning direction, the HDPE single crystal did not show any difference in the magnitude of lateral force between adjacent domains as shown by the upper single crystal in Figure 4 (b). This indicates that even though the chain folding direction, that is, the crystal growth surface, is different between adjacent sectors, the angle between cantilever and direction of chain folding is the same. Then, these LFM results apparently indicate the sharp regular fold along the {110} growth face is formed on the HDPE single crystal surface prepared by the self-seeding method as shown in Figures 2 (c), 3 (c) and 4 (c).

Scanning angle dependence of lateral force. The scanning angle, θ , dependence of lateral force was measured in order to investigate the regularity of chain folding on the HDPE single crystal surface. If the chain folding was formed predominantly along the {110} growth face of the single crystal, the θ dependence of lateral force should be observed due to the existence of directionally ordered or arrayed "loops" as shown in Figures 2 (c), 3 (c) and 4 (c). When the scanning direction of the tip is along the sharp fold loops, in other words, is parallel to the growing edge of the crystal, the LFM tip might experience lower lateral force. On the other hand, the tip might experience higher lateral force if the tip bumps into the fold loops. Figure 5 shows the schematic representation of lateral force curve upon bidirectional scanning in lateral force measurement. The bidirectional lateral force measurement can distinguish the torsion of cantilever due to lateral force of the HDPE single crystal surface from that due to topographical origin. The quantitative evaluation can be performed based on the average of magnitudes of lateral force in both scanning directions. Figure 6 shows the scanning angle dependence of lateral force for the single crystal of unfractionated HDPE of $M_w=520k$ and fractionated HDPEs of $M_w=120k$ and $32k$. The magnitude of lateral force increased gradually with the scanning angle, θ , from 0° to 90° for all cases, in other words, the minimum and maximum lateral forces were observed at $\theta=0^\circ$ and $\theta=90^\circ$, respectively. This apparently indicates that the sharp chain folds were formed parallel to the {110} growth face as described above. Figure 7 shows the adjacent reentry and regular sharp fold model (a) and the random reentry and loose loop fold model (switchboard model) with {110} (b). It is obvious that in the case that the chains on the HDPE single crystal surface form the adjacent reentry and regular sharp fold (Figure 7 (a)), the tip of cantilever should experience the different magnitude of lateral force depending on the θ values. On the other hand, when the surface structure of the HDPE single crystal corresponds to the switchboard like fold (Figure 7 (b)), the tip of cantilever might feel the same lateral force without any θ dependence. Therefore, it can be concluded from Figure 6 that the surface structure of the HDPE single crystal prepared by a self-seeding method is composed of the adjacent reentry and regular sharp fold.

We have reported that in the case of the single crystal of unfractionated HDPE of $M_w=520k$ prepared by an isothermal crystallization technique, the magnitude of lateral force was independent of θ (12). Therefore, it was concluded that the regular direction of fold loops was not present on the single crystal surface of unfractionated HDPE with $M_w=520k$ prepared by an isothermal crystallization method but the switchboard like fold was formed as shown in schematically Figure 7 (b). It seems reasonable to consider that the adjacent reentry and regular sharp fold structure of the HDPE single crystal is formed due to the fractionation of molecular weights based on

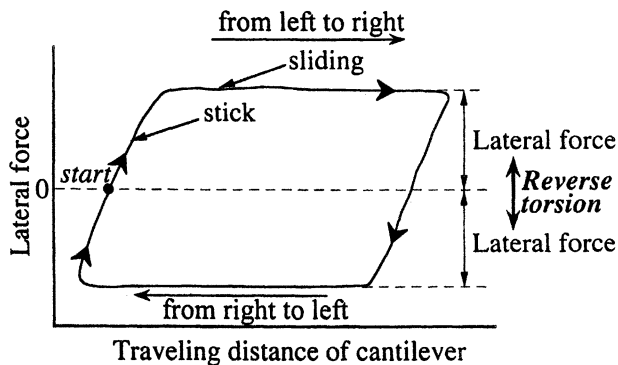


Figure 5. Schematic representation of lateral force curve with bidirectional scannings.

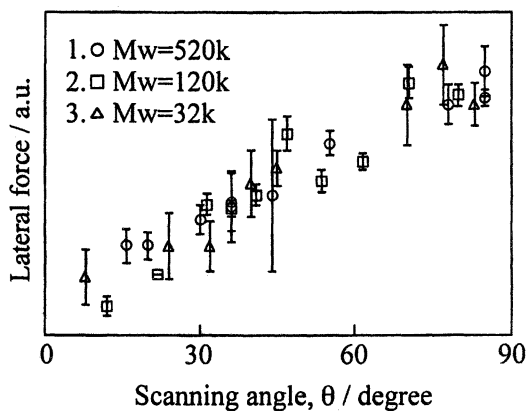


Figure 6. Scanning angle dependence of lateral force for the HDPE single crystal with Mw of 520k, 120k and 32k prepared by self-seeding method.

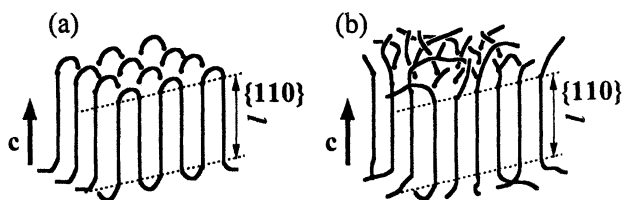


Figure 7. Adjacent reentry and regular sharp fold model (a) and random reentry fold model (switchboard model) (b) at the surface of HDPE single crystal.

their different clouding points during a self-seeding process. These results suggest that surface structures of the HDPE single crystal depend on the crystallization method.

The origin of lateral force has not been completely understood yet because the lateral force reflects many properties of sample surface. The results of LFM measurement do not always have intuitive explanation, the counterintuitive results in the asymmetric LFM measurement have been obtained in the system of thiolipid monolayer (8). In the case of PE single crystal, the molecular tilt direction was equivalent in four sectors of one HDPE lamellar single crystal (4). However, the folding direction of HDPE chain on the surface in adjacent sectors of HDPE single crystal seems to be different. Therefore, it is reasonable to consider that the anisotropy of the lateral force in our experiment was due to the difference in folding direction of HDPE chain.

Conclusion.

The anisotropic lateral force measurements with varying the scanning angle, θ , against the {110} growth face of the HDPE single crystals prepared by the self-seeding method indicates that the adjacent reentry and regular sharp fold is formed parallel to the {110} growth face on the single crystal surface, even in the case that the unfractionated HDPE single crystal with $M_w=520k$. In addition, it was suggested that the state of chain folding on the HDPE single crystal surface strongly depends on the crystallization methods.

Acknowledgement

This study was partially supported by Grant-in-Aid for COE research and Scientific Research on Priority Areas, "Near-field Nano Optics" (No. 286-09241222), from Ministry of Education, Science, Sports and Culture of Japan.

Literature Cited

1. Keller, A. *Phil. Mag.* **1957**, *2*, 1171.
2. Reneker, D. H.; Geil, P. H. *J. Appl. Phys.* **1960**, *31*, 1916.
3. *Faraday Disc. Chem. Ser.* **1979**, *68*, 7.
4. Keller, A. *Rept. Prog. Phys.* **1968**, *31*, 623.
5. Meyer, E.; Howald, L.; Overney, R. M.; Heinzlmann, H.; Frommer, J.; Güntherodt, H. J.; Wagner, T.; Schier, H.; Roth, S. *Nature* **1991**, *349*, 398.
6. Overney, R. M.; Takano, H.; Fujihira, M. *Phys. Rev. Lett.* **1994**, *72*, 3564.
7. Reneker, D. H.; Chun, I. In *Scanning Probe Microscopy of Polymers*; ACS Symp. Ser. 694; American Chemical Society: Washington, DC, 1996; Chapter 2, pp 32-52.
8. Schwarz, U. D.; Bluhm, H.; Hölscher, H.; Allers, W.; Wiesendanger, R. In *Physics of Sliding Friction*; Persson, B. N. P.; Tosatti, E., Ed.; Kluwer Academic Publishers: Dordrecht, Netherlands, 1996; pp 369-402.
9. Liley, M.; Gourdon, D.; Stamou, D.; Meseth, U.; Fisher, T. M.; Lautz, C.; Stahlberg, H.; Vogel, H.; Burnham, N. A.; Duschl, C. *Science* **1998**, *280*, 273.
10. Nisman, R.; Smith, P.; Vancso, G. J. *Langmuir* **1994**, *10*, 1667.
11. Smith, P.; Nisman, R.; Ng, C.; Vancso, G. J. *Polym. Bull.* **1994**, *33*, 459.
12. Kajiyama, T.; Ohki, I.; Takahara, A. *Macromolecules* **1995**, *28*, 4768.
13. Blundell, D. J.; Keller, A. *J. Macromol. Sci.-Phys.* **1968**, *B2*, 301.

Chapter 21

Sparse Coatings by Disperse Adsorption of Cylindrical Brushes

Sergei S. Sheiko¹, Svetlana A. Prokhorova¹, Ute Schmidt², Peter Dzieczok³,
Manfred Schmidt³, and Martin Möller³

¹ Organische Chemie III/Makromolekulare Chemie,
Universität Ulm, 89069 Ulm, Germany

² Molecular Imaging Corporation, Phoenix, AZ 85044

³ Johannes-Gutenberg-Universität, Institut für Physikalische Chemie,
Jakob-Welder-Weg 11, D-55099 Mainz, Germany

Sparse coatings of single macromolecules were prepared by adsorption of polyelectrolyte cylindrical brushes on mica as charged substrate. The degree of coverage was altered between 10 and 50 % by the ionic strength and the degree of ionization of the molecules. The thickness of the layer is determined by the lateral dimension of the molecular brushes, which depends on the grafting density as well as their charge density. For the investigated system, the adsorbed molecules were 2 nm in height and separated by 30-200 nm.

Interest in nanoscopic surface structures is stimulated by recent advances in microelectronics (1), biomimetics (2) and data storage (3). Most interesting examples include quantum dots, field-effect transistors as well as well-defined corrugations to reduce interfacial stickiness. Properties of such devices are significantly altered as their structures are shrunk, e.g. from 100 to <10 nm. Preparation of functional structures on such small size scales requires new approaches in nanotechnology. Complementary to electron and ion beam lithography, novel parallel processes are developed based on concepts from supramolecular and macromolecular chemistry exploiting self organization, templating and replication of molecules in a defined arrangement (4-7). E.g. macromolecular chemists have developed new synthetic strategies to tailor the 3D structure of individual molecules. Both spherically and cylindrically shaped macromolecules have been prepared by attaching side groups like monodendrons (8-10) or linear substituents (11,12) to a linear polymer backbone. The dense branching prevents that such molecules can interpenetrate each other and collapse to a mesoscopically uniform structures. Even in the condensed state, the molecules are well segregated with diameters ranging from 2 to 10 nm. Such macromolecules can be visualized by scanning force microscopy (SFM) as individual species when they get adsorbed from solution on a flat surfaces such as mica or highly oriented pyrolytic graphite (HOPG) (12-16). The height of the monolayer and the distance between

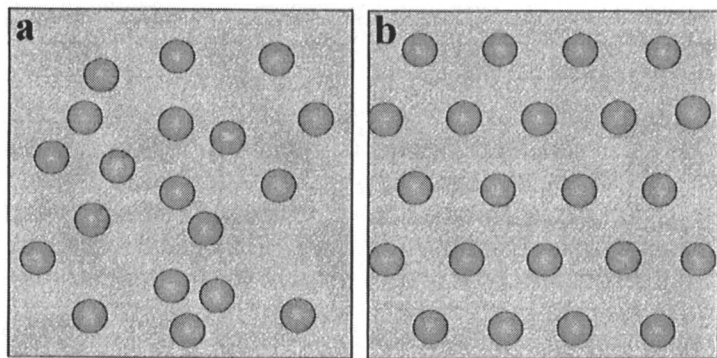


Figure 1. Different types of sparse coatings of individual molecular particles wherein the particles are disordered (a) or demonstrate positional ordering (b).

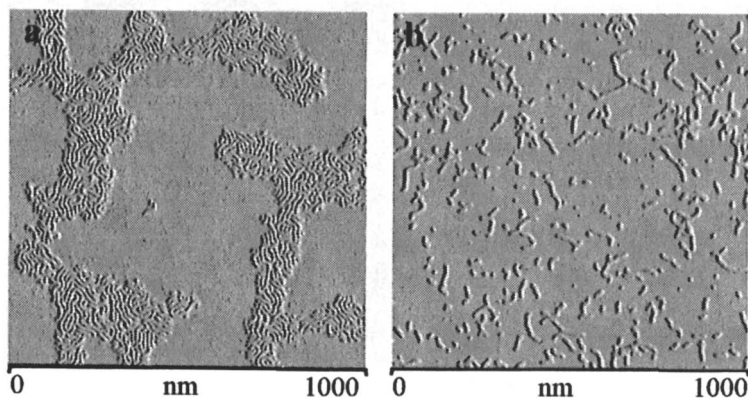


Figure 2. (a) SFM micrograph of adsorbed uncharged PVP brushes from chloroform solution of $c=0.1$ mg/ml on mica by spin coating. Worm-like molecules organized into a densely packed monolayer. (b) SFM image of charged poly(2-vinylpyridinium) brushes adsorbed on a mica from a salt-free aqueous solution of $c=0.01$ mg/ml. Charged PVP molecules repelled each .

packed monolayer islands on mica (Fig. 2a), charged PVP molecules repelled each other. Single molecules in figure 2b are arranged within a particular distance from each other.

The spincoating procedure, by which the films of the charged and the non-charged polymers were prepared, did not allow to study and control the degree of coverage and molecular arrangement within a monolayer.

In-situ Monitoring of the Adsorption Process

Experimental. Employing the magnetic alternative current mode (MAC mode) of a PicoSPM scanning force microscope (Molecular Imaging, AZ) allowed *in situ* monitoring of the adsorption process. This method of surface imaging is based on recording the amplitude variation of a cantilever oscillated by a magnetic field (18). The schematic representation of MAC mode SFM is given in figure 3. The cantilever, is coated by a magnetic material and driven by an alternating magnetic field of a solenoid placed under the sample. The essential advantage of the MAC mode over other oscillating probe techniques is its stable operation in liquid environments. Since the cantilever is directly driven by the external magnetic field, there is no need to move the whole cantilever mounting mechanism, i.e. cantilever holder, cantilever chip and liquid cell. This leads to an increase in control which enables operation of the microscope at much smaller amplitudes. All experiments were done at amplitudes around 5 nm, a set-point decrease of the amplitude as small as 0.5 nm, and a resonance frequency of the cantilever of 9 kHz.

Conformation and Alignment of Single Molecules on Mica. Figure 4 shows a SFM image of ionized poly-2-vinylpyridine brushes adsorbed on mica from a solution in deionized water at a concentration of 0.01 mg/ml. The solution was injected directly into the liquid cell just before starting the scanning, so that the micrographs depict the adsorption in real time. The time between injecting of the polyelectrolytes and recording of the first image was two minutes. Rod-like particles were imaged laying on mica with their backbone oriented parallel to the substrate plane. Different than in the case of the worm-like noncharged brush molecules, no hairpin folds were observed. Due to the electrostatic interaction between the positively charged brushes and the negatively charged mica, the adsorbed molecules did not move during more than one hour while the sample was imaged continuously. The width of the adsorbed molecules was measured to be $d=(8\pm 1)$ nm and their height to be $h=(2.8\pm 0.2)$ nm, which is close to the molecular dimensions measured in the dry state, i.e. $d=(10\pm 1)$ nm, and $h=(2.0\pm 0.2)$ nm.

Single molecules in Figure 4 are located at rather defined distances from each other, and eventually tend to align parallelly or perpendicularly at close distances. In some cases the molecules crossed each other at angles of ca. 90 degrees as it might be expected for electrostatic repulsion of like charged rods (19,20). The degree of coverage was measured to be 25 % of the substrate area. Once adsorbed, the charged PVP molecules did not desorb any more. The coverage did not change within hours in spite of large amount of polyelectrolyte molecules in the solution above the substrate

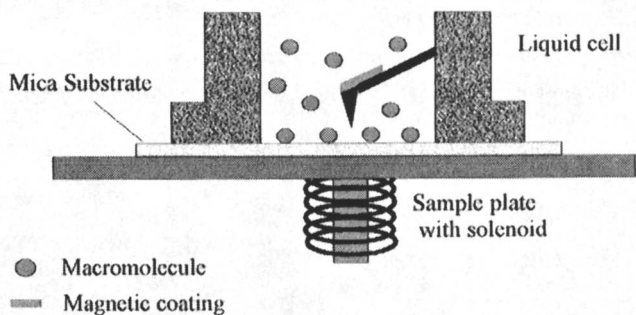


Figure 3. Schematic representation of the MAC Mode scanning force microscope with a liquid cell. A cantilever, coated with a magnetic material, is driven by an alternating magnetic field of a solenoid placed under the sample.

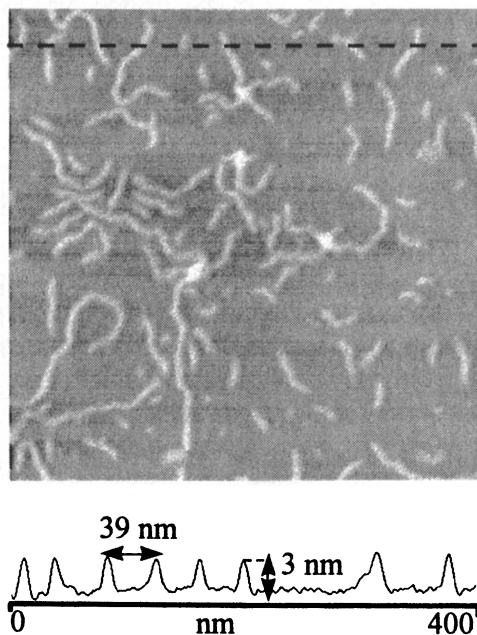


Figure 4. *In-situ* observation of poly(2-vinyl-N-benzylpyridinium bromide) brushes by the MAC mode SFM as adsorbed on mica from a salt-free aqueous solution at a concentration of 0.01 mg/ml.

surface. Dilution of the polyelectrolyte solution with water did not change the coverage of the mica substrate.

Surface Coverage as a Function of the Concentration and the Ionic Strength. In another experiment, the formation of a polyelectrolyte PVP film on mica has been studied as a function of the polyelectrolyte concentration in the reservoir solution above the substrate. The concentration dependence in figure 5 shows that the surface density of the adsorbed molecules does not depend on the concentration which was varied over three orders of magnitude for $c \geq 0.001$ mg/ml. The maximum surface coverage which was achieved for this type of brushes at an ionic strength of about 10^{-5} M NaCl was measured to be 25 ± 5 %.

The coverage of the mica with the poly(2-vinylpyridinium) brushes increased when NaCl was added to the aqueous solution. Figure 6 shows a sequence of images of the polyelectrolyte brushes adsorbed from a 0.05 mg/ml solution before (Fig. 6a), and at different times after addition (Fig. 6b and c) of 50 μ l 0.5 M NaCl to 200 μ l polyelectrolyte solution which corresponds to 0.1 mol/L NaCl. The image in Figure 6a is a downward scan taken just before adding salt. Directly after recording this image, the NaCl solution was inserted into the liquid cell and only after 81 sec., precipitation of the molecules from solution was observed to increase the coverage of the mica surface (Fig. 6b). Due to this time dependence, the image is split in two regions with different degrees of coverage. According to the Einstein-Smoluchovsky equation, the time interval corresponds to the diffusion time of the NaCl molecules to the scanned surface. After adding NaCl to the solution, the number of adsorbed molecules approximately doubled and coverage became approximately equal to 45% (Fig. 6c). This value approached the maximum surface coverage for random sequential adsorption of hard particles on a flat surface (21, 22).

The coverage of the mica with polyvinylpyridinium brushes and the distance between the adsorbed molecules can also be modified by increasing the charged density of the brushes. If quaternization is performed with methylbromid, the resulting polyelectrolyte is more hydrophilic than in case of benzylbromid. This leads to increased dissociation of Br^- ions in aqueous solution causing an increasing charge density of the PVP brushes (23). Figure 7 shows a micrograph of adsorbed poly(vinylmethylpyridiniumbromide) brushes on mica (from a 0.03 mg/ml aqueous solution). The surface coverage decreased by more than two times to about 10%, corresponding to an increased intermolecular distance.

So far, no theory has been developed for the structure of polyelectrolyte rods on charged surface. For polyelectrolyte solutions, it has been shown that the phase behavior is effected by the strength of both steric and electrostatic interactions (24,25). Depending on the concentration, the charge density of the rods, and the solution ionic strength, the rods can align parallel or perpendicular, as well as reveal mixed regimes. In our system, there is a third interaction parameter due to a charged surface. Assuming complete neutralization of the substrate, the number of adsorbed macromolecules per unit area should increase with the charge density of the substrate and decrease with the uncompensated charge of the adsorbed species. Apparently, the adsorption conditions were somewhat different for adsorption of charged dendrimers which formed dense monolayers (26).

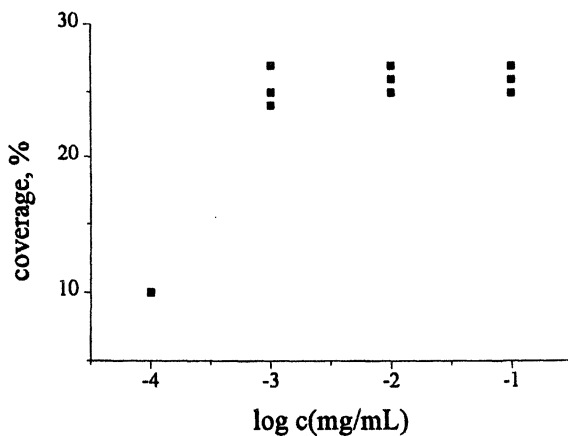


Figure 5. The concentration dependence of the surface coverage indicates that the number of adsorbed molecules does not depend on their concentration in the reservoir for $c \geq 0.001$ mg/ml. The black squares at a given concentration correspond to different samples.

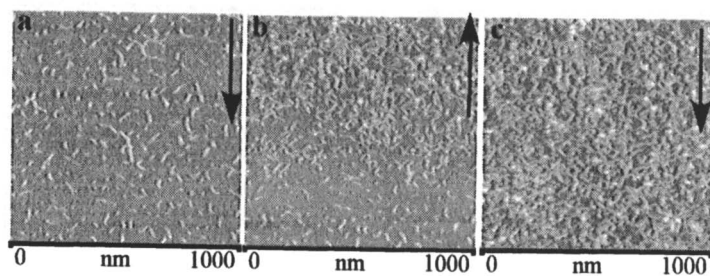


Figure 6. Sequence of images of the polyelectrolyte brushes adsorbed from a 0.05 mg/ml solution before (a), during (b) and after adding (c) NaCl salt to reach a 0.1 M ionic strength.

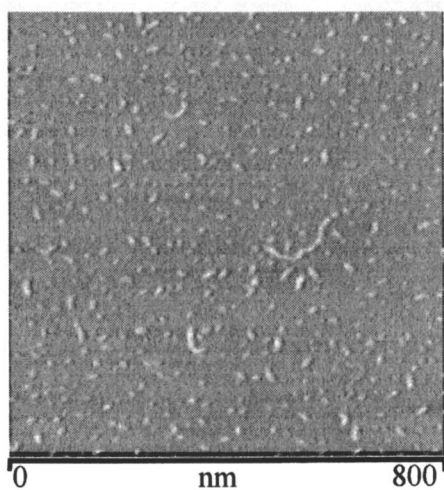


Figure 7. SFM micrographs of poly(2-vinyl-N-methylpyridinium bromide) brushes adsorbed on mica from a 0.03 mg/ml aqueous solution. Compared to poly(2-vinyl-N-benzylpyridinium bromide), the surface coverage decreased from 25 % to about 10%.

Conclusions

Adsorption of polyelectrolyte cylindrical brushes on the charged substrate yielded a sparse monolayer of isolated macromolecules. The coverage degree was controlled between 10 and 50 % by the ionic strength and the degree of ionization of the molecules. Due to the well defined shape of the molecular brushes, the thickness of the layer is given by the molecular diameter and depends on the grafting density as well as the charge density of the brushes. For the investigated system, the adsorbed molecules were 2 nm in height and separated by 30-200 nm. The variation in distance was caused by the great polydispersity of the brushes as well as hindered lateral mobility of the adsorbed molecules. Orientation and positional order of the charged rods, increasing stiffness in dependence of the charge density, variation of the size of the polyelectrolyte cylindrical brushes upon changing of the ionic strength are subject of following research.

Acknowledgments. This work was financially supported by the Deutsche Forschungsgemeinschaft (project SH 46/2-1).

References

1. Smith, H.I.; Craighead, H.G. *Phys. Today* **1990**, *24*.
2. Thomas, J.K.; Mann, S. *Current Opin. in Colloid & Interf. Science* **1996**, *1*, 173.
3. Gellman, A.J. *Current Opin. in Colloid & Interf. Science* **1998**, *3*, 368.
4. Weissbuch, I.; Baxter, P.N.W.; Cohen, S.; Cohen, H.; Kjaer, P.B.; Howes, P.B.; Als-Nielsen, J.; Hanan, G.S.; Shubert, U.S.; Lehn, J.-M.; Leiserowitz L. *J. Am. Chem. Soc.* **1998**, *120*, 4850.
5. G.M. Whitesides, E.E. Simanek, J.P. Mathias, C.T. Seto, D.N. Chin, M. Mammen, D.M. Gordon Acc. Chem Res. **1995**, *28*, 37.
6. Park, M.; Harrison, C.; Chaikin, P.M.; Register, R.A.; Adamson, D.H. *Science* **1997**, *276*, 1401.
7. Bölten, M.; Walhein, S.; Mlynek, J.; Krausch, G.; Steiner, U. *Nature* **1998**, *391*, 877.
8. Percec, V.; Ahn, C.-H.; Cho, W.-D.; Jamieson, A.M.; Kim, J.; Leman, T.; Schmidt, M.; Gerle, M.; Möller, M.; Prokhorova, S.A.; Sheiko, S.S.; Cheng, S.Z.D.; Zhang, A.; Ungar, G.; Yeardley, D.J.P. *J. Am. Chem. Soc.* **1998**, *120*, 8619.
9. Karakaya, B.; Claussen, W.; Gessier, K.; Sängler, W.; Schlüter, A.-D. *J. Am. Chem. Soc.* **1997**, *119*, 3296.
10. Yin, R.; Zhu, Y.; Tomalia, D.A. *J. Am. Chem. Soc.* **1998**, *120*, 2678.
11. M. Wintermantel, K. Fischer, M. Gerle, R. Ries, M. Schmidt, K. Kajiwara, H. Urakawa, I. Wataoka *Angew. Chem. Int. Ed. Engl.* **1995**, *34*, 1472
12. Sheiko, S.S.; Gauthier, M.; Möller, M. *Macromolecules* **1997**, *30*, 2343
13. Dziezok, P.; Sheiko, S.S.; Fischer, K.; Schmidt, M.; Möller, M. *Angew. Chemie, Int. Engl. Ed.* **1997**, *109*, 2812.
14. Prokhorova, S.A.; Sheiko, S.S.; Möller, M.; Ahn, C.-H.; Percec, V. *Macrom. Rapid Comm.* **1998**, *19*, 359.
15. Percec, V.; Ahn, C.-H.; Ungar, G.; Yeardley, D.S.P.; Möller, M.; Sheiko, S.S. *Nature* **1998**, *391*, 161.

16. Sheiko, S.S.; Eckert, G.; Ignat'eva, G.; Muzafarov, A.M.; Spickermann, J.; Räder, H.J.; Möller, M. *Macromol. Rapid Commun* **1996**, *17*, 283.
17. Kralchevsky, P.A.; Nagayama, K. *Langmuir* **1994**, *10*, 23.
18. Han, W.; Lindsay, S.M.; Jing T. *Appl. Phys. Letters* **1996**, *69*, 4111.
19. Brenner, S.L.; Parsegian, V.A. *Biophys. J.* **1974**, *14*, 327.
20. Stroobants, A.; Lekkerkerker, H.N.W.; Odijk, Th. *Macromolecules* **1986**, *19*, 2232.
21. Ricci, S.M.; Talbot, J.; Tarjus, G.; Viot, P. *J. Chem Phys.* **1992**, *97*, 5219.
22. Adamczyk, Z.; Warszynski, P. *Adv. Coll. Interf. Sci.* **1996**, *63*, 41.
23. Schmidt M. *private communication*.
24. Nyrkova, I.A.; Shusharina, N.P.; Khokhlov, A.R. *Macromol. Theory Simul.* **1997**, *6*, 965.
25. Zhulina, E.B.; Borisov, O.V. *Macromolecules* **1996**, *29*, 2618.
26. Tsukruk, V.V.; Rinderspacher, F.; Bliznyuk, V.N. *Langmuir* **1997**, *13*, 2171.

Chapter 22

Microphase Separation and Morphological Transitions at the Surface of Block Copolymers

Ph. Leclère, J. L. Brédas^{1,4}, G. Moineau², M. Minet², Ph. Dubois³, R. Jérôme²,
and R. Lazzaroni¹

¹ Service de Chimie des Matériaux Nouveaux, Centre de Recherche en Electronique et Photonique Moléculaires, Université de Mons-Hainaut, Place du Parc 20, B-7000 Mons, Belgium

² Centre d'Etude et de Recherche sur les Macromolécules (CERM), Institut de Chimie, Bât B6, Université de Liège, B-4000 Liège, Belgium

³ Service des Matériaux Polymères et Composites (SMPC), Université de Mons-Hainaut, Place du Parc 20, B-7000 Mons, Belgium

Tapping-Mode Atomic Force Microscopy is used to study the microphase separation in thin films of symmetric triblock copolymers synthesized via a two-step « living » radical polymerization of *n*-butylacrylate and methylmethacrylate (MMA). This straightforward synthetic pathway allows for strict control of molecular weight, molecular weight distribution, and composition. The presence in the copolymer of immiscible segments covalently bound to each other leads to phase separation on the nanometer scale. Measuring the phase of the oscillating cantilever simultaneously with the topography allows us to determine the microdomain morphology at the surface. Here this approach is applied to all-acrylate (PMMA-*b*-poly-*n*-butylacrylate-*b*-PMMA) thermoplastic elastomers. The data point to a strong contrast in the local mechanical properties, corresponding to the microphase morphology. Cylinders of the minority phase are found to orient perpendicular to the surface, due to the surface energy difference between the constituents. Lamellae are also arranged perpendicular to the surface, in contrast to what is usually observed in block copolymers. This particular orientation is thought to result from the symmetric character of these triblock systems, with the outer blocks more polar than the central sequence.

The increasing importance of block copolymers arises mainly from their unique properties in solution and in the solid state, which is a consequence of their molecular structure. In particular, sequences of different chemical composition are usually incompatible and therefore have a tendency to phase segregate. The microdomain formation process in the solid state is directly related to the specific molecular

⁴ Corresponding author.

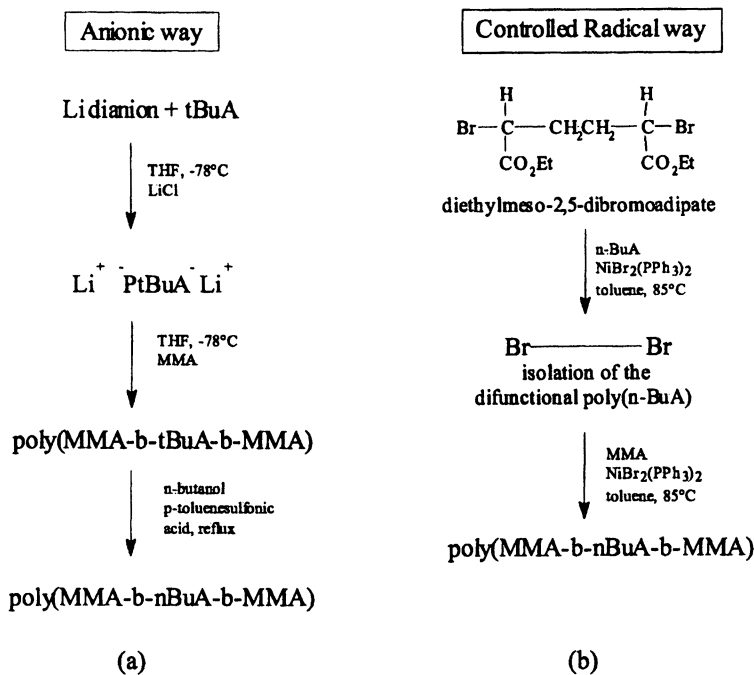
architecture, which can be designed by using existing monomers or polymers. Block copolymers can produce numerous phase-separated nanostructures that present high fundamental and technological interest [1].

Block copolymers have been prepared classically via living anionic polymerization, as pioneered by Szwarc [2]. This opens the way to a fine tailoring of synthetic polymers and copolymers in terms of precise control of molecular weight, molecular weight distribution, molecular architecture, and chain-end functionalization. Due to the thermodynamic immiscibility of their constitutive components, block copolymers combine the intrinsic properties of the parent homopolymers along with the additional benefit of new properties appearing in relation to the phase morphology. For instance, combining thermoplastic and elastomeric sequences into block copolymers, called thermoplastic elastomers (TPEs) [3], results in rubber materials with thermally reversible crosslinking (the crosslinked centers being the thermoplastic domains below their glass transition temperature). Commercially-available TPEs prepared by anionic polymerization are typically of the polystyrene-polydiene-polystyrene type of triblock copolymers (such as polystyrene-polybutadiene-polystyrene, SBS).

The work presented here stems from the need to improve the processability and thermoresistance to degradation of TPEs, relative to the SBS copolymers of the first generation. Because of the temperature limitations imposed by both the poor thermal and oxidative resistance of polydienes and the relatively low glass transition temperature T_g of the polystyrene end blocks, a major loss of strength is usually observed above 60°C. Consequently, there is much interest in: (i) replacing the polystyrene blocks with thermoplastic polymers with higher values of T_g ; and (ii) building elastomeric sequences which better resist oxidation. These two requirements can be fulfilled by acrylate-based polymers: on one hand, the presence of an alkyl-chain (at least four carbon long, *i.e.*, *n*-butylacrylate (*n*-BuA)) on the ester groups provides elastomeric properties, with a strongly reduced possibility of oxidation or crosslinking; on the other hand, predominantly syndiotactic poly(methylmethacrylate) PMMA shows a T_g which can be as high as 125°C, *i.e.*, significantly higher than that of polystyrene ($T_g = 100^\circ\text{C}$). We have therefore synthesized a series of such copolymers associating polyalkylacrylate elastomeric sequences and polymethacrylate thermoplastic sequences.

Here, we report on the synthesis and characterization of PMMA-poly(*n*-butylacrylate)-PMMA (MBuM) symmetric triblock copolymers, as a new family of thermoplastic elastomers. These compounds have been prepared by a novel route based on controlled radical polymerization [4]. Compared to "classical" anionic living polymerization [5], this new route, sketched in Scheme 1a, appears particularly appealing since the triblock copolymers are prepared in a two-step process instead of the usual three steps required in anionic polymerization. In the latter case, as *n*-butylacrylate cannot be polymerized via a living process, the MBuM symmetric triblocks have to be synthesized by sequential copolymerization of *tert*-butylacrylate (tBuA) and MMA followed by the transesterification of the tBu esters with *n*-butanol

(Scheme 1b). An added advantage of the two-step controlled radical polymerization is the possibility to work in much less stringent experimental conditions (higher reaction temperature; no need for strictly anhydrous medium).



Scheme 1

The performances of these new materials as thermoplastic elastomers are intimately related to the extent of phase separation and the resulting microstructure. It is thus of prime importance to characterize in detail the microscopic morphology of thin films of the block copolymers described above. Atomic Force Microscopy (AFM) and derived techniques have recently appeared as powerful tools for the morphological characterization of polymer surfaces. In this work, Tapping-Mode (TM) AFM [6] is used and particular attention is devoted to measurements of the dephasing of the cantilever oscillation relative to the signal exciting the piezo driver. This approach, called "phase detection imaging-PDI", is a very sensitive technique to probe the local mechanical properties at the surface [7-10]; it is thus well adapted to investigations of microphase separation in TPEs.

Experimental Section

The synthesis of the block copolymers is described in detail elsewhere [4]. The MBuM macromolecules were synthesized from a poly(*n*-butylacrylate) difunctional macroinitiator. NiBr₂(PPh₃)₂ and diethyl meso-2,5-dibromoadipate were introduced in a glass tube equipped with a magnetic stirrer. Vacuum-nitrogen cycles were repeated to remove residual molecular oxygen. *n*-Butylacrylate was added under nitrogen via a syringe and the tube was placed in a oil bath maintained at 85°C. After 24 hour polymerization, the residual monomer was extracted by pumping and the polymer was recovered with a 70% yield. The molecular weight of the macromolecular initiator ($M_n = 63,000$; $M_w/M_n = 1.1$) was determined by Size Exclusion Chromatography (SEC) calibrated with PMMA standards. This difunctional macroinitiator and NiBr₂(PPh₃)₂ were then introduced in a round-bottom flask equipped with a magnetic stirrer. Toluene was added and the solution was stirred until complete dissolution of the macroinitiator. MMA was introduced under nitrogen and the reaction mixture was heated up to 85°C for 24 hours. The copolymer was finally recovered by precipitation from methanol. The copolymers presented in this study are described in Table 1. Thin films of the copolymers (typically 500 nm-thick) were prepared by solvent casting from a 2mg/mL toluene solution on a freshly-cleaved mica substrate. Such a thickness was chosen in order to ensure that: (i) the film surface is smooth enough (thicker films tend to be rougher and the topographic contrast can perturb the phase image); and (ii) the morphology is not influenced by specific interactions with the substrate, as is the case when the thickness is of the same order of magnitude as the microdomain size [11]. (here, the film thickness is about 15 times larger than the domain size). Moreover, PDI images on 1 mm-thick samples, albeit affected by topographic features, qualitatively show the same morphology as the 500 nm-thick deposits, confirming that the observations on the latter are not influenced by the substrate. Toluene is chosen as solvent since it is a good solvent for both components; no selective precipitation is thus expected to influence the morphology. The samples were first analyzed after evaporation of the solvent at room temperature. In order to investigate the effect of annealing above the T_g of PMMA on the surface morphology, they were then treated at 140°C under high vacuum (10^{-7} Torr) for 48 hours.

Table I. Description of the copolymers considered in this study.

<i>Sample</i>	<i>PBu</i> M_n	<i>PBu</i> M_w/M_n	<i>PMMA</i> M_n	<i>Copolymer</i> M_w/M_n	<i>Volume</i> % <i>PMMA</i>
A	63,000	1.11	14,500	1.18	30
B	63,000	1.11	30,000	1.3	47

All AFM images were recorded in air with a Nanoscope III microscope from Digital Instruments Inc. operated at room temperature in Tapping Mode (TMAFM), using microfabricated cantilevers with a spring constant of 30 Nm⁻¹. The system is

equipped with the ExtenderTM Electronics Module to provide simultaneously height and PDI cartography. Images of each sample were taken at several locations with scanning time of about 5 minutes. The A_{sp}/A_0 value was set to 0.95, where A_0 is the free oscillation amplitude and A_{sp} is the setpoint amplitude selected for the measurement. Repeated scans indicated that the observed structures were stable. All images were recorded with the maximum available number of pixels (512) in each direction. The images presented here were culled from several recorded files. For image analysis, the Nanoscope image processing software was used. The data were not filtered and are shown as captured.

Results and Discussion

Figure 1 compares the topographic and PDI images, obtained simultaneously on the same area of the surface, for a thin film of MBuM containing 30 % of MMA (see Table 1, sample A). While the topographic image is featureless, which indicates that the surface is flat on a lateral scale of micrometers (the RMS roughness is typically 1-2 nm), the PDI image is highly contrasted: it shows an homogeneous distribution of bright, round-shaped objects in a darker matrix. In TMAFM, the phase contrast originates from local differences in tip-surface interactions, occurring as the tip probes chemically-different domains. The PDI image thus constitutes clear evidence that microphase separation has taken place in this system.

It must be stressed that PDI-TMAFM appears as a unique tool for investigating the microscopic morphology of such compounds since, on the one hand, the electron density difference between the different monomer units is too small to lead to significant contrast in X-ray scattering measurements and, on the other hand, no selective staining agent is available, which precludes morphological characterization by means of transmission electron microscopy (the only results reported on the phase separation of these materials are coming from solid state NMR studies [12]).

Over the last couple of years, the origin of the phase contrast in TMAFM has been actively investigated [8-10, 13-17]. It has been shown that the contrast is related to the local dissipation of the energy brought to the surface by the oscillating tip [16]. It thus strongly depends on the details of the tip-sample interactions. In turn, these interactions depend on the intrinsic properties of the analyzed material, in particular its elastic and viscoelastic moduli, but also on the mechanical properties of the tip and on the existence of tip-sample adhesion. Quantitative measurement of the sample mechanical properties on the local scale from PDI-TMAFM data is therefore a very delicate task.

Nevertheless, a qualitative interpretation of the PDI images in terms of the spatial distribution of domains on an heterogeneous surface is possible. In particular, in the "soft tapping" regime we used, *i.e.*, when the amplitude of the oscillating cantilever is only slightly reduced (for instance, for $A_{sp}/A_0 = 0.95$) upon interaction with the surface, it has been shown that the magnitude of the phase shift is directly related to the elastic modulus of the sample [9, 16]. On this basis, we assign the bright spots in Figure 1b,

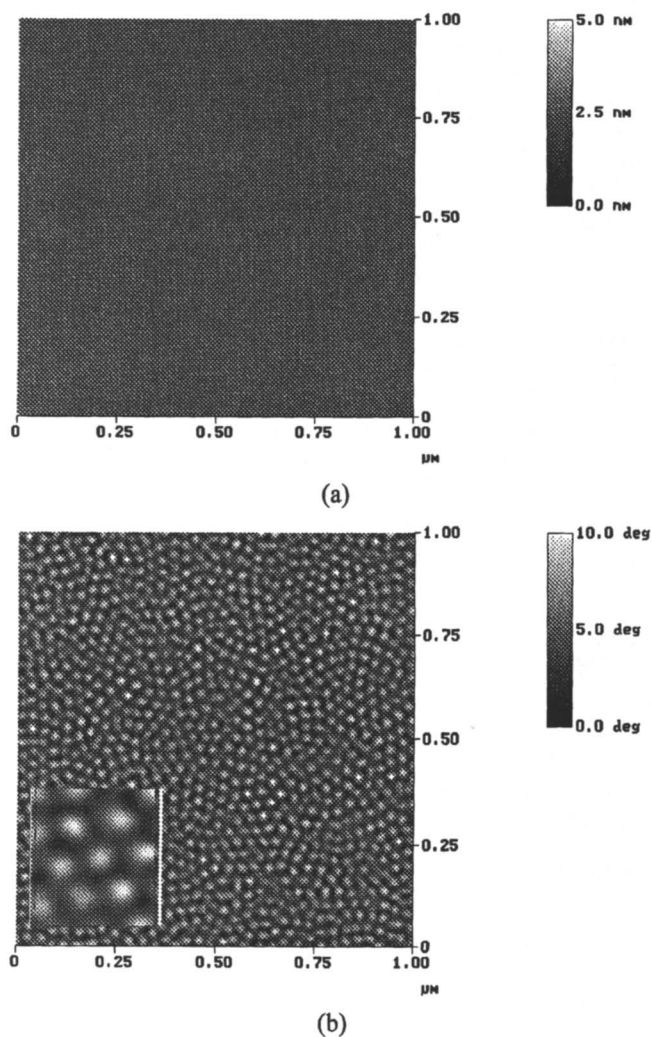
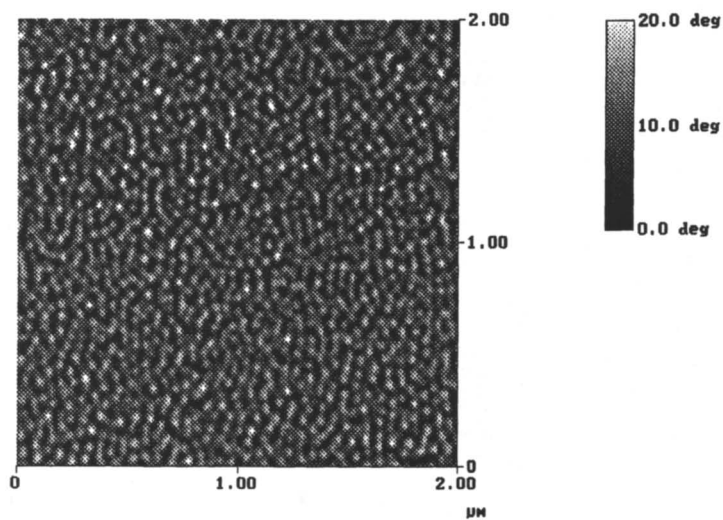


Figure 1. TMAFM height (a) and phase detection (b) images ($1 \times 1 \mu\text{m}^2$) of the 14,500-63,000-14,500 MBuM copolymer (Sample A). The Root Mean Square roughness of the height image is about 1.6 nm illustrating the flatness of such a thin film. The phase contrast shows the morphology of the copolymer. The inset shows that the PMMA domains are locally arranged in a centered hexagonal structure.

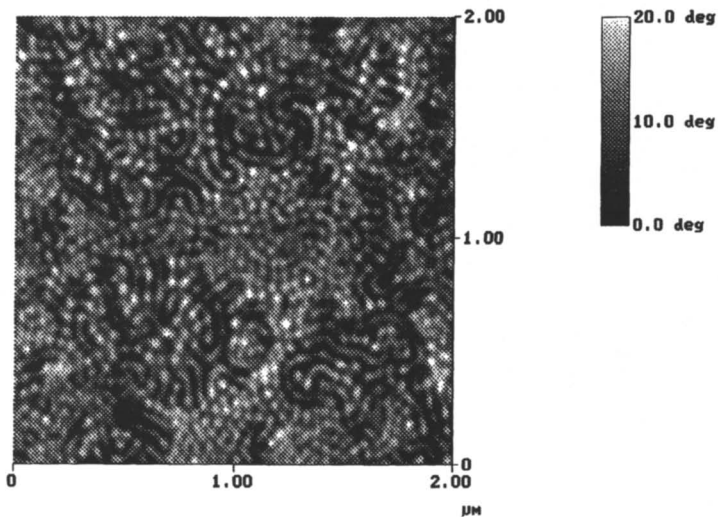
which correspond to a larger phase shift, to domains of the harder, thermoplastic component (PMMA), while the darker matrix, showing a smaller phase shift, is made of the softer, elastomeric component (poly(*n*-butylacrylate)). This assignment has been confirmed by recording approach-retraction curves over the different microdomains [18]. As reported previously [14, 17], we observe that decreasing the A_{sp}/A_0 value leads to the reversal of the contrast in the phase image and the appearance of contrast between domains in the topographic image, due to changes in the mechanisms governing the tip-sample interaction. Data analysis indicates that the mean diameter of the PMMA domains is about 30 (+/- 2) nm and the distance between the centers of adjacent spots is around 46 (+/- 2) nm. The chemical composition of sample A corresponds to a 30:70 PMMA/poly(*n*-butylacrylate) volume ratio; in this composition range, phase-segregated block copolymers are expected to present a "cylinder-in-a-matrix" morphology. The image of Figure 1b should thus not represent spheres of PMMA embedded in an elastomeric matrix, but rather PMMA cylinders standing upright, perpendicular to the surface, so that only their apex is visible. The measured diameter/distance ratio is fully consistent with the theoretical value when assuming hexagonal packing of the cylinders. Such an arrangement likely arises from the difference in surface energy between the two components: the surface energies, as estimated with the method described in reference [19], are 43 mJ/cm² and 39 mJ/cm² for PMMA and poly(*n*-butylacrylate), respectively. PMMA being slightly more polar than poly(*n*-butylacrylate), it tends to be less present at the interface with air; the PMMA cylinders are thus expected to align perpendicular to the outer surface, so that only their upper section is exposed.

Figure 1b does not show any long-range hexagonal compact organization of the cylinders, as would be expected from theoretical consideration [20]; nevertheless, on the local scale, PMMA domains are occasionally found to be arranged as centered hexagons (see inset of Figure 1b). The lack of long-range ordering may be due to the fact that in such thin films, the evaporation of the solvent is too fast to allow the system to reach thermodynamic equilibrium (even though phase separation takes place effectively). Note also that annealing the film above the T_g of PMMA does not lead to significant changes in the morphology. Figure 2a contains a PDI image of the same compound as in Figure 1, annealed for 48 hours at 140°C; it shows no clear evolution towards a more regular arrangement of the PMMA domains.

The annealing experiments are, however, indicative of the occurrence of morphological changes at high temperature. Figure 2b corresponds to a copolymer film annealed at 140°C and then quenched with liquid nitrogen. In contrast, the sample corresponding to Figure 2a was allowed to cool down much more slowly as it was kept in the oven after annealing. The quenched surface consists of a mixture of isolated bright spots, as found before, and elongated bright objects, surrounded by darker areas. The elongated domains appear to be cylinders of PMMA lying flat on the surface; their width (30 +/- 2 nm) agrees well with the diameter of the spots corresponding to cylinders standing upright.



(a)



(b)

Figure 2. TMAFM phase detection images ($2 \times 2 \mu\text{m}^2$) of the 14,500-63,000-14,500 MBuM copolymer (Sample A) annealed at 140°C for 48 hours and then either : (a). slowly cooled or (b) quenched with liquid nitrogen.

The presence of such cylinders parallel to the surface is likely related to the fact that the cooling rate was too high to allow for complete rearrangement into the vertical configuration. This in turn indicates that the surface morphology at high temperature consists of a mixture of flat and standing cylinders (note that very long annealing treatments followed by quenching do not produce an "all-flat" morphology). This mixed morphology may result from the interplay between entropic (*i.e.*, surface disordering) and enthalpic (*i.e.*, surface energy) factors. Because the difference in surface energy between the components is quite small (43 vs 39 mJ/cm²), it is reasonable to think that the entropic gain corresponding to the formation of a disordered assembly of cylinders can overcome the enthalpic loss of bringing more PMMA to the surface, even at moderate temperatures. It must be noted that mixed arrangements of cylinders have been observed previously, in very thin thin layers of styrene-butadiene-styrene copolymers [21]. This morphology has been explained in terms of film thickness influence. Parallel orientations can only exist at specific values of thickness. If the average thickness of the film is not compatible with the repeat distance, the film develops macroscopic variations in thickness, by a 2-D coarsening process, such that the thicker regions are an integer of the repeat distance. In our opinion, this process is not at work here because the film thickness is much larger than the domain size [22]. It is therefore unlikely that the surface morphology we observe is a reflection of the adsorption of the macromolecules on the mica substrate. Instead, it is more likely to be governed by processes taking place at the polymer/air interface. Further heating to around 200°C leads to complete mixing of the two components (order-disorder transition) [23].

Another remarkable feature of Figure 2b is the fact that the poly(*n*-butylacrylate) domains adjacent to the flat PMMA cylinders appear darker than the rest of the matrix. This suggests that the local elastic modulus of the matrix, as probed by the AFM tip, is slightly reduced in the vicinity of the flat cylinders. Assuming a tip radius of about 20 nm (which is typical for TMAFM tips), one can imagine that, as it probes a domain of the poly(*n*-butylacrylate) matrix in a region where PMMA cylinders stand upright, it also interacts laterally with those rigid cylinders, so that the phase shift is not as small (the probed area does not appear as dark on the PDI image) as it would be on a pure elastomeric surface. Conversely, if the soft domains are elongated, they are more easily probed by the tip (there is less disturbance by adjacent PMMA cylinders) and the corresponding phase signal is more typical of their mechanical properties (*i.e.*, those areas appear darker). Along the same line, most of the flat PMMA cylinders appear slightly less bright than their vertical counterparts: as the tip scans the surface, the former are probably not as well supported by the underlying layer as the latter, which form columns. As a result, the local elastic modulus is slightly reduced over the flat cylinders and the phase shift is smaller.

Increasing the PMMA content in the block copolymers to around 50% leads to the morphology illustrated in Figure 3. The alternation of dark and bright stripes corresponds to lamellae of the soft and hard components, assembled perpendicular to the surface. This regular lamellar arrangement is characterized by a typical period length of

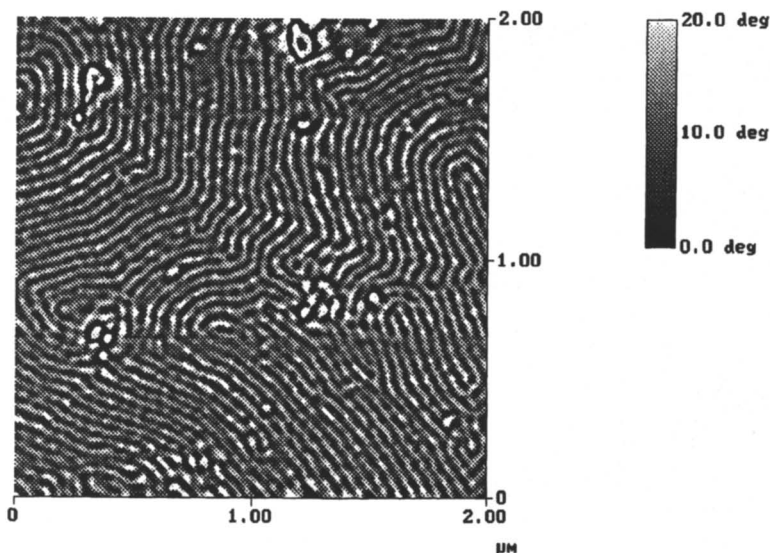


Figure 3. TMAFM phase detection image ($2 \times 2 \mu\text{m}^2$) of the 30,000-63,000-30,000 MBuM copolymer film (Sample B).

50 (± 2) nm. We also observe the presence of a number of topological defects at the surface: dislocations, corresponding to connections between lamellae, are visible (one such defect clearly appears near the center of the image) and lamellae occasionally bend completely into "U-turns"; some locations apparently show a few isolated PMMA cylinders standing perpendicular to the surface.

The other possible organization of lamellae, with the lamellae lying on top of each other parallel to the substrate, is always observed [24] for films of 50/50 diblock copolymers; in that case, the films organize in such a way that a lamella of the component with smaller surface energy occupies the outer surface (this situation is sketched in Figure 4a).

In our block copolymers, a similar arrangement, with only the less polar segments (*i.e.*, the central poly(*n*-butylacrylate sequence) exposed to the surface, would imply that all chains form loops so that both their external PMMA sequences are accommodated in a lamella below the surface (Figure 4b). Such an organization corresponds to a significant loss in conformational freedom and is therefore expected to be entropically unfavorable. Instead, in a lamellar arrangement perpendicular to the surface (Figure 4c), the central segments can either be extracted or looped; this should thus be more favorable entropically. Since the difference in surface energy between the components is small, this entropy gain probably overcomes the energetic destabilization due to the presence of the most polar component at the surface. It is important to notice that this lamellar organization is a direct consequence of the specific molecular architecture of these block copolymers.

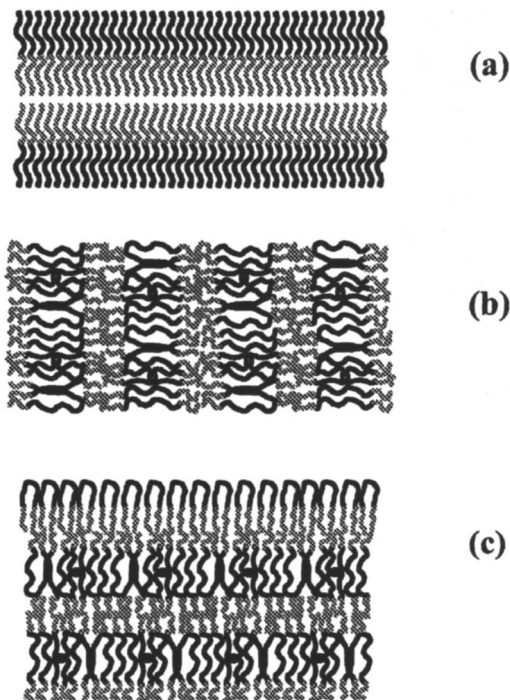


Figure 4. Schematic representation of lamellar arrangements of block copolymers. The light gray and dark sequences correspond to the components with the highest and the lowest surface energy, respectively. The outer surface is the area above each sketch. (a) in a diblock copolymer, lamellae arrange parallel to the surface, exposing only the low-energy component ; (b) in a symmetric copolymer with polar outer segments, parallel arrangement of the lamellae implies that all central segments form loops ; (c) alternative arrangement of lamellae of the symmetric triblock copolymer, with both components exposed to the surface.

Conclusion

Microphase separation has been clearly observed in “all-acrylic” triblock copolymers, by measuring the local phase shifts of the oscillating probe in Tapping-mode atomic force microscopy. Cylinders of PMMA are found to arrange perpendicular to the film surface at room temperature while it is suggested that their arrangement is more disordered above the glass transition temperature of PMMA. Lamellae are also found to stack perpendicular to the surface. The existence of such well-defined phase segregations indicates that these compounds should be promising as a new generation of thermoplastic elastomers.

Acknowledgements

We are grateful to J.P. Aimé and S. Kopp-Marsaudon for fruitful discussions. The collaboration between Mons and Liège is conducted in the framework of the Belgian Federal Government Office of Science Policy (SSTC) "Pôle d'Attraction Interuniversitaire en Chimie Supramoléculaire et Catalyse Supramoléculaire" (PAI 4/11). Research in Mons is also partly supported by the European Commission and the Government of the Région Wallonne (Project NOMAPOL-Objectif 1-Hainaut), the Belgian National Fund for Scientific Research FNRS/FRFC, and an IBM Academic Joint Study. GM is indebted to "ELF-ATOCHEM" (France) for financial support. RL is Maître de Recherches du Fonds National de la Recherche Scientifique (FNRS - Belgium).

References

- [1] Gallot, B.R.M. *Adv. Polym. Sc.* **1978**, *29*, 85; Gallot, B. In *Liquid Crystalline Order in Polymers*, Blumstein, A., Ed.; Academic: New York, 1978, p 223; Hashimoto, T., Nagatoshi, K., Todo, A., Hasegawa, H., and Kawai, H. *Macromolecules* **1974**, *7*, 364; Hashimoto, T., Todo, A., Itoi, H., and Kawai, H., *Macromolecules* **1977**, *10*, 377; Todo, A., Kiuno, H., Miyoshi, K., Hashimoto, T., and Kawai H. *Polymer Engineering and Science* **1977**, *17*, 587; Hashimoto, T., Shibayama, M., and Kawai, H. *Macromolecules* **1980**, *13*, 1237; Hashimoto, T., Fujimura, M., and Kawai, H. *Macromolecules* **1980**, *13*, 1660; Thomas, E.L.; Anderson, D.M.; Henkee, C.S.; Hoffman, D *Nature* **1988**, *334*, 598; Riess, G. & Bahhadur, P., In *Encyclopedia of Polymer Science and Engineering*; Mark, H.F., Bikales, N.M., Overberger, C.G., Menges, G., Eds.; Wiley: New-York, 1989; p 324.
- [2] Szwarc, M.; Levy, M.; Milkovich, R. *J. Am. Chem. Soc.* **1956**, *78*, 2656.
- [3] Holden, G.; Legge, N.R., In *Thermoplastic Elastomers – A Comprehensive Review*; Holden, G.; Legge, N.R.; Schroeder, H.E., Eds.; Hanser: Munich, 1987; chap. 3.
- [4] Kato, M.; Kamigaito, M.; Sawamoto, M.; Higashimura, T. *Macromolecules* **1995**, *28*, 1721; Wang, J.S.; Matyjaszewski, K. *J. Am. Chem. Soc.* **1995**, *117*, 5614; Moineau, G.; Minet, M.; Dubois, Ph.; Teyssié, Ph.; Senninger, T.; Jérôme, R. *Macromolecules*, **1999**, *32*, 27.
- [5] Jérôme, R. *et al.*, In *Thermoplastic Elastomers – A Comprehensive Review*; Holden, G.; Legge, N.R.; Schroeder, H.E., Eds.; Hanser: Munich, 1987; chap. 15D.
- [6] Zhong, Q.; Inniss, D.; Kjoller, K.; Elings, V.B *Surf. Sci.* **1993**, *290*, L688.
- [7] Leclère, Ph.; Lazzaroni, R.; Brédas, J.L.; Yu, J.M.; Dubois, Ph.; Jérôme, R. *Langmuir* **1996**, *12*, 4317.
- [8] Bar, G.; Thomman, Y.; Brandsch, R.; Cantow, H.J.; Whangbo, M.H. *Langmuir* **1997**, *13*, 3807.
- [9] Magonov, S.N.; Elings, V.; Whangbo, W.H. *Surf. Sci. Lett.* **1997**, *375*, L385.
- [10] Burnham, N.A.; Behrend, O. P.; Oulevey, F.; Gremaud, G.; Gallo, P.-J.; Gourdon, D.; Dupas, E.; Kulik, A. J.; Pollock, H. M.; Briggs G. A. D. *Nanotechnology* **1997**, *8*, 67.

- [11] Van den Berg, R.; De Groot, H.; Van Dijk, M.A.; Denley, D.R., *Polymer* **1994**, *35*, 5778;
- [12] Soltani, R.; Lauprêtre, F.; Monnerie, L.; Teyssié, Ph., *Polymer* **1998**, *38*, 3297.
- [13] Tamayo, J.; Garcia, R. *Langmuir* **1996**, *12*, 4430.
- [14] Brandsch, R.; Bar, G.; Whangbo, M.-H. *Langmuir* **1997**, *13*, 6349.
- [15] Bar, G.; Brandsch, R.; Whangbo, M.-H. *Langmuir* **1997**, *14*, 7343.
- [16] Cleveland, J.P.; Anczykowski, B.; Schmidt, A.E.; Elings, V.B. *Appl. Phys. Lett.* **1998**, *72*, 2613.
- [17] Pickering, J.P.; Vancso, G.J. *Polymer Bulletin* **1998**, *40*, 549.
- [18] Kopp, S.; Leclère, Ph.; Lazzaroni, R.; Aimé, J.P., to be published.
- [19] Van Krevelen, D. W. *Properties of Polymers*, 3rd Ed., **1990**, p 790. Elsevier, Amsterdam, Oxford, New York, Tokyo.
- [20] Bates, F.S. & Fredrickson, G.H., *Annu. Rev. Phys. Chem.* **1990**, *41*, 525.
- [21] Van Dijk, M.A.; Van den Berg, R., *Macromolecules* **1995**, *28*, 6773. Wong, G.C.L.; Commandeur, J.; Fisher, H.; de Jeu, W.H. *Phys. Rev. Lett.* **1996**, *77*, 5221.
- [22] Heier, J.; Kramer, E.J.; Walheim, S.; Krausch, G., to be published.
- [23] Tong, J.D.; Moineau, G.; Jérôme, R.; Leclère, Ph.; Brédas, J.L.; Lazzaroni, R submitted for publication.
- [24] Han, C.D.; Kim, J.; Kim, J.K. *Macromolecules* **1989** *22*, 383; Collin, B.; Chatenay, D.; Coulon, G.; Ausserre, D.; Galot, Y. *Macromolecules* **25**, 1621 (1992).

Chapter 23

Modeling the Interactions between Polymers and Clay Surfaces through Self-Consistent Field Theory

Anna C. Balazs, Chandralekha Singh, and Ekaterina Zhulina

Department of Chemical and Petroleum Engineering, University of Pittsburgh,
Pittsburgh, PA 15261

Using numerical self-consistent field (SCF) calculations, we investigate the interactions between two closely-spaced surfaces and the surrounding polymer melt. The surfaces represent clay sheets and we consider the effect of employing end-functionalized chains to promote the dispersion of these sheets within a polymer matrix. We find that this scheme provides a robust method for exfoliating the clay. To consider this case in greater depth, we develop an analytical SCF theory to model the interactions among the functionalized chains, nonfunctionalized polymers and the clay sheets. The results from the numerical and analytical SCF models show good agreement on the behavior of the system. The results indicate that the optimal polymeric candidates for creating stable exfoliated composites are those that would constitute optimal steric stabilizers for colloidal suspensions.

The blending of polymeric melts and inorganic clays can yield composites that exhibit dramatic increases in tensile strength, heat resistance, and decreases in gas permeability when compared to the pure polymer matrix.¹⁻¹¹ The unique properties make the composites ideal materials for products that range from high-barrier packaging for food and electronics to strong, heat-resistant automotive components. Fabricating these materials in an efficient and cost-effective manner, however, poses significant synthetic challenges. To understand the challenges, it is helpful to consider the structure of the clay particles. The inorganic clays (montmorillonite being a prime example) consist of stacked silicate sheets; each sheet is approximately 200 nm in length and 1 nm in thickness.² The spacing between the closely-packed sheets is also on the order of 1 nm. Thus, there is a large entropic barrier associated with the molten polymers penetrating this gap and hence, becoming intermixed with the clay.

In this paper, we use both numerical and analytical self-consistent field (SCF) models to isolate a robust scheme for creating stable dispersions from polymers and clays that are immiscible. Specifically, we show that adding a small fraction of end-functionalized polymers to a melt can lead to the formation of exfoliated structures, where the clay sheets are uniformly dispersed within the polymer matrix. Our findings reveal that the ideal polymeric candidates for creating stable exfoliated composites are those that would constitute optimal steric stabilizers for colloidal suspensions. This prediction provides new design criteria for fabricating polymer/clay composites with the

desired morphology. Recall that tribology is the study of surfaces that are in relative motion with respect to each other. The exfoliation of clay particles represents an industrially important tribological process where the inorganic sheets must be pried apart in order to be dispersed within the polymer matrix.

Below, we begin with a brief description of the numerical SCF model. In prior studies,^{12,13} we used this method to determine the free energies as a function of surface separation for polymer-coated surfaces in solution. Here, we describe our findings for the interactions between solid surfaces immersed in: (1) a single-component melt and (2) a melt that contains polymers with surface-active end-groups¹⁴. We also introduce an analytical SCF model for the melt containing end-functionalized chains and present the results from this theory. Comparisons are made between the numerical and analytical SCF results and the implications of these findings are discussed further in the Conclusions section.

The SCF Model

Our numerical self-consistent field (SCF) calculations are based on the model developed by Scheutjens and Fleer.¹⁵ In this treatment, the phase behavior of polymer systems is modeled by combining Markov chain statistics with a mean field approximation for the free energy. The equations in this lattice model are solved numerically and self-consistently. The self-consistent potential is a function of the polymer segment density distribution and the Flory-Huggins interaction parameters, or χ 's, between the different components. (Note that χ is inversely proportional to temperature, thus variations in χ are comparable to variations in temperature.) While such SCF calculations do not necessarily yield quantitative predictions, the results indicate how to tailor the system to modify the stability and morphology of the mixture.

Using this SCF method, we consider two infinite, parallel plates immersed in a "bath" of molten polymer. These surfaces lie parallel to each other in the XY plane and we investigate the effect of increasing the separation between the surfaces in the Z direction. As the surface separation is increased, polymer from the surrounding bath penetrates the gap between these walls and the calculations yield the corresponding change in the free energy, ΔF , of the system. By systematically increasing the surface separation (H), we obtain the ΔF versus H curves discussed below.

Results and Discussion: Numerical Model

We first confine our interest to the interactions between the bare surfaces and a surrounding melt of identical chains. We then add functionalized polymers to the melt and determine how these additives modify the interactions in the system. The free energy (per unit area), $\Delta F/A$, as a function of surface separation for the case of the bare surfaces in the single-component melt is plotted in Figure 1. We let χ_{surf} represent the Flory-Huggins parameter for the polymer-surface interactions. Here, $\chi_{\text{surf}} = 0$ and the length of the polymers is given by $N = 100$. In the reference state, the surfaces are in intimate contact. The figure indicates that ΔF rapidly becomes positive as the surfaces are pulled apart, and thus the intermixing of these components is unfavorable. The reason for this behavior can be understood through the following argument. As the polymers come in contact with the surface, the chains lose conformational entropy against the solid walls. In the initial reference state, the polymers only come in contact with the two outer surfaces (see cartoon in Fig. 1); however, as the surfaces are pried

apart, there are now four distinct walls within the melt. Thus, the losses in conformational entropy within this system have been increased, all without any compensating enthalpic contributions. For this system, the polymers and sheets would be immiscible and the mixture would phase-separate. These conclusions also agree with our recent calculations of the phase diagrams for the mixtures of polymers and thin, rigid discs.¹⁶ For $N = 100$ and $\chi_{\text{surf}} = 0$, the phase diagrams reveal that the two components are totally immiscible.

We now consider a system that involves bare clay sheets and a polymer mixture that contains both functionalized and nonfunctionalized species. In particular, some fraction of the polymers contain "stickers" that are highly attracted to the surface. Aside from the sticker sites, the functionalized and nonfunctionalized chains are chemically identical. The functionalized polymers will bind to the clay and form a grafted layer. The remainder of the polymers will interact with the anchored species. Since the free and grafted chains are comparable in length, the free polymer can readily penetrate the grafted layer¹⁷ and form a broad interphase, which promotes the formation of exfoliated hybrids¹⁴. While the experimental result will depend on the kinetics of the process, the SCF calculations can indicate, for example, how the fraction of functionalized chains in the mixture affects the thermodynamic stability of the product. To test the feasibility of this approach, we varied the fraction of functionalized polymers within a melt of chains of comparable length.

The functionalized polymers contain a sticker at one end of the chain and are slightly shorter ($N = 75$) than the nonfunctionalized species ($N = 100$). (In a physical experiment, decreasing the length of the functionalized species by a small degree will permit these chains to diffuse to the surface faster than the longer chains and once at the surface, provide an interfacial layer for the longer polymers.) The interaction between the reactive stickers and the surface is characterized by $\chi_{\text{ss}} = -75$, or equivalently, a binding energy of 12.5 kT.¹⁸ The interaction parameter between the stickers and all other species is set equal to 0. (Thus, the stickers do not react with themselves or other monomers.) For the other monomers in the system (the non-stickers), $\chi_{\text{surf}} = 0$.

The results in Figure 2 imply that this scheme is successful in creating stable polymer/clay dispersions. In particular, the plots indicate that there is a global minimum at large (infinite) separations. Such plots point to an exfoliated structure,^{10,14} where the sheets are effectively separated from each other and dispersed within the polymer melt. Note that just a small fraction of the functionalized additives is necessary to promote exfoliation. As basis of comparison, recall that the interaction between the bare surface and nonfunctionalized polymers lead to an immiscible mixture (Fig. 1).

At a low volume fraction of functionalized polymers, these chains form an interlayer that the nonfunctionalized polymer can readily penetrate. As the fraction of the functionalized chains is increased, the polymers are driven to coat the substrates and consequently, the surfaces are pushed apart by the adsorbing chains. Note that increasing the fraction of functionalized chains beyond 30% has little effect on decreasing ΔF . In effect, once the surfaces have been coated with the "sticky" polymers, increasing the volume fraction of these species does not lead to further decreases in this free energy. For that matter, since all curves in Figure 2 point to an exfoliated system, the most cost-effective treatment could be the 5% example, where only a small fraction of functionalized species are needed to create a stable dispersion.

The findings on the functionalized polymers suggest that the optimal polymeric candidates for creating stable exfoliated composites are those that would constitute optimal steric stabilizers for colloidal suspensions. For facile penetration into the gallery, the polymer must contain a fragment that is highly attracted to the surface. This fragment also promotes miscibility between the polymer and clay. In addition, this

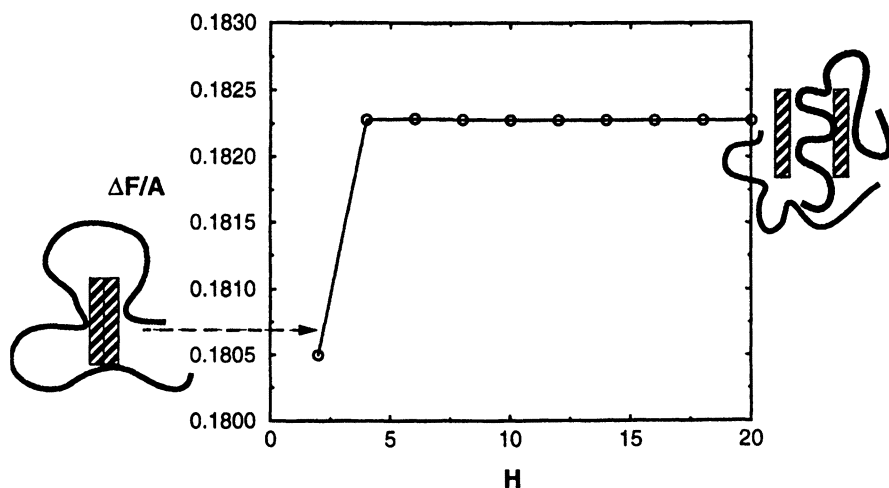


Figure 1. The free energy per unit area, $\Delta F/A$, as a function of surface separation, H , for the bare surfaces in the melt. Here, $\chi_{\text{surf}} = 0$ and the length of the homopolymers is given by $N = 100$. The cartoon on the left shows the surfaces in intimate contact and on the right, the sketch shows the polymers localized between these substrates.

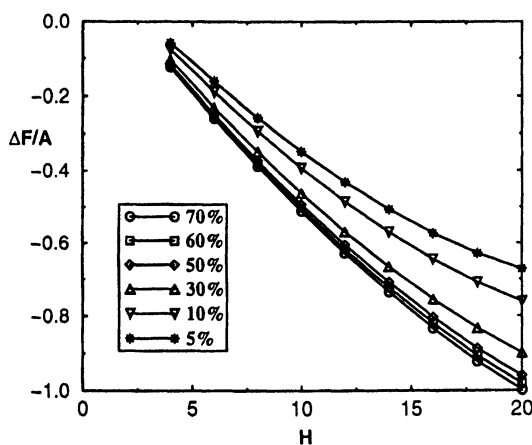


Figure 2. The free energy per unit area as a function of surface separation. The melt contains two types of polymers: a shorter functionalized chain and a slightly longer, non-functionalized species. The functionalized polymer has a sticker at the end of the chain and a length of $N = 75$. The interaction between the sticker and surface is given by $\chi_{\text{ss}} = -75$. The length of the nonfunctionalized polymers is $N = 100$. The percentages in the figure refer to the fraction of functionalized polymers. The other parameters are the same as in Figure 1.

polymer must contain a longer fragment that is not attracted to the sheets. The non-reactive block will attempt to gain entropy by pushing the sheets apart. Once the sheets are separated, these blocks will also sterically hinder the surfaces from coming into close contact. Our SCF results give credence to this scheme. Since surface-active end groups can be attached to essentially any polymer, the proposed technique could enhance the number and types of polymers that are involved in the fabrication of such hybrids.

The above analysis indicates that adding AB diblock copolymers to a melt of B homopolymers would also promote the exfoliation of the clay particles. Here, a short hydrophilic A block will anchor the chain to the bare (non-modified) clay sheets. The large organophilic B block will extend away from the surface, and could drive the separation and dispersion of these sheets.

Since the addition of functionalized polymers (or diblocks) has yielded a robust method of exfoliating the sheets, we developed an analytical SCF theory that allows us to gain further insight into the behavior of this system and test the results from the numerical SCF calculations. Below, we describe the analytical model, discuss the results from this theory and compare the findings from the two SCF studies.

Analytical Self-Consistent-Field Theory

We consider a melt of mobile polymers that contains a volume fraction, ϕ , of functionalized chains and a volume fraction, $(1 - \phi)$, of nonfunctionalized chains. Each functionalized chain contains one terminal group that is attracted to the clay sheet. In all other respects, the functionalized and nonfunctionalized chains are chemically identical. The functionalized chains are monodisperse; each chain contains N monomers and the diameter of each monomer is equal to a . The nonfunctionalized chains are polydisperse. To specify this polydispersity, we let ϕ_i be the volume fraction of chains containing P_i units, where the index i ranges from 1 to infinity. The sum of ϕ_i over all i gives the total volume fraction $(1 - \phi)$ of the nonfunctionalized polymers in the melt. (To simplify the ensuing discussion, we will frequently refer to the functionalized polymers as the N chains and the nonfunctionalized species as the P polymers.) While the end-groups of the functionalized polymers are highly attracted to the clay sheets, they do not react with themselves or the other monomers in the melt. In other words, the interactions among all the monomers are identical, and the melt constitutes a simple athermal mixture of polydisperse polymers. Furthermore, the non-reactive monomers are not attracted to the clay sheets.

The melt is assumed to be in thermodynamic equilibrium with the clay particles. Each clay sheet is modeled as a planar surface of area A . Due to the attraction between the end-groups and the sheets, the functionalized chains become terminally-anchored to these surfaces and effectively push the sheets apart. We assume that at any distance $2H$ between the surfaces, there is an equilibrium between the anchored and free functionalized chains. In other words, the degree to which the functionalized polymers bind to the surface is determined by the distance between the particles.

We introduce a total number ($n_a + n_f$) of the functionalized polymers (each of length N) into a gap of thickness H (half the distance between the sheets). The subscript "a" refers to the attached functionalized chains, while the subscript "f" indicates free, unattached functionalized chains. Within this gap, we also have a number n_i of nonfunctionalized chains of length P_i . The condition that the total volume of the system is conserved yields the following equation:

$$(n_a + n_f) N + \sum_j n_j P_j = A H/a^3 \quad (1)$$

We let ϵ (> 0) be the gain in energy that occurs when a polymer attaches to the clay sheet. At relatively high values of ϵ , the attached chains form a polymer brush. We assume that our system is in the strong stretching limit, and thus, the attached chains experience a parabolic potential.¹⁹

The remainder of the polymers in the gap are mobile and their entropy of mixing is determined by the spatial distribution of all the components between the surfaces. We let $C_a(x)$ be the volume fraction of attached polymers at a distance x from the surface and $C_i(x)$ be the corresponding volume fraction of the mobile (P) polymers. The volume fraction of non-adsorbed functionalized (N) chains is given by $(1 - C_a(x) - \sum_i C_i(x))$. The entropy of mixing per unit volume for the free chains is then given by

$$f[C_a(x), \{C_i(x)\}] a^3/kT = [1 - C_a(x) - \sum_i C_i(x)] \ln[1 - C_a(x) - \sum_i C_i(x)]/N + \sum_i C_i(x) \ln[C_i(x)]/P_i \quad (2)$$

The equilibrium structure of a brush in contact with an infinite melt of mobile polymers was considered in detail in ref. 20. In particular, it was shown that the distributions of all the components in the system are determined by the following set of equations²⁰

$$\delta(f a^3)/\delta(C_a(x)) = \Lambda_a - k^2 x^2 \quad (3)$$

$$\delta(f a^3)/\delta(C_i(x)) = \Lambda_i \quad (i = 1, 2, \dots) \quad (4)$$

where $k^2 = 3\pi^2/8a^2N^2$ and Λ_a and Λ_i are the indefinite Lagrangian multipliers, which ensure the conservation of n_a attached and n_i ($i = 1, 2, \dots$) mobile chains in the gap between the surfaces. By substituting expression (2) for the mixing entropy into eqs (3) and (4), and solving the resulting equations, we arrive at the following expressions for the profiles of the components between the surfaces,

$$C_i(x) = \lambda_i \exp(P_i k^2 x^2) \quad (i = 1, 2, \dots) \quad (5)$$

$$C_a(x) = 1 - \lambda_a \exp(N k^2 x^2) - \sum_i \lambda_i \exp(P_i k^2 x^2) \quad (6)$$

where

$$\lambda_i = [a^3 n_i P_i] / [A \int_0^H \exp(P_i k^2 x^2) dx] = C_i H / [\int_0^H \exp(P_i k^2 x^2) dx] \quad (7)$$

and

$$\lambda_a = [H - (a^3 n_a N/A) - (\sum_i a^3 n_i P_i/\Sigma)] / [\int_0^H \exp(N k^2 x^2) dx]$$

$$= H [1 - C_a - \sum_i C_i] / \left[\int_0^H \exp(N k^2 x^2) dx \right] \quad (8)$$

Here, $C_i = (a^3 n_i P_i)/(A H)$ ($i = 1, 2, \dots$) and $C_a = (a^3 n_a N)/(A H)$ are the average concentrations (volume fractions) of the mobile (P) and the attached (N) polymers in the gap between the particles.

In order to find the equilibrium values of C_i and C_a at any given value of H , we first consider the expression for the total free energy of the system,

$$\Delta F_{\text{total}} = \Delta F_{\text{brush}} - (n_a + n_f) \mu - \sum_i n_i \mu_i \quad (9)$$

The first term on the right hand side is given by

$$\Delta F_{\text{brush}} = \Delta F_{\text{stretch}} + \Delta F_{\text{mix}} + \Delta E_a \quad (10)$$

which incorporates the elastic free energy $\Delta F_{\text{stretch}}$ of the anchored chains, the mixing entropy ΔF_{mix} of the mobile chains, and the energy gain ΔE_a due to the attachment of the functionalized polymers onto the clay sheets. The elastic contribution to the free energy, $\Delta F_{\text{stretch}}$, is determined by the local stretching of the attached chains and the distribution of their free ends.¹⁹ In the strong stretching limit, $\Delta F_{\text{stretch}}$ can also be written in terms of the profile of the tethered chains:

$$\Delta F_{\text{stretch}}/kT = A k^2/a^3 \int_0^H dx \int_x^H x' C_a(x') dx' \quad (11)$$

The mixing entropy of the mobile chains is given by

$$\Delta F_{\text{mix}}/kT = A \int_0^H dx f[C_a(x), \{C_i(x)\}] \quad (12)$$

while the gain in the energy due to the surface attachment of the functionalized chains is given by

$$\Delta E_a/kT = -\epsilon n_a/kT \quad (13)$$

The second and third terms on the right hand side of eq (9) contain the chemical potentials of the different chains in the melt. These chemical potentials can be determined through Flory theory.²¹ Namely, the chemical potential μ of the end-modified chains is given by

$$\mu/kT = \ln \phi + 1 - \phi - N \sum_j (\phi_j/P_j) \quad (14)$$

while the chemical potential μ_i of the polymers with a molecular weight of P_i is given by

$$\mu_i/kT = \ln\phi_i + 1 - \phi P_i/N - P_i \sum_j (\phi_j/P_j) \quad (15)$$

By substituting the appropriate terms in eqs (5) - (8) for the profiles in eqs (11) and (12), we arrive at the following total free energy for the system,

$$\begin{aligned} \Delta F_{\text{total}}/kT = & A k^2 H^3/a^3 + \sum_i C_i \ln\{C_i H / [\int_0^H \exp(P_i k^2 x^2) dx]\} \\ & + [AH/a^3 N - n_a - \sum_i n_i P_i/N] \ln\{H [1 - C_a - \sum_i C_i] / [\int_0^H \exp(N k^2 x^2) dx]\} \\ - \epsilon n_a /kT - & (\alpha H/a^3 N) [1 - \sum_i C_i] \mu/kT - \sum_i n_i \mu_i/kT \end{aligned} \quad (16)$$

(The reference state for the free energy corresponds to the state where the polymers and sheets are totally demixed.) By minimizing ΔF_{total} with respect to n_a and n_i ($i = 1, 2, \dots$), we obtain the equations that specify the equilibrium values of C_a and C_i ($i = 1, 2, \dots$) at a given value of H ,

$$\ln\{H [1 - C_a - \sum_i C_i] / [\int_0^H \exp(N k^2 x^2) dx]\} + \epsilon/kT + 1 = 0 \quad (17)$$

$$\begin{aligned} \ln\{H [1 - C_a - \sum_i C_i] / [\int_0^H \exp(N k^2 x^2) dx]\} \\ = (N/P_i) \ln\{C_i H / [\int_0^H \exp(P_i k^2 x^2) dx]\} \end{aligned} \quad (18)$$

By solving equations (17) - (18), we find C_a and C_i to be

$$C_i = (\phi_i/H) \int_0^H \exp\{P_i [k^2 x^2 - (\epsilon/kT + 1 + \ln\phi)/N]\} dx \quad (19)$$

$$\begin{aligned} C_a = 1 - \sum_i (\phi_i/H) \int_0^H \exp\{P_i [k^2 x^2 - (\epsilon/kT + 1 + \ln\phi)/N]\} dx - \\ (1/H) \int_0^H \exp\{N [k^2 x^2 - (\epsilon/kT + 1)/N]\} dx \end{aligned} \quad (20)$$

The profiles for all the components are then given by

$$C_i(x) = C_i H \exp\{P_i k^2 x^2\} / [\int_0^H \exp(P_i k^2 x^2) dx] \quad (21)$$

$$C_a(x) = 1 - H[1 - C_a - \sum_i C_i] \exp\{N k^2 x^2\} / \left[\int_0^H \exp(N k^2 x^2) dx - \sum_i C_i H \exp\{P_i k^2 x^2\} / \left[\int_0^H \exp(P_i k^2 x^2) dx \right] \right] \quad (22)$$

where C_i and C_a are given by eqs (19) and (20), respectively. The corresponding total free energy per unit area is

$$\Delta F_{\text{total}}/AkT = (H/Na^3) \{k^2 H^2 N/3 - \epsilon/kT - 1 + C_a + \sum_i C_i - N \sum_i C_i/P_i - \mu/kT\} \quad (23)$$

Results and Discussion: Analytical Model

Through the above calculations, we can quantitatively describe the critical characteristics and behavior of the system. Namely, we can determine the extent to which the surfaces are separated by the functionalized polymers and establish the amount of the functionalized polymer that adsorbs on the surface. We start by considering the effects of separating the surfaces within the melt.

Increasing H affects the structure of the melt inside the gap up to the point where the brush formed by the anchored chains reaches its equilibrium thickness, H_0 . At $H > H_0$, a layer of bulk polymer appears between the outer edges of the two brushes. In terms of our model, which ignores the partial penetration of mobile chains into the brush, increases in $H > H_0$ do not change the free energy of the system. Thus, at $H = H_0$, we find the maximal gain in free energy due to the exfoliation of the particles. In order to determine H_0 , we take advantage of the fact that the distribution of the mobile components is continuous at the outer edge of the unperturbed brush. That is,

$$C_i(x = H_0) = \phi_i \quad (24)$$

By substituting eq (24) into eq (21), we obtain the expression for the thickness H_0 of the undeformed brush,

$$H_0 = (2a/\pi) [2N (\epsilon/kT + 1 + \ln \phi)/3]^{1/2} \quad (25)$$

We thus find that H_0 does not depend on the features of the non-reactive chains (their molecular weight and polydispersity), but is solely determined by the length N , volume fraction ϕ and the adsorption energy ϵ of the functionalized chains.

As indicated by eq (25), H_0 scales as the square root of the molecular weight of the reactive chains, $H_0 \sim N^{1/2}$. The chains are nonetheless stretched with respect to their Gaussian size, or $H_0^2/N > 1$, because of the multiplicative factors in eq (25). Thus, for large values of the adsorption energy, $\epsilon/kT \gg 1$, and reasonable values of ϕ , the parabolic approximation¹⁹ for the potential is indeed applicable. Using eq (25), we obtain the specific expressions for the profiles of the attached and free polymers in an undeformed system,²⁰

$$C_a(x) = 1 - \phi \exp\{-Nk^2(H_0^2 - x^2)\} - \sum_i \phi_i \exp\{-P_i k^2(H_0^2 - x^2)\} \quad (26)$$

$$C_i(x) = \phi_i \exp\{-P_i k^2(H_0^2 - x^2)\} \quad (27)$$

Perturbing the system, or decreasing the distance between the two surfaces to $H < H_0$, leads to a decrease in the amount of adsorbed functionalized chains, $\Theta = C_a H$, and a corresponding increase in the free energy. By using eqs (25) and (20), we obtain the following expression for $\Theta(H)$,

$$\begin{aligned} \Theta = & H - \phi \exp(-N k^2 H_0^2) \int_0^H \exp(N k^2 x^2) dx \\ & - \sum_i \phi_i \exp(-P_i k^2 H_0^2) \int_0^H \exp(P_i k^2 x^2) dx \end{aligned} \quad (28)$$

while eq (23) gives the final expression for the free energy

$$\begin{aligned} \Delta F_{\text{total}}/AkT = & (H/Na^3) \{k^2 H^2 N/3 - k^2 H_0^2 N + \\ & \phi [1 - \exp(-N k^2 H_0^2) \int_0^H \exp(N k^2 x^2) dx/H] + \\ & N \sum_i (\phi_i/P_i) [1 - \exp(-P_i k^2 H_0^2) \int_0^H \exp(P_i k^2 x^2) dx/H] \end{aligned} \quad (29)$$

The plots in Figure 3 show the adsorbed amount Θ versus H (the distance between the surfaces) as calculated through eq (28). The curves are for various values of P , the length of the nonfunctionalized chains in a monodisperse melt. The length of the functionalized chains is given by $N = 75$ and the volume fraction of these chains in the melt is fixed at $\phi = 0.05$. The value of ϵ is set at 12.5 kT, which is an experimentally realistic value. Increases in P lead to increases in the adsorbed amount Θ of the functionalized chains. When the lengths of the functionalized and nonfunctionalized chains become comparable and the distances between the particles are close to H_0 , the high values of Θ indicate that the attached chains do indeed form a brush, as was assumed in our model. A comparison of the numerical SCF values and the analytical predictions for Θ indicates reasonable agreement between the two models. At $H = H_0$, Θ reaches the maximal value (Θ_0), which does not change with increases in $H > H_0$.

Good agreement is also found between the SCF values of Θ_0 and the analytical predictions as calculated through eq (28) at $H = H_0$. The analytical model, however, overestimates the values of Θ_0 , particularly at high values of Θ . We attribute this behavior to the partial penetration of the mobile chains into the grafted layer, an effect that is totally ignored in our analytical model. The extent of interpenetration of the

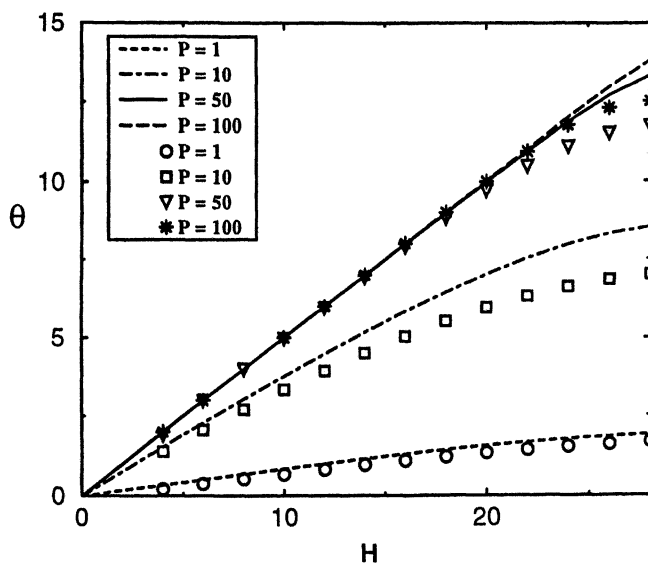


Figure 3. The adsorbed amount of the functionalized chains versus surface separation for various lengths P of the nonfunctionalized chains. The analytical predictions (as calculated from eq (28)) are marked by the lines. The numerical SCF results are indicated by symbols.

tethered and mobile chains increases with increases in N .¹⁷ Correspondingly, the free energy of the system and the adsorbed amount Θ slightly decrease.

The numerical SCF data on the overall thickness of the unperturbed brush, H_0 , also indicates satisfactory agreement with the analytical prediction in eq (25). (The value of H_0 was estimated in an approximate manner from the SCF profiles for the adsorbed polymer as the point where the volume fraction of the functionalized chains reaches the bulk value, ϕ .) Provided that the system was in the brush regime, the overall thickness H_0 was virtually independent of the length of the non-reactive chains at $P \gg 1$. A weak dependence of H_0 on P at small values of P was due to the sparse grafting of the reactive chains on the surfaces and the breakdown of the brush regime.

Conclusions

In the above studies, we focused on the interactions between two clay surfaces and the surrounding polymer melt, and drew conclusions on the equilibrium behavior of the overall mixture. It is, however, important to note that the actual phase behavior and morphology of the mixture can be affected by the kinetics of the polymers penetrating the gap.¹⁶ Initially, the polymer has to penetrate the space between two clay sheets from an outer edge and then diffuse towards the center of the gallery. Consider the case where $\chi_{\text{surf}} < 0$ and thus, the polymer and surface experience an attractive interaction. As the polymer diffuses through the energetically-favorable gallery, it maximizes contact with the two confining layers. In effect, the polymer "glues" the two surfaces together as it moves through the interlayer. This "fused" condition could represent a kinetically trapped state and consequently, increasing the attraction between the polymer and clay sheets would only lead to "intercalated" structures, rather than exfoliated structures.¹⁶ In intercalated structures, extended polymer chains penetrate the host layers, and simply enhance the separation between the silicate sheets. Recent experimental studies¹¹ reveal that the melt mixing of organically-modified clays and highly attractive polymers does in fact lead to intercalated hybrids.

Conversely, in the case where $\chi_{\text{surf}} > 0$, the polymer can separate the sheets, as the chain tries to retain its coil-like conformation and gain entropy. However, both the SCF calculations and our phase diagrams¹⁶ indicate that for $\chi_{\text{surf}} > 0$, polymers and sheets are immiscible.

The proposed scheme of using a mixture of functionalized and nonfunctionalized polymers for the melt could be a way around this problem, providing a means of creating composites with exfoliated morphologies. While the stickers at the chain-ends are highly attracted to the surface, the remainder of polymer does not react with the substrate. Thus, as the polymers penetrate the sheets, the majority of the chain is not likely to glue the surfaces together. Similar behavior is expected to occur in melts containing diblock copolymers, where a short block is attracted to the substrate, but a longer hydrophobic block will separate the hydrophilic sheets.

The above arguments yield criteria for designing polymer systems that will disperse the clay sheets within the melt. These polymers should contain a moiety that anchors the chains to the sheets and a block that is not attracted to this surface. The non-reactive block will attempt to gain entropy by pushing the sheets apart. Once the sheets are separated, these blocks will also sterically hinder the surfaces from coming in close contact. In effective, the criteria for choosing the optimal steric stabilizers for colloidal suspensions should also yield the optimal candidates for creating polymer/clay dispersions.

Acknowledgements

The authors thank Dr. Yulia Lyatskaya and Prof. Mary Galvin for helpful discussions. A.C.B. gratefully acknowledges the financial support of the Army Office of Research, DOE through grant DE-FG02-90ER45438, the N.S.F. through grant number DMR-9709101 and ONR through grant N00014-91-J-1363..

References

1. Okada, A.; Kawasumi, M.; Kojima, Y.; Kurauchi, T.; Kamigaito, O. *Mat. Res. Soc. Symp. Proc.* **1990**, 171, 45.
2. Yano, K.; Uzuki, A.; Okada, A.; Kurauchi, T.; Kamigaito, O. *J. Polym. Sci.: Part A: Polym. Chem.* **1993**, 31, 2493.
3. Kojima, Y.; Usuki, A.; Kawasumi, M.; Okada, A.; Kurauchi, T.; Kamigaito, O. *J. Polym. Sci.: Part A: Polym. Chem.* **1993**, 31, 983.
4. Uzuki, A.; Kawasumi, M.; Kojima, Y.; Okada, A.; Kurauchi, T.; Kamigaito, O. *J. Mater. Res.* **1993**, 8, 1174.
5. Miller, B. *Plastics Formulating and Compounding* **1997**, 30.
6. Vaia, R. A.; Jandt, K. D.; Kramer, E. J.; Giannelis, E. P. *Macromolecules* **1995**, 28, 8080.
7. Vaia, R. A.; Sauer, B. B.; Tse, O. K.; Giannelis, E. P. *J. Polym. Sci.: Part B: Polym. Phys.* **1997**, 35, 59.
8. Messersmith, P. B.; Stupp, S. I. *J. Mater. Res.* **1992**, 7, 2599.
9. Krishnamoorti, R.; Vaia, R. A.; Giannelis, E. P. *Chem. Mater.* **1996**, 8, 1728.
10. Vaia, R. A.; Giannelis, E. P. *Macromolecules* **1997**, 30, 7990.
11. Vaia, R. A.; Giannelis, E. P. *Macromolecules* **1997**, 30, 8000.
12. (a) Singh, C.; Pickett, G.; Zhulina, E. B.; Balazs, A. C. *J. Phys. Chem., B*, **1997**, 101, 10614. (b) Singh, C.; Pickett, G.; Balazs, A. C. *Macromolecules* **1996**, 29, 7559.
13. (a) Singh, C.; Zhulina, E. B.; Balazs, A. C. *Macromolecules* **1997**, 30, 7004. (b) Balazs, A. C.; Zhulina, E.; Singh, C. *Macromolecules* **1998**, 31, 6369.
14. Balazs, A. C.; Singh, C.; Zhulina, E. *Macromolecules* **1998**, 31, 8370.
15. Fleer, G.; Cohen-Stuart, M. A.; Scheutjens, J. M. H. M.; Cosgrove, T. Vincent, B. "Polymers at Interfaces"; Chapman and Hall: London **1993**.
16. Lyatskaya, Y.; Balazs, A. C. *Macromolecules* **1998**, 31, 6676.
17. (a) Zhulina, E.B.; Semenov, A.N. *Polym.Sci.USSR* **1989**, 31, 196. (b) Witten, T.A.; Leibler, L.; Pincus, P. *Macromolecules* **1990**, 23, 824. (c) Wijmans, C.M.; Zhulina, E.B.; Fleer, G.J. *Macromolecules* **1994**, 27, 3238. (d) Ferreira, P.G.; Ajdari, A.; Leibler, L. *Macromolecules* **1998**, 31, 3994.
18. Note that in the case of surface adsorption, we must divide χ_{SS} by the coordination number of the cubic lattice ($q = 6$) in order to relate this Flory-Huggins parameter to experimentally relevant values (see ref. 14). Thus, our value of χ_{SS} is comparable to a binding energy of $(75/6) = 12.5$ kT.
19. Semenov, A.N. *Sov.Phys. JETP* **1985**, 61, 733.
20. Zhulina, E.B.; Borisov, O.V.; Brombacher, L. *Macromolecules* **1991**, 24, 4679.
21. Flory, P. *Principles of Polymer Chemistry*; Cornbell University Press, Ithaca, NY, **1953**.

Chapter 24

Use of Wear Tests for Plastics

Kenneth G. Budinski

**Materials Engineering Laboratory, Eastman Kodak Company,
Kodak Park, Rochester, NY 14652-4347**

It is estimated that over 50 percent of all new products in the United States are made from plastics. Many of these products employ plastics in some type of tribosystem. The plastic can wear or it may produce unanticipated wear on another surface. This paper describes the various wear tests that are frequently used to assess the tribological characteristics of plastics. Tests are described that measure how plastics wear in sliding contact with other solid surfaces such as bushings, guides and the like. Another section discusses tests that can be used to assess how abrasive plastics are to other solid surfaces, plastic abrasivity. Special tests are described that are applied to plastics in web form; these tests assess how they wear mating surfaces. Finally, erosion testing of plastics is described. These tests apply to the use of plastics in applications such as pumps and piping. The goal of this paper is to familiarize designers with the tests that can and should be used to determine if a plastic part will provide anticipated life in service. Guidelines are presented to assist in test selection and use of these tests.

Twenty years ago the ASTM G2 Committee on Wear and Erosion held a symposium on the Selection and Use of Wear Tests for Polymers (1). This symposium's discussions suggested that polymer wear testing was not well defined; there were no agreed-to standard tests or wear mechanisms. Unfortunately, the situation in 1998 is much the same. There are several standard tests in the United States; manufacturers of plastic bearing materials rate their materials in different ways and users still largely rely on testing parts made from candidate plastics and life test these parts in finished products. Needless to say this is an expensive and time-consuming process. Laboratory tests should be used for screening.

Tribological data from various manufacturers may show widely different wear ratings for the same basic plastic. This makes it difficult for a plastic user to have confidence in supplier selection information.

Some aspects of plastic wear are hardly even discussed in manufacturer's literature: plastic abrasivity, plastic abrasion resistance, and plastic erosion resistance. The manufacture of many plastic products involves the use of injection molding or extrusion equipment. If a plastic contains inorganic fillers such as glass or carbon fiber reinforcement, they can be very abrasive to parts that contact the melted plastic: extruder barrels, screws, molds, and check valves. Replacement and coating of extruder barrels and screws is an entire industry. The mechanism of material removal is often polishing abrasion. There are no common tests to measure the abrasivity of plastics in these tribosystems.

Plastics are often used for abrasion and erosion resistance, but like abrasivity, there are no agreed-to tests to rate materials for these types of applications. Plastics and elastomers are frequently used for wheels for a variety of consumer products. Everything from in-line skates to barbecue grills, to strollers, use plastic wheels. How do various plastics resist abrasion from contact with concrete pavement? Erosion of plastics is a factor in dishwashers, plumbing systems, fans, and pumps. Most domestic sump pumps are now made from plastics and in use they are required to carry sand-filled water from basement drain crocks. How do various plastics resist this type of wear?

It is the purpose of this paper to review available plastic wear tests and to comment on their applicability to various tribosystems and to improve the comfort level that users can have that their plastic wear tests are producing valid material comparisons. The objective is to supply potential plastic users with guidelines for the selection of appropriate wear tests for various industrial situations. We will start with a discussion of PV measurement, then wear factors, abrasivity testing, abrasion of plastics by other surfaces, plastic bushings, tests on plastic films, and erosion tests. These tests will be put into a selection matrix for plastic users.

PV Determination

A concept that has prevailed in plastic wear since the 1970s is that there is a pressure-velocity (PV) limit for every plastic. If a plastic tribocomponent is operated above its limit it may be prone to failure, and it is safe to use this plastic if your operating conditions involve a pressure/velocity product that is lower than a stated value. Plastic manufacturers often supply a PV limit for their bearing-grade plastics. There are various ways of measuring PV limits (2), but commonly, a test is run at a fixed velocity and an arbitrary pressure. If the components exhibit mild wear with the selected conditions, the pressure is increased and another test is conducted. This is repeated until the pressure is high enough to make the tribosystem fail due to high wear, high friction, melting and other predetermined criterion. This procedure is repeated at another velocity until a curve is developed that resembles the one shown in Figure 1. A safe operating range is defined for that plastic in that tribosystem.

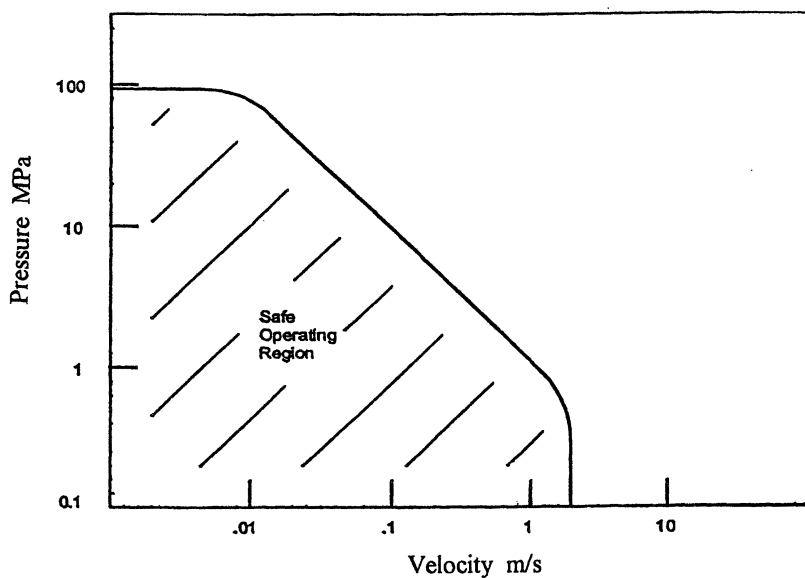


Figure 1. Typical PV limit diagram for a general purpose bearing plastic such as acetal/PTFE.

Sometimes wear factor or specific wear rate is the metric in a PV study. Wear factor is essentially the constant in the Archard equation that is cited for abrasion and adhesive wear in metals. This equation states that wear volume is proportional to the sliding distance and the normal force.

$$W = k D l$$

Where:

k = wear factor (m^3/Nm)

W = wear volume in a test (m^3)

D = the total sliding distance (m)

l = the contact force (N)

Wear factor is based upon the results of a test that measures wear volume. Specific wear rate is an alternate term that is sometimes used for wear factor.

An attractive feature of wear factor measurement is that the equation can be rearranged to solve for wear life if the wear factor and operating conditions are known.

$$t = kPVT$$

Where:

t = radial wear in a bushing (m) (W/A)

A = apparent or projected area

P = contact pressure (N/m^2) (l/A)

V = sliding velocity (m/s) (D/T)

T = time (s)

However, there are some fundamental weaknesses in using PV in this manner:

1. In the United States there is not a standard test for PV
2. Data generated on a particular tribosystem may not apply to another
3. The concept invites misuse
4. Counterface wear is often neglected

Lack of a standard test means that it is difficult to compare data from different suppliers. The lack of a standard test also leads to a potential problem with system differences. If a published PV limit was determined on a continuous motion pin-on-disk test, these data may not be applicable to a bearing application, where the wear debris is maintained in the system. Obviously, data generated at a sliding speed of 100 and an apparent pressure of 100 ($PV = 10,000$ in arbitrary units) does not mean that the material will work in a bearing with a pressure of one and a

velocity of 10,000. A PV curve like that shown in Figure 1 could show the velocity and pressure limits, but the trend in plastic literature is to only give a single number. This presents the risk that users interpret the PV or wear factor as a material property that can be used like any other property such as yield strength.

Ignoring counterface wear is another of the fundamental weaknesses of both PV and wear factor. Nobody will argue that a wear system contains two or more members, yet only the wear of the plastic members is presented in manufacture's literature. A cemented carbide counterface could be used for all tests and it may not wear, but this would not simulate most real-life tribosystems. Counterface wear is particularly important with glass and carbon fiber (CF) reinforced plastics. Counterface wear is often the cause of plastic bearing failure in reinforced and unreinforced bearings.

How should PV and wear factor be dealt with? They should be used as selection aides for grades of plastic available from a given manufacturer. That manufacture probably used a particular test. In fact, the test conditions are usually stated and the designer can use that information to decide on applicability. We recommend against comparing data from different manufacturers unless they used tribosystems and test conditions that are the same. There is nothing wrong with designing a plastic bushing to a supplier's PV value, but be certain that your speed and loads are less than those used by the supplier in developing their PV/wear factor data.

Abrasion of Plastics by Other Surfaces

Abrasion is defined as damage or material removal produced by hard sharp particles or protuberances forced against and moving along a solid surface (3). Damage occurs on the softer surface. Plastics are softer than most metals and ceramics so most rough surfaces made from these materials will abrade plastics. Plastic bushing wear tests have shown that there is an optimum roughness for a conforming steel surface (4). If the roughness is greater than 0.2 μm , the wear increased significantly and becomes exponential when roughness gets as large as 2 μm Ra. On the other hand, if the surface is too smooth wear increases from the minimum, but not to the level produced by the rough surface. Sand abrasion tests (5) indicate that some plastics resist abrasion better than some metals, but the plastic properties that are responsible for good abrasion resistance are not well defined. It appears that plastics that deform easily when imposed upon by a hard, sharp counterface have the best abrasion resistance. It also helps to have favorable friction between the abradant and the counterface. Low friction between abradants and a plastic keeps abradants from "digging" into the surface. On the other hand high friction between an abradant and plastic or elastomer can make third-body abradants roll through the mating interface without producing scratching.

The most widely used test to rate the abrasion resistance of plastics is the Taber Abrasor (6). In this test, a 10 cm square plaque of the plastic is affixed to a record player type of turntable. As it rotates in the horizontal plane, two weighted rubber/abrasive wheels counter-rotate on the plaque to produce a circular wear

scar that is the width of the abrasive wheels. The original test was developed to assess the durability of vinyl and related flooring materials. Mass loss for a given number of platen rotations is commonly used as the metric. When this test is used on transparent plastics and the metric is often haze measurement in the abraded area. The more durable the surface, the less haze in the abraded area. Haze is measured by light transmission. This test simulates a tribosystem of shoe sole materials on flooring. The rubber abrading wheels are filled with a variety of abrasives, but essentially they simulate the action of dirt particles on rubber-heeled shoes rubbing on flooring. Unfortunately, people use this test to rate the durability of plastic articles such as ski goggles, which will never intentionally incur somebody walking on them with dirty shoes. In other words, this test is often misapplied because it does not simulate the tribosystem that applies to the plastic product.

The abrasion resistance of plastics can also be determined by the ASTM G 65 dry sand rubber wheel test (7), which is shown schematically in Figure 2. The three-body abrasion produced by this type of test is similar to that produced by rubbing plastic on a rigid surface with hard particles in the faying surface, but it is probably faster and easier to perform. Test times can be as short as one minute. This test can also be conducted immersed in a slurry (8) if this better simulates the system of interest.

Rubbing a flat-ended pin against a drum covered with bonded abrasive (sandpaper) is a standard test for metals (ASTM G 141), but it could be used for plastics. The ASTM test standard allows the option of rotation of the pins about their axis. The pins traverse the drum in a spiral path (Figure 3) and a reference pin material is run on the same abrasive in a path parallel to the test pin. Wear is expressed as a wear ratio. The use of a reference sample with every test sample mitigates differences in lots of abrasive media. This test simulates tribosystems with severe abrasion, for example, a plastic snow shovel. In use, it will be rubbed on concrete or similarly abrasive paving.

Somewhat similar is the abrasive tape test for plastics (9). This test rubs plaques of plastic against a contact roll covered with bonded abrasive tape. Mass loss in a prescribed amount of contact with the abrasive tape is the metric. The reference material for the test is wrought zinc. This test simulates severe abrasion. This testing standard contains a second procedure that rubs flat plastic specimens against flat plates covered with aluminum oxide particles. This is a three-body abrasion tribosystem as opposed to the two-body system used in the tape test. These two tests and the Taber Abrasor test compete with each other and none is considered to be a reference abrasion test for plastics.

In summary, plastics are subject to abrasion by contacting rough counterfaces made from harder materials, but the tests that exist to rate abrasion resistance may not be realistic if they do not simulate real tribosystems. The best way to assess the abrasion resistance of a plastic is to rub it with whatever it will be rubbed with in its intended application. For example, assume that plastic taillight lenses on an automobile will be scrubbed by a canvas scrub material containing small amounts of road dust. Do not assume that the average car owner will clean the taillights

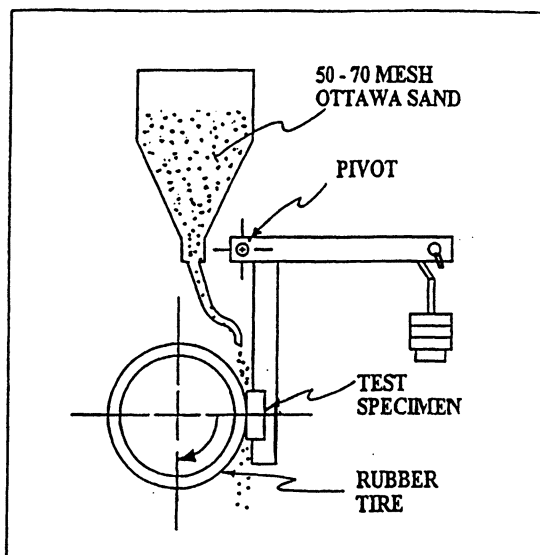


Figure 2. Schematic of ASTM G 65 Dry sand/rubber wheel abrasion test.

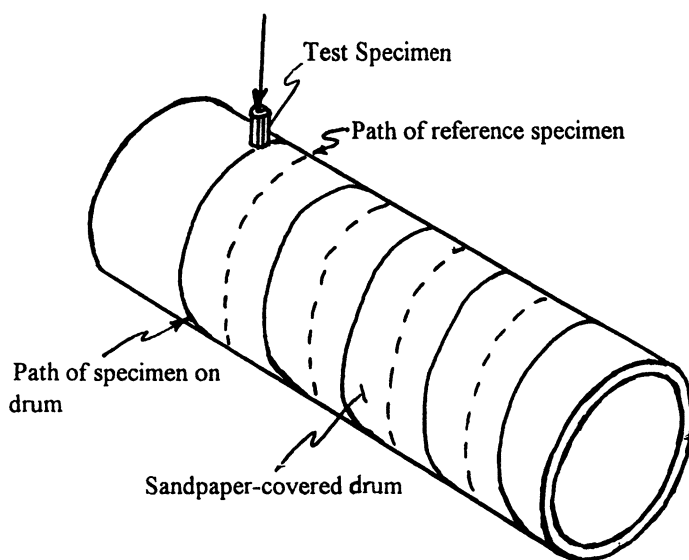


Figure 3. Schematic of ASTM G 141 Pin abrasion test.

with a heavy-duty nylon/aluminum oxide scrub pad. A reciprocating test using the former would be a good screening test for abrasion resistance. A reciprocating wet paper towel test may be an appropriate test for candidate ski goggle plastics. Simulate the tribosystem of interest.

Wear of Conforming Surfaces by Plastics

Some of the tests that are used in the United States to measure the wear of plastics when they rub other surfaces are shown in Table 1. The thrust washer test (10) is probably the closest is to an agreed-to standard. The flat face of a plastic annular ring slides against the flat top of a larger annular ring made from soft steel (Figure 4). Wear volume is measured on the plastic ring or thrust washer by mass change. The disk counterface is usually soft steel and most tabulations by plastic suppliers do not elaborate on the amount of wear that their materials produce on soft steel counterfaces. Counterface wear should not be ignored with glass or mineral-reinforced plastics. If the plastic is self-lubricated, this test is likely to take a very long time. The test loads and speeds are optional, but most plastic compounders run wear ranking tests at a nominal PV such as 0.034 kPa m/s. It may take a hundred hours to get reasonable test results with these test conditions. Needless to say, this makes rating the plastic-to-metal wear of the 15,000 commercially available plastics quite a time-consuming project. This test is gradually being replaced with new tests that require less run time.

The bushing test involves simply making a plain bearing out of a test material and running it under load (at a nominal PV) until measurable wear occurs. This test can take 500 hours. Shaft wear is often not reported, but as shown in Figure 5, it can be significant. This test is an exact duplication of a plain bearing and it is the best test to simulate this type of tribosystem. However, at 500 hours or more per test, it is not very practical for screening candidate materials and for developing new plastic compounds. It takes too long.

The block-on-ring test (11) uses line or area contact loads a small plastic block against a steel ring that looks like the outer race of a rolling element bearing (Figure 6). These rings can be purchased in bulk out of various materials, but most plastic tests are conducted against a case-hardened ring with a surface hardness of about 60 HRC and a surface roughness of 0.2 to 0.3 $\mu\text{m Ra}$. The ASTM G 77 test procedure directs the user to measure the wear on both members. The block wear volume is measured from wear scar dimensions and the ring wear can be measured by mass change or profilometry of the wear groove. Counterface wear can often be a significant factor. The current ASTM standard requires only two hours of testing, however, recent studies indicate that better interlaboratory results can be obtained if the test time is increased to 20 hours.

This test clearly points out another aspect of plastic wear, adhesion of the plastic to the metal counterface and the reverse. In fact, many times severe counterface wear is caused by adhesion of the metal to the plastic rider. With subsequent sliding, the metal is really rubbing itself and this produces severe counterface wear. Hardened steels (60 HRC) are less prone to adhesion; soft

Table 1. Plastic wear tests used for simulating sliding contact with other rigid surfaces.

Test	Metric
Thrust Washer (D 3702)	Wear volume from mass change
Bushing	Radial wear (distance)
Block-on-ring (G 77)	Wear volume from scar size
Block-on-disk (G 137)	Wear volume from mass change
Pin-on-disk (G 99)	Wear volume from scar size
Reciprocating ball-on-flat (G 133)	Wear volume from size change

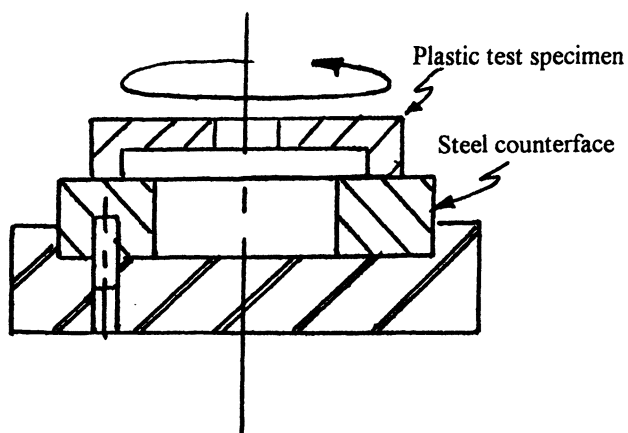


Figure 4. Schematic of ASTM D 3702 Thrust washer plastic wear test.

metals are more prone and some metals such as titanium are extremely prone to this phenomenon. High-strength engineering plastics are often prone to adhesion; olefins and fluorocarbons seem to be the least prone. Plastic-to-metal adhesion is one of the plastic wear issues that needs additional attention.

The block-on-disk test (12) is also called a block-on-ring test, but the counterface is not really a ring. It is a 150 mm diameter hardened tool steel disk. A plastic block is weight-loaded against the rim of the disk (line contact) and the wear test is usually between 20 and 30 hours. The plastic samples have dimensions that allow them to be made from plastic flex test bars that are commonly molded out of new plastics to measure their flexural properties. This test is intended to replace the thrust washer test. The ASTM test procedure does not require measurement of counterface wear, but it is always advisable to make this measurement. The disk weighs more than 3 kg, making it difficult to weigh it to measure mass change that occurred in a test. Profilometry could be used.

The pin-on-disk test (13) is not a standard for plastic wear testing, but it is the only wear test apparatus that many laboratories have and thus it will be used for plastic, metal, ceramic, etc. It works quite well if this tribosystem simulates the real-life tribosystem of interest. The rider in the pin-on-disk test is usually a ball or a hemispherical-ended pin. Flat-ended pins are used, but they often hydroplane and do not wear flat. Plastic testing laboratories often have molds for flex bars and tensile samples. Ball cavities can easily be put in these same molds to provide molded spheres as riders for a pin-on-disk test. The disk can be made from any counterface of interest. It is particularly easy to measure wear volume from spherical surfaces. A simple calculation using the diameter of the flat worn on the sphere will produce a wear volume measurement that is usually more accurate than can be obtained by mass change measures. This test excels for simulating tribosystems that involve very small normal forces on the plastic member.

Reciprocating sphere-on-plate tests are similar to the pin-on-disk tests, but they simulate reciprocating systems. This test should never be used unless the goal is to simulate a reciprocating tribosystem. A priority of selecting a wear test is to simulate the motion in the system of interest. As shown Figure 7, this test can be used to rank plastics for a reciprocating application. Another feature of this test is that it can be used to quantify wear debris generation with a particular couple. Debris accumulates on the flat counterface at the end of the stroke and it forms a halo on the ball rider. These provide good test measures when the goal of a screening test is to find a plastic-to-metal or plastic-to-plastic couple that does not generate debris under anticipated sliding conditions. Debris generation is a common concern in electronic devices and systems that must operate in clean rooms.

In summary, there are a number of standard tests that are used in the United States to measure the tendencies of plastics to wear when they slide against other solids. These tests all have idiosyncrasies that need to be addressed. In fact, selection of one of these tests probably depends more on consideration of these

idiosyncrasies rather than hardware concerns. The block-on-ring, pin-on-disk and reciprocating sphere-on-flat test simulate many tribosystems and they are probably the most widely used tests in the United States. They should be in laboratories that routinely screen plastics for tribological characteristics.

Web Abrasivity Tests

The previously mentioned tests that can be used to determine if a plastic is abrasive to other surfaces are not particularly suited to evaluation of the abrasivity of plastics that are normally manufactured as flexible webs. Web materials with thicknesses less than about one millimeter pose the problem that they usually need to be adhered to some other surface to allow testing them as bushings, thrust washers, or blocks for block-on-ring tests. This can be done and is done, but two other tests have been developed that are particularly useful for web materials: the ball-on-plane test and the tape abrasion test (14). The ball-on-plane test, which is shown schematically in Figure 8, reciprocates a spherical rider on a web test sample while the sample rotates slowly at less than 1 revolution per minute. The rider would see mostly fresh surface if allowed to run only one revolution, but in practice this test is usually run for longer test durations (from 10 minutes to 40 hours). When the test is run for more than an hour, the web counterface is changed every hour; the rider is simply lifted off the test surface. Volume loss on the ball rider is the test metric. Wear volume is measured from the ball scar diameter and this measurement can be made in situ on the test apparatus.

This test was developed to rate the abrasivity of head cleaning tapes for magnetic recording devices. Some tapes were more abrasive than others; all intentionally contained abrasive particles, usually aluminum oxide, to remove brown stain from heads. The stains were really adhesive transfer of polymer from the tapes that contact the heads. The riders in the original test were made from high nickel alloys or other materials that were used for recording heads. This was done to simulate the actual tribosystem. Since that time, it has been learned that type 316 stainless steel balls, that are readily commercially available, produced the same rankings as the more exotic materials. For this reason, 316 stainless steel has become somewhat of a standard for evaluation of the abrasivity of all sorts of web materials.

The test procedure is to affix the web material to the rotating platen (200 mm in diameter) with a pressure-sensitive adhesive. The rider stroke is adjusted so that it produces an annular ring with an inside diameter of 30 mm and an outside diameter of 175 mm. The normal force on the rider varies with the media, but many plastic webs are tested with a two-Newton force. If material has abrasivity similar to magnetic media, a test time of one hour is adequate to get a discernible and measurable flat on the spherical rider. If the material has low abrasivity, the test can require up to 40 hours to get a measurable flat on the rider. Wear

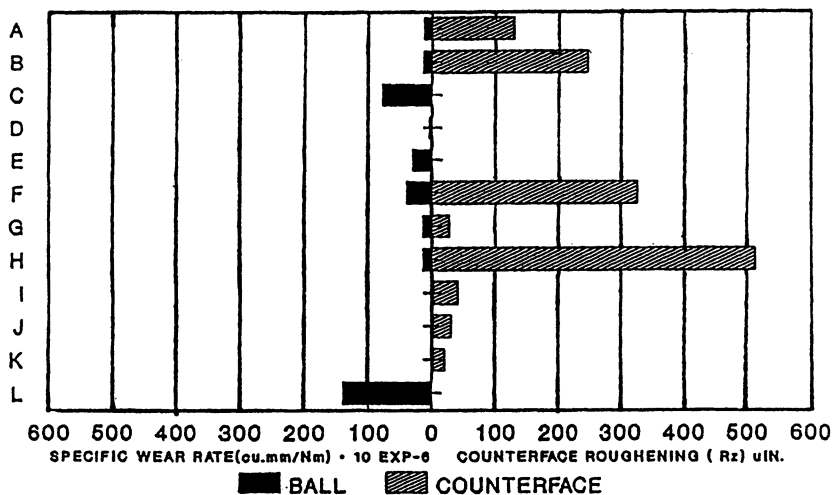


Figure 7. Reciprocating wear tests of a plastic ball on a flat plastic counterface. Wear on both members is recorded. Couple D was a PTFE/silicone-filled polycarbonate ball and an acetal/PTFE counterface. The worst couple (H) was the same rider as D with a polyphenylene sulfide counterface.

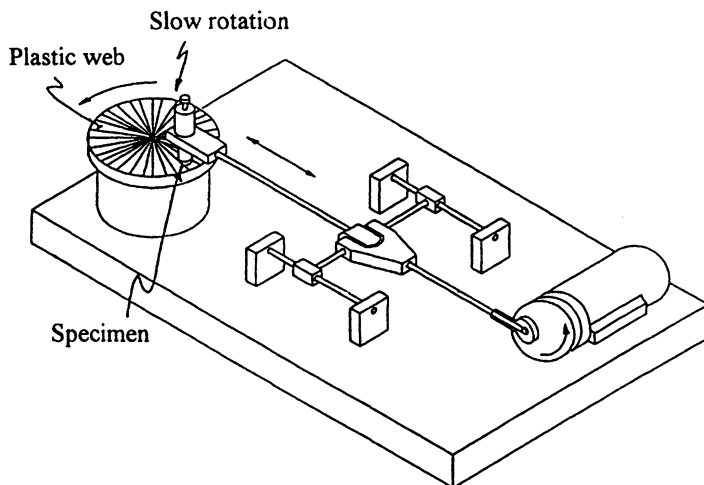


Figure 8. Schematic of the ball-on-plane test. (Reproduced with permission of Bud Labs).

measurement is often the hardest part of assessing materials of low abrasivity. Increasing the normal force or velocity to speed up the test may simply destroy the plastic test sample and create a tribosystem that does not simulate actual tribosystems.

The tape abrasion test will sometimes be more effective than the ball-on-plane test in measuring abrasivity depending on the tribosystem that is being simulated. It is also more suited to testing rider materials that are not easily made into spheres or hemispherical-ended pins. The rider is a small flat of material. The size is not important, only that it reside completely within the width of the web sample (Figure 9). Tests are often run with a continuous loop that is 35 mm wide with a length of 132 cm. The test samples in this case are 10 mm wide and they make line contact with a 2 N normal force. The sliding speed of the web is 0.26 m/s. Another advantage of this test is that it is easier to measure minute wear and surface damage on a polished flat than on a sphere. Profilometers can handle flats easier; curved surfaces usually require filtering out the curve to measure minute surface features. If the web has significant abrasivity, the wear volume can be easily determined by scar measurement. This test has been used for assessing the abrasivity of rubber webs, paper, many different plastics, even diamond-coated polyester. It provides a tool to simulate the wear of webs rubbing on a stationary surface. This is a situation that is common in many web conveyance systems and many products that use belts and webs for power transmission.

In summary, the ball-on-plane and the tape abrasion test are valuable tools for measuring the abrasivity of plastic or other flexible webs to mating surfaces. It better simulates web conveyance systems than the abrasivity tests that use abrasives that are not typical in tribosystems of interest.

Erosion Tests

Plastics are frequently used for applications requiring erosion resistance, but there does not seem to be much activity or interest in the tribology community of the 1990s. However, there are a number of tests that are applied and have been used to rate erosion resistance of plastics. Erosion, by definition, is progressive loss of material from a solid surface due to mechanical interaction between that surface and a fluid, a multicomponent fluid, or impinging liquid or solid particles (3). The field of erosion is usually separated into a number of forms of erosion: liquid erosion, either continuous stream or droplet, solid particle erosion, slurry erosion, and cavitation erosion. Each have separate laboratory tests.

The ASTM droplet erosion test involves putting specimens on the tip of a propeller that can achieve hypersonic tip velocities and the propeller is exposed to a rain field of controlled water droplets (Figure 10). Plastic materials are used for windshields and radomes on aircraft. Needless to say, it is necessary for the plastics used for these applications to have resistance to damage from high-velocity water droplets. In fact, many plastics are readily destroyed by mach 2 water droplets. Reinforced composites are often used for these types of

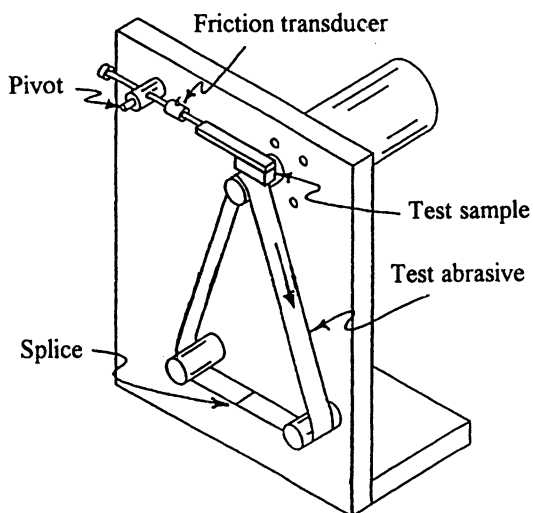


Figure 9. Schematic of the tape abrasion test. The tape can be a bonded abrasive or any web material of interest. (Reproduced with permission of Bud Labs).

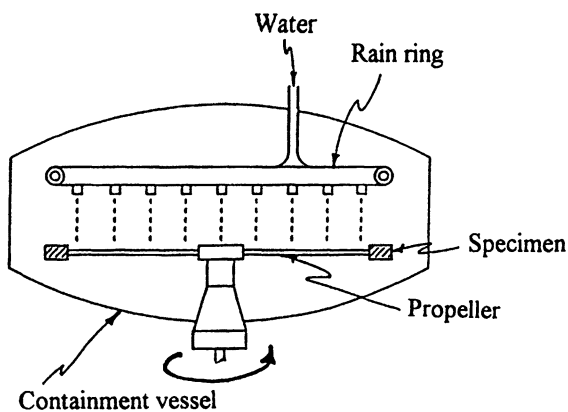


Figure 10. Schematic of the ASTM G 73 water droplet erosion test.

applications, but neat plastics are also candidates as are elastomers and polymeric coatings. The brittle thermosetting plastics are not as erosion-resistant as the more ductile thermoplastics such as polycarbonate and polyether sulfone (16).

Solid particle impact erosion resistance can be assessed with a test that is essentially performed by directing a small sand-blast nozzle (1 mm diameter) at a surface at a prescribed distance and angular relationship and blasting it with 50 μm alumina for a prescribed length time (17). Figure 11 shows some data on plastics from a similar tester. The plastics tested did not have erosion resistance equal to soft metals. In general, very few materials of any sort are resistant to this type of erosion. Cemented carbides are one of the few materials that seems to show long life in sand-blast types of applications. Elastomers are fair in resisting parallel flow erosion, but as a target material they do not perform as well.

Slurry erosion can be measured by the SAR (slurry abrasion response) test (19) that rubs a block of the material of interest against a rubber lap that is immersed in a standard slurry (Figure 12). The test metric is mass loss on the rider. This is a reciprocating test that was originally developed to rank ferrous materials for their resistance to erosion in pipelines carrying slurries. It also simulates sliding action in reciprocating pumps and the like. Another type of slurry test is the slurry pot in which test samples are exposed to a parallel flow of a slurry with no rider on the test surface just the slurry contacts the surface (20). As shown in Figure 13, one plastic, ultrahigh molecular weight polyethylene was quite resistant to this particular slurry.

There are cavitation erosion tests (21,22) that can be used to assess the resistance of plastics to this form of wear, but there are few laboratories performing these tests and fewer use plastics as test specimens. The original ASTM cavitation erosion test required affixing the test specimen on the end of an ultrasonic horn. This would not work well on plastics. The second generation test used a stationary specimen placed near the tip of a vibrating ultrasonic horn. This test could be used on plastics. The latest test uses a high- pressure water jet to create a cavitation field.

In summary, there are erosion tests that are applicable to plastics, but there is not a large amount of research activity in this area. Most materials engineers are of the opinion that plastics are very resistant to erosion/corrosion processes. This is the case when the fluids are a low velocity or impinge with low energy, but when plastics are used for applications like jet airplane windows some of the tests described may be needed to make sure that they do not fail by erosion.

Summary

The purpose of this paper was to describe some of the tests that are used to assess the wear characteristics of plastics. How easy do they wear in different situations and how much damage will they produce when they are rubbed on other surfaces? We have listed about 20 tests that cover the range of wear modes that may be encountered. In closing, it should be emphasized that the correct test to use is the one that best simulates the tribosystem of interest. Table 2 compares the tests

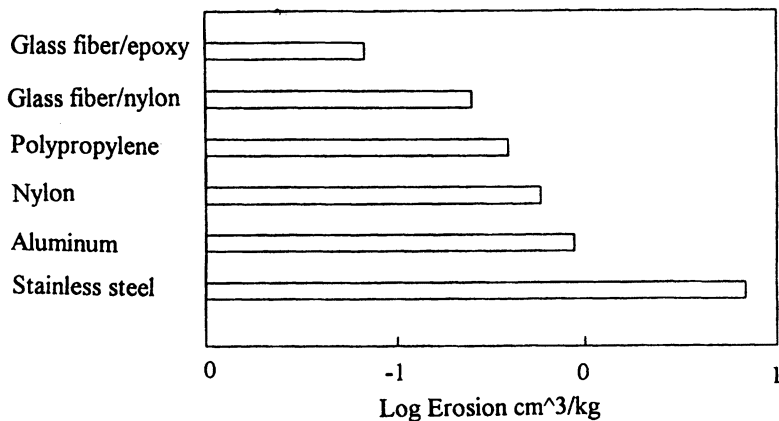


Figure 11. Solid particle erosion rate of several plastics compared to metals (100 m/s, 125-150 μm quarts abrasive, 90 degree impact angle). (Adapted with permission from reference 18. Copyright 1988 American Society for Testing and Materials.)

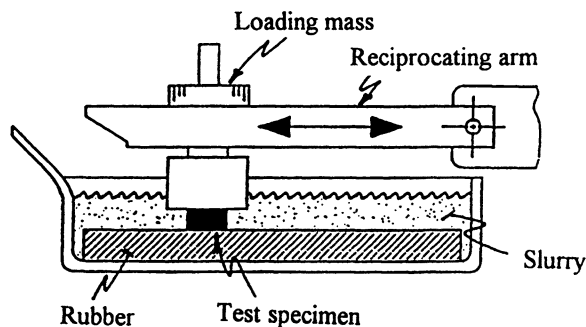


Figure 12. Schematic of the ASTM G 75 slurry erosion tester to measure Miller Number.

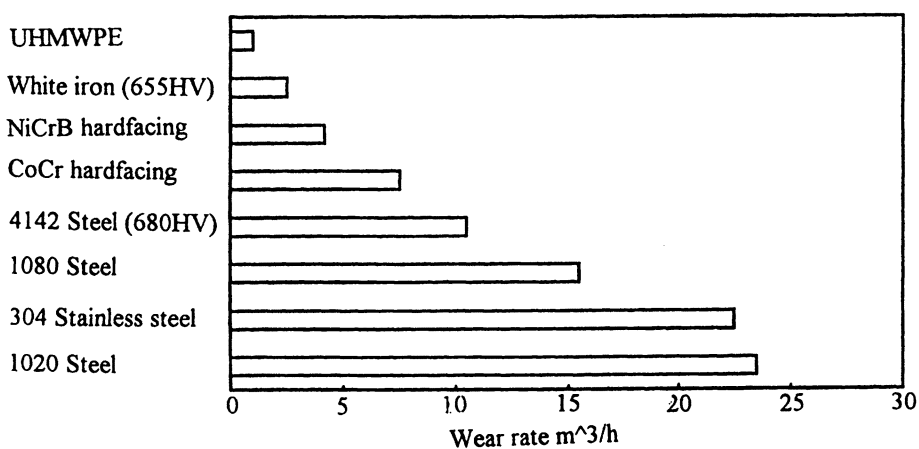


Figure 13. Slurry erosion resistance of ultrahigh molecular weight polyethylene (UHMWPE) compared with various metals (two weight percent silica sand in tap water, 16 m/s, 16C)
(Adapted with permission from reference 20. Copyright 1987 American Society for Testing and Materials.)

Table 2. Plastic wear tests for various applications.

Objective	Test Description	Application Comments
PV	Pin-on-disk	For laboratory screening. Many tests required.
Wear Factor	Block-on-ring	For Laboratory Screening. Test time may be 20h/sample.
Resistance to Abrasion		
ASTM D 1044	Taber abrasion - abrasive wheel vs. Flat plastic	Simulates foot traffic on floors
ASTM D 1242a	Loose abrasive between plastic and plate	Simulated 3 - body abrasion
ASTM D 1242 b	Abrasive tape vs. flat plastic	Simulate fine grinding
ASTM G 65	Loose abrasive between flat plastic and rubber wheel	Simulates 3 - body abrasion
ASTM G 141	Plastic pin riding on sandpaper covered drum	Simulates fine grinding
Plastic Abrasivity		
Tape abrasion	Plastic web rubs in line contact with metal	Measures ability of web to wear contacting surfaces
Ball-on-plane	Metal rider reciprocating on flat plastic	Measures abrasivity of plastic web
Plastic-to-conforming surface		
ASTM D 3702	Plastic disk rotating on fixed metal sample	May take long test time
ASTM G 99	Plastic ball on a rotating disk	Contact geometry does not simulate most tribosystems
ASTM G 133	Plastic or metal ball reciprocating on flat counterface	Simulates reciprocating tribosystems
Bushing	Plastic bushing riding on test shaft	Simulates bushings but test time may be long
ASTM G 137	Plastic block on a rotating cylinder	Simulates bushing / shaft tribosystems
Erosion		
ASTM G 75	Plastic rider vs. rubber in slurry	Simulates handling slurries
ASTM G 105	Plastic flat vs. rubber wheel in slurry	Simulates handling slurries
ASTM G 73	Plastic flat vs. high velocity water droplets	Simulates rain erosion in aircraft
ASTM G 76	Blast of abrasive particles on plastic flat	Simulates particles striking a plastic at high velocity

described. PV tests are valuable in characterizing new materials, but they involve many iterations. They can be costly in lab labor and elapsed time. Wear factor can be obtained quickly in a block-on-ring test if testing conditions are limited to a particular application (one set of test parameters). The dry sand rubber wheel test is fast and definitive for assessing three-body abrasion resistance, but the test severity (load and test time) must be reduced from those stated in the ASTM standard. The tape abrasion test is suitable for assessing two-body abrasion resistance.

The abrasivity of plastics to other materials is easy to measure on the ball-on-plane test if suitable samples are available. It requires a relatively large test plaque and a hemispherical or spherical rider. Wear of plastics rubbing on metals or other materials in a bearing mode can be assessed on any of the tests listed, but it is important to select a test that has the same type of motion and geometry as the application of interest. This statement also applies to the erosion tests. The laboratory test must produce damage that looks like the damage obtained in the real-life application. If a wear test is needed for a new part, ask the question: how might this part wear? Use tests on candidate plastics that simulate your assumed mechanism of wear. Plastics, in general, play a key role in the design of most new products; they need to be selected with wear in service as a consideration. The tests that we have described can be used to screen candidates to make them last for their intended service life.

Literature Cited

1. Bayer, R. "Introduction", in *STP 701 Wear Tests for Plastics: Selection and Use*, ASTM, West Conshohocken, PA, 1983, p 1.
2. Budinski, K. G., Grove. T. H., "Predicting Polymer Serviceability for Wear Applications", in *STP 701 Wear Tests for Plastics: Selection and Use*, ASTM, West Conshohocken, PA, 1983, p 59-75.
3. ASTM G 40, *Standard Terminology Relating to Wear and Erosion*, ASTM, West Conshohocken, PA, 1995.
4. *Polymer Materials for Bearing Surfaces*, Warrington, UK: National Centre of Tribology, 1983, p 16.
5. Budinski, K. G., "Resistance to Particle Abrasion of Selected Plastics," *WEAR*, 203-204 (1997) pp 302-9.
6. ASTM D 1044, *Standard Test for Abrasion Resistance of Transparent Plastics by Optical Clarity*, ASTM, West Conshohocken, PA, 1992.
7. ASTM G 65, Test Method for Measuring Abrasion Using the Dry Sand /Rubber Wheel Test, ASTM, West Conshohocken, PA, 1994.
8. ASTM G 105, *Conducting Wet Sand/Rubber Wheel Abrasion Tests*, ASTM, West Conshohocken, PA, 1996.
9. ASTM D 1242, *Standard Test Method for Resistance of Plastic Materials to Abrasion*, ASTM, West Conshohocken, PA, 1992.

10. ASTM D 3702, *Test Method for Wear Rate of Materials in Unlubricated Rubbing Contact Using a Thrust Washer Testing Machine*, ASTM, West Conshohocken, PA, 1993
11. ASTM G 77, *Test Method for Ranking Resistance of Materials to Sliding Wear Using Block-on-Ring Test*, ASTM, West Conshohocken, PA, 1994
12. ASTM G 137, *Test Method for Ranking Resistance of Plastic Materials to Sliding Wear Using a Block-on-Ring Configuration*, ASTM, West Conshohocken, PA, 1995
13. ASTM G 99, *Test Method for Wear Testing with a Pin-on-Disk Apparatus*, ASTM, West Conshohocken, PA, 1993.
14. Budinski, K. G., "Abrasion Resistance of Transport Roll Surfaces," *WEAR* 181-183 (1995) pp 938-43.
15. ASTM G 73, *Practice for Liquid Impingement Erosion Testing*, ASTM, West Conshohocken, PA, 1993.
16. Gorham A. H. et al., "Damage Mechanisms in Polymers and Composites Under High Velocity Liquid Impact," in *Erosion: Prevention and Useful Applications*, W. F. Adler Ed., STP 664, ASTM, West Conshohocken, PA, 1979, pp 320-44.
17. ASTM G 76, *Test Method for Conducting Erosion Tests by Solid Particle Impingement Using Gas Jets*, ASTM, West Conshohocken, PA, 1995.
18. Raash, E., *Erosive Wear in Coal Utilization*, : Hemisphere Publishing, New York, 1988, p 133.
19. ASTM G 75, *Test Method for Determination of Slurry Abrasivity (Miller Number) and Slurry Abrasion Response of Materials (SAR) Number*, ASTM, West Conshohocken, PA, 1995.
20. Madsen, B. W., Blickensderfer, R., "A New Flow-Through Slurry Erosion Wear Test," *Slurry Erosion: Uses, Applications and Test Methods*, ASTM STP 946, J. E. Miller and F.E. Schmidt Jr, Eds., ASTM, West Conshohocken, PA, 1987, pp 169-84.
21. ASTM G 32, *Test Method for Cavitation Erosion Using Vibratory Apparatus*, ASTM, West Conshohocken, PA, 1992.
22. ASTM G 134, *Test Method for Erosion of Solid Materials by a Cavitating Liquid Jet*, ASTM, West Conshohocken, PA, 1995.

Chapter 25

Nanotribology of Polymer Surfaces for Disk Drive Applications

C. Mathew Mate and Junhua Wu

IBM Research Division, Almaden Research Center, San Jose, CA 95120

In this paper, we discuss the importance the polymer layers to the protection of disk surfaces inside of disk drives by first providing a set of criteria that can be used for developing a disk lubricant system or other polymer protective overlayers. Next, we discuss how contact angle measurements can be used to provide insights into how the polymer lubricants behave on disk surfaces. Finally, we discuss a new type polymer layer that we have developed to supplement traditional disk overcoats. This polymer overlayer is formed by vapor depositing a cyanate ester monomer then polymerizing the film with UV irradiation.

In disk drives, as illustrated in Figure 1, bits of information are written and read from magnetic domains in magnetic layers on disk surfaces using recording heads attached to the back of sliders. When a disk is spinning at normal operating speeds, a thin air bearing film, 30–50 nm in thickness, keeps the slider from physically contacting the disk surface. When the drive is powered on and off, however, the sliders in most of today's disk drives must take off and land on the disks, generating many slider–disk contacts. This is most severe for disk drives in laptop computers, which are frequently powered off to extend the battery life of the computer. The magnetic layer and the information stored in it are protected during these slider–disk contacts by several protective layers: an overcoat, usually consisting of amorphous carbon, and a thin film of polymer lubricant.

To achieve higher recording densities in future disk drives, the spacing between the magnetic layer on the disk and the recording head will need to be considerably reduced in order to decrease the size of the magnetic domains in the disk magnetic layer. This spacing reduction will lead to severe reductions both in the thickness of the air bearing film, resulting in more frequent slider-disk contacts, and in the spacing available for the layers of protective materials. Consequently,

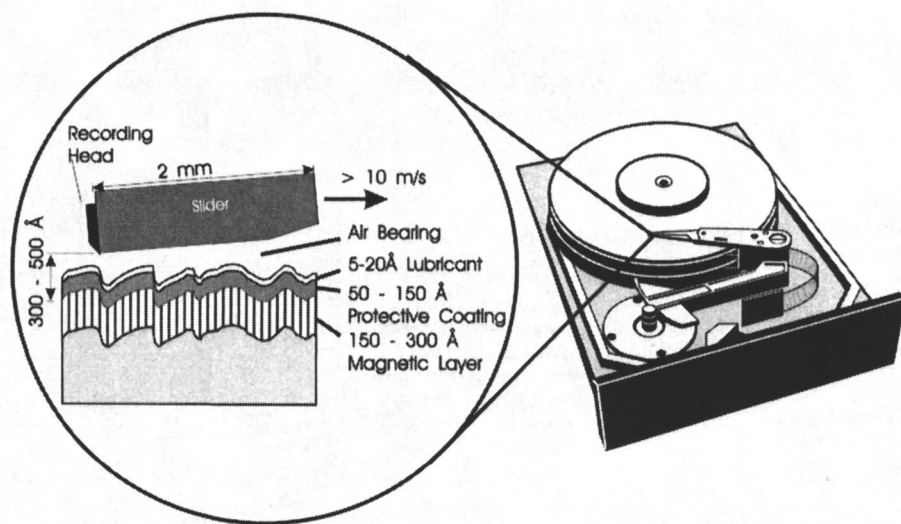


Figure 1. Schematic of the inside of a disk drive. Enlarged section shows the details of a typical slider-disk interface in current disk drives.

these protective materials such as the overcoat and lubricant will have to provide more wear and corrosion protection with less material.

Nanotribology. Nanotribology is the study of how friction, lubrication, and wear occur at the nanometer and sub-nanometer scale, i.e., at the atomic and molecular level. Since the lubricant films currently in disk drives are only about 1 nm in thickness and, within a few years, the carbon overcoats will only be a few nanometers in thickness, improved understanding of how these materials work at the atomic and molecular level to provide tribological protection is critically needed to develop dramatically more effective materials.

In this paper, we discuss three different topics on the application of polymers for improving the nanotribology of the disks used in disk drives. First, we discuss some of the criteria for a good lubricant system, which provides a general overview of what is desired for protective polymers on disk surfaces. Next, we discuss the how contact angle measurements can be used to gain insights into how lubricating disk surfaces with perfluoropolyether polymers can help satisfy these criteria and how these polymers interact with a disk surface and with certain types of contaminants found in disk drives. Finally, we present a novel type of polymer overlayer that we have developed that resides between the carbon overcoat and the lubricant film to help smooth out the final disk surface. This polymer overlayer is formed by vapor depositing a cyanate ester monomer onto disk surfaces then polymerizing the layer with UV irradiation.

Criteria For Good Polymer Layers on Disk Surfaces

A number of criteria are used within the disk drive industry for selecting a polymer lubricant material (*I*). Since these criteria are often contradictory, the principal challenge is finding a lubricant system that provides the best compromise for the particular slider-disk interface under development. Other polymers developed as a protective material, either as overcoat or overlayer as discussed below, should also satisfy these criteria. A good lubricant system or protective polymer layer should provide:

1. *Good boundary lubrication.*
 - Provides adequate wear protection so that the slider-disk interface lasts the expected life of the disk drive product.
 - Ensures against the hazards of flying in close proximity for long periods of time.
2. *Mobility of polymer lubricant.*
 - Improves long term durability (i.e., polymer molecules should have enough mobility to move across the disk surface to replenish lubricant loss during slider-disk contacts).
3. *Good adhesion of polymer lubricant or polymer protective layer to the disk surface.*
 - Provides long term durability by preventing polymer molecules from being displaced during slider-disk contacts.

- Reduces lubricant loss due to spin-off by reducing mobility.
- 4. *Low volatility.*
 - Reduces loss of polymer molecules due to evaporation.
 - 5. *Low surface energy of the final lubricated disk surface.*
 - Lowers adhesive and friction forces.
 - Minimizes the amount of contamination adsorbing onto disk surfaces.
 - 6. *Thermal and chemical stability.*
 - Stable towards catalytic decomposition.
 - Stable towards formation of frictional polymers.
 - Compatible with other disk drive components.
 - 7. *Corrosion resistance.*
 - Water, oxygen, and other contaminants should not be able to penetrate the overcoat and protective layers and to corrode the underlying magnetic layer.

Perfluoropolyethers. Historically, perfluoropolyether polymers have been preferred as disk lubricants since they are liquid at disk drive operating temperatures with low surface tensions and low volatility, as well as being chemically inert and stable at high temperatures, satisfying many of the criteria enumerated above (2). In particular, the oxygen ether linkages in the perfluoropolyether polymer provide the polymer backbone with sufficient flexibility for the material to be liquid over a wide temperature range. Often the perfluoropolyether polymer backbones are terminated by functional end groups designed to attach the lubricant molecules to the overcoat surface, so as to prevent them from being displaced from the surface during slider-disk contacts. In order to meet the increasing severe tribological demands placed on the disk protective layers, new type polymer materials beyond the traditional perfluoropolyether lubricants will most like have to be developed for the disk drive applications and new ways of bonding or adhering the polymers to the disk surface will have to be utilized.

Contact Angle Measurements

One of the above criteria is that the finished disk surface should have a low surface energy. This is beneficial because sliding surfaces with low surface energies tend to have low friction and adhesion forces acting between them. Also, low surface energies help to minimize the adsorption of contaminants that are always present in disk drives, which can lead to a wide variety of tribological failures of the slider-disk interface. The low surface tensions of perfluoropolyether lubricants can help lower disk surface energies. From the Young equation or the Girifalco-Good-Fowkes-Young equation, high contact angles imply low surface energies; so contact angle studies can provide insights of the surface energies of lubricated disks. In addition, contact angle measurements can provide information into how the lubricant polymers interact with disk surfaces and how easily they are displaced by certain types of contaminants.

Contact angle measurements are frequently used in the magnetic storage industry to gain insights into the chemical nature of surfaces inside disk drives (3-7). One can use this technique to monitor manufacturing processes for finishing the

surface of components, that is, if the contact angle on a test sample is out of specification, then the manufacturing process is adjusted until the component surface has the desired contact angle. The question naturally arises as to what is a desirable contact angle for these surfaces and what surface properties influence the contact angle. Obviously, a better understanding of the physical and chemical factors that influence contact angles would be of great value to the storage industry, as well as other industries that make use of this common technique.

Contact Angle Results. We have recently investigated the contact angle of various liquids on disks similar to those found in disk drives (β). Figure 2 shows the cosine of the contact angle of alkane droplets on a disk with an amorphous hydrogenated carbon overcoat (CHx) lubricated with different thicknesses of the perfluoropolyether [Z-Dol-4700: HOCH₂CF₂(OCF₂CF₂)_m(OCF₂)_nOCF₂CH₂OH with a molecular weight of 4700 amu]. Contact angle measurements were performed by releasing a small liquid droplet onto the freshly lubricated surfaces and measuring the advancing contact angle when the speed of the contact line is near zero. The Young-Dupré equation

$$\Delta W = \gamma_l(1 + \cos \theta) \quad (1)$$

relates the cosine of the contact angle θ to the work of adhesion ΔW between the alkane and the disk surface.

The work of adhesion for alkanes on these lubricated surfaces can be separated into a term that describes the direct interaction with the lubricant material and a term that describes how the interaction with the substrate is mediated by the intervening lubricant layer:

$$\Delta W = a'_0 + b'_0 e^{-LL_a} \quad (2)$$

which can also be written as

$$\frac{\Delta W}{\gamma_l} - 1 = \cos \theta = a_0 + b_0 e^{-LL_a} \quad (3)$$

where L is the lubricant layer thickness and L_a the screening distance of the substrate interaction through the lubricant layer. The solid lines in Figure 2 show that the fit of this model to the data is very good. The screening distances L_a are very short (5–7Å) and comparable to the 6 Å chain diameter of the Fomblin Z-Dol-4700 polymer. So, within a few layers of lubricant molecules, the alkanes are effectively interacting with a bulk-like lubricant film. The screening distances L_a may also be a measure of how well the lubricants cover the surface in presence of the alkane liquid with the short screening length indicating good coverage and little displacement of the lubricant molecules from the surface of the disk by the alkane liquids.

Water contact angle measurements reveal to what degree the lubricated surfaces are hydrophobic or hydrophilic. Figure 3 shows how the cosine of the water contact angle changes with increasing Z-Dol lubricant thickness on different types of

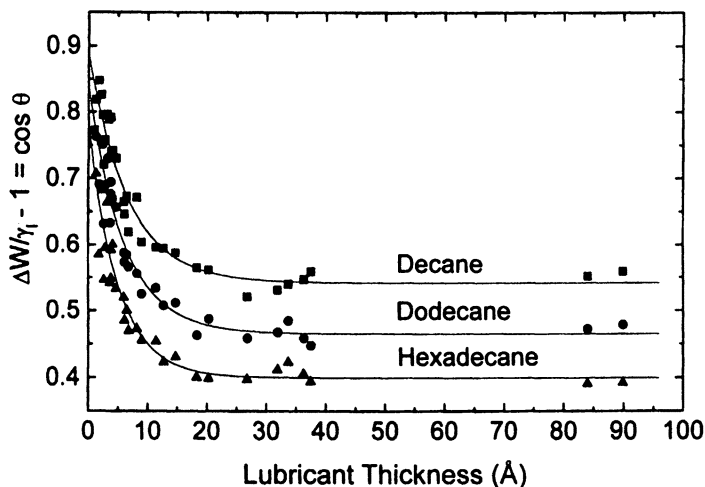


Figure 2. Cosine of the contact angle that alkane droplets on CHx overcoated disks vs. the lubricant thickness. The solid lines show the fit of the data to $\Delta W/\gamma_l - 1 = \cos \theta = a_0 + b_0 e^{-LL/a}$. (Reproduced from reference 8.

Copyright 1998 American Chemical Society.)

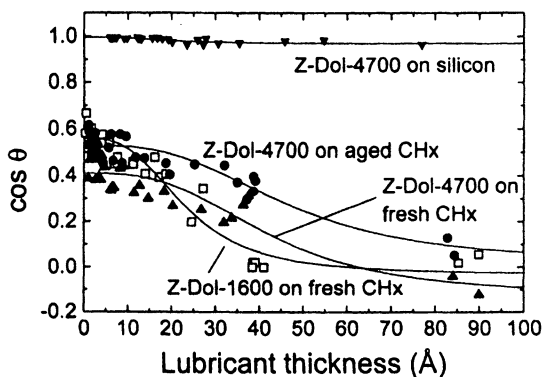


Figure 3. Cosine of water contact angle vs. lubricant thickness. The solid lines show the fit of the data to the empirical equation: $\cos \theta_{water} = a_w + \frac{b_w}{(LL_w)^3 + 1}$. (Reproduced from reference 8. Copyright 1998 American Chemical Society.)

surfaces. Lubricant thickness for all type of surfaces were measured by ellipsometry, which was calibrated using X-Ray Reflectivity (9). For all surfaces, we observed that the cosine monotonically decreases, indicating that all the surfaces become more hydrophobic with increasing lubricant thickness.

The lines in Figure 3 show fits to the experimental data using the following empirical expression:

$$\cos \theta_{\text{water}} = a_w + \frac{b_w}{(L/L_w)^2+1} \quad (4)$$

which mainly serves as guides to the eye as scatter in the data prevents confident fits. From Figure 3 it is apparent that, for very thick films, the cosine of the water contact angle is quite different for each substrate, even for the same lubricant. This indicates that water still interacts, to varying degrees, with the underlying solid surface even in presence of a thick lubricant film. For example, the water contact angle on silicon wafers only increases slightly with the addition of the Z-Dol-4700 lubricant. A possible explanation for this effect could be that water much more easily displaces the Z-Dol molecules from the very hydrophilic SiO_x surface in comparison the carbon overcoats. This phenomena should be contrasted with that for alkanes droplets on very thick lubricant films where the contact angle is independent of the type of substrate. The screening length for water, represented by L_w in the empirical expression, ranges from 20–47 Å, which is considerably longer than the screen length L_a (5–7 Å) observed for alkanes and may be further evidence that water more easily displaces the lubricant.

The importance of these contact angle results to the disk drive industry can be summarized as follows: Since disks in disk drives are typically lubricated with 5–20 Å of perfluoropolyether lubricant, their surfaces should be reasonably well screened against the adsorption of alkanes and other hydrocarbons, particularly at the upper range of this thickness range, but only slightly screened against the adsorption of water, which may lead to problems for drives operating in high humidity environments. While perfluoropolyether lubricants lower the surface energies of disks, the thickness needed to reach lowest surface energy depends strongly on the type of substrate, lubricant, and the test liquid used for the contact angle measurement.

Polycyanate Ester Overlayer for Disks

In addition to the liquid polymers used as lubricant, solid polymer films have been frequently investigated as overcoats and overlayers on disk surfaces. For example, bonding and crosslinking of perfluoropolyether lubricants to disk surfaces using ultraviolet irradiation has been reported by several groups (10–11). Solid fluorocarbon films have also been made on disk surfaces using sputtering, plasma, and ion beam deposition methods (12–14). Most of these past efforts have focused on developing solid lubricant films. Here, we report how a solid polymer film can be used to help smooth out or planarize the disk surface. The polymer film that we

have developed consists of polycyanate esters that reside between the carbon overcoat and lubricant film.

Cyanate esters are a well developed group of high temperature, thermosetting polymers (15). Polycyanate ester polymers are known as coating materials, primarily as matrix resins for composites (e.g., boards, cards, etc.) or for dielectric coatings for semiconductor devices. These coatings are typically several microns to millimeters thick and are polymerized by thermal curing of a cyanate ester monomer, which has been coated by spinning onto the device substrates or by dip-coating onto fibers. For these coatings, some of the favorable properties obtained by using polycyanate esters are low dielectric loss, high temperature stability, excellent adhesion capacity, and good mechanical properties.

Preparation. In this communication, we focus on preparing ultra-thin polymer overlayers on disks starting with the cyanate ester monomer, 2,2'-bis(4-cyanatophenyl)isopropylidene (BCPP), supplied by Ciba Specialty Chemicals. Figure 4 shows the chemical structure of the BCPP monomer and the ring forming cyclotrimerization reaction that occurs when these monomers are heated in the presence of a suitable catalyst.

Our method for forming the polycyanate ester overlayer on disk surfaces is illustrated in Figure 5. This method consists of two steps:

Deposition. (Figure 5a) A source containing the monomer is heated to 110°C. At this temperature, BCPP sublimates at a sufficient rate through air to be vapor deposited onto an unlubricated disk placed a few centimeters above the heated source, as illustrated in Figure 5a. The disk is kept at room temperature during vapor deposition, and the BCPP is uniformly deposited at the rate of a few Å per minute. For the overlayers, we typically deposited 5-15 Å of monomer as measured by ellipsometry. For thicknesses greater than 15 Å, we usually observed dewetting of the final polymer film.

Polymerization. (Figure 5b) We found that heating the ultra-thin cyanate monomer films vapor deposited onto disks caused evaporation rather than polymerization. Consequently, we had to use a different method, UV initiated polymerization, to convert the soft monomer film into a robust polymer film. For the UV curing, the monomer films were placed under a UV lamp (185-254 nm, intensity ~ 5 milliwatts/cm²), while oxygen and other reactive gases were excluded from the chamber by flushing with the inert gas, nitrogen. A few minutes of UV irradiation was sufficient to convert a 1 nm thick film of monomer completely into polymer.

Polymerization was checked several ways:

Solubility. Solvents that could easily remove the BCPP monomer, like methyl-ethyl-ketone (MEK), were unable to dissolve the UV cured product.

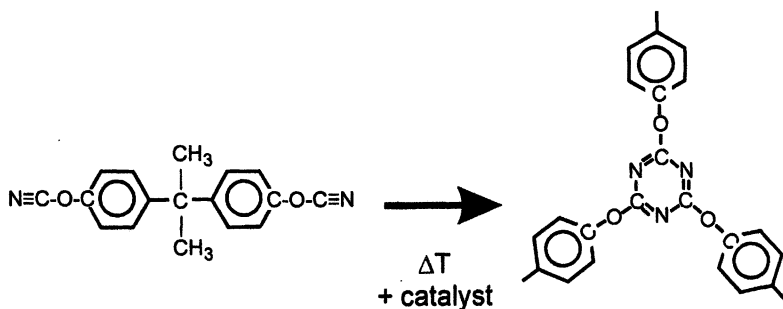


Figure 4. The chemical structure of the BCPP monomer and how the cyanate end groups react in the bulk with heating to form a cross-linked ring network.

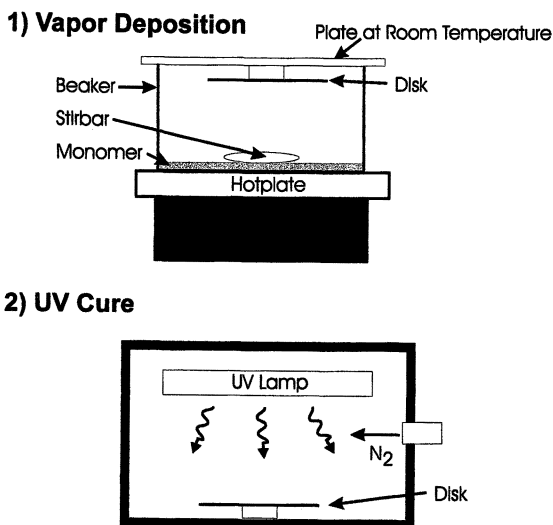


Figure 5. Schematic of the preparation technique for forming the polycyanate ester overlay on disk surfaces.

Heating. The UV cured films were stable upon heating to 220°C for 10 minutes, while the monomer films quickly evaporated at this temperature.

FTIR. Figure 6 compares the spectra of the monomer and the UV cured polymer obtained from grazing angle Fourier Transform Infrared (FTIR) spectroscopy. For the monomer spectrum, the vibrational doublet centered around 2250 cm^{-1} characterizes the $\text{C}\equiv\text{N}$ cyanate groups in the monomer, and the disappearance of these peaks in the cured spectrum is consistent with the cyanate groups reacting to form crosslinked networks. Also, new broad peaks emerge in the range 900-1800 cm^{-1} in the UV cured spectrum characteristic of polymer formation.

Results and Discussion. The UV polymerization process demonstrated here has several advantages over other methods for forming polymer films such as plasma and chemical vapor deposition or curing with heat and electron beams. Photo-polymerization using ultraviolet light is a clean, efficient, and compact process. Further, the polymerization reaction can be instantly started and stop and potentially reach 100% polymerization in a short period of time. The process is also environmentally friendly in that it does not require the use any solvents or noxious gases.

Polymerization Mechanism. The polymerization reaction that occurs by heating the BCPP monomer is thought to involve the reaction of the $\text{C}\equiv\text{N}$ end groups to form *s*-triazine rings as shown in Figure 4. However, the spectrum in Figure 6 for a UV cured polymer does not exhibit the expected vibrational peaks for the *s*-triazine ring indicating that, when UV irradiation is used to initiate polymerization, the reaction may follow a different mechanism such as cyclodimerization and ring expansion. Further work is needed to elucidate the polymerization mechanism that occurs during UV irradiation.

Topography. Atomic force microscopy (AFM) was used to measure how the topography of silicon wafers and disk surfaces change with the addition of the polycyanate ester overlayer. Figure 7 shows an AFM image of a bare silicon wafer and of a 10 Å film of the polycyanate ester overlayer. Even though the image of the polycyanate ester overlayer has a finer texture than the silicon wafer, the rms roughness remains unchanged, 1.3 Å for the overlayer vs. 1.1 Å for the silicon wafer, demonstrating that the polycyanate overlayer does not increase the surface roughness so long as the film thickness is kept below 15 Å. (For films thicker than 15 Å, dewetting of the polymer film is often observed.) When the polycyanate ester film is formed on disk surfaces, which are much rougher than the silicon wafers, the AFM images show that the polymer fills in the deep valleys and pinhole defects on the surface, demonstrating the ability of the polycyanate ester overlayer to planarize surfaces. For example, the root-mean-square roughness for one type of disk surface studied was found to decrease from 16 Å to 8 Å over a $1\mu\text{m} \times 1\mu\text{m}$ area with the addition a 10 Å thick polycyanate ester overlayer.

As discussed earlier, the goal of developing new polymer lubricants and overlayers is to satisfy the numerous demands placed on these very thin films while

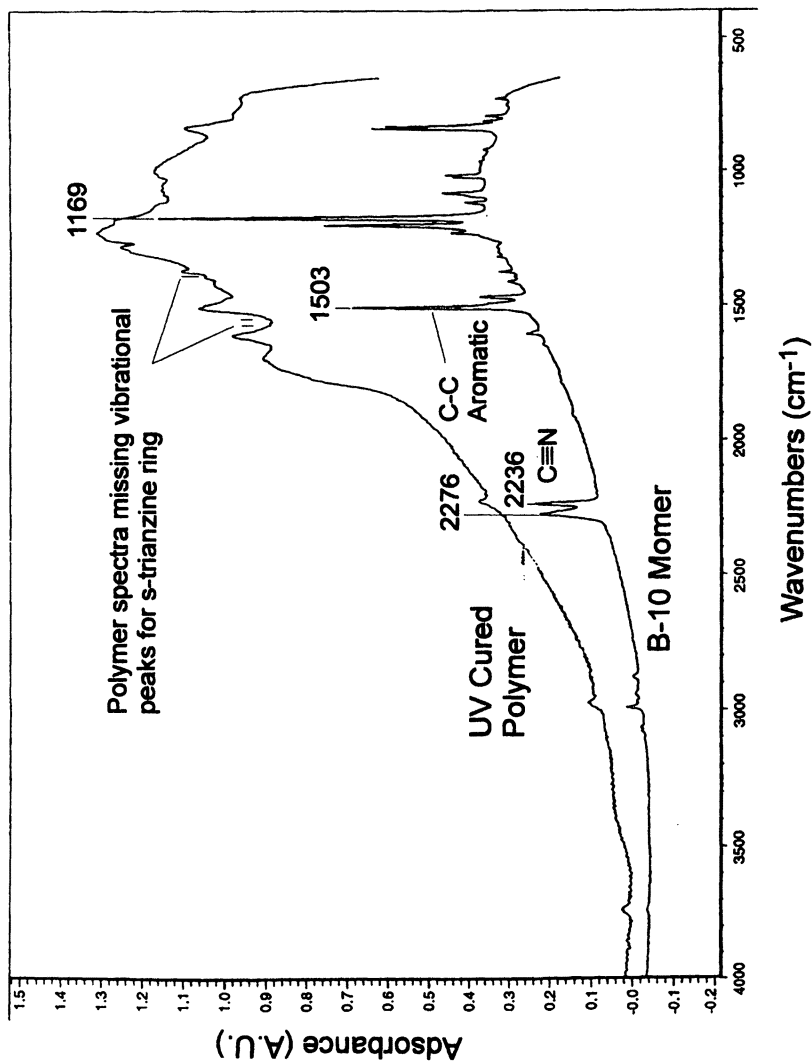


Figure 6. Vibrational spectra collected using FTIR of a thick monomer film before and after polymerization with UV irradiation.

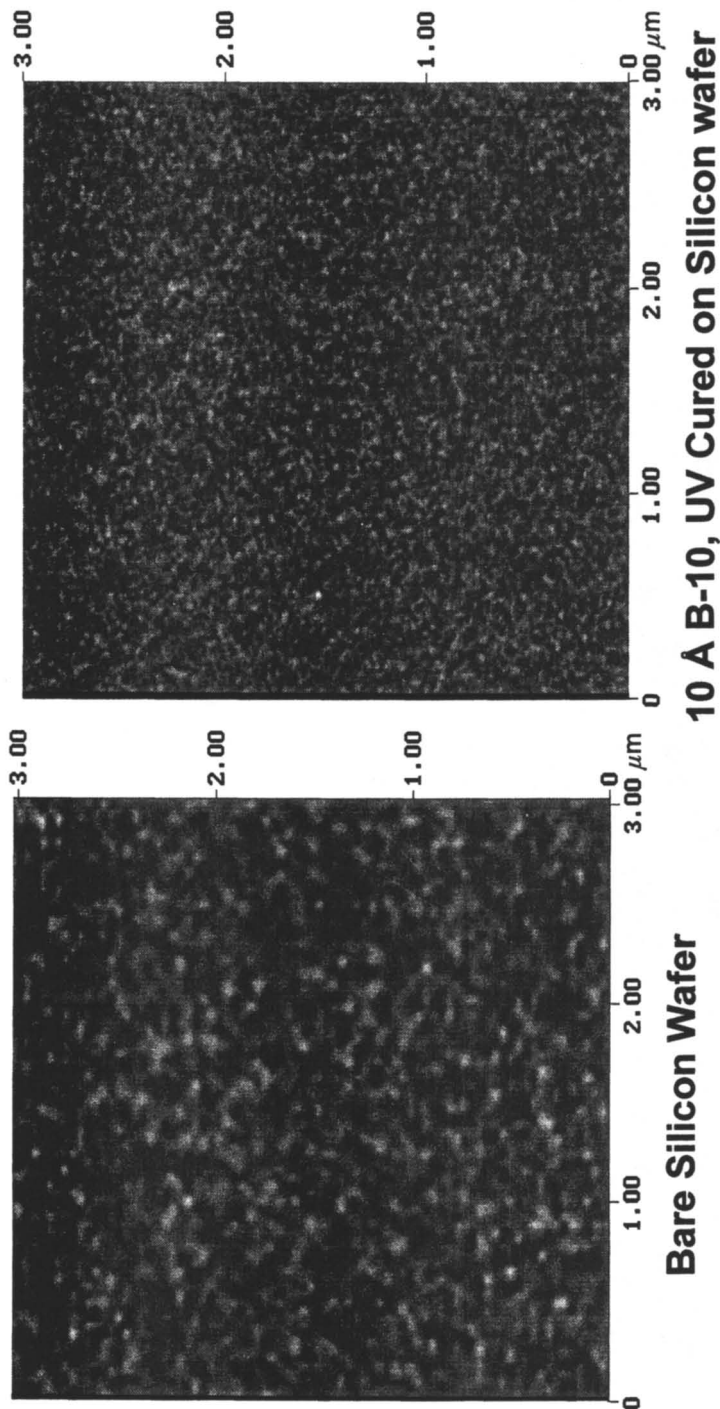


Figure 7. Tapping mode AFM image of a bare Si(100) wafer with 15 Å of native SiO_x and a wafer covered with 10 Å of B-10 monomer then cured with UV irradiation.

maintaining good magnetic recording performance. To handle the static friction forces occurring at the slider-disk interface when the drives are powered up, most current disk drive products have either a dedicated, roughened landing zone or use a load-unload mechanism. In the data zone, the magnetic layer is also formed on a slightly roughened or textured substrate to achieve the best magnetic recording characteristics. However, for the best durability and corrosion protection, the smoothest surface is desired for the data zone. Since sputter-deposited carbon overcoats tend to conform to the surface of the rough magnetic layer, the addition of a polycyanate ester overlayer, to provide a smoother final disk surface, has the potential to improve the tribology of the disk without compromising the magnetic performance, which will be explored further in future work.

Acknowledgments

We would like to thank J. Lyerla and G. Tyndall for valuable discussions. We would also like to thank J. Hedrick for suggesting using the BCPP cyanate ester for the polymer overlayer and for valuable discussions and advice during this project.

Literature Cited

1. Mate, C. M. *Tribology Letters* **1998**, *4*, pp 119-123.
2. Homola, A. M. *IEEE Trans. Magn.* **1996**, *32*, pp 1812.
3. Bhushan, B. "Tribology and Mechanics of Magnetic Storage Devices", 2nd ed.; Springer, New York, 1996.
4. Lee, J. K.; Smallen, M.; Enguero, J.; Lee, H. J.; Chao, A. *IEEE Trans. Magn.* **1993**, *29*, pp 276.
5. Ruhe, J.; Blackman, G.; Novotny, V. J.; Clarke, T.; Street, G. B.; Kaun, S. *J. Appl. Polym. Sci.* **1994**, *53*, pp 825.
6. Perry, S. S.; Mate, C. M.; White, R. L.; Somorjai, G. A. *IEEE Trans. Magn.* **1996**, *32*, pp 115.
7. Tyndall, G. W.; Leezenberg, P. B.; Waltman, R. J.; Castenada, J. *Tribology Letters* **1998**, *4*, pp 103.
8. Wu, J.; Mate, C. M. *Langmuir*, **1998**, *14*, pp 4929-4934.
9. Toney, M. F.; Mate, C. M.; Pocker, D. J. *IEEE Trans. Magn.* **1998**, *34*, pp 1774-1776.
10. Homola, A.M.; Lin, L.J.; Saperstein, U.S. Patent No. 4,960,609.
11. Lee, H.J.; Zubeck, R.; Hollars; Lee, J.K.; Chao, A.; Smallen, M. *J. Vac. Sci. Tech. A* **1993**, *11*, pp 711-714.
12. Harada, K; *J. Appl. Polym. Sci.* **1981**, *26*, pp 3707-3718.
13. Koishi, R.; Yamamoto, T.; Shinohara, M. *Tribol. Trans.* **1993**, *36*, pp 49-54.
14. Karis, T. E.; Tyndall, G. W.; Crowder, M. S. *IEEE Trans. Magn.* **1998**, *34*, pp 1747-1749.
15. Fang, T.; Shimp, D. A. *Prog. Polym. Sci.* **1995**, *20*, pp 61-118.

Chapter 26

The Effect of Surface Texture on the Friction of Automotive Interior Plastics

Norman S. Eiss Jr.¹ and Edward Lee²

¹ Emeritus Professor, Virginia Polytechnic Institute and State University, Blacksburg, VA 24061

² Cryovac Division of Sealed Air Corporation, Duncan, SC 29334

Surfaces with a high density of small radii peaks can reduce the occurrence of stick-slip sliding on plastics such as acrylonitrile-butadiene-styrene. Unfilled polypropylene does not stick slip regardless of the surface texture. The addition of glass fibers to polypropylene causes stick slip to occur. It is proposed that the interfacial strengthening that occurs for many polymers during static contact is relieved by microdisplacements during tangential loading of the interface. The microdisplacements are more likely to occur on surfaces with high density of small radii peaks. The reduction of interfacial strength by microdisplacements reduced the drop in friction when sliding commenced and the occurrence of stick slip.

The widespread use of plastics in automotive interiors has permitted designers to use complex shapes and a variety of surface textures and colors in components. When the components are assembled interfaces are formed between adjacent components. While these interfaces are designed to be in static contact the twisting of the automobile body causes relative motion between these adjacent components. Initially this motion is accommodated by the deflections of the components and the interface remains pinned. As the motion increases the tangential forces in the interface required to deflect the components also increases. If the motion causes the interface to transmit forces which exceed the static friction, then the motion is accommodated by a combination of component deflection and sliding. There is usually a drop in the tangential friction force when sliding commences. The force imbalance caused by the drop can initiate stick-slip motion which causes noises (squeaks, ticks, and pops) that are annoying to the customer.

There are several approaches which can be taken to minimize the noises caused

by stick-slip sliding. One approach is to prevent the sliding from occurring. This can be done by providing sufficient flexibility in the components so that the tangential forces caused by the relative motion in the interface do not exceed the static friction force. The static friction force is determined by the normal load, bulk material properties such as the elastic modulus, hardness, interfacial shear or fracture strength, and the surface roughness. Because the assembly tolerances cause a wide variation in the normal load and, hence, the static friction force, it is difficult to design contacting components which will not slip.

For sliding components which experience stick slip, the designer can minimize the noise produced by isolating the components so that the vibrations caused by stick slip can not be transmitted to large surfaces such as instrument panels, windows, and doors which can radiate acoustic energy which is perceived as noise. The designer can also select materials which have high internal damping to dissipate the vibration energy before it reaches large panels.

Designers can minimize the stick slip by choosing materials which do not experience a drop in friction when sliding commences or by stiffening the components so that the potential energy stored when they are deflected is minimized. However, these two approaches are often in conflict with each other. Efforts to stiffen a polymer by the addition of glass fibers can cause the occurrence of stick slip to increase, an example of which is shown in the data for polypropylene presented in this paper.

Noise-producing contacts in vehicles are most often found by driving the vehicle on a test track or vibrating it on a four poster shaker. To reduce the testing cost, automotive manufacturers have used laboratory tests to measure the friction of material pairs and then correlated these results with the noises generated by these materials in vehicles. One manufacturer (1) correlated the noise level in decibels to the double amplitude of stick slip. It was determined that noise less than 60 dB was acceptable to customers. Tests showed that the noise was less than 60 dB when the double amplitude of the coefficient of friction (COF) during stick slip was less than 0.4. In research sponsored by another manufacturer (2) the double amplitude of stick-slip friction was also used as a figure of merit to select material pairs. It was found that polypropylene (PP) had the lowest double amplitude of seven polymer pairs which were tested, a result which agreed with industry experience that PP is a quiet material.

In a research program (3,4) sponsored by another manufacturer, a friction tester was developed with which friction force and relative velocity between the test specimens were measured. The friction-time and velocity-time data were combined to produce friction-relative velocity plots during the stick-slip events. Of the several friction parameters which were measured, such as the static friction, the maximum drop in friction when sliding commenced, the maximum relative velocity during stick slip, the slope of the friction-velocity plot, and the number of stick-slip cycles, the last was chosen as the figure of merit for polymer pairs. Of the ten material pairs tested (PP was not included) polycarbonate (PC) had the most number of tests with no stick-slip cycles. The friction response of the PC was least affected by doubling the normal load and quadrupling the test machine stiffness than that of the other polymer pairs (5).

One of the factors which has been shown to influence the occurrence of stick-slip motion is the roughness of the surfaces in contact. Eiss and McCann (6) found that acrylonitrile-butadiene-styrene (ABS) copolymer surfaces with a R_A roughness of 0.85

μm had fewer stick-slip cycles than a surface with a R_A roughness of $0.041 \mu\text{m}$. Moliq (7) confirmed Eiss and McCann's conclusions on McCann's apparatus which was modified to eliminate the effect of vibrations cause by motor starting transients on the transition from static to kinetic friction. Moliq added PP to his test matrix and found that it had the most tests with no stick slip. In a subsequent study, a new friction tested described in (4) was used to examine the effect of surface texture, normal load, and test system stiffness on the stick slip of an ABS-PC blend (ABSPC), PC, and PP, unfilled (UPP) and filled with 30 percent glass fiber (FPP). The results of this study are presented in this paper.

Experimental

Materials. The polymers used were ABS blended with bisphenol A/phosgen resin terminated with p-tertiary butyl phenol (ABSPC), a blend of modified PC (minimum 70%), bisphenol A PC (maximum 30%), and methylene chloride (less than 3 ppm) (PC), unfilled PP (UPP), and PP filled with 30% glassfiber and mineral (FPP). All materials were injection molded into $0.3 \times 3.2 \times 7.2$ cm plaques with the mold gated at the center of the 3.2 cm side. Test specimens were machined from these plaques. The lower specimen was $0.3 \times 1.6 \times 7.2$ cm while the upper specimen was $0.3 \times 0.64 \times 0.64$ cm. The upper specimen had a hemispherical cavity machined in the upper surface to form a self aligning bearing with the loading ball which transmitted the normal load to the interface and the fiction force to a transducer.

Surface Textures. The mold cavities were prepared with four surface textures which are commonly used in automotive interior components: Naples FLY, Montana BG, Stipple #1, and SPI-SPE #3. These molds produced plastic surfaces with mean (standard deviation) R_A roughness values of $21.4(2.2)$, $17.8(3.1)$, $10.6(1.0)$, and $1.8(1.6) \mu\text{m}$, respectively. The R_A values were calculated from linear surface profiles parallel to the mold flow direction. Typical surface profiles of these textures are shown in Figure 1. These profiles reveal that there are significant differences that are not indicated by the R_A roughness values. In particular, the Stipple surface has a distribution of surface heights which is symmetrical about its mean value, while the Naples and Montana surfaces have height distributions which are skewed in the negative direction relative to the mean line. The negative skewness is caused by the relatively flat peaks in their profiles. The second difference is that the Stipple surface profile has a higher peak density (more peaks per unit distance along the profile) than the other three surface profiles.

Apparatus. The apparatus which is illustrated in (4) provides a linear sliding motion to the lower specimen in contact with the upper specimen which is prevented from moving by the force transducer.. The normal load is applied by dead weights and the friction force is measured by a piezoelectric force transducer. A DC servo actuator is connected to the lower specimen through a series of elastomeric isolators. The isolators permit the system stiffness to be varied independently of the force transducer stiffness. These isolators also provide system damping. Four isolators in series had a combined

stiffness of 3.2 N/mm for the tests reported in this paper. The effect of stiffness on the number of stick-slip cycles is reported by Eiss and Hanchi (5).

Test Procedure. In all tests, the upper and lower specimens were the same material and surface texture. The specimens were washed with a mild detergent, rinsed with water and air dried prior to installation in the test apparatus. The two specimens were placed in contact and the normal load was applied for 5 min. Previous studies (4,6) have shown that the increase of static friction with time of static loading before applying the tangential motion was constant after 5 min. The actuator speed for all tests in this study was 0.5 cm/s. The actuator was moved in a direction which put the isolators in tension. This eliminated the possibility of buckling of the stack of isolators if the reverse direction had been used. At least four replicates were tested at normal loads of 10.8 and 20.7 N. The sliding direction was the same as the mold flow direction.

Results and Discussion

The friction was recorded as a function of time. Tables I - IV show the number of replicates which had 0, 1, or more than 1 stick-slip cycle, the static COF, and the drop in COF as sliding commenced for each plastic, surface texture, and normal load. The summations at the bottom of each table for each surface texture gives the total number of replicates for all the plastic-load combinations which experienced 0, 1, or more than 1 stick-slip cycle. The mean and standard deviation (in parentheses) are given for the static COF and the drop in COF immediately following the peak static COF.

The summations indicate that the Stipple texture had the most replicates with zero stick-slip cycles and the least replicates with 1 or more stick-slip cycles. The Montana texture had the least number of replicates with zero stick-slip cycles and the most with 1 or more stick-slip cycles. The data reveal that there is an interaction between the polymer and roughness on the number of stick-slip cycles. ABSPC had zero stick-slip cycles on 25 percent of the tests on the Stipple surface and zero percent

Table I. Occurrence of Stick Slip, Static COF, and COF Drop for Stipple

Composition	Normal Load N	Number of	Static COF	COF Drop
		Stick-Slip Cycles 0 / 1 / >1		
ABSPC	20.7	1 / 1 / 2	0.16(0.03)	0.075(0.017)
	10.8	1 / 2 / 1	0.18(0.02)	0.081(0.028)
PC	20.7	0 / 4 / 0	0.20(0.02)	0.084(0.022)
	10.8	2 / 2 / 0	0.18(0.01)	0.060(0.014)
FPP	20.7	3 / 1 / 0	0.20(0.01)	0.050(0.0072)
	10.8	4 / 0 / 0	0.20(0.01)	0.052(0.0095)
UPP	20.7	4 / 0 / 0	0.26(0.01)	0.015(0.018)
	10.8	4 / 0 / 0	0.29(0.03)	0.035(0.024)
Σ		19/10/3		

Table II. Occurrence of Stick Slip, Static COF, and COF Drop for Naples

Composition	Normal Load N	Number of	Static COF	COF Drop
		Stick-Slip Cycles 0 / 1 / >1		
ABSPC	20.7	0 / 2 / 2	0.18(0.03)	0.106(0.016)
	10.8	0 / 0 / 4	0.20(0.03)	0.139(0.027)
PC	20.7	0 / 3 / 1	0.22(0.02)	0.103(0.050)
	10.8	1 / 3 / 0	0.24(0.01)	0.080(0.011)
FPP	20.7	0 / 4 / 0	0.21(0.01)	0.082(0.014)
	10.8	3 / 1 / 0	0.21(0.01)	0.064(0.0073)
UPP	20.7	4 / 0 / 0	0.29(0.03)	0(0)
	10.8	4 / 0 / 0	0.34(0.04)	0(0)
Σ		12/13/ 7		

Table III. Occurrence of Stick Slip, Static COF, and COF Drop for Montana

Composition	Normal Load N	Number of	Static COF	COF Drop
		Stick-Slip Cycles 0 / 1 / >1		
ABSPC	20.7	0 / 0 / 4	0.20(0.02)	0.138(0.036)
	10.8	0 / 0 / 4	0.20(0.01)	0.138(0.022)
PC	20.7	0 / 2 / 2	0.21(0.03)	0.081(0.051)
	10.8	0 / 1 / 3	0.24(0.02)	0.127(0.063)
FPP	20.7	0 / 0 / 4	0.18(0.01)	0.089(0.020)
	10.8	0 / 0 / 4	0.21(0.01)	0.096(0.0085)
UPP	20.7	4 / 0 / 0	0.24(0.09)	0.027(0.036)
	10.8	4 / 0 / 0	0.29(0.02)	0.062(0.046)
Σ		8 / 13 / 13		

Table IV. Occurrence of Stick Slip, Static COF, and COF Drop for SPI-SPE

Composition	Normal Load N	Number of	Static COF	COF Drop
		Stick-Slip Cycles 0 / 1 / >1		
ABSPC	20.7	0 / 2 / 2	0.26(0.03)	0.107(0.030)
	10.8	0 / 1 / 3	0.28(0.06)	0.147(0.042)
PC	20.7	0 / 4 / 0	0.21(0.01)	0.045(0.017)
	10.8	4 / 2 / 0	0.23(0.03)	0.034(0.021)
FPP	20.7	0 / 4 / 0	0.20(0.02)	0.110(0.014)
	10.8	0 / 4 / 0	0.21(0.02)	0.108(0.011)
UPP	20.7	4 / 0 / 0	0.59(0.06)	0.018(0.036)
	10.8	4 / 0 / 0	0.55(0.17)	0.056(0.036)
Σ		12/17/ 5		

of the tests on the other three surfaces. On the other hand, PP had zero stick-slip cycles on 100 percent of the tests on all surfaces.

The data also indicate that there is a positive correlation between the COF drop and the occurrence of stick slip. For values of COF drop greater than 0.08, one or more stick-slip cycles occurred for all polymers and surface textures. When the value of COF drop was less than 0.04, stick slip did not occur. Between COF drops of 0.04 and 0.08 there is a transition where the number of tests that had zero stick slip increased as the magnitude of the COF drop decreased. An ANalysis Of VAriance (ANOVA) of these data indicated that the normal load, surface texture, polymer, and polymer/surface texture interaction had statistically significant effects in the value of the COF drop (δ).

The R_A values for the four textures do not correlate with the occurrence of stick slip. The SPI-SPE texture has the lowest R_A and the Naples texture has the highest R_A , but for both textures the occurrences of more than one stick-slip cycle are about the same and both are less than that for the Montana texture. Clearly, features of the surface texture which are not measured by R_A must have more effect on the occurrence of stick slip. For example, the Stipple surface has the highest peak density and highest peak curvature (lowest peak radius). The height distribution of the Stipple has zero skewness while the Montana and Naples surfaces have negative skewness.

The friction traces indicated that stick slip was initiated when there was a drop in friction as sliding commenced. The data in Tables I-IV show that the occurrences of stick slip increased as the COF drop increased. This relationship between the magnitude of friction drop and the occurrences of stick slip can be explained using the following model. Before sliding commences the actuator motion is accommodated by the extension of the elastomeric isolators which connect the actuator to the lower specimen. Thus, when sliding commences and the friction drops, there is a force unbalance which causes the lower specimen to surge toward the actuator. The lower specimen and the isolators are a mass-spring system; thus, the lower specimen will vibrate relative to the actuator alternately moving away from and toward the actuator. As the force unbalance increases, the amplitude of the velocity of the specimen will increase. If the lower specimen is moving toward the actuator at a velocity equal in magnitude to the actuator velocity, the velocity of the lower specimen relative to the upper specimen is zero and the interface becomes pinned which initiates the stick phase of a stick-slip cycle. Therefore large friction drops which cause the velocity of the slider to equal the magnitude of that of the actuator are more likely to initiate stick-slip motion.

To examine the interaction between polymer and surface texture on the COF drop in more detail, it is noted that ABSPC and FPP have smaller COF drops on the SPI-SPE surface than on the other three surfaces. While UPP has the lowest COF drop on the Naples surface, no stick-slip cycles were observed on any of the surfaces. For UPP the transition from static contact to sliding occurred with either no or a small drop on COF followed by steady sliding. It appears that the designer has the widest latitude in choosing surface roughness which would minimize stick slip when the material is UPP and the least latitude when the material are ABSPC or FPP. For the latter two materials, a surface which has a high peak density and small peak radii such as the Stipple surface is a good choice for minimizing stick slip.

While the fundamental basis for the interaction of the surface roughness and material properties on the COF drop and the occurrence of stick slip is not known, certain observations of the transition from static to kinetic friction may shed some light on this interaction. Simkins (9) has observed microdisplacements during the tangential loading of a static contact prior to the initiation of sliding. His explanation of the microdisplacements is based on the asperity contacts which transmit the normal load from one body to another. The stress states in the contacting asperities range from less than to greater than the yield strength of the materials. As a tangential load is applied to one of the bodies the stresses in the contact increase until the yield strength is exceeded. When all the asperity contacts have yielded, a microdisplacement occurs which separates some of the initial asperity contacts and forms new asperity contacts. The microdisplacement is arrested when the asperities in contact again have a mix of stress states that range from below to above yield. This process repeats until the last microdisplacement results in sufficient kinetic energy for the moving body that new asperity contacts are sheared immediately and macrosiding occurs. Simkins observed these microdisplacement for steel-steel contacts when the tangential force was greater the 75 percent of the static friction force.

Microdisplacements have been observed for glass-glass contacts (10). Rorrer and Eiss (11) observed a rounding of the stick-slip peaks for elastomeric spheres sliding on epoxy-painted steel. The rounding is caused by microdisplacement which occurs before sliding commences. Baumberger and Caroli (12) noted that the rounding of stick-slip peaks has been observed for shear loadings above 70 percent of the nominal static friction force.

Simkins' model of the tangential static loading has some bearing on this study. Referring the Figure 1 the static contact between two Stipple surfaces would consist of a large number of closely spaced contacts. On the other hand, the contact between pairs of the other three surfaces would consist of a smaller number of more widely spaced asperities. As the tangential load is applied to the contact, the microdisplacements for the Stipple are likely to be more frequent and of shorter lengths than those for the other three surfaces.

One possible effect that the microdisplacements could have on the occurrence of stick slip is by reducing the drop in friction as sliding commences. In these tests the polymer pairs were statically loaded for 5 min. before the tangential load was applied. Most polymers will experience an increase in static friction as a result of the creep or diffusion in the interface during the static loading time. UPP is an exception; its static friction is independent of the time of static loading (8). During a microdisplacement a fraction of the area of contact that experienced the static loading time is broken and some new contact area is added. Since the new area has not had the time of static loading to increase its strength, its addition to the total contact area will reduce the overall tangential strength of the interface. Thus, the more microdisplacements that occur before sliding commences, the lower will be the tangential strength of the interface. When sliding commences, all of the contact area will be new and its strength will determine the kinetic friction. Thus, if one surface texture produced more microdisplacements than another texture during tangential loadings one would expect the drop in friction to be lower for the surfaces which experienced more microdisplacements.

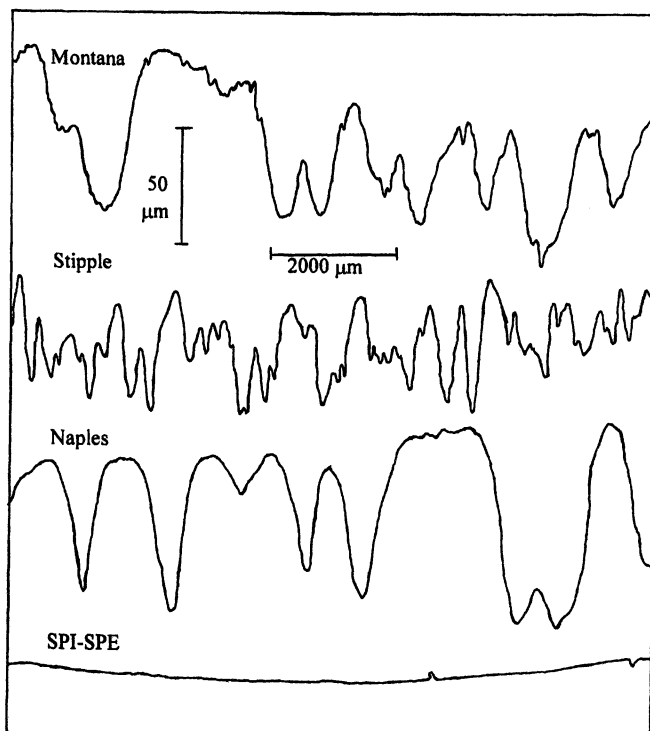


Figure 1. Surface profiles of the Montana, Stipple, Naples, and SPI-SPE surface textures. Note that the vertical magnification is 40 times the horizontal magnification.

The data in Tables I-IV indicate that the COF drops for ABSPC and FPP are smaller on the Stipple surface than those for the other three surfaces which is agreement with the above model. However, PC and UPP do not fit the model. The deviation of the UPP from the model can be explained by the fact that its static friction does not rise during static contact and the microdisplacements, if they occur, do not alter the tangential strength of the interface. The reason that PC does not fit the model is not known, It was not possible to detect microdisplacements in these experiments because of the lack of sensitivity of the velocity transducer.

A comparison of the occurrence of stick-slip and the static COF for FPP and UPP shows that the addition of glassfibers to PP increases the occurrence of stick slip and decreases the static COF. The glassfibers stiffen the FPP which will result in a smaller contact area and a lower value of friction. It is possible that the addition of glassfibers to PP alters the relationship between the static COF and the contact time which would make FPP experience a drop in friction when sliding occurred. However, the effect of contact time on the COF of FPP was not included in the test program.

Peterson (2) observed that PP had a surface energy equal to half that of the other polymers she tested. When the surface was etched with chromic acid to introduce oxygen groups on the surface, the surface energy increased and the etched material experienced stick slip in the friction tests. Peterson noted the PP has a nonpolar surface which minimizes the opportunity for forming interfacial bonds. The introduction of oxygen-containing groups creates a polar surface which can more readily form interfacial bonds. These results suggest that a low strength interface will help to minimize the stick slip during sliding. Ishii and Sawai (1) accomplished a lower interfacial shear strength with a variety of lubricants.

Conclusions

The friction of four plastics was measured as a function of the surface texture and the normal load. It was found that the effect of plastic, texture, load, and the plastic-texture interaction on the COF drop when sliding commenced were all significant. The relevant surface parameters appeared to be the density of peaks and the radii of the peaks and not the R_A roughness. On the Stipple surface which had the highest peak density and the smallest peak radii, ABSPC and FPP had lower COF drops than on the other surfaces. UPP experienced the lowest COF drops when sliding occurred and also did not have any stick slip. The low surface energy of the nonpolar surface of UPP may be a contributing factor to its lack of stick slip.

Acknowledgments

The authors thank the Ford Motor Company, contract monitor, Martin Trapp, for the support of this research. The polymers were molded in the Polymer Processing Laboratory of the Chemical Engineering department, Prof. Don Baird, director. Polymers were supplied by Dow Chemical (ABSPC), Miles (PC) and Ferro (UPP and FPP).

Literature Cited

1. Ishii, N., Sawai, S. Japanese Patent No. Sho 61-191449, **1986**
2. Peterson, C. *Evaluation of Squeak and Rattle Properties of Polymeric Materials*, Diploma work no. 190, Chalmers University of Technology, Gothenburg, Sweden, **1998**
3. Judek, T., Eiss, N., Trapp, M., Loftus, H. *Proc. 14th International Modal Analysis Conference 1996*, 502
4. Eiss, N., Lee, E., Trapp, M. *SAE Paper No. 972056 1997*, 1479
5. Eiss, N. S., Hanchi, J. *Proc. 11th International Colloquium, Industrial and Automotive Lubrication* Ed. Bartz, W. J. Technische Akademie Esslingen, Ostfildern, Germany **1998**, 1907
6. Eiss, N. S. Jr., McCann, B. P. *Tribology Trans. 1993*, 36, 686
7. Moliq, R. S. *Friction Behavior of Polymers: the Transition from Static and Kinetic Conditions* M. S. Thesis, Virginia Polytechnic Institute and State University, Blacksburg, VA **1994**
8. Lee, E. C. *A Study of the Static to Kinetic Friction Transition of Polymers* M. S. Thesis, Virginia Polytechnic Institute and State University, Blacksburg, VA **1995**
9. Simkins, T. E. *Lubrication Engineering 1967*, 25, 26
10. Brown, E. D. Jr. *Trans. ASLE 1969*, 12, 233
11. Rorrer, R., Eiss, N. S. Jr. *Tribology Trans. 1995*, 38, 323
12. Baumberger, T., Carole, C. *MRS Bulletin 1998*, 23, 41

Chapter 27

Micromechanical Characterization of Scratch and Mar Behavior of Automotive Topcoats

L. Lin¹, G. S. Blackman², and R. R. Matheson³

¹ DuPont Automotive, Marshall Research Laboratory,
3500 Grays Ferry Avenue, Philadelphia, PA 19146

² DuPont CRD, Experimental Station E323/110B, Wilmington, DE 19880

³ DuPont Automotive, 950 Stephenson Highway, Troy, MI 48007

The automobile industry and its customers demand durable glossy appearance of automotive topcoats. A micro-scratch technique has been developed to quantitatively characterize scratch and mar behavior. With the micro-scratch instrument normal force, tangential force, penetration depth and permanent damage can be controlled or measured precisely as function of time or position during scratch experiments. These physical quantities allow us to evaluate scratch and mar resistance based on damage mechanisms. The micro-scratch instrument is stable enough to produce centimeters long scratches of various types and sizes so that the relationship between scratch morphology and appearance can be investigated. Results from statistical surveys on well-defined scratches suggest that a scratch with fracture is the most visible type of damage.

Automobile exteriors are coated with multi-layer polymeric coatings for protection and appearance. The electrical coat and primer layers provide corrosion protection and better adhesion to the steel substrate. The basecoat provides the color component. The topcoat protects the other layers from the environment and is responsible for the glossy appearance. The automobile industry and its customers have long demanded that these coatings retain their initial attractive appearance despite weathering and chemical and mechanical damage (1).

Mar is one kind of physical damage that affects the appearance of topcoats. This type of damage occurs within a few micrometers of the surfaces of topcoats. The major contribution to mar is micro-scale scratches (2). Causes of mar include car-washing, in-plant finessing, keys and fingernails, building materials, branches, and blowing sand. There is general agreement that the major source of mar damage is a

car-washing since it is a normal periodic activity for many automobile owners (2). During a car-wash, dust and grit is rubbed against the topcoat surface resulting in many such micro-scale scratches. These micro-scale scratches have a dramatic impact on the appearance and cause a significant loss of gloss.

It has been a problem for the automobile industry and paint suppliers to characterize the mar behavior. There is no well-established test to measure mar resistance. Existing methods used are the Taber test (3), Rub test (3,4), Scrub test (5), Falling abrasive test (6), and Bench-top car-wash test, all of which make simultaneous multi-point scratch damage during experiments. An Optical Imaging Method (3) was developed to work with the above tests to quantify the damage level. Contradictory conclusions often occur even when attempting a relative ranking between good and bad. Some of the problems of the multi-contact tests are poor reproducibility, poor discrimination, and most importantly no measurement of physical quantities. Several investigators have developed single point contact techniques (7-10) to study abrasive wear of polymeric materials. The macroscopic single point scratch tests make damages too severe compared to regular mar. Many of the other techniques have limited scratch length, penetration depth and poor long-range stability. Often important physical quantities are not measured adequately. We developed a technique that is sensitive enough to make scratches as small as a few nanometers yet has the long-range stability and large depth-range to make a single scratch as long as a few centimeters. Coupling this technique with Atomic Force Microscopy (AFM) and statistic surveys, the damage mechanism of mar and its effect on appearance of automotive topcoats was investigated. Mar resistance is characterized based on damage mechanisms.

Experimental

The principle of a scratch experiment is to move an indenter into a topcoat while the sample is translated perpendicular to the indenter motion. During the process, the force parallel to indenter motion (Normal force) and force parallel to sample motion (Tangential force), the displacements of indenter and sample are controlled or measured with high resolution and fast dynamic response. In addition, other controllable parameters are penetration rate, scratch rate, lubrication condition, cutting geometry and temperature.

To implement the micro-scratch experiment described above, a unique instrument was developed at DuPont Marshall R&D Laboratory. As illustrated in the block diagram of Figure 1, the instrument mainly consists of a nano driving / probing system, tangential force / stages system, signal conditioning / motion controller system, data acquisition system, and microscope / video system. The driving / probing system provides vertical displacement and measures corresponding resistant normal forces or generates the force to drive the indenter into coatings and measures the corresponding penetration depth. The tangential force / stage system is used to move coating samples at a given constant rate, position the indenter tip, and measure tangential force during the scratch. The signal conditioning and motion controller system includes electronic elements for signal converting, servo-control, and signal amplifying to all mechanical components. The integrated optical microscope and video system is used to capture the real-time deformation and elastic recovery during

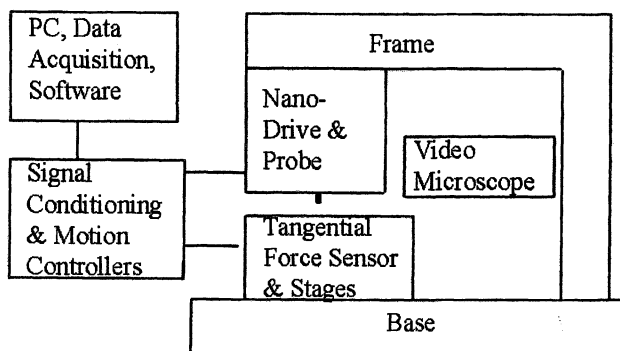


Figure 1. Block diagram of the micro-scratch apparatus.

the scratch and to characterize the permanent damage afterwards. In addition, the video system is very useful for indenter tip positioning and sample leveling with position stages and tilting stages, for setting-up the experiment. The design of the instrument with more details will be published elsewhere (11).

For the micro-scratch experiments presented here, the instrument configured for a maximum of 100 milli-Newtons (mN) normal force with 5 micro-Newtons (μN) resolution, and 90 micrometers (μm) vertical displacement with 2 nanometer (nm) resolution. A variety of normal force and displacement ranges and system resolutions can be constructed depending on the application. The resolution for the sensor of tangential force measurement is 20 μN .

Most commercial polymer topcoats have long-range height variation as much as a few microns for every millimeter distance. Since most scratch damage itself is not more than a few microns, displacement control is not adequate for a micro scratch experiment. Control of the normal force during the experiment is necessary. In the force control mode, the indenter automatically follows the coating surface to produce the necessary penetration from coating surface according to the applied force, thus correcting for any surface height variation. The instrument is capable of either force control mode or displacement control mode. However, all work described here is done in force control mode.

A complete experiment consists of three separate "scratches", a pre-scratch to measure topography of the undamaged coating, a scratch to produce the damage, and a post-scratch to measure the permanent deformation of the coating. All pre-scratch and post-scratch measurements were done under an applied constant normal force 20 μN . Scratch experiments can be performed in many different patterns. Ramp scratches are used to precisely measure physical quantities corresponding to a given force and to probe transitions in damage mechanisms as will be discussed in a later section. Step scratches were used to check instrument reproducibility, and more importantly to make precise scratches of different types and sizes for studying the relationship to visual appearance. In a ramp scratch, the normal force starts at 20 μN constant, and after 5 seconds, increases at a rate of 20 $\mu\text{N/s}$ to a predefined maximum. During the scratch the displacement, normal, and tangential loads are recorded at ~ 100 data point per second. The high data acquisition rate is important to capture abrupt or transient events. Other parameters of the experiments are 25 $\mu\text{m/s}$ scratch rate, 21°C temperature, ambient condition and 60° conical indentors with spherical tips. The radius of the tips will be specified as discussions of results.

The AFM used in these experiments is a precision large stage M-5 instrument from Park Scientific Instruments. The stage motion is calibrated with NIST traceable standards and the absolute reproducibility is within a few microns. The micro-scratch instrument and the AFM are in perfect registry so that images and morphological calculations are precisely related to the micro-mechanical measurement (12).

The material used in this study is a model styrenated -acrylic/melamine topcoat over a black basecoat. The thickness of the topcoat is ~ 40 μm . The topcoat material is known to have long-term reproducible mechanical properties.

Results and Discussion

Figure 2 shows the results of a typical micro-scratch experiment. The indenter used here had a $1\ \mu\text{m}$ radius. The Curve A measured in pre-scratch shows the profile or height variation of the undamaged coating. Curve C, D and E were obtained during scratch damage process. Curve E and C are the applied normal force and the measured tangential force, respectively. Curve D is the displacement of the indenter. The total deformation under the load or penetration depth can be calculated from the indenter displacement (D) by subtracting the pre-scratch profile (A). Curve B measured in post-scratch is the surface topography after the scratch damage made. The amount of unrecovered damage to the coating can be obtained from the post-scratch (B) profile by subtracting the pre-scratch (A). Figure 3 presents the total deformation (A) and the plastic deformation (B) as function of the applied normal force.

As can be seen in Figure 2, the surface height variation within the 2.5 mm scratch distance is more than 100 nanometers, which is much better than average commercial coatings. Even with this sample, the variation could result in large error if the absolute displacement instead normal force was controlled. In the force control mode, all of the topographic details of the undeformed coating (A) are faithfully reproduced in both curves B and D before a distance of 1.747 mm where large fluctuations begin to occur. However, as seen in Figure 3, the total deformation (A) under indenter during scratch and the unrecovered deformation (B) of scratch damage measured afterwards are not effected by topographic details but are only a function of applied force. To achieve this realistic measurement, it is necessary for the instrument to have a high sensitivity and fast dynamic response.

In the early region of the scratch, Curves A and B of figure 2 are superimposed on one another, signifying that the deformation is totally recovered, i.e. elastic. As the load increases, the two curves diverge, indicating the beginning of plastic deformation. Under video microscopy, a faint but smooth scratch is observed, which steadily increases in size as the load increases. The smooth increase of the unrecovered deformation as the normal force increases was also measured afterwards as shown in Figure 3.

At a scratch distance of 1.747 mm or an applied normal force of 1.29 mN, (see Figures 2 and 3), the character of the curves abruptly change. The displacement curve (D) and the tangential force curve (C) start to show large and rapid fluctuations well above the local height or roughness variations in the coating. Cracks begin to appear on the scratch observed by the video microscope. The starting point of the fluctuation indicates that fracture or rupture events occur in addition to plastic deformation. This is clearly confirmed by detailed AFM images near this transition point (12). As the normal load increases further, both the frequency and the magnitude of the rupture increases. However, at the early stage of the on and off fracture events, there is no material removal or debris observed through video microscopy. Wear rates calculated from high-resolution AFM images at the same locations confirm that no chips are generated (11). If the controlled normal force is increased further, debris from the surface is eventually generated, which clings to the indenter. At the same time the scratch morphology becomes very irregular.

Based on this study as well as on field studies, scratch damage can be classified into two types: a) plastic flow (ploughing) where the damage is regular and

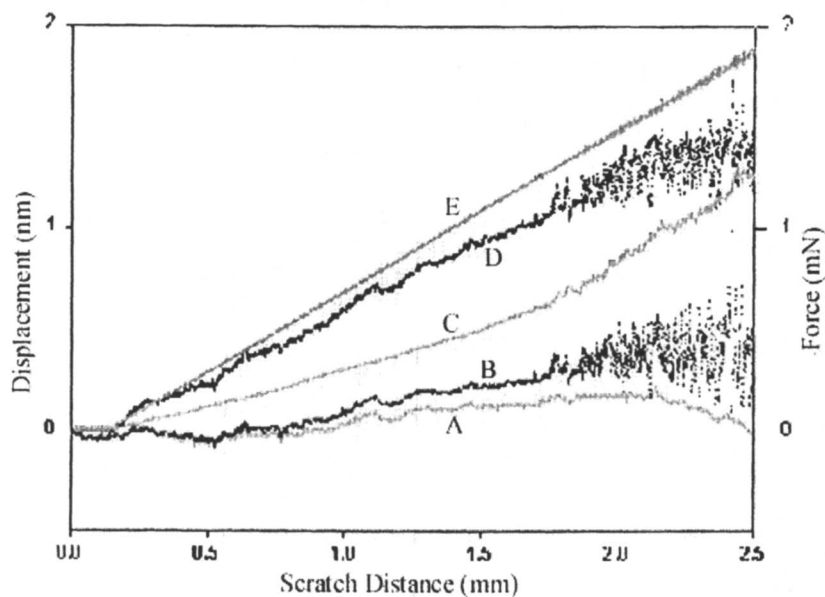


Figure 2. Force and displacement vs. scratch distance during a micro-scratch experiment.

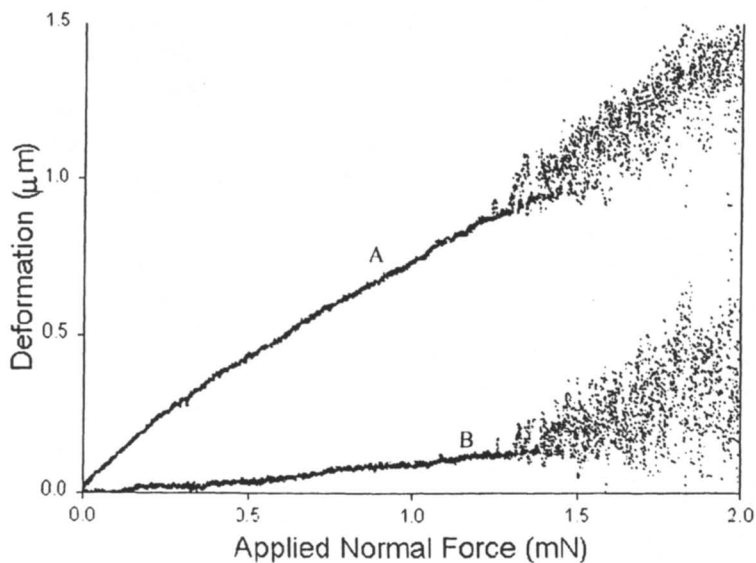


Figure 3. Total deformation and permanent deformation vs. applied normal force.

the surface topography changes smoothly; and b) plastic flow with rupture (fracture) where cracks and crevices open in the coating surface. In characterization of mar behavior of coatings, both plastic deformation resistance and fracture resistance, which in most cases are not proportional, must be considered. It is simply impossible to correctly evaluate mar resistance with a single number, as is currently done in the automotive industry. The visual impact from a collection of scratches depends on the damage morphology. The different types of damage result in different visual effects and are governed by different types of mechanical properties. Much of the confusion and controversy in evaluating mar resistance comes from a historical insistence on using visual rankings based on a single number without regard for the damage mechanisms. The result of visual evaluation is dramatically influenced by variables such as color, lighting condition, damage size, orientation of observation, duration of inspection, psychological factors, and so on. To our knowledge, there is no example that all of the variables were controlled during such evaluations.

It can be argued that if a coating has better mechanical properties, both against plastic deformation and fracture, it should have a better mar resistance. As a first step, it is better to think of mar resistance as a purely mechanical problem and find a way to evaluate mar objectively based on damage mechanisms. A minimum of two parameters is required to characterize mar performance, one related to plastic flow and the other related to fracture.

In a micro-scratch experiment with increasing applied normal force, deformation continuously changes from elastic behavior to visco-plastic and finally to fracture. The physical quantities at the transition points between two regimes of deformation are naturally the most important. They are the mechanical thresholds of the different types of deformation. As can be seen in Figure 2 and Figure 3, the fracture threshold is easily identified because the curves change their characters at this point. As the applied normal force increases to 1.29 mN, the tangential and total deformation reach 0.63 mN and 0.9 μm , deformation changes from pure visco-plastic alone to visco-plastic with fracture. As results of the fracture, the tangential force and total deformation fluctuate to keep up with the normal forces through the closed-loop control. The applied force at the transition point is the minimum (or critical) force for fracture to occur. One of the tasks to improve mar resistance is to modify a topcoat to have a higher critical force against fracture.

The threshold for plastic deformation is much more difficult to directly determine by a micro-scratch experiment because there is no dramatic change in the curve character. Although we can see that the curve B deviates from curve A in Figure 2 or from horizontal axis in Figure 3, we can not locate the exact starting point. In fact, even with AFM the precise threshold of plastic deformation is difficult to determine. However, we know more deviation of curve B from A in Figure 2 (or B from horizontal axis) means more permanent damage made by a scratch, which further indicate lower mar resistance of the coating. To extract a single number to evaluate the plastic behavior, we calculate the area under curve B in figure 3 to a predefined normal force. This predefined force should be as large as possible but smaller than the lowest of fracture thresholds in a group for comparison. The larger the calculated number, the larger the permanent damage from the scratch and the lower the mar resistance the material. The reason for using the area rather than the depth of permanent damage is to reduce possible error due to local noise of the measured data.

There may be other ways to evaluate plastic resistance of coatings based on the data of micro-scratch experiment. Nevertheless, mar resistance can be evaluated or ranked mechanically and objectively with the area under the plastic deformation curve and the critical normal force before fracture.

To completely understand the mar behavior of coatings, it is also important to understand the relationship between physical damage and visibility or appearance. This is a very complex problem since many variables are involved, including basecoat color, lighting, damage orientation, duration of inspection, and psychological factors, as well as size and type of damage. By means of the micro-scratch technique, different types and sizes of scratches can be produced with precision. This allows us to conduct statistical surveys to investigate size and type impact on visibility of micro scratches as described below.

First, ten well-defined scratches were made on a 25mmx50mm sample with a 2 μm -radius indenter. These scratches are 10 mm long and parallel to each other 1 mm apart. Table 1 summarizes the normal forces used to produce the scratches, and morphology parameters of the scratches measured by AFM. Three of the ten scratches have only plastic deformation. Six scratches involved continuous fracture. One is on the transition, where fracture occurred intermittently. Figure 4 shows three AFM images of scratches near the fracture transition. Note the scales of the images are different. Other conditions for the survey were chosen to simulate the worst case scenario for visibility, a black basecoat and light intensity equivalent to the noonday sun. The following questions were asked to try to determine the nature of scratches and the critical "size" of the scratches that can be seen by human eye. How many scratches can you see? a) after 5 seconds; b) after 60 seconds; c) after being told there were twelve scratches on the panel. Participants were told there were twelve rather than ten scratches in an attempt to eliminate possible psychological factors. Seventy-three people participated in this survey. The statistical results, however, are based on 72 people because there was one person who saw twelve scratches and his answer was removed from the survey.

More than 60% of the participants observed five and six scratches after cursory examination of the sample (Figure 5). The percentage is much higher than the lines with pure plastic deformation (seven lines or higher). This indicates that scratches in continuous fracture are much more visible in very short observation time. The narrow distribution around five and six scratches suggests that once fracture occurs, the scratches become easily visible. When the participants were allowed sixty seconds to examine the panel, the result shifts to more scratches (smaller scratches) and broadens. Approximately 20% of people were able to see eight scratches. The result suggests that scratches with pure plastic deformation are visible if given longer observation time. After being told that there were twelve scratches present, the distribution shifts to even smaller scratches. Scratches as small as a few of nanometers in depth (Table 1) are visible by most people if they know what and where to look. The current survey does not provide a direct answer to what geometrical parameters govern the visibility of a scratch. However, from this and other studies, we believe neither width nor depth, but local geometrical changes are most important for visibility of plastic deformation.

Styrenated-Acrylic/Melamine TopCoat

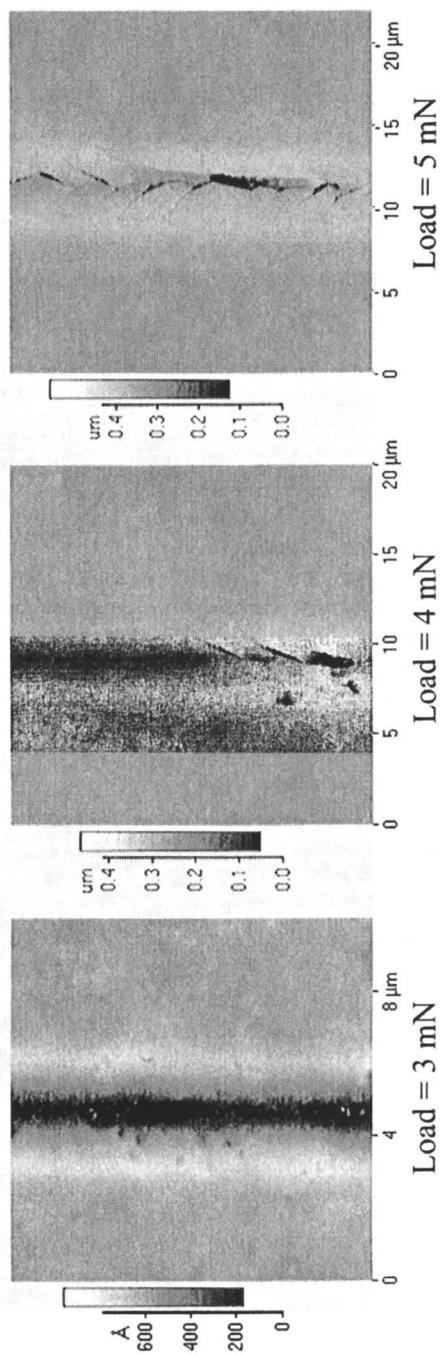


Figure 4. AFM images of scratches near fracture threshold.

Table 1. Scratch parameters for ten line statistical survey.

Load (mN)	Width (μm)	Depth (nm)	Scratch Roughness (nm)	Wear Rate ($\mu\text{m}^3/\mu\text{m}$)
1.0	2.33	8.0	4.9	0.000
2.0	4.11	20.3	8.5	0.026
3.0	4.54	42.5	7.3	-0.018
4.0	6.11	51.8	21.5	0.085
5.0	9.12	99.6	55.4	0.381
6.0	8.95	153.8	104.7	0.504
7.0	10.05	273.0	162.1	0.597
10.0	13.18	354.0	173.3	1.176
15.0	16.38	652.1	254.1	1.545
20.0	21.53	903.9	301.8	1.430

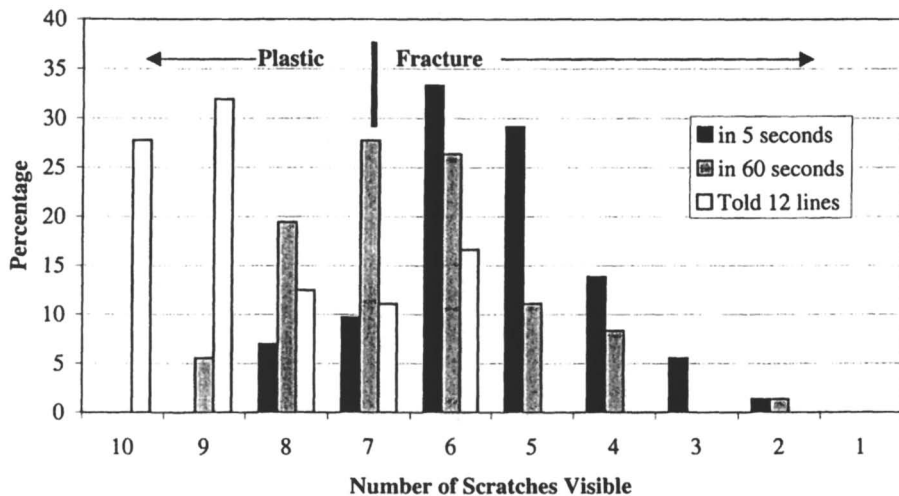


Figure 5. Statistical survey results.

Conclusions

Mar damage of coatings can be classified into pure ploughing (plastic deformation) and ploughing with cracks (fracture). Characterization of mar behavior based on the damage mechanisms is objective and unambiguous. A micro-scratch technique with an instrument was developed to quantitatively evaluate the mar performance of polymer coatings. The instrument has high resolution, fast dynamic response and long-range stability, and is capable of collecting relevant mechanical values as a function of time at a high data acquisition rate. With the instrument, polymer surface deformation can be studied and important physical quantities can be obtained to evaluate both plastic and fracture resistance. Studying mar resistance of automotive topcoats is an example of such an application; however, the instrument can be used as research tool for many other applications.

Fracture is the most serious damage mechanism on automotive topcoats. This type of damage is visible in a much shorter time and under a wider range of lighting conditions than plastic ploughing. Increasing the toughness of a topcoat may dramatically improve its scratch and mar resistance. Small scratch damage produced by plastic ploughing is also visible. In comparison with fracture scratches, brighter lighting conditions, longer duration of inspection, and correct angle of observation are required to observe plastic damage. It should be noted that significantly larger plastic deformation occurs in other type of coatings and in this case scratches by pure plastic ploughing may be more visible. Research is in progress to apply the same techniques to other type of topcoats. The new methodology shown will help to advance the understanding of wear of polymeric topcoats.

Acknowledgments

The authors would like to acknowledge B.V. Gregorovich for helpful conversations and S.A. Riggs for her AFM contributions.

Literature Cited

1. Adamsons, K; Blackman, G.; Gregorovich, B.; Lin, L.; Matheson, R.R. *Proc. XXIII International Conference on Organic Coatings* **1997** 23, 151.
2. Gregorovich, B.; Mcgonigal, P.J. *SME technical paper*, **1993**.
3. Gregorovich, B.; Mcgonigal, P.J., *Proc. of the ASM/ESD Advanced Coating Technology Conference* **1992**, 121-125.
4. ASTM D673-93a, D3389-94, D4060-95, D1630-94, and D1242-95a.
5. ASTM D2486-95.
6. ASTM D968-93.
7. Briscoe, B.J.; Evans, P.D. *Composites Science and Technology* **1989**, 34, 73.
8. Yang, A.C.-M.; Wu, T.W. *J. Materials Sci.* **1993**, 28, 955.
9. Ruan, J.; Bhushan, B. *Trans. ASME* **1994**, 116, 378.
10. Shen, W.; Smith, S.M.; Jones, F.N.; Ji, C.; Ryntz, R.A.; Everson, M.P. *J. Coatings Technol.* **1997**, 69, 123.
11. Lin, L.; Blackman, G.S.; Matheson, R.R. to be published.
12. G. S. Blackman, L. Lin and R. R. Matheson, *ACS Symposium* **1999**.

Chapter 28

Investigation of Tribological Properties of Polymeric Surface Coatings with Scanning Probe Microscope

Weidian Shen and Frank N. Jones

Eastern Michigan University, Ypsilanti, MI 48197

We have used a scanning probe microscope, equipped with a custom-made probe, consisting of a diamond tip and rectangular tungsten cantilever, to investigate tribological properties of cross-linked polymeric surface coatings at micron and submicron scales. A new method to measure the mar resistance, a very desirable characteristic of surface coatings, has been developed, by using the custom-made tip to mar the surface under well-controlled conditions, and using a conventional tip to image the marred surface and measure the dimension of the mars. Based on the dimension of the mar, different responses of coatings to marring stress, elastic recovery, plastic deformation, and abrasive wear, can also be identified quantitatively with great accuracy. In addition, the dynamic process, including viscoelastic creep, strain-hardening, micro-cracking, and surface fatigue, has been studied with the SPM in micron and submicron scales.

The enormous technological importance of the cross-linked polymeric surface coatings has engendered scientific interest in their tribological properties. One such property, resistance to marring, is a very desired characteristic of coatings, especially for the coatings used in the automotive, glazing, and flooring industries (1-5). The terms "mar" and "marring" are used to describe surface defects that are large enough to degrade the appearance of a polymer surface but are small with respect to the coating thickness. For example, mars 0.2 to 0.5 μm deep and 1 to 2 μm wide degrade the appearance of automobile clearcoats that are 30-60 μm thick. Mar resistance is a measure of a material's ability to resist appearance degradation caused by small-scale mechanical stresses under a specific set of conditions. Conventional indentation hardness and impact resistance tests measure resistance against the compressive force that is perpendicular to the surface, and do not provide pertinent information for marring resistance. The crockmeter test (6, 7), used by some coating companies recently, subjects the tested coating to stresses unlike those encountered in the field, and the stresses are poorly characterized. To

better characterize the mar resistance, which is a complicated issue, and no single quantity can characterize it independently of marring stresses, we have developed a new test method by using a scanning probe microscope (SPM) equipped with a custom-made tip (8). It is becoming more and more accepted in the coating community as an appropriate method for the measurement.

With its unique high resolution, SPM can also identify the different responses of a coating to marring stress, i. e. elastic response, plastic deformation, and abrasive wear, quantitatively with great accuracy (9, 10). We have tested different coatings, and studied the correlation of their tribological properties and their surface structure.

The dynamic process of marring is also studied with the SPM, including the viscoelastic creep (11), strain-hardening, micro-cracking, and surface fatigue (12). The accumulated knowledge will provide useful information in developing polymer coatings with improved tribological properties.

Experimental

The SPM used in our tests was a Nanoscope IIIa of Digital Instruments. Conventionally, the SPM is used for non-destructive imaging. To investigate the tribological properties of coatings, a custom probe is made. It consists of a diamond tip glued to a rectangular-shaped tungsten cantilever with epoxy resin. At the beginning, the diamond tips were made in our laboratory, by smashing a thin piece of diamond, picking a pyramid-shaped shard in micron size under a studio zoom microscope (8-10). Since the shape of the home-made tip was not predictable and reproducible, the results were only good for comparison of coatings tested with the same tip and under the same conditions. As the demand for diamond tips grows from researchers in the field of nanotribology, the commercial diamond tips are available now. Currently we purchase our tips from Imetra, Inc. in Elmsford NY, whose manufacturer is in Switzerland. The tips of Imetra have well defined shape and sharpness. The cantilevers are cut from tungsten foils, and their spring constants range from 400N/m to 4000N/m, three to four orders of magnitude larger than conventional SPM probes. The SPM equipped with such a probe is capable of making artificial mars, under well-controlled conditions, with the same dimensions as the mars encountered in the field.

The coating panels under test were cut into a 10 x 10mm² piece by a shear cutter to fit the sample stage of the SPM. Before the test, the samples were washed in an ultrasonic bath with a mild solvent-free detergent, rinsed in a stream of cool tap water, gently dried with soft tissue, and then were blown dry with high pressure nitrogen gas.

In the micro mar resistance (MMR) measurement, the tip, under a fixed normal force ranging from about 50 micronewtons up to 2 - 4 millinewtons, depending on the property of the tested coating, was moved laterally along the surface and made a single scrape of about 70µm. After the scraping, the tip was lifted and the sample was moved, and a second mar was then made under a increased normal force, parallel to the first one at a distance of about 10µm. After five to ten mars were made under different normal forces, the marred sample was again washed in an

ultrasonic bath, but without detergent, rinsed in a stream of cool tap water, gently dried with soft tissue, and blown dry with high pressure nitrogen gas to remove the broken debris. Then the marred surface was imaged with a scanning probe microscope (SPM) equipped with a conventional high resolution tip. The dimensions of the mars were measured. The average values over 200 - 400 data points along the mar were used to calculate the MMR as well as the percentage of elastic, plastic and abrasive response at different normal forces.

At the beginning, the tip, under each normal force, was moved back and forth for 5 to 10 bi-directional scrapes to make a mar, in order to compare the results with those from crockmeter test, in which a probe, covered by a fresh green 50 x 50mm² felt pad, stroked a coated panel back and forth for 5 to 10 times (8-10). Later, we reduced the scrapings to a single one, which is closer to the practical situation.

Force Calibration. The readout of NanoScope IIIa for the force is in terms of voltage, V . To figure out the normal force applied in the marring, we performed the force calibration mode of the instrument using a thin, flat piece of diamond as sample. The diamond sheet was pushed upward against the diamond tip, the cantilever deflection versus the vertical advancement of the sample against the tip was plotted. Suppose V_0 is the signal before the diamond sheet touches the tip of the probe, and V_{stpt} is the signal after the sheet touches the tip and deflects the cantilever to a certain extent. The difference $\Delta V = V_{\text{stpt}} - V_0$ reflects the normal force applied to the tip, which the feedback loop of the instrument was set to maintain during subsequent marring test. Forces, varying from $\Delta V = 0.5V$ to $\Delta V = 5V$ in 5 or 10 steps, were used in our tests, and the corresponding vertical advancements of the diamond sheet were recorded and used to calculate the forces. As illustrated in Figure 1, V_0 , before touching at the lower right flat part of the curve, was $-1.5V$, and the setpoint voltage V_{stpt} is $1.0V$ in this case. An advancement of $\Delta Z_{\text{dmnd}} = 455\text{nm}$ by the diamond sheet against the tip yields $\Delta V = V_{\text{stpt}} - V_0 = 2.5V$. The diamond tip and sheet are assumed to be non-deformable under these conditions; therefore, all vertical sample motion is transferred to the cantilever deflection. The normal force in this instance is given by

$$F_N = K * \Delta Z_{\text{dmnd}} \quad (1)$$

where K is the spring constant of the rectangular tungsten cantilever, and could be calculated using the equation:

$$K = E * (W t^3/4L^3) \quad (2)$$

where E is Young's modulus, and L , W , and t are the length, width, and thickness of the cantilever.

Measurement of Depth of Indentation. To calculate the micro mar resistance and the different responses of the coating to marring stresses, the dimension of the

indentation when the tip stuck into the surface of a coating under a given normal force is needed. To figure it out, the force calibration was performed at the surface of the coating. Figure 2 shows the plot of the cantilever deflection versus the vertical advancement of the sample against the tip obtained at the surface of coating PE, comprising a polyester resin, made in our laboratories, crosslinked with a monomeric methylolated melamine formaldehyde resin under acid catalysis. In this case, a vertical advancement of the coating, $\Delta Z_{ctg} = 1,430\text{nm}$, was needed to produce the same cantilever deflection, $\Delta V = 2.5\text{V}$, as was produced by $\Delta Z_{dmnd} = 455\text{nm}$ of the diamond sheet. The difference, in this case 975nm , is attributed to penetration of the diamond tip into the surface of the coating under the applied normal force.

Using the measured depth of indentation, the cross-section area of the indentation can be calculated for different shaped tips. Conical shaped tips of 60° , 90° , 120° with the radius from $0.5\mu\text{m}$ to $5\mu\text{m}$ at its apex are available from Imetra, Inc. Figure 3 shows the profile of a 90° conical tip with a radius of $1\mu\text{m}$ at its apex. For such a tip, as depth of indentation, $D_{ind} \leq 0.293\mu\text{m}$, the cross-section area of indentation can be calculated using the equation:

$$A_{ind} = \text{COS}^{-1}(1 - D_{ind}) - 0.5\text{SIN}[2 \text{COS}^{-1}(1 - D_{ind})] (\mu\text{m})^2 \quad (3)$$

as depth of indentation, $D_{ind} > 0.293\mu\text{m}$, the cross-section area of indentation can be calculated using the equation:

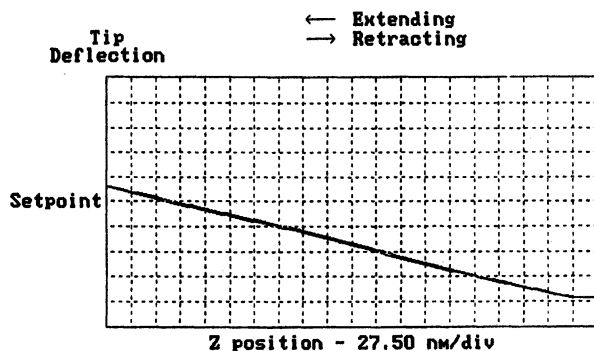
$$A_{ind} = D_{ind}^2 + 0.83D_{ind} - 0.04 (\mu\text{m})^2 \quad (4)$$

where D_{ind} is the depth of indentation in the unit of μm .

Dynamic Process Study. More than two hundred coatings have been tested with this method. More than fifteen percent showed self-healing to different extents, mainly depending on their glass transition temperature, T_g . This is attributed to viscoelastic creep. Viscoelastic creep is different from elastic recovery; it results in partial or complete recovery of a marred surface within a time frame from several minutes to several hours (13, 14), while the elastic recovery occurs immediately after the marring tip moves over the surface. To study the creep in detail, we imaged the marred surface continuously, immediately after the scratching, at a time interval of 10 minutes up to several hours when the recovery was almost complete, and stored the data in a computer. Later we plotted the dimension of mar versus time, and studied the recovery rate, recoverable part, and unrecoverable part for the mars made under different normal forces.

To study the strain-hardening, micro cracking, and surface fatigue, we marred the coating surface with an increasing number of scrapings in the same channel at a fixed normal force. The depth of ditch was measured, and the morphology at the bottom of the ditches was examined after each scraping. It provided direct experimental evidence for strain-hardening, micro cracking, and surface fatigue of a polymeric coating on the micron and submicron scales when it undergoes marring.

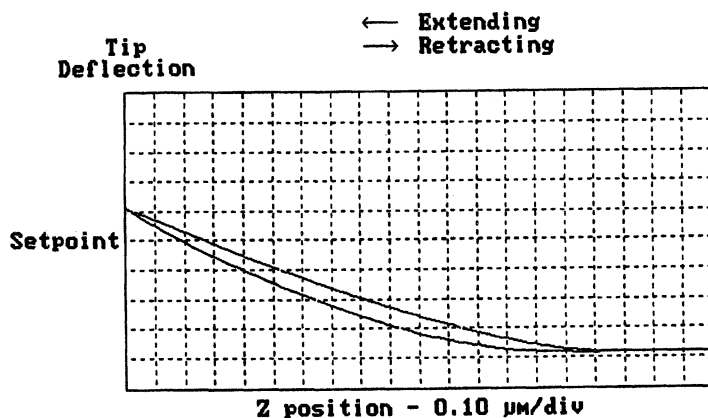
Force Calibration Plot



$$V_0 = -1.5V, \text{ and } V_{\text{setpoint}} = 1.0V$$

Figure 1. Force curve obtained at the surface of diamond sheet with $\Delta V = 2.5V$ and corresponding $\Delta Z_{\text{dmnd}} = 455\text{nm}$.

Force Calibration Plot



$$V_0 = -1.5V, \text{ and } V_{\text{setpoint}} = 1.0V$$

Figure 2. Force curve obtained at the surface of coating PE with $\Delta V = 2.5V$ and corresponding $\Delta Z_{\text{ctg}} = 1430\text{nm}$.

Results and Discussion

Figure 4 shows a marred surface of an experimental PU coating, a polyurethane coating obtained from DuPont in two components, coded RKR94550 and RK7018, which were mixed in our laboratory just before the films were cast. The ten mars in the surface were made under normal forces of 49, 92, 126, 169, 212, 254, 298, 338, 385, and 421 μN , respectively. Below the image is the cross-section profile of the mars. Micro mar resistance (MMR), defined as normal force used in scraping divided by the cross section area of the trough, is used to characterize the coating's performance in marring. Thus the polyurethane coating has an MMR of 2.6, 1.3, 1.0, 0.54, 0.37, 0.33, 0.27, 0.26, 0.25, 0.11 GPa under the increasing normal forces. For most cross-linked polymer surface coatings, which we have tested, the MMR, as well as micro indentation hardness MIH, decreases with the increasing normal forces, i. e. decreases with the penetration depth. Mar resistance is a complicated issue, as mentioned above. It depends very much on the test conditions, such as applied normal force. Mar resistance of a single coating is probably best characterized by measuring it under different normal forces. We usually measure it under 5 to 10 different normal forces, and provide a set of data to characterize it. Decrease of MMR and MIH with depth suggests the existence of a hard crust at the top layer of the cross-linked polymer coatings. It may be associated with the higher crosslink density at the top layer due to the aging effect.

As can be seen in the profile, there are two shoulders on both sides of the ditch, which reflect the plastic deformation. The material was displaced from the ditch to build up the shoulders during marring. In most cases, the total cross-section area of two shoulders is less than the cross-section area of the ditch. Since the polymer coatings are not compressible material, the volume change under the marring stresses could not go beyond 10%. The difference between the total cross-section area of two shoulders and the cross-section area of the ditch is mainly due to the abrasive wear. Some material was abraded from the surface in the marring. We found the debris along the marred surface whenever abrasive wear occurred, which made the subsequent imaging with the conventional tip difficult. After the marring, we washed the samples again to remove the debris, then took an image of the marred surface. Figure 5 is a schematic illustration of how to calculate the MMR and different responses of the coating to marring stress. The cross-section area of trough is the cross-section area of ditch plus the cross-section area between two shoulders, if any. To be more consistent with the optical evaluation and visual judgment of the coating surface, the cross-section area of trough is used to calculate the MMR instead of the cross-section area of ditch.

Different coatings possess different mar resistances as well as show distinguishably different responses to marring stress. We have tested, under the same conditions, the PE coating and the PU coating, as mentioned above, and an AC coating, a commercial one-component automotive clearcoat obtained from DuPont and coded "Gen-3", which is presumed to be based on special acrylic polymers crosslinked, at least partly, with alcoholated melamine-formaldehyde resins. Although the PU and AC coatings are much harder than the PE coating, the PE coating shows a much better mar resistance than the PU and AC coatings. It is due

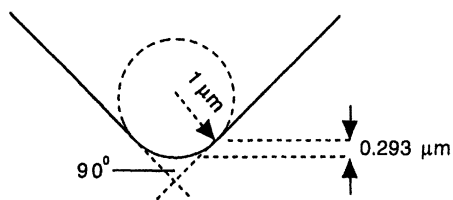


Figure 3. Profile of a 90° conical shaped diamond tip with $1\mu\text{m}$ radius at its apex.

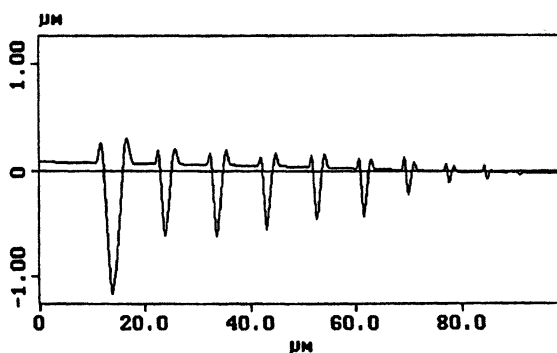
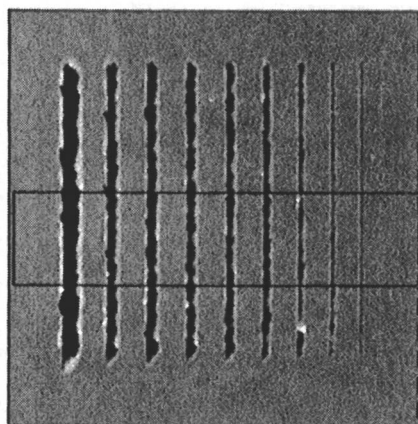


Figure 4. Coating PU surface with ten mars made under ten different normal forces, and its cross-section profile.

to the fact that the PE coating has a greater elastic recovery. The tip stuck deeper in the surface of the PE coating under the applied normal force; however the indentation recovered immediately after the tip moved over. In contrast, the PU coating has a significant plastic deformation, and the AC coating has a significant abrasive wear. Table I shows their micro indentation hardness (MIH), micro mar resistance (MMR), and their different responses under a normal force of $126\mu\text{N}$.

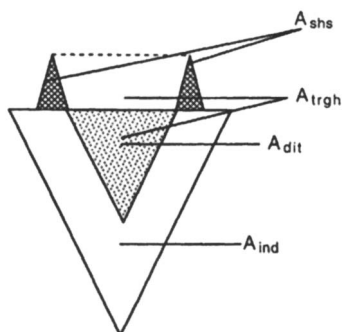
The mar resistance and different responses of a coating also depends on the marring condition, such as the normal force used in the marring. The MMR and percentage of elastic recovery, plastic deformation, and abrasive wear varied with the normal force applied in marring.

The correlation between the structure of coatings and their tribological properties was explored. Images of $1\mu\text{m}$ by $1\mu\text{m}$ at the surface of the AC, PU and PE coatings, were taken using the SPM equipped with the conventional high resolution tip. They showed three distinguishable polymer domain structures. A nano scratch with a depth of a couple of nanometers, which is much smaller than the mars in the MMR tests, was made at their surface, and the response of the polymer domains to the nano scratching was examined. Figure 6 (a) is the image of the AC coating, showing the small particles sitting at the top of the continuous matrix phase. In the nano scratching, the tip easily removed the small particles. This observation may relate to the brittleness of coating AC, as reflected in its tendency to undergo abrasive wear. (b) is the image of the PU coating, showing string shaped polymer domains. In the nano scratching, these domains realigned themselves along the scratch as the tip moved over the surface, similar to the shoulders of plastic deformation in the marring test. (c) is the image of the PE coating with its polymer domains much larger than those of the AC's and PU's. In the nano scratching, the domains were hardly removed or broken, but were displaced from their original positions. After the tip moved past, they returned back to their original positions, making the left over path zigzag-shaped, which may be attributable for the great elasticity of the PE coating in the marring test.

Mar resistance of polymeric coatings depends on a number of factors, such as chemical components, molecular weight, crosslink material and its density, additives, processing procedure, etc. In addition, the tribological properties of coatings vary with the depth and age. A scratching test performed at the top surface at nano scale does not necessarily represent the performance in marring test at micro and submicron scales. An intensive study is needed before any conclusive statement can be made.

To study viscoelastic creep, the diamond tip was replaced by a regular tip after the marring, and the imaging started within 15 minutes. It was observed that the total cross-section area of the shoulders decreased with time, as well as the cross-section area of the ditch. The material was removed from the shoulders to fill up the ditch.

The total volume of the shoulders at time t , $V(t)$, consists of a recoverable part by viscoelasticity, $V_{\text{vis}}(t)$, and an unrecoverable part of permanent plastic deformation, V_{pl} . The decrease of the volume of recoverable part $\delta V_{\text{vis}}(t)$ in a small time interval δt is proportional to δt as well as the existing volume of the recoverable part $V_{\text{vis}}(t)$, thus we have



A_{ind} : Cross-section area of the indentation

A_{dit} : Cross-section area of the ditch

A_{shs} : Cross-section area of the two shoulders

A_{trgh} : Cross-section area of the trough

Micro Mar Resistance: F_N / A_{trgh}

Elastic Recovery: $(A_{ind} - A_{dit}) / A_{ind} \cdot \%$

Plastic Deformation: $A_{shs} / A_{ind} \cdot \%$

Abrasive Wear: $(A_{dit} - A_{shs}) / A_{ind} \cdot \%$

Figure 5. Schematic illustration of how to calculate micro mar resistance (MMR) and how to calculate different responses of the coating to marring stress.

Table I. Micro Indentation Hardness (MIH), Micro Mar Resistance (MMR), and Responses to Marring Stress of Three Coatings at $126\mu\text{N}$

Coating	MIH (MPa)	MMR (GPa)	Elastic %	Plastic %	Fracture %
PE	9.2	3.5	97	1	2
PU	76	1.0	58	43	0
AC	53	0.64	21	14	65

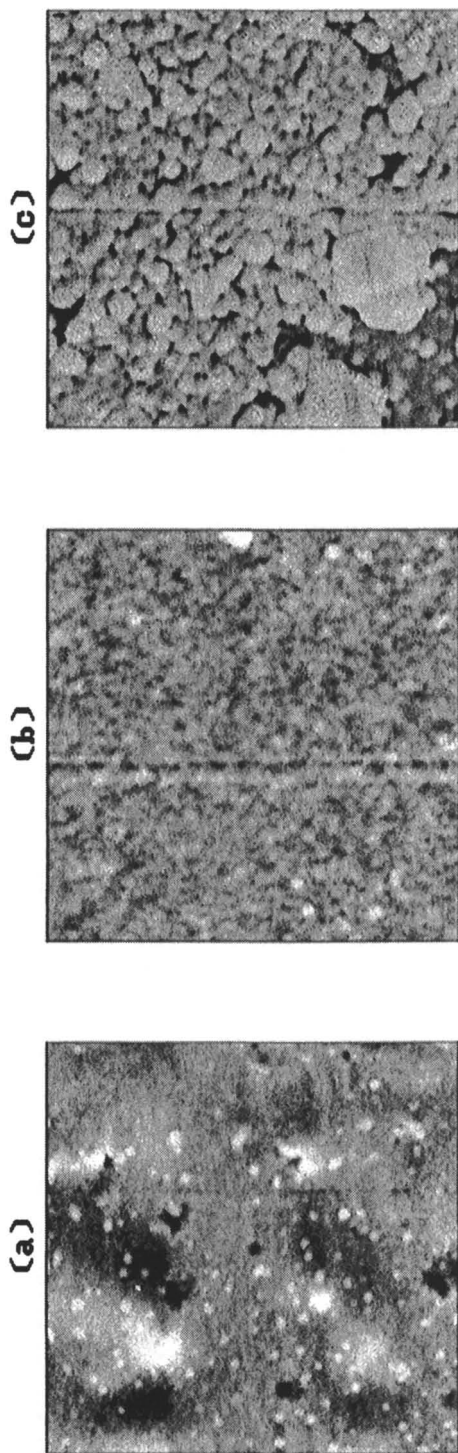


Figure 6. Images, 1 μm by 1 μm , of coating AC, PU, and PE with a nano scratch at their surfaces are shown in (a), (b), and (c) respectively.

$$\delta V_{\text{vis}}(t) = -k V_{\text{vis}}(t) * \delta t \quad (5)$$

where k is a proportionality constant. Through simple integration, we have

$$V_{\text{tot}}(t) = V_{\text{vis}/\text{ini}} * e^{-kt} + V_{\text{pla}}, \quad (6)$$

where the integration constant $V_{\text{vis}/\text{ini}}$ is the initial volume of the recoverable part immediately after the marring.

Figure 7 is a plot of the measured total volume of shoulders of a mar, made under a normal force of $190\mu\text{N}$ at the surface of an Acrylic Polyol / HDI coating obtained from Bayer Corporation, over a six hour period, and the theoretical predicted value, with the recovery rate $k=0.02/\text{min.}$, $V_{\text{vis}}=6.86\mu\text{m}^3$, and $V_{\text{pla}}=0.21\mu\text{m}^3$. They agreed with each other very well.

Through the study, it was found the rate k is independent of the size of mars made under different normal forces, and is determined by the properties of the coating and influenced by temperature and humidity. Immersing the coating in water for a few minutes will greatly promote recovery.

In the study of strain-hardening, micro cracking, and surface fatigue, a $245\mu\text{N}$ normal force was applied to the tip, as the tip moved laterally to mar the surface. One-scrape marring, two-scrape marring, -----up to a 22-scrape marring was executed in the same path, respectively, on the surface of a coating supplied by Bayer Corporation. The coating was made by crosslinking a mixture of acrylic and polyester polyols with a mixture of polysocyanates. It showed a micro phase separation; the round-shaped domains of the dispersed phase embedded in the continuous matrix phase.

Figure 8 shows a plot of depth of the ditches versus the number of the scrapings. The first single scraping made a ditch of 54nm deep, and one more scraping increased the depth by about 20nm . The rate of increase in depth decreased with the additional scrapings, and the depth reached a saturated value after six scrapings. However, as the scraping was repeated at the same trench, the depth began to increase again after 10 scrapings at a roughly constant rate of 10nm per scraping.

To analyze the coating under repeated scrapings, a model proposed by Johnson (15) for indentation analysis was used. The coating under scraping consists of three zones, (i) a core immediately underneath the tip that is under hydrostatic pressure, (ii) a plastic zone that surrounds the core, and (iii) a large elastic hinterland that surrounds the plastic zone, as show in Figure 9. In this analysis, the material around the ditch did not reach its plasticity limit after a single scraping. Thus, continuous scraping increased the depth of the ditch, and caused further plastic deformation. However, the increase of the depth after each additional scraping decreased due to the hardened walls of the ditch that had been plastically worked in the previous scrapings. After six scrapings in the test, the material surrounding the ditch had reached its plasticity limit and could not be further deformed; a rigid-plastic zone was fully established. The stress exerted by the tip was transmitted, through this

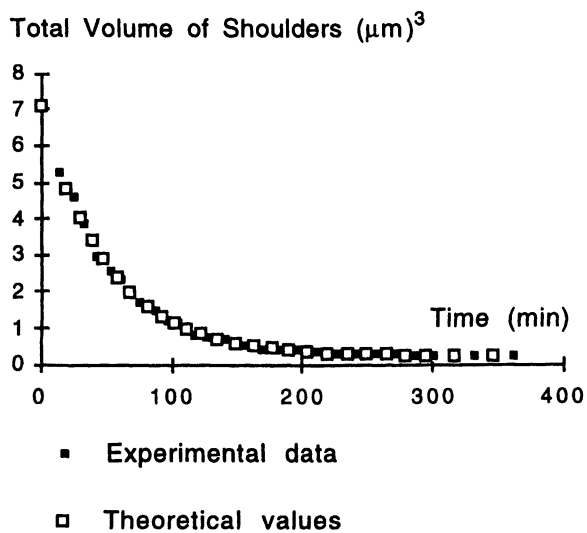


Figure 7. Comparison of experimental data and theoretical values of the total volume of the shoulders of a mar, made under a normal force of $190\mu\text{N}$, over a period of six hours.

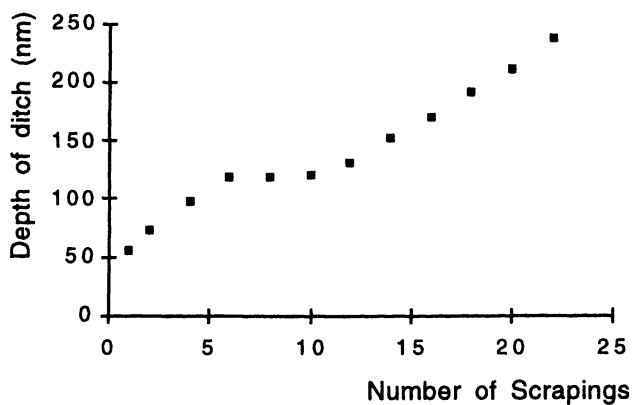


Figure 8. Depth of ditch versus the number of scrapings.

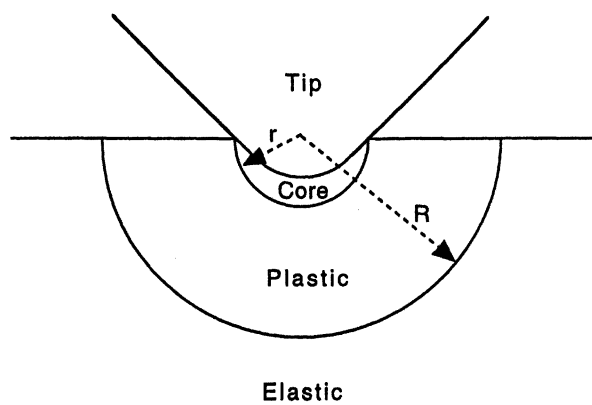


Figure 9. Johnson's three zone model: hydrostatic core of radius r , plastic zone of radius R , and elastic hinterland.

rigid plastic deformed zone, to the large hinterland zone. Under the reduced stress over the large zone, the hinterland was elastically deformed, and it recovered immediately after the tip moved over. An equilibrium was reached, hence, a saturation depth was obtained. Although the equilibrium was reached, fatigue processes would be expected to lead to wear eventually, as a result of the repeated plastic working. Due to the sufficiently high hydrostatic pressures, the materials immediately adjacent to the tip were prevented from cracking. Instead, cracks were generated in the subsurface, and they did not propagate and emerge at the bottom of the ditch after the first several scrapings. However, the continuous repeated scraping provided the energy for crack propagation, and promoted surface fatigue. After 10 scrapings, the cracks began to emerge at the bottom of the ditch, and formed a broken fragile surface. Thus, the tip began to remove the weakened surface, layer by layer, at a roughly constant rate of 10nm per scraping.

The images at the bottom of the ditch after different numbers of scrapings support this analysis. Figure 10 (a) is the image of the coating surface before scraping. It consists of continuous matrix phase and dispersed phase. The bright round-shaped spot protruding at the top surface are the domains of the dispersed phase, which are embedded in the continuous matrix phase. (b) is the image at the bottom of the ditch after the first scraping. Some dispersed phase domains were removed away by the tip; the others were squeezed into the surface to different extents. After six scrapings, only a few domains of the dispersed phase remained at the surface. Most of them were either swept off or squeezed into the continuous matrix underneath. At this stage the surface was pretty smooth and firmly compressed, but no cracks emerged at the surface yet, as shown in (c). (d) is a typical image for the bottom of the ditch after more than 10 scrapings. The cracks emerged at the bottom of the ditch, forming a broken matrix phase with squeezed dispersed domains embedded in it.

Summary

We have used a scanning probe microscope equipped with a custom-made probe to investigate tribological properties of polymeric surface coatings, measuring mar resistance, identifying different responses of coatings to marring stress, studying the dynamic process of marring, such as viscoelastic creep, strain-hardening, micro crack developing, and surface fatigue at micron and submicron scales. The SPM has been proved to be a very useful instrument in nanotribology.

Acknowledgments

Support of this work by the National Science Foundation Industry/University Cooperative Research Center in Coatings at Eastern Michigan University and by an Eastern Michigan University Faculty Research Fellowship is gratefully acknowledged.

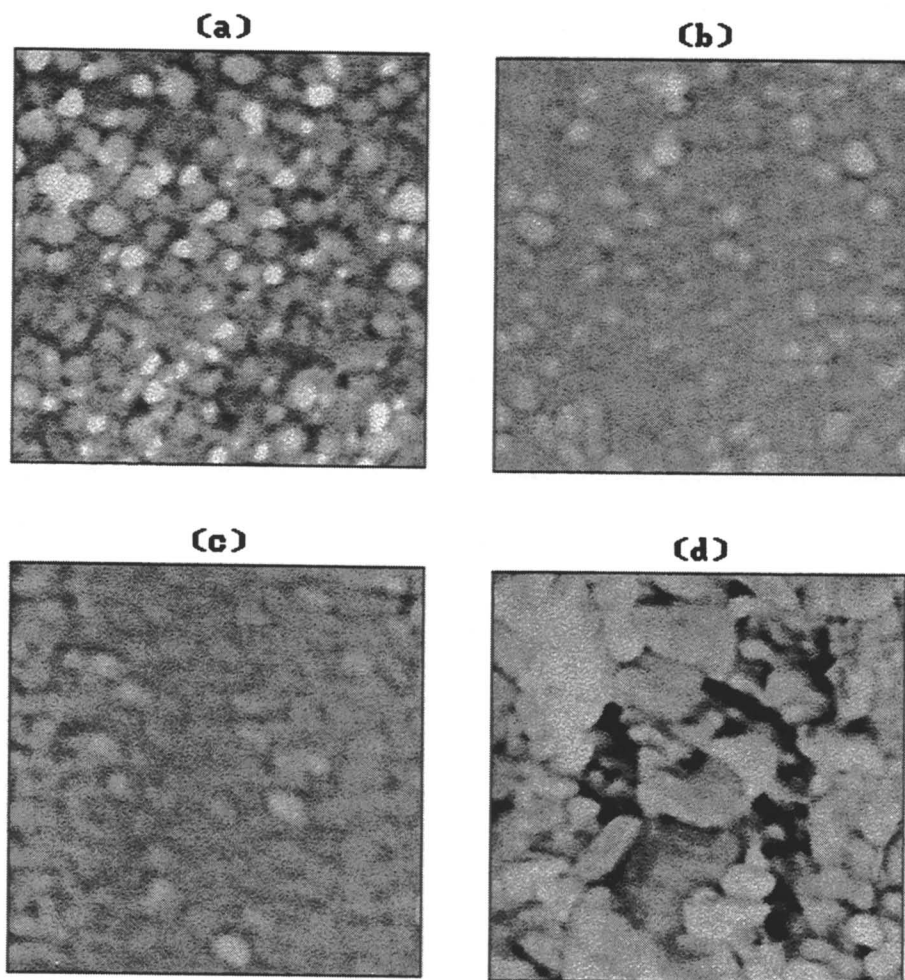


Figure 10. Images, 0.64 μm by 0.64 μm , of the surface before scraping, and at the bottom of the ditch after 1, 6, and 10 scrapings are shown in (a), (b), (c), and (d), respectively.

References

1. Gregorovich, B. V.; McGonigal, P. J. *Proc. Adv. Coat. Technol. Conf. ASM/ESD*, **1992**, 121.
2. Kahl, L.; Halpaap, R.; Wamprecht, C.; *Surf. Coat. Intl.* **1993**, 73, 394.
3. McGinniss, V. D. *Paint & Coat. Ind.* **1994**, 34.
4. Tonge, J. S.; Blizzard, J. D.; Schmidt, S. M.; Washer, T. R. *Proc. 22nd Intl. Waterborne, High-Solids and Powder Coat. Symp.* **1995**, 22, 432.
5. Courter, J. L. *J. Coat. Tech.* **1997**, 69, 56.
6. Nordstrom, J. D. *Proc. 22nd Intl. Waterborne, High-Solids and Powder Coat. Symp.* **1995**, 22, 492.
7. Jacobs, P. B.; Engbert, T. *Proc 5th Ann. ESD Adv. Coat Conf. Expo* **1995**, 29.
8. Shen, W.; Ji, C.; Jones, F. N.; Everson, M. P.; Ryntz, R. A. *Surf. Coat. Intl.* **1996**, 79, 253.
9. Shen, W.; Smith, S. M.; Jones, F. N.; Ji, C.; Ryntz, R. A.; Everson, M. P. *J. Coat. Tech.* **1997**, 69, 123.
10. Jones, F. N.; Shen, W.; Smith, S. M.; Huang, Z.; Ryntz, R. A. *Prog. Org. Coat.* **1998**, 34, 119.
11. Shen, W.; Smith, S. M.; Ye, H.; Jones, F. N. *Tribol. Lett.* **1998**, 5, 75.
12. Shen, W.; Ye, H.; Jones, F. N. *Tribol. Lett.* **1998**, 5, 197.
13. Betz, P.; Bartelt, A. *Prog. Org. Coat.* **1993**, 22, 27.
14. Sano, S.; Yamada, K.; Ishihara, M. *Toso Kagaku* **1994**, 29, 475.
15. Johnson, K. L. *J. Mech. Phy. Solids* **1970**, 18, 115.

Chapter 29

Friction and Durability of Chemisorbed Organic Lubricants for Microelectromechanical Systems

M. T. Dugger, D. C. Senft, and G. C. Nelson

Sandia National Laboratories, P.O. Box 5800, MS 0340,
Albuquerque, NM 87185-0340

Processing constraints on materials for micromachines frequently result in self-mated contacts. Adhesion aside, this situation is undesirable from a tribological perspective. Friction and wear at such contacts can be mitigated with the use of surface treatments. We describe methods for quantifying the tribological behavior of surface treatments for polycrystalline silicon in surface micromachining. Results of scanning probe microscopy to examine the frictional behavior of contacts at the nanoscale are discussed. We also discuss the use of specially fabricated testers for quantifying the friction between sidewalls of polycrystalline silicon structures. As examples of application of these techniques, we present results of surface treatment of silicon surfaces with silane-based coupling agents as molecular scale lubricants.

Surface micromachined electromechanical devices on silicon substrates represent a popular fabrication route to micro-electromechanical systems (MEMS), due to the infrastructure and process knowledge available from the semiconductor industry. Although the number of materials compatible with silicon surface micromachining is large, material selection may be constrained by process temperatures or chemical compatibility, particularly in cases where the micromachine is to be integrated with CMOS logic. Surface treatments can be used to improve interfacial properties where the composition of the structural elements is constrained.

Adhesion between polycrystalline silicon members or the substrate (referred to as "stiction") can lead to failure of microelectromechanical systems. This adhesion can occur during processing, when the hydrophilic surfaces present after wet chemical release etching are dried in air and capillary forces bring the surfaces into contact (1). Adhesion may also occur in use, between surfaces left in contact for long periods of time or brought together by mechanical shock. Mastrangelo (2) discussed the mechanisms of adhesion-related failure, and suggested that low energy monolayer

coatings, such as silane films, are the most effective and reliable adhesion prevention methods. Maboudian and Howe (3, 4) reviewed several methods for adhesion reduction including chemisorbed molecular monolayer coatings, concluding that back-end processes such as packaging are likely to limit the applicability of adhesion reducing treatments, and more work is necessary to understand the impact of these surface treatments on friction and wear.

Micromachined electromechanical devices of interest to Sandia National Laboratories can have complex mechanical interfaces, with many kinds of relative motion between structures including impact, rolling, and sliding. Recent failure analysis of micromachines consisting of rotating gears (5) shows that the median cycles to failure as a function of operating frequency can be explained by a wear model. While the material removal mechanism(s) is not known, the fact that the operating life of a microengine may be explained in terms of material removal suggests that wear processes are responsible for ultimate failure of the devices. We are investigating surface treatments to improve the friction and wear behavior of MEMS that contain contacting surfaces. The relationship between surface preparation, processing, and performance of chemisorbed alkylsilanes on silicon is the subject of this paper.

Experimental

Substrate Preparation. Flat coupons for silane deposition were 1×1 or 2.5×2.5 cm squares cleaved from (100) wafers. The coupons were either bare silicon or silicon coated with a polycrystalline silicon film deposited by low pressure chemical vapor deposition. Coupons were loaded into perfluoroalkoxy carriers for wet chemical treatment.

A variety of wet chemical surface preparation and post-cleaning drying techniques were used in an attempt to vary the surface chemistry and amount of physisorbed water available to participate in reactions with the silane head group. These generally consisted of cleaning ($\text{H}_2\text{SO}_4:\text{H}_2\text{O}_2$ mixtures from 10:1 to 2:1 at $\sim 110^\circ\text{C}$ due to exothermic reaction heat only), oxide etching ($\text{H}_2\text{O}:\text{HF}:\text{HCl}$ mixture of 100:10:1 at room temperature), and oxide regrowth ($\text{H}_2\text{O}:\text{NH}_4\text{OH}:\text{H}_2\text{O}_2$ mixture of 20:1:1 at 45°C) solutions. All chemicals were analytical reagent and low particle count electronic grades. Filtered high purity deionized water was used in solutions as well as for rinsing between the treatment steps. Times in these solutions were generally 10, 5, and 10 minutes, respectively.

In addition to wet chemical methods, some coupons were exposed to ozone under an ultraviolet lamp to promote complete oxidation and hydration of the silicon surface. Coupons were held within 1 cm of an ultraviolet lamp for 1 hour in ambient air.

Coupons were either dried in laboratory air on a clean bench, oven dried at 120°C for 1 hour, or transferred to the coating solution by solvent exchange. Coupons dried in the oven were moved between the oven and coating stations in a glass desiccator with minimal exposure to the ambient atmosphere. Coupons transferred to the coating solution by solvent exchange were moved from solution to solution, in the following sequence after the release and cleaning steps above: $\text{H}_2\text{O} \rightarrow$ isopropyl alcohol \rightarrow 1,1,2-trimethylpentane (anhydrous) \rightarrow coating solution.

Silane Deposition. Octadecyltrichlorosilane (ODTS, $C_{18}H_{37}SiCl_3$) (95%, Acros) was vacuum distilled prior to preparation of coating solutions. Vacuum distillation was carried out at a pressure lower than 2.7 Pa, and high purity argon was used to purge the distillation apparatus prior to capping the receiver flask. The distilled silane was immediately moved to a glovebox purged with dry nitrogen for storage and preparation of coating solutions.

Coating solutions consisted of 0.001 M silane in selected organic solvents. Anhydrous toluene, hexadecane, or mixtures of hexadecane with CCl_4 or chloroform were used to prepare coating solutions within a nitrogen purged glovebox. Solution volume was typically 400 to 700 ml in a perfluoroalkoxy tank, and samples were transferred to the tank in the same crystal carriers as used for substrate preparation. To examine the effect of treatment time on silane coverage, coupons were moved after various times in the coating tank to a carrier in a rinse tank that contained only the solvent. After all coupons had been moved, the rinse tank was removed from the glovebox and the carrier transferred to an alcohol bath. Coupons were ultrasonically cleaned in two successive alcohol baths for 10 minutes each, and then allowed to dry on a clean bench.

The procedure for surface treatment of micromachined tribology test devices differed slightly due to the fragile nature of the devices. Coating solutions were prepared as for coupons, but in smaller quantities (typically in 200 ml beakers). Small crystal carriers were used to move the test structure die from beaker to beaker, without allowing the surfaces to dewet. The solvent exchange method, described above, was used to transfer the structures to the coating solution. After coating, the devices were transferred through the same solutions in reverse order, and removed from water. Because the surfaces are hydrophobic after coating, the dies come out of water dry with freely moving structures.

In order to obtain released, uncoated micromachine devices for friction measurement, some devices were dried in supercritical CO_2 . In this process, the devices were transferred to ethyl alcohol after the oxide release etch and water rinse. The devices were then placed in the supercritical CO_2 process chamber while covered with alcohol. The alcohol was then dissolved in CO_2 above its triple point, avoiding the meniscus forces that pull structures together.

Table I shows the surface preparation and deposition conditions used to treat Si(100) and polycrystalline silicon films with silanes, along with the symbols used to represent these samples in Figures 2 and 3.

Coating Coverage. Several techniques were used to examine the silane coatings prior to tribological tests. These surface treatments create a hydrophobic surface and are effective in reducing adhesion between elements due to capillary attraction (6). Static water contact angle measurements were performed on all treated surfaces as a qualitative indicator of coating coverage. A 3 to 6 μ l drop of water was placed on the surface, and a side view of the droplet on the surface was captured immediately using a CCD camera and video frame grabber. Digital image analysis was used to determine the shape of the static droplet and the contact angle with the surface.

Time-of-flight SIMS (TOF-SIMS) was used to determine the amount of silane present on the surface, as well as the concentration of contaminants in the film or on the substrate. A PHI-TRIFT spectrometer was used, in which a 15 keV pulsed Ga

ion beam was rastered over an area of $\sim 90 \times 90 \mu\text{m}$. Data collection time was on the order of 1 minute. Dosage during data collection was on the order of 10^{11} ions. For comparison of the silane coverage with different treatment processes, the ratio of the C_3H_7 peak to the SiCH_3 peak was used. C_3H_7 is an ionization fragment of the silane molecule's backbone, and SiCH_3 results from the head group. Silicon dominates the spectrum at low coverage, masking any variation in coating coverage calculated using the $\text{C}_3\text{H}_7/\text{Si}$ peak area ratio. However, the $\text{C}_3\text{H}_7/\text{SiCH}_3$ ratio was found to correlate more reproducibly with coating time and with coverage measured by x-ray photoelectron spectroscopy in earlier work (7). Since these peaks are more comparable in intensity and occur near mass 43, instrument sensitivity corrections and those due to ion counting statistics are also minimized.

Table I. Surface Preparation and Solution Deposition Conditions for Silanes

<i>Surface</i>	<i>Cleaning and Oxidation</i>	<i>Dry and Transfer to Coating Solution</i>	<i>Solvent(s) for 0.001 M ODTS</i>	<i>Symbol</i>
Si(100)	1	120°C air dry	Hexadecane:CCl ₄ , 4:1	○
Si(100)	1	25°C bench dry	Hexadecane:CCl ₄ , 4:1	●
Si(100)	1, 2, 3	120°C air dry	Hexadecane	□
Si(100)	1, 2, 3	Solvent Exchange	Hexadecane	■
polySi	1, 2, 3	120°C air dry	Hexadecane	△
polySi	1, 2, 3	Solvent Exchange	Hexadecane	▲
Si(100)	1, 2, 3	4	Hexadecane:CCl ₄ , 4:1	▽
Si(100)	1, 2, 3	4	Hexadecane	▼
polySi	1, 2, 3	4	Hexadecane:CCl ₄ , 4:1	◇
polySi	1, 2, 3	4	Hexadecane	◆
Si(100)	1	25°C bench dry	Toluene	+

¹ H₂SO₄:H₂O₂, 10:1 ratio, 10 min.

² H₂O:HF:HCl, 100:10:1 ratio, 90 min.

³ H₂O:H₂O₂:NH₄OH, 20:1:1 ratio at 45°C, 10 min.

⁴ Dry clean 1 cm from an ultraviolet lamp in air for 1 hour.

Friction Measurements. Macroscopic friction coefficient between treated Si(100) flats and polished semiconductor grade SiO₂ balls 3.2 mm in diameter (Specialty Glass Products, Willow Grove, PA) was measured using an ICS-200 pin-on-disk tribometer (Falex Corporation). A normal load of 10 gf and sliding speed of 2 cm/s was used for all experiments. The friction force was captured at a rate of 5 Hz, and sliding continued until a friction coefficient above 0.5 was observed, accompanied by visible damage to the Si flat.

Samples of Si(100) or blanket polycrystalline silicon on Si(100) were examined in a scanning probe microscope (Park Scientific Instruments Autoprobe LS) using an etched silicon probe. Probes were untreated, and had a nominal radius of curvature of 10 nm. Imaging forces measured by the deflection of the cantilever (Ultralever 'B' with normal spring constant of 0.24 N/m) were between 30 nN compressive and 5 nN tensile.

Friction between micromachine structural elements was determined using the specially-designed tribology test structure shown in Figure 1. This device is designed to produce sliding contact between two etched surfaces that are perpendicular to the wafer (sidewalls). Other micromachined structures have been used to characterize friction (δ), but these typically produce contact between a rounded dimple and the planar, as-deposited polycrystalline silicon or silicon nitride surface. Briefly, the sidewall device consists of a polycrystalline silicon post about 6 μm high, grown by low pressure chemical vapor deposition of silicon in a deeply etched trench. The radius of curvature of the post is 2 μm . A flexible polycrystalline silicon beam makes contact with the post when loaded by an electrostatic comb drive acting perpendicular to the axis of the beam ('N' drive). The normal load is determined from the deflection of the comb as a function of voltage, the electrostatic force constant, and the spring constants of the comb suspension. The beam is oscillated with respect to the fixed post using a second comb drive acting parallel to the axis of the beam ('T' drive). The device is operated on a vibration-isolated probe station in a class 10 clean bench, in laboratory air (10 to 50 % relative humidity) at room temperature ($22\pm 3^\circ\text{C}$). The 'T' drive, which oscillates the beam against the post, is driven by a square wave output (100 Hz) to a programmable power supply. The position of the movable beam structure at its limits of travel is determined by flashing a strobe and grabbing an image at phases of 7° and 187° of the drive signal, so that the location of the beam at the maximum extents of its motion is captured. Position of the beam is determined by an image processing algorithm that searches for a feature on the beam, and calculates its position with respect to a fixed feature on the wafer surface. A force balance on the test device when in contact and when out of contact allows the friction force at the contact between the beam and the post to be determined from the difference in displacement as follows. The electrostatic force produced by the comb drive is given by

$$F_c = \frac{n\epsilon_0 h}{g} V^2 = (k_c + k_b)\delta_0 \quad (1)$$

where n is the number of fingers, ϵ_0 is the dielectric constant, h is the height of the fingers, g is the gap between fingers, V is the relative voltage between the opposing teeth of the comb, k_c is the stiffness of the comb suspension springs, k_b is the stiffness of the beam in bending, and δ_0 is the displacement of the comb in the absence of a load. Equation 1 indicates that a plot of comb displacement versus the square of applied voltage should yield a line of slope equal to

$$\frac{\delta_0}{V^2} = \frac{n\epsilon_0 h}{g(k_c + k_b)} \quad (2)$$

Each device is calibrated prior to use, and a typical value of the proportionality constant is $3.1 \times 10^{-3} \mu\text{m}/\text{V}^2$. In the absence of contact, a force balance on the device yields

$$(F_c - k_c\delta) - k_b\delta_0 = m \frac{d^2x}{dt^2} \quad (3)$$

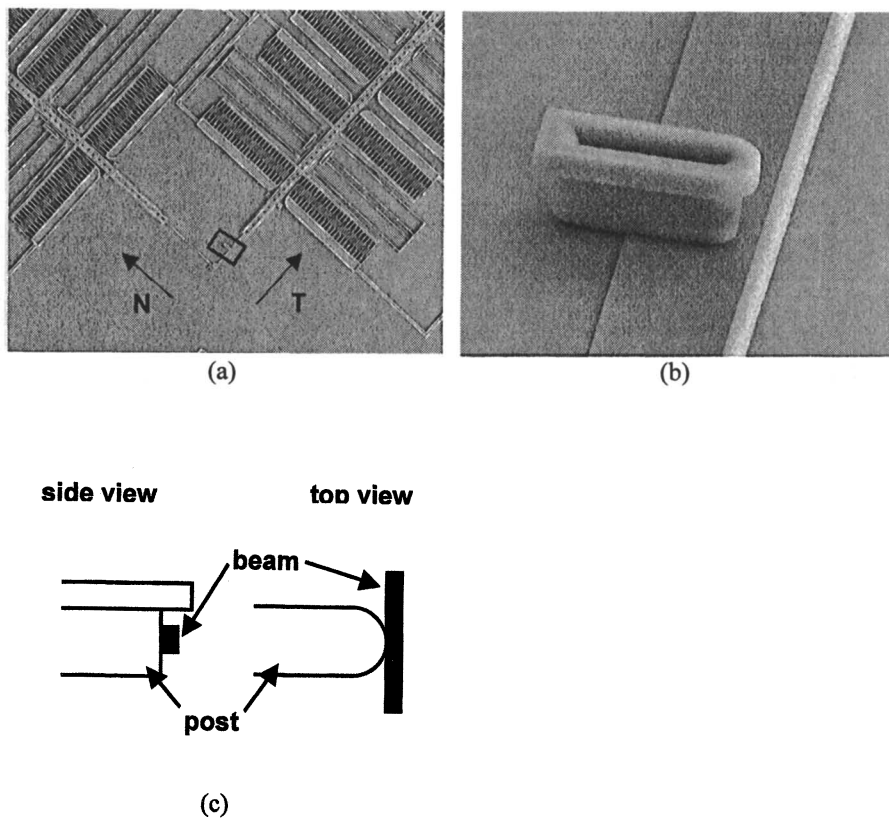


Figure 1. Device for measuring friction coefficient between etched polycrystalline silicon sidewall surfaces. The entire structure is shown in (a), a close-up of the contact area in (b), and schematic of the contact geometry in (c).

If the beam is pulled into contact with the post creating a friction drag force f_d , the force balance becomes

$$(F_c - k_c \delta) - k_b \delta_0 - f_d = m \frac{d^2 x}{dt^2} \quad (4)$$

Since the output force of the comb drive is the same in both cases, we may express equations 3 and 4 in terms of F_c , equate, and solve for f_d , yielding

$$f_d = (k_c + k_b)(\delta - \delta_0) = \frac{n \varepsilon_0 h}{g} V^2 (\delta - \delta_0) \quad (5)$$

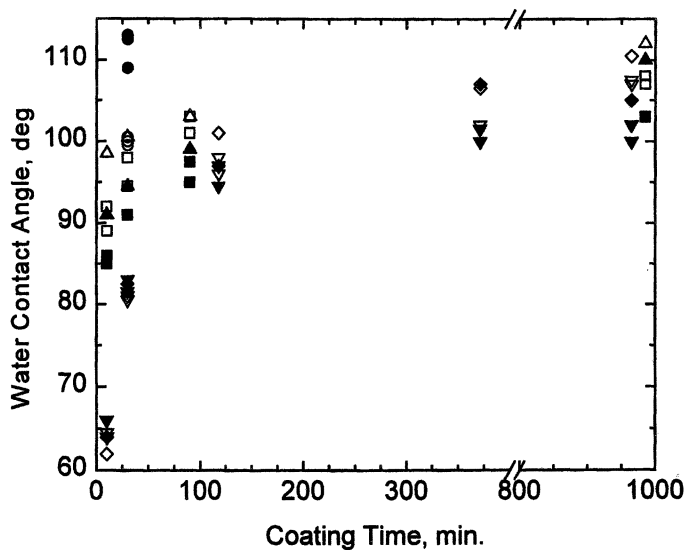
Uncertainties in friction force then result from uncertainties in the measurements of n , h and g , as well as the displacement of the beam. The friction coefficient can then be calculated from the measured friction force divided by the applied load.

Results and Discussion

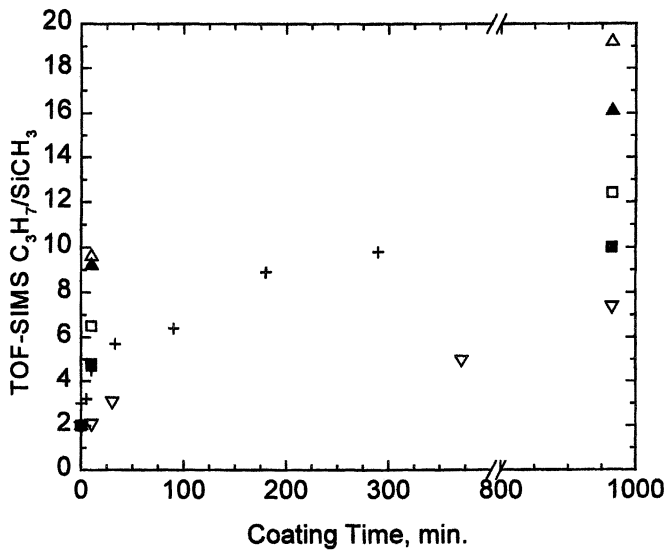
Silane Coverage vs Processing Conditions. Figure 2a shows water contact angle as a function of coating time for ODTS films formed using a variety of surface preparation techniques and deposition solutions. The data show that after about 100 minutes, all deposition processes result in a hydrophobic ($> 90^\circ$ contact angle) surface. The rate at which contact angle increases with treatment time varies with process at short treatment times. In Figure 2b, the coverage of silanes has been measured as a function of coating time for the same samples as in Figure 2a, by using SIMS peak area ratios as a measurement of coverage. Large differences in the amount of silane on the silicon surface as a function of process and treatment time can be seen in Figure 2b.

In Figure 3, the data in Figure 2 is plotted as contact angle as a function of silane coverage as measured by SIMS. This figure shows that at coverages above that required to produce a hydrophobic surface, the water contact angle is not a sensitive measurement of the amount of silane on the surface. Water contact angle is frequently used as a qualitative measure of coating integrity when depositing silane films for adhesion reduction in micromachines. The important result of this data is that silane-treated surfaces that are hydrophobic may have dramatically different amounts of molecules adsorbed on the surface, which may be expected to exhibit different friction and wear behavior. Therefore, while contact angle may be sufficient to determine when micromachine surfaces are hydrophobic to prevent adhesion of structural elements, a more quantitative measure of coverage is required to produce surfaces with consistent tribological behavior.

Macroscopic Tribological Performance of ODTS. Macroscopic friction tests were performed on coated Si(100) samples in contact with polished balls of semiconductor grade SiO_2 . Sliding tests were performed in laboratory air at 11% relative humidity. Figure 4 shows the relationship between friction, coating durability, and ODTS coverage measured by SIMS. The initial friction coefficient was determined for the first few cycles of sliding, before damage to the substrate had occurred. The figure



(a)



(b)

Figure 2. Static water contact angle (a) and coverage measured by SIMS peak area ratios (b) ODTs-coated silicon. Symbol descriptions are given in Table I.

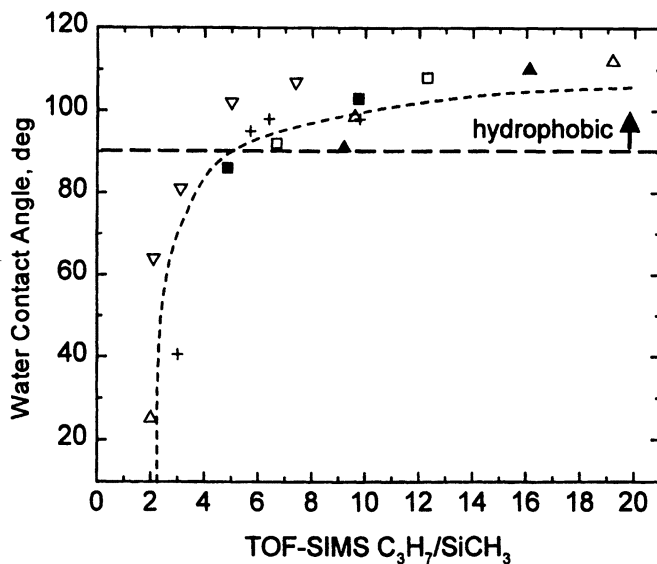


Figure 3. Static water contact angle as a function of ODTS coverage on silicon as measured by SIMS peak area ratios. Symbol descriptions are given in Table I.

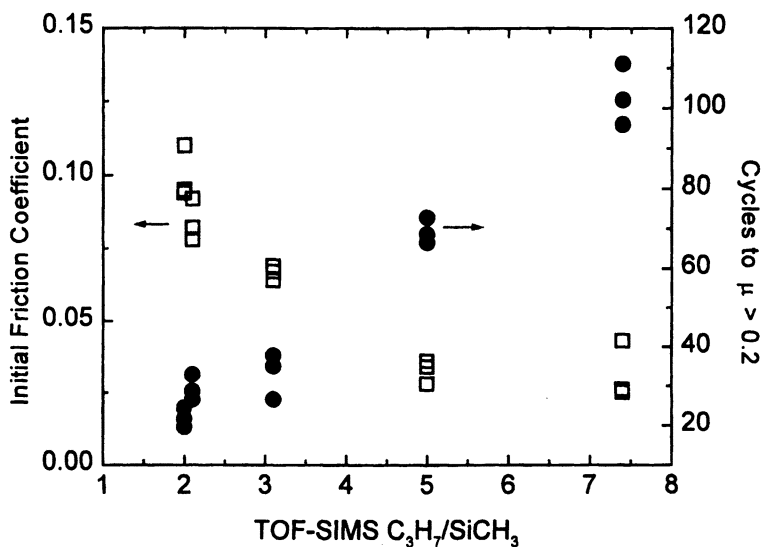


Figure 4. Initial friction coefficient and number of sliding cycles for friction coefficient to exceed 0.2, as a function of ODTS coverage measured by SIMS.

shows that the starting friction coefficient decreases monotonically as the amount of ODTS on the surface increases. As a qualitative measure of the ability of the coating to protect the silicon surface, the number of sliding cycles required for the friction coefficient to exceed 0.2 was determined and is also plotted in Figure 4. This data also shows a monotonic dependence on ODTS coverage. The macroscopic friction tests on ODTS-coated Si(100) as a function of coverage show that both the initial friction and the ability of the coating to protect the surface depend on the amount of silane chemisorbed on the surface.

SPM Response of ODTS Films. Quantitative friction coefficient measurements from scanning probe microscopes with compliant cantilevers are complicated by a number of instrumental parameters and uncertainty about the contact geometry. An excellent treatment of this subject has recently been published (9). For purposes of this work, only relative changes in the lateral force will be discussed, and these have been determined by subtraction of the forward and reverse scan images to yield lateral force images where "high" intensity or more positive detector output corresponds to higher friction force. To minimize tip geometry effects, all measurements in a single group (i.e. plotted on a single graph) were acquired with the same tip. We first wished to verify that adsorption of ODTS reduced the friction force observed in a SPM measurement between an untreated tip and the Si(100) surface. In order to create areas selectively covered with ODTS, a photoresist was deposited and patterned on a Si(100) surface. This photoresist was deposited without the adhesion promoter (another silane) typically used. After etching the photoresist to form a pattern of parallel lines, the sample was placed under an UV lamp to remove any residual organic contamination from the bare areas, as well as promote oxidation of the Si surface. ODTS was deposited on this surface using the procedures for Si(100) flat specimens, and the photoresist was then removed by ultrasonic cleaning in acetone. The ODTS bound to the surface is not removed, but any unbonded ODTS as well as the photoresist is removed. This left a pattern of lines coated with ODTS, separated by bare areas without ODTS. A friction force measurement on such a surface is shown in Figure 5. TOF-SIMS was used to verify that ODTS was present in the area that exhibited lower friction force in the SPM. TOF-SIMS also showed that the bare surface was clean, showing only minimal organic contamination. This data confirms in a single measurement, where instrument parameters and tip shape are constant, that the friction force is reduced on the area covered with ODTS compared to bare Si.

Scanning probe microscope experiments have been conducted to determine how chemisorbed ODTS films respond to compressive and shear stress in a single asperity contact. Films of a variety of coverages have been examined using conventional AFM cantilevers with silicon probes, and both topography and lateral force images are acquired simultaneously. Figure 6 shows the results of a typical experiment of this type. We begin by scanning the probe over the treated Si(100) surface at constant applied force to create an area $\sim 2 \mu\text{m}$ square that has been contacted by the probe. Additional areas may be created nearby using different contact parameters. After the probe has scanned several areas, we then increase the size of the scan and make a single pass over the previously scanned areas while simultaneously measuring the vertical and torsional displacement of the cantilever. The results are

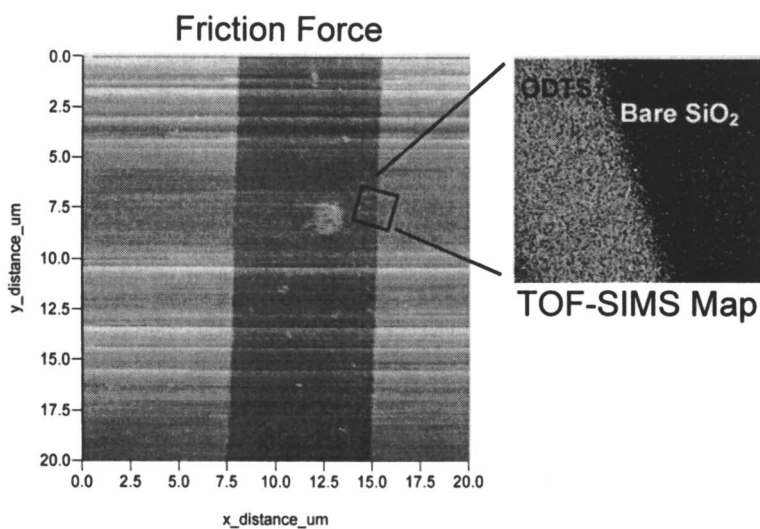


Figure 5. Lateral force and SIMS images of patterned ODTs on silicon, showing lower friction in the area that contains the silane film.

shown in Figure 6a, which is a lateral force image from a single scan that includes the four smaller areas that were previously scanned three times by the probe. For some ODTS films, we find a change in the lateral response of the film after scanning. The signal from the lateral force detectors has been mapped to intensity in the image so that bright represents high force, and dark represents low force. Therefore, the areas previously scanned exhibit lower lateral force than those scanned for the first time. The image intensity reflects some tilt in the sample from top to bottom of the image. Comparison of the lateral force in the areas scanned many times with the regions horizontally adjacent indicates that the magnitude of this change in force does not depend upon whether the smaller area was scanned at low or high applied force. The topography image acquired simultaneously shows no significant change in height that accompanies this change in lateral force response. Figure 6b shows that while the topography is unchanged compared to the surrounding area, the lateral force for previously scanned areas is decreased, whether the area is scanned under compressive or tensile force. Changes in the frictional response of NH_2 -terminated silanes after scanning at high loads has been previously reported (10), but the mechanism responsible for this change was not determined. Much more research is required to understand the mechanism for this change in lateral force with rubbing, and how it depends upon the molecular configuration of the coating. However, we hypothesize that scanning of the coated surface facilitates alignment of the ODTS molecules, which would tend to increase van der Waals interactions between the chains. Increased van der Waals interactions would stiffen the film, and reduce the vibrational and rotational modes available to the molecules to dissipate energy. The friction coefficient of the aligned regions should therefore be less than that in regions that have not been aligned by shear.

Friction of Silane Films Measured by Micromachined Structures. The friction response of silane films in a micromachined device has been examined with the sidewall device, and compared to the behavior of the device after supercritical drying alone. Results of displacement amplitude as a function of time are shown in Figure 7. The general features of the data are the same for the treated and untreated surfaces, although the calculated friction coefficient and duration of sliding are different. Figure 7a shows displacement data for a supercritically dried device in the initial stages of sliding. The figure shows the relative position of the device when sampled at the two phases of the drive signal. This displacement data can be converted into a plot of friction coefficient as a function of cycles using the approach discussed in the experimental section. After a period of smooth operation at some level of friction, the device begins to stick intermittently. This behavior is shown in Figure 7b for a device treated with ODTS. At some time when the position of the device is captured, it is located out of phase with respect to the drive signal, resulting from the device sticking during part of the operating cycle. This sticking reduces the amplitude of motion to zero, and manifests itself as a step change in the friction coefficient. The device will frequently break free at this stage and continue to operate until at some point it sticks irreversibly, so that the force exerted by the comb drive cannot break it free. Table II shows the friction coefficients and cycles to sticking exhibited by supercritically dried devices and those treated with ODTS.

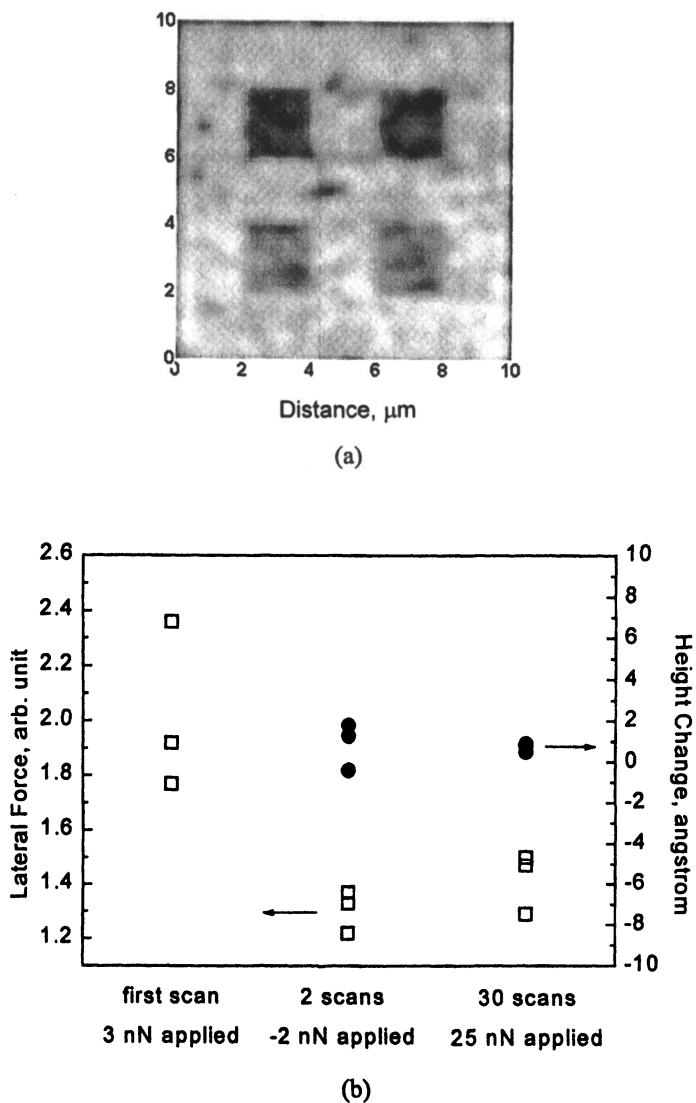
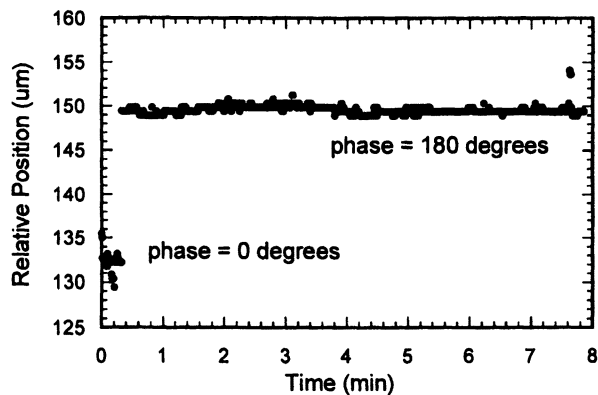
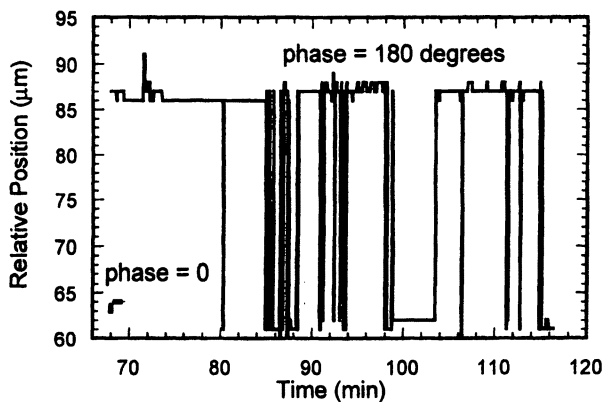


Figure 6. Lateral force image of ODTs film altered by rubbing (a), and the effect of contact conditions on the magnitude of force and height change (b).



(a)



(b)

Figure 7. Displacement amplitude versus test time at 100 Hz for the initial cycles of a supercritically dried device (a), and near failure for an ODTS-lubricated device (b).

Although the friction coefficient exhibited by the ODTS is similar to that for unlubricated structures, the sliding duration increases by a factor of three.

Table II. Friction Coefficient and Cycles to Seizure for Sidewall Devices

<i>Treatment Process</i>	<i>Friction Coefficient</i>	<i>Cycles to Seizure</i>
SC CO ₂	0.16	76,000
ODTS (C ₁₈ H ₃₇ SiCl ₃)	0.14	267,000

The morphology of tested surfaces after failure is shown in Figure 8. The beams of both structures (8a, 8c) show vertical ridges resulting from the reactive ion etch step used to form the beam and associated comb drive elements. Measurement of the sidewall roughness by atomic force microscopy results in a RMS roughness of 30 nm for this surface, compared to less than 5 nm for the polycrystalline silicon in the plane of the wafer. The beam and post (8a, 8b) from the supercritically dried structure show no evidence of wear or debris accumulation. There appear to be no changes in contact surface morphology at this scale, despite the fact that the device was tested until irreversible sticking took place at 76,000 cycles. There is, however, evidence of wear on the beam and post (8c, 8d) from the test of the ODTS-coated structure run for 267,000 cycles. The beam exhibits horizontal scratches in the direction of sliding, and the post shows an accumulation of wear debris. Duplicate experiments of this type in which sliding was stopped before the onset of sticking suggest that debris formation occurs before the devices begin to stick. In fact, devices treated for long times (high coverage) with ODTS can operate for millions of cycles after debris begins to form. The formation of scratches visible on the beam surfaces in SEM clearly suggests that the silane film has been removed in the location of the scratches. The small size and quantity of debris, and difficulties in removing it from the surface for analysis, has prevented unambiguous compositional analysis of the debris. Knowledge of debris composition alone will not determine its role in micromachine operation and ultimate seizure. A systematic investigation of debris formation during sliding, and its impact on friction, is required to illuminate the degradation and failure mechanisms in silane-coated micromachines, and is the subject of continuing work.

Lastly, the effect of ODTS coverage on micromachine operation has been investigated using sidewall devices removed from the coating solution at two different times to vary the amount of silane on the surface. Flat pieces of Si(100) were treated with the sidewall devices, so that the structure of the resulting films could be examined using scanning probe microscopy. Due to the careful handling required of sidewall devices and limited space in the perfluoroalkoxy carriers, the Si(100) wafer pieces were not removed at exactly the same time for short coating deposition times. Figures 9a and 9b show lateral force images of the resulting coatings on Si(100) after 9 and 900 minutes in the solution, respectively. The short duration coating had a C₃H₇/SiCH₃ peak area ratio of 5 measured by SIMS, and

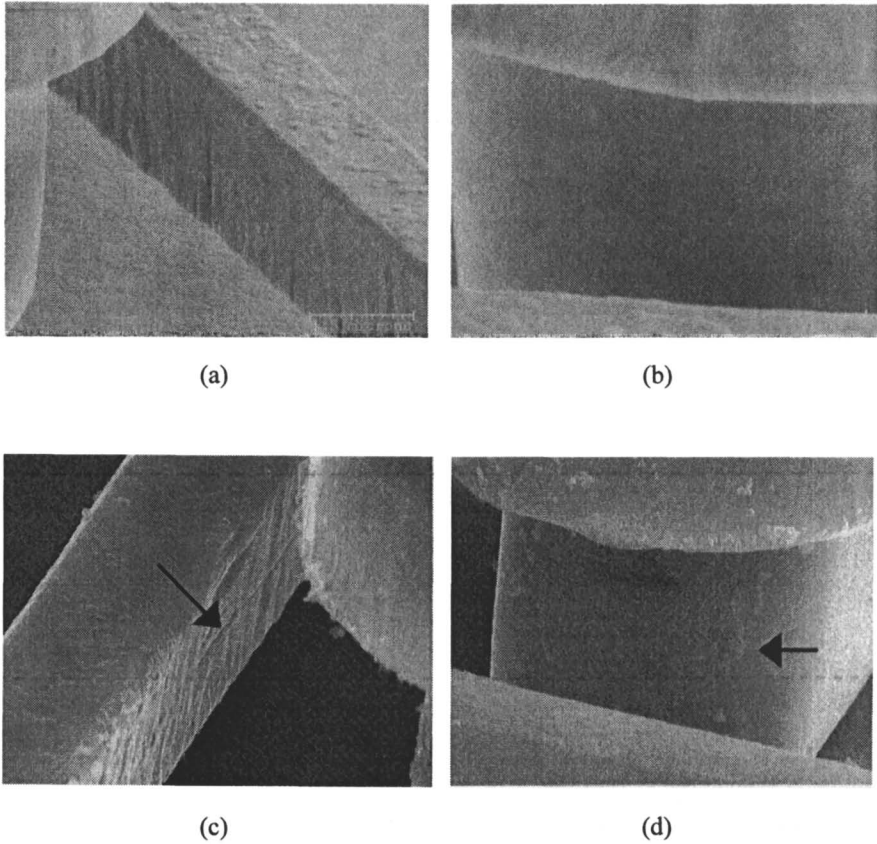


Figure 8. Contact surfaces of the beam (a) and post (b) from an unlubricated device that ran 76,000 cycles to seizure, and the beam (c) and post (d) from an ODTS-lubricated structure that ran 267,000 cycles to seizure.

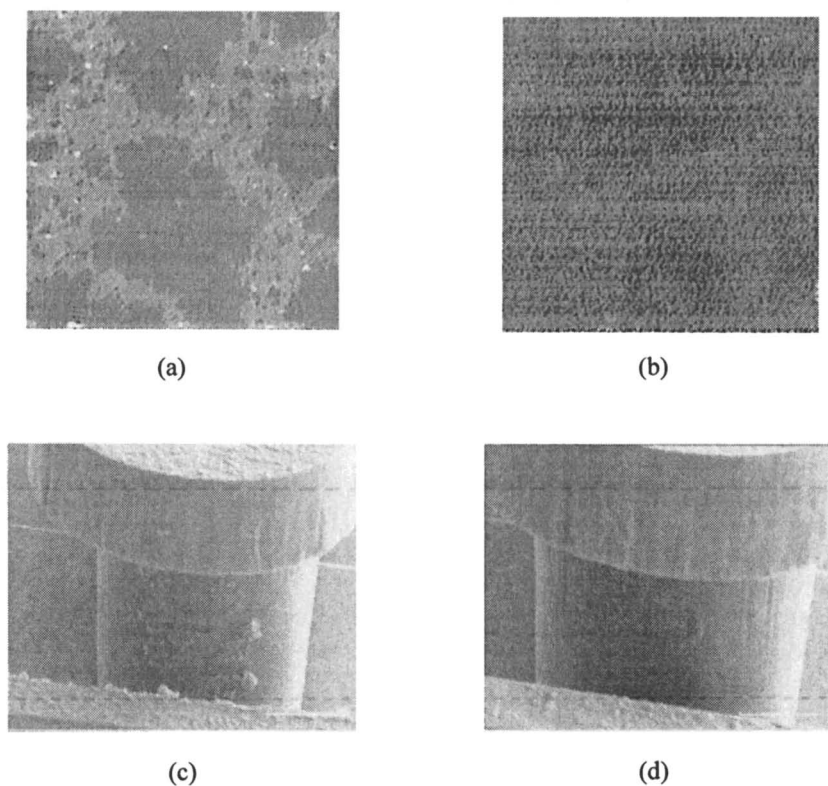


Figure 9. Lateral force image of Si(100) exposed to ODTS coating solution for 9 minutes (a), and 900 minutes (b). Contact area of the post of sidewall friction test structures exposed to the same coating solution for 5 minutes (c) and 900 minutes (d).

exhibits domains of lower lateral force surrounded by regions of higher force. These are attributed to islands of chemisorbed silane separated by uncoated regions. In contrast, the sample left in the coating solution for 900 minutes had $C_3H_7/SiCH_3 = 8$, and exhibits more uniform lateral force over the entire $2 \mu m$ scan area. Wear areas on the posts from sidewall device tests having different silane coverage are shown in Figures 9c and 9d. Both devices were operated for 3×10^7 cycles, but the estimated contact pressures are different due to slightly different loading on the two beams. Assuming line contact and an elastic modulus of the polycrystalline silicon of 150 GPa, the peak contact pressure for the device treated for 5 minutes was 90 MPa, and that for the device treated for 900 minutes was 43 MPa. The device having the greater silane coverage exhibited a smoother friction trace (average value ~ 0.17) and no evidence of sticking for the duration of the test. The device with smaller silane coverage exhibited a similar average friction coefficient, but with erratic changes and sticking after 1×10^7 cycles. Although the estimated contact pressure was higher for the device having lower silane coverage, a wear-related degradation mechanism would suggest that only the accumulated sliding duration to degrade the film would be affected, and not the friction behavior throughout the test. The intermittent sticking and erratic friction coefficient for the device having lower coverage is therefore attributed to differences in coverage alone. As in the macroscopic friction measurements as a function of silane coverage discussed earlier, these results suggest a relationship between amount of silane present and the dynamic behavior of the devices, although the mechanisms of coating degradation are not yet understood.

Summary and Conclusions

Formation of dense silane films on silicon by solution treatment is not a trivial process. Large variations in the kinetics of film formation are exhibited depending upon how the surfaces are prepared for coating deposition. While all the surface preparation processes investigated in this work allowed hydrophobic surfaces to be produced within about 60 minutes of exposure to the coating solution, quantitative measurement of the ODTS coverage by SIMS indicates that large variations in coverage are still present. While these variations in coverage may not significantly impact the performance of devices that are designed to prevent the contact of silicon surfaces, other devices which rely on the contact of surfaces are expected to exhibit performance that is dependent on the details of the surface treatment process.

Macroscopic friction measurements between untreated SiO_2 balls and ODTS treated Si(100) flats show that the friction and durability of these surfaces are directly related to the quantity of ODTS chemisorbed on the surface. Friction decreases and the number of sliding cycles required for the friction coefficient to exceed 0.2 increases as the coverage of ODTS increases.

A change in the lateral response of ODTS films to shear after repeated contact has been observed in scanning probe microscope experiments. A hypothesis consistent with the observed decrease in friction response after rubbing has been developed. Orientation of the adsorbed molecules by rubbing, resulting in increased van der Waals attraction between molecules and reduced energy dissipation modes on subsequent contact, is believed to be responsible for the observed changes. Further scanning probe experiments are required to verify this hypothesis.

Friction measurements in micromachined devices have been made using a specially fabricated structure designed to isolate a sliding contact between a moving beam and a stationary cylindrical post. As in more complex moving devices, the failure mode consists of intermittent sticking followed by seizure. Seizure has been observed without measurable wear or debris formation in supercritically dried structures, while ODTS-coated structures can operate for millions of cycles after debris and damage is observed on contacting surfaces, suggesting that debris formation and sticking or seizure are independent phenomena. Performance of micromachined structures has been demonstrated to depend upon the quantity of chemisorbed silane present.

Acknowledgments

The authors wish to thank Greg Poulter for development of the data acquisition software for the micromachined test structures. This work was supported by the United States Department of Energy under Contract DE-AC04-94AL85000. Sandia is a multiprogram laboratory operated by Sandia Corporation, a Lockheed Martin Company, for the United States Department of Energy.

Literature Cited

1. Pietsch, G.J.; Kohler, U.; Henzler, M. *J. Vac. Sci. Technol.* **1994**, *B12*, pp.78-87.
2. Mastrangelo, C.H. *Tribology Letters* **1997**, *3*, pp.223-238.
3. Maboudian, R.; Howe, R.T. *J. Vac. Sci. Technol.* **1997**, *B15*, pp.1-20.
4. Maboudian, R.; Howe, R.T. *Tribology Letters* **1997**, *3*, pp.215-221.
5. Tanner, D.M.; Miller, W.M.; Eaton, W.P.; Irwin, L.W.; Peterson, K.A.; Dugger, M.T.; Senft, D.C.; Smith, N.F.; Tangyonyong P.; Miller, S.L. *Proceedings of the International Reliability Physics Symposium*, Reno, NV, 1998.
6. Srinivasan, U.; Houston, M.R.; Howe, R.T.; Maboudian, R. *Transducers '97*, Chicago, IL, 1997.
7. Rye, R.R.; Nelson, G.C.; Dugger, M.T. *Langmuir* **1997**, *13*, pp. 2695-2972.
8. Komvopoulos, K. *Wear* **1996**, *200*, pp. 305-327.
9. Carpick, R.W. *The Study of Contact, Adhesion and Friction at the Atomic Scale by Atomic Force Microscopy*; Ph.D. Thesis, University of California, Berkeley, CA, 1997, pp.1-168.
10. Tsukruk, V.V.; Bliznyuk, V.N. *Langmuir* **1998**, *14*, pp. 446-455.

Chapter 30

Physics of Friction Applied to Medical Devices

Andrea Liebmann-Vinson

Becton Dickinson Technologies, P. O. Box 12016/21 Davis Drive,
Research Triangle Park, NC 27709-2016

Physics of friction in lubricated medical devices is discussed using the surprisingly complex friction and lubrication issues in disposable plastic syringes as a single but illustrative example. Syringes represent a particular important example of medical devices due to the ubiquitous application in modern drug delivery and in a variety of nosocomial procedures. Frictional performance in syringes is found to strongly depend on handling characteristics, namely the velocity at which the plunger is moved inside the syringe barrel. Three distinct regimes of lubricated friction, in analogy to a Stribeck curve, are revealed when studying this velocity dependence of syringe performance: (1) boundary lubrication, (2) mixed lubrication regimes and (3) hydrodynamic shear. Forces to initiate stopper motion and stick-slip motion observed when syringes are used in connection with mechanical dispensing devices (syringe pumps) are associated with the boundary and mixed lubrication regime. Hydrodynamic shear forces determine "feel" of a syringe when operated manually by hand. The velocity range of all three regimes is strongly coupled with lubricant mobility. Immobilizing lubricant treatments, such as exposure to high-energy radiation or an oxidizing plasma, cause the velocity ranges of each lubrication regime to shift. The fundamentals of friction and lubrication are thus shown to be embodied in common but important medical devices.

Introduction

Historical Perspective. Friction is a fundamental physical phenomenon occurring whenever two contacting surfaces are in relative motion. Mankind has struggled against and has used friction since ancient times, as is apparent from the earliest recorded

engineering projects in history. For example, a mural painting in a grotto at El Beresh dated from about 1900 B.C. shows a colossus being pulled along on a sledge while one man, standing in front of the sledge, pours a lubricating liquid in its path (1). Many centuries later, Leonardo da Vinci deduced two empirical basic laws of friction: (1) friction is proportional to normal load acting on the contact pair and (2) friction is independent of size of contacting bodies. These laws were lost until rediscovered about 200 years later by Guillaume Amontons, who carried out the first scientific friction studies in 1699 (2). About 1780, Coulomb added another basic rule by saying that (3) friction is independent of sliding velocity (3). However, with improved experimental techniques, it was found later that "Amontons' rules" may be regarded only as crude approximations (4-7). Elastomers and polymers are prime examples of materials for which the frictional behavior fail to follow Amontons' rules (8-14).

Theories of Friction. Many theories were put forth to explain the mechanism of friction (12, 15-18). For example, Amontons and Coulomb believed friction to originate from surface roughness. But Desaguliers discovered that smoother surfaces do not necessarily exhibit lower friction, and he was first to associate friction with adhesion occurring between contacting surfaces (2). All early theories had in common that friction was described as being a purely surface-related phenomenon. Later, it was realized that friction is not a process confined to the surface but can cause distortions propagating substantially into the sample bulk (4, 19). Bowden and Tabor's "adhesion and ploughing theory of friction" explained friction between metals as being the consequence of adhesion between areas of real contact, resulting in junction formation which have to be sheared during sliding, and plowing of asperities on the harder surface through the surface of the softer material (12, 17).

The same theory was applied to explain the sliding friction of polymers. Adhesion forces between two surfaces in contact were claimed to be the dominating contribution to the friction force for sliding of unlubricated polymer surfaces at relatively slow constant velocities. Plowing of harder asperities on the softer counterface was found to be the source of frictional forces occurring in rolling and lubricated sliding friction of polymers where formation of interfacial contacts or junctions can be prevented (12, 17, 20-23). Sliding friction of polymers and especially rubbers was found to deviate from "Amontons' (and Coulomb's) rules" in that friction force was found to be velocity dependent and, thus, reflect viscoelastic properties of these materials (8, 10, 14, 20, 24-47). Controversy about mechanisms of friction (7, 48, 49) and especially the role of adhesion in friction (50-53) exists to this day and the study of simplified model systems utilizing modern techniques of nanotribology, especially in combination with advanced computational methods, are hoped to resolve much of the existing confusion (54-59).

Lubrication. Friction in the presence of a lubricant, which is commonly used to mitigate high friction contacts, is a velocity dependent phenomenon that can be illustrated with the so-called Stribeck curve (7, 60, 61). Three regimes of lubricated friction are identified: (1) boundary, (2) mixed, and (3) hydrodynamic lubrication. Frictional problems, such as wear or friction-force fluctuations, so-called stick-slip motion, are usually associated with the mixed and boundary lubrication regime. Either velocity of the moving counterfaces is too low, pressure on the friction contact is too

high, or lubricant viscosity is too low to sustain the necessary hydrostatic pressure in the lubricant film to allow for complete separation of the moving counterfaces. It is in these regimes that physico-chemical properties of all three components, lubricant and both opposing surfaces, are important. Lubrication is essential for adequate performance of most machinery and devices comprised of moving parts. The objective of this contribution is to demonstrate that medical devices are no exception to this rule.

Medical Devices. The term "medical device" covers a broad range of instruments, implements, or implants which are used in medical care in hospitals, the physician office or in home care. Examples include wheel chairs, contact lenses, pacemakers, endoscopes, vascular prostheses, extracorporeal blood circuits, joint or bone prostheses, thermometers, scalpels, catheters and syringes, just to name a few. As a consequence of this diversity in application, many different materials (biomaterials), including metals, ceramics, glasses, carbons, composites and plastics are used. And since many of these devices have moving parts, all kinds of different friction contacts, both lubricated and unlubricated, are encountered in medical devices.

Syringes are a particularly important example of medical devices because of the ubiquitous application in modern drug delivery. Disposable plastic syringes have essentially replaced the old-fashioned glass syringes, except in some special procedures, and are today the most prevalent parenteral drug delivery device worldwide. A three-piece syringe, illustrated in Figure 1, typically consists of a polypropylene barrel and an elastomeric stopper. The stopper is affixed to a plastic plunger rod and is frequently made out of vulcanized natural rubber, isoprene rubber or styrene-butadiene rubber (62). The liquid-tight seal necessary to contain drugs or bodily fluids within a syringe is provided by an interference fit between elastomeric stopper and barrel. This interference fit creates a sealing pressure sufficient to withstand the rigors of filling and injection. A drawback, of course, is that the sealing pressure acts as a normal load on the frictional contact and thus increases the already high frictional resistance to movement of the elastomeric stopper in the barrel (63). Lubricant, usually a medical grade silicone oil (64-66), is required to mitigate this high coefficient of friction between elastomeric stopper and plastic barrel.

Sterilization is required for most medical devices in order to prevent delivery of pathogenic organism. Common sterilization methods for disposable plastic syringes are exposure to ethylene oxide gas or exposure to high energy radiation, such as an electron beam or γ -radiation from a Co^{60} source (67). Such treatments have the potential to alter the friction properties of a syringe as will be discussed briefly in this contribution.

Organization. This review is divided into three main parts and is focused on the physics of friction in disposable plastic syringes. In the first section, selected fundamentals of friction essential to friction in disposable plastic syringes are reviewed. The second and third section are concerned with frictional contacts occurring in parenteral drug administration: cutting and penetration of skin and tissue by hypodermic needles; friction between an elastomeric stopper and a plastic barrel in the presence of a lubricant. In the third section, friction related problems occurring in two typical syringe applications (manual hand and syringe pump operation) are used to

illustrate the applicability of basic physical concepts to explain friction in lubricated medical devices.

Physics of Friction

Dry Friction. Three steps, shown schematically in Figure 2, are involved in sliding a macroscopic body, which may be called slider, against a stationary substrate: (1) bringing the bodies into contact, (2) applying a normal load (in many cases this is simply the weight of the slider), where "normal" refers to the normal (perpendicular) direction with respect to the substrate surface, and (3) applying a tangential load to initiate motion, where "tangential" means parallel to the substrate surface. These three steps are discussed in more detail in the following with emphasis on the sliding friction of polymers.

Step 1: Contacting. In the first step, slider and substrate are brought into contact along the normal direction. As illustrated in Figure 2, contact will only be made in discrete spots where surface asperities from both surfaces meet, due to roughness that almost all surfaces possess (49, 68-70). In those so-called "areas of real contact", molecules from both surfaces are in intimate contact, allowing for "stickiness" to develop (71). This "stickiness" is commonly referred to as adhesion because it is due to attractive intermolecular force fields originating from all molecules situated on the surface of either substrate or slider (72-74). Attractive forces acting across the contact area (Figure 2) cause the bodies to be pulled together more closely, leading to spontaneous elastic or even plastic deformation of the contact zone and, thus, create finite contact areas even under zero external load (71, 75-78).

Contact area and stress distribution between two elastic spheres under a given external load was first calculated by Hertz in 1881 (79). His calculations were based on elastic properties of the materials and geometrical arguments, ignoring any interactions taking place across the contact area. In 1971, Johnson, Roberts, and Kendall (JRK) extended Hertz theory to include attractive interactions acting across the contact area of contacting elastic bodies (75). Later this theory was further extended by Derjaguin, Muller and Toporov (DMT) to include interactions acting just outside the contact area, in regions where the two surfaces are still in close proximity (80). The most important differences between the earlier Hertz and later JRK and DMT theories are: (1) the contact area at zero load is zero in Hertz theory, but a finite value in the JRK and DMT theories (even for slightly negative loads); (2) the contact area predicted by JRK and DMT theories is always larger than that predicted by Hertz for a given load. This phenomenon of increasing contact area due to attractive intermolecular interactions across interfaces of contacting bodies, or simply said, the "sticking together" of surfaces in contact, is commonly called "adhesion" and represents the adhesion part of the previously mentioned Bowden and Tabor "adhesion and ploughing theory of friction". This choice of nomenclature is an unfortunate one, since adhesion means different things to different scientists (according to the Dictionary of Scientific and Technical Terms, the term "adhesion" finds application with mostly different meanings in a variety of fields, such as botany, electromagnetism, engineering, mechanics, medicine, and physics (81)) (51, 82, 83). It should thus be emphasized that *adhesion in context of friction* is synonymous for the *effective force of attraction between surfaces*

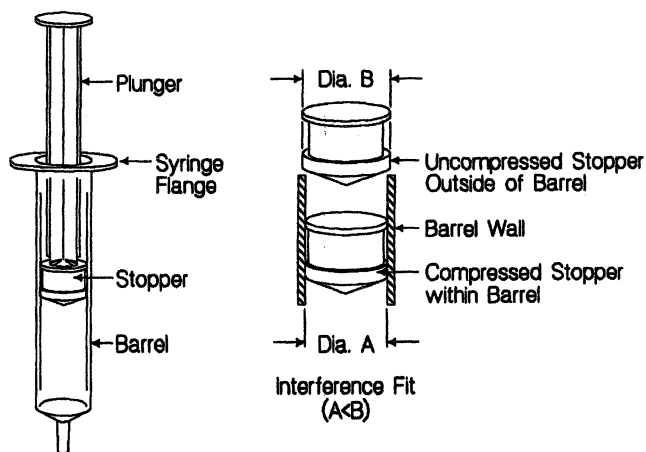


Figure 1. Schematic of a typical three-piece syringe comprised of a plastic barrel, plastic plunger rod and an elastomeric stopper. In the unassembled state, the outer diameter of the stopper (B) is larger than the inner diameter of the syringe barrel (A), providing an interference fit pressure in the stopper/syringe barrel area in the assembled syringe.

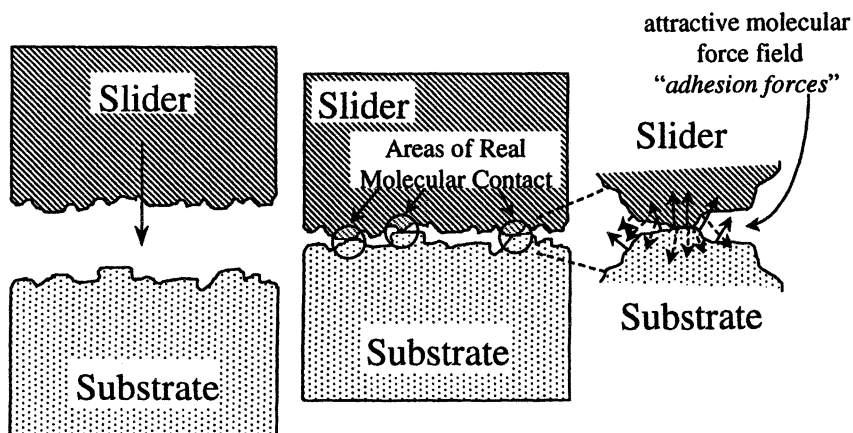


Figure 2. As slider and substrate are brought into contact along the normal direction (left), asperities from both surfaces meet to form areas of real contact (middle) and an attractive molecular force field (adhesion forces) propagates across the interface (right).

(Figure 2) (according to the physics definition, describing adhesion as the tendency for matter to cling to other matter due to intermolecular forces (81)). Possible alternative nomenclature, such as "adhesion forces" or "attachment forces", for example, could be used to avoid the confusion associated with the ambiguously defined term "adhesion".

Step 2: Loading. In the second step of the friction process (Figure 3), the real area of contact is further increased upon application of a normal load or just simply due to the weight of the slider. Surface asperities will deform, either elastically or plastically, and new areas of real contact are created until the normal load is supported by the real contact area (7, 49, 68, 84, 85). This process can be time-dependent, as is the case for viscoelastic materials such as rubber or polymers and, as a result, an increase in contact area with contact time may be observed (76).

Step 3: Shearing. In the third step (Figure 4), a tangential force is applied in order to initiate sliding. According to the classic laws of friction, sliding will start as soon as a threshold force is overcome. This threshold is called static friction and is defined as static friction coefficient multiplied by normal load. The classic law can only be true when the slider/substrate system is observed from a macroscopic point of view. Most likely, sliding will not start immediately, but rather small relative motion, so-called "micro-slips", will occur in parts of the interface until, collectively, static friction is overcome and macroscopic sliding will begin (7, 12, 49, 86). The force necessary to maintain sliding is called kinetic friction and, according to macroscopic theory, must be smaller than static friction (87). This circumstance has been explained by the observation that the static coefficient of friction is a function of contact time during which the contact area is thought to be strengthened due to either creep under load, resulting in an increase of contact area, a breakdown of surface films with time, or diffusion of molecules across the interface, leading to strengthening of junctions with time (7, 12, 49, 69, 88-91).

The detailed mechanism of sliding polymer friction remains unclear, clearly demonstrated by the inability to predict frictional performance for a given contact pair. However, it is commonly acknowledged that adhesion forces acting in areas of real contact between slider and substrate play a major role, especially in the case when no lubricant is present in the slider/substrate interface (Figure 4) (6, 7, 14, 20, 21, 23, 30, 31, 34, 39, 40, 43, 44, 47, 49, 51, 69, 87, 92-108). Improved experimental techniques, especially the surface force apparatus, have been extensively used to study the much-debated relationship between adhesion and friction (18, 73, 109-115). These approaches are limited to systems such as molecularly smooth mica surfaces and model liquids, and suggest that no direct correlation exists between friction and *adhesion*, defined as the work done on bringing two surfaces together (loading) or the energy needed to separate surfaces (unloading). But irreversible energy dissipation during such a loading/unloading cycle, referred to as *adhesion hysteresis*, seems to be directly correlated to friction.

Lubrication. The separation of slider and substrate by a liquid lubricant layer drastically changes above described processes for dry friction contacts (Figure 2).

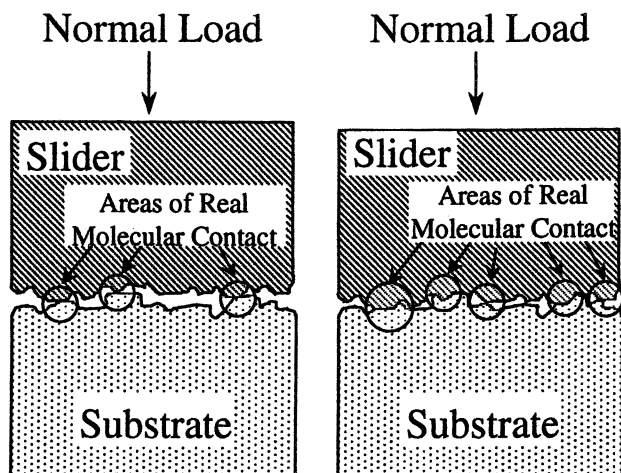


Figure 3. A normal load applied to slider and substrate in contact (left) leads to an increase in real contact area by creating new interface and with expansion of previous areas of real contact (right).

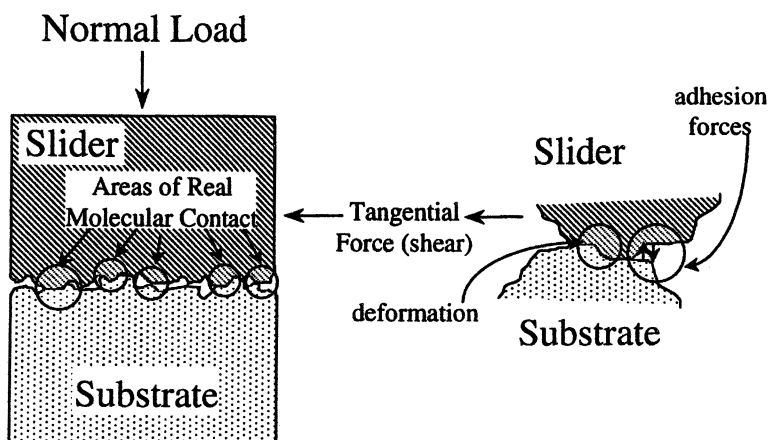


Figure 4. A tangential load applied to a slider/substrate pair in contact under normal load (left) brings asperities into locked contact adding to adhesion forces resisting tangential motion (right).

Step 1: Contacting: Assuming that a complete lubricant layer wets both substrate and slider surface, as is shown in Figure 5, contact will be made at the surface of those lubricant layers when slider and substrate are brought together along the normal direction. Consequently, no contact between slider and substrate surface occurs and, therefore, adhesion forces, which are only acting between two solids in direct contact, are minimized or even eliminated.

Step 2: Loading: The separation of slider and substrate (lubricant layer thickness) is a function of lubricant viscosity and pressure (normal load) on the contact. In addition, "aging" effects may become important since a liquid can migrate or be squeezed-out from high-pressure contacts with time (116, 117). As a result, areas of direct contact between slider and substrate and, simultaneously, adhesion forces acting between both surfaces can be reintroduced in case the lubricant layer thickness decreases with either contact pressure or time (Figure 6).

Step 3: Shearing: The shear stress necessary to initiate sliding will depend strongly on the lubricant layer thickness between the contact pairs. Once sliding has begun, friction depends on slider velocity, lubricant viscosity, and normal force acting on the friction contact. This dependence is typically illustrated in a so-called Stribeck curve (60, 61) which identifies three regimes of lubricated friction: (1) boundary, (2) mixed, and (3) hydrodynamic lubrication regime.

In the *hydrodynamic lubrication regime*, the surfaces of both bodies in relative motion are completely separated by a lubricant layer. Friction is thus determined essentially by the force required to shear the liquid lubricant (118-120). With decreasing velocity or increasing load, lubricant layer thickness decreases until finally the highest surface asperities protrude through the bulk lubricant layer. It is this direct, but partial contact between slider and substrate that defines the *boundary lubrication regime* (61, 121). This circumstance is directly analogous to loading (Step 2) described above, and these areas of direct contact lead to high friction interactions associated with deformation and adhesive forces acting between both bodies in relative motion. Chemical composition of lubricant and both moving surfaces, mechanical properties of the surface asperities, and lubricant viscosity in this confined geometry (in contrast to bulk viscosity) determine friction in this regime. The transition from hydrodynamic to boundary lubrication is called the *mixed lubrication regime* (61).

A molecularly thin lubricant layer which effectively prevents direct contact between slider and substrate is called a "*boundary lubricant*" (61, 122, 123). Friction in the presence of a boundary lubricant (direct contact in slider/substrate interface prevented by boundary lubricant) should therefore not be confused with the above defined boundary lubrication regime (partial direct contact in slider/substrate interface). In fact, the boundary lubrication regime is either prevented or moved into a regime of higher normal load or lower velocity in the presence of a boundary lubricant.

Stick-Slip Motion. Stick-slip motion, also called intermittent motion or chattering, manifests itself in friction force fluctuations, due to sliding at the interface proceeding in alternating intervals of no relative motion (stick) followed by relative motion (slip) rather than smooth, continuous sliding.

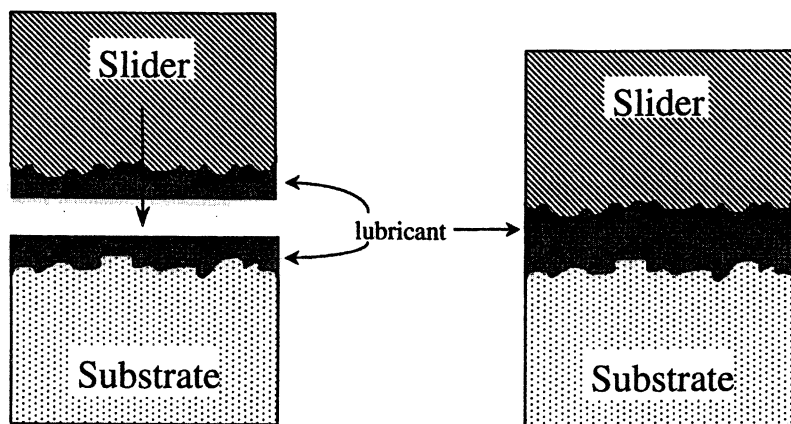


Figure 5. As lubricated substrate and slider are brought in contact along the normal direction (left) lubricant layer faces meet and, in contrast to the unlubricated case (Figure 2), areas of real contact are prevented (right).

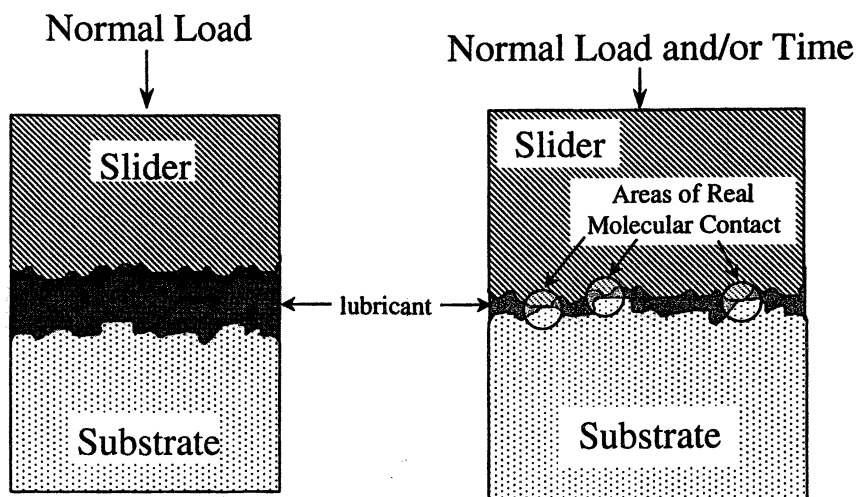


Figure 6. Under normal load (left) or with time lubricant can be squeezed out from the slider/substrate interface creating areas of real contact (right).

Stick-slip motion was first reported in 1929 (124) and first detailed studies were carried out by Papenhuyzen in 1938 and by Bowden and Leben in 1939 (4, 125). Stick-slip motion was found to occur for both dry and lubricated metal pairs and, in case of lubrication, to be associated with the boundary lubrication regime (4). A first theory to explain stick-slip motion was already presented by Blok in 1940 (121), based on the hypothesis that stick-slip motion is caused by a decreasing frictional force exerted by a dragging member with increasing sliding velocity. Using a mechanical model consisting of a block being pulled by a damped spring on a solid substrate and the hypothetical case of a definite static friction force and a constant kinetic friction force of smaller magnitude, he calculated conditions promoting stick-slip motion to occur. This early theory thus used two criteria which are still used today to explain the occurrence of stick-slip motion: (1) "velocity weakening" (decreasing frictional force with increasing velocity), and (2) pronounced difference between static (high) and kinetic (low) friction (7, 61, 87, 88, 102, 126-138). Other possible causes for stick-slip motion discussed in the literature are roughness, existence of an intrinsic deformation length, and dynamic instabilities associated with the coupling between normal and tangential motion (49, 88, 138-143).

Yet another theory has emerged recently from the field of nanotribology. Surface force apparatus studies, combined with molecular dynamics simulations, of simplified model systems, such as molecularly flat mica separated by a few molecules thick lubricant layers, have identified a solid-melt transition as the cause for stick-slip motion to occur for such confined liquids (18, 106, 111-113, 144-149). A similarly confined liquid can be found in macroscopic friction systems in the boundary lubrication regime wherein thin lubricant layers are trapped between surface asperities in very close proximity.

It is obvious from above discussion that there seems to be no single universal cause responsible for the occurrence of stick-slip motion in sliding systems. Results discussed in the third section of this contribution will show that a combination of the above mechanisms is needed to explain stick-slip motion observed in practical systems, such as a disposable plastic syringe.

Hypodermic Needle Friction

The most common pervasive parenteral drug delivery device is a hypodermic syringe with a sharp pointed needle used to puncture the skin. Absence of effective needle lubrication that is stable throughout both the insertion and withdrawal stages results in pain experienced by the patient. The pain is caused by friction between needle and skin, which usually causes some stretching of the skin, and friction caused by stainless steel moving through subcutaneous tissue. Needle lubrication is furthermore important to reduce tissue and vein trauma caused by the needle stick (150).

Hypodermic needles are produced by drawing stainless steel tubing through appropriate dies to the desirable gauge; a process which itself requires lubrication. However, changes in processing lubricants introduced in the mid-60's necessitated utilization of extreme cleaning procedures resulting in "squeaky-clean" needles. Many needle manufacturer received complaints about dullness and needle bending. Missing needle lubrication was identified as the cause and needle siliconization was introduced (151).

Thus, it has become common practice to lubricate hypodermic needles with liquid medical grade polydimethylsiloxanes. Low viscosity oils are preferred since it is common knowledge that these are generally better lubricants than oils of higher viscosity. However, such a low-viscosity liquid film coating may be easily wiped away due to frictional wiping forces during penetration of tissue, making subsequent removal of the needle difficult and painful to the patient. This problem has been solved by using silicone lubricants containing a room temperature vulcanizing silicone which serves as matrix for the low-viscosity silicone oil and thus prevents complete removal of lubricant during penetration (152). Another suggested solution was use of gelling agents to achieve a needle lubricant that readily remedies the problem of wipe-away (153).

Friction in Disposable Plastic Syringes

The overall frictional response of a disposable plastic syringe, as described in the Introduction and as shown in Figure 1, is dependent on the speed of plunger motion, due in part to velocity dependent shear of the liquid lubricant. As a consequence, handling characteristics vary depending on the application of a syringe. In the following, friction related problems occurring during two typical applications, namely manually operation by hand and use of syringes in connection with motorized devices such as syringe pumps are discussed. Finally, impact of sterilization techniques is introduced, especially with respect to frictional problems associated with γ -radiation sterilization.

Manual Syringe Operation. Syringes are used by hand in most nosocomial (pertaining to a hospital) applications and plunger motion is determined by finger pressure at the end of the plunger rod. Different plunger (stopper) motions are required for different syringe procedures. For example, slow stopper motion assures accurate volumetric measurements whereas medium stopper velocities are encountered during medicant filling. Bolus injection requires yet higher stopper velocities. In other nosocomial applications, syringes are used in conjunction with a wide variety of tubing and catheters to meter delivery of medicant, as well as in simple surgical steps such as aspiration or flushing. Manual syringe operations thus cover a broad stopper velocity range, typically between 20 and 1000 mm/min (154).

Handling Characteristics. The handling characteristic of a manually operated syringe is predominated by the force required to move a stopper in a syringe barrel. This force can be measured using an universal mechanical tester, such as an Instron (155, 156). Figure 7 shows the result of such a test for a typical three-piece syringe at a single, constant speed (100 mm/min). The initial peak in the curve represents the force that is required to initiate stopper movement, generally referred to as breakout force, and the force required to maintain steady sliding after overcoming the initial breakout is called sustaining force.

Table I compiles the relationships between measured forces, impact on syringe application and physics involved. Sustaining forces at velocities encountered during manual use of syringes are related to the hydrodynamic lubrication regime. Lubricant is

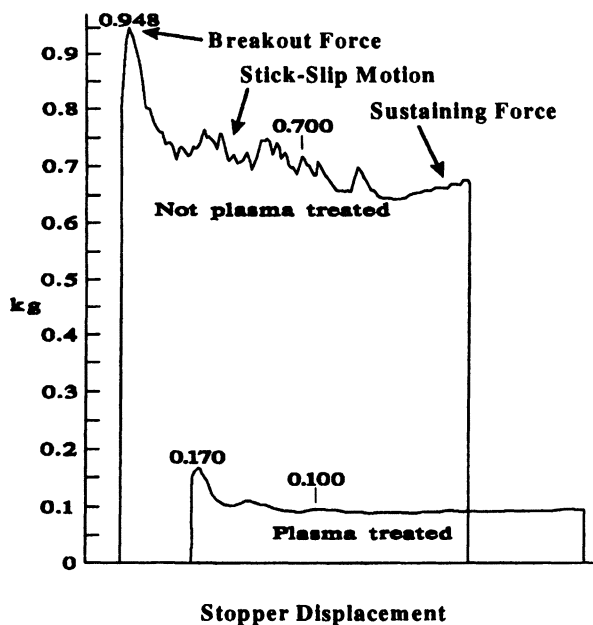


Figure 7. Typical syringe friction diagram measured while moving a stopper at a velocity of 100 mm/min in a syringe barrel. Shown is the frictional force (in kg) for a typical three-piece syringe (Figure 1) lubricated with a conventional silicone lubricant (curve labeled "Not plasma treated") and the reduced frictional force after plasma treatment (crosslinking) of the lubricated syringe barrel (curve labeled "Plasma treated").

separating stopper and barrel and the force to move the stopper is determined mainly by lubricant viscosity. Breakout forces are a result of lacking boundary lubrication, where high-friction contacts between elastomeric stopper and plastic barrel occur. Lubricant mobility is the determining factor for breakout forces in syringes, as is illustrated in the following section.

Table I. Relationship between syringe friction and fundamental physics of friction.

<i>Attribute</i>	<i>Impact on Syringe Application</i>	<i>Physics of Friction Involved</i>
<i>Breakout Force</i>	<ul style="list-style-type: none"> precise manual delivery of small medicant doses by hand (line-to-line movement) 	<ul style="list-style-type: none"> boundary and mixed lubrication regime <ul style="list-style-type: none"> - lubricant migration from high pressure contact - formation of real (elastomer/plastic) interface
<i>Sustaining Force</i>	<ul style="list-style-type: none"> manual bolus injection by hand 	<ul style="list-style-type: none"> hydrodynamic lubrication regime
<i>Stick-Slip Motion</i>	<ul style="list-style-type: none"> continuous drug delivery at very small dispensing rates 	<ul style="list-style-type: none"> boundary and mixed lubrication regime elasticity of driving system <ul style="list-style-type: none"> -low velocity/high pressure -energy storage (deformation) in elastomeric stopper

Breakout Force. Relatively high breakout forces, attained after extended storage times or long times between syringe filling and syringe discharge, are a problem often encountered during manual use of syringes. Thus, if an attempt is made to move the stopper from an initial position to a very nearby target position, the force required to effect this movement sometimes results in a motion exceeding the target position and hence making it difficult to correctly charge or discharge a desired amount of fluid (62). For example, when syringes are first removed from their package, the stopper had been in a fixed position for a considerable time since manufacture, and when moved, an impression of the piston can remain on the barrel wall, indicating an uneven lubricant distribution in this area of the syringe barrel. Two mechanisms are believed to be responsible for this lubricant displacement during extended syringe storage: (1) migration of oil from the interface caused by the sealing pressure in the stopper/barrel interface due to the interference fit (155, 156); and/or (2) absorption of silicone oil into the elastomeric stopper (157). Lubricant can be displaced with time by either one of the above mentioned mechanisms or a combination of both leading to unlubricated high friction contacts between plastic barrel and elastomeric stopper. This effect in combination with very slow initial velocities places the breakout event into the mixed and boundary lubrication regime.

An elegant method proposed to prevent migration and/or absorption of silicone oil and the resulting high initial breakout forces is the exposure of the silicone lubricated syringe barrel to an ionizing plasma (154-156). Reduction in breakout force obtained after plasma treatment (Figure 7) was attributed to crosslinking and conversion of the liquid lubricant into a semi-solid gel that remains immobilized on the barrel. This immobilized gel forms a low-friction lubrication layer that apparently separates stopper and barrel over extended periods of time and thus prevents high friction contacts between stopper and barrel to form during storage.

Syringe Pump Operation. An interesting application of syringes is in pumps wherein the syringe plunger is driven by a motor at typically very low medicant dispensing rates. Syringe pumps have become especially popular for intravenous drug infusion in intensive care, coronary care, and neonatal units requiring delivery of controlled doses of medicant over an extended period of time. Very slow speed medicant dispensing with stopper velocities ranging from about 0.003 to about 2 mm/min are particularly problematic due to stick-slip motion (154, 158).

Stick-slip motion in syringes is defined as the uneven, jerky motion of the stopper which results when the syringe pump fails to overcome the friction between the syringe plunger and syringe barrel. This uneven motion results in fluctuating flow rates, in the worst case alternating between bolus injection and periods of no medicant flow (see Row 3 in Table I). (157-159).

Stick-slip motion observed with syringes is associated with the mixed and boundary lubrication regime. This is in agreement with current models of the occurrence of stick-slip motion for lubricated sliding systems (see Physics of Friction section). Possible causes for this phenomenon are discussed in more detail in the following.

Stick-Slip Motion. It has been proposed in the literature that (1) swelling of the elastomeric stopper due to absorption of fluid with which the syringe is filled and/or (2) sweeping of the silicone lubricant during stopper motion may be the cause of stick-slip motion and subsequent syringe pump malfunction (157). Supporting the second theory is the observation that syringes lubricated with above mentioned plasma-crosslinked silicone oil (immobilized lubricant) can be used in conjunction with syringe pumps at any velocity without stick-slip motion. This illustrated the need for suitable lubrication to eliminate stick-slip motion in a syringe.

Another component contributing to stick-slip friction in a disposable three piece syringe is the elastomeric nature of the syringe stopper (160). It is well known that the mechanical properties of the sliding system, especially the mechanical coupling between driving force and sliding interface, have a significant impact on the occurrence of stick-slip motion (43, 90, 129, 134, 138, 161, 162). In case of a syringe, the driving force (syringe pump) is transferred to the lubricated stopper/slider interface by a plastic plunger with attached elastomeric stopper. The influence of the elastomeric nature of the stopper on stick-slip motion occurring at very low to moderate speeds is revealing of the complexities involved in real systems, which should be contrasted to model systems like those described by Israelachvili et al. (73, 111, 115), for example.

During utilization of a syringe in a very slowly moving syringe pump, the end of the plunger rod is moved at a constant velocity, driving the plunger down into the

syringe barrel. Ideally, the elastomeric stopper at the other end of the plunger rod moves as a whole with exactly the same constant velocity. In reality, friction at the stopper/barrel interface is high (due to lubricant migration from the stopper/barrel interface after the stopper remained stationary in one place over extended periods of time; see also column 1 of Table I) and initially, there will be no motion at the interface, except for some micro-slips. Yet, the plunger rod moves inexorably forward loading the elastomeric stopper with mechanical energy that must be either stored or dissipated. The most likely mechanism for energy storage during this "stick" period (no macroscopic motion) is macroscopic stopper deformation. Once the stored energy, or deformation, in the stopper is high enough to exceed existing frictional forces, the stopper will disengage from the barrel wall and macroscopic slipping at the interface will occur. Force measurements on the Instron reveal an increasing loading force peaking at the force required to disengage the stopper. This force was earlier defined as the breakout force (Figure 7, Table I).

Once macroscopic sliding has started, two different events can take place. Firstly, the stopper can continue to move, most likely with some constant deformation resulting from a balance between elastomeric properties of the stopper material and lubricant properties of the frictional contact. In this case, no stick-slip motion is observed but smooth continuous sliding of the stopper inside the plastic barrel takes place. Secondly, during release of the deformation imposed on the stopper during the initial stick phase, the relative velocity in the stopper/barrel interface can drop to a very low value or can even reach zero. In this event the stopper will stick again and the above described process will be repeated. In this case stick-slip motion is observed (Table I).

In summary, the cause for stick-slip motion in syringes can be rationalized as a combination of high initial friction (breakout force) and the elastomeric properties of the stopper.

Sterilization. Syringes need to be sterilized to prevent delivery of pathogenic organisms. Historically, when disposable syringes were unavailable and syringes were reused in the hospital (both glass and plastic), the only practical method of syringe sterilization in a hospital was to lightly lubricate the syringe barrel with liquid paraffin and then place the barrel into a steam autoclave at 160 °C. However, after repeated sterilization a build-up of charred paraffin was observed which made the syringes unattractive for further use, and even worse, the syringes tended to stick in use. The application of silicone oil with a high boiling point and a greatly reduced number of carbon atoms prevented the charring and sticking and thus made sterilization and repeated use easier (163).

In modern times, most syringes are not reused and sterilization is done after manufacturing and packaging of the syringes and before they are sold to a hospital. Common sterilization methods are exposure to ethylene oxide gas or exposure to high energy radiation, such as an electron beam or γ -radiation from a Co^{60} source (67). In contrast to steam sterilization, which seems to have little to no impact on the lubricating properties of silicone oils, exposure of silicone fluid to high energy radiation is known to increase the lubricant viscosity, a process which depends on molecular weight and radiation dose (164). In addition, degradation of the lubricant during

sterilization or during shelf life can occur. These radiation induced changes impact the frictional performance of both the hypodermic needle and the syringe stopper moving in the barrel and can, in worst case, compromise the performance of the article. Additives are commonly added to prevent the degradation during and after radiation sterilization (165).

Summary

Physics of friction and lubrication in biomedical devices was illustrated using the disposable plastic syringe, the most widely used drug delivery device worldwide, as an illustrative example. Friction in disposable plastic syringes can be described in terms of three distinct regimes dependent on stopper velocity, similar to a Stribeck curve for lubricated friction. In the hydrodynamic lubrication regime stopper and barrel are completely separated by the silicone oil film and the overall frictional response of a syringe is observed to be dependent on the speed of plunger motion due to velocity dependent shear of the liquid lubricant. However, there is a low-velocity limit to hydrodynamic lubrication. It is difficult to maintain a sufficiently thick lubricant film to entirely separate the two surfaces when the relative sliding speed is slow due to lubricant film thinning under the normal load. Eventually the highest surface asperities protrude through the bulk lubricant layer, leading to mechanical interactions between both surfaces. This phenomenon is termed boundary lubrication and it is in this regime and the transition zone between hydrodynamic and boundary lubrication that problems such as stick-slip motion are encountered. It can be concluded that lubricant mobility plays a major role in both the transition zone and the boundary lubrication regime because mobility determines the extend to which stopper and barrel form close, high friction contacts. Sterilization by high energy radiation slightly increases lubricant viscosity and thus improves the frictional characteristics of syringes to a certain degree. However, an oxidizing plasma treatment of the syringe lubricant which immobilizes the lubricant was found to be the most effective way to improve the frictional performance of a disposable plastic syringe.

Acknowledgments

Dr. Erwin Vogler is acknowledged for critical review of the manuscript and valuable discussions. Dr. Noel Harvey is thanked for his continued support of friction research in disposable medical devices at Becton Dickinson Technologies. Sandra Morris is acknowledged for her help in obtaining the literature used in the compilation of this review. Linda Tingen provided skilled artistic input in preparation of figures.

Literature Cited

1. Bowden, F. P.; Tabor, D. *Friction - An Introduction to Tribology*; Robert E. Krieger Publishing Company: Malabar, FL, 1982, pp. 10.
2. Bowden, F. P.; Tabor, D. *Friction - An Introduction to Tribology*; Robert E. Krieger Publishing Company: Malabar, FL, 1982, pp. 9-24.
3. Halling, J. *Principles of Tribology*; MacMillan Press Ltd.: London, 1975, pp. 4-7.

4. Bowden, F. P.; Leben, L. *Proc. Roy. Soc.* **1939**, *A169*, pp. 371-391.
5. Rabinowicz, E. *Friction and Wear of Materials*; John Wiley & Sons, Inc.: New York, 1995, pp. 66-74.
6. Teer, D. G.; Arnell, R. D. In *Principles of Tribology*; Halling, J., Ed., MacMillan Press Ltd.: London, 1975, pp. 72-93.
7. Ibrahim, R. A. *Applied Mechanics Review* **1994**, *47*, pp. 209-226.
8. Schallamach, A. *Wear* **1957**, *1*, pp. 384-417.
9. Schallamach, A. *Wear* **1969**, *13*, pp. 13-25.
10. Schallamach, A. *Gummi, Asbest, Kunststoffe* **1975**, *28*, pp. 142-155.
11. Bowden, F. P.; Tabor, D. *Friction - An Introduction to Tribology*; Robert E. Krieger Publishing Company: Malabar, FL, 1982, pp. 63, 79-81.
12. Bowden, F. P.; Tabor, D. *The Friction and Lubrication of Solids - Part II*; Oxford University Press: London, 1964,
13. James, D. I.; Newell, W. G. *Polymer Testing* **1980**, *1*, pp. 9-25.
14. Chernyak, Y. B.; Leonov, A. I. *Wear* **1986**, *108*, pp. 105-138.
15. Tomlinson, G. A. *Phil. Mag.* **1929**, *7*, pp. 905-939.
16. Derjaguin, B. Z. *Physik* **1934**, *88*, pp. 661-675.
17. Bowden, F. P.; Tabor, D. *The Friction and Lubrication of Solids*; Oxford University Press: Oxford, 1986,
18. Homola, A. M.; Israelachvili, J. N.; Gee, M. L.; McGuiggan, P. M. *J. Tribol.* **1989**, *111*, pp. 675-682.
19. Beare, W. G.; Bowden, F. P. *Phil. Trans. A* **1935**, *234*, pp. 329-354.
20. Tabor, D. In *Advances in Polymer Friction and Wear*; Lee, L.-H., Ed. Polymer Science and Technology 5A; Plenum Press: New York, 1974, pp. 5-30.
21. Briscoe, B. J. In *Physicochemical Aspects of Polymer Surfaces*; Mittal, Ed. 1; Plenum Publishers: New York, 1983, pp. 387-412.
22. Yamaguchi, Y. *Tribology of Plastic Materials*; Tribology Series, Elsevier: Amsterdam, 1990, 16,
23. Tewari, U. S.; Sharma, S. K.; Vasudevan, P. *JMS-Rev. Macromol. Chem. Phys.* **1989**, *C29*, pp. 1-38.
24. Bueche, A. M.; Flom, D. G. *Wear* **1958**, *2*, pp. 168-182.
25. Bulgin, D.; Hubbard, G. D.; Walters, M. H. Institution of Rubber Industry: London, England, 1962, pp. 173-188.
26. McLaren, K. G.; Tabor, D. *Nature* **1963**, *197*, pp. 856-858.
27. Grosch, K. A. *Nature* **1963**, *197*, pp. 858-859.
28. Grosch, K. A. *Proc. Roy. Soc.* **1963**, *A274*, pp. 21-39.
29. Schallamach, A. *Wear* **1963**, *6*, pp. 375-382.
30. *Friction of Polymers at Engineering Speeds: Influence of Speed, Temperature and Lubricants*; McLaren, K. G.; Tabor, D., Eds.; Lubrication and Wear Convention; Institution of Mechanical Engineers: 1963.
31. Savkoor, A. R. *Wear* **1965**, *8*, pp. 222-237.
32. Ludema, K. C.; Tabor, D. *Wear* **1966**, *9*, pp. 329-348.
33. Schallamach, A. *Rubber Chem. Technol.* **1968**, *41*, pp. 209-244.
34. Savkoor, A. R. In *Advances in Polymer Friction and Wear*; Lee, L.-H., Ed. Polymer Science and Technology 5A; Plenum Press: New York, 1974, pp. 69-121.
35. Gujrati, B. D.; Ludema, K. C. In *Advances in Polymer Friction and Wear*; Lee, L.-H., Ed. Polymer Science and Technology 5A; Plenum Press: New York, 1974, pp. 413-427.
36. Schallamach, A. In *Mechanics of the contact between deformable bodies*; Delft University Press: Enschede, Netherland, 1974, pp. 359-376.

37. Schallamach, A. In *Mechanics of the Contact between Deformable Bodies*; Delft University Press: Delft, 1975, pp. 359-376.
38. Arnell, R. D.; Teer, D. G. In *Principles of Tribology*; Halling, J., Ed. MacMillan Press Ltd.: London, 1975, pp. 128-146.
39. Briscoe, B. J. *Phil. Mag.* **1981**, *43*, pp. 511-527.
40. Barquins, M. *Mater. Sci. Eng.* **1985**, *73*, pp. 45-63.
41. Barquins, M.; Roberts, A. D. *J. Phys. D: Appl. Phys.* **1986**, *19*, pp. 547-563.
42. Wiedemeyer, J. *Microstruct. Mech. Prop. Mater* **1991**, pp. 195-202.
43. De Togni, R. S.; Eiss Jr, N. S.; Rorrer, R. A. L. In *Wear and Friction of Elastomers*; Denton, R.; Kehavan, M. K., Eds.; 1145; American Society for Testing and Materials: Philadelphia, 1992, pp. 30-49.
44. Wang, Q.; Kong, X.; Zhu, L.; Zhe, J.; Fan, Y. *J. Appl. Polym. Sci.* **1995**, *58*, pp. 903-910.
45. Haugstad, G.; Gladfelter, W. L.; Weberg, E. B.; Weberg, R. T.; Jones, R. R. *Tribol. Lett.* **1995**, *1*, pp. 253-264.
46. Haugstad, G.; Gladfelter, W. L.; Weberg, E. B.; Weberg, R. T.; Jones, R. R. *Langmuir* **1995**, *11*, pp. 3473-3482.
47. Heinrich, G. *Rubber Chem. Technol.* **1997**, *170*, pp. 1-14.
48. Brown, E. D.; Owens, R. S.; Booser, E. R. In *Boundary Lubrication*; ASME Publication: NY, 1969, pp. 7-18.
49. Oden, J. T.; Martins, J. A. C. *Computer Methods in Applied Mechanics and Engineering* **1985**, *52*, pp. 527-634.
50. Bikerman, J. J. In *Advances in Polymer Friction and Wear*; Lee, L.-H., Ed. Polymer Science and Technology 5A; Plenum Press: New York, 1974, pp. 149-163.
51. Pollock, H. M. In *Fundamentals of Friction: Macroscopic and Microscopic Processes*; Singer, I. L.; Pollock, H. M., Eds.; Nato ASE Series E: Applied Sciences 220; Kluwer Academic Press: Dordrecht, 1992, pp. 77-94.
52. Overney, R. M.; Leta, D. P. *Tribol. Lett.* **1995**, *1*, pp. 247-252.
53. Rabinowicz, E. *Friction and Wear of Materials*; John Wiley & Sons, Inc.: New York, 1995, pp. 76-78.
54. Johnson, K. L. *Langmuir* **1996**, *12*, pp. 4510-4513.
55. *Fundamentals of Friction: Macroscopic and Microscopic Processes*; Singer, I. L.; Pollock, H. M., Eds.; NATO ASE Series E: Applied Science; Kluwer Academic Press: Dordrecht, 1992.
56. Overney, R. M. *Trends Polym. Sci.* **1995**, *3*, pp. 359-364.
57. *Handbook of Micro/Nano Tribology*; Bushan, B., Ed. CRS Series Mechanics and Materials Science; CRC Press: Boca Raton, 1995.
58. Krim, J. *Scientific American* **1996**, *October*, pp. 74-80.
59. Krim, J. *MRS Bulletin* **1998**, *June*, pp. 20-21.
60. Bondi, A. In *Physical Chemistry of Lubricating Oils*; Reinhold Publishing Corporation: New York, 1951, pp. 101-166.
61. Campbell, W. E. In *Boundary Lubrication*; ASME Publication: NY, 1969, pp. 87-117.
62. Ichikawa, T.; Watanabe, T. *US Patent* **1981**, *4,303,070*.
63. Lewis, A. K.; Weilbacher, E. E. *US Patent* **1994**, *5,314,416*.
64. Chen, Y. Y. *J. Pharm. Sci.* **1970**, *59*, pp. 717-718.
65. Hine, C. H.; Elliott, H. W.; Wright, R. R.; Cavalli, R. D.; Porter, C. D. *Toxicology and Applied Pharmacology* **1969**, *15*, pp. 566-573.
66. Wohlfeil, E. R. *Anesthesiology* **1993**, *79*, pp. A560.

67. Sacharow, S. *Paper, Film & Foil Converter* 1988, pp. 126-129.
68. Archard, J. F. *J. Appl. Phys.* 1953, 24, pp. 67-74.
69. Dieterich, J. H.; Kilgore, B. D. *Pageophy.* 1994, 143, pp. 283-302.
70. Majumdar, A.; Bushan, B. In *Handbook of Micro/Nano Tribology*; Bushan, B., Ed. CRC Press: Boca Raton, 1995, pp. 109-165.
71. Kendall, K. *Contemp. Phys.* 1980, 21, pp. 277-297.
72. Israelachvili, J. *Intermolecular & Surface Forces*; Academic Press: London, 1985.
73. Israelachvili, J. N. In *Handbook of Micro/Nanotribology*; Bushan, B., Ed. CRC Press: Boca Raton, FL, 1995, pp. 267-319.
74. Israelachvili, J. N. In *The Handbook of Surface Imaging and Visualization*; Hubbard, A. T., Ed. CRC Press: Boca Raton, 1995, pp. 793-816.
75. Johnson, K. L.; Kendall, K.; Roberts, A. D. *Proc. R. Soc. Lond. A* 1971, 324, pp. 301-313.
76. Greenwood, J. A.; Johnson, K. L. *Phil. Mag.* 1981, A43, pp. 697-711.
77. Sun, S. M.; Chang, W. V. *Rubber Chem. Technol.* 1995, 68, pp. 1-12.
78. Tirrell, M. *Langmuir* 1996, 12, pp. 4548-4551.
79. Hertz, H. *Journal fuer die Reine und Angewandte Mathematik* 1881, 92, pp. 156-171.
80. Derjaguin, B. V.; Muller, V. M.; Toporov, Y. J. *Colloid Interface Sci.* 1975, 53, pp. 314-326.
81. *Dictionary of Scientific and Technical Terms*; Lapedes, D. N., Ed. McGraw-Hill Book Company: New York, 1974.
82. Mittal, K. L. *J. Vac. Sci. Technol.* 1976, 13, pp. 19-25.
83. Mittal, K. L. *Pure & Appl. Chem.* 1980, 52, pp. 1295-1305.
84. Greenwood, J. A.; Williamson, J. B. P. *Proc. Roy. Soc. Lond. A.* 1966, 295, pp. 300-319.
85. Halling, J.; Nuri, K. A. In *Principles of Tribology*; Halling, J., Ed. MacMillan Press Ltd.: London, 1975, pp. 40-71.
86. Simkins, T. E. *Lub. Eng.* 1967, 23, pp. 26-31.
87. Derjaguin, B. V. *Wear* 1988, 128, pp. 19-27.
88. Rabinowicz, E. *Proceedings of the Physical Society* 1958, 71, pp. 668-675.
89. Rabinowicz, E. *Product Eng.* 1960, Sep 26, pp. 62-64.
90. Heslot, F.; Baumberger, T.; Perrin, B.; Caroli, B.; Caroli, C. *Physical Review* 1994, E49, pp. 4973-4988.
91. Reiter, G.; Demirel, A. L.; Peanasky, J.; Cai, L.; Granick, S. *Tribol. Lett.* 1995, 1, pp. 1-12.
92. Bartenev, G. M.; Elkin, A. I. *Wear* 1968, 11, pp. 393-403.
93. Schallamach, A. *Wear* 1971, 17, pp. 310-312.
94. Pooley, C. M.; Tabor, D. *Proc. Roy. Soc.* 1972, A.329, pp. 251-274.
95. Lee, L.-H. In *Advances in Polymer Friction and Wear*; Lee, L.-H., Ed. Polymer Science and Technology 5A; Plenum Press: New York, 1974, pp. 31-66.
96. Savkoor, A. R.; Briggs, G. A. D. *Proc. R. Soc. Lond. A.* 1977, 356, pp. 103-114.
97. Czichos, H. *Wear* 1983, 88, pp. 27-43.
98. Santer, E.; Czichos, H. *Tribol. Int.* 1989, 22, pp. 103-109.
99. Leonov, A. I. *Wear* 1990, 141, pp. 137-145.
100. Thornton, C. J. *Phys. D: Appl. Phys.* 1991, 24, pp. 1942-1946.
101. Tabor, D. In *Fundamentals of Friction: Macroscopic and Microscopic Processes*; Singer, I. L.; Pollock, H. M., Eds.; Kluwer Academic Publishers: Dordrecht, 1992, pp. 3-24.
102. Eiss Jr, N. S.; McCann, B. P. *Tribol. Trans.* 1993, 36, pp. 686-692.
103. *Friction and Wear (Tribology)*; Eiss Jr., N. S., Ed. Charact. Polym.; Butterworth Heineman: Boston, 1994.

104. Arvanitaki, A.; Briscoe, B. J.; Adams, M. J.; Johnson, S. A. In *Lubricants and Lubrication*; Dowson, D., Ed. Elsevier Science: 1995, pp. 503-511.
105. Bushan, B.; Israelachvili, J. N.; Landman, U. *Nature* **1995**, *374*, pp. 607-616.
106. Gao, J.; Luedtke, W. D.; Landman, U. *Science* **1995**, *270*, pp. 605-608.
107. Rabinowicz, E. *Friction and Wear of Materials*; John Wiley & Sons, INC.: New York, 1995, pp. 74-78.
108. Ludema, K. C. *Friction, Wear, Lubrication*; CRC Press: Boca Raton, FL, 1996, pp. 72-81.
109. Horn, R. G.; Israelachvili, J. N.; Pribac, F. *J. Colloid Interface Sci.* **1987**, *115*, pp. 480-492.
110. Homola, A. M.; Israelachvili, J. N.; McGuiggan, P. M.; Gee, M. L. *Wear* **1990**, *136*, pp. 65-83.
111. Israelachvili, J. N. In *Fundamentals of Friction*; Singer, I. L.; Pollock, H. M., Eds.; NATO ASI Series, Series E, Applied Sciences 220; Kluwer Academic Publishers: Braunlage, Germany, 1992, pp.
112. Yoshizawa, H.; Chen, Y.-L.; Israelachvili, J. *J. Phys. Chem.* **1993**, *97*, pp. 4128-4140.
113. Yoshizawa, H.; Israelachvili, J. *J. Phys. Chem.* **1993**, *97*, pp. 11300-11313.
114. Reiter, G.; Demirel, A. L.; Peanasky, J.; Cai, L. L.; Granick, S. *J. Chem. Phys.* **1994**, *103*, pp. 2606-2615.
115. Israelachvili, J.; Berman, A. *Israel J. Chem.* **1995**, *35*, pp. 85-91.
116. Perrson, B. N. J. In *Physics of Sliding Friction*; Perrson, B. N. J.; Tosatti, E., Eds.; SeriesE; Applied Sciences 311; Kluwer Academic Publishers: Dordrecht, 1996, pp. 69-91.
117. Granick, S. *Science* **1991**, *253*, pp. 1374-1379.
118. Morgan, F.; Muskat, M.; Reed, D. W. *J. Appl. Phys.* **1940**, *11*, pp. 541-548.
119. Whomes, T. L. In *Principles of Tribology*; Halling, J., Ed. MacMillan Press Ltd.: London, 1975, pp. 233-287.
120. Sun, D. C. *Lub. Eng.* **1997**, *January*, pp. 18-25.
121. Blok, H. *J. Soc. Autom. Engineer* **1940**, *46*, pp. 54-68.
122. Briscoe, B. J.; Evans, D. C. B. *Proc. R. Soc. Lond. A* **1982**, *380*, pp. 389-407.
123. Komvopoulos, K.; Saka, N.; Suh, N. P. *J. Tribol.* **1985**, *107*, pp. 452-462.
124. Wells, J. H. *The Engineer* **1929**, *147*, pp. 454.
125. Papenhuyzen, P. J. *De Ingenieur* **1938**, *53*, pp. V75-V82.
126. Morgan, F.; Muskat, M.; Reed, D. W. *J. Appl. Phys.* **1941**, *12*, pp. 743-752.
127. Burwell, T. J.; Rabinowicz, E. *J. Appl. Phys.* **1953**, *24*, pp. 136-139.
128. Schelleng, J. C. *Scientific American* **1974**, *230*, pp. 87-95.
129. Eaton, L. In *Principles of Tribology*; Halling, J., Ed. MacMillan Press Ltd.: London, 1975, pp. 147-173.
130. Rowson, D. M. *Wear* **1975**, *31*, pp. 213-218.
131. Briscoe, B. J.; Evans, D. C. B.; Tabor, D. *J. Colloid Interface Sci.* **1977**, *61*, pp. 9-13.
132. Bowden, F. P.; Tabor, D. *Friction - An Introduction to Tribology*; Robert E. Krieger Publishing Company: Malabar, FL, 1982, pp. 68-71.
133. Eiss Jr, N. S. In *Physical Methods in Chemistry*; Rossiter, B. W.; Hamilton, J. F., Eds.; 7; Wiley: New York, 1991, pp. 101-138.
134. Ibrahim, R. A. *Applied Mechanics Review* **1994**, *47*, pp. 227-253.
135. Carlson, J. M.; Langer, J. S.; Shaw, B. E. *Reviews of Modern Physics* **1994**, *66*, pp. 657-670.
136. Rorrer, R.; Eiss Jr., N. S. *Tribol. Trans.* **1995**, *38*, pp. 323-328.
137. Rabinowicz, E. *Friction and Wear of Materials*; John Wiley & Sons, INC.: New York, 1995, pp. 105-111.
138. Baumberger, T. In *Physics of Sliding Friction*; Perrson, B. N. J.; Tosatti, E., Eds.; SeriesE; Applied Sciences 311; Kluwer Academic Publishers: Dordrecht, 1996, pp.

139. Ohara, K. *Wear* **1978**, *50*, pp. 333-342.
140. Martins, J. A. C.; Guimarães, J.; Faria, L. O. *Journal of Vibrations and Acoustics* **1995**, *117*, pp. 445-451.
141. Adams, G. G. *Journal of Applied Mechanics* **1995**, *62*, pp. 867-872.
142. Adams, G. G. *J. Tribol.* **1996**, *118*, pp. 819-823.
143. Berman, A. D.; Ducker, W. A.; Israelachvili, J. N. *Langmuir* **1996**, *12*, pp. 4559-4563.
144. Alsten, J. V.; Granick, S. *Phys. Rev. Lett.* **1988**, *61*, pp. 2570-2573.
145. Thompson, P. A.; Robbins, M. O. *Science* **1990**, *250*, pp. 792-794.
146. Robbins, M. O.; Thompson, P. A. *Science* **1991**, *253*, pp. 916.
147. Robbins, M. O.; Thompson, P. A.; Grest, G. S. *MRS Bulletin* **1993**, *May*, pp. 45.
148. Thompson, P. A.; Robbins, M. O.; Grest, G. S. *Israel J. Chem.* **1995**, *35*, pp. 93-106.
149. Demirel, A. L.; Granick, S. *Phys. Rev. Lett.* **1996**, *77*, pp. 4330-4333.
150. Eriksson, E.; Larsson, N.; Nitescu, P.; Applegreen, L.; Linder, L. E.; Curelaru, I. *Acta Anaesthesiol. Scand.* **1991**, *35*, pp. 306-314.
151. Elias, W. F. *Bull. Parenter. Drug Assoc. (US)* **1968**, *Mar.-Apr.*, pp. 70-71.
152. Spielvogel, D. E.; Zdrachala, R. J. *US Patent* **1988**, *4,720,521*.
153. Williams, J. L.; Shepard, T. A. *US Patent* **1993**, *5,186,972*.
154. Montgomery, D. B. *US Patent* **1994**, *5,338,312*.
155. Williams, J. L.; Martin, D. A.; Montgomery, D. B. *US Patent* **1989**, *4,822,632*.
156. Williams, J. L.; Martin, D. A.; Montgomery, D. B. *US Patent* **1988**, *4,767,414*.
157. Capes, D. F.; Herring, D.; Sunderland, V. B.; McMillan, D.; McDonald, C. *PDA Journal of Pharmaceutical Science and Technology* **1996**, *50*, pp. 40-50.
158. Lönnqvist, P. A.; Löfqvist, B. *Intensive Care Med* **1997**, *23*, pp. 998-1001.
159. Capes, D. F.; Dunster, K. R.; Sunderland, V. B.; McMillan, D.; Colditz, P. B.; McDonald, C. *A. J. Health-Syst. Pharm.* **1995**, *52*, pp. 1646-1653.
160. Akaike, Y.; Nishiya, Y. *US Patent* **1991**, *5,061,247*.
161. Baumberger, T.; Heslot, F.; Perrin, B. *Nature* **1994**, *367*, pp. 544-546.
162. Berman, A. D.; Ducker, W. A.; Israelachvili, J. N. In *Physics of Sliding Friction*; Persson, B. N. J.; Tosatti, E., Eds.; NATO ASI Series E: Applied Sciences Vol. 311; Kluwer Academic Publishers: Trieste, Italy, 1996, pp. 51-67.
163. Darling, G. H.; Spencer, J. G. C. *Brit. Med. J.* **1951**, *1*, pp. 300-301.
164. United Chemical Technologies *Silicone Compounds Register and Review*; 1993, pp. 251.
165. Khan, M. A.; Hopkins, D. P. *European Patent Application* **1996**, *EP 0 689 397 A1*.

Author Index

- Aimé, J. P., 124
Balazs, Anna C., 369
Baljon, Arlette R. C., 91
Barquins, M., 42
Basire, C., 239
Blackman, G. S., 258, 428
Brédas, J. L., 356
Briscoe, B. J., 2
Budinski, Kenneth G., 384
Buenviaje, C., 154
Burnham, N. A., 118
Charmet, J. C., 42
Chaudhury, M. K., 83
Chiao, Yi-Hung, 190
Chizhik, S. A., 177
DeKoven, Benjamin M., 190
Dineen, Michael T., 190
Dubois, Ph., 356
Dugger, M. T., 455
Dupas, E., 118
Duschl, C., 118
Dziezok, Peter, 346
Eiss, Norman S., Jr., 418
Feldman, Kirill, 258
Fretigny, C., 239
Fujii, Tomokazu, 336
Ge, S., 154
Gladfelter, Wayne L., 227, 284
Gorbunov, V. V., 177
Gourdon, D., 118
Gremaud, G., 118
Hähner, Georg, 258
Hammerschmidt, Jon A., 284
Hammiche, Azzedine, 190
Haugstad, Greg, 227, 284
Hild, Sabine, 212
Hu, Terry, 190
Huang, Z., 177
Jérôme, R., 356
Johnson, K.L., 24
Jones, Frank N., 439
Kajiyama, Tisato, 336
Kopp-Marsaudon, S., 124
Kulik, A. J., 118
Lazzaroni, R., 356
Leclère, Ph., 356
Lee, Edward, 418
Liebmann-Vinson, Andrea, 474
Liley, M., 118
Lin, L., 258, 428
Marti, Othmar, 212
Mate, C. Mathew, 405
Matheson, R. R., 258, 428
Meerman, C., 304
Meyers, Gregory F., 190
Michel, D., 124
Minet, M., 356
Moineau, G., 356
Möller, Martin, 346
Myshkin, N. K., 177
Nelson, G. C., 455
Nony, L., 124
Nysten, B., 304
O'Connor, Paul J., 190
Oulevey, F., 118
Overney, R. M., 154
Pollack, Hubert M., 190
Prokhorova, Svetlana A., 346
Rafailovich, M., 154
Robbins, Mark O., 91
Schmidt, Manfred, 346
Schmidt, Ronald H., 227
Schmidt, Ute, 346
Schönherr, Holger, 317
Senft, D. C., 455
Sheiko, Sergei S., 346
Shen, Weidian, 439
Singh, Chandralekha, 369
Sokolov, J., 154
Spencer, Nicholas D., 272
Strandjord, Andrew, 190
Takahara, Atsushi, 336
Tomasetti, E., 304
Tsukruk, V. V., 177
Unertl, W. N., 66
Vallet, D., 42
Vancso, G. Julius, 317
Vorvolakos, K., 83
Wu, Junhua, 405
Zhulina, Ekaterina, 369

Subject Index

A

Abrasion

- abrasive tape test for plastics, 389
- ball-on-plane test, 395, 396*f*, 397
- definition, 388
- dry sand rubber wheel test, 389, 390*f*
- extreme, 18
- measuring abrasivity of plastics, 403
- pin abrasion test, 389, 390*f*
- plastics by other surfaces, 388–391
- profilometers, 397
- slurry abrasion response test, 399, 400*f*
- Taber Abrasor, 388–389
- tape abrasion test, 397, 398*f*

See also Wear tests for plastics

Abrasive tape test for plastics, 389

Acrylic adhesive

- adhesion strengths, 85
- direct velocimetry using fluorescent particles, 89
- interfacial shear stress on silicone coatings as function of shear velocity, 89*f*
- interfacial slippage, 87–89
- release forces, 86

See also Silicone coatings

Acrylonitrile–butadiene–styrene/polycarbonate blend (ABS/PC)

- occurrence of stick slip, static coefficient of friction (COF), and COF drop for four surface textures, 421*t*, 422*t*

See also Automotive interior plastics

Activation energy, poly(methyl methacrylate) (PMMA), 301

Adherence of elastic/viscoelastic solids

- adhesion and rupture, 47–48
- bouncing ball, 53–58
- comparison of distorted surface profiles of pure elastic contact and adhesion, 44*f*
- dissipation function versus crack speed, 50*f*
- elastic contact, 43–45
- friction law, 43
- Griffith's theory of brittle fracture, 45–47
- interaction energy in Griffith model, 46*f*
- preliminary knowledge, 42–49
- rolling cylinder, 58–63
- spontaneous peeling, 49, 51–53
- strain energy release rate, 45
- viscoelastic losses, 48–49

Adhesion

- adhesive force images, 221–224
 - aspect of plastic wear, 391, 394
 - calculated surface energies from pull-off data, 196*t*
 - characterization by surface energy or surface tension, 213
 - common modes of fracture at interface, 83–84
 - contact mode atomic force microscopy (AFM) images checking for plastic deformation, 195*f*
 - creep in viscoelastic contacts with, 77–80
 - deformation process, 9, 10*f*
 - failure of microelectromechanical systems, 455–456
 - image of lamellar polyethylene crystal, 326, 329*f*, 330*f*
 - irreversibility, 24–25
 - need for mechanics model for viscoelastic solids, 25
 - properties using pull-off force, 219, 220*t*
 - pull-off force equation, 194
 - pull-off force versus maximum applied load during contact demonstrating effect of surface contamination and roughness on measurement accuracy, 197*f*
 - pull-off force versus maximum applied load for various surfaces, 194, 196, 197*f*
 - qualitative differences in surface adhesion using tapping mode AFM (TMAFM), 198
 - representative deflection versus distance curves for polystyrene (PS) film, sapphire crystal, rubber, and LDPE, 195*f*
 - reproducibility and accuracy of pull-off measurements, 196
 - role in friction, 318
 - rupture mechanics, 47–48
 - sketch of release of adhesive from surface, 84*f*
 - static deflection AFM probing polymer surfaces in air using soft cantilevers, 207
 - tapping mode with phase detection, 202
 - type of tribological system, 2
 - using pull-off force, 194–198
 - variations of adhesive force of PS films during heating to 67°C, 220*f*, 221
 - viscoelastic cycle, 34, 36
- See also* Interfacial slippage in adhesive release; Scanning probe microscopy (SPM); Viscoelastic spheres

- Adhesion and ploughing theory of friction, 475, 477
- Adhesion hysteresis
irreversible energy dissipation during loading/unloading cycle, 479
isotropic phenomenon, 123
- Adjacent reentry and regular sharp fold model, high density polyethylene (HDPE) single crystals, 343, 344f
- Adsorption of cylindrical brushes. *See* Sparse coatings
- Alkanethiols, lateral force images of monolayer with differently functionalized endgroups, 275f
- Alloy systems, polymer tribology, 9
- Amontons, Guillaume, 43
- Amontons' law of friction
sliding friction deviating from, 475
Young's modulus, 158, 160
- Antiboundary lubrication, boundary lubricants for metals producing, 19
- Applications. *See* Automotive interior plastics; Automotive topcoats; Chemisorbed organic lubricants for microelectromechanical systems (MEMS); Disk drive applications; Medical devices; Polymeric surface coatings
- Approaching-retracing measurements
analysis of full cycle, 179, 180f
full cycle of approaching-retracing measurements, 179, 180f
See also Micromechanical properties of polymers
- Arrhenius relationship
between shift factor and temperature, 297
plot of shift factor versus inverse temperature, 299f
- Atomic force microscopy (AFM)
deflection and force calibration, 126
elastic and viscoelastic properties of copolymer blends at microscopy level, 305
experiment, 125
experimental environment, 130–131
idealized approach-retract curve, 129f
idealized force curve in contact AFM, 128f
key issues, 125–131
microtribology, 121–123
new techniques, 118
optical detection method sketches, 127f
probing friction processes at nanometer scale, 124
study of soft materials, 124
surface nanochemical imaging of organic surfaces, 273
tip characterization, 126, 130
See also Physics and physical chemistry at nanotip scale; Polypropylene/(ethylene-propylene) copolymer blends (PP/EP); Surface nanochemical studies
- Auto-dewetting
testing graft copolymers, 156–157
See also Disentanglement in ultrathin polymer films
- Automotive clearcoat (AC)
image of AC with nano-scratch at surface, 446, 448f
mar resistance, 444, 446
See also Polymeric surface coatings
- Automotive interior plastics
addition of glass fibers to polypropylene (PP), 426
approaches minimizing noises from stick-slip sliding, 418–419
component deflection and sliding, 418
correlation between coefficient of friction (COF) drop and stick-slip occurrence, 423
examining interaction between polymer and surface texture on COF drop, 423
experimental materials, 420
finding noise-producing contacts, 419
friction tester, 419
microdisplacements prior to initiation of sliding, 424
model of tangential static loading, 424
possible effect of microdisplacements on stick-slip occurrence, 424
roughness of surfaces influencing stick-slip occurrence, 419–420
roughness values for four textures, 423
stick-slip initiation from friction traces, 423
stick-slip occurrence, static COF, and COF drop for surface textures, 421t, 422t
surface profiles of surface textures, 425f
surface textures, 420
testing apparatus, 420–421
test procedure, 421
transition from static to kinetic friction, 424
- Automotive topcoats
AFM (atomic force microscopy) images of scratches near fracture threshold, 436f
block diagram of micro-scratch apparatus, 430f
complete experiment, 431
difficulty determining threshold for plastic deformation, 434–435
experimental, 429, 431
force and displacement versus scratch distance during micro-scratch experiment, 433f
indications of fracture or rupture events, 432
long-range height variation of commercial topcoats, 431

mar damage, 428–429
 micro-scratch experimental instrument, 429, 431
 morphology parameters of scratches by AFM, 437f
 participant observation of scratches, 435, 437f
 principle of scratch experiment, 429
 problem characterizing mar behavior, 429
 relationship between physical damage and appearance, 435
 required parameters for characterizing mar performance, 434
 scratch analysis, 435
 surface height variation, 432
 topcoat materials, 431
 total deformation and permanent deformation versus applied normal force, 433f
 types of scratch damage, 432, 434
 Autophobicity, interfacial energy of graft copolymers and effect on wetting, 167–168

B

Ball-on-plane test
 measuring abrasivity of plastics, 403
 web abrasivity, 395, 396f, 397

Bead-spring potential, modeling films
 containing linear short-chain molecules, 92

Benzocyclobutene, photodefineable (photoBCB)
 experimental sample, 194
 scanning thermal microscopy (SThM) images before plasma treatment, 209f
 tapping mode AFM image before and after plasma treatment, 208f
 thermal properties, 204, 207
See also Scanning probe microscopy (SPM)

Blend of poly(vinyl chloride) and poly(butadiene), force microscope and rigidity images as function of temperature, 120f

Block copolymers
 annealing indicating occurrence of morphology changes at high temperature, 362, 363f
 centered hexagons in poly(methyl methacrylate) (PMMA) domains, 362, 363f
 chromatography calibration with PMMA standards, 359
 comparing topographic and phase detection imaging (PDI) images, 360, 361f
 controlled radical polymerization, 357–358
 copolymers descriptions, 359f
 diblock copolymer schematic, 366f
 family of thermoplastic elastomers PMMA–poly(*n*-butylacrylate)–PMMA (MBuM) symmetric triblock copolymers, 357–358
 increasing PMMA content in block copolymers to ~50%, 364–365
 living anionic polymerization, 357, 358
 MBuM macromolecule synthesis, 359
 origin of phase contrast in tapping mode AFM (TMAFM), 360
 PDI technique, 358
 PDI–TMAFM (tapping mode AFM) investigating microscopic morphology, 360
 performance in relation to extent of phase separation and microstructure, 358
 poly(*n*-butylacrylate) domains adjacent to flat PMMA cylinders darker than matrix, 364
 possible organization of lamellae, 365, 366f
 presence of cylinders parallel to surface, 364
 qualitative interpretation of PDI images in terms of spatial distribution of domains on heterogeneous surface, 360, 362
 recording atomic force microscopy (AFM) images, 359–360
 schematic of lamellar arrangements, 366f
 symmetric copolymer with polar outer segments schematic, 366f
 symmetric triblock copolymer alternative lamellae arrangement, 366f
 tailoring via living anionic polymerization, 357
 TMAFM height and phase detection images of MBuM copolymer A, 361f, 361f
 TMAFM PDI images of MBuM copolymer A after annealing and quenching, 363f
 TMAFM phase detection images of MBuM copolymer B, 365f

Block-on-disk test, intended thrust washer test replacement, 394

Block-on-ring test, measuring wear of both members, 391, 393f

Bouncing ball
 adhesive rebound critical heights, 57f
 critical release altitude, 54
 experiments, 54–55
 material exponent, 55, 58
 rebound heights, 55, 56f
 theoretical considerations, 53–54

Boundary lubricant, molecularly thin lubricant layer, 481

Boundary lubrication regime, 481

Boundary solid lubricant, part of composite tribology, 19

Boussinesq, Joseph, 43

Breakout force
 manual syringe operation, 486–487

- relationship between syringe friction and physics of friction, 486*t*
- Brewster angle microscopy, anisotropy and asymmetry, 122
- Brittle fracture, Griffith's theory, 45–47
- Bulk yield stress, contact mechanical measurements, 13
- Bushing test, running until measurable wear occurs, 391, 393*f*

C

Cantilevers

- distribution of applicability towards various materials, 181*t*
- mechanical properties based on lever deflection of soft, 198–202
- probing adhesion using soft, 207
- range of applicability, 181, 182*f*
- ratio of indentation depth and cantilever deflection, 179, 181
- silicon and silicon nitride V-shaped, 178
- static deflection AFM for mechanical properties, 207
- tapping experiments, 133
- See also* Mechanical properties of polymers; Micromechanical properties of polymers
- Car industry, erosive wear, 5
- Cavitation erosion tests, second generation, 399
- Chain folding structure, single crystals, 336–337
- Chemisorbed organic lubricants for microelectromechanical systems (MEMS)
 - change in lateral response of octadecyltrichlorosilane (ODTS) films to shear after repeated contact, 472
 - coating coverage techniques, 457–458
 - coverage of silanes as function of coating time, 462*f*
 - device for measuring friction coefficient between etched polycrystalline silicon sidewall surfaces, 460*f*
 - displacement amplitude versus test time for device treated with ODTS, 468*f*
 - displacement amplitude versus test time for initial cycles of supercritically dried device, 468*f*
 - effect of contact conditions on magnitude of force and height change, 466, 467*f*
 - effect of ODTS coverage on micromachine operation, 469, 472
 - electrostatic force by comb drive, 459
 - experimental, 456–461
 - failure mode, 473
 - force balance calculations, 459, 461

- friction between micromachine structural elements using tribology test structure, 459
- friction coefficient and cycles to seizure for sidewall devices, 469*t*
- friction measurements, 458–461
- friction of silane films measured by micromachined structures, 466, 469, 472
- lateral force and secondary ion mass spectroscopy (SIMS) images of patterned ODTS on silicon, 465*f*
- lateral force image of ODTS film altered by rubbing, 467*f*
- lateral force image of silicon exposed to ODTS coating solution for 9 and 900 minutes, 471*f*
- macroscopic tribological performance of ODTS, 461, 464
- morphology of tested surfaces after failure, 469, 470*f*
- ODTS in coating solutions, 457
- procedure for surface treatment of micromachined tribology test devices, 457
- relationship between friction, coating durability, and ODTS coverage, 461, 463*f*, 464
- scanning probe microscopy (SPM) response of ODTS films, 464, 466
- silane coverage versus processing conditions, 461
- silane deposition procedure, 457
- static water contact angle as function of ODTS coverage on silicon, 463*f*
- substrate preparation, 456
- surface preparation and solution deposition conditions for silanes, 458*t*
- time-of-flight SIMS (TOF–SIMS) to determine amount of silane on surface, 457–458
- variations in kinetics of dense silane film formation, 472
- water contact angle as function of coating time for ODTS films, 462*f*
- wear areas on posts from sidewall device tests having different silane coverage, 471*f*, 472
- Civil engineering, apparent contact area, 6
- Clay surfaces
 - scheme for creating stable dispersions from immiscible polymers and clays, 369–370
 - See also* Modeling interactions
- Clearance, loss in wear modes, 16
- Clogging, repeated sliding over abrasive surface, 18
- Coatings. *See* Polymeric surface coatings
- Cobblestone model
 - example of Eyring approach, 13
 - interfacial friction, 326, 332–334

- Coefficient of friction (COF). *See* Automotive interior plastics
- Cohesion
 damage mode, 13, 14*f*
 deformation process, 9, 10*f*
 failure through scratch deformation, 15–16
- Coloumbic friction, scale of asperities
 approaching contact dimensions, 12
- Composite systems, polymer tribology, 9
- Compression-molded blends
 versus injection-molded blends, 310–313
See also Polypropylene/(ethylene-propylene) copolymer blends (PP/EP)
- Contact cycle, linear viscoelastic solids, 29
- Contact mechanics
 application of, 20–21
 creep in viscoelastic contacts in absence of adhesion, 71–80
 creep in viscoelastic contacts with adhesion, 77–80
 direct measurement of surface energetics of silicone coatings, 86–87
 linear viscoelastic materials, 71–80
 viscoelastic, 29–30
See also Viscoelastic spheres
- Contact mode
 analogy with crazes and fractures, 137, 139*f*
 dynamic force microscopy, 124–125
 force curve cycles, 134, 136*f*
 friction coefficient, 134, 135*f*
 molecular weight dependence, 134, 137
- Contacts, varying loads, 6
- Continuous shear, interpreting interface shear phenomena, 12
- Continuum mechanics models
 adhesion of perfectly elastic spheres, 25–27
 analyzing nanoscale scanning force microscope (SFM), 66
- Controlled radical polymerization
 comparison to classical anionic polymerization, 357–358
See also Block copolymers
- Copolymer blends. *See*
 Polypropylene/(ethylene-propylene) copolymer blends (PP/EP)
- Correspondence principle, viscoelastic contact mechanics, 29–30
- Crazes and fractures, contact atomic force microscopy (AFM), 137, 139
- Creep compliance function
 linear viscoelastic solids, 27, 28*f*
 viscoelastic adhesion cycle computations, 36
- Creep effects
 due to bulk deformation, 78
See also Nanometer-scale contacts to linear viscoelastic materials
- Crosslinkable epoxy thermoplastic with grafted rubber concentrate (CET–GRC)
 calculated surface stiffness and tip penetration depths, 200*r*
 contact mode atomic force microscopy (AFM)
 after cryo-polishing and after staining with OsO₄, 200, 201*f*
 preparation, 193–194
 tapping mode AFM height and phase images after cryo-polishing, 202, 203*f*
See also Scanning probe microscopy (SPM)
- Crystallization. *See* Polyethylene (PE) single crystals
- Crystals. *See* Polymer lamellar crystals; Transcrystallized polymer crystals
- Cylindrical brushes. *See* Sparse coatings
- D**
- da Vinci, Leonardo, friction law, 43
- Damage
 cohesive failure, 15–16
 interfacial mode, 15
 interfacial or cohesive modes, 14*f*
 lubrication suppressing scratch, 15–16
 modes, 13–16
 producing debris and displacing from contact zone, 8
 scratching operations, 15–16
 type of tribological system, 2
- Debris detachment, wear, 16
- Debye–Waller factor, rise where slip localizes at wall/film interface, 110
- Deflection
 atomic force microscopy (AFM), 126, 127*f*
 plastic components in automotive interiors, 418
- Deformation
 application of mechanics, 20–21
 distinction between modes, 9, 11*f*
 gross subsurface, 9
 processes, 9
 result of contact mechanical work, 8
- Depth sensing nanoindentation, mechanical properties, 202, 204, 210
- Dewetting
 effect of grafting density on compatible copolymers, 168, 169*f*, 170*f*
 effect of grafting density on incompatible copolymers, 168, 171*f*
See also Disentanglement in ultrathin polymer films
- Disentanglement in ultrathin polymer films
 boundary layer thickness and disentanglement strength, 160, 163

- calibrating cantilever of unknown torsional spring constant, 173
- calibration procedure, 172–173
- decreasing dewetting velocity with increasing grafting density for non-compatible homopolymer/graft-copolymer systems, 171*f*
- dependence of mechanical properties on interfacial interactions, 154
- determining calibration friction coefficient, 157–158
- determining normal load, 172–173
- effect of grafting density on dewetting of compatible polymers, 168
- effect of grafting density on dewetting of incompatible polymers, 168
- effects of film coating procedures, 155–156
- effects of spin coating and substrate interaction, 172
- equilibrium theories and extent of interfacial confinement, 155–156
- experimental, 156–158
- flow and sliding properties from structural model, 164
- friction coefficient of well-defined cantilever, 173
- graft copolymers, 156*f*
- increase in interfacial tension between homopolymer and graft copolymer with grafting density, 170*f*
- increasing dewetting velocity with increasing grafting density on binary homopolymer/graft-copolymer systems, 169*f*
- instrumentation, 157
- interfacial energy of graft-copolymers and effect of wetting autophobicity, 167–168
- jump off adhesion forces from force displacement curves as function of transition loads for film thicknesses, 165*f*
- lateral disentanglement strength, 158–160
- lateral force calibration, 157–158
- lateral force friction measurements as function of applied load on polyethylene–copropylene (PEP), 159*f*
- lateral force versus load measurements of thick PEP films, 161*f*
- load independent work of adhesion, 167
- materials in study, 156–157
- parabolic friction regime, 158, 160
- samples to test wetting compatibility, 156–157
- shear mechanical measurements by SFM, 155–156
- sliding or lubrication regime, 160
- spin-coating induced strain and density gradient, 163–164
- structural model, 163–164, 166*f*
- surface energy of interfacially confined films, 172
- surface free energy of strained homopolymer elastomer films, 167
- transition loads of PEP as function of film thickness, 162*f*
- two-fluid model, 172
- two-fluid model of interfacially constraint PEP film, 166*f*
- viscous plug flow regime, 160
- wetting-autophobicity, 156–157
- Disk drive applications
 - achieving higher recording densities in future, 405, 407
 - contact angle measurements, 408–411
 - contact angle results, 409–411
 - cosine of contact angle of alkane droplets on CH_x overcoated disks versus lubricant thickness, 410*f*
 - cosine of water contact angle versus lubricant thickness, 410*f*
 - criteria for good polymer layers on disk surfaces, 407–408
 - importance of contact angle results, 411
 - nanotribology, 407
 - perfluoropolyethers as disk lubricants, 408
 - polycyanate ester overlayer for disks, 411–417
 - polycyanate ester preparation, 412–414
 - polymerization mechanism of polycyanate ester, 414
 - schematic of inside of disk drive, 405, 406*f*
 - tapping mode atomic force microscopy (TMAFM) of bare silicon wafer and of film of polycyanate ester overlayer, 416*f*
 - topography of polycyanate esters, 414, 417
 - See also* Polycyanate ester
- Dissipation, result of contact mechanical work, 8
- DMT (Derjaguin, Muller and Toporov) theory, including interactions outside contact area, 477
- Droplet erosion test, 397, 398*f*, 399
- Drug delivery device. *See* Medical devices
- Dry friction
 - applying normal load to slider and substrate, 480*f*
 - applying tangential load to slider/substrate pair in contact under normal load, 480*f*
 - contacting, 477–479
 - loading, 479, 480*f*
 - shearing, 479, 480*f*
- Dry sand rubber wheel test, abrasion resistance of plastics, 389, 390*f*
- Dugdale zone
 - fundamental restriction in theory, 38, 40
 - length, 33

- width, 27
- Dupré adhesion energy
- adhesion and rupture, 47–48
- bouncing ball, 55
- Dupré adhesion force, strained homopolymer elastomer films, 167
- Durability. *See* Chemisorbed organic lubricants for microelectromechanical systems (MEMS)
- Dynamical force microscopy, quantitative measurements, 125
- Dynamic loading, experimental aspects, 67–71
- Dynamic mechanical analysis (DMA). *See* Nano-dynamic mechanical analysis (DMA)

E

- Elastic contact
 - Boussinesq, Joseph, 43
 - comparison of distorted surface profiles of pure elastic contact and adhesion, 44*f*
 - observed penetration depth, 43, 45
 - pioneering work of Heinrich Hertz, 34
- Elastic modulus
 - comparison of different models, 184*f*
 - derivation of Young's modulus from Hertzian model, 183
 - evaluation from force-distance data, 187, 188*f*
 - Sneddon's, Hertzian, and JKR approaches, 183, 185
 - Sneddon's equations, 183
 - summarized data for depth variation for rubber, polyurethanes, poly(vinyl chloride), and polystyrene, 186*f*
 - surface, by Hertz mechanical model, 305
- Elastic solids
 - adhesive contact of elastic spheres, 26*f*
 - elastic modulus, 25
 - infinite tension at edge of contact, 25, 26*f*
 - JKR (Johnson, Kendall, & Roberts) and Maugis–Dugdale theories, 25–27
 - pull-off force, 25
 - width of Dugdale zone, 27
 - See also* Adherence of elastic/viscoelastic solids
- Elastomers
 - not tending to transfer material, 15
 - organic polymer systems, 9
 - surface free energy of strained homopolymer films, 167
 - viscoelastic losses, 49, 50*f*
- Electron diffraction, anisotropy and asymmetry, 122
- Electrostatic forces
 - atomic force microscopy (AFM) tip, 274
 - organic surfaces, 274–276

- tip-surface interactions, 274–276
- Ellipsometric measurements of thermal expansivity, studying glass transition, 227
- Environmental sensitivity, lubrication and, 18–20
- Erosion, definition, 397
- Erosion tests
 - cavitation erosion tests, 399
 - slurry abrasion response test, 399, 400*f*
 - slurry erosion resistance of ultrahigh molecular weight polyethylene versus various metals, 401*f*
 - water droplet, 397, 398*f*, 399
 - See also* Wear tests for plastics
- Erosive wear, car industry, 5
- External boundary lubrication, polymers, 18–19
- Eyring-type relationships, interface rheology, 13

F

- Fabric conditioners, use in rope systems, 3, 5
- Fabrics/fibrous assemblies, tribological polymer contacts, 4*f*
- Fatigue, wear, 16
- Films
 - improving interaction between polymers and environment, 5
 - tribological polymer contacts, 4*f*
 - viscoelastic, 36, 38
 - See also* Oligomer films, thin
- Fine particle system, extension of fiber system, 5
- Flory theory, determining chemical potentials, 375–376
- Flory–Huggins interaction parameters
 - polymer-surface interactions, 370–371
 - self-consistent field (SCF) calculations, 370
- Force calibration, atomic force microscopy (AFM), 126, 128*f*, 129*f*
- Force curve
 - calibration, 308–310
 - control of experiments versus tribological and approach-retract, 147, 149
 - cycles in contact atomic force microscopy (AFM), 134, 136*f*
 - results reinforcing molecular weight dependence, 149
 - theory, 305–306
 - See also* Polypropylene/(ethylene-propylene) copolymer blends (PP/EP)
- Force-distance curves
 - adhesive properties from pull-off force, 219, 220*t*
 - elastic modulus evaluation from force-distance data, 187

- evaluation from force-distance data, 187, 188*f*
 force-distance curves for determining
 microscopic scale adhesive properties, 213
 force-distance measurements and lateral-force
 imaging, 273
 local probing of surface adhesive force, 224–
 225
 mechanical data from force curve analysis,
 219*f*
 polystyrene (PS) films at 27°C and 67°C, 217,
 218*f*
 Sneddon's, Hertzian, and JKR approaches for
 processing force-distance data and
 calculating Young's modulus at different
 penetration depths, 183, 184*f*
Force modulation microscopy (FMM)
 calibration, 308–310
 elastic and viscoelastic properties of
 copolymer blends at microscopy level, 305
 theory, 306
See also Polypropylene/(ethylene-propylene)
 copolymer blends (PP/EP)
**Fox and Flory law, equivalence between
 molecular weight and glass transition
 temperature, 137, 138*f***
Fracture, brittle, Griffith's theory, 45–47
Fracture mechanics
 adhesion and rupture, 47–48
 viscoelastic, 30, 33–34
**Fractures and crazes, contact atomic force
 microscopy (AFM), 137, 139**
Free volume
 fit of variation of diffusion constant and
 relaxation rate for 6-mers to free volume
 theory, 102*f*
 understanding trends in terms of, 98
Friction
 between micromachine structural elements
 using tribology test structure, 459, 460*f*
 classical distinction of modes, 10*f*
 Cobblestone model of interfacial, 326, 332–
 334
 Coloumbic or Ratchet, 12
 considering interfacial and ploughing forces in
 assigning mechanism of friction, 297
 contribution from internal viscoelastic
 dissipation, 284
 deformation or ploughing modes, 12
 dry, 477–479
 general equation for static and kinetic friction
 force, 332
 historical perspective, 474–475
 interpretation of rationalization of interfacial
 frictional modes, 12–13
 law, 43
 lubrication, 479, 481
 measurements of treated silicon coupons,
 458–461
 physical phenomena contributing to
 complexity of problem, 239
 physics, 477–483
 processes, 9–13
 schematic of modes, 11*f*
 stick-slip motion, 481, 483
 tester producing friction-relative velocity
 plots, 419
 theories, 475
 time-temperature dependence, 297
 type of tribological system, 2
See also Automotive interior plastics;
 Chemisorbed organic lubricants for
 microelectromechanical systems (MEMS);
 Dry friction; Medical devices
**Friction anisotropy, transcrystallized
 poly(ethylene oxide) (PEO) crystals, 326,
 331*f***
Friction coefficient
 calibration standard for well-defined
 cantilever, 173
 cantilever of unknown torsional spring
 constant, 173
 contact atomic force microscopy (AFM), 134,
 135*f*
**Friction devices, tribological polymer contacts,
 4*t***
Friction force microscopy (FFM)
 activation energy of poly(methyl
 methacrylate) (PMMA), 301
 Arrhenius plot of shift factor versus inverse
 temperature, 299*f*
 Arrhenius relationship between shift factor
 and temperature, 297
 determining velocity dependence of friction,
 295
 difference of trace and retrace lateral force
 images of PMMA film surface, 288, 289*f*
 distribution of frictional forces varying with
 temperature, 301
 experimental materials, 286
 experimental measurements using, 286
 frictional force versus scan velocity at several
 temperatures for PMMA film, 298*f*
 frictional force versus temperature at various
 scan velocities for PMMA film, 298*f*
 frictional force versus temperature for
 PMMA, poly(ethylene terephthalate)
 (PET), and polystyrene (PS), 295*f*
 friction difference images at 50°C, 90°C, and
 110°C for PMMA film surface, 291*f*
 friction force versus temperature for Si(100)

wafer with native oxide, 290*f*
 friction histogram dispersion versus mean
 friction force for PMMA film surface,
 294*f*
 Gaussian distribution equation, 293
 histograms of friction difference images fit to
 Gaussian distribution, 292*f*
 limited velocity range in commercial, 295
 lowered glass transition and activation energy
 measurements, 301
 master curve of frictional force versus velocity
 shifted to 60°C, 299*f*
 methodology, 288
 probing frictional processes at nanometer
 scale, 295
 profile of calibration grating and radius of
 curvature measurement, 287*f*
 pull-off force versus temperature for PMMA,
 PET, and PS, 296*f*
 rate dependence of hindered rotation of -
 COOCH₃ group in PMMA, 301–302
 surface rendered topographic AFM image of
 calibration grating displaying tip geometry,
 287*f*
 temperature dependence of friction on
 PMMA, PET, PS, 288, 293, 297
 thin film/bulk comparison, 300–301
 time-temperature dependence of friction, 297
 velocity/frequency relationship, 300

Friction regimes
 determining complex moduli of polymeric
 materials, 244, 249
 displacement of disk at constant velocity, 242
 effects of dwell time on stiction curve, 240,
 241*f*
 evolution of tangential force during
 displacement of sample at constant
 velocity, 240, 241*f*
 image of polymeric surface after stick-slip
 experiment, 254, 255*f*
 materials and method, 240–242
 normalized tangential force in static zone,
 244, 245*f*
 position of transition from static to dynamic
 friction versus indentation depth, 249, 251*f*
 precise definition of initial conditions of
 contact, 240
 relaxation modulus of polymer by
 differentiation, 244, 247*f*
 results confirming description of preliminary
 phase of friction, 244
 static friction, 242, 244, 249
 stick-slip experiment, 249, 253*f*, 254
 stiction curves at several velocities after
 constant dwell time, 243*f*
 stiction effect, 240, 241*f*

tangential force, 242
 tangential force during displacement of
 sample at constant velocity and small
 periodic lateral displacement, 249, 250*f*
 tangential force normalized to velocity and
 indentation depth versus time, 244, 246*f*
 transition-sliding friction, 249, 254
 variation of characteristic length of contact
 area and continuous tangential force, 249,
 250*f*
 variation of dynamic friction coefficient with
 velocity, 254, 256*f*
 variation of effective energy of separation
 between tip and viscoelastic material versus
 displacement velocity, 249, 252*f*
 variations of storage and loss moduli with
 frequency from analysis of material
 response to periodic modulation, 244, 248*f*,
 249

G

Gaussian distribution equation, 293
 Gelatin, velocity dependence of friction, 285
Glass transition
 correlation between glass transition induced
 by confinement and ordinary thermal, 112
 critical free volume, 237
 debating exact nature of, 98
 ellipsometric measurements of thermal
 expansivity to study, 227
 scaling near, 98, 100–101
 Glass transition temperature
 detection during sliding of thin films, 13
 variation with molecular weight, 137, 138*f*
Glassy systems
 becoming trapped in metastable states, 106–
 107
 response of glassy system for advancing
 translation stage at constant velocity, 104,
 105*f*
 response to oscillatory shear force, 101, 103*f*
 static friction and lower, velocity independent,
 sliding friction, 113
 transferring under higher sliding velocities, 15

Gold
 calculated surface energies from pull-off data,
 196*f*
 lever deflection versus sample displacement,
 199*f*
 pull-off force versus maximum applied load
 during contact, 197*f*

Graft copolymers
 interfacial energy of, and effect on wetting
 autophobicity, 167–168

testing wetting compatibility, 156–157

See also Disentanglement in ultrathin polymer films

Grafting density

effect on dewetting of compatible polymers, 168, 169*f*, 170*f*

effect on dewetting of incompatible polymers, 168, 171*f*

Graphite, calculated surface energies from pull-off data, 196*t*

Griffith's theory

brittle fracture, 45–47

distribution of cohesive forces in crack tip, 47

interaction energy, 46*f*

strain energy release rate, 45

H

Hamaker constant, function of chemical composition and density of materials, 134

Hertz, Heinrich, 43

Hertz model

calculating depth dependencies of elastic moduli, 185, 186*f*

comparison between surface Young's modulus from force modulation experiments and volume modulus using Hertz model, 310*f*

comparison of Young's modulus from force-indentation curves using Hertz elastic and JKR (Johnson, Kendall & Roberts) model, 309*f*

elastic modulus, 183, 184*f*

elastic modulus for stiffer polymers, 308–309

surface elastic modulus using Hertz model, 305

Hertz theory

modulation amplitude, 68–69

Young's modulus, 158, 160

Hexadecanethiol

height and friction-force images for sample by microcontact printing with, 275*f*

See also Surface nanochemical studies

High-density polyethylene (HDPE). *See*

Polyethylene (PE) single crystals

Hooke's law

application to spontaneous peeling, 51

deducing tip-sample interaction force, 305

modulation amplitude, 68–69

Hydrodynamic lubrication regime, 481

Hypodermic needle. *See* Medical devices

Hysteresis, more work separating two surfaces than returning together, 24–25

I

Injection-molded blends

versus compression-molded blends, 310–313

See also Polypropylene/(ethylene-propylene) copolymer blends (PP/EP)

Interface zone, third body, 8

Interfacial friction, Cobblestone model, 326, 332–334

Interfacial frictional modes, interpretation of rationalization, 12–13

Interfacial mode, damage, 13–15

Interfacial slippage in adhesive release

adhesion energies of silicone coatings, 87*t*

contact angles of water, 85*t*

direct measurement of surface energetics of poly(dimethylsiloxane) (PDMS) coatings by contact mechanics, 86–87

interfacial shear stress of acrylic adhesive on silicone coatings as function of shear velocity, 89*f*

investigation of interfacial slippage, 87–89

oscillatory motion of fluorescent particles at adhesive-polymer interfaces, 88*f*

relationship between peel fracture energy and velocity of crack propagation, 85*f*

release profiles of silicone coatings, 84–86

simplified sketch showing release of adhesive from surface, 84*f*

Isotactic polypropylene (i-PP). *See* Surface nanochemical studies

J

JKR (Johnson, Kendall & Roberts) theory

adhesion and rupture, 47–48

adhesive contact of elastic spheres, 26*f*

attractive interactions acting across contact area, 477

comparison of Young's modulus from force-indentation curves using Hertz elastic and JKR model, 309*f*

connecting pull-off adhesion force with work of adhesion, 167

elastic model accounting for adhesion force between tip and surface, 306

elastic modulus, 183, 184*f*

elastic solids, 25–27

equation, 41

maximum force at pull-off point, 185

perfectly elastic solids assuming reversible behavior, 24

pull-off force for adhesion, 194
Journal bearings, tribological polymer contacts, 4*f*

L

Lamellar crystals. *See* Polymer lamellar crystals
Langevin method, model for heat flow, 95
Langmuir–Blodgett films, microtribology model system, 121–123
- Lateral force microscopy (LFM)
 calibration method, 172–173
 determining calibration friction coefficient, 157–158
 Langmuir–Blodgett films, 121–123
 scanning angle dependence of lateral force, 343–345
 surface nanochemical imaging of organic surfaces, 273
 See also Molecular alignment and nanotribology of polymeric solids; Polyethylene (PE) single crystals; Surface nanochemical studies
Lennard–Jones (LJ) potential
 modeling films containing linear short-chain molecules, 92
 wall atoms and fluid monomers interacting with, 93
Linear viscoelastic materials
 contact mechanics, 71–80
 creep in absence of adhesion, 71–77
 creep with adhesion, 77–80
 See also Nanometer-scale contacts to linear viscoelastic materials
Linear viscoelastic solids
 contact cycle, 29
 creep compliance function, 27, 28*f*
 material characteristics, 27, 29
 phase angle, 27
 phase angle between cyclic stress and strain, 28*f*
 ramp cycle with load increased and reduced at uniform rate, 31*f*
 three-parameter model, 28*f*
Losses, viscoelastic, 48–49
Low density polyethylene films
 samples for adhesion and mechanical testing, 193
 See Scanning probe microscopy (SPM)
Lubricants
 important secondary issues in organic polymer systems, 6
 tribological polymer contacts, 4*f*
Lubrication
 boundary lubrication regime, 481

 contacting, 481, 482*f*
 effect on tribological performance of polymers, 20
 environmental sensitivity, 18–20
 external boundary of polymers, 18–19
 fluids for polymeric contact, 19
 friction in presence of lubricant, 475–476
 hydrodynamic lubrication regime, 481
 loading, 481
 lubricant layer thickness decreasing with contact pressure or time, 482*f*
 mixed lubrication regime, 481
 physics of friction, 479, 481
 regimes of lubricated friction, 475
 shearing, 481
 suppressing scratch damage, 15–16
 type of tribological system, 2
 See also Chemisorbed organic lubricants for microelectromechanical systems (MEMS)
Lubrication or sliding regime, lateral disentanglement strength, 160

M

Magnetic alternative current (MAC) mode scanning force microscopy (SFM) mode, 349
 schematic of MAC mode SFM with liquid cell, 350*f*
 SFM image of ionized poly-2-vinylpyridine (PVP) brushes on mica, 349, 350*f*
 See also Sparse coatings
Mar behavior
 causes of mar, 428–429
 definition, 428
 difficulty determining plastic deformation threshold, 434–435
 factors affecting mar resistance of polymeric coatings, 446
 problem characterizing, 429
 relationship between physical damage and appearance, 435
 required parameters for characterizing mar performance, 434
 terms and tests describing, 439–440
 See also Automotive topcoats; Polymeric surface coatings
Mar resistance
 complex interplay of processes, 258–259
 standard tests, 259
Marine slideway supports, 6
Material science, application of, 20–21
Maugis–Dugdale theory
 adhesive contact of elastic spheres, 26*f*
 elastic solids, 25–27
 modification and extension of Savkoor and Briggs approach for adhesion, 242

- steady-state moving interface crack, 30, 32*f*
- Maxwell model
- effects of adhesion, 79
 - series combination of elastic spring and dashpot, 73
 - solutions to Ting model for contact of rigid probe with viscoelastic substrate, 75*f*
 - time of maximum contact radius as function of contact, 76*f*
- Mechanical properties of polymers
- calculated surface stiffness and tip penetration depths for epoxy (CET)-rubber (GRC) composite surface, 200*t*
 - calculated surface stiffness and tip penetration depths for several materials, 200*t*
 - contact mode AFM of CET-GRC after cryo-polishing and staining in OsO₄ vapor, 200, 201*f*
 - dependence on interfacial interactions, 154
 - depth sensing nanoindentation, 202, 204, 210
 - force versus distance curves of polystyrene (PS) films with varying molecular weight at 27°C and 67°C, 217, 218*f*
 - Hertzian contact mechanics for calculating surface stiffness and tip penetration depths during contact, 198
 - lever deflection of soft cantilevers, 198-202
 - lever deflection versus sample displacement for all surfaces, 199*f*
 - mechanical data from force curve analysis, 219
 - nanoindentation of commercial polycarbonate using Berkovich diamond indenter, 205*f*
 - nanoindentation of commercial polycarbonate with protective coating using Berkovich diamond indenter, 206*f*
 - static deflection AFM, 207
 - tapping mode (TMAFM) height and phase images of CET-GRC after cryo-polishing, 203*f*
 - tapping mode with phase detection, 202
- Medical devices
- breakout force, 486-487
 - broad range of instruments, 476
 - friction in disposable plastic syringes, 484-489
 - handling characteristics of manually operated syringe, 484, 486
 - hypodermic needle friction, 483-484
 - illustrating physics of friction and lubrication, 489
 - manual syringe operation, 484, 486
 - physics of friction, 477-483
 - relationship between syringe friction and fundamental physics of friction, 486*f*
 - schematic of three-piece syringe, 478*f*
 - sterilization, 488-489
 - sterilization requirements, 476
 - stick-slip motion in syringe, 487-488
 - syringe pump operations, 487-488
 - syringes, 476
 - typical syringe friction diagram, 485*f*
- Memory
- dramatic memory effects reflecting structural changes, 112-113
 - illustration, 110, 111*f*
 - transient behavior during yield and memory storage, 106-112
 - See also* Oligomer films, thin
- Mica
- calculated surface energies from pull-off data, 196*t*
 - lever deflection versus sample displacement, 199*f*
 - pull-off force versus maximum applied load during contact, 197*f*
- Micro- and nano-wear of polymeric materials
- calculating wear volume, 264
 - chemistry of various topcoats, 268
 - coupling microscratch device with large stage atomic force microscopy (AFM), 259-260
 - determining detailed scratch morphology, 260
 - experimental, 259-260, 264
 - extended region around fracture threshold, 267*f*
 - functions of industrial polymers and coatings, 258
 - integrated area as function of distance, 266, 267*f*, 268
 - mar resistance, 258-259
 - penetration depth and tangential force as normal force is ramped during microscratch experiment, 261*f*
 - positive wear rate during abrasion experiment, 268
 - regimes in micromechanical measurements and scratch morphology plots, 264, 266
 - responses to forces exerted during scratch, 264
 - scratch morphology calculations, 260, 263*f*, 264
 - scratch morphology parameters as function of scratch distance, 265*f*
 - selected AFM images, 262*f*
 - single indenter scratch tests, 259
 - trend towards deeper and gaping crevices with increasing normal load, 266
 - visibility of scratch, 264
 - wear volume providing insight into nature of fracture event, 266
- Micro cracking
- dynamic process study, 442
 - studying in polymeric coatings, 449
- Micro electromechanical systems (MEMS)

- fabrication and surface treatments, 455
 impact, rolling, and sliding motions between structures, 456
See also Chemisorbed organic lubricants for microelectromechanical systems (MEMS)
- Micro mar resistance (MMR)
 definition, 444
 measurement, 440–441
 micro indentation hardness (MIH), MMR, and responses to marring stress on coatings, 447*f*
 schematic of how to calculate MMR, 447*f*
See also Polymeric surface coatings
- Micromechanical properties of polymers
 checking mechanical and piezoelement creep contribution, 178–179
 correlation between elastic moduli from scanning force microscopy (SFM) and bulk values, 185
 correlation between elastic modulus values in compression mode and retracing mode, 188*f*
 derivation of Young's modulus from Hertzian model, 183
 developing scanning force microscopy (SFM) data processing procedures, 181, 183
 distribution of applicability of cantilevers with different nominal stiffness towards various materials, 181*f*
 double-spring model of elastic contact, 182*f*
 elastic modulus evaluation from force-distance data, 187
 estimating acceptable range of spring parameters, 179
 experimental, 178–179
 force distance data for polyisoprene rubber in approaching-retracing cycle, 180*f*
 full cycle of approaching-retracing measurements, 179, 180*f*
 Hertzian model calculating depth dependencies of elastic moduli for polymeric materials, 185, 186*f*
 Hertzian model of elastic contact and two-spring model, 181
 maximum force at pull-off point by JKR model, 185
 neck behavior under tensile stress, 187
 probing elastic modulus in tensile mode for compliant materials with strong adhesion, 185
 range of applicability of cantilevers, 182*f*
 ratio of indentation depth and cantilever deflection, 179, 181
 silicon and silicon nitride V-shaped cantilevers, 178
 Sneddon's, Hertzian, and JKR approaches for processing force-distance data and calculating Young's modulus at different penetration depths, 183, 184*f*
 Sneddon's equation for model, 183
 testing validity of proposed plot, 181
- Micromechanics
 avoiding problems of frictional effects and low sensitivity, 120
 force microscope and rigidity images as function of temperature, 120*f*
 polymer films, 118–120
 schematic of nano-dynamic mechanical analysis (DMA), 119*f*
 thermal drift problem, 120
- Microphase separation. *See* Block copolymers
- Microprobe instruments
 advantageous for adhesion measurements, 24
 measuring surface energy and viscoelastic properties, 24
- Microtribology
 anisotropy and asymmetry, 122–123
 flower-shaped domains in Langmuir–Blodgett monolayer on mica, 122
 Langmuir–Blodgett film on mica as model system, 121
 schematic of frictional and structural results, 122*f*
 series of lateral force images, 121*f*
 tip of atomic force microscope contacting surface, 121
- Mixed lubrication regime, 481
- Modeling interactions
 adsorbed amount of functionalized chains versus surface separation for various lengths of nonfunctionalized chains, 379*f*
 analytical model results, 377–380
 analytical self-consistent field (SCF) theory, 373–377
 assuming melt in thermodynamic equilibrium with clay particles, 373
 bare clay sheets and polymer mixture with functionalized and nonfunctionalized species, 371
 bare surfaces and surrounding melt of identical chains, 370–371
 chemical potential of end-modified chains, 375–376
 comparing SCF values and analytical predictions, 378, 380
 distributions of components in system, 374
 entropy of mixing per unit volume for free chains, 374
 equilibrium behavior of interactions between two clay surfaces and polymer melt, 380
 expressions for profiles of attached and free polymers in undeformed system, 377–378

free energy per unit area as function of surface separation in melt containing two types of polymers, 372*f*

free energy per unit area as function of surface separation in single-component melt, 372*f*

increasing distance between sheets affecting structure of melt, 377

increasing fraction of functionalized chains, 371

melt of mobile polymers of functionalized and nonfunctionalized chains, 373

mixing entropy of mobile chains, 375

numerical model results, 370–373

numeric SCF model, 370

optimal polymeric composites for creating stable exfoliated composites, 371, 373, 380

perturbing system or decreasing distance between two surfaces, 378

profiles for all components, 376–377

profiles of components between surfaces, 374–375

quantitative description of critical characteristics and behavior of system, 377–378

scheme for creating stable dispersions from immiscible polymers and clays, 369–370

total free energy of system, 375, 376

total free energy per unit area, 377

Molecular alignment and nanotribology of polymeric solids

adhesion image of lamellar polyethylene (PE) crystal, 329*f*

Cobblestone model of interfacial friction, 326, 332–334

dual height and friction image of poly(ethylene oxide) (PEO) transcrystallized on electrospun PEO fibers, 331*f*

experimentally determined friction force versus relative scan angle for poly(tetrafluoroethylene) (PTFE), 333*f*

friction force image and adhesion force image on PE lamellar crystal in water, 330*f*

friction force versus normal force plot for HDPE for different relative scan directions with Si_3N_4 tip in air, 324*f*

friction force versus normal force plot for HDPE using modified tips in air, 324*f*

friction versus normal force versus scan velocity for difference in high and low friction, 328*f*

friction versus normal force versus scan velocity for high friction, 327*f*

friction versus normal force versus scan velocity for low friction, 327*f*

friction versus relative scan angle for oriented PTFE with Si_3N_4 tip in ethanol and air, 322*f*

general equation for static and kinetic friction force, 332

LFM image of high density polyethylene (HDPE) with $-\text{CF}_3$ tip in air, 323*f*

LFM image of PTFE with molecular resolution, 320*f*

LFM image of solution grown polyethylene (PE) lamellar crystal in air, 325*f*

materials and orientation, 318–319

polymer lamellar crystals grown from solution, 321, 326

scanning force microscopy/lateral force microscopy experiments, 319

schematic of chain fold directions in LFM image of solution grown PE lamellar crystal, 325*f*

schematic of events occurring during sliding motion of AFM tip over ordered surface, 333*f*

transcrystallized polymer crystals, 326

typical SFM image of morphology of oriented PTFE, 320*f*

uniaxially oriented polymer fibers, 319, 321

Molecular dynamics (MD) simulations

oligomers between parallel surfaces, 91–92

See also Oligomer films, thin

Molecular relaxations

internal viscoelastic dissipation from, 284

interpreting interface shear phenomena, 12

See also Friction force microscopy (FFM)

Molecular weight, glass transition temperature varying with, 137, 138*f*

Molecular weight dependence, contact atomic force microscopy (AFM), 134, 137, 138*f*

Morphological transitions

order-disorder transition, 364

See also Block copolymers

N

Nanochemical studies. *See* Surface nanochemical studies

Nano-dynamic mechanical analysis (DMA) avoiding problems of frictional effects and low sensitivity, 120

force microscope and rigidity images as function of temperature, 120*f*

schematic diagram, 119*f*

sinusoidal mechanical oscillation, 118

technical hurdles, 119

thermal drift problem, 120

Nanometer-scale contacts to linear viscoelastic materials

adding adhesion to Maxwell model, 79

adding adhesion to Voigt/Kelvin model, 79, 80*f*

adhesion energy, 77
 contact mechanics, 71–80
 continuum mechanics models, 66
 creep effects due to bulk deformation, 78
 creep in viscoelastic contacts in absence of adhesion, 71–77
 creep in viscoelastic contacts with adhesion, 77–80
 deformation, 72–73
 Derjaguin approximation, 77
 designing shear modulation experiments for SFM, 70–71
 dynamic contact between silicon nitride SFM tip and poly(vinyl ethylene) sample, 69f
 effects dominating in SFM-scale contacts, 78–79
 experimental aspects of dynamic loading, 67–71
 fracture mechanics, 78
 geometry of deformable contact between axially symmetric bodies, 67f
 ignoring effects of creep on contact in fracture mechanics approach, 78
 incorporation effects of adhesion into Ting model, 79
 major features of Ting solution, 73, 75f, 76
 Maxwell model, 73
 modulation amplitude using Hertzian result and Hooke's law, 68
 observations useful in design and analysis of creep experiments, 76–77
 range of expected behavior for linear loading ramp, 73, 74f, 75f, 76f
 relationship between amplitudes and phases of drive signal tip and contact, 68f
 schematic of scanning force microscope (SFM) contact with shear modulation, 68f
 standard solid model, 73
 Voigt/Kelvin model, 73
 Nanoscopic surface structures
 scanning force microscopy (SFM), 346–347
See also Sparse coatings
 Nanotip scale. *See* Physics and physical chemistry at nanotip scale
 Nanotribology
 developing microscopic models of friction and relationship between friction and adhesion, 318
 solid-melt transition as cause for stick-slip, 483
 study of friction, lubrication and wear nanometer and sub-nanometer scale, 407
See also Disk drive applications; Molecular alignment and nanotribology of polymeric solids
 Nano-wear. *See* Micro- and nano-wear of polymeric materials

Nose–Hoover method, heat from all regions of space, 95
 Nylon fabric systems, self lubrication, 6
 Nylon system water, weakening or softening polymer surface, 19

O

Octadecyltrichlorosilane (ODTS)
 effect of contact conditions on magnitude of force and height change, 466, 467f
 effect of ODTS coverage on micromachine operation, 469, 472
 friction coefficient and cycles to seizure for sidewall devices, 469f
 initial friction coefficient and sliding cycles as function of ODTS coverage, 463f
 lateral force and secondary ion mass spectroscopy (SIMS) images of patterned ODTS on silicon, 465f
 lateral force image of ODTS film altered by rubbing, 467f
 macroscopic tribological performance, 461, 464
 scanning probe microscopy (SPM) response of ODTS films, 464, 466
See also Chemisorbed organic lubricants for microelectromechanical systems (MEMS); Silanes
 Oligomer films, thin
 changes in mode of sliding reflecting internal film properties, 107
 channeling in simulations possibly explaining memory effects, 110, 112
 confinement limits, 109
 correlation between glass transition induced by confinement and ordinary thermal, 112
 debating exact nature of glass transitions, 98
 Debye–Waller factor, 110
 distribution of shear displacements in film, 107
 dramatic memory effects reflecting structural changes, 112–113
 energy contours as function of position for single monomer moving over (111) surface, 94f
 factors affecting phase of film, 96
 film entering solid state, 96
 film remembering past motion, 106
 film response for low amplitudes, 101
 film thickness in role of temperature, 100
 fit of variation of diffusion constant and relaxation rate for 6-mers to free volume theory, 102f
 glassy system becoming trapped in metastable states, 106–107

- illustration of memory, 110, 111*f*
 increase in spacing between walls during sliding at constant load, 104
 maintaining constant temperature, 95–96
 memory storage in sliding direction, 107, 109
 method of imposing shear, 93–95
 monomer alignment after sliding, 109–110
 non-linear response to applied stress, 92
 oscillatory stick-slip motion, 104
 packing density fluctuations for new metastable configurations, 107
 phase transitions and steady state shear response, 96–101
 plots of velocity versus shear rate, 99*f*
 possible origins of static friction, 113
 potentials and geometry, 92–93
 power law of viscosity over three decades in shear rate, 112
 quantifying response of system to shear, 96
 response of glassy system for advancing translation stage at constant velocity, 104, 105*f*
 response to oscillatory shear, 101, 103–104
 scaling near glass transition, 98, 100–101
 shear-melting transitions at constant temperature, 106
 simulation method, 92–96
 snapshots of wall and monomer atoms at bottom of film, 109
 stick-slip events exhibiting memory, 92
 stick-slip motion, 104–106
 structural changes within film, 104, 106
 temperature dependence of frictional force and wall velocity, 97*f*
 time dependence of various film properties, 108*f*
 transient behavior during yield and memory storage, 106–112
 transition from elastic response to slip as drive amplitude increases, 101
 transition from static glassy or crystalline state to shearing liquid state, 104, 106
 trends in terms of free volume, 98
 units, 93
 universal curve of simulation results for viscosity, 100–101, 102*f*
 unsteady motion, 101, 104–106
- Organic films**
 nanochemical imaging, 279
See also Surface nanochemical studies
- Organic polymer systems**
 elastomers, 9
 generic peculiarity, 3
 high wear rates, 8
- Orientational order, memory storage in sliding direction, 107, 109**
- Oscillating tip**
 difficulty of results, 149
 experiments without or only slightly touching surface, 149
 mechanical response of polystyrene (PS) films, 140, 142*f*, 143*f*
 nanoprotuberance growth under action of tip, 144–147
 typical approach-retract curve, 140, 141*f*
See also Physics and physical chemistry at nanotip scale
- Oscillatory shear, response, 101, 103–104**
- Oscillatory stick-slip motion, thin oligomer films, 104–106**
- P**
- Parabolic friction regime, lateral disentanglement strength, 158, 160**
- Parenteral drug delivery device, hypodermic needle, 483**
- Peeling**
 relationship between fracture energy and velocity of crack propagation, 85
See also Spontaneous peeling
- Phase angle, linear viscoelastic solids, 27, 28*f***
- Phase detection imaging (PDI)**
 probing local mechanical properties at surface, 358
See also Block copolymers
- Phase transitions**
 steady state shear response, 96–101
See also Oligomer films, thin
- Physics and physical chemistry at nanotip scale**
 AFM (atomic force microscopy) key issues, 125–131
 AFM experiment, 125
 AFM optical detection method sketches, 127*f*
 analogy with crazes and fractures, 137, 139
 approach-retract experimental curve changes during experimentation, 132*f*
 assuming disentanglement controlling friction process for intermediary molecular weight M_w , 139
 compliance of nanoprotuberance, 144, 146
 contact AFM, 134–139
 deflection and force calibration, 126
 difficulty of oscillating tip results, 149
 effective static force, 144
 equivalence between molecular weight and glass transition temperature, 137, 138*f*

- experimental conditions, 131–133
 experimental environment, 130–131
 force curve cycles, 134
 force curve experimental procedure less controlled, 147, 149
 force curve experiments on polystyrene (PS) films, 136*f*
 force curve results reinforcing Mw dependence aspect, 149
 friction coefficient, 134
 friction loop, 132*f*
 idealized approach-retract curve, 129*f*
 idealized force curve in contact AFM, 128*f*
 linking origin of non-linearity with experimental methods, 149
 local mechanical responses to polymeric films, 133–147
 mechanical response of PS films, 140
 mechanical susceptibility, 144
 modeling tip action, 145*f*
 molecular weight dependence, 134, 137
 nanoprotuberance growth under action of tip, 144–147
 nanoprotuberance height, 146–147
 obtaining in situ tip structure determination, 126, 130
 oscillating tip, 137–147
 oscillating tip experiments without or only slightly touching surface, 149
 reference sample, 131
 residence time, 144, 146
 sketch of craze preceding crack in vitreous polymer, 139*f*
 sketch of PS nanoprotuberance growing during tip vibration, 145*f*
 static contact and tapping modes, 125
 table of symbols, 150
 tapping experiments, 133
 Taylor development of residence time, 146
 tip characterization, 126, 130
 tip vibrating amplitude, 146
 tribological experiments, 133
 typical approach-retract curve, 140, 141*f*
 use of oscillating behavior of tip-cantilever (CL) system, 124–125
 variation of friction coefficient of PS samples with molecular weight, 135*f*
 variation of friction deflection with tip-sample distance variation, 135*f*
 variation of oscillation amplitude of vibrating tip during retract for three molecular weights, 143*f*
 variation of vibrating tip oscillation amplitude during retract, 142*f*
 variation with oscillation free amplitude of parameters for fits of amplitude variation
- with distance, 148*f*
 vertical location of sample, 146–147
 Pin abrasion test, standard for metals, 389, 390*f*
 Pin-on-disk test, not standard for plastic wear testing, 394
Plastics
 wear of conforming surfaces, 391–395
See also Wear tests for plastics
 Poly(acrylic acid) (PAA)
 force measurements of polar polymers, 278–279
 histograms of pull-off forces between SiO_x probe and gold probe with PAA, 280*f*, 281*f*
 Poly(acrylonitrile) (PAN)
 force measurements of polar polymers, 278–279
 histograms of pull-off forces between SiO_x probe and gold probe with PAN, 280*f*, 281*f*
 Poly(*n*-butylacrylate). *See* Block copolymers
 Polycarbonate (PC)
 mechanical properties using depth sensing nanoindentation, 202, 204
 nanoindentation of commercial surface, 205*f*
 nanoindentation of commercial surface with protective coating, 206*f*
 occurrence of stick slip, static coefficient of friction (COF), and COF drop for four surface textures, 421*t*, 422*t*
See also Automotive interior plastics
Polycyanate ester
 chemical nature of 2,2'-bis(4-cyanatophenyl)isopropylidene (BCPP) monomer and cross-linked ring network formation, 413*f*
 deposition, 412
 Fourier transform infrared (FTIR) spectroscopy, 414
 heating, 414
 overlayer for disks, 411–412
 polymerization, 412
 polymerization mechanism, 414
 preparation, 412–414
 schematic of preparation technique for forming overlayer on disk surfaces, 413*f*
 solubility, 412
 tapping mode atomic force microscopy (TMAFM) image of bare silicon wafer and of film of polycyanate ester overlayer, 416*f*
 topography, 414, 417
 vibrational spectra using FTIR of thick monomer film before and after polymerization with UV irradiation, 415*f*
See also Disk drive applications
 Poly(dimethylsiloxane) (PDMS)
 calculated surface stiffness and tip penetration depths, 200*r*

- facilitating release of adhesives, 83
 lever deflection versus sample displacement, 198, 199*f*
 samples for adhesion and mechanical testing, 193
See also Scanning probe microscopy (SPM);
 Silicone coatings
- Polyelectrolyte cylindrical brushes. *See* Sparse coatings
- Polyethylene (PE)
 image of PE with nano-scratch at surface, 446, 448*f*
 mar resistance, 444, 446
 plot of cantilever deflection versus vertical advancement of sample against tip, 443*f*
See also Polymeric surface coatings
- Polyethylene, high-density
 uniaxially oriented polymer fibers, 321, 323*f*, 324*f*
See also Molecular alignment and nanotribology of polymeric solids
- Polyethylene, low-density films
 adhesion using pull-off force, 194–198
 calculated surface energies from pull-off data, 196*t*
 calculated surface stiffness and tip penetration depths, 200*t*
 deflection versus distance curves, 195*f*
 lever deflection versus sample displacement, 198, 199*f*
 pull-off force versus maximum applied load during contact, 197*f*
 samples for adhesion and mechanical testing, 193
See also Scanning probe microscopy (SPM)
- Polyethylene-copolymer (PEP)
 film properties changing in vicinity of interactive substrate, 155
 lateral force versus load measurements of PEP films, 161*f*
 structural model from previous PEP and PS film studies, 163–164
 transition loads of PEP as function of film thickness, 162*f*
See also Disentanglement in ultrathin polymer films
- Poly(ethylene oxide) (PEO)
 transcrystallized polymer crystals, 326, 331*f*
See also Molecular alignment and nanotribology of polymeric solids
- Polyethylene (PE) lamellar crystal
 adhesion image, 329*f*
 crystals from solution, 321, 326
 friction force image and adhesion force image on crystal in water, 330*f*
 friction versus normal force versus scan velocity for high friction, low friction and friction difference, 327*f*, 328*f*
 lateral force microscopy (LFM) image of solution grown crystal in air, 325*f*
 schematic of chain fold directions in LFM image of solution grown crystal, 325*f*
See also Molecular alignment and nanotribology of polymeric solids
- Polyethylene (PE) single crystals
 adjacent reentry and regular sharp fold model and random reentry fold model at surface of high-density PE (HDPE) single crystal, 343, 344*f*
 AFM (atomic force microscopy), lateral force microscopy (LFM), and relationship between scanning direction of cantilever and chain folding direction of single crystals of different molecular weight, 340*f*, 341*f*, 342*f*
 AFM observation and LFM measurement, 338, 343
 crystallization conditions of HDPE single crystals in self-seeding method, 339*t*
 procedure for obtaining AFM and LFM images, 338
 sample preparation, 337–338
 scanning angle dependence of lateral force, 343–345
 scanning angle dependence of lateral force for HDPE single crystals by self-seeding method, 344*f*
 schematic of lateral force curve with bidirectional scanings, 344*f*
 schematic of scanning angle definition in lateral force measurement, 339*f*
- Poly(ethylene terephthalate) (PET)
 frictional force versus temperature, 295*f*
 material for friction force microscopy (FFM), 286
 no adhesion dependence on temperature, 300
 pull-off force versus temperature, 296*f*
 temperature dependence of friction, 288, 293, 297
 velocity dependence of friction, 285
- Polyisoprene rubber
 depth variation of elastic modulus, 185, 186*f*
 distribution of applicability of cantilevers with nominal stiffness, 181*t*
 force distance data in approaching-retracing cycle, 179, 180*f*
 samples for micromechanical analysis, 178
See also Micromechanical properties of polymers
- Polymer films

- nanochemical imaging, 279
 processing, 5–6
See also Surface nanochemical studies
- Polymer lamellar crystals**
 adhesion image of lamellar PE crystal, 329f
 friction force image and adhesion force image on PE crystal in water, 330f
 friction versus normal force versus scan velocity for high friction, low friction, and difference for PE in air, 327f, 328f
 lateral force microscopy (LFM) image of solution grown polyethylene (PE) in air, 326f
 schematic of chain fold directions in LFM image of PE crystal, 325f
 solution grown, 321, 326
See also Molecular alignment and nanotribology of polymeric solids
- Polymer melt, molecular interpretation of stresses, 232, 234**
- Polymer processing and manufacture**
 crucial influence of wall friction, 5
 tribological polymer contacts, 4f
- Polymer surfaces, inducing modification of operating performance, 19**
- Polymer tribologists, lacking attempt to unify tribology of thermosets and thermoplastics, 9**
- Polymer tribology**
 composite and alloy systems, 9
 scientific enquiry, 21
 variety of nature of contacts, 6
- Polymeric solids. *See* Molecular alignment and nanotribology of polymeric solids**
- Polymeric surface coatings**
 coating panels preparation, 440
 comparing experimental and theoretical values of total volume of shoulders of mar, 450f
 correlation between structure of coatings and tribological properties, 446
 cross-section area of indentation equation, 442
 depth of ditch versus number of scrapings, 450f
 dynamic process study, 442
 experimental, 440–442
 experimental polyurethane (PU) coating with mars and its cross-section profile, 444, 445f
 factors affecting mar resistance, 446
 force calibration, 441
 force curve at surface of diamond sheet, 443f
 images of bottom of ditch after different numbers of scrapings, 452, 453f
 images of coatings with nano-scratch at surfaces, 448f
 indentation analysis model to analyze coating under repeated scrapings, 449, 451f, 452
 mar resistances of different coatings, 444, 446
 measurement of depth of indentation, 441–442
- micro indentation hardness (MIH), micro mar resistance (MMR), and responses to marring stress of three coatings, 447f
 MMR characterizing performance of coating, 444
 MMR measurement, 440–441
 plot of cantilever deflection versus vertical advancement of sample against tip, 443f
 profile of 90° conical tip with 1 μm radius at apex, 445f
 scanning probe microscopy (SPM) instrument, 440
 schematic of how to calculate MMR and responses of coating to marring stress, 447f
 studying strain-hardening, micro cracking, and surface fatigue, 449
 studying viscoelastic creep, 446, 449
- Polymers**
 chip-forming or machining operations, 5
 external boundary lubrication, 18–19
 self-lubricating capacity, 8
 variety of characteristics, 20
 wide use in bearing-practice, 8
See also Modeling interactions
- Poly(methyl methacrylate) (PMMA)**
 activation energy, 301
 adhesive force images, 221–224
 difference of trace and retrace lateral force images of PMMA film surface, 288, 289f
 force measurements of polar polymers, 278–279
 frictional force versus scan velocity at several temperatures for PMMA film, 298f
 frictional force versus temperature, 295f
 frictional force versus temperature at various scan velocities for PMMA film, 298f
 friction difference images at 50°C, 90°C, and 110°C for PMMA film surface, 291f
 friction histogram dispersion versus mean frictional force for PMMA film surface, 294f
 glass-like properties under mechanical load, 212
 height and friction images of spin-cast PS:PMMA polymer blend, 282f
 histograms of pull-off forces between SiO_x probe and gold probe with PMMA, 280f, 281f
 increase in contact zone near bulk glass transition temperature, 297, 300
 material for friction force microscopy (FFM), 286
 pull-off force versus temperature, 296f
 rate dependence of hindered rotation of -COOCH₃ group in PMMA, 301–302
 scanning force images of blend of 75/25 PMMA/PS at 27°C and 97°C, 223f, 224

scanning force images of blend of PMMA/PS at 25°C and 67°C, 222*f*
 temperature dependence of friction, 288, 293, 297
See also Block copolymers
 Poly(propylene) (PP)
 effect of addition of glass fibers on stick-slip and static coefficient of friction (COF), 426
 filled and unfilled samples, 420
 occurrence of stick slip, static COF, and COF drop for four surface textures, 421*t*, 422*t*
See also Automotive interior plastics
 Poly(propylene)/(ethylene-propylene) copolymer blends (PP/EP)
 atomic force microscopy (AFM) and force modulation microscopy (FMM) images of PP/EP resins, 314*f*
 characteristics of PP/EP resins, 307*t*
 comparison between surface Young's modulus from force modulation experiments and volume modulus using Hertz model, 310*f*
 comparison of Young's modulus from force-indentation curves using Hertz elastic and JKR (Johnson, Kendall & Roberts) model, 309*f*
 compression molding versus injection molding, 310–313
 effect of EP/PP viscosity ratio, 313–315
 elastic modulus and dynamic elastic response at different spots on surface of samples, 315*t*
 elastic response FMM images of surface of compression-molded and injection-molded blends, 311*f*
 elastic response measured on PP, EP, and PP/EP samples, 310*t*
 experimental AFM analyses, 308
 experimental dynamic mechanical analysis (DMA) measurements, 307
 experimental materials, 307
 experimental transmission electron microscopy (TEM) analyses, 308
 force-curves and force-modulation calibration, 308–310
 force-curves measurements, 305–306
 force-indentation curves for rigid and soft polymers, 309*f*
 force modulation, 306
 histograms of dynamic elastic response corresponding to FMM images, 312*f*
 modeling sample-tip-cantilever as mechanical system with springs and dash-pots, 306
 surface elastic modulus using Hertz mechanical model, 305
 TEM images parallel and perpendicular to injection direction, 313*f*

theoretical, 305–306
 variation of dynamic elastic response by local force modulation as function of bulk elastic modulus, 310*f*
 Poly(propylene) isotactic (i-PP)
 comparison of measured pull-off forces and calculated work of adhesion, 278*f*
 histograms of pull-off forces between SiO_x probe and i-PP, 277*f*
See also Surface nanochemical studies
 Polystyrene (PS)
 adhesion using pull-off force, 194–198
 adhesive properties, 213
 approach-retract curves, 140, 141*f*
 atypical response during retraction, 142*f*
 calculated surface energies from pull-off data, 196*t*
 calculated surface stiffness and tip penetration depths, 200*t*
 comparison of measured pull-off forces and calculated work of adhesion, 278, 278*f*
 comparison of Williams-Landel-Ferry (WLF) analysis to literature values for bulk PS, 237*t*
 deflection versus distance curves, 195*f*
 depth variation of elastic modulus, 185, 186*f*
 distribution of applicability of cantilevers with nominal stiffness, 181*t*
 film properties changing in vicinity of interactive substrate, 155
 force curve experiments, 134, 136*f*
 force measurements of polar polymers, 278–279
 frictional force versus temperature, 295*f*
 friction coefficient, 134, 135*f*
 height and friction images of spin-cast PS:PMMA (poly(methyl methacrylate)) polymer blend, 282*f*
 histograms of pull-off forces between SiO_x probe and gold probe with PS, 280*f*, 281*f*
 histograms of pull-off forces between SiO_x probe and PS, 277*f*
 increase in contact zone near bulk glass transition temperature, 300
 lever deflection versus sample displacement, 199*f*
 material for friction force microscopy (FFM), 286
 mechanical response with oscillating tip, 140
 modeling tip action, 145*f*
 nanoprotuberance with tip action, 144–147
 pull-off force versus maximum applied load during contact, 197*f*
 pull-off force versus temperature, 296*f*
 samples for adhesion and mechanical testing, 193

- samples for micromechanical analysis, 178
 sketch of PS nanoprotuberance growing during tip vibration, 145*f*
 temperature dependence of friction, 288, 293, 297
 variation of glass transition temperature with molecular weight, 137, 138*f*
 velocity dependence of friction, 285
See also Disentanglement in ultrathin polymer films; Micromechanical properties of polymers; Scanning probe microscopy (SPM); Temperature dependent surface properties of thin polystyrene films; Viscoelastic measurements in thin polystyrene melts
- Poly(tetrafluoroethylene) (PTFE)
 experimentally determined friction force versus relative scan angle, 332, 333*f*
 uniaxially oriented polymer fibers, 319–321
See also Molecular alignment and nanotribology of polymeric solids
- Poly(tetrafluoroethylene-co-hexafluoropropylene) (FEP)
 comparison of measured pull-off forces and calculated work of adhesion, 278*f*
 histograms of pull-off forces between SiO_x probe and FEP, 277*f*
See also Surface nanochemical studies
- Polyurethanes (PU)
 depth variation of elastic modulus, 185, 186*f*
 dissipation function of spontaneous peeling, 51
 distribution of applicability of cantilevers with nominal stiffness, 181*t*
 images of PU with nano-scratch at surface, 446, 448*f*
 mar resistance, 444, 446
 samples for micromechanical analysis, 178
 surface coating with ten mars and its cross-section profile, 444, 445*f*
 work of adhesion as function of peeling speed, 30, 32*f*
See also Micromechanical properties of polymers; Polymeric surface coatings
- Poly(vinyl acetate) (PVAc), velocity dependence of friction, 285
- Poly(vinyl alcohol) (PVOH), velocity dependence of friction, 285
- Poly(vinyl chloride) (PVC)
 depth variation of elastic modulus, 185, 186*f*
 distribution of applicability of cantilevers with nominal stiffness, 181*t*
 samples for micromechanical analysis, 178
See also Micromechanical properties of polymers
- Poly(vinyl chloride)/poly(butadiene) blend, force microscope and rigidity images as function of temperature, 120*f*
- Poly(vinyl ethylene), dynamic contact between silicon nitride tip and, 69–70
- Poly(vinylidene fluoride) (PVDF)
 comparison of measured pull-off forces and calculated work of adhesion, 278*f*
 histograms of pull-off forces between SiO_x probe and PVDF, 277*f*
See also Surface nanochemical studies
- Polyvinylpyridine (PVP)
 monolayers of cylindrical brushes of PVP on mica, 347, 349
 neutral brushes, 347
 polyelectrolyte brush, 347, 349
See also Sparse coatings
- Potentials
 Lennard–Jones, 92–93
 simple bead-spring, 92
- Powders/granules, tribological polymer contacts, 4*t*
- Pressure-velocity (PV) determination
 fundamental weaknesses, 387
 lack of standard test, 387–388
 PV limit for every plastic, 385
 typical PV limit diagram for general purpose bearing plastic, 386*f*
 wear factor or specific wear rate, 387
 wear life, 387
See also Wear tests for plastics
- Primary members, tribological contacts, 3, 4*t*
- Processing, tribological polymer contacts, 4*t*
- Profilometers, handling flats easier than curved surfaces, 397
- Pull-off force
 elastic solids, 25
 magnitude increasing with parameter A, 40
- Pulsed force mode (PFM)
 adhesive force images of
 polystyrene/poly(methyl methacrylate) (PS/PMMA) blends, 221–224
 performing adhesive force images, 216–217
 technique overcoming disadvantages of scanning force microscopy (SFM), 213–214

R

- Random reentry and loose loop fold model, high density polyethylene (HDPE) single crystals, 343, 344*f*
- Raster-scanned scanning force microscopy (SFM) tip. *See* Viscoelastic measurements in thin polystyrene melts

- Ratchet friction, scale of asperities approaching contact dimensions, 12
- Ratner–Lancaster correlation, sharp adhesives, 18
- Reciprocating sphere-on-plate tests, simulating reciprocating systems, 394, 396*f*
- Rheology
 correlation between interface and bulk, 13
 interface, Eyring-type relationships, 13
- Rolling cylinder
 asymmetrical profile of contact of long and rigid cylinder rolling under flat and smooth surface, 60, 61*f*
 contact load, 59
 dimensionless variables, 60
 half-width of contact area from Hertz theory, 58
 half-width of equilibrium contact area between rigid cylinder and smooth surface of elastic solid, 60, 61*f*
 kinetic of rolling, 60, 62–63
 magnitude of observed rolling parameters, 62–63
 normal tensile stress, 59
 normal tensile stresses at edge of contact area, 59
 relation linking load and tangential rolling force, 60
 rolling on and under inclined surface, 62–63
 static equilibrium, 58–60
 width of rolling contact area, 63
 width of rolling contact area versus rolling speed, 64*f*
- Rope systems
 tribological polymer contacts, 4*t*
 use of fabric conditioners, 3, 5
 variety of requirements, 3
- Rubber
 calculated surface energies from pull-off data, 196*t*
 deflection versus distance curves, 195*f*
 lever deflection versus sample displacement, 199*f*
 pull-off force versus maximum applied load during contact, 197*f*
- Rubber-like materials, viscoelastic losses, 48–49
- Rupture mechanics, adhesion, 47–48
- S**
- Sapphire single crystal
 calculated surface energies from pull-off data, 196*t*
 calculated surface stiffness and tip penetration depths, 200*t*
 deflection versus distance curves, 195*f*
 lever deflection versus sample displacement, 199*f*
 pull-off force versus maximum applied load during contact, 197*f*
- Scanning force microscopy (SFM)
 challenge of quantitative measurements, 177–178
 considerations in designing shear modulation experiments, 70–71
 correlation between elastic moduli from SFM and bulk values, 185, 187
 determining elastic properties of surfaces or thin films, 212–213
 developing data processing procedure, 181, 183
 effect of sample preparation and interaction strength on mechanical properties of polymer films, 154
 examining role of temperature in material response, 227–228
 force-distance curves for determining microscopic scale adhesive properties, 213
 mapping surface mechanical properties with submicron resolution, 177
 promising approach for studying organic and polymer surfaces with high spatial resolution, 282
- pulsed force mode (PFM) technique
 overcoming disadvantages of SFM, 213–214
 shear mechanical measurements, 155–156
 surface topology on molecular level, 337
 three-dimensional structure of individual molecules, 346–347
- See also* Disentanglement in ultrathin polymer films; Micromechanical properties of polymers; Nanometer-scale contacts to linear viscoelastic materials; Polyethylene (PE) single crystals; Surface nanochemical studies; Temperature dependent surface properties of thin polystyrene films; Viscoelastic measurements in thin polystyrene melts
- Scanning probe microscopy (SPM)
 achieving quantitative nanoindentation, 192–193
 adhesion and mechanics of polymer surfaces, 190
 adhesion using pull-off force, 194–198
 controlling tapping conditions, 192
 crosslinkable epoxy thermoplastic with grafted rubber concentrate (CET–GRC) preparation, 193–194
 determining surface shear and viscoelastic

- properties on submicrometer scale, 155
 experimental for tapping mode and phase images, 192
 experimental samples, 193
 mechanical properties based on lever deflection of soft cantilevers, 198–202
 mechanical properties using depth sensing nanoindentation, 202, 204
 obtaining force versus distance curves, 192
 photodefineable benzocyclobutene (photoBCB) sample, 194
 schematic of deflection versus distance curve, 191f
 thermal properties of photoBCB, 204, 207
See also Adhesion; Mechanical properties of polymers; Thermal properties
- Scanning thermal microscopy (SThM)
 experimental, 193
 imaging modes, 193
 thermal properties, 204, 207
See also Scanning probe microscopy (SPM)
- Schapery theory
 modeling loading/unloading adhesion experiment, 40
 rate dependence of adhesion for 3-parameter solid, 30, 32f
- Scratch behavior
 complete experiment, 431
 micro-scratch experimental instrument, 429, 430f, 431
 morphology parameters of scratches by AFM, 436f, 437t
 principle of scratch experiment, 429
 relationship between physical damage and appearance, 435
 results of typical micro-scratch experiment, 433f
 temperatures for thermoplastics, 15
 types of scratch damage, 432, 434
See also Automotive topcoats
- Secondary examples, tribological contacts, 3, 4t
- Self-consistent field (SCF) theory
 analytical model results, 377–380
 analytical SCF theory, 373–377
 numerical calculation basis, 370
 numerical model results, 370–373
 scheme for creating stable dispersions from immiscible polymers and clays, 369–370
See also Modeling interactions
- Self-lubrication
 bearings of polymers, 20
 nylon fabric systems, 6
 prospect of effective, 18–19
See Lubrication
- Self-seeding method
 preparation of high density polyethylene (HDPE) single crystals, 337
- See also* Polyethylene (PE) single crystals
- Shear
 method of imposing, 93–95
See also Oligomer films, thin
- Shear modulation
 advantage over normal, 67–68
 amplitude using Hertzian result and Hooke's law, 68–69
 schematic diagram of scanning force microscope (SFM), 68f
- Silanes
 coating coverage, 457–458
 coverage as function of coating time, 462f
 coverage versus processing conditions, 461
 deposition procedure, 457
 effect of silane coverage on micromachine operation, 469, 472
 friction of silane films measured by micromachined structures, 466, 469, 472
 lateral force image of silicon exposed to octadecyltrichlorosilane (ODTS) solution for 9 and 900 minutes, 471f
 static water contact angle as function of ODTS coverage on silicon, 463f
 surface preparation and solution deposition conditions, 458t
 water contact angle as function of coating time for ODTS films, 462f
 wear areas on posts from sidewall device tests having different silane coverage, 471f
See also Chemisorbed organic lubricants for microelectromechanical systems (MEMS)
- Silicon nitride
 calculated surface energies from pull-off data, 196t
 lever deflection versus sample displacement, 199f
 pull-off force versus maximum applied load during contact, 197f
- Silicone coatings
 adhesion energies, 87t
 adhesion strengths of acrylic adhesive to, 85
 contact angles of water, 85t
 direct measurement of surface energetics by contact mechanics, 86–87
 interfacial shear stress of acrylic adhesive as function of shear velocity, 89f
 release profiles, 84–86
 slippage patterns at adhesive-polymer interface, 88f
See also Poly(dimethylsiloxane) (PDMS)
- Single crystals. *See* Polyethylene (PE) single crystals
- Single pass abrasion, debris accumulation, 18
- Slideways, tribological polymer contacts, 4t
- Sliding or lubrication regime, lateral disentanglement strength, 160

- Slurry abrasion response test
 slurry erosion, 399, 400f
 slurry erosion resistance of ultrahigh molecular weight polyethylene versus various metals, 401f
- Sneddon's approach, elastic modulus, 183, 184f
- Sparse coatings
 adsorption of polyelectrolyte cylindrical brushes on charged substrate, 354
 concentration dependence of surface coverage, 352f
 conformation and alignment of single molecules on mica, 349, 351
 experimental for in situ monitoring process, 349
 in situ monitoring of adsorption process, 349–351
 in situ observation of poly(2-vinyl-*N*-benzylpyridinium bromide) brushes by magnetic alternative current (MAC) mode SFM, 350f
 monolayers of cylindrical brushes of poly(2-vinylpyridine) (PVP) on mica, 347, 349
 neutral brushes, 347
 polyelectrolyte brush, 347, 349
 schematic of MAC mode SFM with liquid cell, 350f
 sequence of images of polyelectrolyte brushes before, during, and after adding NaCl, 352f
 SFM image of charged PVP brushes on mica, 348f
 SFM micrograph of adsorbed uncharged PVP brushes on mica, 348f
 SFM micrographs of adsorbed poly(2-vinyl-*N*-pyridinium bromide) brushes on mica, 353f
 surface coverage as function of concentration and ionic strength, 351
 types of individual molecular particles where particles are disordered or demonstrate positional ordering, 348f
- Spin-coating induced strain
 flow and sliding properties from structural model, 164
 structural model, 163–164
 ultrathin polymer films, 163, 165f
- Spontaneous peeling
 application of Hooke's law, 51
 dissipation function, 51
 experiments and results, 51, 53
 force variation, 51
 geometry of adhesive joint before and after substrate extension, 50f
 model, 49, 51
 peeling angle, 51, 53
 predicting evolution of system, 53
 range of delamination domain as function of relative transversal stiffness of peeling strip, 52f
 strain energy release rate, 49
- Sterilization
 common methods, 488–489
 medical devices, 476
- Stick-slip motion
 approaches minimizing noises by, 418–419
 elastomeric nature of syringe stopper, 487
 experiment, 249, 253f, 254
 image of polymeric surface after stick-slip experiment, 254, 255f
 mixed and boundary lubrication regime, 475
 physics of friction, 481, 483
 possible effects of microdisplacements on occurrence, 424
 relationship between syringe friction and physics of friction, 486f
 solid-melt transition causing, 483
 surface roughness influencing occurrence, 419–420
 syringe operation, 487–488
 testing apparatus, 420–421
 thin oligomer films, 104–106
See also Automotive interior plastics
- Stiction effect
 adhesion between polycrystalline silicon members or substrate, 455
 friction changes from static to sliding state, 240, 241f
- Strain, spin-coating induced, 163, 165f
- Strain-hardening
 dynamic process study, 442
 studying in polymeric coatings, 449
- Styrene-butadiene sample
 relaxation modulus by differentiation, 244, 247f
See also Friction regimes
- Styrene-isoprene sample
 variations of storage and loss moduli with frequency from analysis of material response to periodic modulation, 244, 248f, 249
See also Friction regimes
- Surface coatings. *See* Polymeric surface coatings
- Surface fatigue
 dynamic process study, 442
 studying in polymeric coatings, 449
- Surface force apparatus (SFA)
 channeling in simulations possibly explaining memory effects, 110, 112
 measuring surface energy and viscoelastic properties, 24
 oligomers between parallel surfaces, 91
 viscoelastic films, 36, 38
See also Oligomer films, thin

Surface nanochemical studies

comparison of measured pull-off forces and calculated work of adhesion for interactions between SiO_x probe and polystyrene (PS), isotactic polypropylene (i-PP), poly(vinylidene fluoride) (PVDF), and poly(tetrafluoroethylene-co-hexafluoropropylene) (FEP) surfaces, 278*f*
distinguishing between polymers in blend, 279

electrostatic forces of AFM tip, 274

electrostatic forces of organic surfaces, 274–276

experimental, 273–274

experimental films of PS, i-PP, PVDF, and FEP, 273–274

force-distance measurements and lateral-force imaging, 273

force measurements of polar polymers, 278–279

force measurements on non-polar polymers, 276–277

height and friction-force images for sample by microcontact printing with hexadecanethiol, 275*f*

height and friction images of spin-cast PS:PMMA (poly(methyl methacrylate)) polymer blend, 282*f*

histograms of pull-off forces between SiO_x probe and gold probe with PS, poly(acrylonitrile) (PAN), PMMA, and poly(acrylic acid) (PAA) surfaces in perfluorodecalin, 280*f*, 281*f*

histograms of pull-off forces between SiO_x probe and PS, i-PP, PVDF, and FEP surfaces in perfluorodecalin, 277*f*

hydrogen bonding and other effects, 278–279
lateral force images of monolayer of alkanethiols with differently functionalized endgroups, 275*f*

nanochemical imaging of polymers and organic films, 279

tip-surface interactions, 274–276

van der Waals forces, 276

Surface strain. *See* Disentanglement in ultrathin polymer films

Surface textures

common in automotive interiors, 420

occurrence of stick slip, static coefficient of friction (COF), and COF drop for various polymers, 421*t*, 422*t*

roughness values, 423

See also Automotive interior plastics

Sustaining force, relationship between syringe friction and physics of friction, 486*t*

Switchboard model, high density ethylene (HDPE) single crystals, 343, 344*f*

Syringes

manual operation, 484, 486

pump operation, 487–488

See also Medical devices

Systems approach

Godet, Maurice, 6

introduction of contact mechanical work, 6, 8
scheme of units of tribological system, 7*f*

T

Tabor Abrasor, test rating abrasion resistance of plastics, 388–389

Tape abrasion test, web abrasivity, 397, 398*f*

Tapping mode

cantilever system, 133

dynamic force microscopy, 124–125

Tapping mode atomic force microscopy (TMAFM)

experimental, 192

phase detection imaging (PDI), 358

resonant imaging mode, 202

studying microphase separation in thin films, 356

TMAFM height and phase images of crosslinkable epoxy thermoplastic with grafted rubber concentrate (CET–GRC) after cryo-polishing, 203*f*

See also Block copolymers; Mechanical properties of polymers

Temperature dependent surface properties of thin polystyrene films

adhesion forces from force curve analysis, 219, 220*t*

adhesive force images, 221–224

adhesive force images by pulsed force mode (PFM), 216–217

calibration, 217

experimental, 214–217

force versus distance curves, 217–221

force versus distance curves of polystyrene (PS) films with various molecular weights at 27°C and 67°C, 218*f*

heating device, 215–216

measurements by scanning force microscopy (SFM), 216–217

mechanical data from force curve analysis, 219*t*

properties and preparation of samples, 214–215

scanning force images of blend of poly(methyl methacrylate) (PMMA) and PS at 25°C and 67°C, 222*f*

scanning force images of 75/25 PMMA/PS at 27°C and 97°C, 223*f*, 224

- temperature induced changes in adhesive force of bare silicon substrate, 217f
- variations of adhesive force of thin PS films during heating to 67°C, 220f, 221
- Tests. *See* Wear tests for plastics
- Thermal properties
- photodefineable benzocyclobutene (photoBCB) preparation, 194
- scanning thermal microscopy (SThM), 204, 207
- SThM images of 35 μm via holes in photoBCB thin film before "de-scum" plasma treatment, 207, 209f
- tapping mode AFM image of 35 μm via holes in photoBCB thin film before and after "de-scum" plasma treatment, 207, 208f
- Thermoplastic elastomers (TPEs)
- need to improve processability and thermoresistance to degradation, 357
- See also* Block copolymers
- Thermosetting resins, not tending to transfer material, 15
- Thin films. *See* Disentanglement in ultrathin polymer films; Oligomer films, thin; Temperature dependent surface properties of thin polystyrene films
- Third body
- interface zone, 8
- possible origins of static friction, 113
- producing self-lubricating interfacial medium, 8
- Thrust washer test, measuring wear volume, 391, 392f
- Time-of-flight secondary ion mass spectroscopy (SIMS)
- method for determining silane amount of surface, 457–458
- See also* Chemisorbed organic lubricants for microelectromechanical systems (MEMS)
- Ting model
- characterizing response of contacts during loading and unloading, 80
- general solution to Hertz contact problem, 71–72
- incorporating adhesion effects into model, 79
- major features of Ting solution, 73, 75f, 76
- Tip-cantilever (CL) system
- tapping experiments, 133
- use of oscillating behavior, 124–125
- Tip characterization
- atomic force microscopy (AFM), 126, 130
- oscillating tip, 139–147
- See also* Physics and physical chemistry at nanotip scale
- Topcoats
- chemistry, 268
- mar resistance, 258–259
- Traction drives, tribological polymer contacts, 4f
- Transcrystallized polymer crystals, poly(ethylene oxide) (PEO), 326, 331f
- Triblock copolymers. *See* Block copolymers
- Tribology
- common contacts, 3, 4f
- damage modes, 13–16
- differing practical needs in various areas, 20
- divisions, 2–3
- experimental robustness, 149, 151
- friction processes, 9–13
- generic peculiarity of organic polymer systems, 3
- lubrication and environmental sensitivity, 18–20
- primary members, 3, 4f
- scheme of various units, 7f
- secondary examples, 3, 4f
- simplification, 9–18
- systems approach, 6–9
- technical points of experiments, 133
- test structure for measuring friction, 459, 460f
- types of polymer contacts, 4f
- wear modes, 16–18
- See also* Microtribology
- U
- Ultrathin polymer films, glass transition effects with thickness, 227
- Uniaxially oriented polymer fibers
- friction force versus normal force plot for HDPE (high density polyethylene) for different relative scan directions with Si_3N_4 tip in air, 324f
- friction force versus normal force plot for HDPE using modified tips in air, 324f
- friction versus relative scan angle for oriented poly(tetrafluoroethylene) (PTFE) with Si_3N_4 tip in ethanol and air, 322f
- lateral force microscopy (LFM) image of PTFE with molecular resolution, 320f
- LFM image of HDPE with $-\text{CF}_3$ tip in air, 323f
- typical scanning force microscopy (SFM) image of morphology of oriented PTFE, 320f
- See also* Molecular alignment and nanotribology of polymeric solids
- Unit processes
- definition, 8
- friction dissipating contact mechanical work, 8
- Unsteady motion, thin oligomer films, 101, 104–106

V

- van der Waals forces, tip-surface interactions, 276
- Velocimetry. *See* Acrylic adhesive
- Viscoelastic adhesion cycle
 attempting to model adhesion test, 34, 36
 computations using creep compliance function, 36
 dimensionless pull-off force as function of rate parameter A , 37*f*
 simulation of ramp loading cycle of viscoelastic spheres in contact, 37*f*
- Viscoelastic contact mechanics
 computations for 3-parameter solid, 30
 correspondence principle, 29
 variation in contact radius through cycle, 31*f*
- Viscoelastic creep
 dynamic process study, 442
 studying in polymeric coatings, 446, 449
- Viscoelastic films
 effect of layer thickness on apparent surface energy of opening interface crack, 38, 39*f*
 effective work of adhesion, 36, 38
 interface crack between viscoelastic layers, 39*f*
- Viscoelastic fracture mechanics
 analogy between kinetics of adhering interface and moving crack in viscoelastic solid, 30, 32*f*
 apparent surface energy of moving viscoelastic crack, 34, 35*f*
 apparent work of adhesion, 33–34
 closing force, 33
 effective work of adhesion, G , 30
 master curve of G as function of peeling speed for polyurethane rubber, 30, 32*f*
 opening force, 30, 33
- Viscoelastic losses
 dimensionless function of crack speed and temperature, 48
 dissipation function versus crack speed, 50*f*
 elastomers, 49
 predicting evolution of contact area, 48–49
 rubber-like materials, 48
- Viscoelastic materials. *See* Friction regimes
- Viscoelastic measurements in thin polystyrene melts
 comparison of Williams–Landel–Ferry (WLF) analysis to literature values for bulk polystyrene, 237*t*
 critical free volume, 237
 deriving mathematical description of bundle orientation, 230, 232
 description of scan-induced patterning, 228–230
 10 μm images at different temperatures and fast-scan frequencies, 235*f*
 10 μm images quantification by measuring slope of scan-induced bundles at left and right edges of scan area, 236*f*
 interpretation of empirical shift factors, 234, 237
 methodology, 228
 molecular interpretation, 232, 234
 schematic of tip trajectory for 128, 256, and 512 fast-scan cycles per image, 231*f*
 SFM topographic image scanning from top-to-bottom and bottom-to-top, 229*f*
 slope of bundle with respect to fast-scan axis, 230
 studying viscoelastic response, 234, 237
 topography and friction images, 229*f*
 tracing three bundles on each side of image and plotting on common curve, 233*f*
 varying raster geometry, 230–234
 WLF equation, 234
- Viscoelastic solids. *See* Adherence of elastic/viscoelastic solids
- Viscoelastic spheres
 elastic solid theories, 25–27
 exposing effects of viscoelasticity, 38
 extracting solid surface properties, 38
 film thickness influencing apparent surface energy, 40–41
 fundamental restriction in theory, 38, 40
 JKR (Johnson, Kendall & Roberts) equation, 41
 key to analyzing adhesion of viscoelastic solids, 40
 linear viscoelastic solids, 27–29
 magnitude of pull-off force increasing with parameter A , 40
 Maugis–Dugdale and JKR theories, 25–27
 modeling loading/unloading adhesion experiments, 40
 need for mechanics model for adhesion, 25
 viscoelastic adhesion cycle, 34, 36
 viscoelastic contact mechanics, 29–30
 viscoelastic films, 36, 38
 viscoelastic fracture mechanics, 30, 33–34
- Viscosity
 power law over three decades in shear rate, 112
 universal curve of simulation results for, 100–101, 102*f*
See also Oligomer films, thin
- Viscous plug flow regime, lateral disentanglement strength, 160
- Voigt/Kelvin model
 effects of adhesion, 79, 80*f*
 solutions to Ting model for contact of rigid probe with viscoelastic substrate, 73, 75*f*, 76
 spring and dashpot in parallel, 73

time of maximum contact radius as function of contact, 76*f*

W

Water droplet erosion test, 397, 398*f*, 399

Wear

clearance, 16

debris detachment and fatigue, 16

definition, 16

modes, 16–18

predicting rate, 16, 18

processes, 17*f*

type of tribological system, 2

See also Micro- and nano-wear of polymeric materials

Wear tests for plastics

abrasion of plastics by other surfaces, 388–391

abrasive tape test, 389

adhesion of plastic to metal and reverse, 391, 394

ball-on-plane test, 395, 396*f*, 397

block-on-disk test, 394

block-on-ring test, 391, 393*f*

bushing test, 391, 393*f*

cavitation erosion tests, 399

dry sand rubber wheel test (ASTM G 65), 389, 390*f*

erosion tests, 397, 399

lack of standard pressure-velocity (PV) test, 387–388

no agreed-to tests rating abrasion and erosion resistance, 385

pin abrasion test (ASTM G 141), 389, 390*f*

pin-on-disk test, 394

plastic wear tests for simulating sliding

contact with rigid surfaces, 392*t*

plastic wear tests for various applications, 402*t*

profilometers, 397

PV determination, 385–388

reciprocating sphere-on-plate tests, 394, 396*f*

slurry abrasion response test (ASTM G 75), 399, 400*f*

slurry erosion resistance of ultrahigh molecular weight polyethylene versus various metals, 401*f*

solid particle erosion rate, 399, 400*f*

Taber Abrasor, 388–389

tape adhesion test, 397, 398*f*

testing not well defined, 384

thrust washer test (ASTM D 3702), 391, 392*f*
typical PV limit diagram for general purpose bearing plastic, 386*f*

water droplet erosion test (ASTM G 73), 397, 398*f*, 399

wear of conforming surfaces by plastics, 391–395

web abrasivity tests, 395, 397

Web abrasivity tests

ball-on-plane test, 395, 396*f*, 397

profilometers, 397

tape abrasion test, 397, 398*f*

Wetting-autophobicity

interfacial energy of graft copolymers and effect on, 167–168

testing graft copolymers, 156–157

White goods

improving interaction between polymers and environment, 5

tribological polymer contacts, 4*t*

Williams–Landel–Ferry (WLF) equation, interpretation of empirical shift factors, 234, 237

Y

Yield

transient behavior, 106–112

See also Oligomer films, thin

Young's modulus

comparison of values from force-indentation curves using Hertz elastic and JKR

(Johnson, Kendall & Roberts) model, 309*f*

tangential traction for sphere-plane contact by Hertz theory and Amontons' law of friction, 158, 160